Stirring Up the Gas: Star Formation and Powering High Pressures in Galaxies 10 Billion Years Ago

Loic Le Tiran

Stirring Up the Gas: Star Formation and Powering High Pressures in Galaxies 10 Billion Years Ago

Thèse de Doctorat

présentée pour l'obtention du grade de

Docteur de l'Observatoire de Paris

défendue le 23 septembre 2011

par Loïc Le Tiran

President :	Didier Pelat
Rapporteurs :	Jean-Paul Kneib
	Bodo Ziegler
Examinateurs :	Philippe Amram
	Hervé Dole
Directeur :	Matthew D. Lehnert

Stirring Up the Gas: Star Formation and Powering High Pressures in Galaxies 10 Billion Years Ago

Abstract

The range of phenomenologies exhibited by galaxies was apparently larger in the distant Universe than it is today. The global star-formation rate was higher by an order of magnitude, and so were the specific star-formation rates. Morphologies were much more irregular, something that cannot be explained through extinction alone. Processes like starburst-driven outflows are obvious and ubiquitous in high redshift galaxies compared to their rareness today, and the AGN fraction appears high even in optically selected distant samples. The merger rate was also likely to be much higher. While the gas infall rates of nearby galaxies are apparently low, they were likely much higher in the early Universe. While today the Universe could be considered in the "Age of secular evolution", more than about 8 Gyrs ago the Universe was in the "Age of feedback and self-regulation".

Integral-field unit (IFU) spectroscopy has led to to improve the understanding of the physical conditions in galaxies within the first few billion years after the Big Bang. In this thesis, we analyze the properties of rest-frame optical emission lines such as Hα and [NII] λ6583 of a sample of more than fifty galaxies observed with the SINFONI IFU spectrograph on the ESO-VLT. These data were taken as part of our own or other programs and the galaxies span the redshift range z=1.3 to 2.7. Integration times per object are a few hours and the spectra reach a depth of about 4-40 $\times$ 10^{-18} erg s^{-1} cm^{-2} arcsec^{-2}. The point-spread function FWHM is $\sim$0$''$.6, which at z=2 represents an area of $\sim$20 kpc^2, meaning that we generally have $\sim$8 independent spatial resolution elements per object. Their mean isophotal radius is $\sim$7 kpc (corresponding to an isophotal area of $\sim$150 kpc^2). Their total Hα luminosities all exceed 10^{41} erg s^{-1}, but are mostly above about 10^{42} erg s^{-1}. Such Hα luminosities imply an average star-formation rate of $\sim$70 M$_\odot$ yr^{-1}. As these are not corrected for extinction our estimates are lower limits. However, the line ratios of Hα to Hβ in those objects where the latter line was observed suggest relatively modest extinction corrections, of a factor of few.

We analyzed the spatially resolved properties of the galaxies, concentrating on determining the sources of their large emission line widths and the underlying cause of their line ratios. We show that photo-ionization calculations and emission line diagnostics imply gas pressures and densities that are similar to the most intense nearby star-forming regions but over much larger scales (10-20 kpc). We find that the line velocity dispersions are much larger than in nearby disk galaxies (tens to several hundreds of km s^{-1} vs $\sim$10 km s^{-1}) and likely driven by the intense star formation taking place within these galaxies. We reach this conclusion by comparing our data with those of simulations, adopting a scaling relation of the

form $\sigma \propto \sqrt{\Sigma_{SFR}}$ (i.e., the velocity dispersion is proportional to the square root of the star-formation rate per unit surface area). We find good agreement between the observations and beam-smeared models when using this underlying relationship. Furthermore, we show that this conclusion is in general largely driven by a selection effect whereby galaxies must have a high enough average Hα surface brightness to be detectable and spatially resolved with SINFONI in a few hours exposure time, which requires the galaxies to have sufficiently intense star formation, which in turn drives the large line widths. However, for galaxies at z<2 the surface brightness requirement is relaxed to the extent that we may be observing galaxies where the star-formation intensity may not be the predominant driver of the line dispersions. Finally, we argue that one advantage of having such a biased sample is to show us that the stars are injecting sufficient energy to force the Toomre Q instability parameter to be approximately 1 by generating high dispersions, thus allowing intense star formation for the generally high mass surface densities observed in (a portion of) this sample. We suggest this is strong evidence for self-regulation in star formation and that it may explain the mass surface densities observed in nearby massive galaxies.

In addition to analyzing spatially resolved properties, we have made a stacking analysis of integrated spectra of approximately 50 of our galaxies which fall in two redshifts bins, z≈1.4 and z≈2.2. Our goal is to significantly increase the signal-to-noise ratio of spectra of various subsamples in order to investigate in detail the average shapes of emission line profiles and to enable an analysis of weaker lines undetectable in individual cases, such as [SII]$\lambda\lambda$6716,6731 and [OI]λ6300. Galaxy spectra were combined as function of their average Hα surface brightness. In addition to stacking the integrated spectra of galaxies, we also stacked spectra of only the brightest regions in emission in each galaxy.

The line ratios are consistent with the gas being photoionized by massive stars. We find that the presence, full width at half maximum and flux of a broad line component underlying the region around Hα depend on the average surface brightness of the galaxies in each stack. The broad component can be most easily explained as due to outflowing material in the most intense starbursts and can be fitted with a simple model that has a negative offset velocity relative to the narrower Hα line and where the [NII]/Hα ratio is determined from fast shock models. If we assume that the mechanical energy output from stars is efficiently thermalized, we only require of-order 1-10% of the mechanical energy to energize the broad line emission. The [SII]$\lambda\lambda$6716,6731 and [SII]$\lambda\lambda$6716,6731/Hα ratios are consistent with an ISM that is highly over-pressurized compared with nearby galaxies but similar to that observed in the nuclei of intense, local starbursts. Considering the continuity between these stacks and the data for nearby star-forming galaxies in the [SII]$\lambda\lambda$6716,6731 versus Hα surface brightness plane, our data are consistent with dense clouds that are likely compressed by shocks and in which post-shock material is photoionized

by the on-going intense star formation.

We also discuss the possibility that the high surface brightnesses observed are not due to star formation, but rather to cosmological gas accretion. If we assume that all of the accretion energy is dissipated as shocks from the accreting gas we show that in order to explain the high surface brightnesses of these galaxies, both the mass accretion rate and energy would have to be much higher than expected from simulations or from equating the star formation with the accretion rate. We investigate scaling relations between the surface brightness expected for accretion and for star formation through mechanical heating and photo-ionization, and try to identify a regime where such accretion may become evident in optical rest-frame observations of galaxies. Unfortunately, the surface brightness detection limit required for this is about an order of magnitude lower than what has currently been achieved with near-infrared observations of distant galaxies.

Finally, we combine the analysis of SINFONI data of a sub-sample of 10 galaxies at z∼1.4 with data obtained from the DEEP2 Survey. Their ratios of $F_{\mathrm{H}\alpha}/f_{\mathrm{FUV}}$ to Hα and *R*-band luminosity surface brightness indicate that perhaps their initial mass function is flatter than Salpeter at the high mass end, as has also been suggested recently for some local galaxies. It may be that high turbulence is responsible for skewing the IMF towards more massive stars, as has been suggested by some theories of star formation. We suggest that the IMF is not universal through cosmological times or environments. Much work is needed however to substantiate this hypothesis as it could be that this effect is due to bursty star-formation (although this hypothesis is found wanting too).

The main conclusions of this thesis are that the selection of galaxies at z>2 useable for IFU studies based on spatially resolved data, necessarily implies they must have high Hα surface brightnesses. Because of the strong effect of cosmological surface brightness dimming, these Hα surface brightnesses have to be similar to what is observed in nearby starbursts, but over much larger – 10s of kpc instead of kpc – scales in order to be spatially resolved. This selection effect alone means that it is difficult to observe the underlying effects of gravity or accretion because of the intensity and the strong feedback of star-formation. Nevertheless, our sample does allow us to investigate the impact of star-formation on the ISM in distant galaxies. We find evidence that star-formation is self-regulated in these galaxies and that this self-regulation has consequences for our observations at high redshift as well as for what these galaxies will evolve into.

Le Rôle de la Formation Stellaire dans les Galaxies il y a 10 milliards d'années : Agitation du Gaz et Mise sous Pression du Milieu Interstellaire

Résumé

L'univers lointain présente une gamme de phénoménologies bien plus large que ce que l'on observe dans l'univers local. Le taux de formation stellaire était plus élevé d'au moins un ordre de grandeur, de même que le taux spécifique de formation stellaire. Les galaxies étaient morphologiquement bien plus irrégulières, ce qui ne peut pas être expliqué uniquement par l'effet de l'extinction. Des processus tels que les vents galactiques, produits par des flambées d'étoiles, sont manifestes et omniprésents dans les galaxies à décalage vers le rouge élevé, ce qui n'est plus le cas dans l'univers local. La fraction de noyaux actifs dans l'univers lointain semble élevée si on la compare à l'univers local, et le taux de fusions galactiques est susceptible d'être beaucoup plus élevé que dans l'univers local. C'est aussi le cas des taux d'accrétion de gaz : si ceux-ci sont faibles dans l'univers local, il est probable qu'ils aient été bien plus importants par le passé. Si l'Univers semble être aujourd'hui dans une phase d'évolution séculaire, il était, il y a plus de 8 milliards d'années dans une phase de rétroaction et d'auto-régulation.

L'utilisation de la spectroscopie à intégrale de champ a permis d'améliorer significativement notre compréhension des phénomènes physiques à l'œuvre dans les galaxies durant les premiers milliards d'années qui ont suivi le Big-Bang. Dans cette thèse sont analysées les propriétés en émission visible, notamment les raies d'émission Hα et [NII], d'un échantillon comprenant plus de cinquante galaxies observées avec le spectromètre à intégrale de champ SINFONI installé au VLT. Ces données sont issues en partie de nos propres observations mais aussi d'autres programmes, et couvrent la gamme de décalages vers le rouge allant de 1,3 à 2,7. Les durées d'intégration sont de l'ordre de quelques heures, ce qui permet d'atteindre environ 4 à 40 $\times$ 10^{-18} erg s^{-1} cm^{-2} arcsec^{-2}. La fonction d'étalement du point est typiquement de l'ordre de 0,6 arcsecondes, ce qui correspond à une région d'environ 20 kpc^2 pour un objet avec un décalage vers le rouge de l'ordre de 2. Les observations indiquent un rayon isophote d'environ 7 kpc, soit une aire de l'ordre de 150 kpc^2 : les observations faites avec SINFONI de ces objets présentent donc environ 8 éléments de résolution indépendants. Leur luminosité en Hα est supérieure à 10^{41} erg s^{-1}, et dépasse généralement 10^{42} erg s^{-1}. De telles luminosités en Hα impliquent des taux de formation stellaire de l'ordre de 70 M$_\odot$ yr^{-1} en moyenne. Ces valeurs n'étant pas corrigées de l'effet de l'extinction, elles ne sont qu'une limite inférieure. Le rapport des raies d'émission Hα sur Hβ, pour les objets pour lesquels Hβ a aussi été observé, suggère une extinction relativement faible, de l'ordre de quelques unités.

Dans cette thèse, nous analysons les propriétés optiques spatialement résolues de galaxies à haut décalage vers le rouge afin de déterminer les causes sous-jacentes de la largeur particulièrement importante de leurs raies d'émission, ainsi que les rapports des différentes raies d'émission. Grâce à des calculs de photo-ionisation et au diagnostic des raies d'émission, nous sommes en mesure de montrer que la pression et la densité du gaz sont similaires à celles que l'on trouve dans les régions de l'univers proche pour lesquelles la formation stellaire est très intense, mais sur des régions bien plus larges (10 à 20 kpc). Nous montrons que les raies associées au gaz ionisé sont bien plus larges dans l'univers lointain que dans l'univers local (de plusieurs dizaines à plus d'une centaine de km s^{-1} contre environ 10 km s^{-1} dans l'univers local), mais aussi que ces larges dispersions de vitesse sont probablement dues à la formation stellaire intense qui a lieu dans ces galaxies. Nous parvenons à cette conclusion après comparaison de nos données avec celles issues de simulations adoptant une loi d'échelle de la forme $\sigma \propto \sqrt{\Sigma_{SFR}}$ (la dispersion de vitesse est proportionelle au carré du taux de formation stellaire par unité de surface). Nous obtenons un bon accord entre les observations et nos modèles prenant en compte l'effet dû à la largeur de la fonction d'étalement du point des observations SINFONI, lorsque l'on utilise la relation précédente. Nous montrons aussi que cette conclusion est entrainée par un effet de sélection : les galaxies doivent avoir une brillance de surface en Hα suffisament importante pour pouvoir être détectées et résolues spatialement avec SINFONI en quelques heures d'intégration. Ceci nécessite un taux de formation stellaire particulièrement intense, et entraine à son tour des largeurs de raies conséquentes. Cependant, pour les galaxies ayant un décalage vers le rouge inférieur à 2, ce biais de sélection en brillance de surface est moins important, ce qui permet d'observer des galaxies pour lesquelles l'intensité de la formation stellaire n'est plus le paramètre principal déterminant la largeur des raies d'émission. L'un des avantages d'un échantillon présentant un tel biais de sélection est qu'il permet de montrer que les étoiles peuvent injecter suffisament d'énergie dans le milieu interstellaire pour contraindre le paramètre d'instabilité de Toomre Q à prendre approximativement la valeur 1 : les étoiles massives génèrent des dispersions de vitesses élevées, permettant ainsi d'obtenir les taux de formation stellaire observés dans (une partie de) cet échantillon ayant des densités de masse surfacique généralement élevées. Nous suggérons que ce processus est une preuve solide de l'existence d'un mécanisme d'auto-régulation de la formation stellaire qui peut expliquer les densités de masse surfaciques observées dans les galaxies massives de l'univers proche.

Indépendamment de l'analyse des propriétés spatialement résolues des galaxies de l'univers lointain, nous avons réalisé une analyse "en piles" des spectres intégrés d'environ 50 galaxies centrées autour de z≈1,4 et de z≈2,2. Le but de cette analyse est d'augmenter significativement le rapport signal sur bruit des spectres de différents sous-échantillons afin d'examiner en détail le profil moyen

des raies d'émission, permettant ainsi l'étude de raies plus faibles, la plupart du temps indétectables lors d'observations individuelles, telles que [SII]$\lambda\lambda$6716,6731 et [OI]λ6300. Les spectres galactiques ont été combinés selon leur brillance de surface en Hα. Outre l'analyse "en piles" de spectres intégrés de galaxies, nous avons réalisé une analyse similaire pour les régions les plus brillantes de ces galaxies.

Les rapports de raies sont compatibles avec un processus de photo-ionisation du gaz par les étoiles massives. La présence sous les raies d'émission d'une composante spectrale large, ainsi que sa largeur à mi-hauteur et son flux, dépendent de la brillance de surface moyenne des galaxies dans chaque pile. La composante large peut être facilement expliquée comme étant due à l'éjection de matière dans les flambées d'étoiles les plus intenses, et peut être ajustée par un modèle simple dans lequel la composante large est décalée d'une vitesse négative par rapport à l'émission principale, et dans lequel le rapport [NII]/Hα est déterminé à partir de modèles de chocs en grande vitesse. En supposant que l'énergie mécanique éjectée par les étoiles est efficacement thermalisée, seuls 1 à 10% de cette énergie est nécessaire pour produire de telles raies d'émissions larges. Les rapports [SII]$\lambda\lambda$6716,6731 et [SII]$\lambda\lambda$6716,6731/Hα sont cohérents avec un milieu interstellaire largement sur-pressurisé par rapport aux galaxies locales, mais comparable à ce qui est observé dans les noyaux d'intenses flambées stellaires de l'univers local. La relation entre [SII]$\lambda\lambda$6716,6731 et la brillance de surface de Hα présente une continuité entre les données issues de l'analyse "en piles" des galaxies à fort décalage spectral et les données concernant les galaxies à fort taux de formation stellaire de l'univers proche. Cette continuité est compatible avec un modèle de nuages denses vraisemblablement compressés par des chocs et dans lesquels les éléments post-chocs sont photo-ionisés sous l'effet de la formation stellaire intense.

Afin de compléter cette étude, nous examinons le rôle de l'accrétion cosmologique de gaz dans la génération des brillances de surface élevées qui sont observées et que nous avons précédemment interprété comme un effet de l'intense formation stellaire. En supposant que la totalité de l'énergie d'accrétion se dissipe sous forme de chocs, le taux d'accrétion en masse de gaz, ainsi que l'énergie apportée nécessaire pour générer des brillances de surface élevées doivent être bien plus grands que ceux attendus par les simulations ou en supposant que le taux d'accrétion de gaz est égal au taux de formation stellaire. Nous étudions les lois d'échelle entre la brillance de surface attendue par accrétion ou par formation stellaire par le biais du chauffage par injection d'énergie mécanique et par photo-ionisation, et tentons d'identifier un régime dans lequel le rôle de l'accrétion pourrait apparaître dans l'observation de leur émission dans le domaine visible. Malencontreusement, la limite de brillance de surface nécessaire pour détecter l'effet de l'accrétion est d'environ un ordre de grandeur plus faible que ce qu'il est possible d'atteindre en utilisant les moyens actuels d'observations de galaxies distantes dans le proche infrarouge.

En perspective, nous combinons l'analyse de données SINFONI pour un sous-ensemble de 10 galaxies ayant un décalage vers le rouge proche de 1,4 avec des données obtenues par le relevé DEEP2. Le rapport $F_{\mathrm{H}\alpha}/f_{\mathrm{FUV}}$ en fonction de la brillance de surface de Hα ou de la bande *R* indique qu'il est possible que leur fonction de masse initiale soit plus aplatie que celle de Salpeter pour les plus grandes masses, comme cela a été suggéré récemment pour certaines galaxies proches. Il est possible que le niveau élevé de turbulence soit responsable de cette déviation de la fonction de masse initiale pour les plus hautes masses, ce qui a été précédemment proposé par certaines théories de formation stellaire. Nous suggérons que la fonction de masse initiale n'est pas universelle sur l'ensemble des temps cosmologiques et des environnements de formation stellaire. Une étude plus poussée est cependant nécessaire pour confirmer cette hypothèse et exclure certains effets tels que les pics de formation stellaire.

En conclusion, les biais de sélection pour l'observation de galaxies ayant un décalage vers le rouge de l'ordre de 2 par spectroscopie à intégrale de champ implique nécessairement que ces objets aient une brillance de surface en Hα élevée. L'effet considérable de l'atténuation cosmologique de la brillance de surface implique que pour être observés, ces objets doivent avoir une brillance de surface en Hα similaire à celle observé dans les galaxies à flambées d'étoiles de l'univers local, mais sur des régions beaucoup plus larges, de l'ordre de la dizaine de kiloparsec alors que celles-ci sont de l'ordre du kiloparsec dans l'univers proche. Ce biais de sélection rend difficile l'observation de processus sous-jacents tels des effets gravitationnels ou d'accrétion de gaz, secondaires si on les compare aux effets rétroactifs de l'intense formation stellaire. Notre échantillon nous permet néanmoins d'examiner l'impact de la formation stellaire sur le milieu interstellaire des galaxies distantes. Nous mettons en évidence le rôle auto-régulateur de la formation stellaire dans ces galaxies et ses conséquences pour leur observation ainsi que pour leur évolution.

Contents

Chapter 1

Introduction

Contents

1.1 SINFONI, an Integral-Field Unit

A great part of the work presented in this thesis has been derived using observations made with the instrument SINFONI on VLT. SINFONI (Spectrograph for INtegral Field Observations in the Near Infrared) is an integral-field spectrograph observing in the near infrared installed since 2004 on the Cassegrain focus of VLT/UT4. SINFONI is composed of an image slicer, SPIFFI (SPectrometer for Infrared Faint Field Imaging), and an adaptive optics module. This module can be used with a nearby bright star (Natural Guide Star) as reference or with Laser Guide Star. Available gratings are J, H, K and H+K bands (with respective spectral resolutions of 2000, 3000, 4000 and 1500). H and K bands are the most usual bands for studying galaxies seen as they were about 10 billion years ago: Hα falls in the H band for galaxies at z~1.5 and in the K band for z~2. Available fields-of-view are 8″.×8″., 3″.×3″.*a* nd 0″.8 ×0″.8, corresponding to spatial resolutions of 0″.25, 0″.1 and 0″.025. Usually, high-redshift galaxies are observed with 0″.25 pixel scale, without adaptive optics, therefore with a typical PSF of 0″.6. A few observations however, have been done using a natural guide star, reducing the PSF to 0″.2, therefore using 0″.1 pixel scale.

Integral-field spectroscopy, also called 3D spectroscopy because of the possibility to directly add to an image the spectral dimension, produces datacubes with

2 spatial dimensions and a spectral dimension. The preceding generation, long-slit spectroscopy allowed spectral sampling over a one dimension slit, and is itself the descendant of aperture spectroscopy.

In order to produce integral-field spectroscopy, different techniques can be used. Fabry-Perrot interferometry, used for example for 3D-NTT, successively samples different wavelengths. Three other systems usually sample all the spectral band directly, after "slicing-up" the image. They differ principally on the method used to bring the light to the spectrograph:

- "Lenslet arrays" diffracts the light directly after an array of lenses (each lens corresponding to a pixel). This technique is used for OSIRIS (OH-Suppressing Infrared Integral Field Spectrograph) on Keck.
- "Fibre array" uses fibres to bring the light from each spatial pixel to the spectrograph. The FLAMES/GIRAFFE integral field unit on VLT/UT2 uses fibre arrays.
- "Image slicer" slices the image only along one spatial dimension before diffrating each of these slices (see Figure 1.1): this is the technique used in SINFONI. It has many advantages: the fraction of the light lost between the focal plane and the spectrograph is small, the spatial sampling is done only toward one direction before arriving on the detector, and the spectra fill the whole detector array.

1.2 The Universe at z~2

Our knowledge of the Universe as it was about 10 billion years ago has expanded considerably since the last 20 years. We can now draw a picture of the past when the global co-moving star-formation rate, as well as the specific star-formation rate, were higher by at least an order of magnitude (Madau et al., 1996; Le Borgne et al., 2009). The co-moving star-formation rate peaks around redshift 2, about 10 billion years ago (see Figure 1.2), which is the epoch we focus on in this thesis. In this very star-forming Universe, the morphologies of a majority of galaxies are peculiar (Conselice et al., 2008), and display starbursts-driven outflows (e.g., Shapley et al., 2003; Steidel et al., 2010) as well as a fraction of active galactic nuclei ($\sim$ 1% in Lyman Break Galaxies) which is larger than today ($<<$1%). This active epoch of rapid galaxy evolution was likely driven by a higher merger rate (de Ravel et al., 2009) perhaps together with intense cosmological accretion (Croton et al., 2006).

Galaxies, from the local universe to high redshifts, follow a global scale power-law relation between their cold gas and SFR surface densities, the Schmidt-Kennicutt law (see Figure 1.3), observed over five orders of magnitudes. The fact

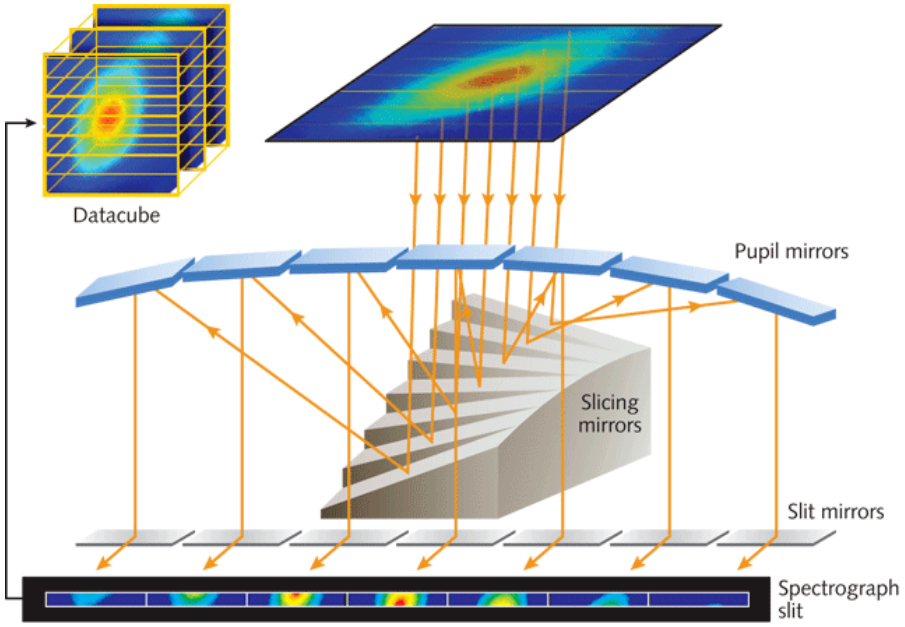

Figure 1.1 Principles of image slicer: the field of view is divided up into N strips and the light from these strips is directed by a set of mirrors along N different light paths toward the common entrance slit of the grating instrument.

that galaxies observed at a variety of evolutionary points, exhibiting different processes and having so many large scale disparities all follow the same simple law suggest that there must be regulating processes that control the star formation (e.g., Kennicutt et al., 2007). There are however many possible mechanisms for regulating star formation over large scales (cloud formation and destruction, mechanical energy output from stars and AGN, spiral density waves, turbulence induced by gravity and mechanical energy, magnetic fields, mixing layers, and many others) and explaining the Schmidt-Kennicutt law from all these processes is complicated. Studying the most extreme segment of star-forming galaxies nearby as well as at high redshift is necessary to reveal the relative importance of these mechanisms (e.g., Lehnert & Heckman, 1996a; Shapley et al., 2003; Verma et al., 2007).

1.3 Characteristics of high-redshift galaxies

Observations of high-redshift galaxies (e.g., Genzel et al., 2006; Förster Schreiber et al., 2006) display large, dynamically hot, gaseous disks of ~10-20 kpc size. Their gas random motions is particularly large, making the large scale bulk motion to velocity dispersion, v/σ, of the order of a few while local galaxies typically have $v/\sigma \sim 10$. In an *in vogue* model, galaxies accrete their gas from "cold flows" (Kereš et al., 2005, 2009; Ocvirk et al., 2008; Dekel & Birnboim, 2008a), which

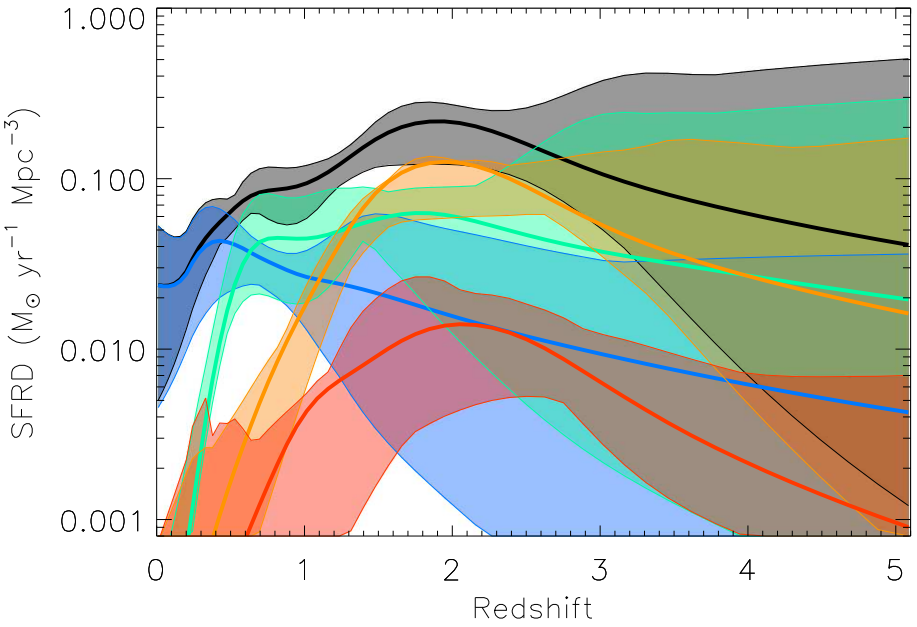

Figure 1.2 Star-formation rate density since z = 5 derived from counts inversions. The SFRD is obtained from the range of all possible luminosity functions derived from the counts and respecting the cosmic infrared background constraints. The solid lines correspond to the best fit to the counts and the transparent shaded areas show the range of uncertainties. From top to bottom at z = 0.8: black = all galaxies, green = LIRGS ($10^{11}L_\odot < L_{IR} \leq 10^{12}L_\odot$), blue = normal star-forming galaxies, orange = ULIRGS ($10^{12}L_\odot < L_{IR} \leq 10^{13}L_\odot$), red = HLIRGS ($L_{IR} > 10^{13}L_\odot$). Figure from Le Borgne et al. (2009).

accumulate to form a gaseous disk. When the amount of gas is high, it becomes gravitationally unstable and reaches a high rate of star formation (Genzel et al., 2008; Dekel & Birnboim, 2008a). According to this model, the processes responsible of galaxy growth in the historical "hierarchical" model of galaxy formation (major and minor mergers, gas cooling from a virialized halo, see White & Rees, 1978), as well as AGN and star formation feedback, contribute only weakly until the bulk of stars are produced.

This model is based on the assumption that baryons and dark matter are strongly coupled, which may be in contradiction with the missing baryons problem which suggests that either galaxies ejected a large fraction of their baryons, either these baryons did not follow the dark matter haloes at the epoch of galaxy formation and were never part of galaxies (Anderson & Bregman, 2010). Furthermore, the gas in haloes seems to come from starburst driven outflows more than from accretion (Steidel et al., 2010).

Although cold flows are probably too faint to be observed with present days

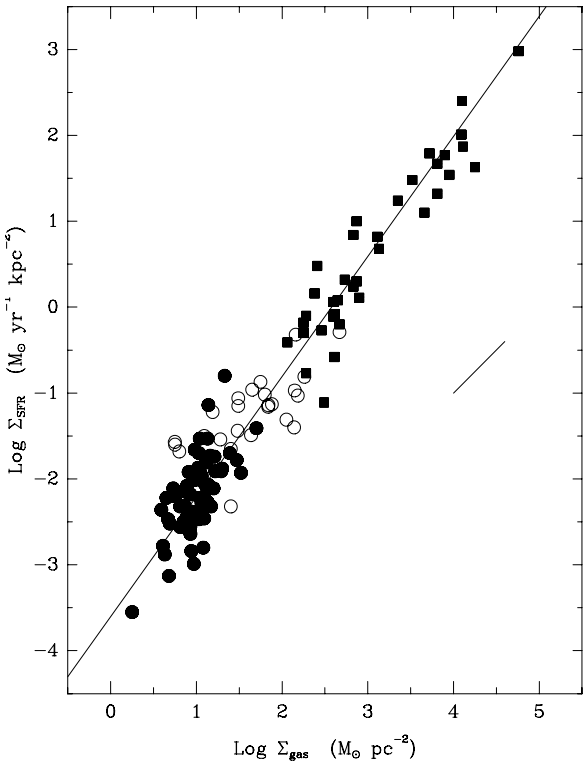

Figure 1.3 The "Schmidt-Kennicutt law": composite star formation law for the normal disk (solid circles) and starburst (squares) samples. Open circles show the SFRs and gas densities for the centers of the normal disk galaxies. The line is a least squares fit with index N = 1.40. The diagonal short line shows the effect of changing the scaling radius by a factor of two. This figure is taken from Kennicutt (1998c)

facilities, they are used in many models (e.g. Dekel et al., 2009; Brooks et al., 2009; Kereš et al., 2009) to explain different observations, as the important number of rotating disks (Förster Schreiber et al., 2006, 2009) – contrary to events as major mergers, cold flows presumably do not disrupt the disk – or their high star-formation rates. They could also partially explain the large velocity dispersion in the gas (see section 1.5).

1.4 Observational biases and their effects

There are many differences between galaxies at high and low redshifts. Importantly, gas fractions are higher (Erb et al., 2006b) at high redshifts, and the gas it-

self has lower metallicity (Erb et al., 2006a; Rodrigues et al., 2008; Maiolino et al., 2008). Simulations of gas-rich mergers analogued as they would be observed with the current generation of integral-field units demonstrate that they could in some cases mimic the disk-like characteristics of high-redshift galaxies (Robertson & Bullock, 2008). IFU observations of local analogs of Lyman Break Galaxies also suggest that morphological and dynamical analysis may not be sufficient to discern the impact of recent mergers (Gonçalves et al., 2010). Therefore, a certain fraction of objects characterized as disks (e.g. Nesvadba et al., 2006a; Genzel et al., 2006, 2008; Wright et al., 2009a) could be recent or advanced mergers.

Many results, using only the most visible emission lines, Hα and [OIII]λ5007, rely on the assumption that the conditions in the ISM of high redshift galaxies are the same than disks in the local universe. This assumption has not been tested directly on the observed properties of high-redshift galaxies. "BPT diagrams" (Baldwin et al., 1981; Veilleux & Osterbrock, 1987) which discriminates between starburst galaxies and AGN in the nearby Universe, using ionization lines ratios such as [NII]/Hα, [OI]/Hα and [SII]/Hα versus [OIII]/Hβ. Starbursts however seem to have higher ratios of [NII]/Hα at high redshift than in the local Universe (Erb et al., 2006a), which could be explained by higher densities and ionization parameters (Brinchmann et al., 2008), but also by a combination of star-formation plus AGN in a relatively low metallicity environment (Groves et al., 2006).

Another significant bias resides in the selection of the observed galaxies: only the highest surface brightness galaxies have been observed (perhaps with the exception of MASSIV, see Contini et al., 2011) , an effect that is accentuated by the impact of surface brightness dimming (which is a strong function of redshift, $\propto (z+1)^4$ for bolometric luminosities and spectral lines, $\propto (z+1)^5$ for broadband photometry due to the additional 'stretching' of the continuum; see, e.g., Tolman, 1930). Galaxies with powerful AGN (e.g., Nesvadba et al., 2006b, 2008b) or large star-formation areas (typically several 10s of $M_\odot$ yr^{-1} over 10s of kpc^2) are therefore over-represented in IFU observations samples. The former are well above the critical threshold of $SFI_{crit} \sim 0.1$ $M_\odot$ yr^{-1} kpc^{-2} (Heckman, 2003) over which galaxies drive vigorous outflows. In the local Universe, galaxies with SFI$\gtrsim$SFI$_{crit}$ creates strongly over-pressurized bubbles of hot gas which expand perpendicular to the disk plane and produce galactic-scale outflows (Heckman et al., 1990; Lehnert & Heckman, 1996a,c). Observational signatures of these starburst-driven winds are present at high redshift in rest-frame UV absorption lines (Pettini et al., 2000; Erb et al., 2004, 2006a) as well as blue wings in rest-frame optical emission lines (e.g. Nesvadba et al., 2007). Broad lines are also observed in stacking analysis of the optical emission lines of high-redshift galaxies, although they could be indicative of outflows as well as of the presence of an AGN (Shapiro et al., 2009).

1.5 What is driving the turbulence in high-redshift galaxies?

The large dispersions observed in the ionized gas of high-redshift galaxies are subject to an important controversy concerning their origin. Different mechanisms are suggested to explain the high level of turbulence: instabilities in disks (gravitational, hydrodynamical, tidal forces between clumps...) eventually aided by cosmological gas accretion (Brooks et al., 2009; Kereš et al., 2009; Dekel et al., 2009; Elmegreen & Burkert, 2010), or energy injection from the large number of supernovae and massive stars maintained by the intense star formation (e.g., Elmegreen et al., 2004; Cox, 2005; Ferrara, 1993; Norman & Ferrara, 1996; Green et al., 2010). Discriminating between the relative importance of these processes is complex, as it depends on many parameters, especially the rate and scale of energy injection and the rate at which the turbulent energy cascades down and dissipates. In the local Universe, the observed velocity dispersions of the gas ($\sigma \sim 10$ km s^{-1}) is more likely to be produced by the energy injection from supernovae and stellar winds in normal spiral galaxies (Tamburro et al., 2009; Leroy et al., 2008) as well as in Lyman Break Analogs (Basu-Zych et al., 2009; Gonçalves et al., 2010) and galaxies selected for their high star formation (Green et al., 2010).

1.6 Self-regulation of star formation

What is regulating the intense star formation in high-redshift galaxies? Models suggest that disks must stay close to the gravitational stability line (Toomre parameter $Q \sim 1$, see Burkert et al., 2010) in order to form the continuous amount of stars we observe. If star formation is the main driver of turbulence, the ISM can reach a state in which star formation is self-regulated, as it may already be obserevd in local starburst galaxies (Silk, 2001; Blitz & Rosolowsky, 2006).

1.7 Purpose of this thesis

Until now, most of the work using integral-field spectroscopy of galaxies seen as they were about 10 billion years ago focused on their dynamical and morphological properties. First IFU observations revealed a large number of objects classified as rotating disks, together with dispersion dominated objects and mergers, in similar proportions. These objects (up to now, more than a hundred of them have been observed with SINFONI), and especially the so-called rotating disks, have been intensely studied in the literature, focusing on their emission line morphologies (bulges, rings, clumps) and of their dynamical properties, especially their "velocity

curves". With the exception of a few objects observed with adaptive optics, the number of spatial resolution elements in these observations is rarely greater than ten, which tends to limit dynamical and morphological analysis. The observed objects have high emission lines surface brightness, as expected considering that the Universe at these redshifts is more active, and especially have a higher star-formation rate density and specific star-formation rate that in the local Universe (Madau et al., 1996; Le Borgne et al., 2009). Of course, we observe only objects that are bright enough to be detected and analyzed, and the effect of the cosmological dimming is critical. This high level of activity is probably to be related to the high gas fractions in these galaxies (Erb et al., 2006a). Another critical point that led to this thesis is the observation that the amount of random motions compared to the large scale velocity shear is larger than in the local Universe. There has been many attempts at explaining the importance of random motions in the ionized gas of high- redshift galaxies. For example, through the gravitational energy input from gas accretion, based on models suggesting that galaxies could be fed via non-virialized gas ("cold flows", Kereš et al., 2005). Another way of stirring up this gas could be through gravitational instabilities forming in thick galactic disks. Last, the level of star formation, through mechanical and photoionization output from supernovae and high-mass stars in the interstellar medium, is a determinant factor in nearby galaxies (Dib et al., 2006), but has been often neglected for high-redshift objects.

The tools used in today's analysis of high-redshift galaxies through the recent developments of IFU spectroscopy are often very similar to the ones used at low redshift. There are however many observed differences between nearby and high-redshift galaxies, suggesting that typical tools used for well resolved observations of nearby disks may not be appropriate to studying high-redshift objects. Until recently, recombination lines were used only as tracers of the star-formation intensity (Genzel et al., 2006; Förster Schreiber et al., 2006; van Starkenburg et al., 2008; Law et al., 2007; Wright et al., 2007; Nesvadba et al., 2008b). This work has been done using the prescriptions developed in the nearby Universe (Epinat et al., 2008; Chemin et al., 2009; Sarzi et al., 2006), and sometimes using gravitational lensing as a natural telescope (Swinbank et al., 2007).

In this thesis, we apply heretofore methods to investigate the physical processes that shape the warm ionized media in galaxies from z=1-3. Through the use of various modeling codes such as Starburst99, Cloudy, GALAXEV and others, we wanted to carefully analyze the properties of their optical emission lines. Our intention by doing this was to begin to get insight into the physics underlying the dynamics and excitation of the warm ionized gas and to compare this with the properties of nearby galaxies. Due to the inability currently to probe other phases of the ISM in distant galaxies at other wavelengths in such detail and at sub-arcsecond scales, even though the warm ionized medium is only one component of a multi-

phase medium, we could still gain valuable insight into the excitation and injection and dissipation of energy in the ISM of distant galaxies. The questions we were interested in answering were: What is the primary driver of the large spatially resolved line widths observed in the optical emission line gas in galaxies at z=1–3? Is the intense star-formation the primary driver? Is it cosmological accretion of gas? Is it turbulence generated by gravity in a collapsing disk? We know that the galaxies observed with SINFONI which yield spatially resolved information have high optical emission line surface brightnesses. What is the underlying mechanism for that? Does it suggest high gas densities, high pressures, high intensity radiation fields, and/or strong shocks? If star-formation is playing the key role in exciting the galaxy-scale emission line nebulae, is it intense enough to drive outflows? Is the star-formation self-regulating, meaning is the star-formation so intense that it is controlling the rate at which further star-formation proceeds? If the ISM is highly turbulent, does this imply a skewed IMF, and/or efficient star-formation. Perhaps these two effect might lead to the high Hα surface brightnesses observed? What causes the star-formation rate - stellar mass relation in galaxies from z=0 to z=6? This is the general motivation and only some of the questions we will attempt to answer in this thesis work.

There are questions we did not pursue in this thesis. We did not pursue detailed comparison of the large scale dynamics in these galaxies with models or try to determine if they are disks or mergers. This is not because these are uninteresting questions, they are, but because we were unsure if the data were sufficient to address these adequately. Moreover, much effort has already been expended on the disk or merger nature of galaxies observed with SINFONI. It is not clear what more we could have added. We did not address the question as to the metallicity of galaxies we observed. Again, this has been addressed extensively in the literature. In addition, through our investigation of the emission line properties, it is not clear if the data and analysis that can be done can determine the metallicities robustly. Our goal in this thesis was to take a new look at integral field data in the near-infrared of galaxies at z=1–3 attempting to determine the physical characteristics of their warm ionized medium and what we could learn from such analyses about the nature of high redshift galaxies. Originality is one important criteria in deciding what thesis to undertake and we have tried to look at problems not previously addressed elsewhere.

Chapter 2

Data

Contents

2.1 Observational properties

This thesis is based on observations of more than 50 galaxies with SINFONI integral field unit spectrograph on the 8m ESO-VLT. They span a redshift range of z= 1.3-2.7, as shown in Figure 6.1). For more details on the data reduction and analysis, see Appendix A.

These redshifts correspond to lookback times between roughly 9 and 11 billion years, as seen in Figure 2.2. Figures 2.3 and 2.4 show the luminosity distance and the physical-to-angular size scale as a function of redshift. It is interesting to note that for the galaxies in the redshift range of this thesis, the physical-to-angular size scale almost does not vary (between z=1.3 and 2.7, it is bound between 7.9 and 8.5 kpc arcsec^{-1}).

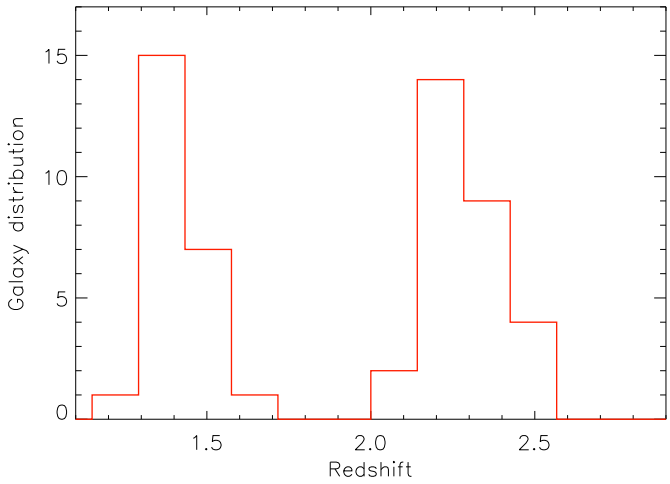

Figure 2.1 Redshift distribution of the sample of galaxies used in this thesis.

The data comes from a variety of programs in the ESO archives (074.A-9011, 075.A-0318, 075.A-0466, 076.A-0464, 076.A-0527, 077.B-0079, 077.B-0511, 078.A-0055, 078.A-0600, 079.A-0341 and 079.B-0430). These observations were conducted by different teams in order to study galaxy formation and evolution through the study of their resolved kinematics, growth and merger rates, metallicities, dynamical masses, ionization properties, star-formation rates and star-formation histories, or superwinds. These galaxies have been selected using a number criteria, which depend on the program but can also vary inside a defined program. Selections criteria include UV, optical, near-infrared and infrared based ones – for example, selection criteria “BM/BX” (selecting galaxies by their lack of strong break in their optical emission, Adelberger et al., 2004), or “BzK” (Daddi et al., 2004), a selection technique separating star-forming and quiescent galaxies

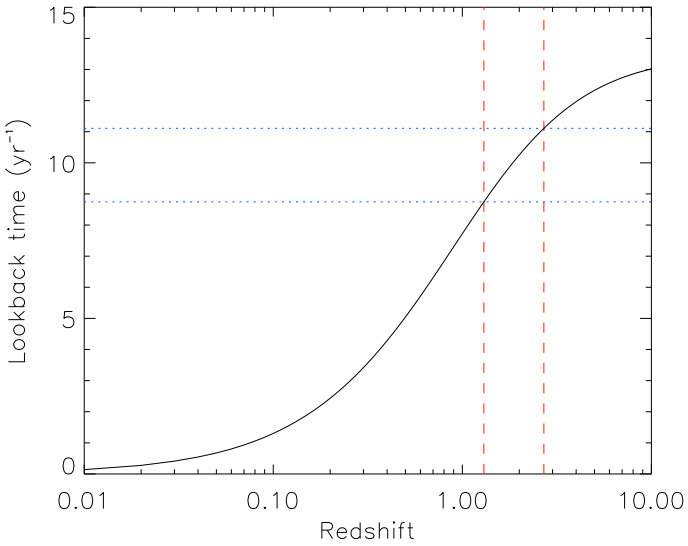

Figure 2.2 Plot of the lookback time (in billion years) as a function of redshift. The red dashed lines correspond to the redshift limits of my sample, and the blue dashed lines to their equivalent lookback time limits.

from K-selected surveys like the "K20" survey (mass selection through K-band magnitude Cimatti et al., 2002)– as well as mass selection in the DEEP2 survey, or late-type morphology selection in the VIMOS/VLT Deep Survey (VVDS) fields based on a strong [OII] doublet.

This thesis is not aimed at a population study. We focus here on the emission line properties of galaxies that are spatially resolved in SINFONI observations. The key to the sample is that all have sufficiently high Hα surface brightness to obtain spatially resolved line maps in a few hours integration time (see Table 2.1), typical for SINFONI observations of distant galaxies. Because of this necessity, our results are only applicable to galaxies with intense star-formation surface density (star-formation rate per unit area). Observational properties and general characteristics of these galaxies are detailed in Table 2.1. Emission lines properties of these objects are presented in Table 2.2. Spatially resolved continuum and line fluxes, line velocities and velocity dispersions and, when available, NICMOS F160W images, as well as integrated and intrinsic spectra, and plots of the Hα line dispersion versus the SFR surface density are presented in Section 2.4.

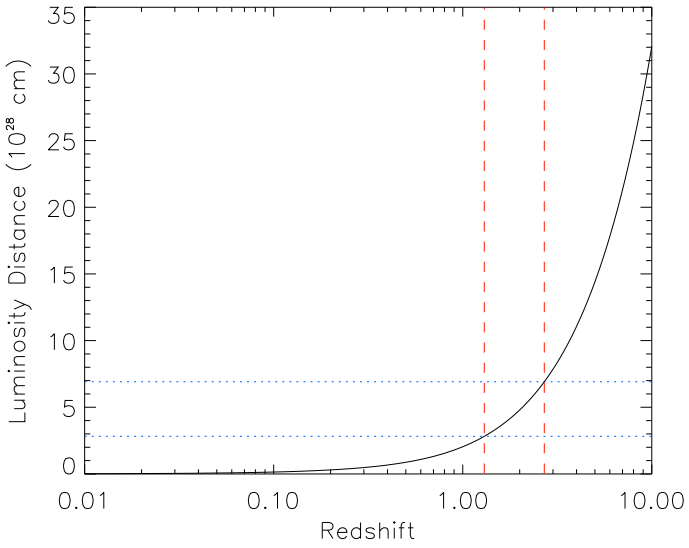

Figure 2.3 Plot of the luminosity distance (in cm) as a function of redshift. The red dashed lines correspond to the redshift limits of my sample, and the blue dashed lines correspond to their equivalent luminosity distance limits.

2.2 General properties of the galaxies

In the integration times of a few hours, the observations reach flux detection limits in Hα of $\sim 2\times10^{-19}$ erg s^{-1} cm^{-2} pixel^{-1}, as seen in Figure 2.5 (for the 250 mas pixel^{-1} scale and averaged over 3×3 pixels). The average surface brightnesses range from about 4.5 to 40 $\times$ 10^{-16} erg s^{-1} cm^{-2} arcsec^{-2} (see Figure 2.6). Hα isophotal radii are typically about $\sim$1″.($\sim$8 kpc radius, or $\sim$200 kpc^2 area, see distribution in Figure 2.7). These observations have a point-spread function FWHM of $\sim$0″.6, which at z$\sim$2 corresponds to an area of $\sim$20 kpc^2. Therefore we have typically $\sim$8-10 independent spatial resolution elements per object.

Total Hα luminosities for our sample are mostly above 10^{42} erg s^{-1}. Figure 2.8 shows the distribution of Hα luminosities for our sample, and their corresponding star-formation rates, converted using the relation from Kennicutt (1998a):

$$SFR(M_\odot\ yr^{-1}) = \frac{L(H\alpha)}{1.26\times10^{41}\ erg\ s^{-1}} \tag{2.1}$$

Our average star-formation rate is $\sim$70 M$_\odot$ yr^{-1}, with values as low as 10 M$_\odot$ yr^{-1} and as high as 250 M$_\odot$ yr^{-1}. However, these values are not corrected for extinction and are expected to be under-estimated by a factor of a few. This extinction correction has been estimated for a sub-sample of these galaxies, for which we have Hβ estimates: their line ratios of Hα to Hβ suggest relatively modest extinction cor-

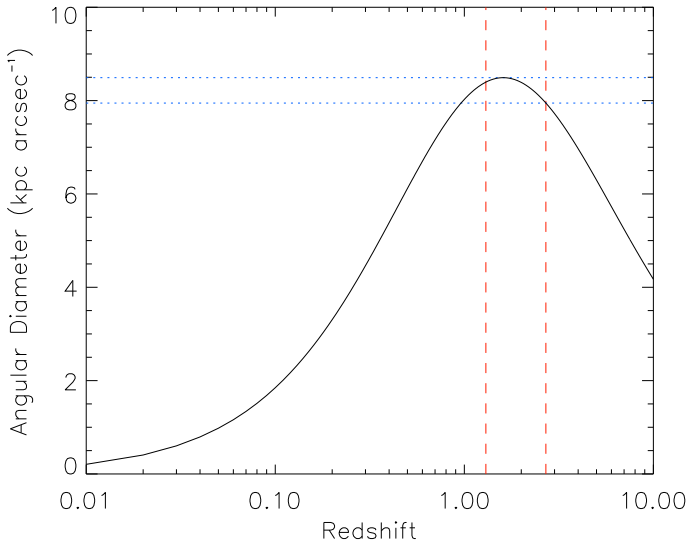

Figure 2.4 Plot of the angular diameter scale (in kpc per arcsec) as a function of redshift. The red dashed lines correspond to the redshift limits of my sample, and the blue dashed lines to the minimal and maximal possible angular diameters scales for our sample of galaxies. Note that our redshifts lie around the top of the curve, and that therefore for all galaxies in this thesis the physical-to-angular size scale factors are almost the same (~8 kpc arcsec^{-1}), almost independently of their redshift.

rections to the star-formation rates, of a factor of few (see Chapter 3). Figures 2.6 (Hα surface brightnesses distribution), 2.7 (Hα detection areas distribution) and 2.8 (Hα luminosities and star-formation rates distributions) are obviously related.

Figures 2.9, 2.10 and 2.11 display, respectively, the maps of the Hα line flux distribution, velocity field and velocity dispersion for all galaxies in this thesis sample. By showing all objects on the same apparent size scale (and therefore roughly on the same physical scale, see Figure 2.4), these figures display the diversity of sizes, morphologies and dynamics in our sample. Objects have been ordered according to crude estimations of their V/σ ratios and their unextincted star-formation rate. To determine V/σ, for V we use the standard deviation of the Hα line velocity field and for σ the Hα line velocity dispersion weighted by the Hα line flux. V/σ has also been derived for a few objects using 1-D method (V/σ derivation along the major axis): in this case we obtain values usually ~25% larger, but our objects are distributed similarly that in the case of the 2-D calculation.

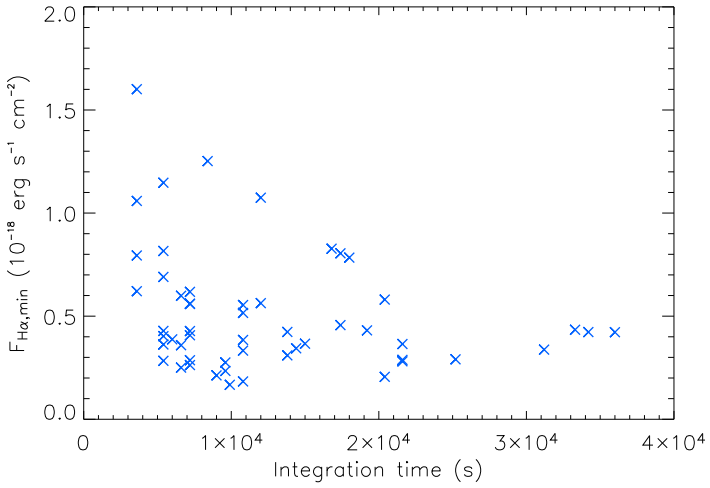

Figure 2.5 Flux detection limit (for Hα, in units of erg s^{-1} cm^{-2}) as a function of integration time for the different sources in our sample.

2.3 Integrated properties

In this section we present the detailed data obtained for each galaxy, using the analysis techniques presented in Chapter A. Table 2.1 gives the observational properties (right ascension and declination of the source, integration time, redshift and Star Formation Rate). Table 2.2 gives the properties of the detected emission lines (integrated fluxes and luminosities, line dispersions, line detection areas and isophotal radii, and minimum fluxes detected).

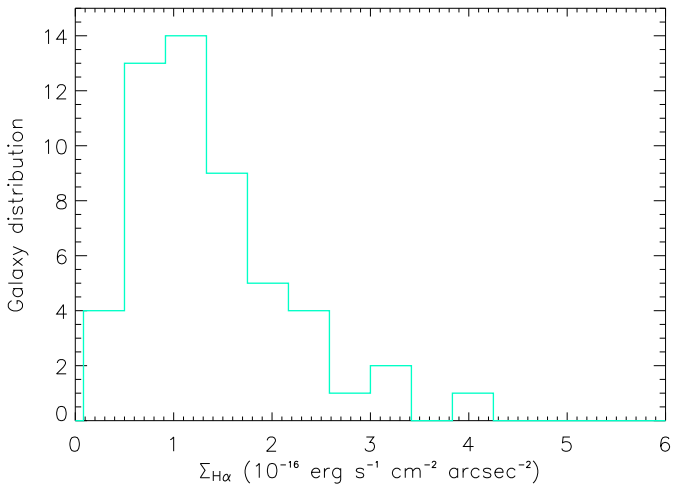

Figure 2.6 Distribution of the sample of galaxies used in this thesis as a function of their average Hα surface brightness, in units of 10^{-16} erg s^{-1} cm^{-2} arcsec^{-2}.

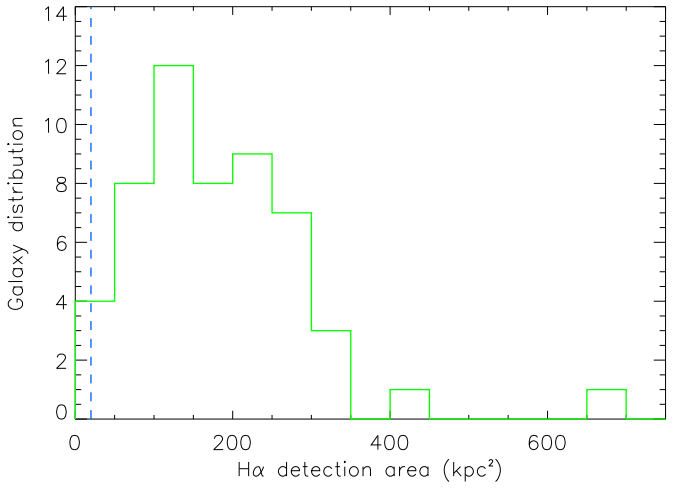

Figure 2.7 Distribution of the sample of galaxies used in this thesis as a function of the size of the area over which Hα is detected at or above the 3-σ level, in units of kpc^2. The blue dashed line represents the typical area size of a PSF (FWHM$\sim$0$''$.6).

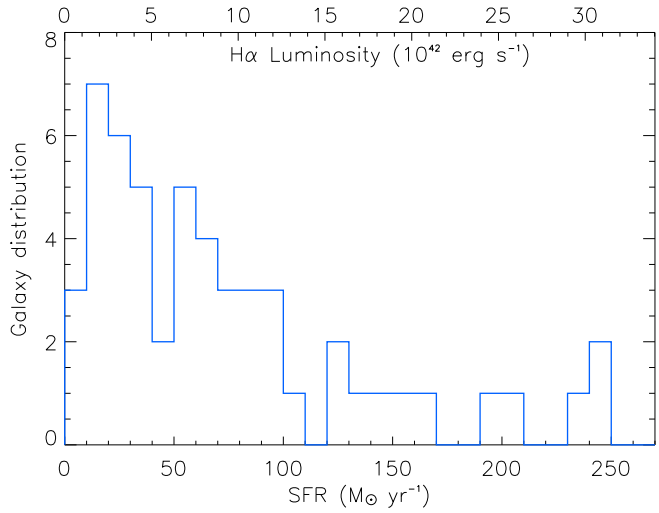

Figure 2.8 Distribution of the sample of galaxies used in this thesis as a function of their Hα luminosity (bottom axis) and their corresponding SFR (top axis). The conversion from Hα luminosity and SFR is from Kennicutt (1998a), see Equation 2.1.

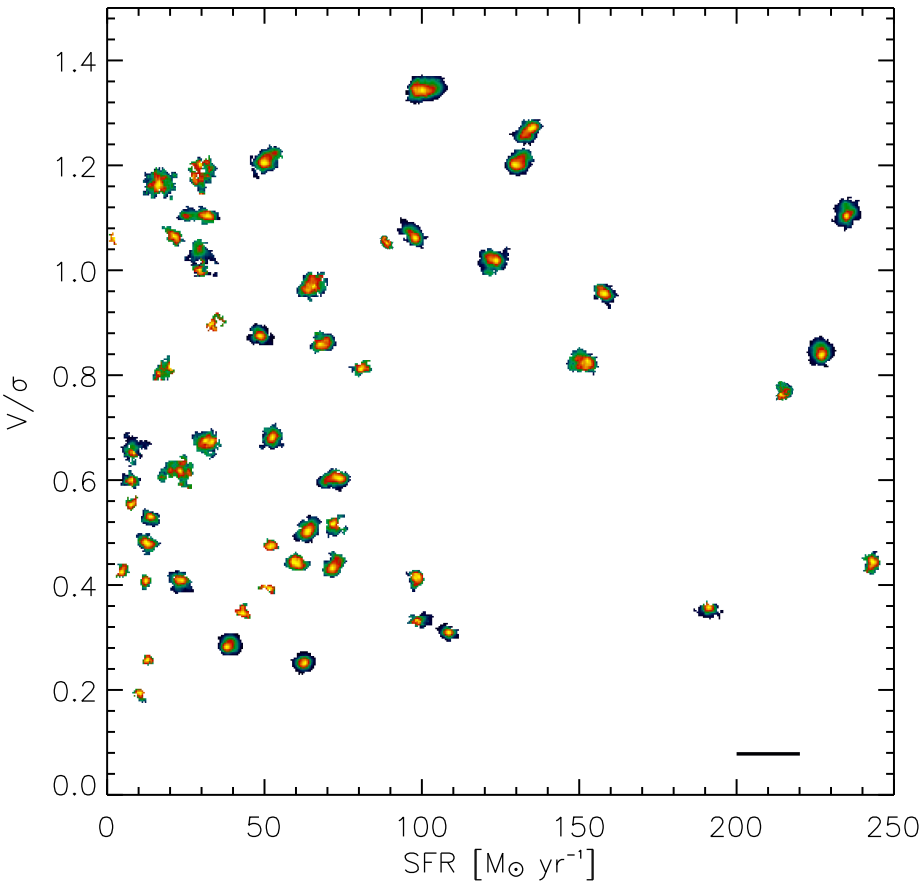

Figure 2.9 Shown at the position of each object in this plot is a small map of its Hα line flux spatial distribution. To indicate their sizes, the horizontal bar in the lower-right corner represents a scale of 10″.0. The Hα fluxes have been normalized individually, in order to maximize the contrast for each galaxy. Objects have been ordered according to estimations of their V/σ ratios and their total star-formation rate.

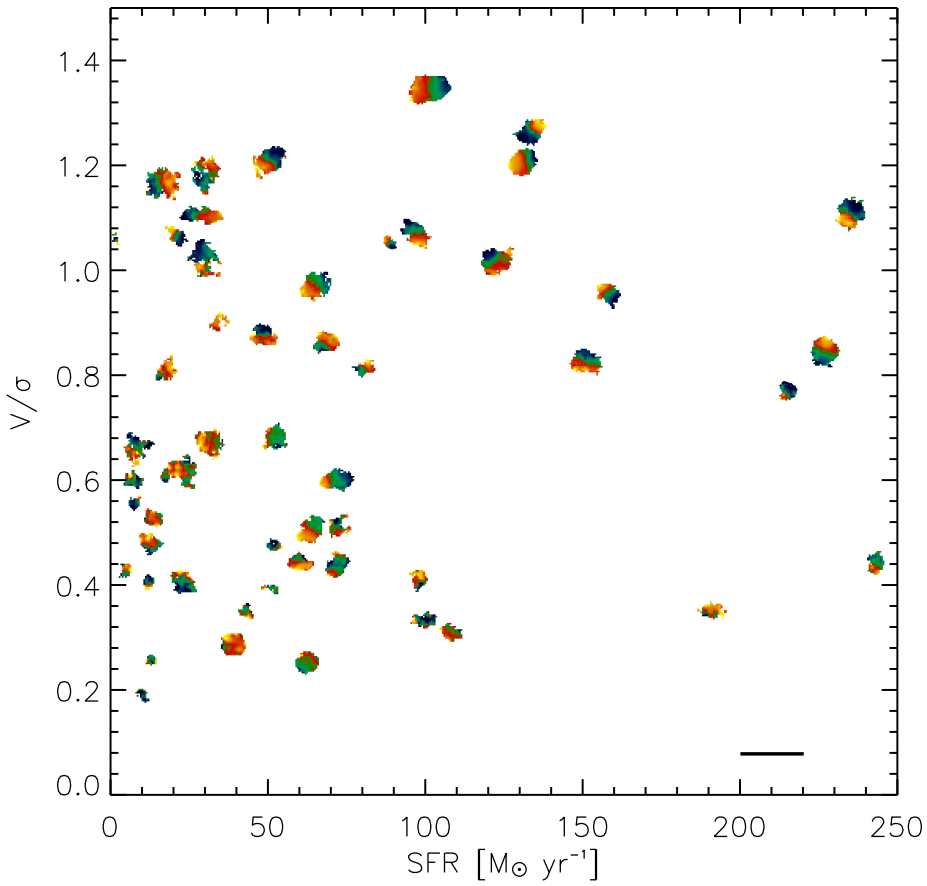

Figure 2.10 Shown at the position of each object in this plot is a small map of its Hα line velocity field. To indicate their sizes, the horizontal bar in the lower-right corner represents a scale of 10″.0. The Hα line velocities have been normalized individually, in order to maximize the contrast for each galaxy. Objects have been ordered according to estimations of their V/σ ratios and their total star-formation rate.

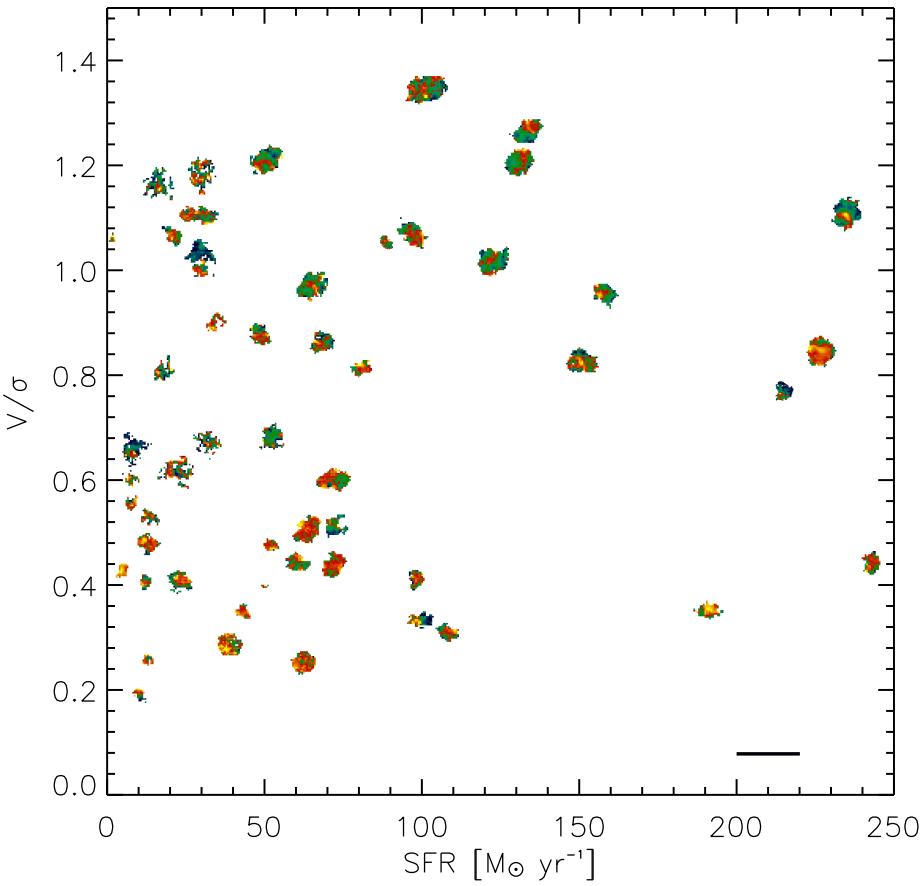

Figure 2.11 Shown at the position of each object in this plot is a small map of its Hα line velocity dispersion field. To indicate their sizes, the horizontal bar in the lower-right corner represents a scale of 10″.0. The Hα line velocity dispersions have been normalized individually, in order to maximize the contrast for each galaxy. Objects have been ordered according to estimations of their V/σ ratios and their total star-formation rate.

Object (1)	Page (2)	R.A. (3)	Dec. (4)	I.T. (5)	Redshift (6)	SFR (7)
BzK-15504	28	11:24:15.8	-21:39:28.9	20400	2.3822±0.0019	249± 9
BzK-15504$^{0.1}_{AO}$	29	11:24:15.6	-21:39:30.6	20400	2.3816±0.0014	210± 9
BzK-6004	30	11:25:03.9	-21:45:31.6	36000	2.3865±0.0013	152± 6
BzK-6397	31	11:25:10.6	-21:45:08.8	9600	1.5133±0.0012	32± 1
CDFS-GK1084	32	03:32:39.6	-27:46:09.6	7200	1.5521±0.0009	4± 1
CDFS-GK2252	33	03:32:19.2	-27:43:18.2	18000	2.4080±0.0014	32± 2
CDFS-GK2363	34	03:32:39.2	-27:42:34.5	17400	2.4512±0.0014	42± 3
CDFS-GK2471	35	03:32:32.6	-27:42:46.4	16800	2.4319±0.0019	81± 4
DEEP2-32002481	36	23:30:59.0	+00:01:23.7	6600	1.3880±0.0014	25± 3
DEEP2-32007614	37	23:30:58.3	+00:02:32.4	5400	1.3716±0.0010	10± 1
DEEP2-32013051	38	23:31:09.1	+00:06:37.3	5400	1.3950±0.0011	23± 1
DEEP2-32015443	39	23:30:00.9	+00:08:45.7	6600	1.3822±0.0009	13± 2
DEEP2-32015501	40	23:30:07.0	+00:06:08.8	10800	1.3919±0.0007	23± 1
DEEP2-32021317	41	23:29:57.5	+00:09:39.3	5400	1.3815±0.0016	26± 2
DEEP2-32021394	42	23:29:46.5	+00:09:30.4	5400	1.3735±0.0009	25± 2
DEEP2-32029850	43	23:31:04.2	+00:16:54.9	6600	1.3952±0.0009	1± 1
DEEP2-32037003	44	23:30:13.5	+00:20:02.0	5400	1.3985±0.0014	52± 2
DEEP2-32100778	45	23:30:38.7	+00:14:06.3	6000	1.3918±0.0006	33± 2
ECDFS-04713	46	03:31:52.4	-27:54:48.6	3600	2.3061±0.0017	51± 6
ECDFS-12514	47	03:31:39.4	-27:41:17.9	5400	2.0261±0.0029	163± 15
HDFS1-1884	48	22:32:50.9	-60:33:29.1	21600	2.0264±0.0014	45± 3
K20-ID4	49	11:25:11.7	-21:35:50.9	9900	1.5934±0.0008	37± 1
K20-ID5	50	03:32:31.6	-27:46:21.7	12000	2.2240±0.0022	88± 4
K20-ID7	51	03:32:29.1	-27:46:28.2	25200	2.2233±0.0017	130± 5
K20-ID8	52	03:32:24.0	-27:47:41.5	15000	2.2230±0.0011	65± 3
Q1623-BX376	53	16:25:45.5	+26:46:51.1	17400	2.4080±0.0011	13± 1
Q1623-BX447	54	16:25:50.5	+26:47:15.4	13800	2.1471±0.0014	29± 2
Q1623-BX455	55	16:25:51.9	+26:46:57.5	12000	2.4065±0.0014	50± 3
Q1623-BX543	56	16:25:57.8	+26:50:06.4	8400	2.5204±0.0017	241± 10
Q1623-BX599	57	16:26:02.8	+26:45:28.3	5400	2.3305±0.0019	199± 8
Q1623-BX663	58	16:26:04.8	+26:47:57.7	33300	2.4253±0.0026	72± 3
Q2343-BX389	59	23:46:29.0	+12:47:31.2	14400	2.1716±0.0020	127± 4
Q2343-BX502	60	16:25:54.3	+26:44:07.6	9600	2.1550±0.0008	50± 2
Q2343-BX528	61	16:25:56.5	+26:50:14.5	34200	2.2684±0.0015	70± 3
Q2343-BX610	62	23:46:09.4	+12:49:16.8	21600	2.2098±0.0019	232± 9
Q2346-BX482	63	23:48:13.4	+00:25:42.7	31200	2.2562±0.0015	125± 5
SA12-5241	64	12:05:28.5	-07:24:55.5	7200	1.3617±0.0007	13± 1

Continued on next page...

Object (1)	Page (2)	R.A. (3)	Dec. (4)	I.T. (5)	Redshift (6)	SFR (7)
SA12-6192	65	12:05:25.4	-07:23:49.8	10800	1.5038±0.0008	7± 1
SA12-6339	66	12:05:32.8	-07:23:35.5	19200	2.2963±0.0013	107± 4
SA12-8768	67	12:05:31.1	-07:20:27.9	10800	2.1875±0.0010	65± 3
SA15-5365	68	15:23:46.0	-00:05:58.8	9000	1.5340±0.0011	13± 1
SINS-4751	69	11:24:50.1	-21:47:21.9	3600	2.2651±0.0011	97± 4
SSA-22a-MD041	70	22:17:40.3	+00:17:06.7	21600	2.1632±0.0014	98± 4
VVDS-020147106	71	02:26:45.5	-04:40:47.0	7200	1.5182±0.0008	62± 3
VVDS-020261328	72	02:27:11.1	-04:25:30.8	3600	1.5276±0.0008	11± 1
VVDS-220014252	73	22:17:45.6	+00:28:40.3	7200	1.3090±0.0011	63± 2
VVDS-220015726	74	22:15:42.6	+00:29:05.0	10800	1.2920±0.0012	51± 2
VVDS-220544103	75	22:15:25.5	+00:06:40.1	7200	1.3955±0.0010	73± 3
VVDS-220584167	76	22:15:22.9	+00:18:47.6	7200	1.4643±0.0012	99± 4
VVDS-220596913	77	22:14:29.3	+00:22:15.9	10800	1.2649±0.0010	30± 1
ZC-1101592	78	09:59:54.8	+02:17:44.9	3600	1.4034±0.0013	10± 1
ZC-782941$_{AO}$	79	09:59:56.0	+02:06:52.0	7200	2.1811±0.0015	141± 6
ZC-782941$^{0.1}_{AO}$	80	09:59:55.9	+02:06:49.8	13800	2.1813±0.0016	89± 3

Table 2.1: General properties of the sample of galaxies used in this thesis. Column (1): object designation. $_{AO}$: adaptive optics mode. $^{0.1}$: pixel scale of 0.1 arcsec. All other observations are without the use of adaptive optics, and with 0.25 arcsec pixels. Column (2): reference page of detailed properties. Column (3): right ascension in units of hh:mm:ss. Column (4): declination in dd:mm:ss. Column (5): integration time in seconds. Column (6): redshift obtained from the Hα line position. Column (7): star formation rate obtained from the Hα luminosity, in $M_\odot$ yr^{-1}, not corrected for extinction.

Object (1)	Page (2)	Line (3)	F_{line} (4) 10^{-16} erg s^{-1} cm^{-2}	L_{line} (5) 10^{42} erg s^{-1}	σ_{line} (6) km s^{-1}	A_{line} (7) kpc^2	r_{line} (8) kpc	$Min_{F_{line}}$ (9) 10^{-18} erg s^{-1} cm^{-2}
BzK-15504	28	Hα	7.09± 0.27	31.41± 1.18	163.± 6.	271	9.3	0.58
		[NII]	1.96± 0.21	8.68± 0.91	133.± 14.	118	6.2	0.38
BzK-15504$^{0.1}_{AO}$	29	Hα	5.99± 0.27	26.53± 1.19	111.± 5.	107	5.8	0.21
		[NII]	2.45± 0.21	10.87± 0.91	135.± 11.	44	3.7	0.20
BzK-6004	30	Hα	4.33± 0.19	19.27± 0.86	105.± 5.	236	8.7	0.42
		[NII]	1.78± 0.15	7.91± 0.67	67.± 6.	164	7.2	0.42
BzK-6397	31	Hα	2.80± 0.13	4.08± 0.18	122.± 5.	345	10.5	0.23
		[NII]	1.14± 0.10	1.66± 0.15	177.± 16.	161	7.2	0.14
CDFS-GK1084	32	Hα	0.38± 0.03	0.59± 0.05	86.± 7.	59	4.4	0.29
		[NII]	0.14± 0.03	0.22± 0.05	90.± 19.	14	2.2	0.47
CDFS-GK2252	33	Hα	0.90± 0.07	4.09± 0.30	112.± 8.	70	4.7	0.78
		[NII]	0.21± 0.06	0.97± 0.26	100.± 27.	15	2.2	0.77
CDFS-GK2363	34	Hα	1.13± 0.09	5.36± 0.41	105.± 8.	61	4.4	0.81
		[NII]	0.25± 0.06	1.21± 0.30	61.± 15.	15	2.2	0.57
CDFS-GK2471	35	Hα	2.20± 0.11	10.25± 0.51	159.± 8.	88	5.3	0.83
		[NII]	0.34^{ND}	1.58^{ND}	...	...	...	...
DEEP2-32002481	36	Hα	2.77± 0.32	3.25± 0.38	156.± 18.	302	9.8	0.25
		[NII]	1.20± 0.37	1.41± 0.43	209.± 64.	69	4.7	0.25
DEEP2-32007614	37	Hα	1.13± 0.08	1.29± 0.09	110.± 8.	47	3.9	0.69
		[NII]	0.47± 0.06	0.53± 0.06	43.± 5.	33	3.3	0.36
DEEP2-32013051	38	Hα	2.45± 0.18	2.91± 0.21	118.± 9.	188	7.7	0.28
		[NII]	1.57± 0.19	1.87± 0.23	124.± 15.	131	6.5	0.22
DEEP2-32015443	39	Hα	1.48± 0.22	1.72± 0.25	85.± 13.	140	6.7	0.60
		[NII]	0.54± 0.18	0.63± 0.21	82.± 27.	42	3.7	0.42
DEEP2-32015501	40	Hα	2.48± 0.18	2.93± 0.22	58.± 4.	304	9.8	0.38
		[NII]	0.38± 0.14	0.46± 0.17	32.± 12.	63	4.5	0.21
DEEP2-32021317	41	Hα	2.88± 0.28	3.35± 0.32	194.± 19.	216	8.3	0.43
		[NII]	3.38± 0.37	3.93± 0.43	351.± 38.	111	6.0	0.26
DEEP2-32021394	42	Hα	2.78± 0.25	3.18± 0.28	92.± 8.	281	9.5	0.40
		[NII]	1.29± 0.27	1.48± 0.32	156.± 33.	52	4.1	0.31
DEEP2-32029850	43	Hα	0.13± 0.03	0.15± 0.04	82.± 22.	20	2.5	0.36
		[NII]	0.09± 0.03	0.11± 0.04	107.± 36.	6	1.5	0.67
DEEP2-32037003	44	Hα	5.52± 0.24	6.62± 0.28	158.± 7.	287	9.6	0.36
		[NII]	1.39± 0.19	1.66± 0.23	102.± 14.	155	7.0	0.24
DEEP2-32100778	45	Hα	3.55± 0.27	4.20± 0.32	41.± 3.	245	8.8	0.39
		[NII]	1.37± 0.31	1.62± 0.37	60.± 14.	148	6.9	0.27
ECDFS-04713	46	Hα	1.59± 0.19	6.53± 0.80	137.± 17.	39	3.5	1.60
		[NII]	1.18± 0.22	4.83± 0.91	155.± 29.	22	2.7	1.85
ECDFS-12514	47	Hα	6.92± 0.67	20.64± 2.00	279.± 27.	189	7.8	1.15
		[NII]	2.59± 0.44	7.73± 1.33	118.± 20.	19	2.5	0.73
HDFS1-1884	48	Hα	1.90± 0.15	5.69± 0.45	119.± 9.	270	9.3	0.28
		[NII]	0.38± 0.12	1.14± 0.37	88.± 28.	70	4.7	0.32
K20-ID4	49	Hα	2.85± 0.14	4.72± 0.24	62.± 3.	214	8.3	0.17
		[NII]	0.79± 0.08	1.31± 0.14	64.± 7.	94	5.5	0.32
K20-ID5	50	Hα	2.97± 0.14	11.12± 0.54	194.± 9.	117	6.1	0.56
		[NII]	1.82± 0.16	6.84± 0.60	260.± 23.	61	4.4	0.69
K20-ID7	51	Hα	4.40± 0.18	16.47± 0.67	149.± 6.	279	9.4	0.29
		[NII]	0.86± 0.11	3.24± 0.40	109.± 13.	113	6.0	0.30
K20-ID8	52	Hα	2.19± 0.11	8.21± 0.42	88.± 4.	175	7.5	0.37
		[NII]	0.74± 0.10	2.75± 0.38	123.± 17.	70	4.7	0.23
Q1623-BX376	53	Hα	0.36± 0.02	1.64± 0.11	82.± 5.	38	3.5	0.46
		[NII]	0.05± 0.02	0.23± 0.07	30.± 9.	1	0.6	0.50
Q1623-BX447	54	Hα	1.09± 0.10	3.73± 0.34	116.± 11.	105	5.8	0.42
		[NII]	0.35^{ND}	1.24^{ND}	...	...	...	...
Q1623-BX455	55	Hα	1.41± 0.10	6.41± 0.47	106.± 8.	56	4.2	1.07
		[NII]	0.35± 0.10	1.59± 0.45	121.± 34.	5	1.3	0.48
Q1623-BX543	56	Hα	5.99± 0.26	30.43± 1.33	137.± 6.	116	6.1	1.25
		[NII]	0.69± 0.20	3.51± 0.99	72.± 20.	28	3.0	0.93

Continued on next page...

Object (1)	Page (2)	Line (3)	F_{line} (4) 10^{-16} erg s^{-1} cm^{-2}	L_{line} (5) 10^{42} erg s^{-1}	σ_{line} (6) km s^{-1}	A_{line} (7) kpc^2	r_{line} (8) kpc	$Min_{F_{line}}$ (9) 10^{-18} erg s^{-1} cm^{-2}
Q1623-BX599	57	Hα	5.98± 0.24	25.12± 1.02	159.± 6.	119	6.2	0.82
		[NII]	0.76± 0.15	3.17± 0.61	85.± 16.	41	3.6	0.94
Q1623-BX663	58	Hα	1.99± 0.11	9.19± 0.50	221.± 12.	121	6.2	0.43
		[NII]	0.78± 0.13	3.59± 0.60	333.± 56.	34	3.3	0.27
Q2343-BX389	59	Hα	4.54± 0.17	16.07± 0.61	177.± 7.	228	8.5	0.34
		[NII]	0.69± 0.15	2.43± 0.53	122.± 26.	69	4.7	0.29
Q2343-BX502	60	Hα	1.82± 0.09	6.31± 0.32	52.± 3.	186	7.7	0.28
		[NII]	0.23^{ND}	0.82^{ND}	...	...	...	...
Q2343-BX528	61	Hα	2.26± 0.10	8.90± 0.40	128.± 6.	176	7.5	0.42
		[NII]	0.41± 0.05	1.61± 0.21	72.± 9.	62	4.5	0.28
Q2343-BX610	62	Hα	7.93± 0.32	29.26± 1.19	163.± 7.	269	9.3	0.37
		[NII]	2.49± 0.13	9.20± 0.48	107.± 6.	192	7.8	0.35
Q2346-BX482	63	Hα	4.09± 0.17	15.87± 0.64	130.± 5.	252	9.0	0.34
		[NII]	0.48± 0.06	1.87± 0.25	70.± 9.	92	5.4	0.27
SA12-5241	64	Hα	1.46± 0.07	1.64± 0.08	52.± 3.	112	6.0	0.43
		[NII]	0.62± 0.06	0.70± 0.07	37.± 4.	51	4.0	0.31
SA12-6192	65	Hα	0.69± 0.05	0.99± 0.07	63.± 4.	102	5.7	0.18
		[NII]	0.40± 0.06	0.57± 0.08	83.± 12.	50	4.0	0.22
SA12-6339	66	Hα	3.33± 0.15	13.49± 0.60	101.± 5.	112	6.0	0.43
		[NII]	0.61± 0.12	2.46± 0.49	129.± 26.	35	3.4	0.68
SA12-8768	67	Hα	2.31± 0.12	8.31± 0.42	73.± 4.	138	6.6	0.55
		[NII]	0.44± 0.10	1.57± 0.37	85.± 20.	30	3.1	0.48
SA15-5365	68	Hα	1.10± 0.10	1.65± 0.16	117.± 11.	146	6.8	0.21
		[NII]	0.19± 0.08	0.29± 0.11	100.± 39.	1	0.6	0.48
SINS-4751	69	Hα	3.12± 0.16	12.24± 0.62	77.± 4.	105	5.8	0.62
		[NII]	0.48± 0.11	1.89± 0.45	69.± 16.	21	2.6	1.12
SSA-22a-MD041	70	Hα	3.56± 0.16	12.46± 0.56	123.± 5.	215	8.3	0.29
		[NII]	0.50± 0.13	1.75± 0.47	142.± 38.	95	5.5	0.22
VVDS-020147106	71	Hα	5.37± 0.27	7.89± 0.40	75.± 4.	183	7.6	0.41
		[NII]	0.31± 0.10	0.46± 0.15	40.± 13.	34	3.3	0.30
VVDS-020261328	72	Hα	1.00± 0.06	1.50± 0.08	71.± 4.	57	4.3	0.79
		[NII]	0.12± 0.04	0.18± 0.06	38.± 13.	1	0.6	0.50
VVDS-220014252	73	Hα	7.83± 0.35	7.97± 0.36	130.± 6.	225	8.5	0.56
		[NII]	1.02± 0.28	1.04± 0.28	128.± 35.	88	5.3	0.43
VVDS-220015726	74	Hα	6.64± 0.30	6.54± 0.29	140.± 6.	188	7.7	0.52
		[NII]	1.09± 0.16	1.08± 0.16	110.± 16.	79	5.0	0.50
VVDS-220544103	75	Hα	7.78± 0.35	9.27± 0.42	103.± 5.	235	8.7	0.56
		[NII]	1.55± 0.25	1.85± 0.30	141.± 23.	89	5.3	0.48
VVDS-220584167	76	Hα	9.37± 0.42	12.58± 0.56	125.± 6.	417	11.5	0.26
		[NII]	1.95± 0.18	2.61± 0.25	99.± 9.	161	7.2	0.27
VVDS-220596913	77	Hα	4.11± 0.18	3.85± 0.17	107.± 5.	224	8.5	0.33
		[NII]	0.69± 0.17	0.65± 0.16	125.± 30.	28	3.0	0.38
ZC-1101592	78	Hα	1.06± 0.11	1.29± 0.14	148.± 16.	52	4.1	1.06
		[NII]	0.24 ± 0.07^{sky}	0.29 ± 0.08^{sky}	7 ± 2^{sky}	...	...	...
ZC-782941$_{AO}$	79	Hα	4.97± 0.21	17.78± 0.77	133.± 6.	162	7.2	0.62
		[NII]	0.71± 0.17	2.53± 0.62	76.± 19.	51	4.1	0.89
ZC-782941$^{0.1}_{AO}$	80	Hα	3.14± 0.13	11.24± 0.46	144.± 6.	53	4.1	0.31
		[NII]	0.74± 0.09	2.65± 0.32	77.± 9.	24	2.8	0.20

Table 2.2: Emission line properties of the sample of galaxies used in this thesis. Column (1): object designation. $_{AO}$: adaptive optics mode. $^{0.1}$: pixel scale of 0.1 arcsec. All other observations are without the use of adaptive optics, and with 0.25 arcsec pixels. Column (2): reference page of detailed properties. Column (3): line identification. Column (4): line flux in the integrated spectrum in units of 10^{-16} erg s^{-1} cm^{-2}. Column (5): line luminosity in units of 10^{42} erg s^{-1}. Column (6): line dispersion in the integrated spectrum, corrected for the instrumental resolution, in km s^{-1}. Column (7): size of the region where the line detection is over 3-σ, in kpc^2. Column (8): isophotal radius corresponding to the region where the line detection exceeds 3-σ, in kpc. Column (9): flux detection limit per pixel in units of 10^{-18} erg s^{-1} cm^{-2}.
^{NC}: the line is not detected, given value is the 3-σ upper limit (with a line width constrained to the Hα value).
^{sky}: the estimated line characteristics are influenced significantly by a nearby sky line.

2.4 Spatially resolved properties

This section gives detailed information on each galaxy, with maps of the Hα line flux distribution, Hα line velocity field and velocity dispersion distribution. When [NII] is spatially resolved (for ~85% of our sample), we also show the [NII] line flux map and the corresponding [NII]/Hα line flux ratio map. When the continuum is detected (for ~65% of our sample; the non-detection in the other ~35% is partially due to cosmological surface brightness dimming), we also present a map of the *R*-band continuum as well as of the rest-frame Hα equivalent widths. For five galaxies, we present the high resolution NICMOS F160W band HST maps. Superimposed on all maps are contours following either (i) the *R*-band continuum flux distribution, or (ii) in case the continuum is not detected, the Hα flux distribution. We also show the integrated spectrum, centered on the Hα and [NII] lines, as well as the intrinsic spectrum (which sums all the spectra where Hα is detected over 3-σ after shifting them individually to their rest-frame). Finally, for each galaxy we show a plot of the pixel per pixel Hα line velocity dispersion as a function of the star formation rate surface density. For the convenience of the reader, we have included a caption for each object.

2.4.0.1 BzK-15504

$z = 2.38$

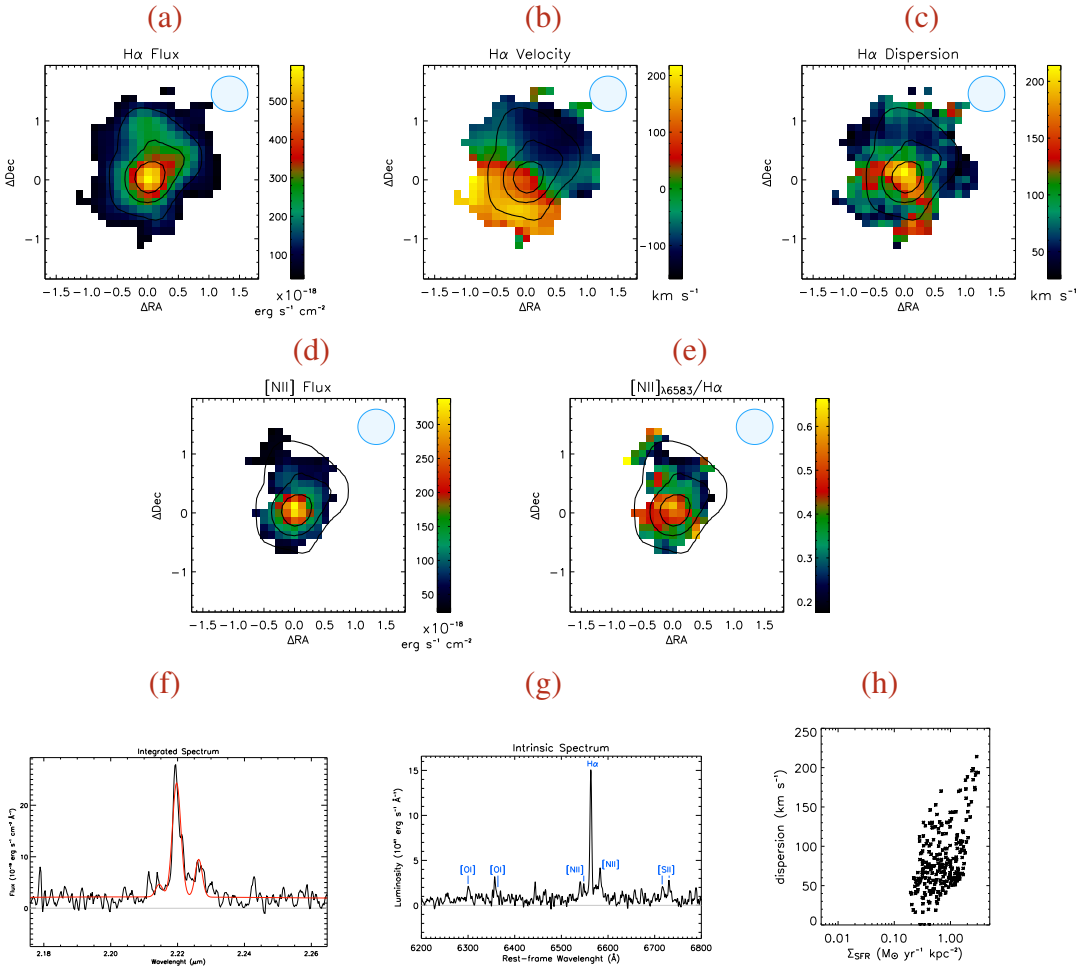

Figure 2.12 (a) Spatial distribution of the Hα line flux, in units of 10^{-18} erg s^{-1} cm^{-2}, (b) Hα velocity field, in km s^{-1}, (c) velocity dispersion distribution, in km s^{-1}, (d) spatial distribution of the [NII] line flux, in units of 10^{-18} erg s^{-1} cm^{-2}, (e) and spatial distribution of the ratio of the [NII] over the Hα line fluxes, (f) integrated spectrum (in observer-frame) centered on the Hα line: the red curve is the best fit for Hα and [NII], (g) intrinsic spectrum (in rest-frame) and (h) Hα velocity dispersion as a function of the star formation rate surface density. The contours superimposed on the maps follow the Hα flux distribution. Blue circles represent the FWHM of the PSF.

2.4.0.2 BzK-15504$^{0.1}_{AO}$ $z = 2.38$

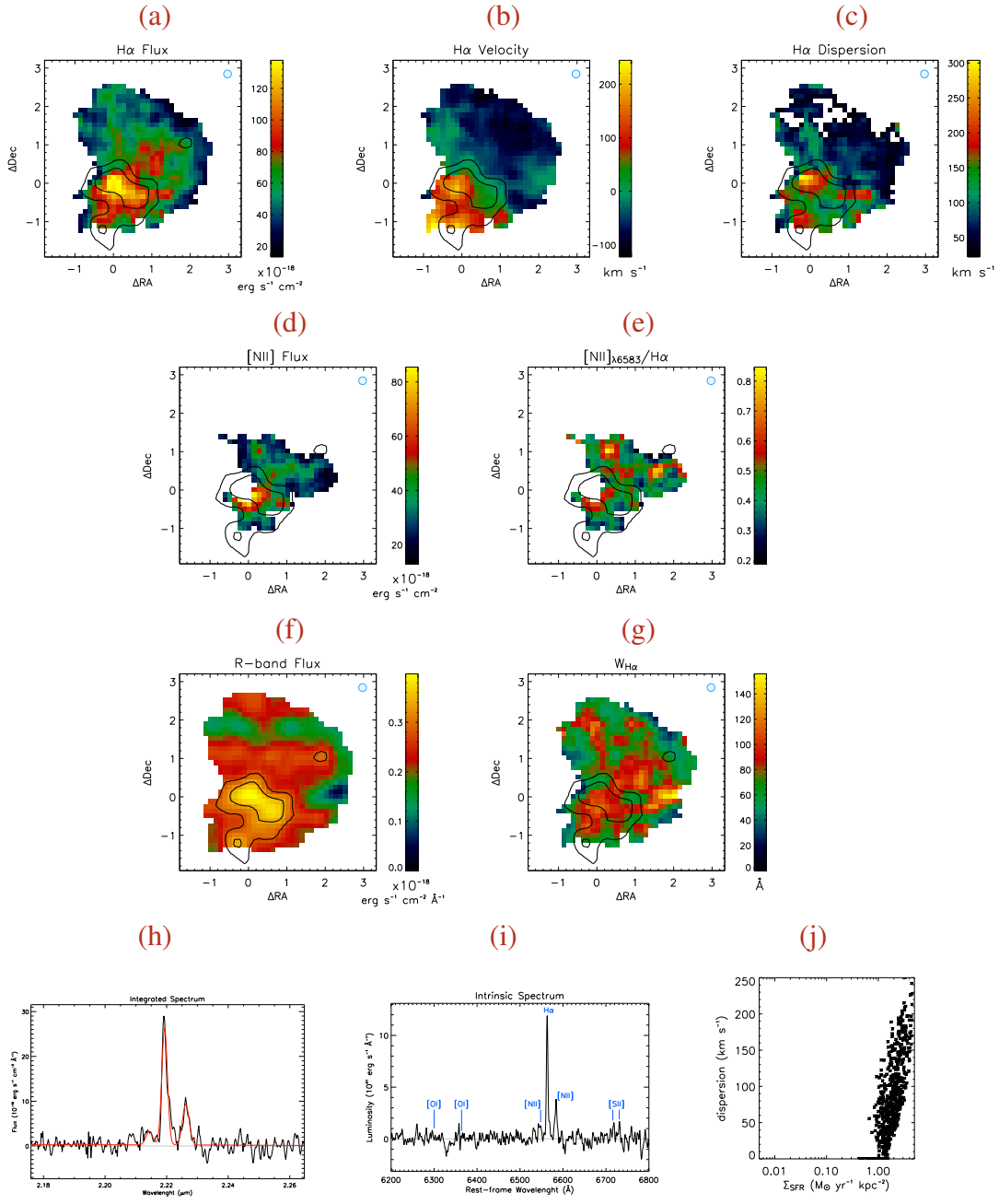

Figure 2.13 (a) Spatial distribution of the Hα line flux, in units of 10^{-18} erg s^{-1} cm^{-2}, (b) Hα velocity field, in km s^{-1}, (c) velocity dispersion distribution, in km s^{-1}, (d) spatial distribution of the [NII] line flux, in units of 10^{-18} erg s^{-1} cm^{-2}, (e) and spatial distribution of the ratio of the [NII] over the Hα line fluxes, (f) *R*-band continuum flux, in units of 10^{-18} erg s^{-1} cm^{-2} Å^{-1}, (g) equivalent width of the Hα line in Å, (h) integrated spectrum (in observer-frame) centered on the Hα line: the red curve is the best fit for Hα and [NII], (i) intrinsic spectrum (in rest-frame) and (j) Hα velocity dispersion as a function of the star formation rate surface density. The contours superimposed on the maps follow the *R*-band flux distribution. Blue circles represent the FWHM of the PSF.

2.4.0.3 BzK-6004

$z = 2.39$

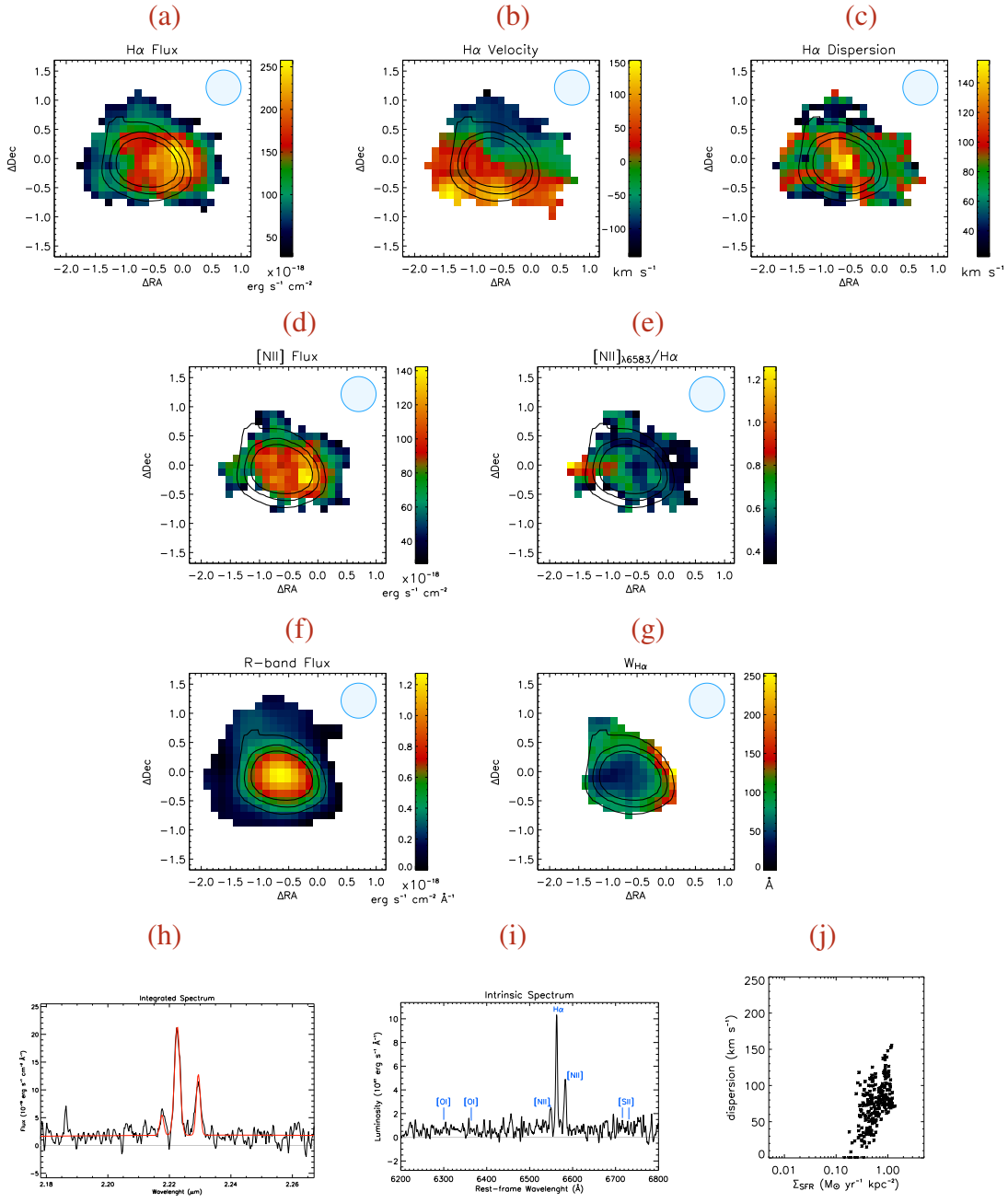

Figure 2.14 (a) Spatial distribution of the Hα line flux, in units of 10^{-18} erg s^{-1} cm^{-2}, (b) Hα velocity field, in km s^{-1}, (c) velocity dispersion distribution, in km s^{-1}, (d) spatial distribution of the [NII] line flux, in units of 10^{-18} erg s^{-1} cm^{-2}, (e) and spatial distribution of the ratio of the [NII] over the Hα line fluxes, (f) *R*-band continuum flux, in units of 10^{-18} erg s^{-1} cm^{-2} Å^{-1}, (g) equivalent width of the Hα line in Å, (h) integrated spectrum (in observer-frame) centered on the Hα line: the red curve is the best fit for Hα and [NII], (i) intrinsic spectrum (in rest-frame) and (j) Hα velocity dispersion as a function of the star formation rate surface density. The contours superimposed on the maps follow the *R*-band flux distribution. Blue circles represent the FWHM of the PSF.

2.4.0.4 BzK-6397 $z = 1.51$

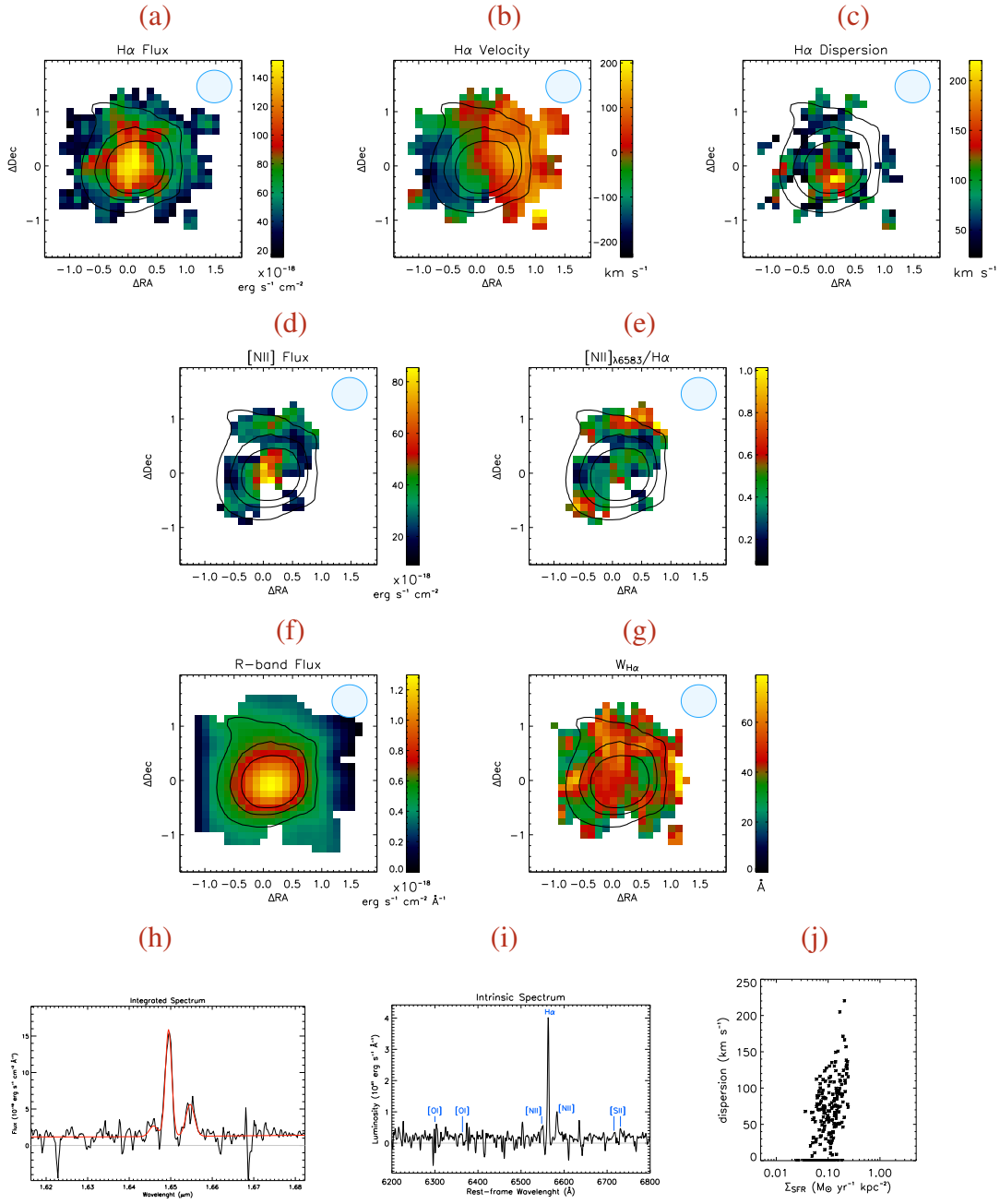

Figure 2.15 (a) Spatial distribution of the Hα line flux, in units of 10^{-18} erg s^{-1} cm^{-2}, (b) Hα velocity field, in km s^{-1}, (c) velocity dispersion distribution, in km s^{-1}, (d) spatial distribution of the [NII] line flux, in units of 10^{-18} erg s^{-1} cm^{-2}, (e) and spatial distribution of the ratio of the [NII] over the Hα line fluxes, (f) *R*-band continuum flux, in units of 10^{-18} erg s^{-1} cm^{-2} Å^{-1}, (g) equivalent width of the Hα line in Å, (h) integrated spectrum (in observer-frame) centered on the Hα line: the red curve is the best fit for Hα and [NII], (i) intrinsic spectrum (in rest-frame) and (j) Hα velocity dispersion as a function of the star formation rate surface density. The contours superimposed on the maps follow the *R*-band flux distribution. Blue circles represent the FWHM of the PSF.

2.4.0.5 CDFS-GK1084 $z = 1.55$

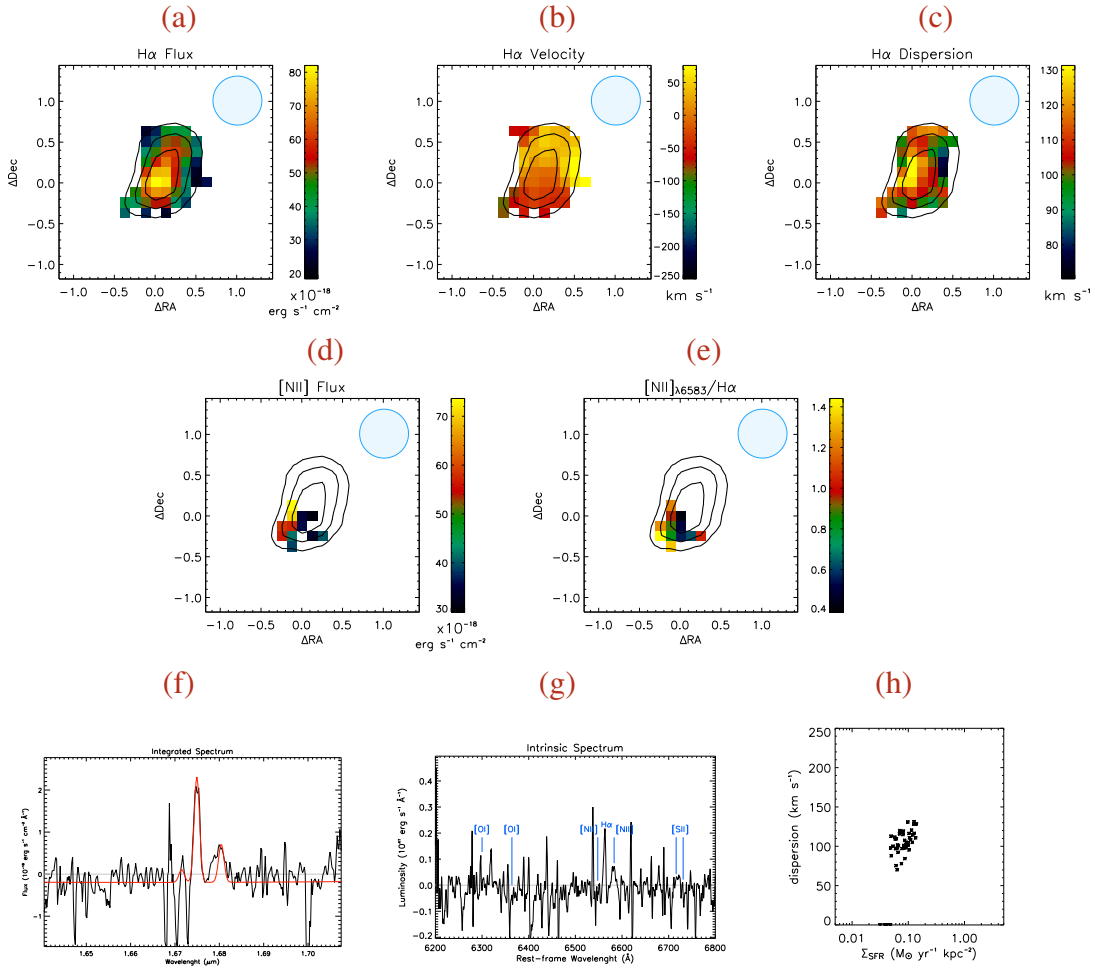

Figure 2.16 (a) Spatial distribution of the Hα line flux, in units of 10^{-18} erg s^{-1} cm^{-2}, (b) Hα velocity field, in km s^{-1}, (c) velocity dispersion distribution, in km s^{-1}, (d) spatial distribution of the [NII] line flux, in units of 10^{-18} erg s^{-1} cm^{-2}, (e) and spatial distribution of the ratio of the [NII] over the Hα line fluxes, (f) integrated spectrum (in observer-frame) centered on the Hα line: the red curve is the best fit for Hα and [NII], (g) intrinsic spectrum (in rest-frame) and (h) Hα velocity dispersion as a function of the star formation rate surface density. The contours superimposed on the maps follow the Hα flux distribution. Blue circles represent the FWHM of the PSF.

2.4.0.6 CDFS-GK2252 $z = 2.41$

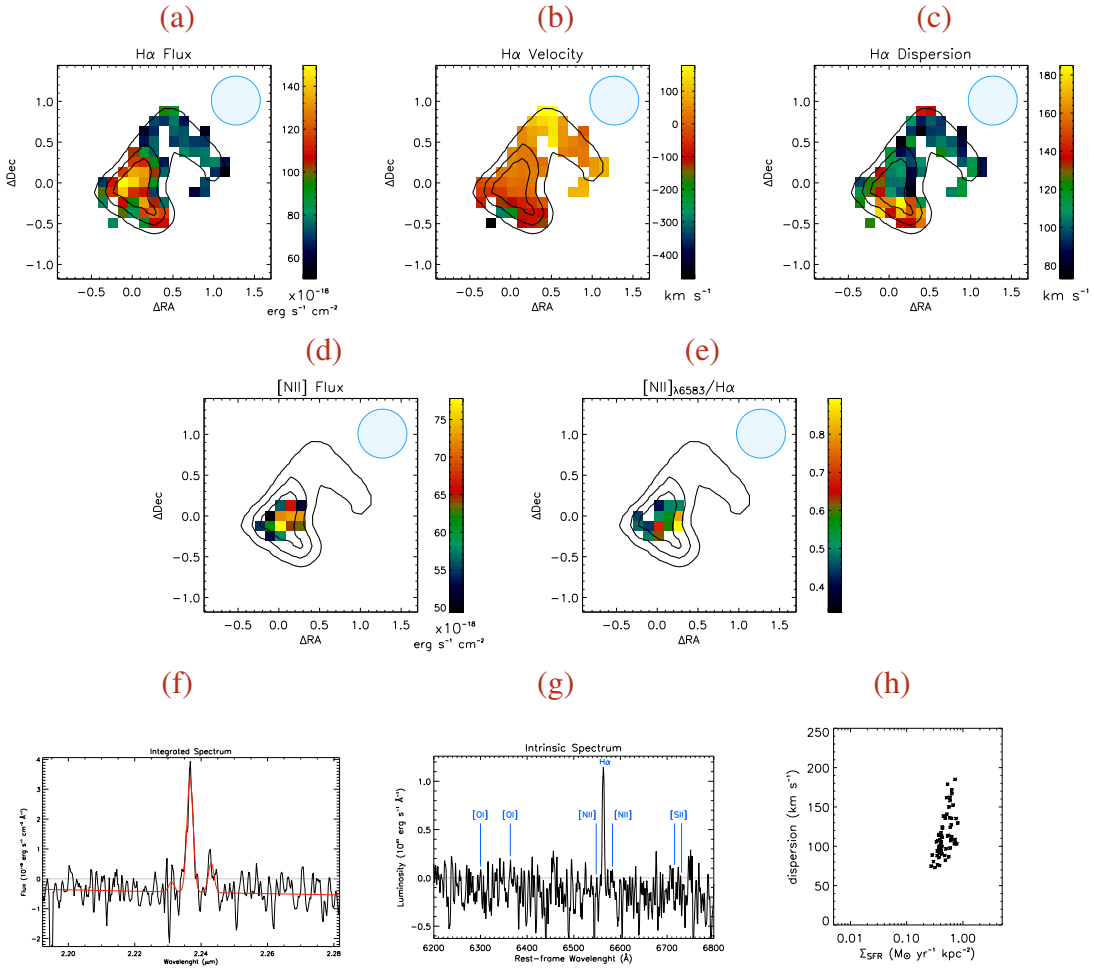

Figure 2.17 (a) Spatial distribution of the Hα line flux, in units of 10^{-18} erg s^{-1} cm^{-2}, (b) Hα velocity field, in km s^{-1}, (c) velocity dispersion distribution, in km s^{-1}, (d) spatial distribution of the [NII] line flux, in units of 10^{-18} erg s^{-1} cm^{-2}, (e) and spatial distribution of the ratio of the [NII] over the Hα line fluxes, (f) integrated spectrum (in observer-frame) centered on the Hα line: the red curve is the best fit for Hα and [NII], (g) intrinsic spectrum (in rest-frame) and (h) Hα velocity dispersion as a function of the star formation rate surface density. The contours superimposed on the maps follow the Hα flux distribution. Blue circles represent the FWHM of the PSF.

2.4.0.7 CDFS-GK2363 $z = 2.45$

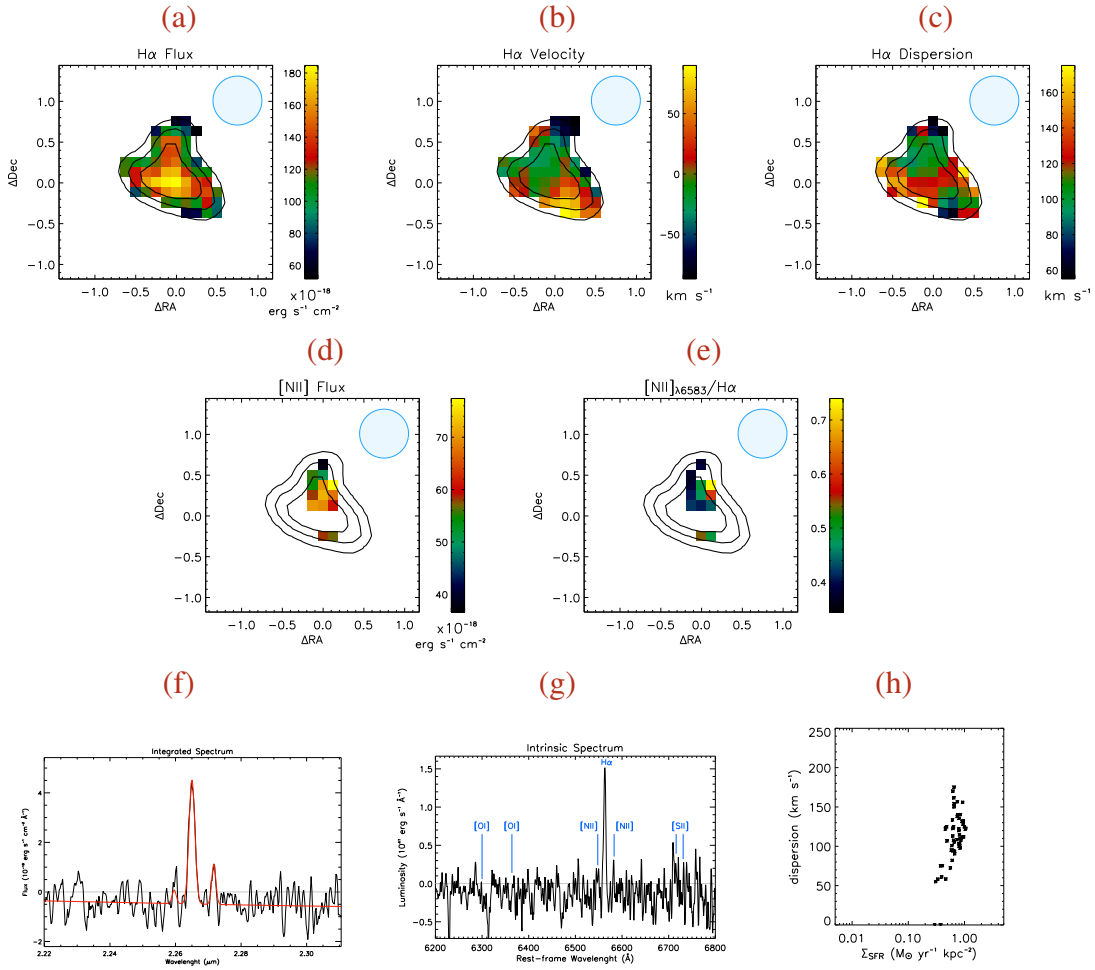

Figure 2.18 (a) Spatial distribution of the Hα line flux, in units of 10^{-18} erg s^{-1} cm^{-2}, (b) Hα velocity field, in km s^{-1}, (c) velocity dispersion distribution, in km s^{-1}, (d) spatial distribution of the [NII] line flux, in units of 10^{-18} erg s^{-1} cm^{-2}, (e) and spatial distribution of the ratio of the [NII] over the Hα line fluxes, (f) integrated spectrum (in observer-frame) centered on the Hα line: the red curve is the best fit for Hα and [NII], (g) intrinsic spectrum (in rest-frame) and (h) Hα velocity dispersion as a function of the star formation rate surface density. The contours superimposed on the maps follow the Hα flux distribution. Blue circles represent the FWHM of the PSF.

2.4.0.8 CDFS-GK2471 $z = 2.43$

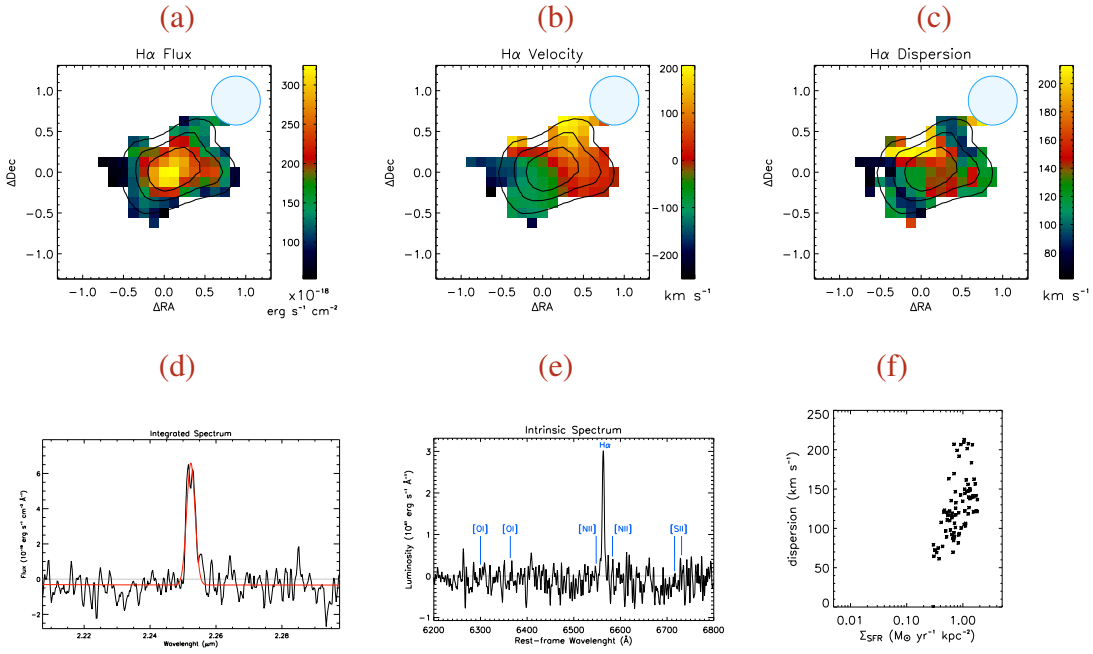

Figure 2.19 (a) Spatial distribution of the Hα line flux, in units of 10^{-18} erg s^{-1} cm^{-2}, (b) Hα velocity field, in km s^{-1}, (c) velocity dispersion distribution, in km s^{-1}, (d) integrated spectrum (in observer-frame) centered on the Hα line: the red curve is the best fit for Hα and [NII], (e) intrinsic spectrum (in rest-frame) and (f) Hα velocity dispersion as a function of the star formation rate surface density. The contours superimposed on the maps follow the Hα flux distribution. Blue circles represent the FWHM of the PSF.

2.4.0.9 DEEP2-32002481 $z = 1.39$

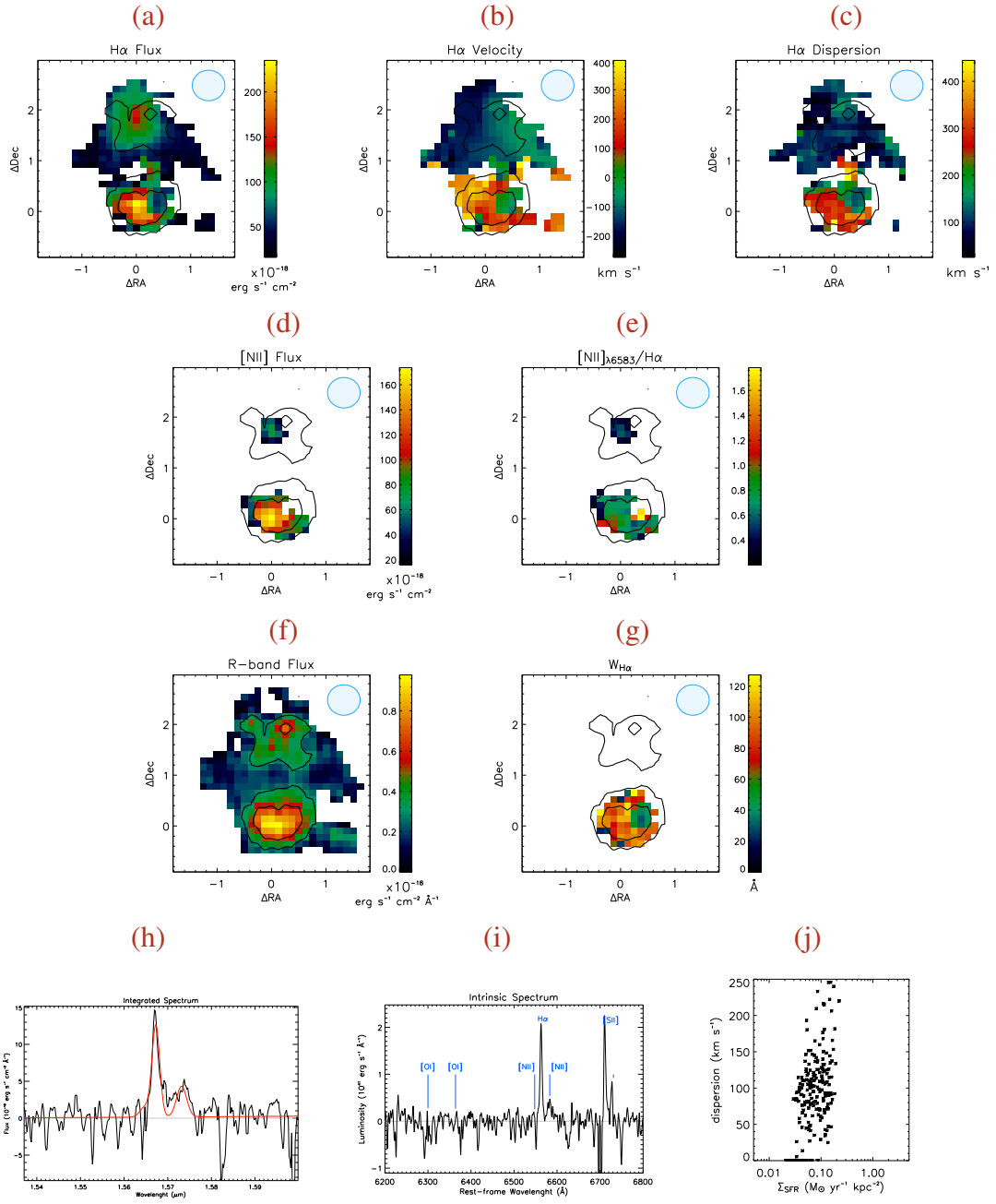

Figure 2.20 (a) Spatial distribution of the Hα line flux, in units of 10^{-18} erg s^{-1} cm^{-2}, (b) Hα velocity field, in km s^{-1}, (c) velocity dispersion distribution, in km s^{-1}, (d) spatial distribution of the [NII] line flux, in units of 10^{-18} erg s^{-1} cm^{-2}, (e) and spatial distribution of the ratio of the [NII] over the Hα line fluxes, (f) *R*-band continuum flux, in units of 10^{-18} erg s^{-1} cm^{-2} Å^{-1}, (g) equivalent width of the Hα line in Å, (h) integrated spectrum (in observer-frame) centered on the Hα line: the red curve is the best fit for Hα and [NII], (i) intrinsic spectrum (in rest-frame) and (j) Hα velocity dispersion as a function of the star formation rate surface density. The contours superimposed on the maps follow the *R*-band flux distribution. Blue circles represent the FWHM of the PSF.

2.4.0.10 DEEP2-32007614 $z = 1.37$

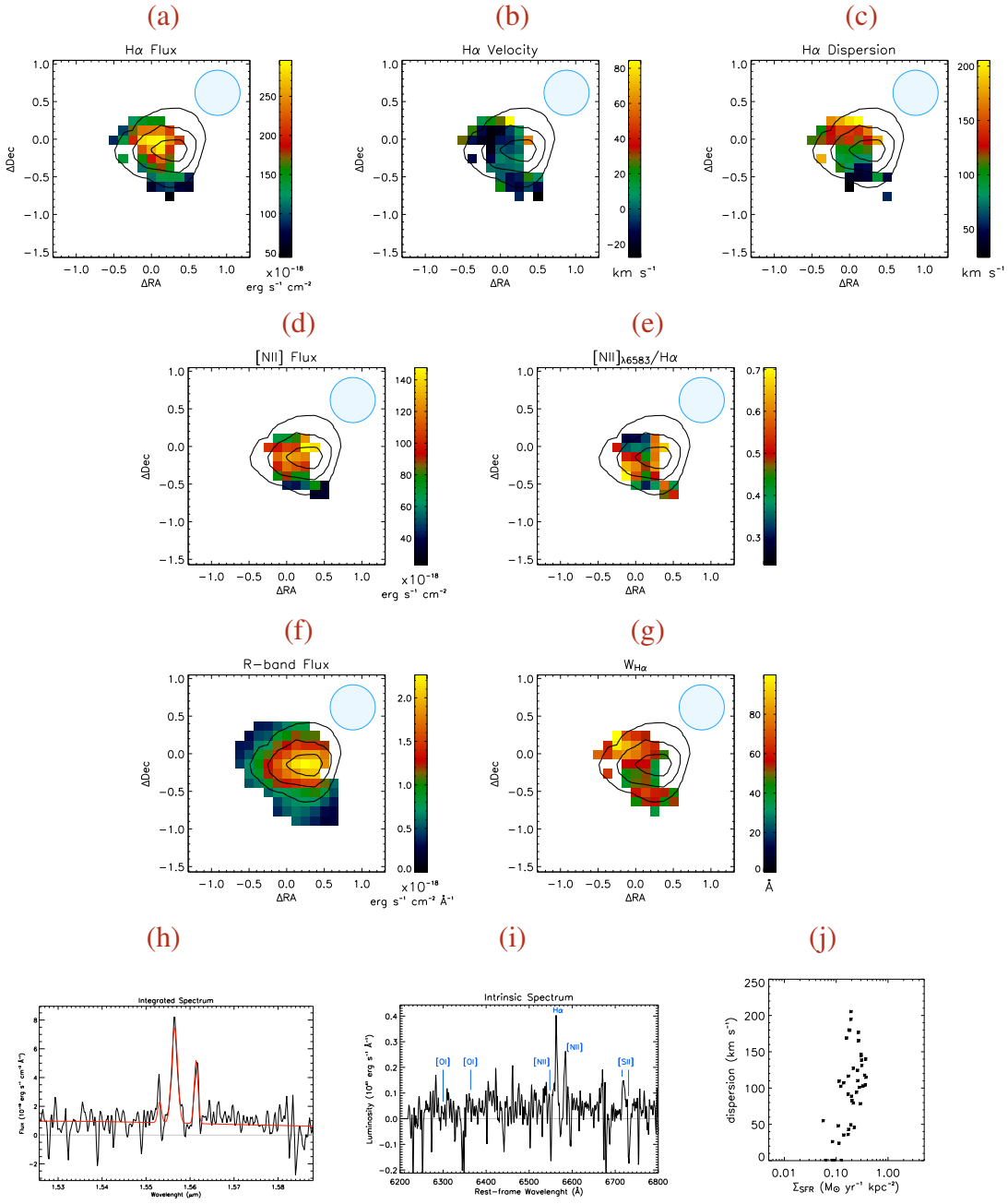

Figure 2.21 (a) Spatial distribution of the Hα line flux, in units of 10^{-18} erg s^{-1} cm^{-2}, (b) Hα velocity field, in km s^{-1}, (c) velocity dispersion distribution, in km s^{-1}, (d) spatial distribution of the [NII] line flux, in units of 10^{-18} erg s^{-1} cm^{-2}, (e) and spatial distribution of the ratio of the [NII] over the Hα line fluxes, (f) *R*-band continuum flux, in units of 10^{-18} erg s^{-1} cm^{-2} Å^{-1}, (g) equivalent width of the Hα line in Å, (h) integrated spectrum (in observer-frame) centered on the Hα line: the red curve is the best fit for Hα and [NII], (i) intrinsic spectrum (in rest-frame) and (j) Hα velocity dispersion as a function of the star formation rate surface density. The contours superimposed on the maps follow the *R*-band flux distribution. Blue circles represent the FWHM of the PSF.

2.4.0.11 DEEP2-32013051 $z = 1.40$

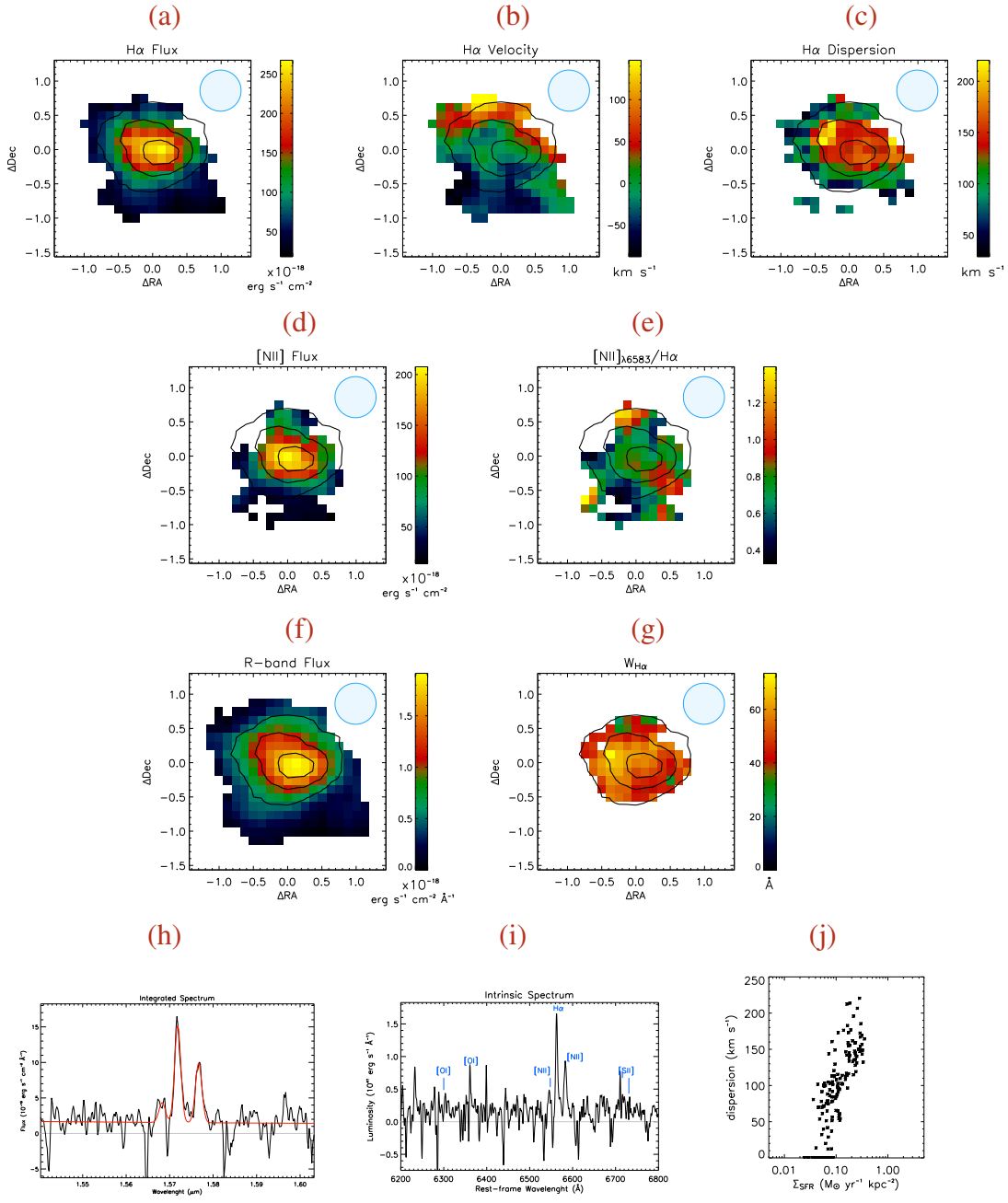

Figure 2.22 (a) Spatial distribution of the Hα line flux, in units of 10^{-18} erg s^{-1} cm^{-2}, (b) Hα velocity field, in km s^{-1}, (c) velocity dispersion distribution, in km s^{-1}, (d) spatial distribution of the [NII] line flux, in units of 10^{-18} erg s^{-1} cm^{-2}, (e) and spatial distribution of the ratio of the [NII] over the Hα line fluxes, (f) *R*-band continuum flux, in units of 10^{-18} erg s^{-1} cm^{-2} Å^{-1}, (g) equivalent width of the Hα line in Å, (h) integrated spectrum (in observer-frame) centered on the Hα line: the red curve is the best fit for Hα and [NII], (i) intrinsic spectrum (in rest-frame) and (j) Hα velocity dispersion as a function of the star formation rate surface density. The contours superimposed on the maps follow the *R*-band flux distribution. Blue circles represent the FWHM of the PSF.

2.4.0.12 DEEP2-32015443

$z = 1.38$

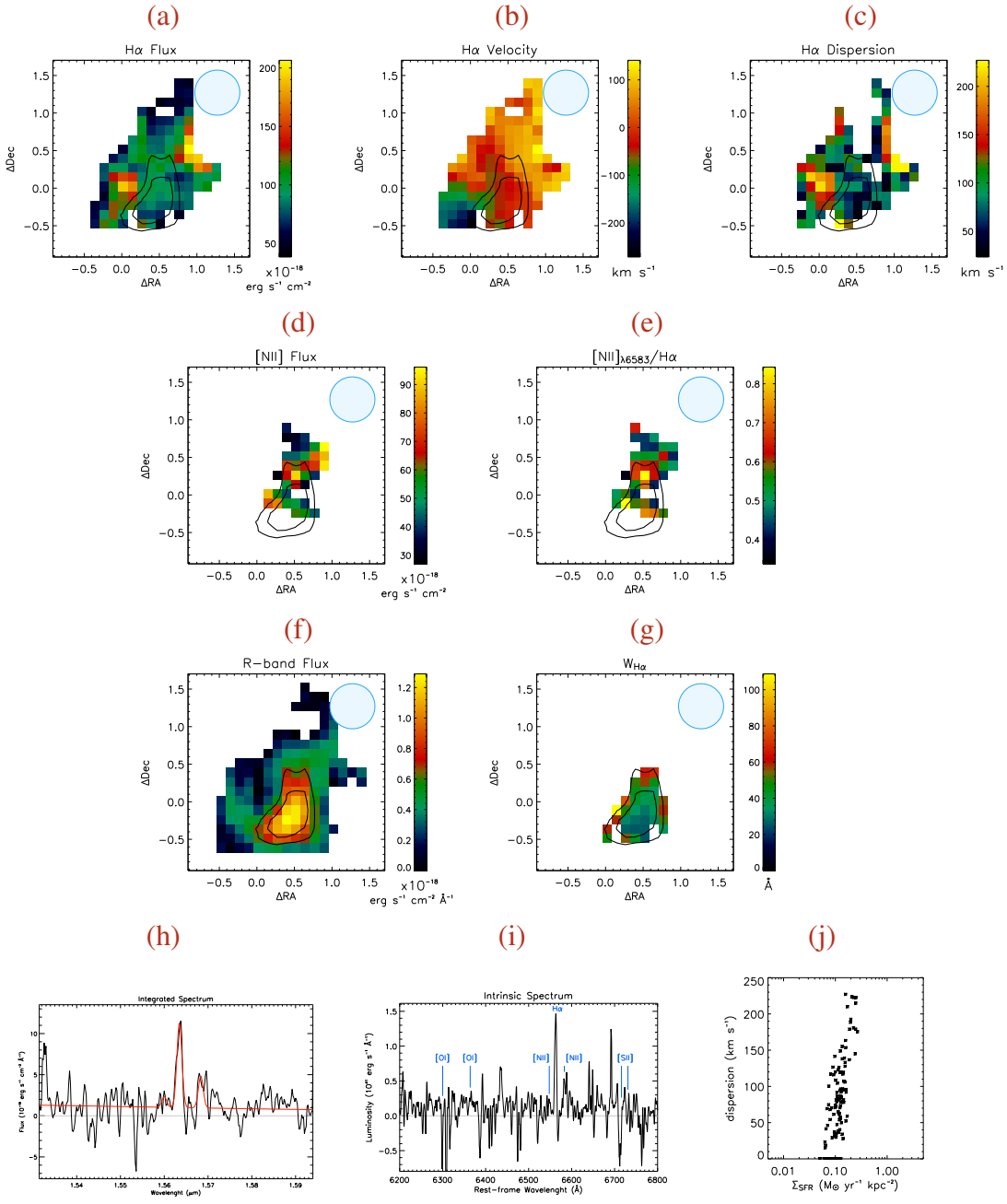

Figure 2.23 (a) Spatial distribution of the Hα line flux, in units of 10^{-18} erg s^{-1} cm^{-2}, (b) Hα velocity field, in km s^{-1}, (c) velocity dispersion distribution, in km s^{-1}, (d) spatial distribution of the [NII] line flux, in units of 10^{-18} erg s^{-1} cm^{-2}, (e) and spatial distribution of the ratio of the [NII] over the Hα line fluxes, (f) *R*-band continuum flux, in units of 10^{-18} erg s^{-1} cm^{-2} Å^{-1}, (g) equivalent width of the Hα line in Å, (h) integrated spectrum (in observer-frame) centered on the Hα line: the red curve is the best fit for Hα and [NII], (i) intrinsic spectrum (in rest-frame) and (j) Hα velocity dispersion as a function of the star formation rate surface density. The contours superimposed on the maps follow the *R*-band flux distribution. Blue circles represent the FWHM of the PSF.

2.4.0.13 DEEP2-32015501 $z = 1.39$

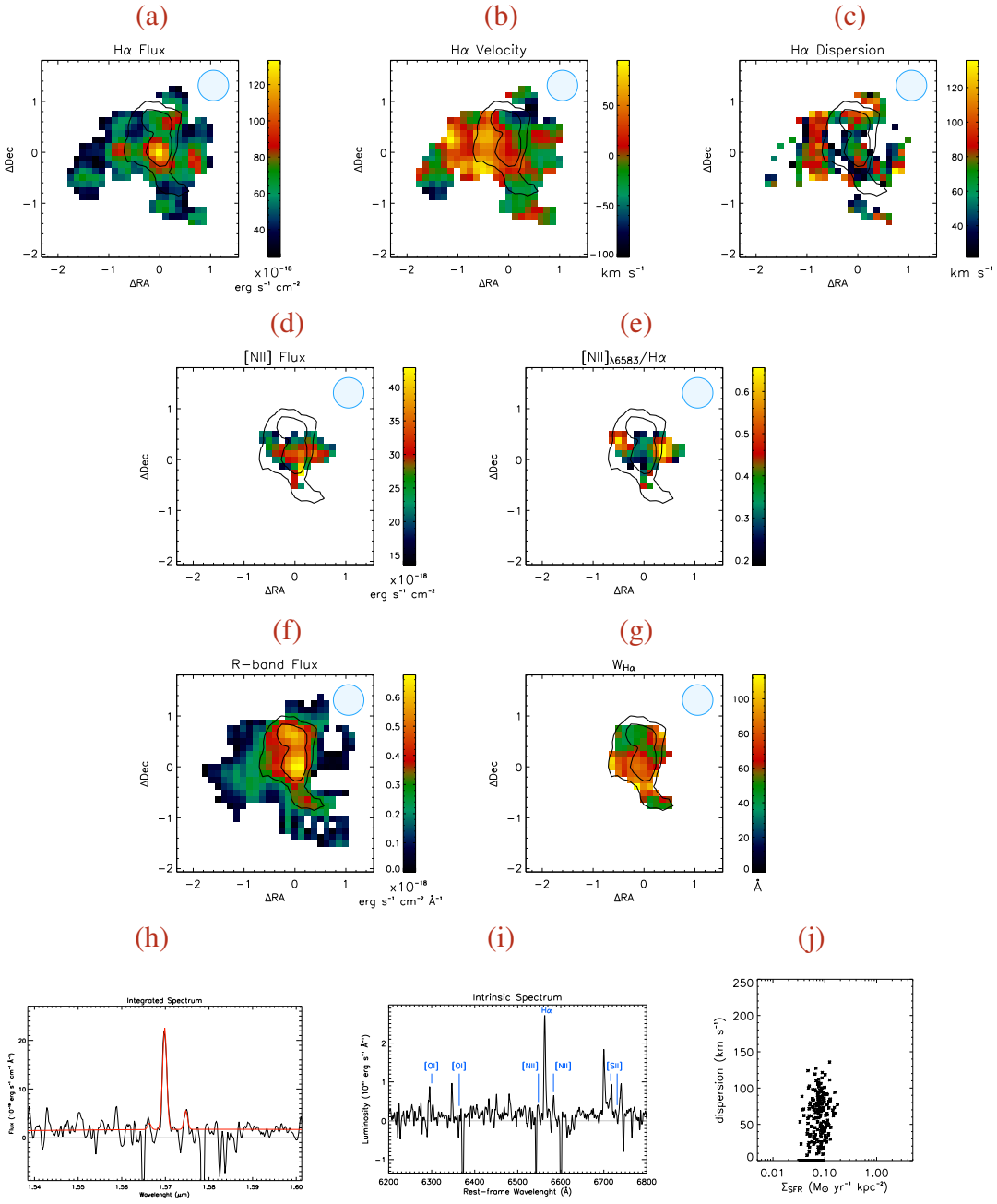

Figure 2.24 (a) Spatial distribution of the Hα line flux, in units of 10^{-18} erg s^{-1} cm^{-2}, (b) Hα velocity field, in km s^{-1}, (c) velocity dispersion distribution, in km s^{-1}, (d) spatial distribution of the [NII] line flux, in units of 10^{-18} erg s^{-1} cm^{-2}, (e) and spatial distribution of the ratio of the [NII] over the Hα line fluxes, (f) *R*-band continuum flux, in units of 10^{-18} erg s^{-1} cm^{-2} Å^{-1}, (g) equivalent width of the Hα line in Å, (h) integrated spectrum (in observer-frame) centered on the Hα line: the red curve is the best fit for Hα and [NII], (i) intrinsic spectrum (in rest-frame) and (j) Hα velocity dispersion as a function of the star formation rate surface density. The contours superimposed on the maps follow the *R*-band flux distribution. Blue circles represent the FWHM of the PSF.

2.4.0.14 DEEP2-32021317 $z = 1.38$

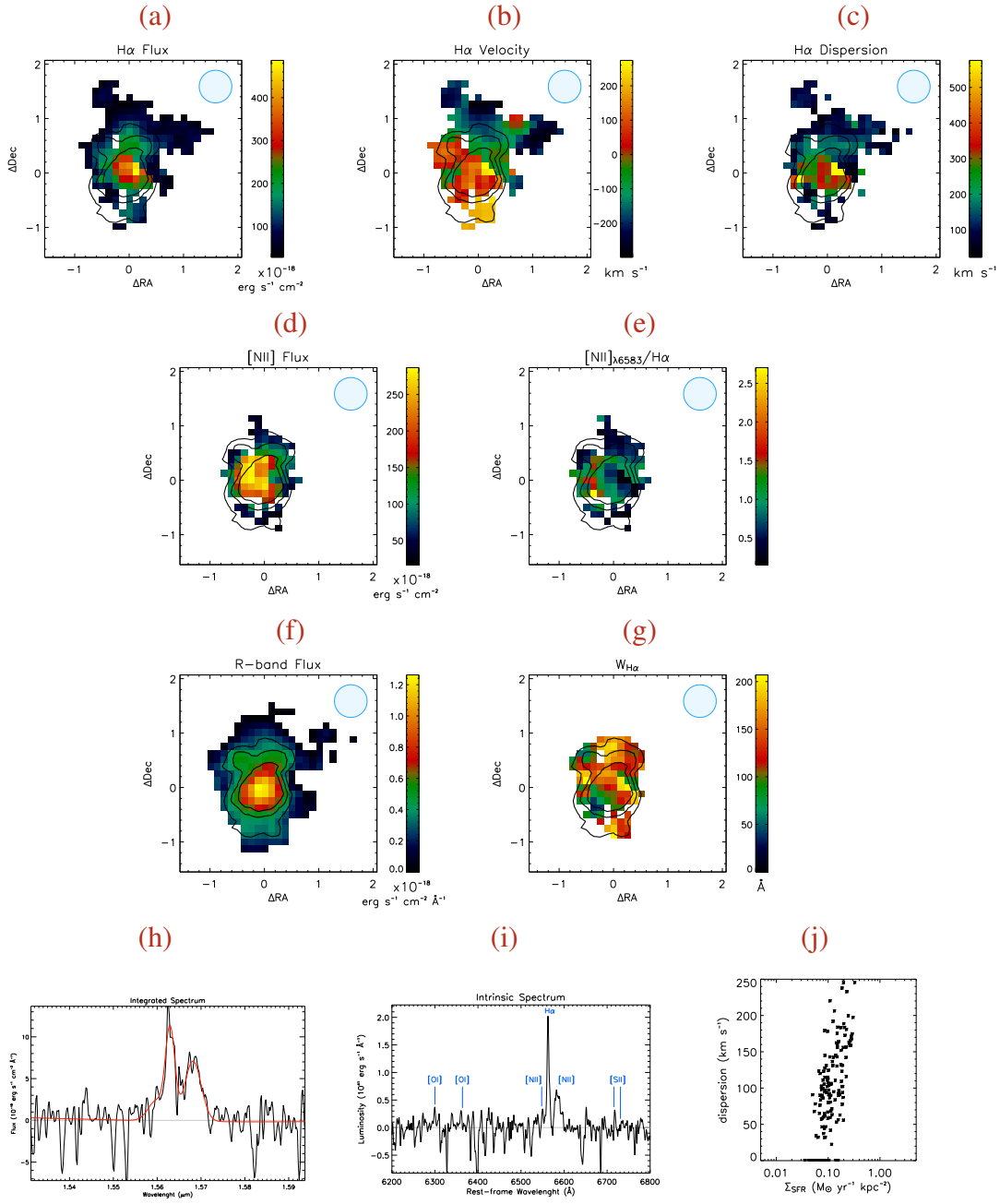

Figure 2.25 (a) Spatial distribution of the Hα line flux, in units of 10^{-18} erg s^{-1} cm^{-2}, (b) Hα velocity field, in km s^{-1}, (c) velocity dispersion distribution, in km s^{-1}, (d) spatial distribution of the [NII] line flux, in units of 10^{-18} erg s^{-1} cm^{-2}, (e) and spatial distribution of the ratio of the [NII] over the Hα line fluxes, (f) *R*-band continuum flux, in units of 10^{-18} erg s^{-1} cm^{-2} Å^{-1}, (g) equivalent width of the Hα line in Å, (h) integrated spectrum (in observer-frame) centered on the Hα line: the red curve is the best fit for Hα and [NII], (i) intrinsic spectrum (in rest-frame) and (j) Hα velocity dispersion as a function of the star formation rate surface density. The contours superimposed on the maps follow the *R*-band flux distribution. Blue circles represent the FWHM of the PSF.

2.4.0.15 DEEP2-32021394 $z = 1.37$

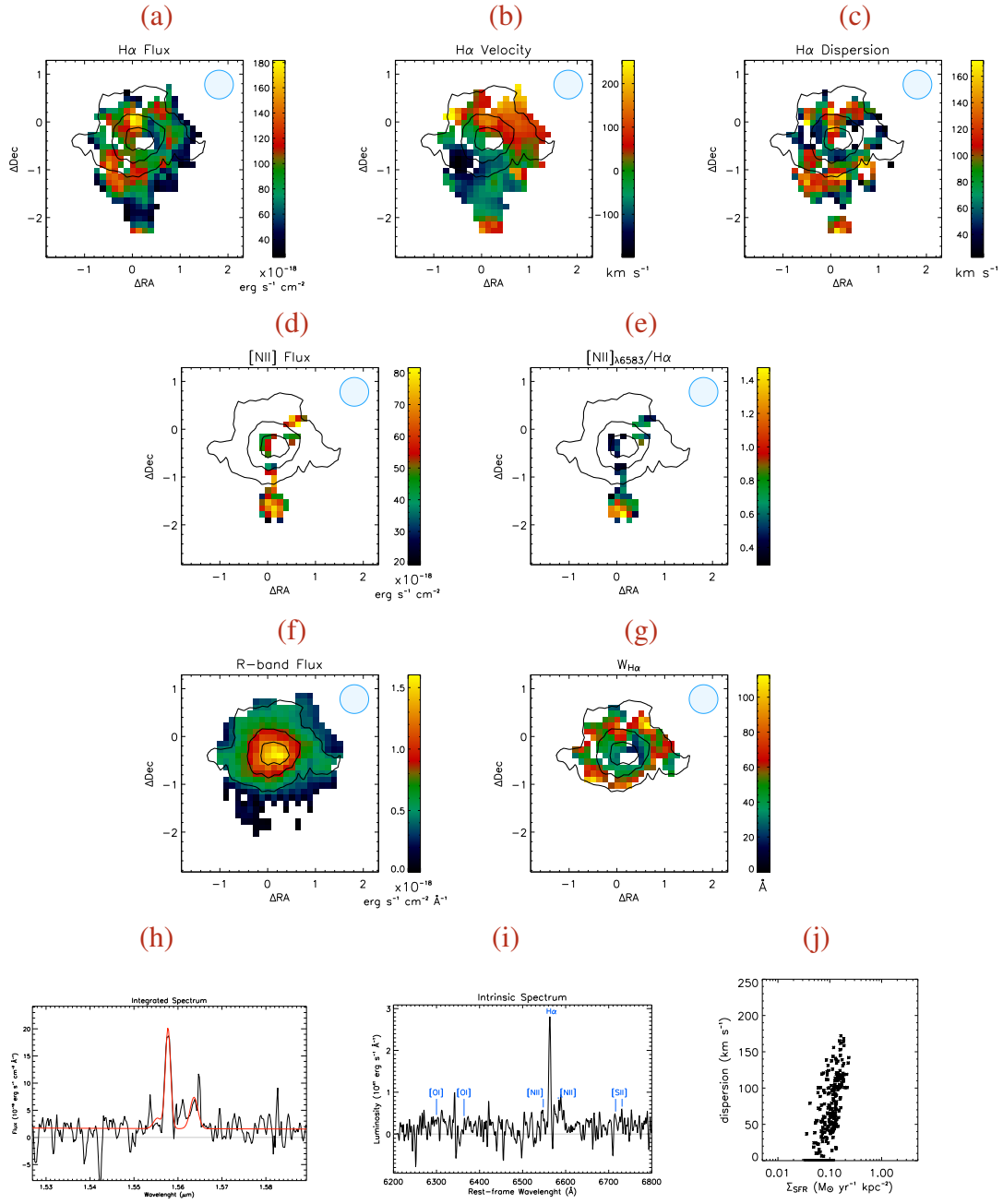

Figure 2.26 (a) Spatial distribution of the Hα line flux, in units of 10^{-18} erg s^{-1} cm^{-2}, (b) Hα velocity field, in km s^{-1}, (c) velocity dispersion distribution, in km s^{-1}, (d) spatial distribution of the [NII] line flux, in units of 10^{-18} erg s^{-1} cm^{-2}, (e) and spatial distribution of the ratio of the [NII] over the Hα line fluxes, (f) *R*-band continuum flux, in units of 10^{-18} erg s^{-1} cm^{-2} Å^{-1}, (g) equivalent width of the Hα line in Å, (h) integrated spectrum (in observer-frame) centered on the Hα line: the red curve is the best fit for Hα and [NII], (i) intrinsic spectrum (in rest-frame) and (j) Hα velocity dispersion as a function of the star formation rate surface density. The contours superimposed on the maps follow the *R*-band flux distribution. Blue circles represent the FWHM of the PSF.

2.4.0.16 DEEP2-32029850 $z = 1.40$

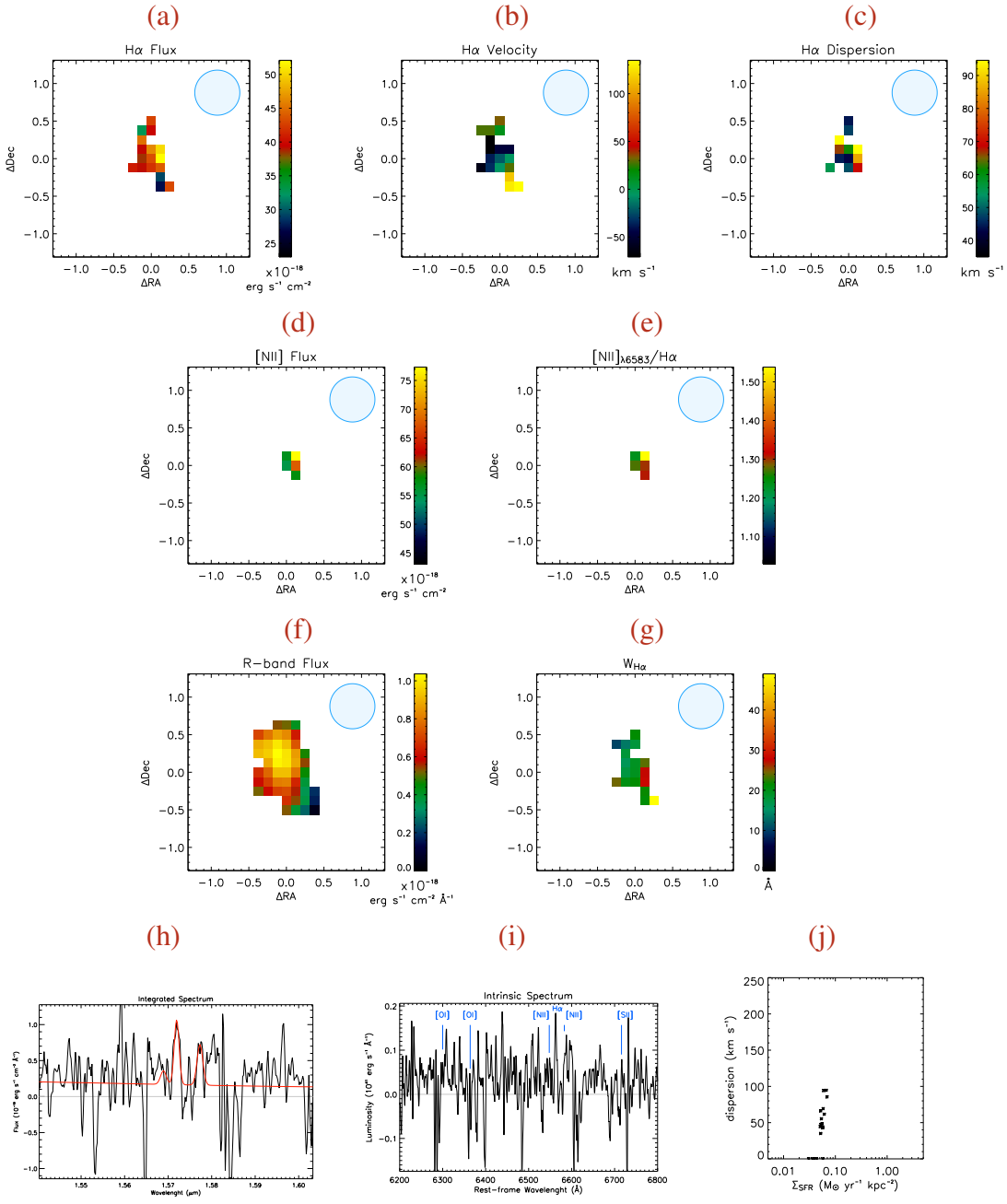

Figure 2.27 (a) Spatial distribution of the Hα line flux, in units of 10^{-18} erg s^{-1} cm^{-2}, (b) Hα velocity field, in km s^{-1}, (c) velocity dispersion distribution, in km s^{-1}, (d) spatial distribution of the [NII] line flux, in units of 10^{-18} erg s^{-1} cm^{-2}, (e) and spatial distribution of the ratio of the [NII] over the Hα line fluxes, (f) *R*-band continuum flux, in units of 10^{-18} erg s^{-1} cm^{-2} Å^{-1}, (g) equivalent width of the Hα line in Å, (h) integrated spectrum (in observer-frame) centered on the Hα line: the red curve is the best fit for Hα and [NII], (i) intrinsic spectrum (in rest-frame) and (j) Hα velocity dispersion as a function of the star formation rate surface density. The contours superimposed on the maps follow the *R*-band flux distribution. Blue circles represent the FWHM of the PSF.

2.4.0.17 DEEP2-32037003 $z = 1.40$

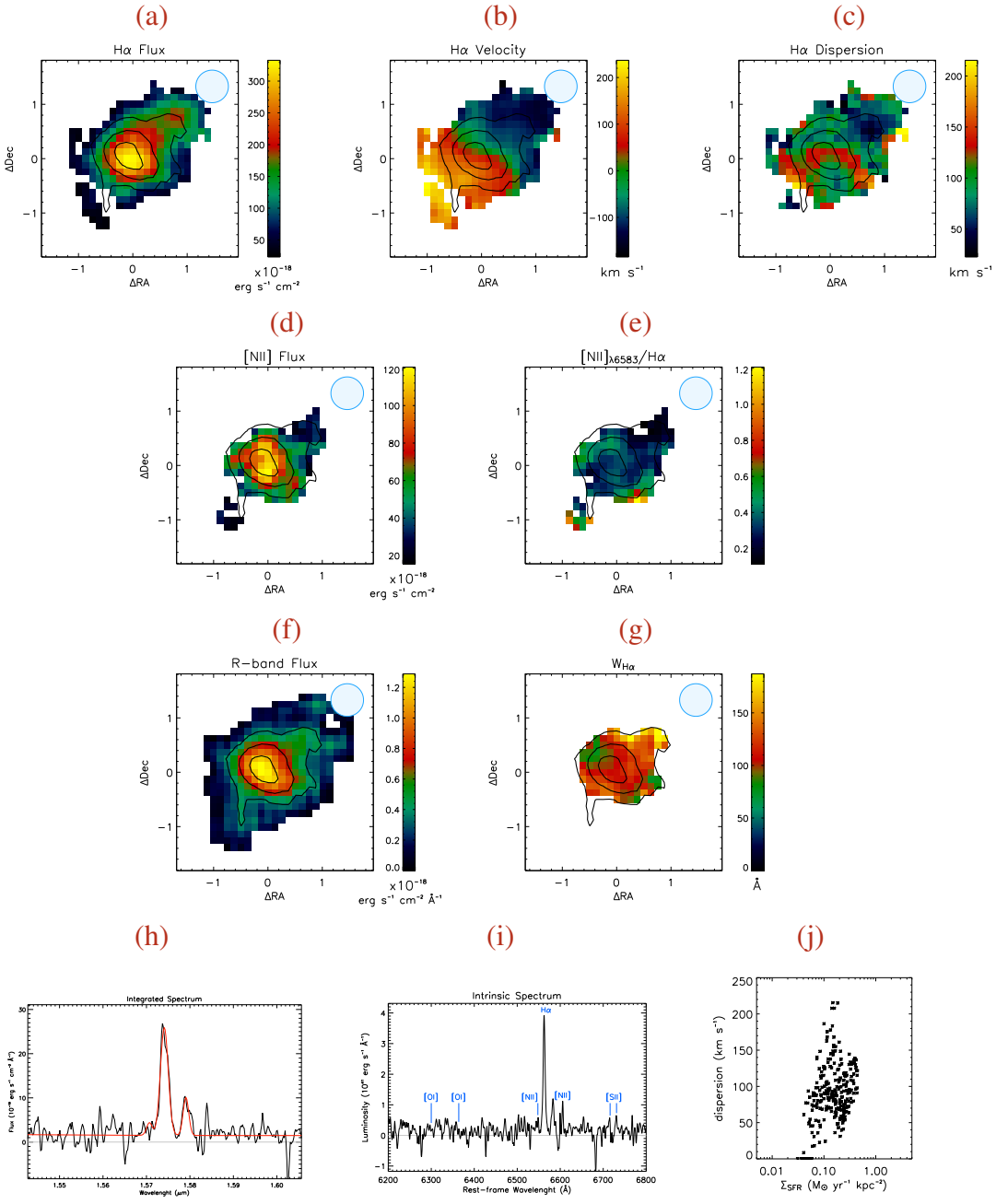

Figure 2.28 (a) Spatial distribution of the Hα line flux, in units of 10^{-18} erg s^{-1} cm^{-2}, (b) Hα velocity field, in km s^{-1}, (c) velocity dispersion distribution, in km s^{-1}, (d) spatial distribution of the [NII] line flux, in units of 10^{-18} erg s^{-1} cm^{-2}, (e) and spatial distribution of the ratio of the [NII] over the Hα line fluxes, (f) *R*-band continuum flux, in units of 10^{-18} erg s^{-1} cm^{-2} Å^{-1}, (g) equivalent width of the Hα line in Å, (h) integrated spectrum (in observer-frame) centered on the Hα line: the red curve is the best fit for Hα and [NII], (i) intrinsic spectrum (in rest-frame) and (j) Hα velocity dispersion as a function of the star formation rate surface density. The contours superimposed on the maps follow the *R*-band flux distribution. Blue circles represent the FWHM of the PSF.

2.4.0.18 DEEP2-32100778

$z = 1.39$

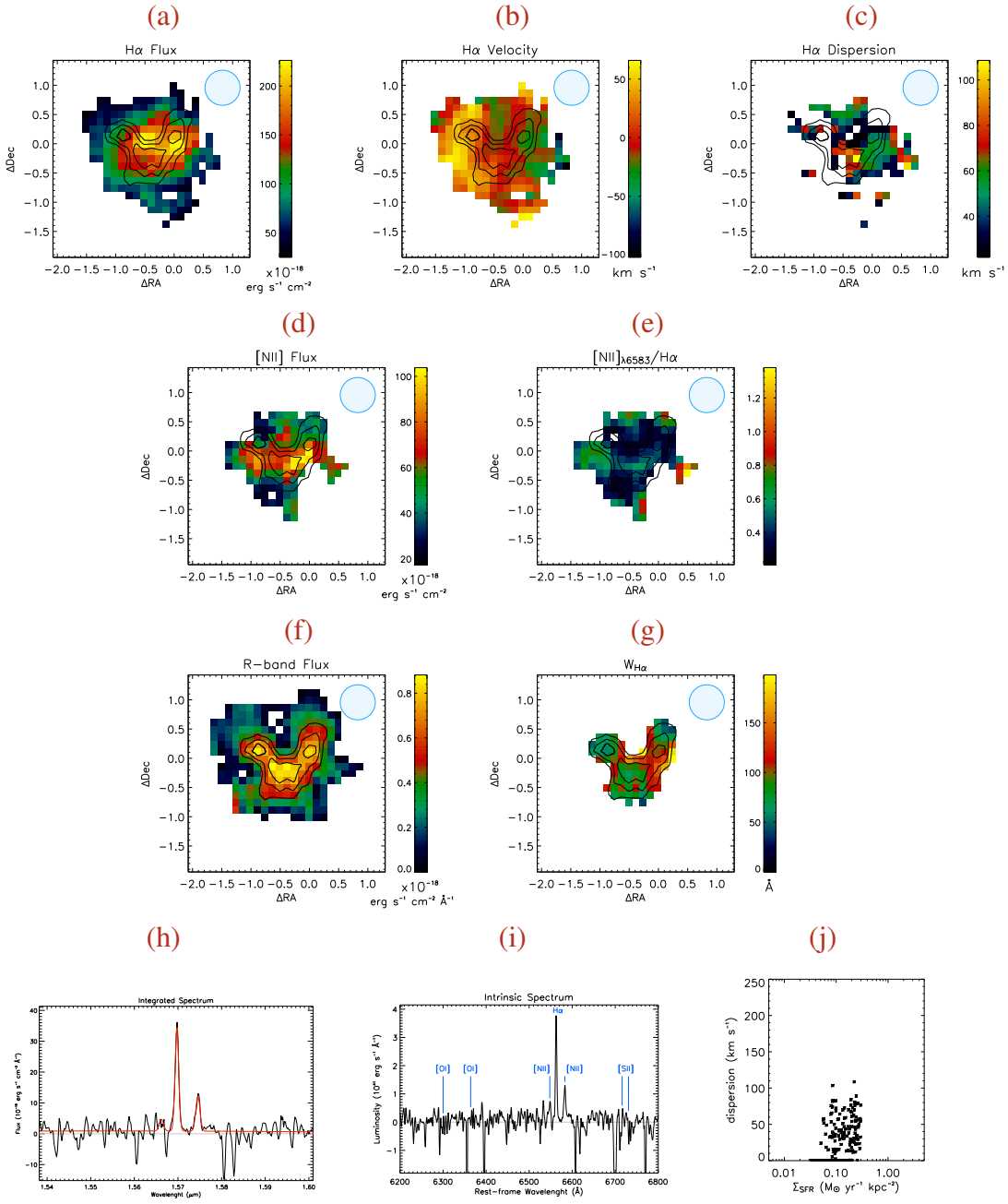

Figure 2.29 (a) Spatial distribution of the Hα line flux, in units of 10^{-18} erg s^{-1} cm^{-2}, (b) Hα velocity field, in km s^{-1}, (c) velocity dispersion distribution, in km s^{-1}, (d) spatial distribution of the [NII] line flux, in units of 10^{-18} erg s^{-1} cm^{-2}, (e) and spatial distribution of the ratio of the [NII] over the Hα line fluxes, (f) *R*-band continuum flux, in units of 10^{-18} erg s^{-1} cm^{-2} Å^{-1}, (g) equivalent width of the Hα line in Å, (h) integrated spectrum (in observer-frame) centered on the Hα line: the red curve is the best fit for Hα and [NII], (i) intrinsic spectrum (in rest-frame) and (j) Hα velocity dispersion as a function of the star formation rate surface density. The contours superimposed on the maps follow the *R*-band flux distribution. Blue circles represent the FWHM of the PSF.

2.4.0.19 ECDFS-04713 $z = 2.31$

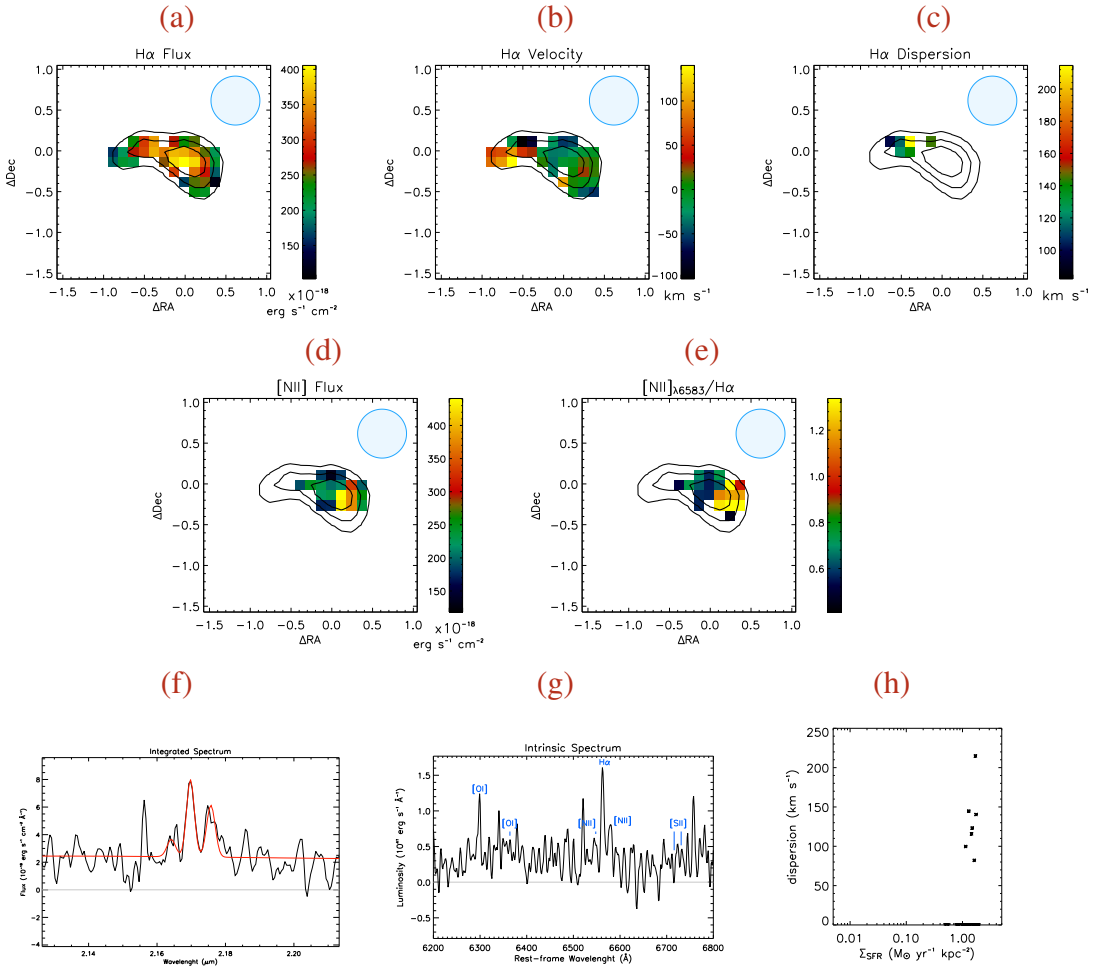

Figure 2.30 (a) Spatial distribution of the Hα line flux, in units of 10^{-18} erg s^{-1} cm^{-2}, (b) Hα velocity field, in km s^{-1}, (c) velocity dispersion distribution, in km s^{-1}, (d) spatial distribution of the [NII] line flux, in units of 10^{-18} erg s^{-1} cm^{-2}, (e) and spatial distribution of the ratio of the [NII] over the Hα line fluxes, (f) integrated spectrum (in observer-frame) centered on the Hα line: the red curve is the best fit for Hα and [NII], (g) intrinsic spectrum (in rest-frame) and (h) Hα velocity dispersion as a function of the star formation rate surface density. The contours superimposed on the maps follow the Hα flux distribution. Blue circles represent the FWHM of the PSF.

2.4.0.20 ECDFS-12514

$z = 2.03$

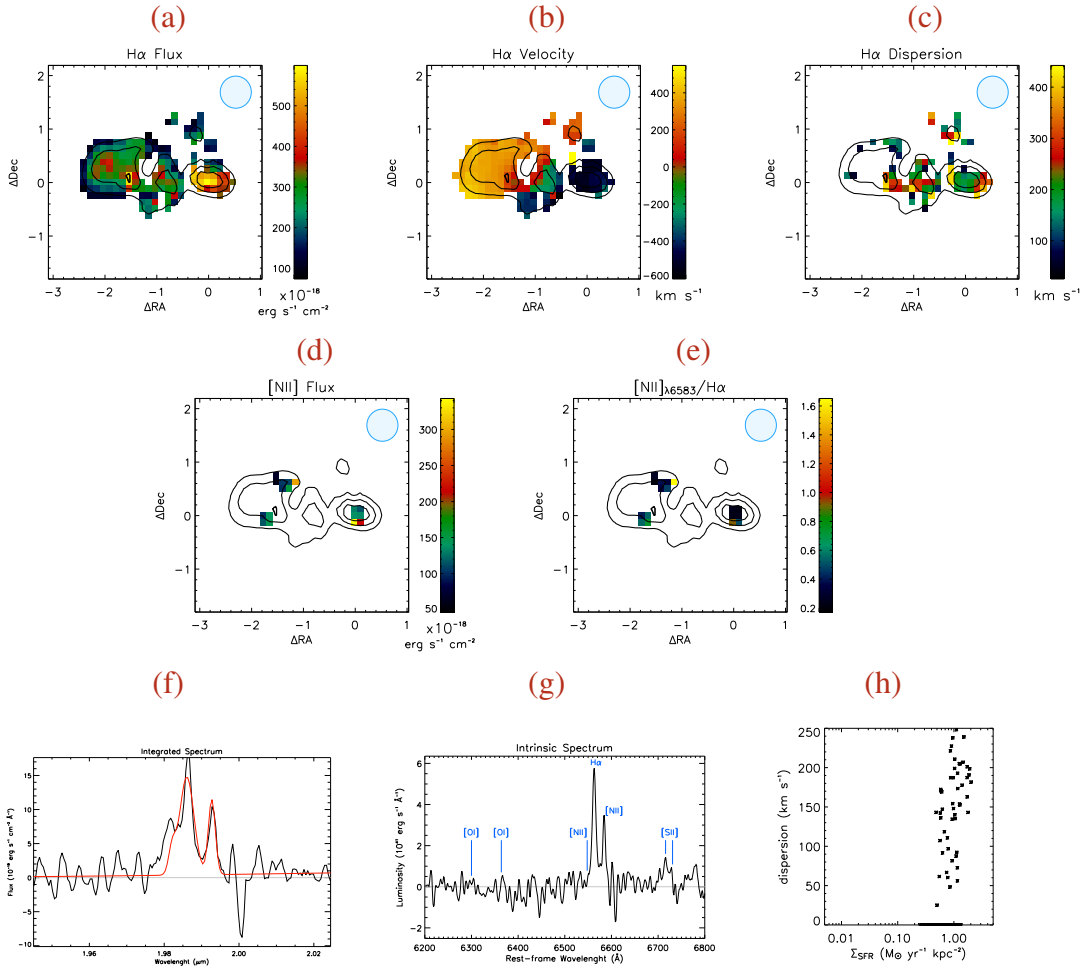

Figure 2.31 (a) Spatial distribution of the Hα line flux, in units of 10^{-18} erg s^{-1} cm^{-2}, (b) Hα velocity field, in km s^{-1}, (c) velocity dispersion distribution, in km s^{-1}, (d) spatial distribution of the [NII] line flux, in units of 10^{-18} erg s^{-1} cm^{-2}, (e) and spatial distribution of the ratio of the [NII] over the Hα line fluxes, (f) integrated spectrum (in observer-frame) centered on the Hα line: the red curve is the best fit for Hα and [NII], (g) intrinsic spectrum (in rest-frame) and (h) Hα velocity dispersion as a function of the star formation rate surface density. The contours superimposed on the maps follow the Hα flux distribution. Blue circles represent the FWHM of the PSF.

2.4.0.21 HDFS1-1884

$z = 2.03$

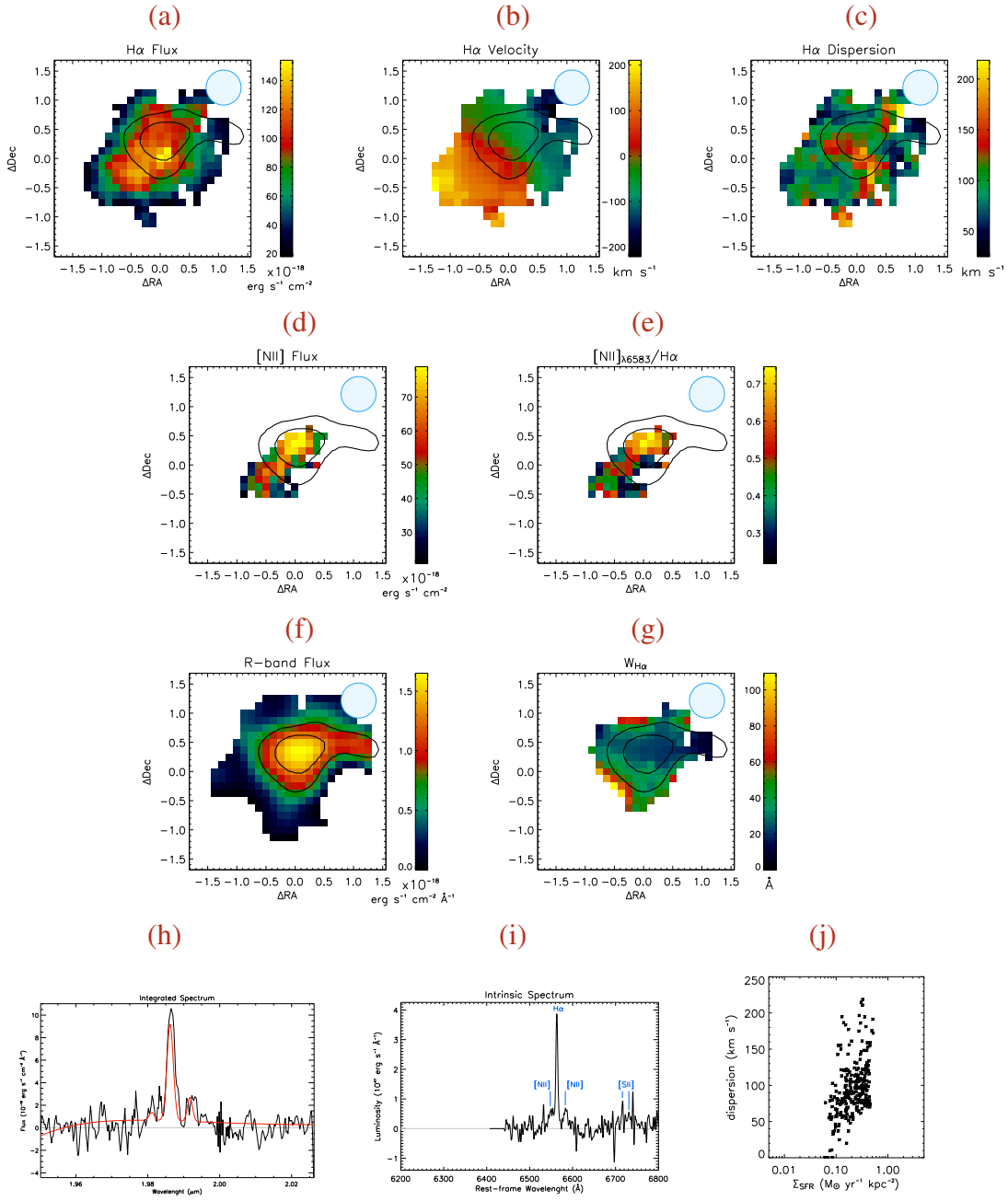

Figure 2.32 (a) Spatial distribution of the Hα line flux, in units of 10^{-18} erg s^{-1} cm^{-2}, (b) Hα velocity field, in km s^{-1}, (c) velocity dispersion distribution, in km s^{-1}, (d) spatial distribution of the [NII] line flux, in units of 10^{-18} erg s^{-1} cm^{-2}, (e) and spatial distribution of the ratio of the [NII] over the Hα line fluxes, (f) *R*-band continuum flux, in units of 10^{-18} erg s^{-1} cm^{-2} Å^{-1}, (g) equivalent width of the Hα line in Å, (h) integrated spectrum (in observer-frame) centered on the Hα line: the red curve is the best fit for Hα and [NII], (i) intrinsic spectrum (in rest-frame) and (j) Hα velocity dispersion as a function of the star formation rate surface density. The contours superimposed on the maps follow the *R*-band flux distribution. Blue circles represent the FWHM of the PSF.

2.4.0.22 K20-ID4

$z = 1.59$

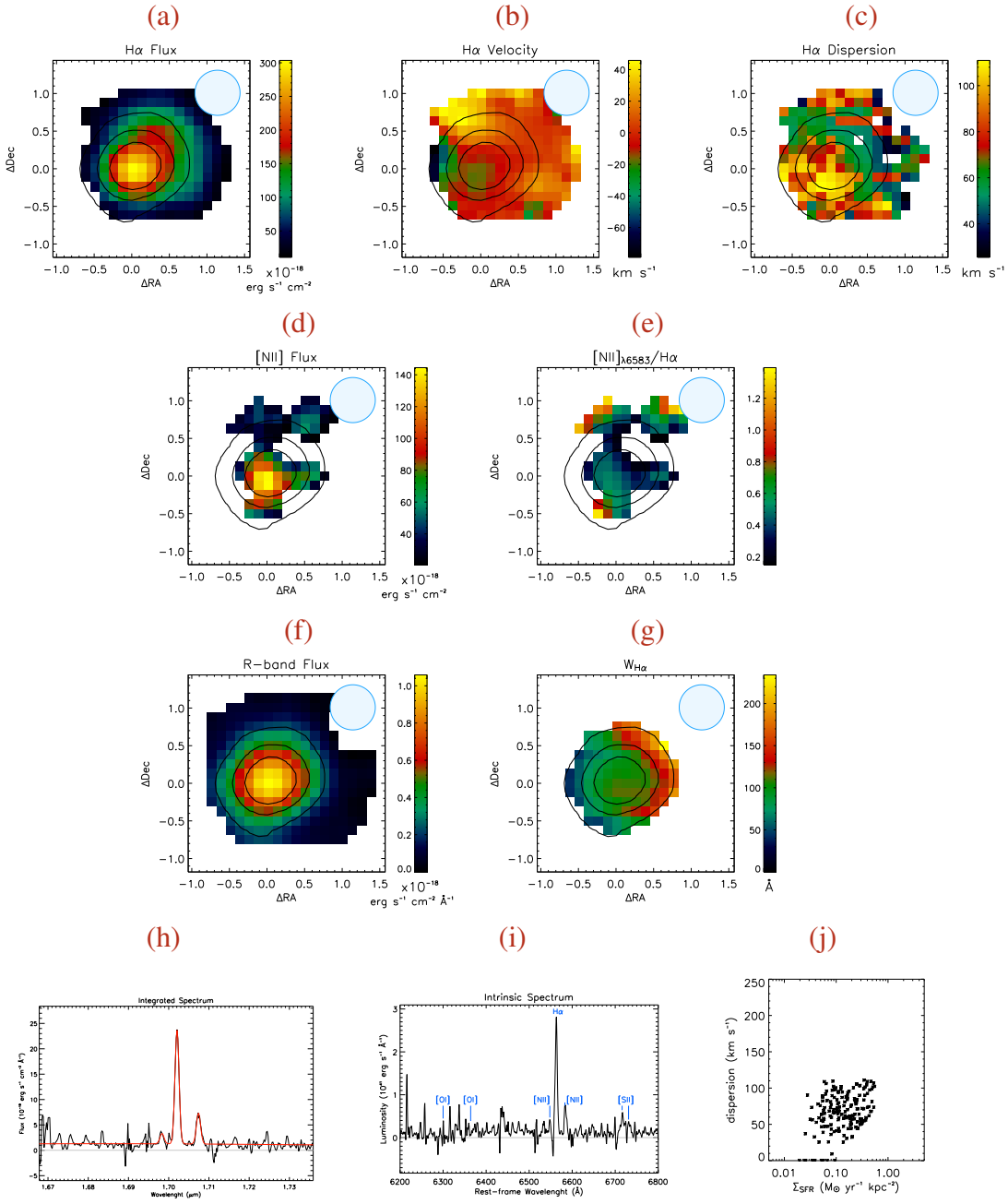

Figure 2.33 (a) Spatial distribution of the Hα line flux, in units of 10^{-18} erg s^{-1} cm^{-2}, (b) Hα velocity field, in km s^{-1}, (c) velocity dispersion distribution, in km s^{-1}, (d) spatial distribution of the [NII] line flux, in units of 10^{-18} erg s^{-1} cm^{-2}, (e) and spatial distribution of the ratio of the [NII] over the Hα line fluxes, (f) *R*-band continuum flux, in units of 10^{-18} erg s^{-1} cm^{-2} Å^{-1}, (g) equivalent width of the Hα line in Å, (h) integrated spectrum (in observer-frame) centered on the Hα line: the red curve is the best fit for Hα and [NII], (i) intrinsic spectrum (in rest-frame) and (j) Hα velocity dispersion as a function of the star formation rate surface density. The contours superimposed on the maps follow the *R*-band flux distribution. Blue circles represent the FWHM of the PSF.

2.4.0.23 K20-ID5

$z = 2.22$

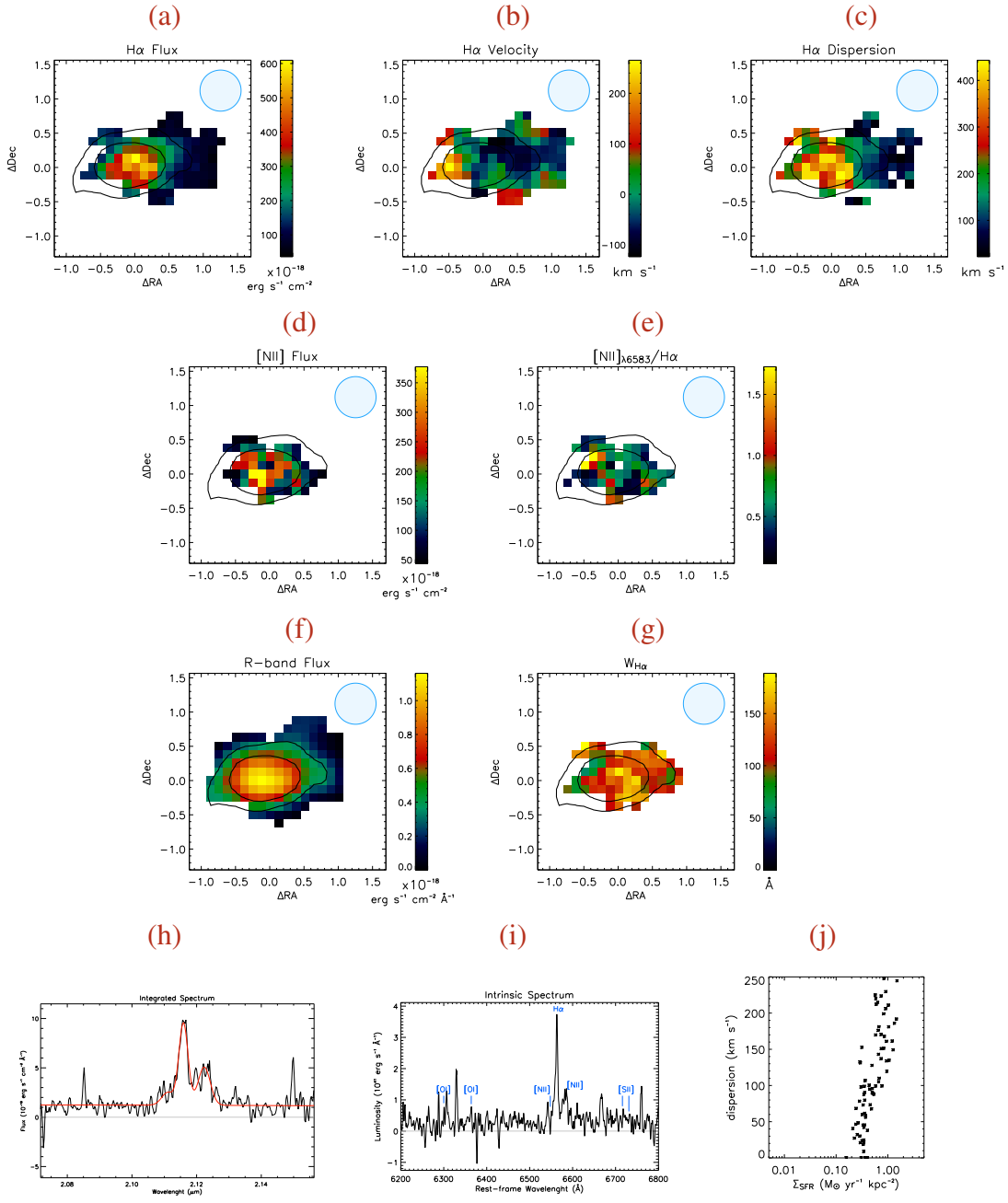

Figure 2.34 (a) Spatial distribution of the Hα line flux, in units of 10^{-18} erg s^{-1} cm^{-2}, (b) Hα velocity field, in km s^{-1}, (c) velocity dispersion distribution, in km s^{-1}, (d) spatial distribution of the [NII] line flux, in units of 10^{-18} erg s^{-1} cm^{-2}, (e) and spatial distribution of the ratio of the [NII] over the Hα line fluxes, (f) *R*-band continuum flux, in units of 10^{-18} erg s^{-1} cm^{-2} Å^{-1}, (g) equivalent width of the Hα line in Å, (h) integrated spectrum (in observer-frame) centered on the Hα line: the red curve is the best fit for Hα and [NII], (i) intrinsic spectrum (in rest-frame) and (j) Hα velocity dispersion as a function of the star formation rate surface density. The contours superimposed on the maps follow the *R*-band flux distribution. Blue circles represent the FWHM of the PSF.

2.4.0.24 K20-ID7

$z = 2.22$

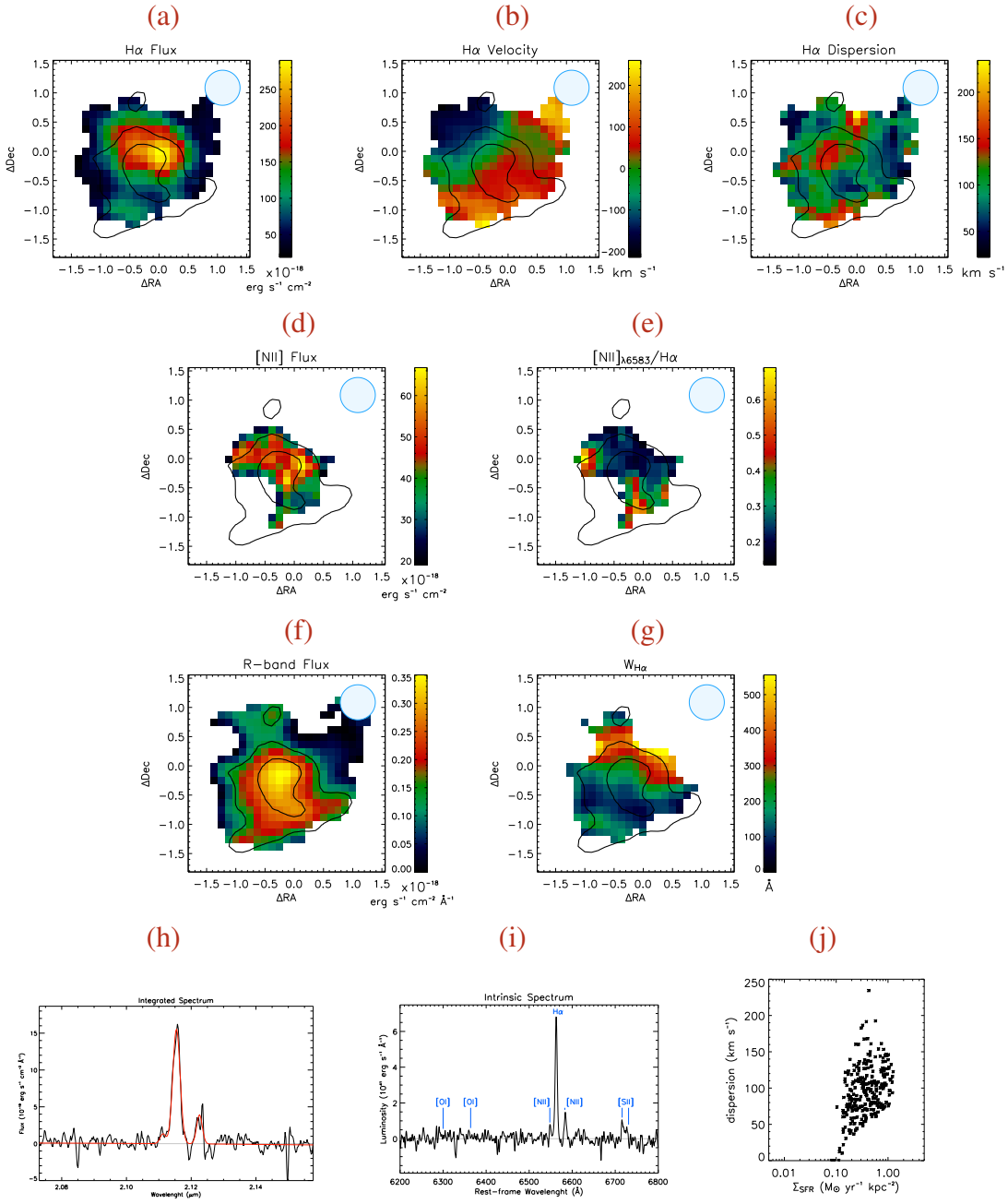

Figure 2.35 (a) Spatial distribution of the Hα line flux, in units of 10^{-18} erg s^{-1} cm^{-2}, (b) Hα velocity field, in km s^{-1}, (c) velocity dispersion distribution, in km s^{-1}, (d) spatial distribution of the [NII] line flux, in units of 10^{-18} erg s^{-1} cm^{-2}, (e) and spatial distribution of the ratio of the [NII] over the Hα line fluxes, (f) *R*-band continuum flux, in units of 10^{-18} erg s^{-1} cm^{-2} Å^{-1}, (g) equivalent width of the Hα line in Å, (h) integrated spectrum (in observer-frame) centered on the Hα line: the red curve is the best fit for Hα and [NII], (i) intrinsic spectrum (in rest-frame) and (j) Hα velocity dispersion as a function of the star formation rate surface density. The contours superimposed on the maps follow the *R*-band flux distribution. Blue circles represent the FWHM of the PSF.

2.4.0.25 K20-ID8

$z = 2.22$

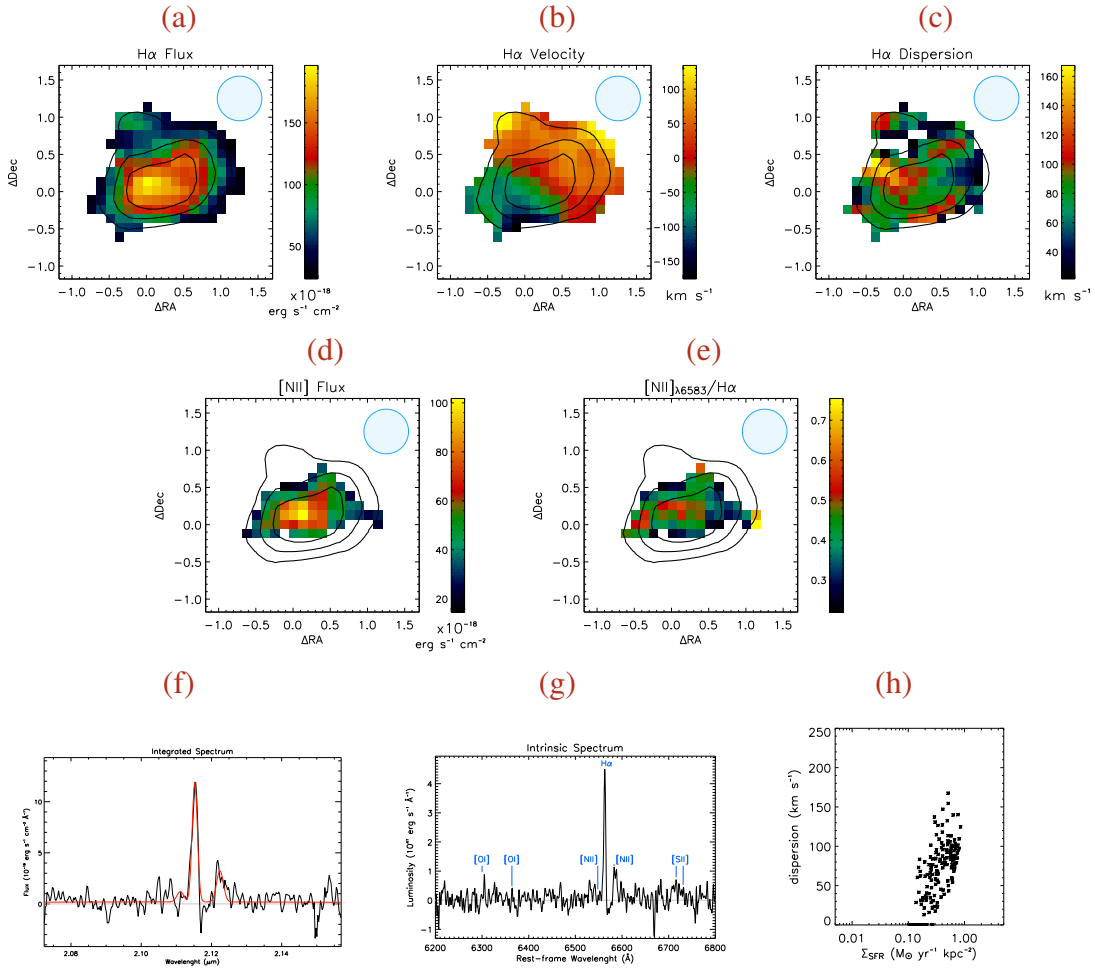

Figure 2.36 (a) Spatial distribution of the Hα line flux, in units of 10^{-18} erg s^{-1} cm^{-2}, (b) Hα velocity field, in km s^{-1}, (c) velocity dispersion distribution, in km s^{-1}, (d) spatial distribution of the [NII] line flux, in units of 10^{-18} erg s^{-1} cm^{-2}, (e) and spatial distribution of the ratio of the [NII] over the Hα line fluxes, (f) integrated spectrum (in observer-frame) centered on the Hα line: the red curve is the best fit for Hα and [NII], (g) intrinsic spectrum (in rest-frame) and (h) Hα velocity dispersion as a function of the star formation rate surface density. The contours superimposed on the maps follow the Hα flux distribution. Blue circles represent the FWHM of the PSF.

2.4.0.26 Q1623-BX376

$z = 2.41$

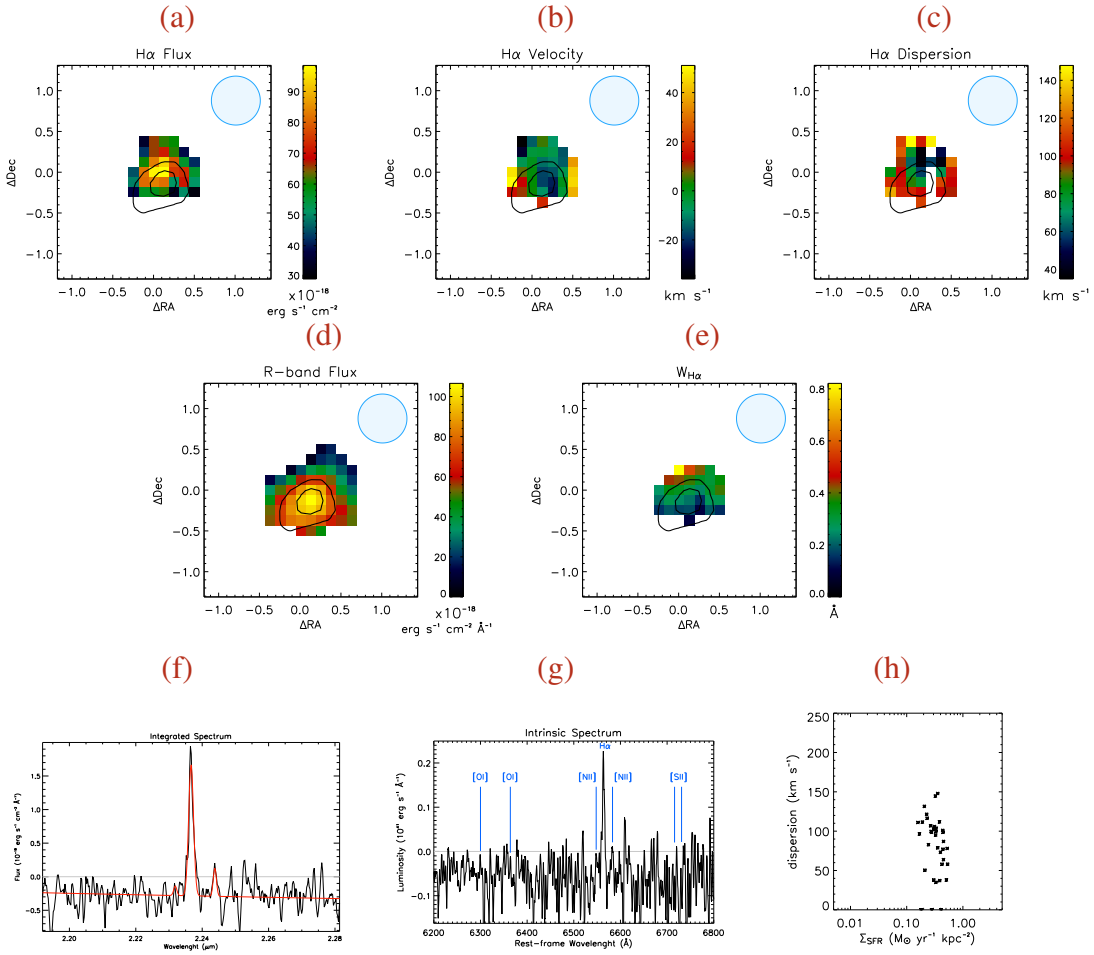

Figure 2.37 (a) Spatial distribution of the Hα line flux, in units of 10^{-18} erg s^{-1} cm^{-2}, (b) Hα velocity field, in km s^{-1}, (c) velocity dispersion distribution, in km s^{-1}, (d) *R*-band continuum flux, in units of 10^{-18} erg s^{-1} cm^{-2} Å^{-1}, (e) equivalent width of the Hα line in Å, (f) integrated spectrum (in observer-frame) centered on the Hα line: the red curve is the best fit for Hα and [NII], (g) intrinsic spectrum (in rest-frame) and (h) Hα velocity dispersion as a function of the star formation rate surface density. The contours superimposed on the maps follow the *R*-band flux distribution. Blue circles represent the FWHM of the PSF.

2.4.0.27 Q1623-BX447 $z = 2.15$

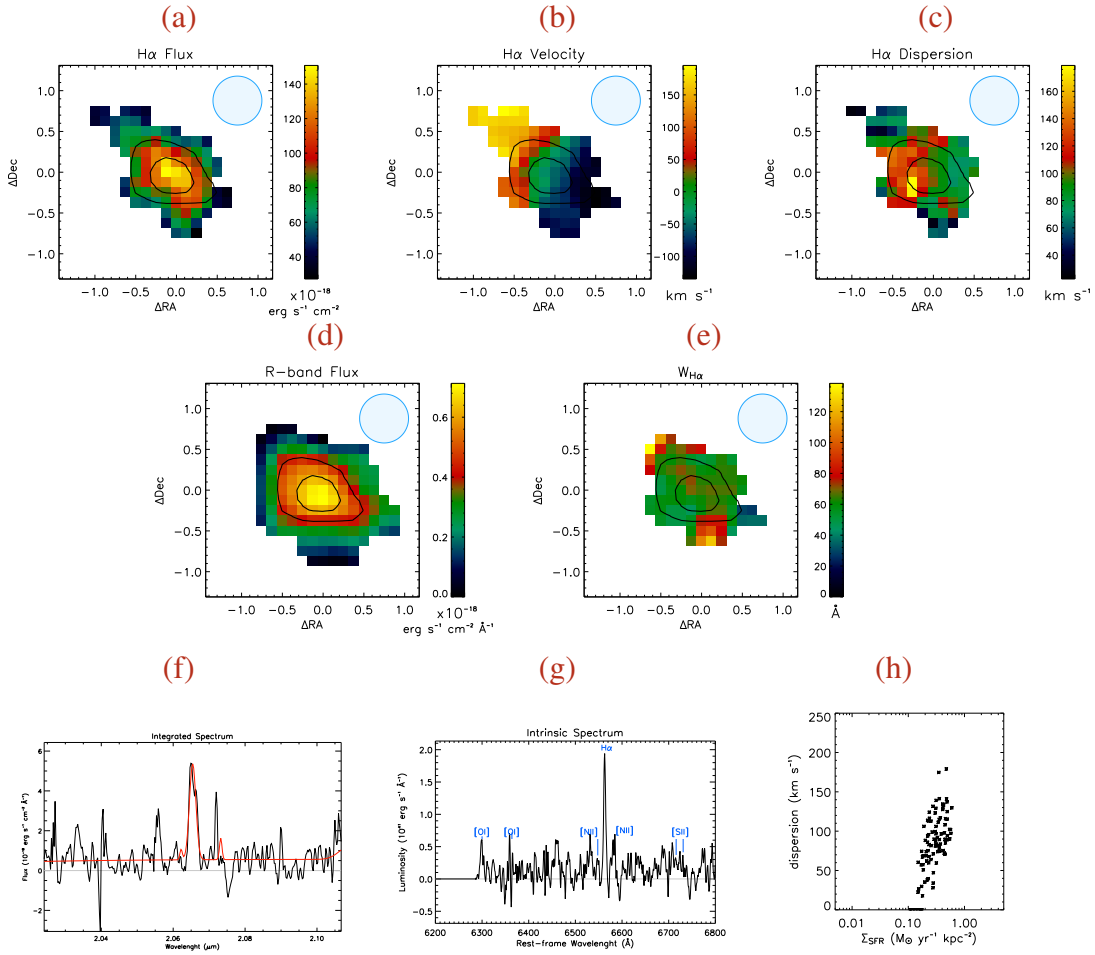

Figure 2.38 (a) Spatial distribution of the Hα line flux, in units of 10^{-18} erg s^{-1} cm^{-2}, (b) Hα velocity field, in km s^{-1}, (c) velocity dispersion distribution, in km s^{-1}, (d) R-band continuum flux, in units of 10^{-18} erg s^{-1} cm^{-2} Å^{-1}, (e) equivalent width of the Hα line in Å, (f) integrated spectrum (in observer-frame) centered on the Hα line: the red curve is the best fit for Hα and [NII], (g) intrinsic spectrum (in rest-frame) and (h) Hα velocity dispersion as a function of the star formation rate surface density. The contours superimposed on the maps follow the R-band flux distribution. Blue circles represent the FWHM of the PSF.

2.4.0.28 Q1623-BX455

$z = 2.41$

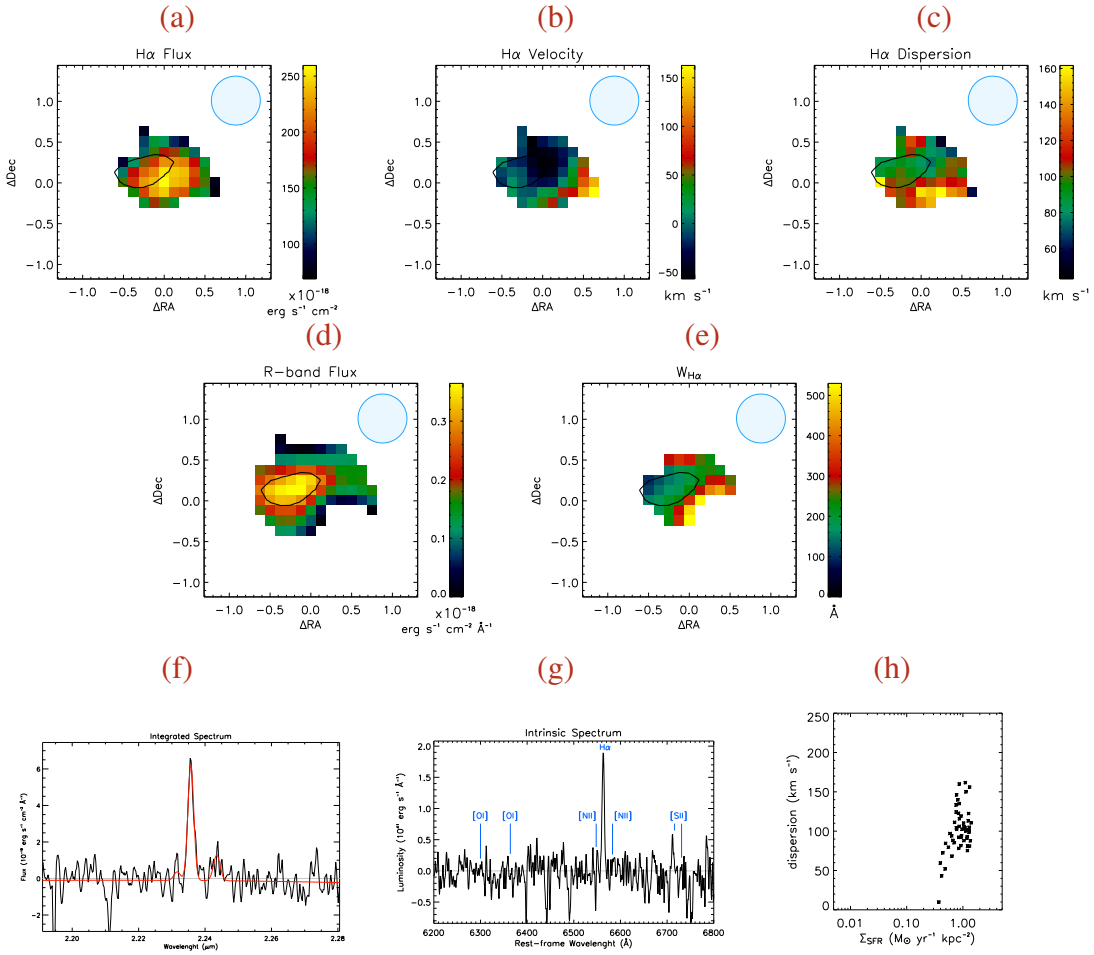

Figure 2.39 (a) Spatial distribution of the Hα line flux, in units of 10^{-18} erg s^{-1} cm^{-2}, (b) Hα velocity field, in km s^{-1}, (c) velocity dispersion distribution, in km s^{-1}, (d) *R*-band continuum flux, in units of 10^{-18} erg s^{-1} cm^{-2} Å^{-1}, (e) equivalent width of the Hα line in Å, (f) integrated spectrum (in observer-frame) centered on the Hα line: the red curve is the best fit for Hα and [NII], (g) intrinsic spectrum (in rest-frame) and (h) Hα velocity dispersion as a function of the star formation rate surface density. The contours superimposed on the maps follow the *R*-band flux distribution. Blue circles represent the FWHM of the PSF.

2.4.0.29 Q1623-BX543

$z = 2.52$

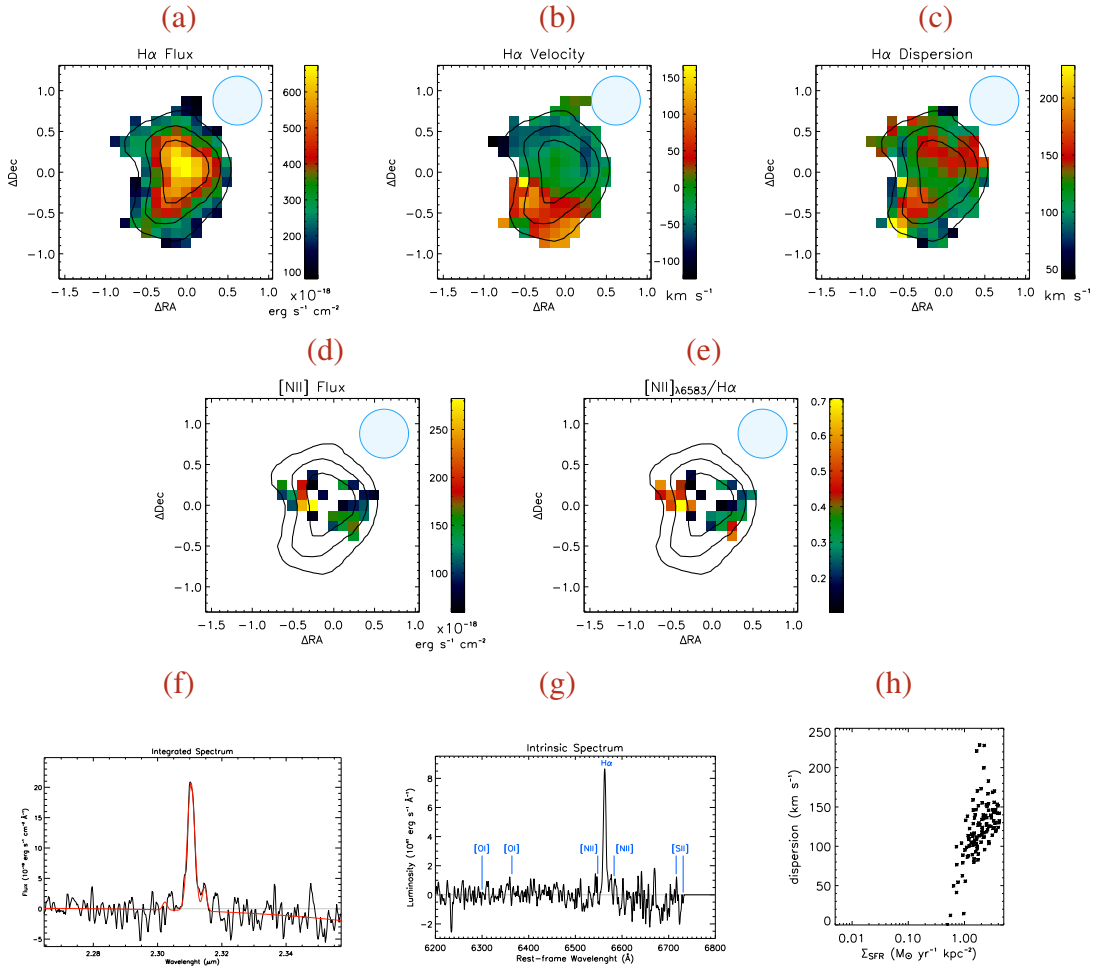

Figure 2.40 (a) Spatial distribution of the Hα line flux, in units of 10^{-18} erg s^{-1} cm^{-2}, (b) Hα velocity field, in km s^{-1}, (c) velocity dispersion distribution, in km s^{-1}, (d) spatial distribution of the [NII] line flux, in units of 10^{-18} erg s^{-1} cm^{-2}, (e) and spatial distribution of the ratio of the [NII] over the Hα line fluxes, (f) integrated spectrum (in observer-frame) centered on the Hα line: the red curve is the best fit for Hα and [NII], (g) intrinsic spectrum (in rest-frame) and (h) Hα velocity dispersion as a function of the star formation rate surface density. The contours superimposed on the maps follow the Hα flux distribution. Blue circles represent the FWHM of the PSF.

2.4.0.30 Q1623-BX599

$z = 2.33$

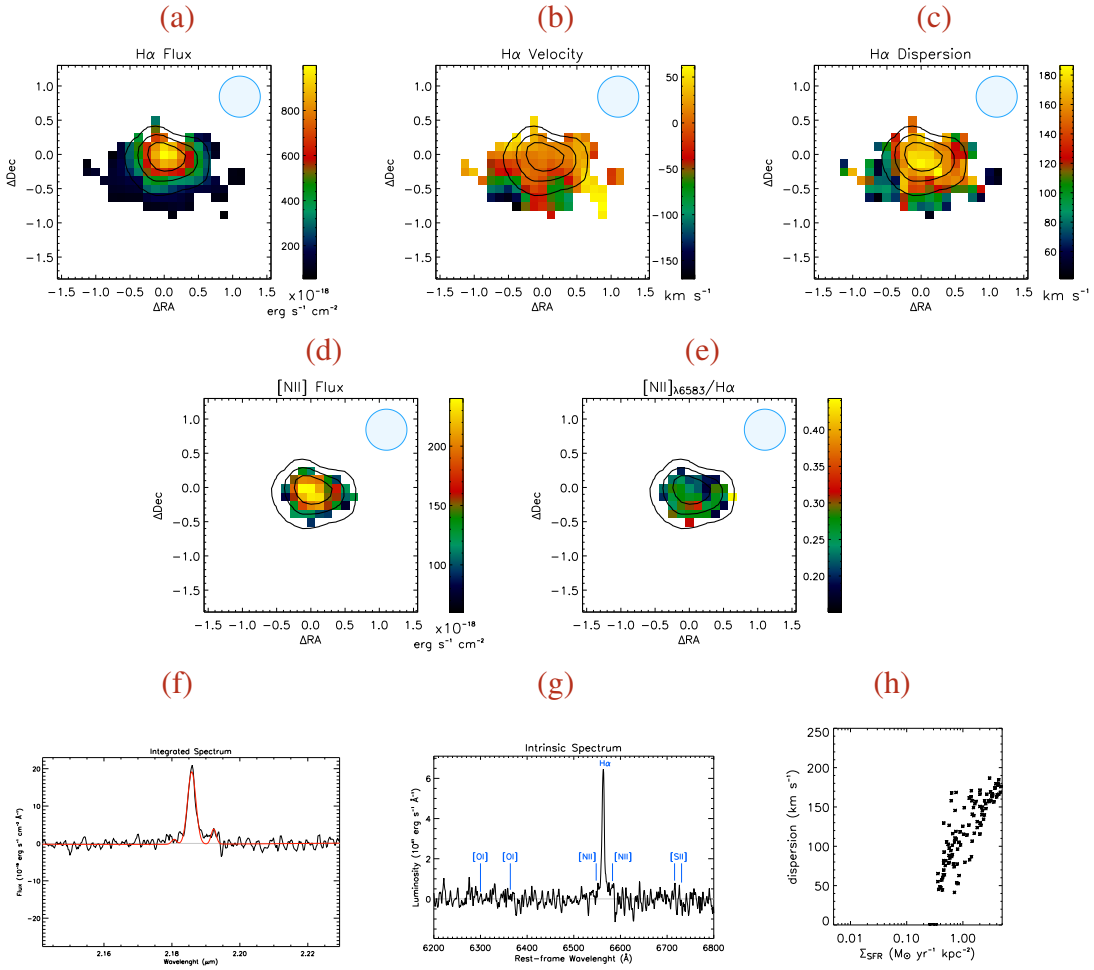

Figure 2.41 (a) Spatial distribution of the Hα line flux, in units of 10^{-18} erg s^{-1} cm^{-2}, (b) Hα velocity field, in km s^{-1}, (c) velocity dispersion distribution, in km s^{-1}, (d) spatial distribution of the [NII] line flux, in units of 10^{-18} erg s^{-1} cm^{-2}, (e) and spatial distribution of the ratio of the [NII] over the Hα line fluxes, (f) integrated spectrum (in observer-frame) centered on the Hα line: the red curve is the best fit for Hα and [NII], (g) intrinsic spectrum (in rest-frame) and (h) Hα velocity dispersion as a function of the star formation rate surface density. The contours superimposed on the maps follow the Hα flux distribution. Blue circles represent the FWHM of the PSF.

2.4.0.31 Q1623-BX663

$z = 2.43$

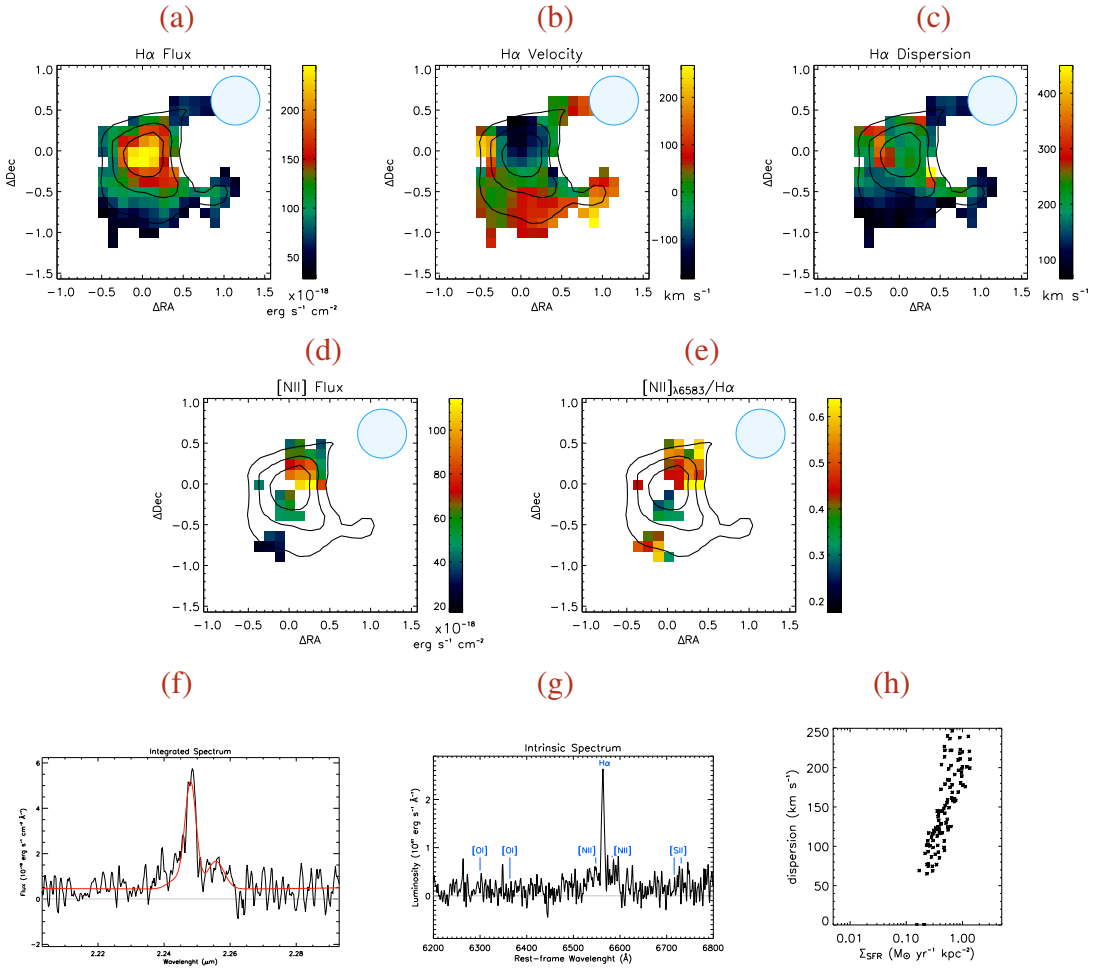

Figure 2.42 (a) Spatial distribution of the Hα line flux, in units of 10^{-18} erg s^{-1} cm^{-2}, (b) Hα velocity field, in km s^{-1}, (c) velocity dispersion distribution, in km s^{-1}, (d) spatial distribution of the [NII] line flux, in units of 10^{-18} erg s^{-1} cm^{-2}, (e) and spatial distribution of the ratio of the [NII] over the Hα line fluxes, (f) integrated spectrum (in observer-frame) centered on the Hα line: the red curve is the best fit for Hα and [NII], (g) intrinsic spectrum (in rest-frame) and (h) Hα velocity dispersion as a function of the star formation rate surface density. The contours superimposed on the maps follow the Hα flux distribution. Blue circles represent the FWHM of the PSF.

2.4.0.32 Q2343-BX389

$z = 2.17$

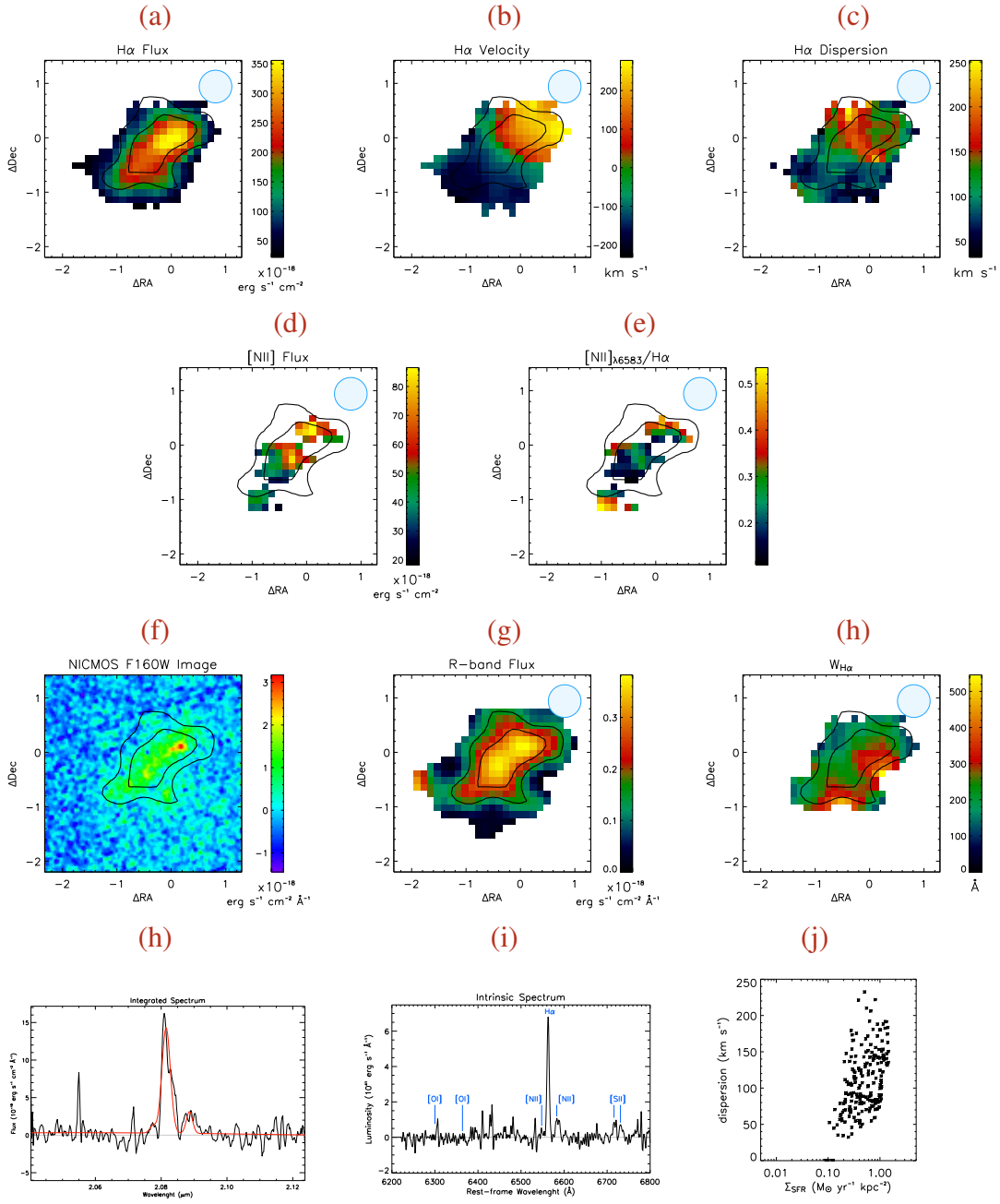

Figure 2.43 (a) Spatial distribution of the Hα line flux, in units of 10^{-18} erg s^{-1} cm^{-2}, (b) Hα velocity field, in km s^{-1}, (c) velocity dispersion distribution, in km s^{-1}, (d) spatial distribution of the [NII] line flux, in units of 10^{-18} erg s^{-1} cm^{-2}, (e) and spatial distribution of the ratio of the [NII] over the Hα line fluxes, (f) *R*-band continuum flux, in units of 10^{-18} erg s^{-1} cm^{-2} Å^{-1}, (g) equivalent width of the Hα line in Å, (h) NICMOS F160W image, in units of 10^{-18} erg s^{-1} cm^{-2} Å^{-1}, (h) integrated spectrum (in observer-frame) centered on the Hα line: the red curve is the best fit for Hα and [NII], (i) intrinsic spectrum (in rest-frame) and (j) Hα velocity dispersion as a function of the star formation rate surface density. The contours superimposed on the maps follow the *R*-band flux distribution. Blue circles represent the FWHM of the PSF.

2.4.0.33 Q2343-BX502 $z = 2.15$

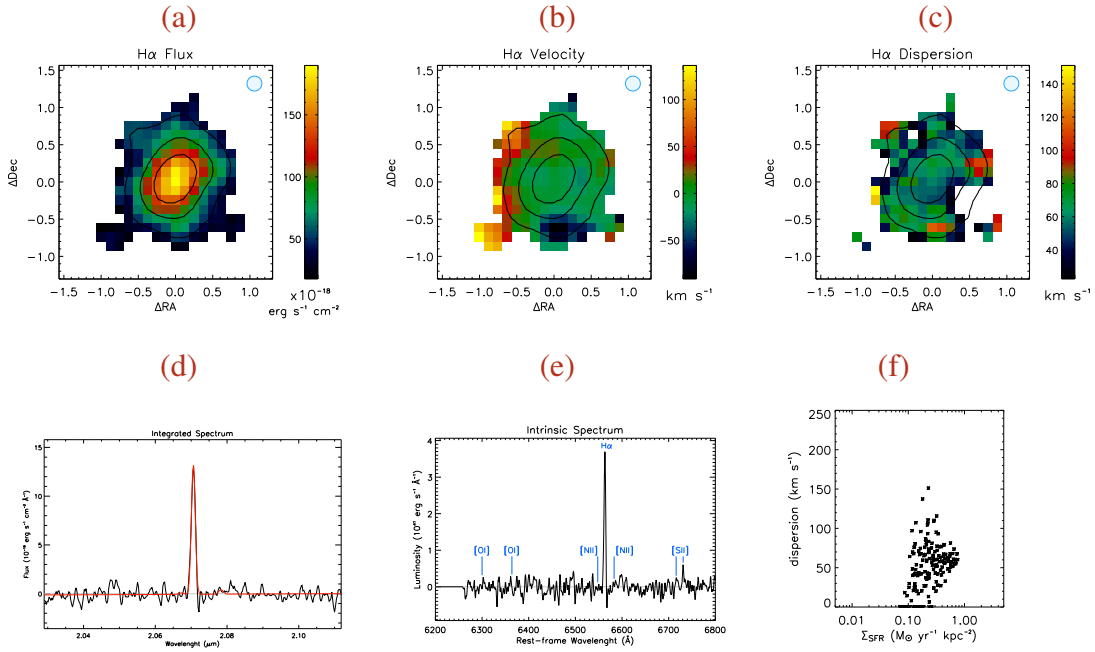

Figure 2.44 (a) Spatial distribution of the Hα line flux, in units of 10^{-18} erg s^{-1} cm^{-2}, (b) Hα velocity field, in km s^{-1}, (c) velocity dispersion distribution, in km s^{-1}, (d) integrated spectrum (in observer-frame) centered on the Hα line: the red curve is the best fit for Hα and [NII], (e) intrinsic spectrum (in rest-frame) and (f) Hα velocity dispersion as a function of the star formation rate surface density. The contours superimposed on the maps follow the Hα flux distribution. Blue circles represent the FWHM of the PSF.

2.4.0.34 Q2343-BX528

$z = 2.27$

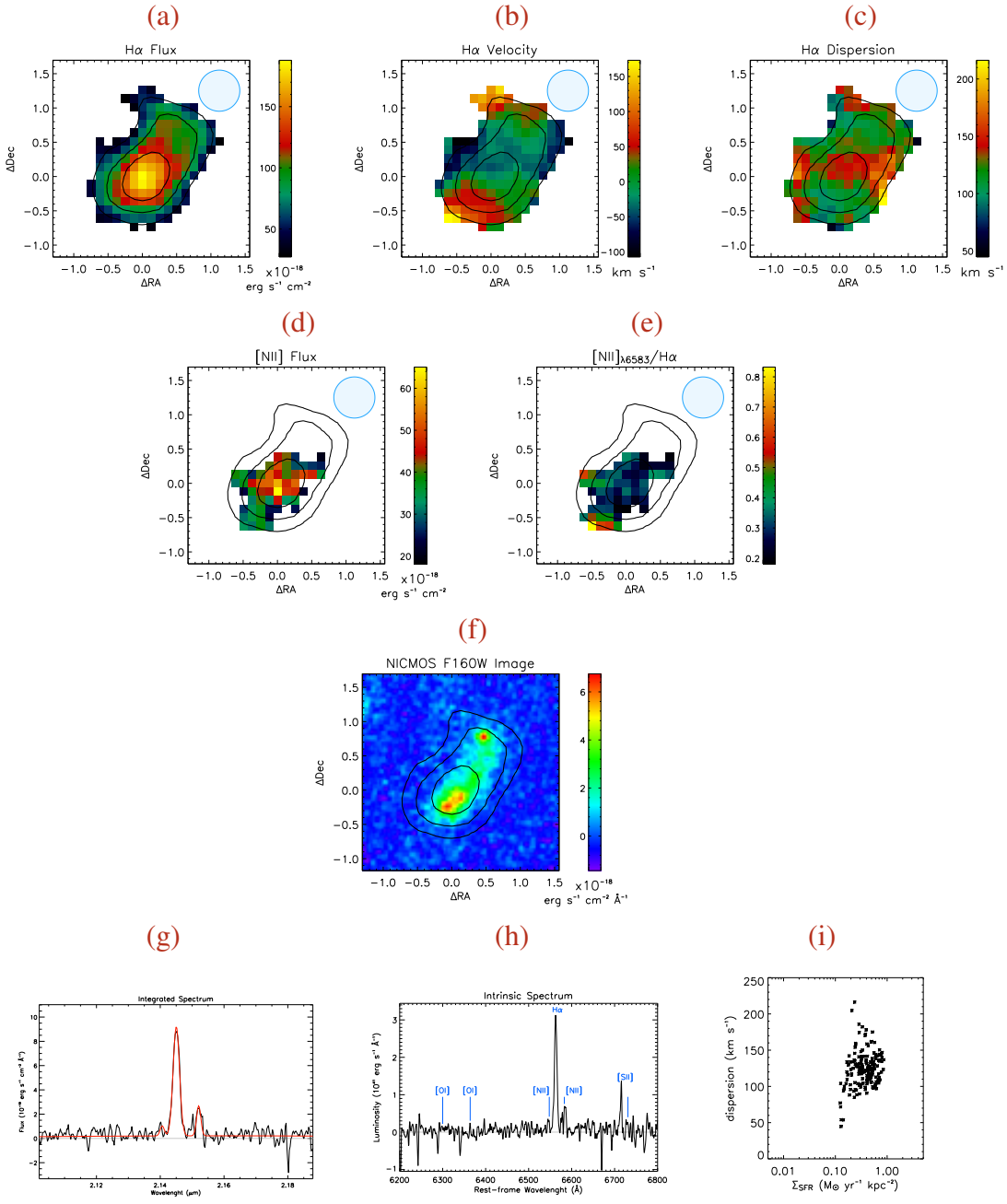

Figure 2.45 (a) Spatial distribution of the Hα line flux, in units of 10^{-18} erg s^{-1} cm^{-2}, (b) Hα velocity field, in km s^{-1}, (c) velocity dispersion distribution, in km s^{-1}, (d) spatial distribution of the [NII] line flux, in units of 10^{-18} erg s^{-1} cm^{-2}, (e) and spatial distribution of the ratio of the [NII] over the Hα line fluxes, (f) NICMOS F160W image, in units of 10^{-18} erg s^{-1} cm^{-2} Å^{-1}, (g) integrated spectrum (in observer-frame) centered on the Hα line: the red curve is the best fit for Hα and [NII], (h) intrinsic spectrum (in rest-frame) and (i) Hα velocity dispersion as a function of the star formation rate surface density. The contours superimposed on the maps follow the Hα flux distribution. Blue circles represent the FWHM of the PSF.

2.4.0.35 Q2343-BX610

$z = 2.21$

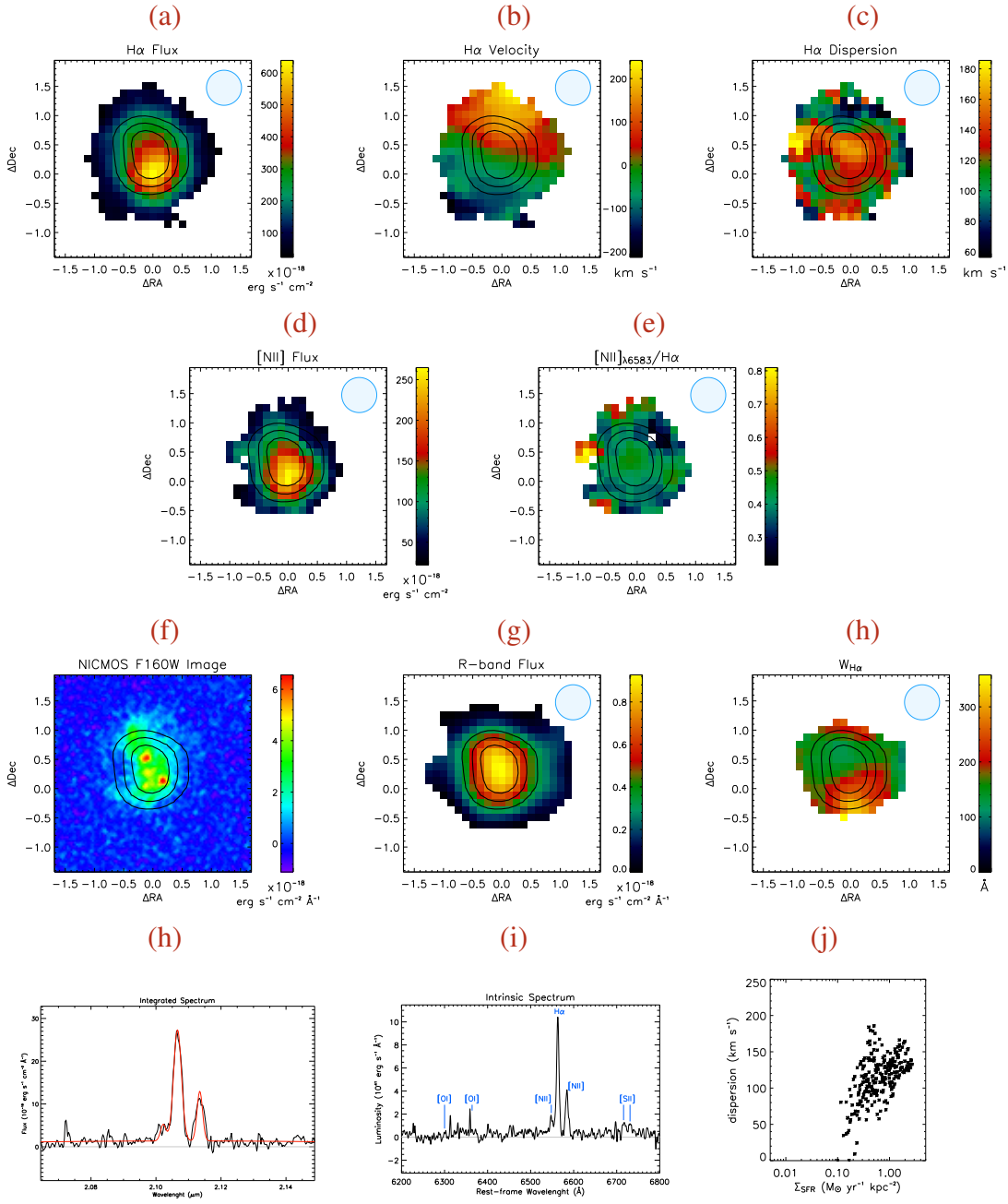

Figure 2.46 (a) Spatial distribution of the Hα line flux, in units of 10^{-18} erg s^{-1} cm^{-2}, (b) Hα velocity field, in km s^{-1}, (c) velocity dispersion distribution, in km s^{-1}, (d) spatial distribution of the [NII] line flux, in units of 10^{-18} erg s^{-1} cm^{-2}, (e) and spatial distribution of the ratio of the [NII] over the Hα line fluxes, (f) *R*-band continuum flux, in units of 10^{-18} erg s^{-1} cm^{-2} Å^{-1}, (g) equivalent width of the Hα line in Å, (h) NICMOS F160W image, in units of 10^{-18} erg s^{-1} cm^{-2} Å^{-1}, (h) integrated spectrum (in observer-frame) centered on the Hα line: the red curve is the best fit for Hα and [NII], (i) intrinsic spectrum (in rest-frame) and (j) Hα velocity dispersion as a function of the star formation rate surface density. The contours superimposed on the maps follow the *R*-band flux distribution. Blue circles represent the FWHM of the PSF.

2.4.0.36 Q2346-BX482

$z = 2.26$

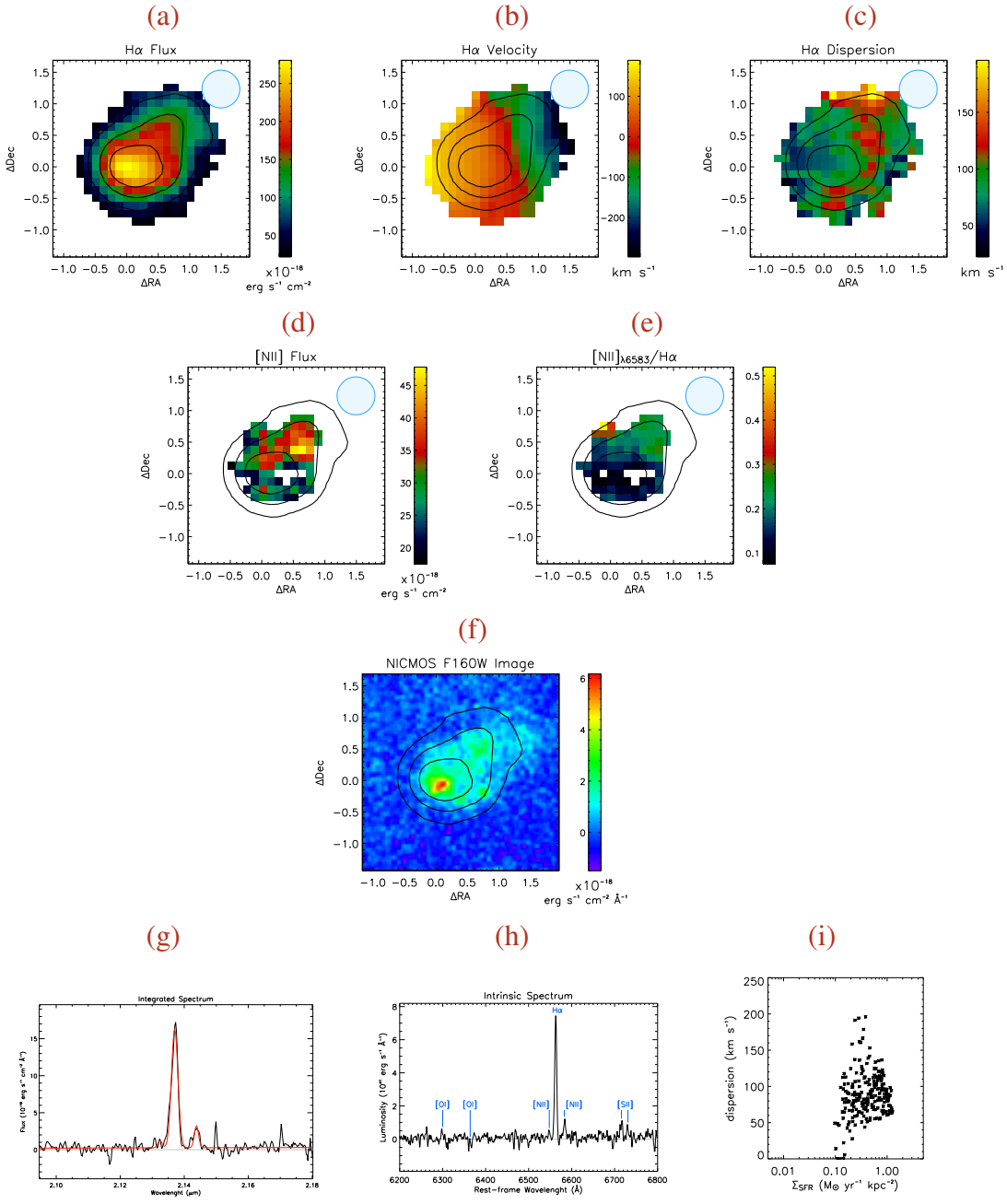

Figure 2.47 (a) Spatial distribution of the Hα line flux, in units of 10^{-18} erg s^{-1} cm^{-2}, (b) Hα velocity field, in km s^{-1}, (c) velocity dispersion distribution, in km s^{-1}, (d) spatial distribution of the [NII] line flux, in units of 10^{-18} erg s^{-1} cm^{-2}, (e) and spatial distribution of the ratio of the [NII] over the Hα line fluxes, (f) NICMOS F160W image, in units of 10^{-18} erg s^{-1} cm^{-2} Å^{-1}, (g) integrated spectrum (in observer-frame) centered on the Hα line: the red curve is the best fit for Hα and [NII], (h) intrinsic spectrum (in rest-frame) and (i) Hα velocity dispersion as a function of the star formation rate surface density. The contours superimposed on the maps follow the Hα flux distribution. Blue circles represent the FWHM of the PSF.

2.4.0.37 SA12-5241 $z = 1.36$

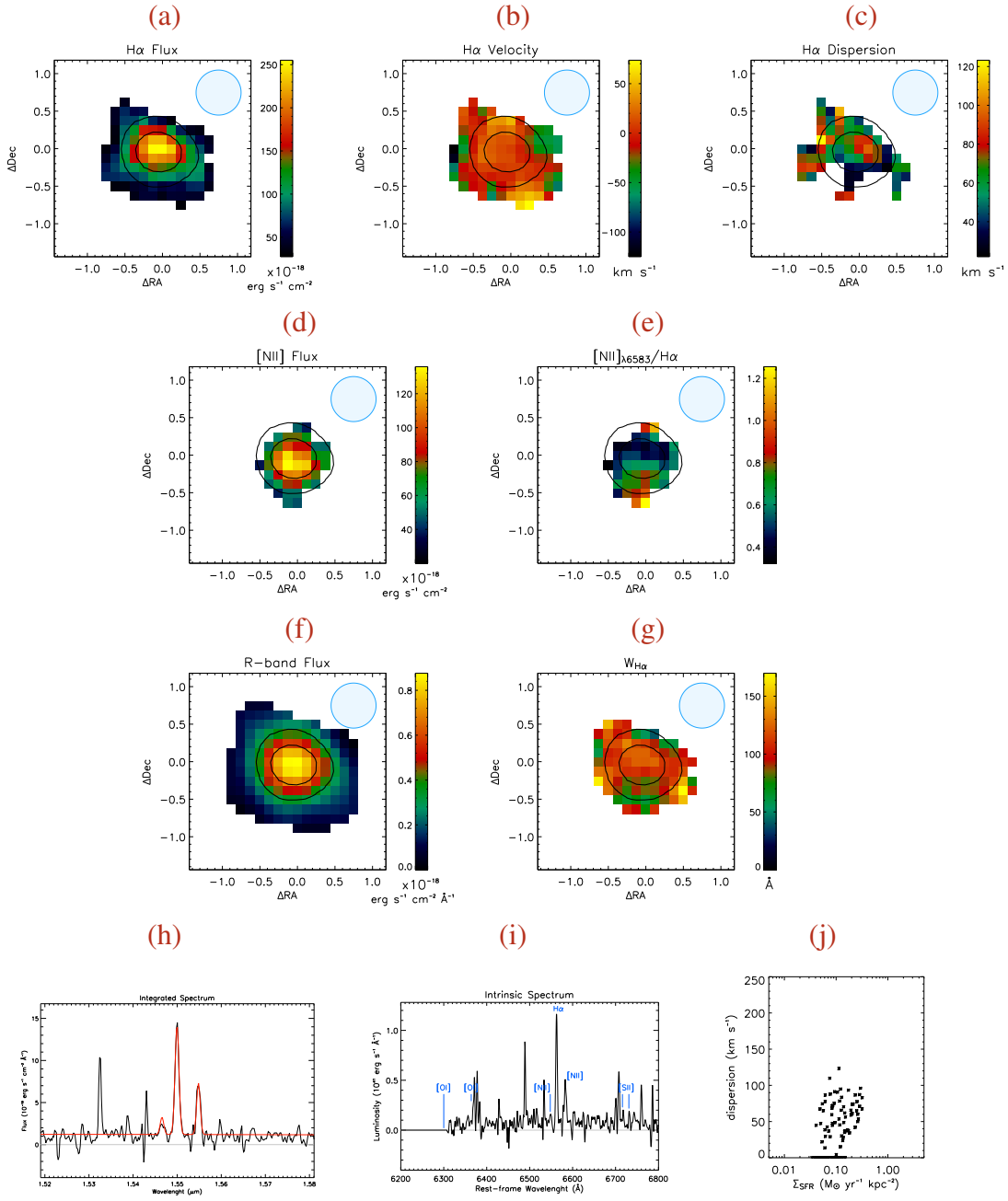

Figure 2.48 (a) Spatial distribution of the Hα line flux, in units of 10^{-18} erg s^{-1} cm^{-2}, (b) Hα velocity field, in km s^{-1}, (c) velocity dispersion distribution, in km s^{-1}, (d) spatial distribution of the [NII] line flux, in units of 10^{-18} erg s^{-1} cm^{-2}, (e) and spatial distribution of the ratio of the [NII] over the Hα line fluxes, (f) *R*-band continuum flux, in units of 10^{-18} erg s^{-1} cm^{-2} Å^{-1}, (g) equivalent width of the Hα line in Å, (h) integrated spectrum (in observer-frame) centered on the Hα line: the red curve is the best fit for Hα and [NII], (i) intrinsic spectrum (in rest-frame) and (j) Hα velocity dispersion as a function of the star formation rate surface density. The contours superimposed on the maps follow the *R*-band flux distribution. Blue circles represent the FWHM of the PSF.

2.4.0.38 SA12-6192

$z = 1.50$

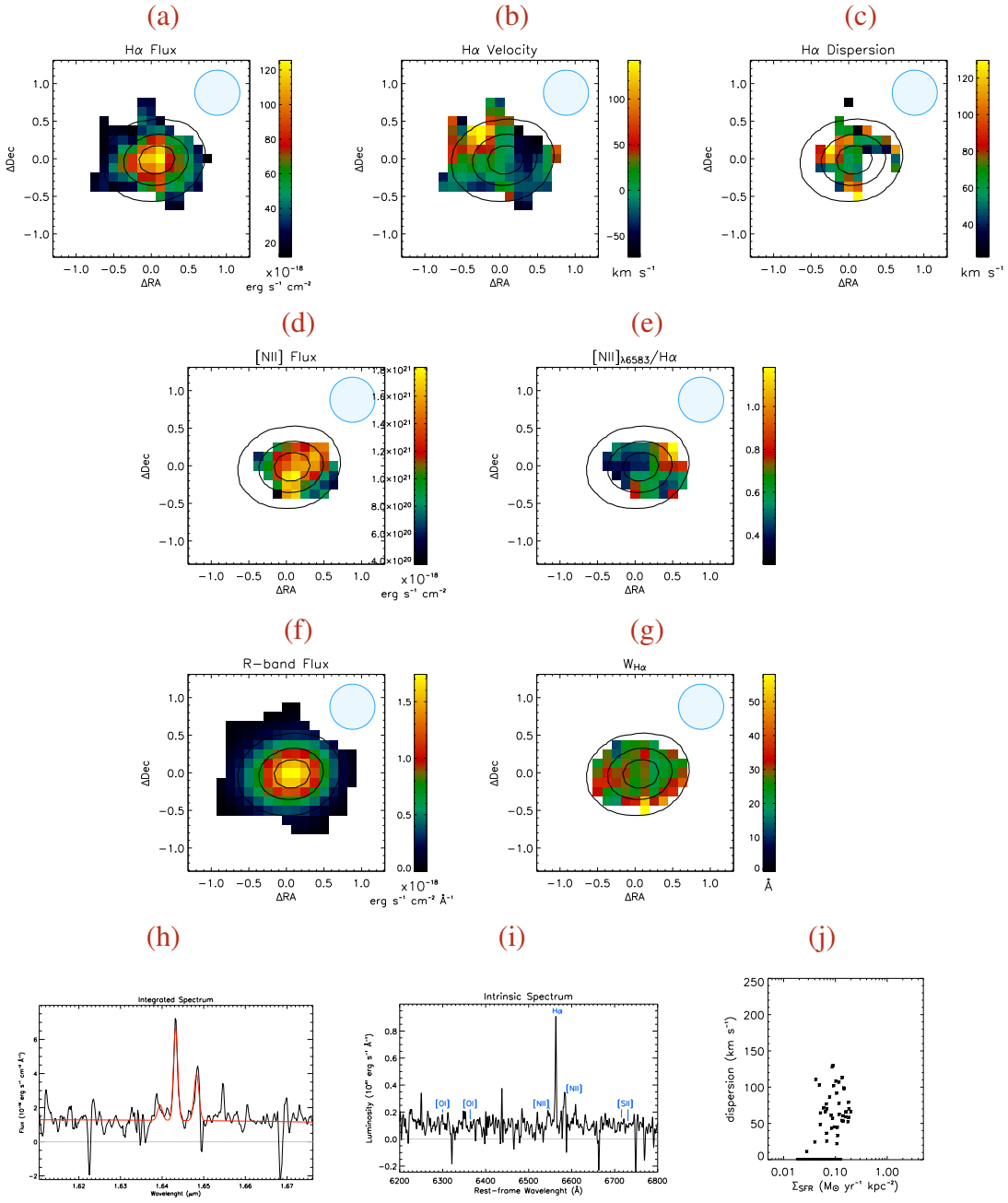

Figure 2.49 (a) Spatial distribution of the Hα line flux, in units of 10^{-18} erg s^{-1} cm^{-2}, (b) Hα velocity field, in km s^{-1}, (c) velocity dispersion distribution, in km s^{-1}, (d) spatial distribution of the [NII] line flux, in units of 10^{-18} erg s^{-1} cm^{-2}, (e) and spatial distribution of the ratio of the [NII] over the Hα line fluxes, (f) *R*-band continuum flux, in units of 10^{-18} erg s^{-1} cm^{-2} Å^{-1}, (g) equivalent width of the Hα line in Å, (h) integrated spectrum (in observer-frame) centered on the Hα line: the red curve is the best fit for Hα and [NII], (i) intrinsic spectrum (in rest-frame) and (j) Hα velocity dispersion as a function of the star formation rate surface density. The contours superimposed on the maps follow the *R*-band flux distribution. Blue circles represent the FWHM of the PSF.

2.4.0.39 SA12-6339 $z = 2.30$

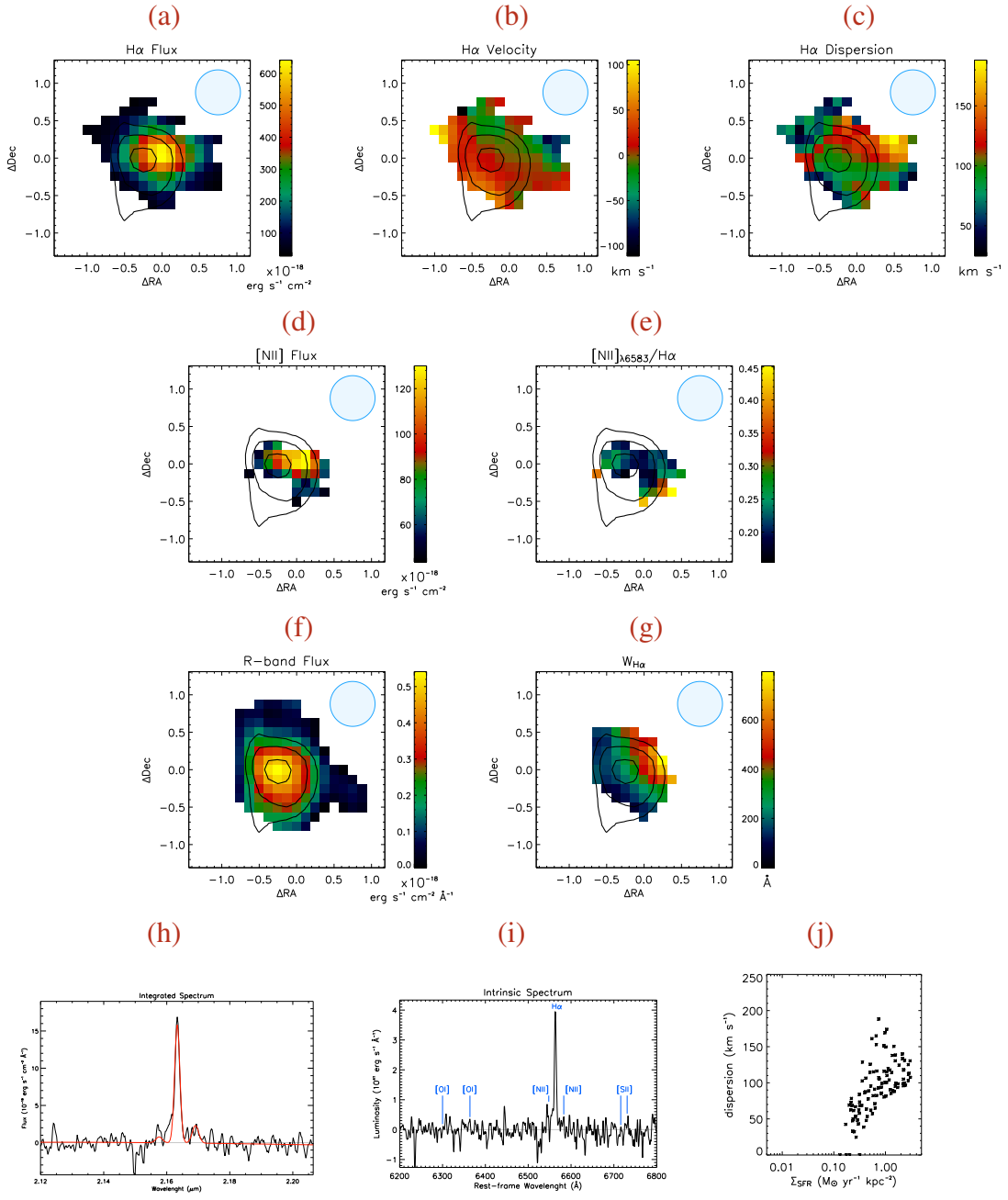

Figure 2.50 (a) Spatial distribution of the Hα line flux, in units of 10^{-18} erg s^{-1} cm^{-2}, (b) Hα velocity field, in km s^{-1}, (c) velocity dispersion distribution, in km s^{-1}, (d) spatial distribution of the [NII] line flux, in units of 10^{-18} erg s^{-1} cm^{-2}, (e) and spatial distribution of the ratio of the [NII] over the Hα line fluxes, (f) *R*-band continuum flux, in units of 10^{-18} erg s^{-1} cm^{-2} Å^{-1}, (g) equivalent width of the Hα line in Å, (h) integrated spectrum (in observer-frame) centered on the Hα line: the red curve is the best fit for Hα and [NII], (i) intrinsic spectrum (in rest-frame) and (j) Hα velocity dispersion as a function of the star formation rate surface density. The contours superimposed on the maps follow the *R*-band flux distribution. Blue circles represent the FWHM of the PSF.

2.4.0.40 SA12-8768

$z = 2.19$

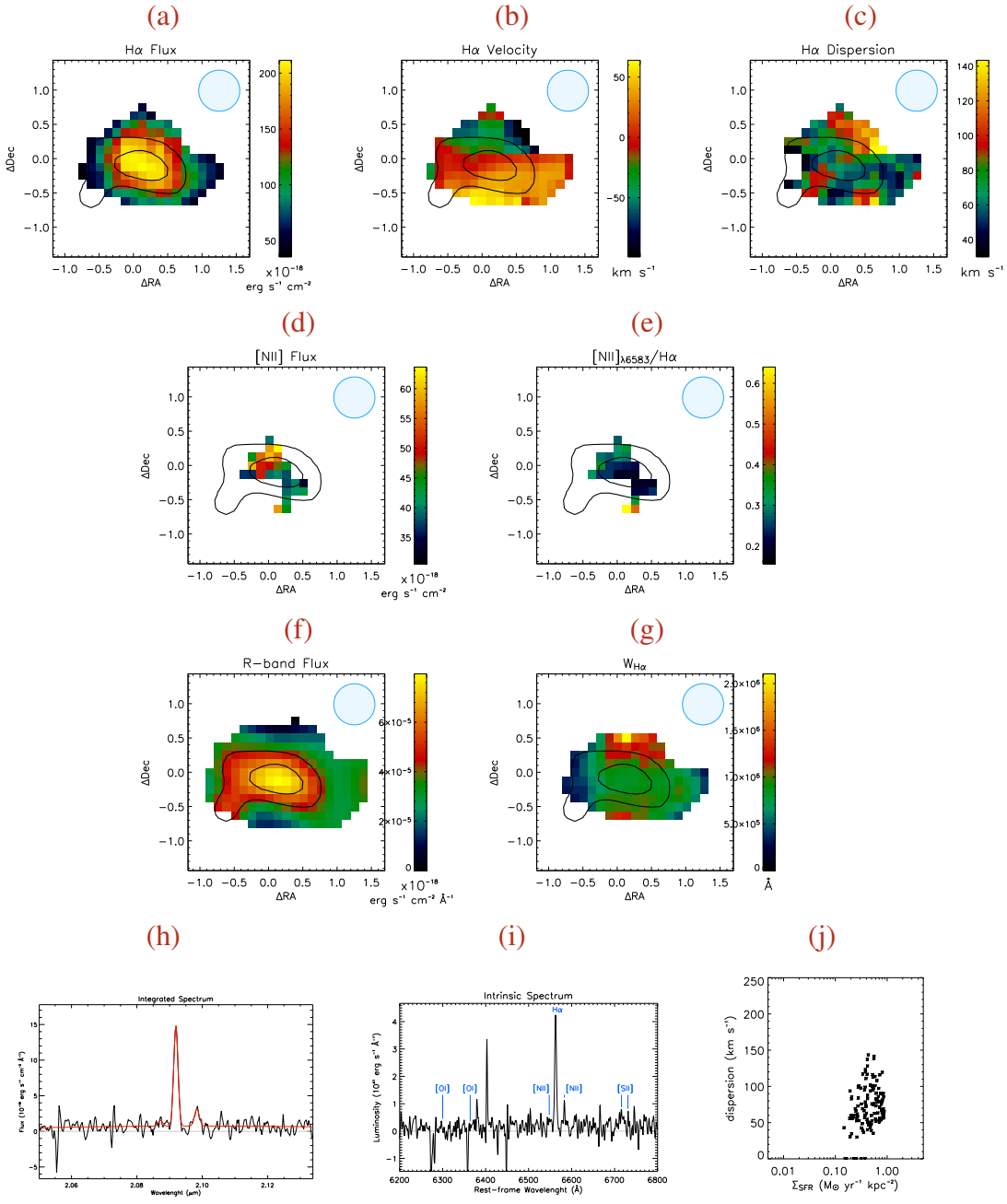

Figure 2.51 (a) Spatial distribution of the Hα line flux, in units of 10^{-18} erg s^{-1} cm^{-2}, (b) Hα velocity field, in km s^{-1}, (c) velocity dispersion distribution, in km s^{-1}, (d) spatial distribution of the [NII] line flux, in units of 10^{-18} erg s^{-1} cm^{-2}, (e) and spatial distribution of the ratio of the [NII] over the Hα line fluxes, (f) *R*-band continuum flux, in units of 10^{-18} erg s^{-1} cm^{-2} Å^{-1}, (g) equivalent width of the Hα line in Å, (h) integrated spectrum (in observer-frame) centered on the Hα line: the red curve is the best fit for Hα and [NII], (i) intrinsic spectrum (in rest-frame) and (j) Hα velocity dispersion as a function of the star formation rate surface density. The contours superimposed on the maps follow the *R*-band flux distribution. Blue circles represent the FWHM of the PSF.

2.4.0.41 SA15-5365 $z = 1.53$

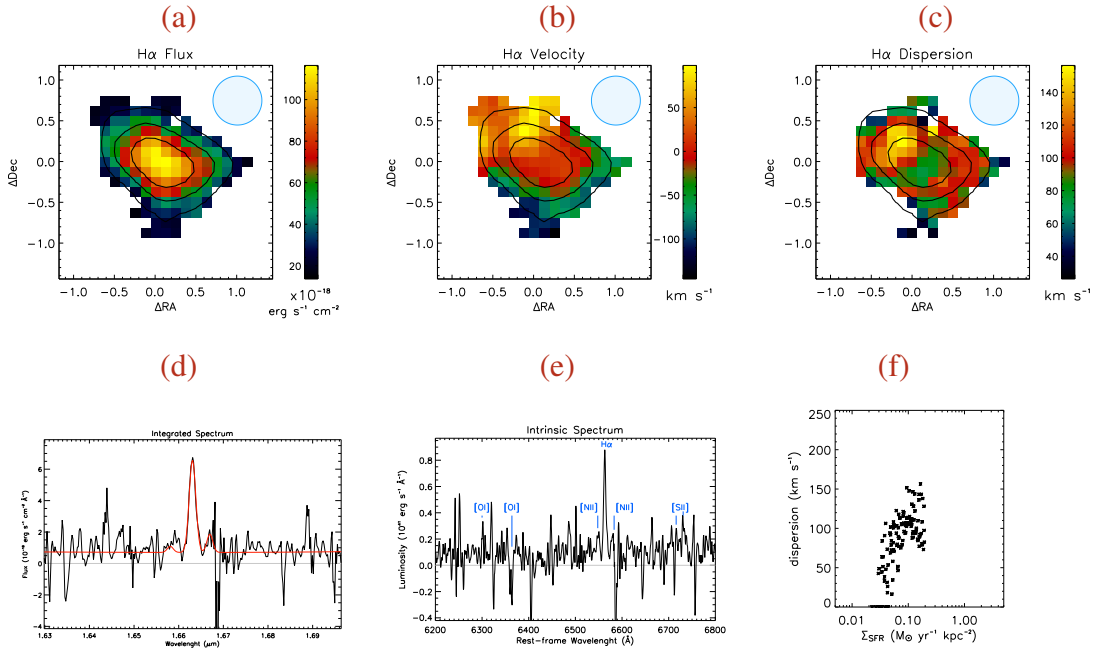

Figure 2.52 (a) Spatial distribution of the Hα line flux, in units of 10^{-18} erg s^{-1} cm^{-2}, (b) Hα velocity field, in km s^{-1}, (c) velocity dispersion distribution, in km s^{-1}, (d) integrated spectrum (in observer-frame) centered on the Hα line: the red curve is the best fit for Hα and [NII], (e) intrinsic spectrum (in rest-frame) and (f) Hα velocity dispersion as a function of the star formation rate surface density. The contours superimposed on the maps follow the Hα flux distribution. Blue circles represent the FWHM of the PSF.

2.4.0.42 SINS-4751

$z = 2.27$

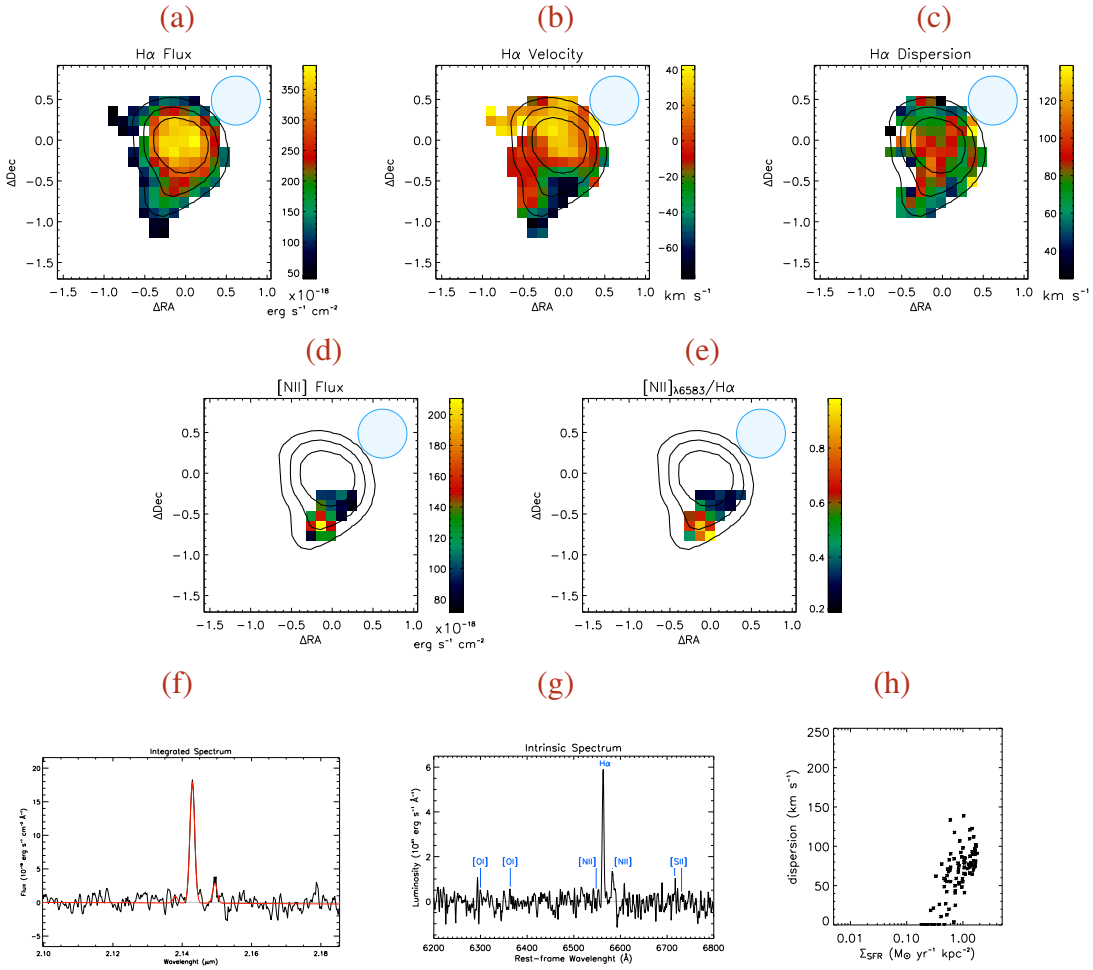

Figure 2.53 (a) Spatial distribution of the Hα line flux, in units of 10^{-18} erg s^{-1} cm^{-2}, (b) Hα velocity field, in km s^{-1}, (c) velocity dispersion distribution, in km s^{-1}, (d) spatial distribution of the [NII] line flux, in units of 10^{-18} erg s^{-1} cm^{-2}, (e) and spatial distribution of the ratio of the [NII] over the Hα line fluxes, (f) integrated spectrum (in observer-frame) centered on the Hα line: the red curve is the best fit for Hα and [NII], (g) intrinsic spectrum (in rest-frame) and (h) Hα velocity dispersion as a function of the star formation rate surface density. The contours superimposed on the maps follow the Hα flux distribution. Blue circles represent the FWHM of the PSF.

2.4.0.43 SSA-22a-MD041 $z = 2.16$

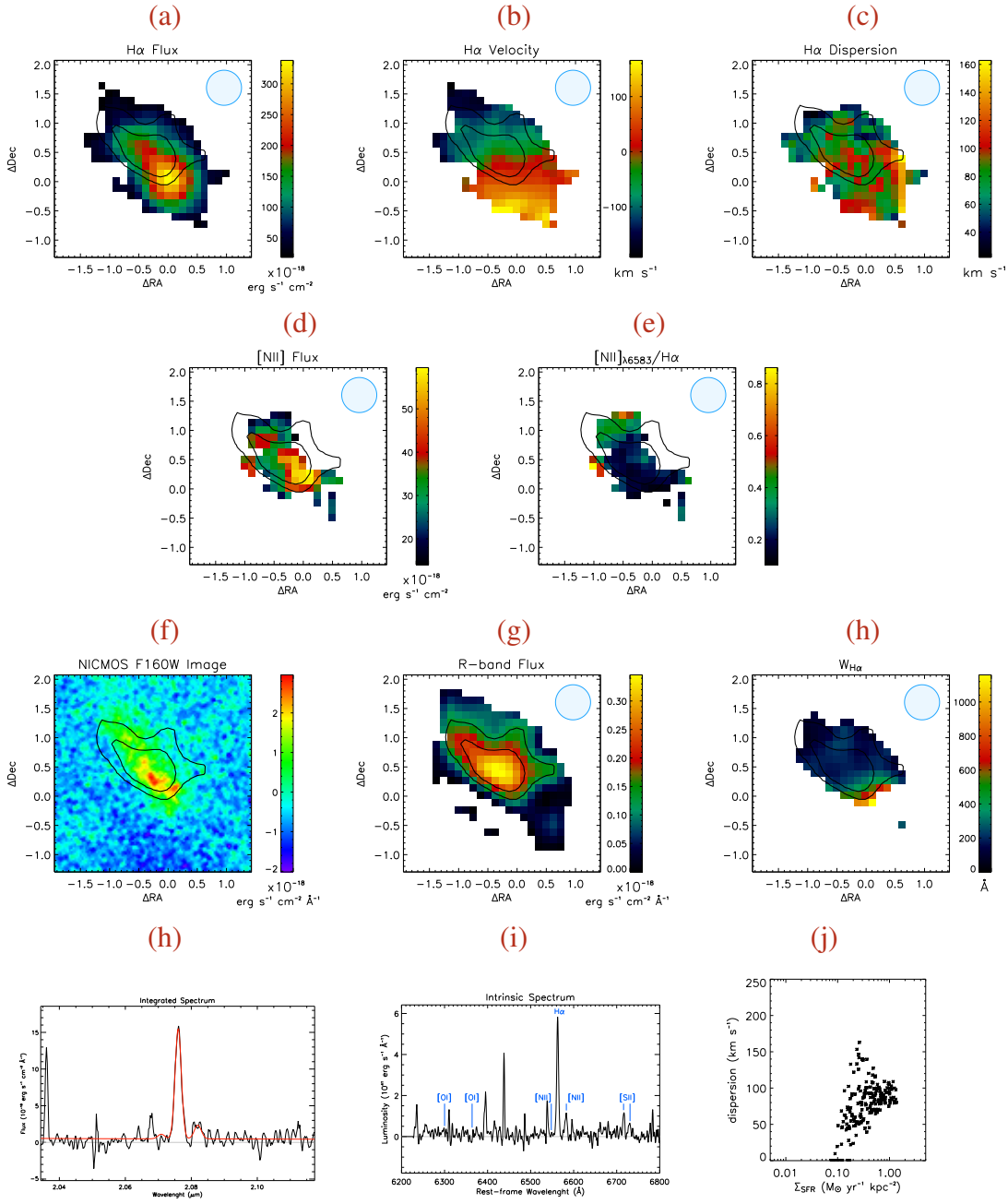

Figure 2.54 (a) Spatial distribution of the Hα line flux, in units of 10^{-18} erg s^{-1} cm^{-2}, (b) Hα velocity field, in km s^{-1}, (c) velocity dispersion distribution, in km s^{-1}, (d) spatial distribution of the [NII] line flux, in units of 10^{-18} erg s^{-1} cm^{-2}, (e) and spatial distribution of the ratio of the [NII] over the Hα line fluxes, (f) *R*-band continuum flux, in units of 10^{-18} erg s^{-1} cm^{-2} Å^{-1}, (g) equivalent width of the Hα line in Å, (h) NICMOS F160W image, in units of 10^{-18} erg s^{-1} cm^{-2} Å^{-1}, (h) integrated spectrum (in observer-frame) centered on the Hα line: the red curve is the best fit for Hα and [NII], (i) intrinsic spectrum (in rest-frame) and (j) Hα velocity dispersion as a function of the star formation rate surface density. The contours superimposed on the maps follow the *R*-band flux distribution. Blue circles represent the FWHM of the PSF.

2.4.0.44 VVDS-020147106 $z = 1.52$

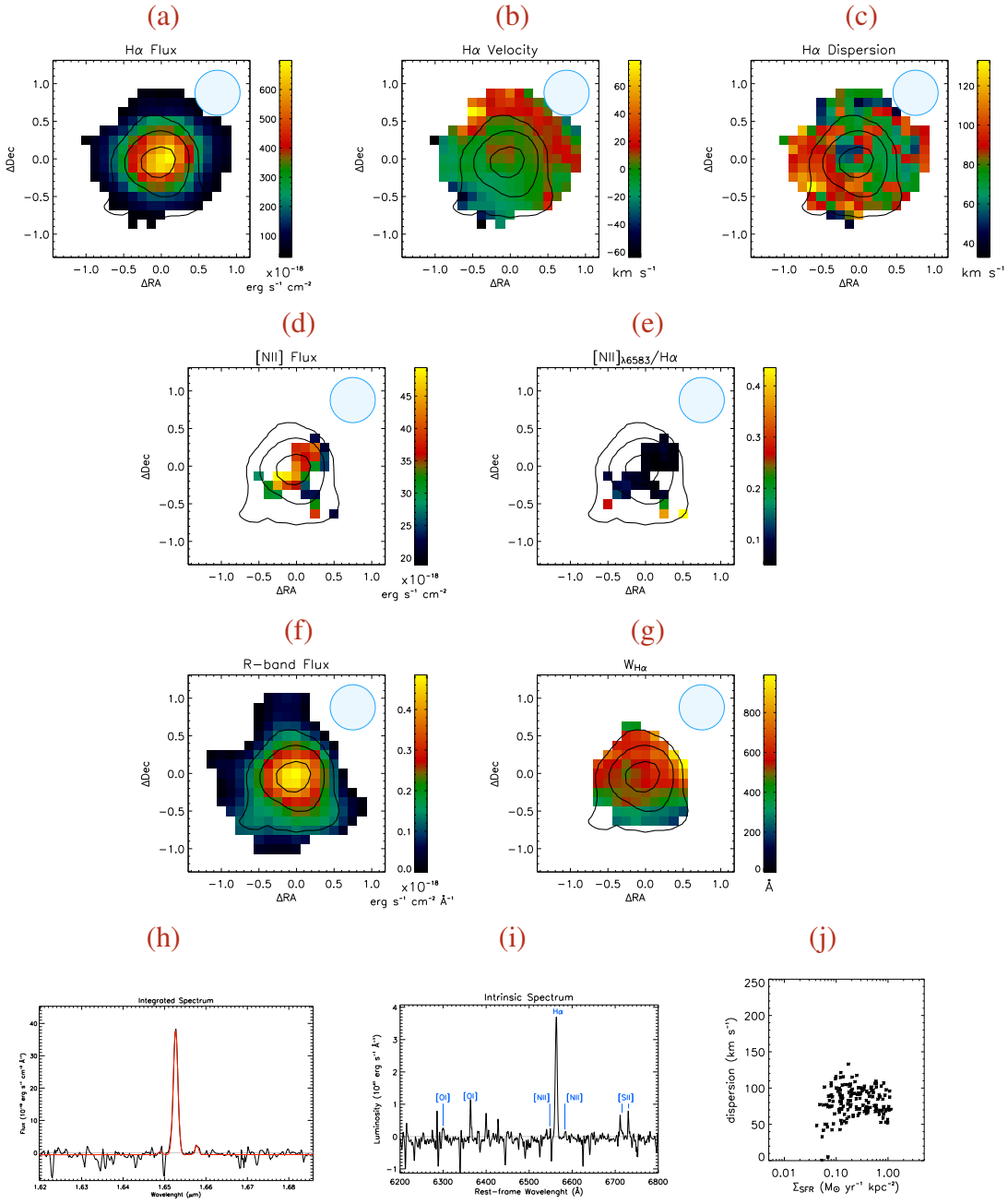

Figure 2.55 (a) Spatial distribution of the Hα line flux, in units of 10^{-18} erg s^{-1} cm^{-2}, (b) Hα velocity field, in km s^{-1}, (c) velocity dispersion distribution, in km s^{-1}, (d) spatial distribution of the [NII] line flux, in units of 10^{-18} erg s^{-1} cm^{-2}, (e) and spatial distribution of the ratio of the [NII] over the Hα line fluxes, (f) *R*-band continuum flux, in units of 10^{-18} erg s^{-1} cm^{-2} Å^{-1}, (g) equivalent width of the Hα line in Å, (h) integrated spectrum (in observer-frame) centered on the Hα line: the red curve is the best fit for Hα and [NII], (i) intrinsic spectrum (in rest-frame) and (j) Hα velocity dispersion as a function of the star formation rate surface density. The contours superimposed on the maps follow the *R*-band flux distribution. Blue circles represent the FWHM of the PSF.

2.4.0.45 VVDS-020261328 $z = 1.53$

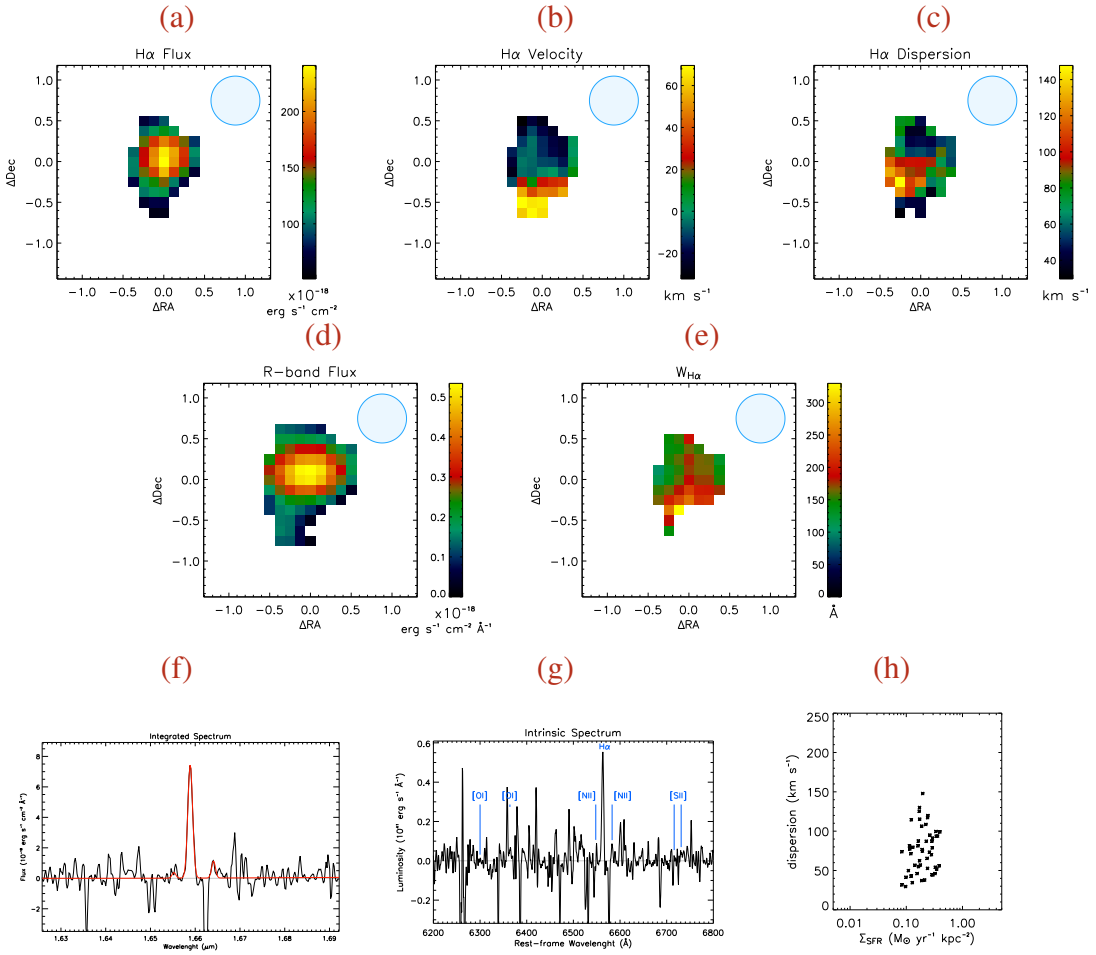

Figure 2.56 (a) Spatial distribution of the Hα line flux, in units of 10^{-18} erg s^{-1} cm^{-2}, (b) Hα velocity field, in km s^{-1}, (c) velocity dispersion distribution, in km s^{-1}, (d) R-band continuum flux, in units of 10^{-18} erg s^{-1} cm^{-2} Å^{-1}, (e) equivalent width of the Hα line in Å, (f) integrated spectrum (in observer-frame) centered on the Hα line: the red curve is the best fit for Hα and [NII], (g) intrinsic spectrum (in rest-frame) and (h) Hα velocity dispersion as a function of the star formation rate surface density. The contours superimposed on the maps follow the R-band flux distribution. Blue circles represent the FWHM of the PSF.

2.4.0.46 VVDS-220014252 $z = 1.31$

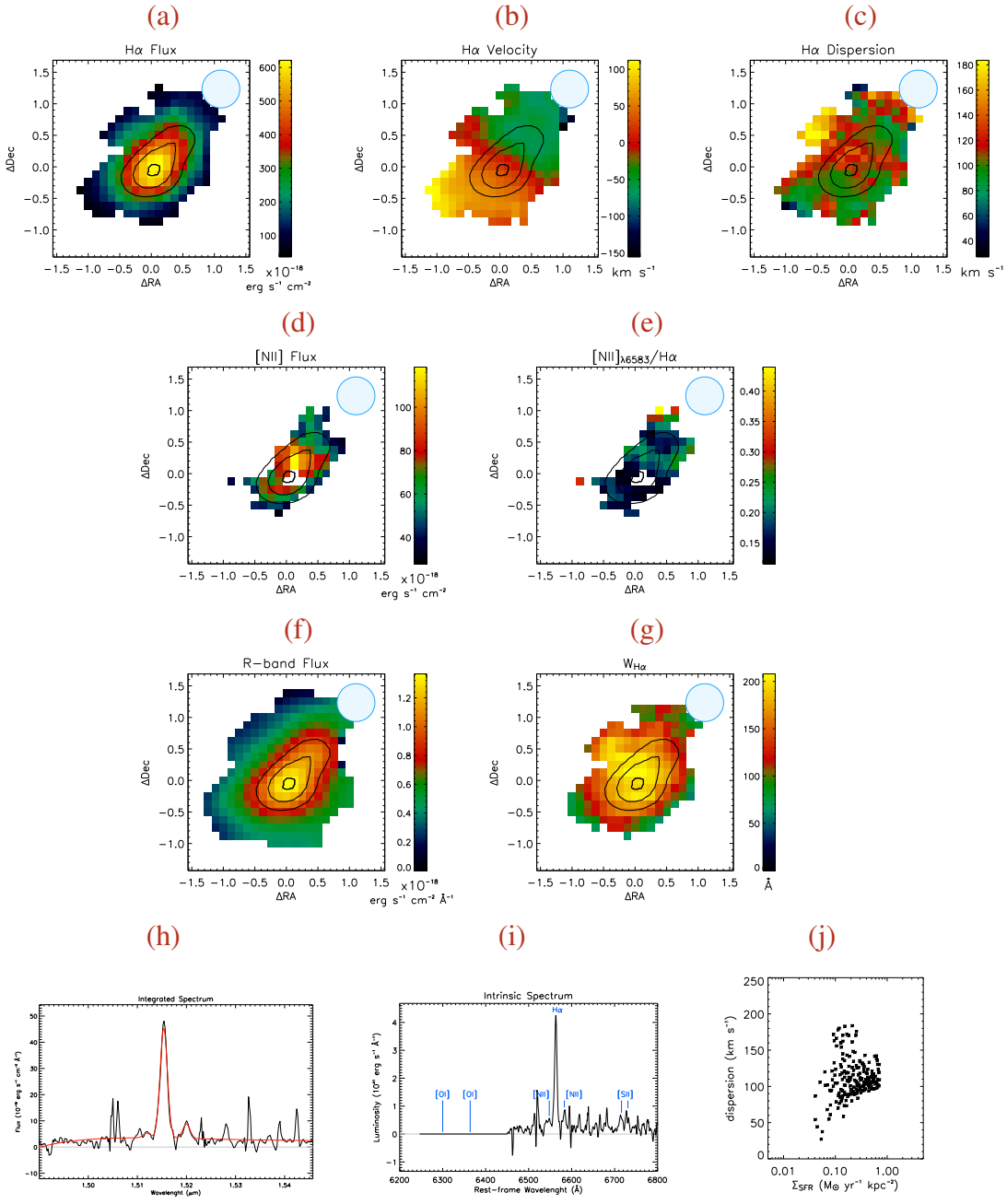

Figure 2.57 (a) Spatial distribution of the Hα line flux, in units of 10^{-18} erg s^{-1} cm^{-2}, (b) Hα velocity field, in km s^{-1}, (c) velocity dispersion distribution, in km s^{-1}, (d) spatial distribution of the [NII] line flux, in units of 10^{-18} erg s^{-1} cm^{-2}, (e) and spatial distribution of the ratio of the [NII] over the Hα line fluxes, (f) *R*-band continuum flux, in units of 10^{-18} erg s^{-1} cm^{-2} Å^{-1}, (g) equivalent width of the Hα line in Å, (h) integrated spectrum (in observer-frame) centered on the Hα line: the red curve is the best fit for Hα and [NII], (i) intrinsic spectrum (in rest-frame) and (j) Hα velocity dispersion as a function of the star formation rate surface density. The contours superimposed on the maps follow the *R*-band flux distribution. Blue circles represent the FWHM of the PSF.

2.4.0.47 VVDS-220015726 $z = 1.29$

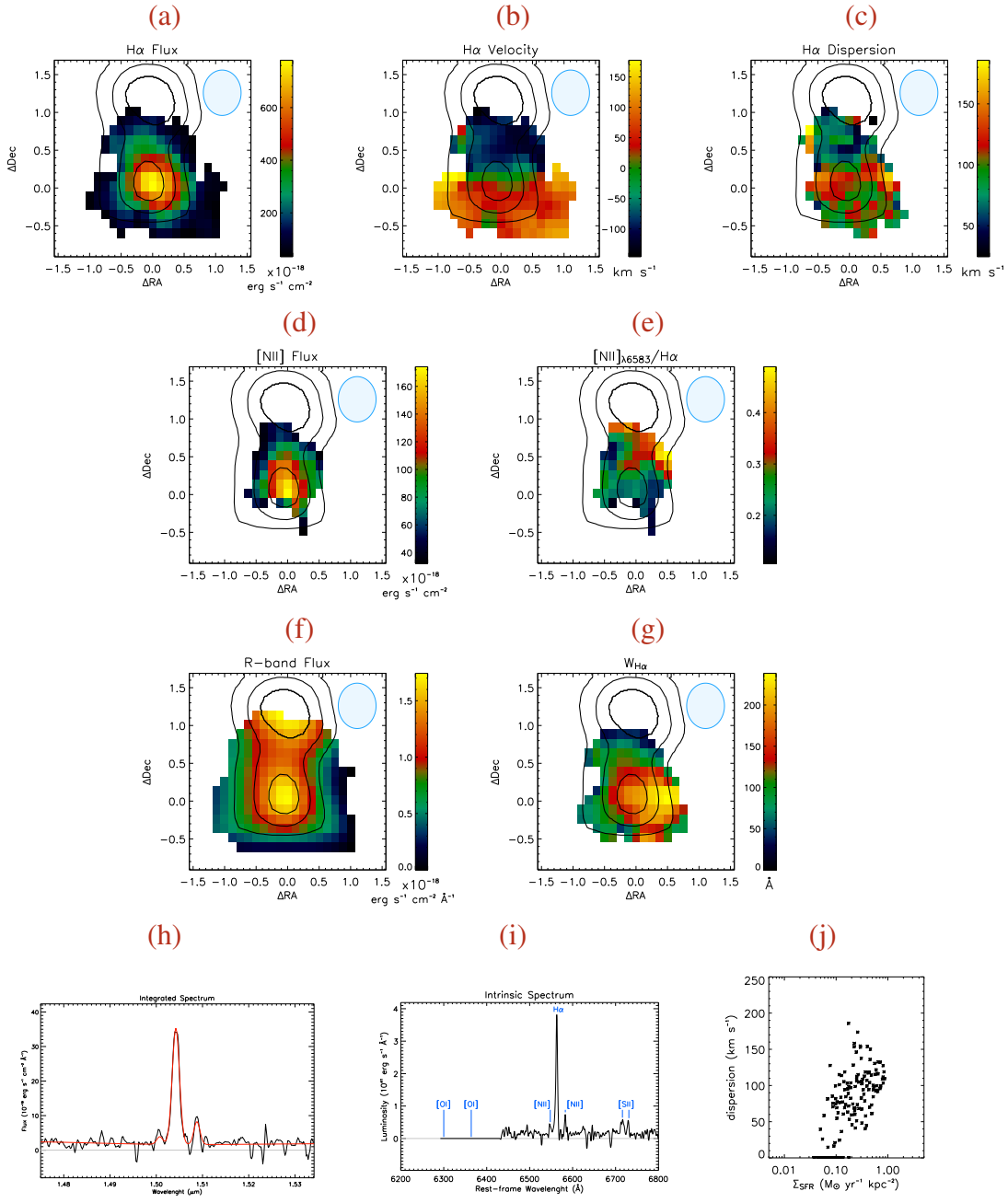

Figure 2.58 (a) Spatial distribution of the Hα line flux, in units of 10^{-18} erg s^{-1} cm^{-2}, (b) Hα velocity field, in km s^{-1}, (c) velocity dispersion distribution, in km s^{-1}, (d) spatial distribution of the [NII] line flux, in units of 10^{-18} erg s^{-1} cm^{-2}, (e) and spatial distribution of the ratio of the [NII] over the Hα line fluxes, (f) *R*-band continuum flux, in units of 10^{-18} erg s^{-1} cm^{-2} Å^{-1}, (g) equivalent width of the Hα line in Å, (h) integrated spectrum (in observer-frame) centered on the Hα line: the red curve is the best fit for Hα and [NII], (i) intrinsic spectrum (in rest-frame) and (j) Hα velocity dispersion as a function of the star formation rate surface density. The contours superimposed on the maps follow the *R*-band flux distribution. Blue circles represent the FWHM of the PSF.

2.4.0.48 VVDS-220544103 $z = 1.40$

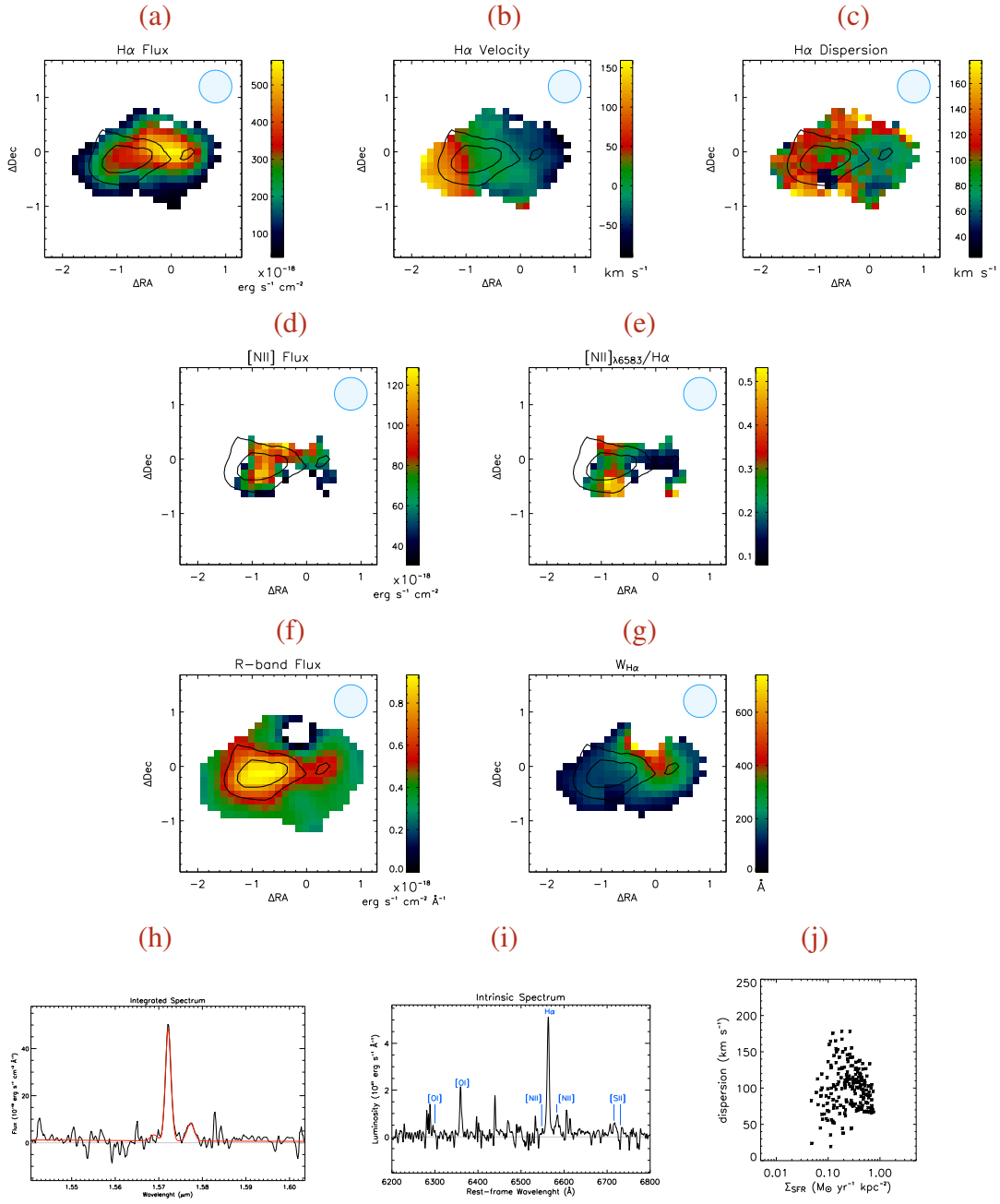

Figure 2.59 (a) Spatial distribution of the Hα line flux, in units of 10^{-18} erg s^{-1} cm^{-2}, (b) Hα velocity field, in km s^{-1}, (c) velocity dispersion distribution, in km s^{-1}, (d) spatial distribution of the [NII] line flux, in units of 10^{-18} erg s^{-1} cm^{-2}, (e) and spatial distribution of the ratio of the [NII] over the Hα line fluxes, (f) *R*-band continuum flux, in units of 10^{-18} erg s^{-1} cm^{-2} Å^{-1}, (g) equivalent width of the Hα line in Å, (h) integrated spectrum (in observer-frame) centered on the Hα line: the red curve is the best fit for Hα and [NII], (i) intrinsic spectrum (in rest-frame) and (j) Hα velocity dispersion as a function of the star formation rate surface density. The contours superimposed on the maps follow the *R*-band flux distribution. Blue circles represent the FWHM of the PSF.

2.4.0.49 VVDS-220584167 $z = 1.46$

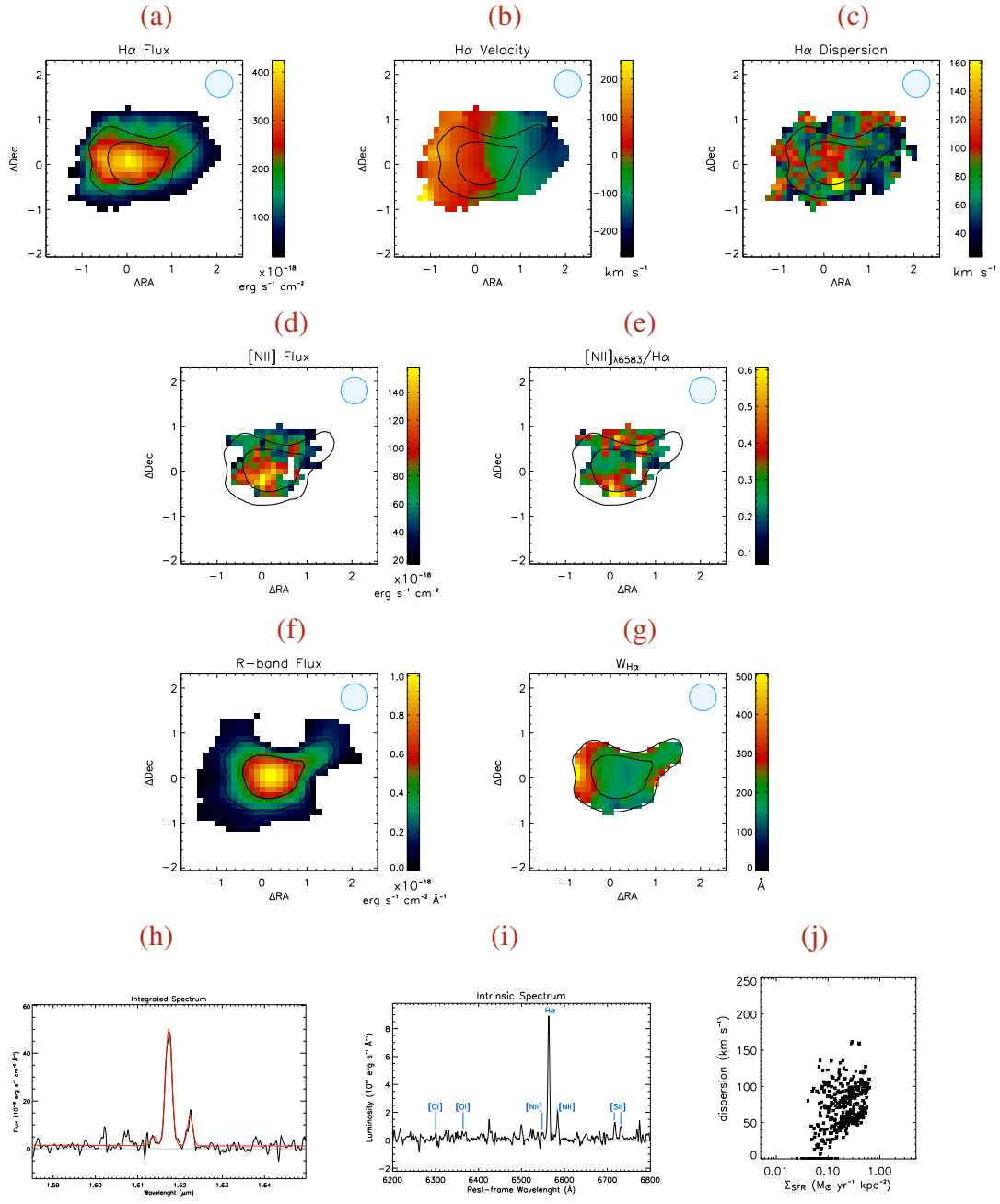

Figure 2.60 (a) Spatial distribution of the Hα line flux, in units of 10^{-18} erg s^{-1} cm^{-2}, (b) Hα velocity field, in km s^{-1}, (c) velocity dispersion distribution, in km s^{-1}, (d) spatial distribution of the [NII] line flux, in units of 10^{-18} erg s^{-1} cm^{-2}, (e) and spatial distribution of the ratio of the [NII] over the Hα line fluxes, (f) *R*-band continuum flux, in units of 10^{-18} erg s^{-1} cm^{-2} Å^{-1}, (g) equivalent width of the Hα line in Å, (h) integrated spectrum (in observer-frame) centered on the Hα line: the red curve is the best fit for Hα and [NII], (i) intrinsic spectrum (in rest-frame) and (j) Hα velocity dispersion as a function of the star formation rate surface density. The contours superimposed on the maps follow the *R*-band flux distribution. Blue circles represent the FWHM of the PSF.

2.4.0.50 VVDS-220596913 $z = 1.26$

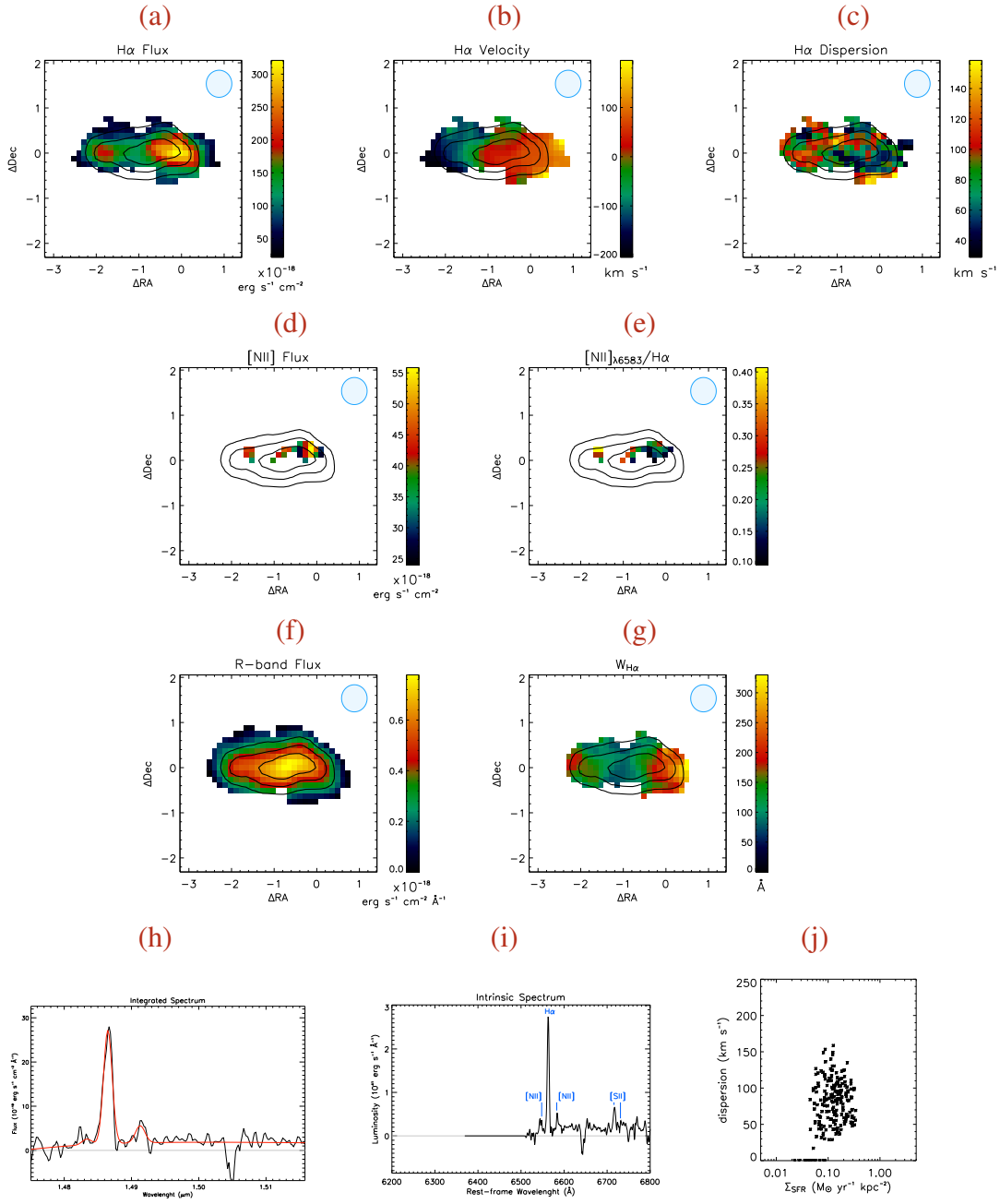

Figure 2.61 (a) Spatial distribution of the Hα line flux, in units of 10^{-18} erg s^{-1} cm^{-2}, (b) Hα velocity field, in km s^{-1}, (c) velocity dispersion distribution, in km s^{-1}, (d) spatial distribution of the [NII] line flux, in units of 10^{-18} erg s^{-1} cm^{-2}, (e) and spatial distribution of the ratio of the [NII] over the Hα line fluxes, (f) *R*-band continuum flux, in units of 10^{-18} erg s^{-1} cm^{-2} Å^{-1}, (g) equivalent width of the Hα line in Å, (h) integrated spectrum (in observer-frame) centered on the Hα line: the red curve is the best fit for Hα and [NII], (i) intrinsic spectrum (in rest-frame) and (j) Hα velocity dispersion as a function of the star formation rate surface density. The contours superimposed on the maps follow the *R*-band flux distribution. Blue circles represent the FWHM of the PSF.

2.4.0.51 ZC-1101592 $z = 1.40$

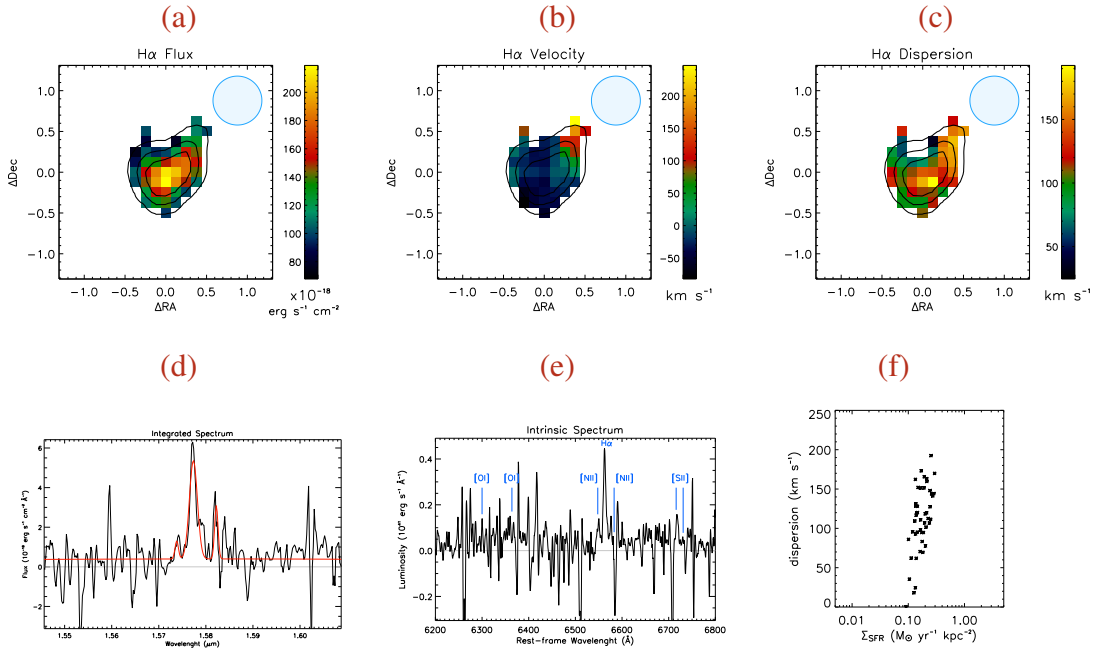

Figure 2.62 (a) Spatial distribution of the Hα line flux, in units of 10^{-18} erg s^{-1} cm^{-2}, (b) Hα velocity field, in km s^{-1}, (c) velocity dispersion distribution, in km s^{-1}, (d) integrated spectrum (in observer-frame) centered on the Hα line: the red curve is the best fit for Hα and [NII], (e) intrinsic spectrum (in rest-frame) and (f) Hα velocity dispersion as a function of the star formation rate surface density. The contours superimposed on the maps follow the Hα flux distribution. Blue circles represent the FWHM of the PSF.

2.4.0.52 ZC-782941$_{AO}$ $z = 2.18$

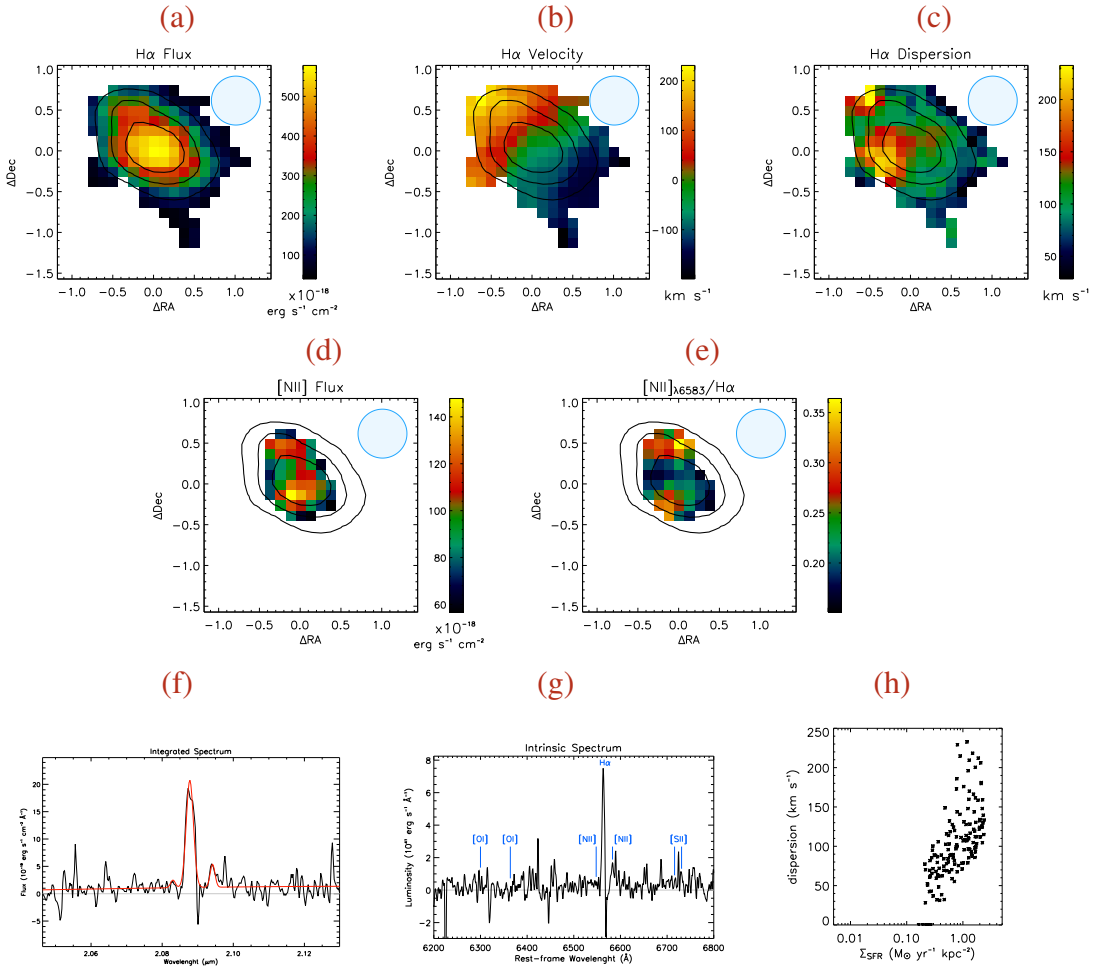

Figure 2.63 (a) Spatial distribution of the Hα line flux, in units of 10^{-18} erg s^{-1} cm^{-2}, (b) Hα velocity field, in km s^{-1}, (c) velocity dispersion distribution, in km s^{-1}, (d) spatial distribution of the [NII] line flux, in units of 10^{-18} erg s^{-1} cm^{-2}, (e) and spatial distribution of the ratio of the [NII] over the Hα line fluxes, (f) integrated spectrum (in observer-frame) centered on the Hα line: the red curve is the best fit for Hα and [NII], (g) intrinsic spectrum (in rest-frame) and (h) Hα velocity dispersion as a function of the star formation rate surface density. The contours superimposed on the maps follow the Hα flux distribution. Blue circles represent the FWHM of the PSF.

2.4.0.53 ZC-782941$^{0.1}_{AO}$ $z = 2.18$

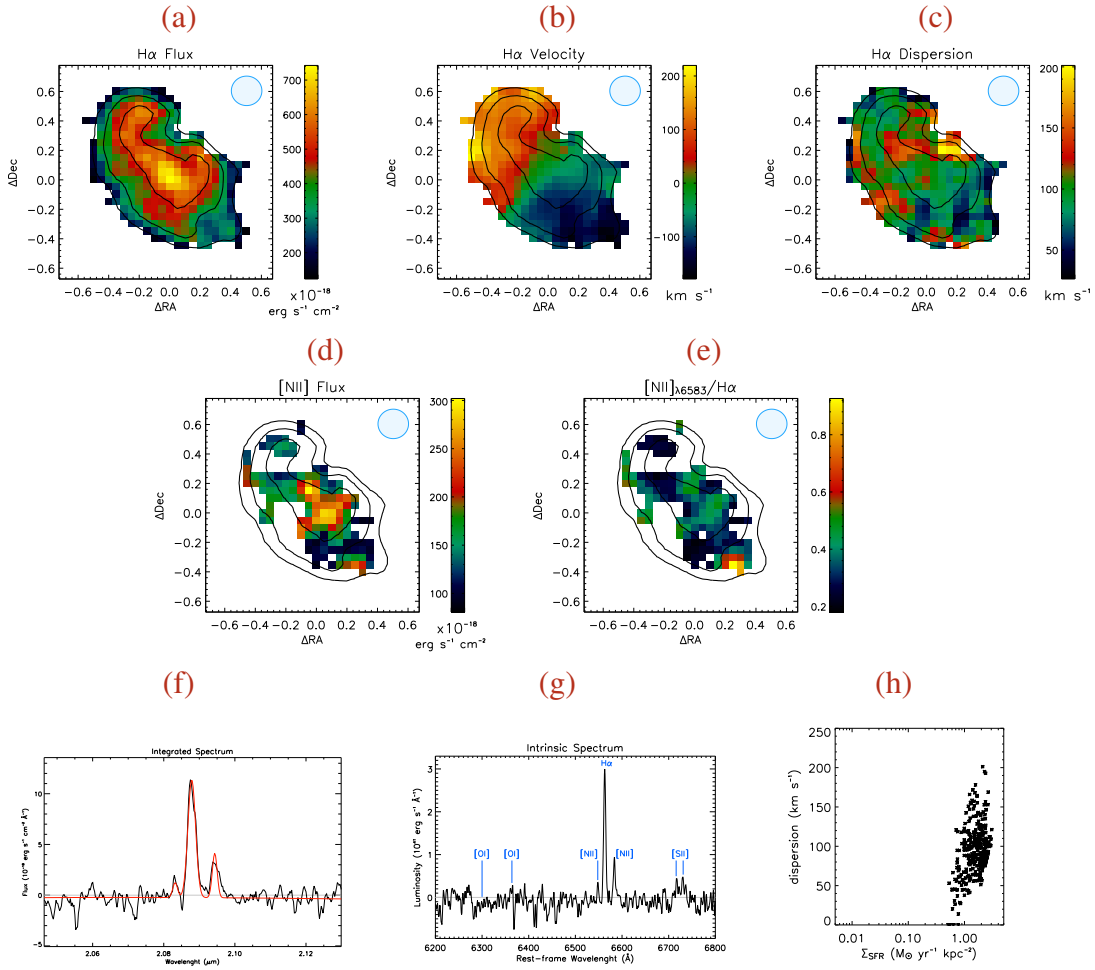

Figure 2.64 (a) Spatial distribution of the Hα line flux, in units of 10^{-18} erg s^{-1} cm^{-2}, (b) Hα velocity field, in km s^{-1}, (c) velocity dispersion distribution, in km s^{-1}, (d) spatial distribution of the [NII] line flux, in units of 10^{-18} erg s^{-1} cm^{-2}, (e) and spatial distribution of the ratio of the [NII] over the Hα line fluxes, (f) integrated spectrum (in observer-frame) centered on the Hα line: the red curve is the best fit for Hα and [NII], (g) intrinsic spectrum (in rest-frame) and (h) Hα velocity dispersion as a function of the star formation rate surface density. The contours superimposed on the maps follow the Hα flux distribution. Blue circles represent the FWHM of the PSF.

Chapter 3

Physical conditions in the ISM of intensely star-forming galaxies at redshift~2

Lehnert, M. D., Nesvadba, N. P. H., Le Tiran, L., Di Matteo, P., van Driel, W., Douglas, L. S., Chemin, L., & Bournaud, F.
Published in *The Astrophysical Journal*, 699:1660-1678, 2009.

Abstract: We analyze the physical conditions in the interstellar gas of 11 actively star-forming galaxies at z~2, based on integral-field spectroscopy from the ESO-VLT and HST/ NICMOS imaging. We concentrate on the high Hα surface brightnesses, large line widths, line ratios and the clumpy nature of these galaxies. We show that photoionization calculations and emission line diagnostics imply gas pressures and densities that are similar to the most intense nearby star-forming regions at z=0 but over much larger scales (10-20 kpc). A relationship between surface brightness and velocity dispersion can be explained through simple energy injection arguments and a scaling set by nearby galaxies with no free parameters. The high velocity dispersions are a natural consequence of intense star formation thus regions of high velocity dispersion are not evidence for mass concentrations such as bulges or rings. External mechanisms like cosmological gas accretion generally do not have enough energy to sustain the high velocity dispersions. In some cases, the high pressures and low gas metallicites may make it difficult to robustly distinguish between AGN ionization cones and star formation, as we show for BzK-15504 at z=2.38. We construct a picture where the early stages of galaxy evolution are driven by self-gravity which powers strong turbulence until the velocity dispersion is high. Then massive, dense, gas-rich clumps collapse, triggering star formation with high efficiencies and intensities as observed. At this stage, the intense star formation is likely self-regulated by the mechanical energy output of massive stars.

Contents

3.1 Introduction

Elucidating the physical processes that regulate global star formation is one of the keys to understanding galaxy evolution. The power-law relation, over several orders of magnitude, between the warm HI and cold molecular gas surface density and star formation intensity ("Schmidt-Kennicutt law") is telling us that there must be underlying physical processes that control and regulate star formation (e.g., Kennicutt et al., 2007). However, with a myriad of possible mechanisms for regulating star formation over large scales – cloud formation and destruction, mechanical energy output from stars and AGN, spiral density waves, turbulence induced by gravity and mechanical energy, magnetic fields, mixing layers, and many others – it is challenging to distill a unifying explanation over many orders of magnitudes in gas density. One possible way of advancing our understanding of the processes that regulate global star formation is by studying the most extreme star-forming galaxies locally and at cosmological distances (e.g., Lehnert & Heckman, 1996a; Shapley et al., 2003; Verma et al., 2007).

Thanks to recent technological improvements, we are now able to study the basic physical processes driving galaxy assembly directly and over large ranges of cosmic time. In particular, the number of galaxies at redshifts of 2−3 with detailed integral-field spectroscopic studies in the rest-frame optical is still small, less than a few dozen, but growing rapidly. These observations allow us to trace spatially resolved emission-line properties, and to investigate galaxy kinematics and the physical conditions of the ionized gas. Up to now, most studies have focused on the kinematic properties of the galaxies and less so on the properties of the emission lines themselves beyond their relative velocities and widths. Recombination line fluxes were used to estimate star-formation rates using simple prescriptions developed for low-redshift galaxies (Genzel et al., 2006; Förster Schreiber et al., 2006; van Starkenburg et al., 2008; Law et al., 2007; Wright et al., 2007; Nesvadba et al., 2008b).

With these estimates and assumptions, far-reaching conclusions have been made regarding the modes of galaxy assembly and the drivers of star formation in the early Universe. Many of these studies (e.g., Genzel et al., 2006; Förster Schreiber et al., 2006) favor a scenario where high-redshift galaxies exhibit gaseous disks of ∼10-20 kpc in size, which, unlike galaxies at low redshift, are dynamically hot with large gas velocity dispersions, σ, relative to their bulk velocities, v (see also Nesvadba et al., 2006a). The ratios of random to large scale velocity shear at high redshift are of order v/σ ∼few, compared to $v/\sigma \geq 10$ at low redshift. To explain these observations, Kereš et al. (2005, 2009); Ocvirk et al. (2008); Dekel & Birnboim (2008a) proposed a scenario where galaxies at z∼ 2 accrete significant amounts of cold gas, which after accumulating and forming gaseous disks, will become gravitationally unstable and lead to the observed high star formation

rates (Genzel et al., 2008; Dekel & Birnboim, 2008a). In this picture, mergers and hydrodynamic processes like feedback from star formation and AGN play only a minor role in assembling early galaxies, beginning to play a significant role only as a consequence of the build-up of the bulk of the stellar mass in bulges and disks.

Given the faintness of the targets and the often low number of diagnostic optical emission lines, usually only studying Hα or [OIII]λ5007, many of these results must rely on the assumption that the gas conditions in the interstellar medium will overall be largely similar to those in galaxies at low redshift. This assumption has not been tested directly on the observed properties of high-redshift galaxies.

We already know of (or may plausibly expect) several major differences between galaxies at high and at low redshift, which may strongly influence the state of their interstellar medium and thus, their rest-frame optical line emission. First, many galaxies at high redshift are less evolved, with higher fractions (Erb et al., 2006b) of lower-metallicity gas (Erb et al., 2006a; Maiolino et al., 2008). This may have rather subtle observational consequences. For example, Robertson & Bullock (2008) discuss the expected morphology of an advanced (or mostly relaxed) merger of two gas-rich disk galaxies as would be observed using state-of-the-art Integral-Field Units (IFUs). They find that their model reproduces the observed properties of high redshift galaxies as well as pure (and isolated) disk models, which are often favored by observers in contrast to on-going or advanced mergers (Nesvadba et al., 2006a; Genzel et al., 2006, 2008; Wright et al., 2009a).

Second, virtually all high-redshift galaxies studied in detail with IFUs have very high surface brightnesses of the recombination lines. Given the impact of cosmological surface brightness dimming, which is a strong function of redshift ($\propto (z+1)^4$ for bolometric luminosities and spectral lines, $\propto (z+1)^5$ for broadband photometry due to the additional 'stretching' of the continuum; see, e.g., Tolman, 1930), and current observational limits, all observations at high redshift will naturally be biased towards the most luminous emission-line regions, and the most luminous galaxies. As a result, all galaxies so far studied with IFUs have star-formation rates of several 10s of $M_\odot$ yr^{-1} or more, and typical star-formation intensities, SFI, well above the critical threshold of $SFI_{crit} \sim 0.1$ $M_\odot$ yr^{-1} kpc^{-2}(Heckman, 2003) necessary to drive vigorous outflows in local galaxies. Galaxies with $SFI \gtrsim SFI_{crit}$ are observed to create and maintain strongly over-pressurized bubbles of hot gas from the thermalized ejecta of supernovae and massive young stars, which expand perpendicular to the disk plane and produce galactic-scale outflows (Heckman et al., 1990; Lehnert & Heckman, 1996a,c). These outflows may play an important role in rendering a starburst "self-regulating" (Dopita & Ryder, 1994; Silk, 1997). The observational signatures of starburst-driven winds, such as characteristic velocity offsets between the rest-frame UV absorption lines and the systemic velocity (Pettini et al., 2000; Erb et al., 2004, 2006a), or blue wings in rest-frame optical emission lines (e.g. Nesvadba et al., 2007), are commonly observed at high redshift.

In a detailed study of a massive, z$\sim$ 2.6 starburst and the related outflow of a submillimeter-selected galaxy at z$\sim$ 2.6, Nesvadba et al. (2007) found that overall, the physical properties of maximal starbursts at z$\sim$2$-$3 appear very similar to local starbursts. The starburst appears to be self-regulating, and characteristic, density-sensitive line ratios suggest that the pressures in the starburst region, which are ultimately driving the observed outflow, are very similar to those in low-redshift starbursts.

This may have a non-negligible impact on our interpretation of the physical processes in high-redshift galaxies, because much of our well-established low-redshift emission line diagnostics relies on the physical gas conditions in rather subtle ways. For example, when relating the ratios of strong, low-ionization nebular emission lines with Hα, like, [NII]/Hα, [OI]/Hα, or [SII]/Hα with the [OIII]/Hβ ratios, starburst galaxies will fall onto a characteristic curve (Baldwin et al., 1981; Veilleux & Osterbrock, 1987), whereas AGN will fall into a different part of the diagram. For high-redshift galaxies, however, the same relationship may not be strictly valid. Erb et al. (2006a) observed that, although UV selected galaxies at z$\sim$ 2 follow the overall shape of the starburst-curve in the [NII]/Hα versus [OIII]/Hβ diagram, as a whole, they are offset towards larger [NII] fluxes. Brinchmann et al. (2008) collected a comparison sample of low-redshift SDSS galaxies with similar offsets, and found that these galaxies also had statistically higher Hα equivalent widths. They argue that the most likely explanation may be higher ionization parameters and densities in high-redshift star-forming regions compared to local galaxies. We will further develop these arguments and illustrate that pressures induced by the starbursts may very naturally explain some of the kinematic properties of high-redshift galaxies as well.

However, the line ratios indicative of excitation by an AGN may also shift at high redshift (Groves et al., 2006). Since most luminous AGN at low redshift preferentially reside in massive galaxies (e.g., Kauffmann et al., 2003), and because gas metallicity correlates with galaxy mass (e.g., Tremonti et al., 2004), most AGN hosts at low redshift will have narrow-line regions with high metallicities. Groves et al. (2006) modeled the diagnostic line ratios for AGN in relatively low-metallicity host galaxies. They showed that star-formation plus AGN in relatively low metallicity host galaxies could explain the offset observed for example by Erb et al. (2006a). We will show that many z$\sim$ 2 $-$ 3 galaxies fall very close to these regions, which may make it difficult to robustly quantify the role of AGN and starbursts in exciting the optical emission line gas.

We will in the following present an analysis of 11 galaxies with particularly deep near-infrared integral-field spectroscopy obtained at the VLT. These data allow in particular to trace intrinsically fainter nebular emission lines such as [OI] λ6300 and [SII] $\lambda\lambda$6716,6731 which being close in wavelength to Hα often fall into the same band. A subset of 5 galaxies also have measurements of the [OIII]

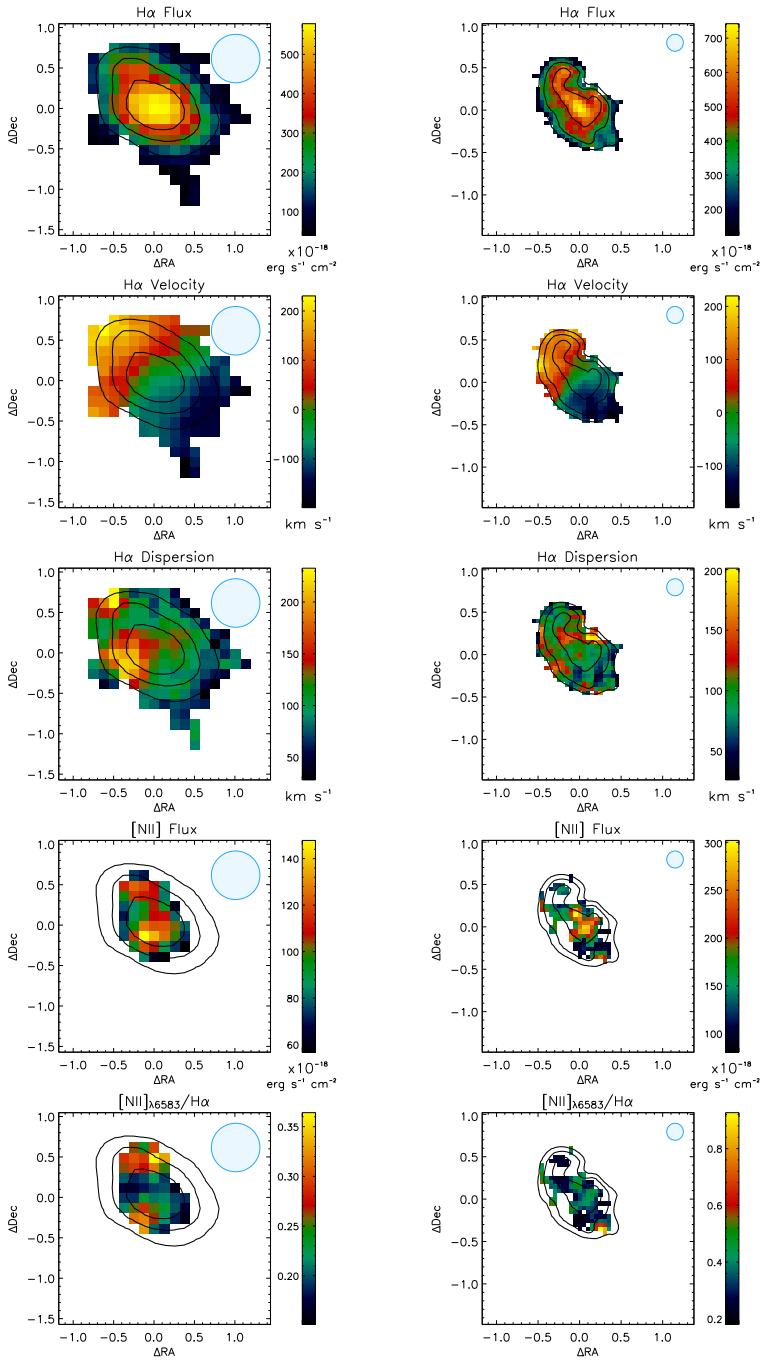

Figure 3.1 The various emission line and kinematic maps for the source, ZC782941, used in our analysis. *(left column and from top to bottom)* The Hα flux, velocity dispersion, velocity, [NII]λ6583, and [NII]λ6583/Hα ratio maps respectively for the 250 mas (non-AO assisted) data for ZC782941. *(right column)* The maps of ZC782941 in the same order as for the left column but now for the observations taken with the 100 mas pixel scale and with the assistance of adaptive optics. In each of the panels, we show the approximately size of the full-width at half-maximum of the seeing disk (the blue disk in the upper-right corner of each plot) and the relative positions are in arc seconds. The contours in each maps are the distribution of the Hα emission in each of the two cubes. All maps were centered on the peak in the Hα surface brightness distribution which defines the (0,0) in each panel.

λ4959,5007 and Hβ lines, which fall into the near-infrared H band, and which have not been discussed previously in the literature. Many of the arguments in previous papers are based on the implicit assumption that most of the emission originates from "ordinary" HII regions similar to low-redshift disk galaxies and thus, that observations of the warm ionized gas are representative of all of the kinematics and other properties of the phases of the ISM. In contrast, our analysis is aimed at quantifying the physical conditions in the interstellar medium of these galaxies principally by investigating the surface brightnesses of the recombination lines, various optical emission line ratios, and line widths to test this underlying assumption.

Throughout this chapter we adopt a flat H_0 =70 km s^{-1} Mpc^{-3} concordance cosmology with $\Omega_\Lambda = 0.7$ and $\Omega_M = 0.3$.

3.2 Observations and data reduction

For our analysis of the physical conditions in the interstellar medium of strongly star-forming, high-redshift galaxies, we collected a sample of 11 galaxies at z$\sim$1.5$-$2.5 from the SINS program (Förster Schreiber et al., 2006) with rest-frame optical integral-field spectroscopy (Table 3.1).

Data were taken with the near-infrared integral-field spectrograph SINFONI on the ESO Very Large Telescope in several runs between 2004 and 2006. Observations have been presented elsewhere (Förster Schreiber et al., 2006; Genzel et al., 2008). We reduced these data independently from any other previous work, using the IRAF (Tody, 1993) standard tools for the reduction of longslit spectra, modified to meet the special requirements of integral-field spectroscopy, and complemented by a dedicated set of IDL routines. Data are dark-frame subtracted and flat-fielded. The position of each slitlet is measured from a set of standard SINFONI calibration data, measuring the position of an artificial point source. Rectification along the spectral dimension and wavelength calibration are done before night sky subtraction to account for some spectral flexure between the frames. Curvature is measured and removed using an arc lamp, before shifting the spectra to an absolute (vacuum) wavelength scale with reference to the OH lines in the data. To account for variations in the night sky emission, we normalize the sky frame to the average of the object frame separately for each wavelength before sky subtraction, correcting for residuals of the background subtraction and uncertainties in the flux calibration by subsequently subtracting the (empty sky) background separately from each wavelength plane. These data reduction procedures have fewer interpolations and are optimized for faint, extended, low surface brightness objects compared to the SINFONI pipeline which obviously must be capable of reducing a much wider variety of objects. Overall, we expect that these differences lead to more robust data compared to previous reductions but overall the results are largely consistent.

The three-dimensional data are then reconstructed and spatially aligned using the telescope offsets as recorded in the header within the same sequence of dithered exposures (about one hour of exposure), and by cross-correlating the line images from the combined data in each sequence, to eliminate relative offsets between different sequences. Telluric correction is applied to each final cube. Flux scales are obtained from standard star observations taken every hour at similar position and air mass as the source.

We also used the standard stars to monitor the seeing during observations, and we find an effective seeing in the combined cubes of typically FWHM 0″.5 −0″.8. The spectral resolution was measured from night-sky lines and is FWHM∼ 115 and 150 km s^{-1} in the K and H-bands, respectively, for the 250 mas pixel scale ("mas" is milli-arcseconds). In addition, for two of the sources, data were taken with adaptive optics assistance which yielded a seeing about 200 mas. The data were taken with the 100 mas pixel scale in SINFONI. In Figure 3.1 we show an example of various maps that have not been presented previously for the source, ZC782941. In addition, we show example maps of the sources, Q2343-BX610 and Q2343-BX528 for comparison with previously published maps (e.g., Förster Schreiber et al., 2006). In our subsequent analysis, we will analyze the integrated H-band spectra of the sources when they are available. We show an example of the H and K-band integrated spectra for the source, Q2343-BX610, in Figure 3.3.

In addition, we reduced publicly available HST/NICMOS images of 5 of the galaxies in our sample, which were observed as part of proposal ID 10924 (P.I. Shapley). Each galaxy was observed for 4 orbits using the NIC2 camera with the F160W (H-band) filter and a pixel scale of 0″.075. The calibrated individual exposures (_cal files) were downloaded from the HST archive and reduced using the standard IRAF routines *pedsky*, to correct the well-studied pedestal effect caused by residual bias, and *multidrizzle*, to combine the exposures. Images were corrected for the impact of additional cosmic ray events during passage through the South Atlantic Anomaly when required. The resulting images are shown in Figure 3.4.

3.3 The remarkably high Hα surface brightnesses and trends

In this section, we will discuss the emission line properties of our sample of galaxies such as surface brightnesses, the relationship between the velocity dispersion and surface brightness, and the impact of "beam smearing". This analysis will form the basis of our subsequent discussion. We refer the reader to Förster Schreiber et al. (2006), Genzel et al. (2006), and Genzel et al. (2008) for a discussion of the overall kinematic properties of the galaxies in our sample.

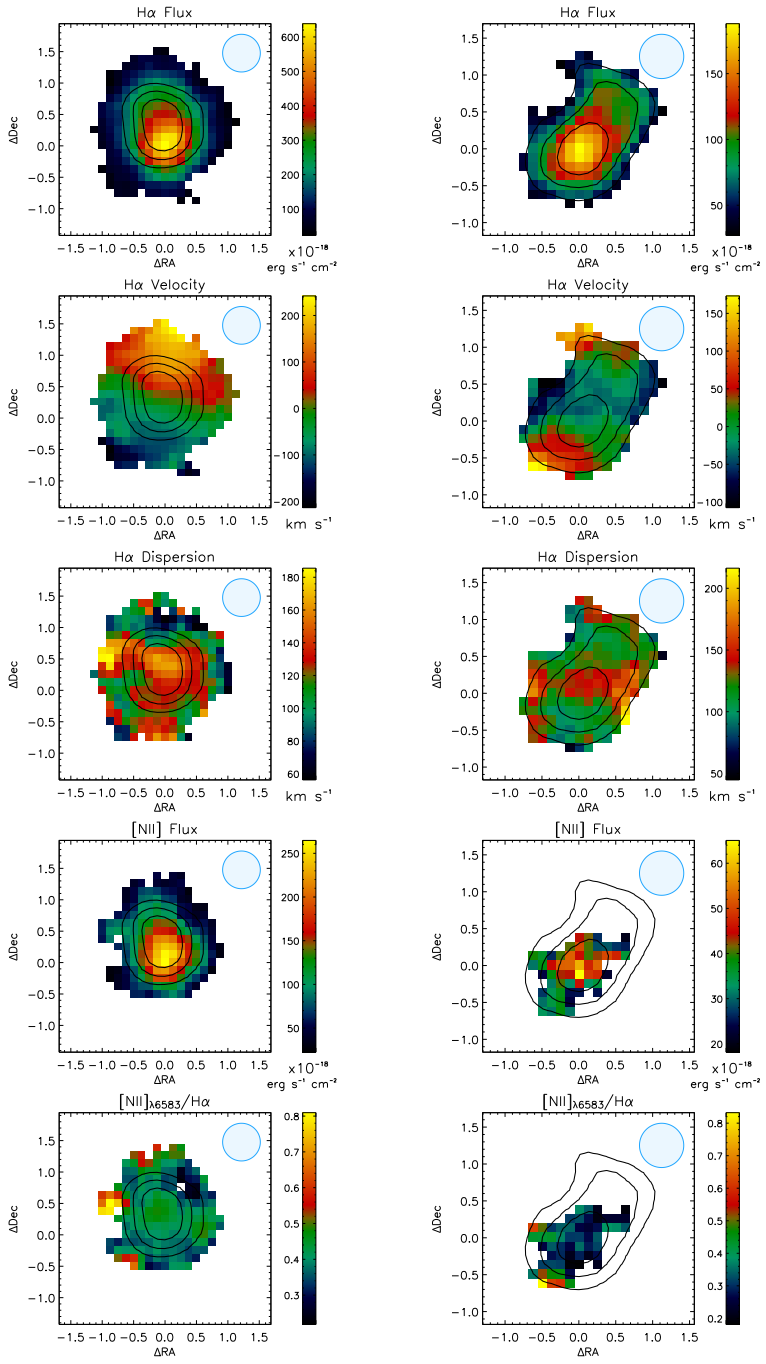

Figure 3.2 The various emission line and kinematic maps for the source, Q2343-BX610 and Q2343-BX528, used in our analysis. We show these two sources for comparison with previously published maps in the literature. *(left column and from top to bottom)* The Hα flux, velocity dispersion, velocity, [NII]λ6583, and [NII]λ6583/Hα ratio maps respectively for the for Q2343-BX610. *(right column)* The maps of Q2343-BX528 in the same order as for the left column. In each of the panels, we show the approximately size of the full-width at half-maximum of the seeing disk (the blue disk in the upper-right corner of each plot) and the relative positions are in arc seconds. The contours for the maps of Q2343-BX610 represent the continuum, while those of Q2343-BX528 represent the Hα surface brightness. All maps were centered on the peak in the Hα surface brightness distribution which defines the (0,0) in each panel.

3.3.1 Hα surface brightness

One of the most remarkable, but so far little discussed, observational findings of z$\sim$ 2 – 3 galaxies studied with IFUs are their high emission line surface brightnesses. In our sample we measure Hα surface brightnesses of $\sim 10^{-15.1}$ – $10^{-16.9}$ erg cm^{-2} s^{-1} arcsec^{-2} (Figure 3.5). The data were smoothed by 3×3 pixels, i.e., averaged in areas of size 0$''$.375 ×0$''$.375, which is appropriate since the spatial resolution is typically $\sim$ 0$''$.5-0$''$.6 or $\sim$4–5 pixels. Correcting for cosmological surface brightness dimming, this corresponds to a typical rest-frame surface brightness of $10^{-13.2}$ – $10^{-14.8}$ erg cm^{-2} s$^{-1}\square''$ (Figure 3.6). This represents a lower limit to the highest intensity regions, due to the "beam smearing" effect of the low spatial resolution of our data. In fact, for two of the galaxies, we can further quantify the effect of beam smearing on both the surface brightness distribution and line widths. For BzK-15504 and ZC782941, where we have both adaptive optics assisted and seeing limited observations, we find that the offset in surface brightness between both sets of observations is typically more than a factor of 3 (Figure 3.7). This factor is similar to the ratio of the area of the point spread function in both sets (the full width half maximum of the seeing disk is typically about 0$''$.5 for the seeing limited data versus about 0$''$.2 in the AO assisted data), suggesting that the star-forming clumps are at best marginally resolved in either data set. Much of the structure must be smaller than about 2 kpc, the physical resolution of our highest resolution data. Moreover, this implies that all of the measured surface brightnesses of the most intense Hα emission regions are under-estimated, even in the AO-assisted observations.

An Hα surface brightness comparison between galaxies in the local and distant Universe illustrates the exceptional nature of the galaxies in our sample. Galaxies that reach the highest surface brightnesses we observe and over similar physical scales do not exist at low redshift. In a study of 84 Virgo cluster and isolated spiral galaxies, many galaxies reach surface brightness levels at the low end of what we have observed at high redshift ($\log \mathrm{SB}_{\mathrm{H}\alpha} \lesssim -14$ erg cm^{-2} arcsec^{-2}) but only in their nuclei and on scales about or less than 1 kpc (Koopmann et al., 2006; Koopmann & Kenney, 2006, 2004b,a; Koopmann et al., 2001). Local starburst galaxies can reach higher surface brightnesses (but not as high as our peak surface brightnesses, Lehnert & Heckman, 1995, 1996a) but again only in regions that are nuclear or circumnuclear with sizes $\lesssim$ 1 kpc (and well within the "turn-over" radius of the rotation curve; Lehnert & Heckman, 1996c). Even in the more extreme starburst sample of Armus et al. (1989, 1990), only a handful of galaxies reach surface brightnesses sufficient to be observed at z$\sim$2 (such as M82). At high redshift, Hα surface brightnesses as extreme as those found only in the nuclei of nearby galaxies on small scales are found over significantly larger isophotal radii of order 10-20 kpc and are generally more extreme. Although our comparison includes some of the most

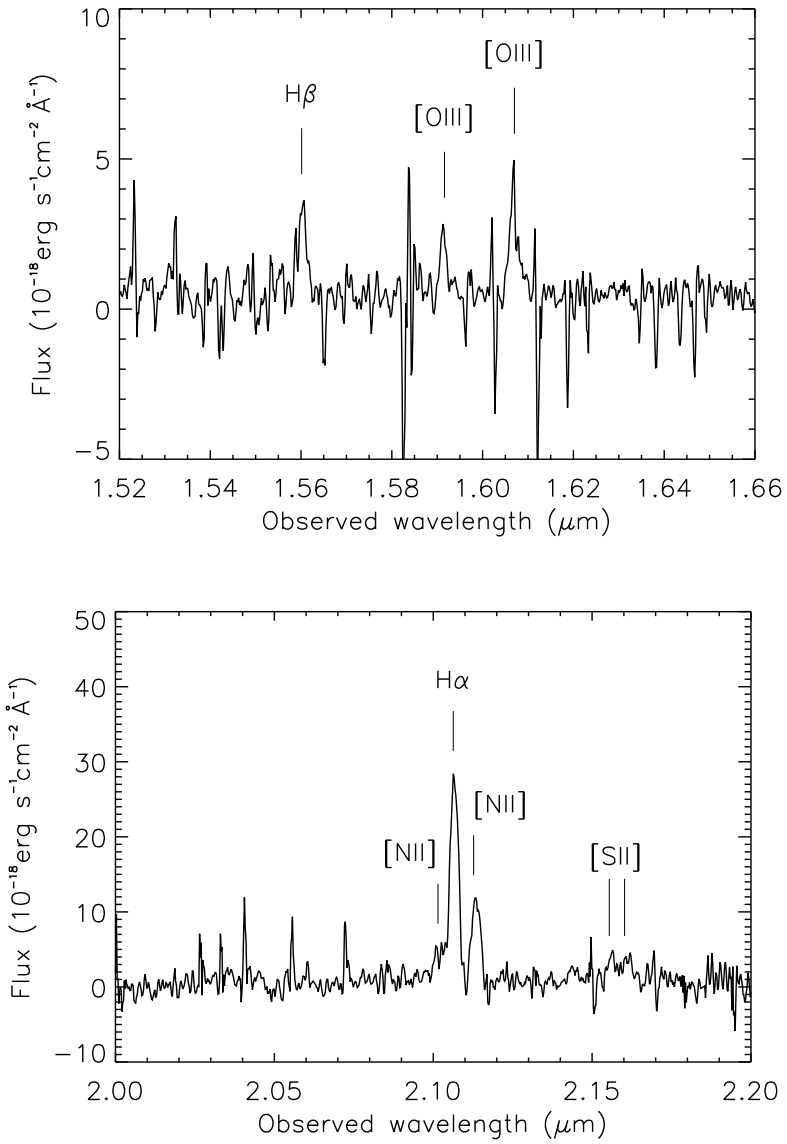

Figure 3.3 The integrated spectrum of Q2343-BX610 in the H-band *(top)* and the K-band *(bottom)*. All of the strong optical lines are indicated.

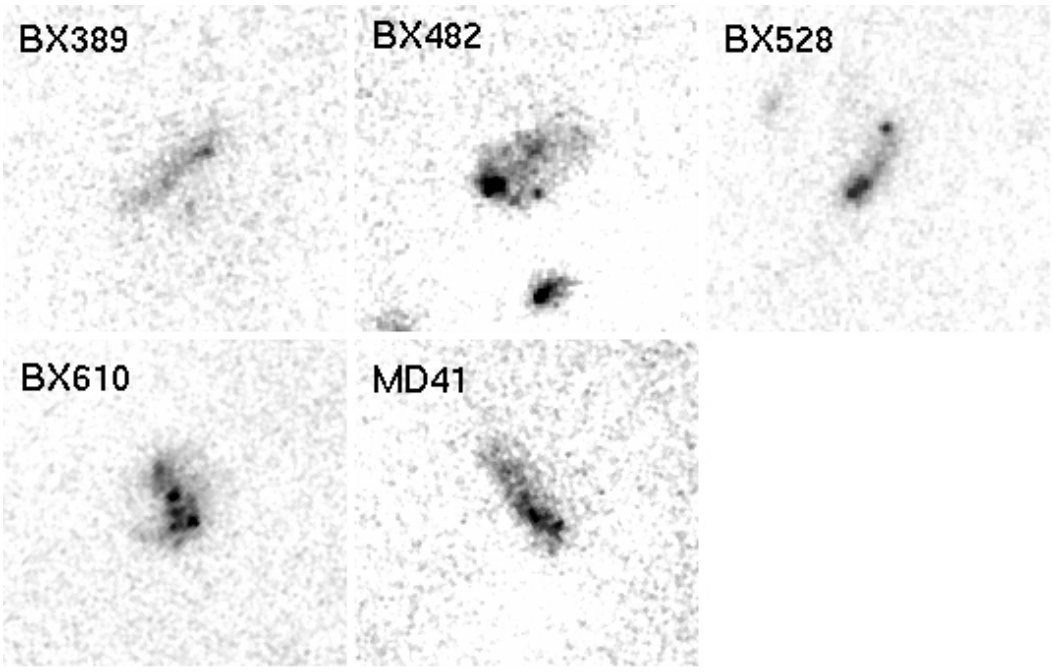

Figure 3.4 HST/NICMOS NIC2 H-band (F160W) images of 5 galaxies within the sample. Images are 5×5″, and North is at the top and East is on the left. The images have a pixel scale of 30 mas (the drizzled pixel size) and each image reaches a depth of about 28.6-28.7 m_{AB} pixel^{-1} (for a NICMOS pixel scale of 76 mas) or about 25.8-25.9 m_{AB} arcsec^{-2}.

powerful and intense starbursts in the local Universe, they generally do not reach sufficiently high surface brightnesses over large enough areas to correspond to any of the galaxies in our distant galaxy sample. Moreover, at the 4−5 kpc resolution of our seeing limited high-redshift data, none of the local starbursts would reach these maxima in the surface brightnesses that are observed due to the heavy spatial smoothing and dilution by regions with lower surface brightness.

This lack of correspondence renders any simple analogy between "ordinary" quiescently star-forming spiral galaxies in the local Universe and galaxies at z∼2 questionable. Possible significant differences include the distribution of mass in various phases of the ISM, of density, of star-formation intensity, of gas fraction, and many more. Moreover, this lack implies that we cannot only study the kinematics of z∼2 galaxies without investigating the nature of the physical processes that power their high surface brightness line emission, and the impact such a finding has on their kinematics and overall gas physics.

3.3.2 Hα surface brightness: Characteristic correlations and Beam Smearing

To elucidate the underlying physical cause of the high Hα surface brightness of our galaxies, we searched for correlations with other parameters. As shown in Figure 3.5, 3.6, and 3.7, we find that both the Hα surface brightness and Hα velocity dispersion decline with radius. We generally do not find a substantial increase in line widths when comparing the seeing-limited data with data taken with the adaptive optics system, although as expected, we observe higher Hα surface brightness in some regions (Figure 3.7). Thus beam smearing does have a tendency to lower the observed surface brightness suggesting that most of the structure within these galaxies is not resolved.

However, beam smearing is worrying in that the trends we observe will obviously be influenced by our poor resolution. We must take care in determining what the true impact of our poor resolution might actually be on the distribution and kinematics of the emission line gas. We observe the trends with Hα surface brightness over physical scales that are ∼6× larger than the spatial resolution of our data. To investigate explicitly whether this may be an artifact due to low spatial resolution we constructed several simple models that have bright central point sources with broad lines. Such models would correspond to a bright AGN or concentration of mass increasing the velocity dispersion in the centers of these galaxies. Although this may appear unphysical, since we do not see bright point sources, it will help to investigate, for example, the effects of a narrow-line AGN. Our toy models (not shown) do not reproduce the observed trends, which implies it is very difficult to contrive a realistic situation where only the poor resolution of our data would lead to the trends we observe between surface brightness and radius.

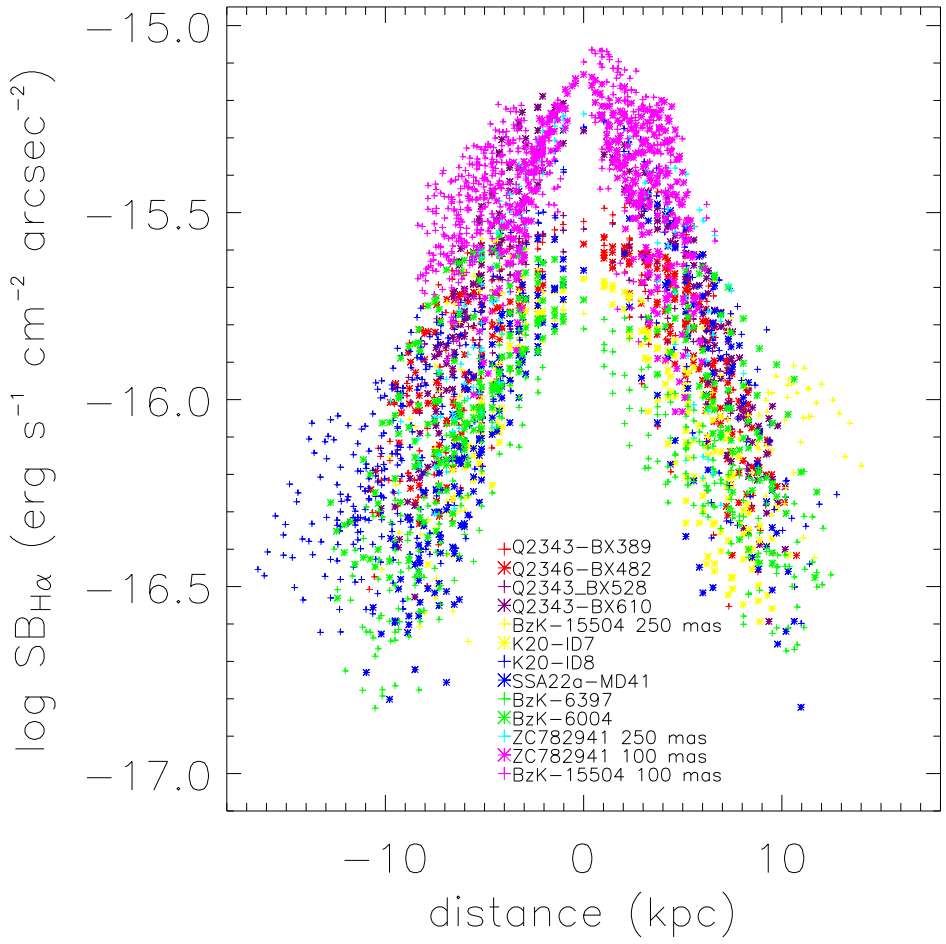

Figure 3.5 A plot of the observed Hα surface brightness versus the projected physical radius. The surface brightness has not been corrected for cosmological dimming. Each point represents a position centered on one pixel of 0″.125 ×0″.125 , whereas the data were smoothed by 3×3 pixels, i.e., averaged in areas of size 0″.375 ×0″.375. As the spatial resolution is typically ∼ 0″.5-0″.6 (or ∼4−5 pixels), the points are therefore not independent, and each data set has a limited number of independent points (about 5-10, see Shapiro et al., 2008). The legend to the figure indicates each galaxy in our sample. The zero radius was chosen to represent the symmetry point in either the kinematics or the outer isophotal Hα distribution. The distribution of surface brightness is not symmetrical for most of the sources.

Could beam smearing induce an apparent relationship between line width and surface brightness? Could this trend be related to distant galaxies having more complex light profiles? To understand the impact of beam smearing and complex light profiles of these galaxies on our analysis, we constructed simulated data cubes using the light distributions observed in NICMOS H-band images of five galaxies in our sample (Figure 3.4). We assumed that the line emission follows the distribution of the H-band flux, that the velocity dispersion is 25 km s^{-1} independent of position or radius (Epinat et al., 2009), and that the rotation curves and peak velocities are those from Förster Schreiber et al. (2006). We did not include noise in this display as it results in a scatter plot about the assumed constant velocity dispersion, masking the trend of some pixels to reach high dispersions (which we think is extremely important to make obvious). Thus for clarity, we do not show a plot of our analysis with noise.

As we can see in Figure 3.8, assuming typical velocity dispersions seen in local disk galaxies and light distributions of distant galaxies and smoothing them to our resolutions does not reproduce the data (see also Wright et al., 2009a; Genzel et al., 2008; Förster Schreiber et al., 2006). We do see that there are some regions of high dispersion, but this makes up a small number of pixels whereas a great majority of the regions, regardless of their relative surface brightness have dispersions similar to what we initially assumed (i.e., 25 km s^{-1}). This, coupled with the lack of increase in the dispersions when comparing our seeing limited data with that taken using adaptive optics, suggests that beam smearing, while obviously playing a role in these trends, does not cause these trends.

3.4 Emission-line properties of high-redshift galaxies

Given the high star-formation rates (Förster Schreiber et al., 2006; Genzel et al., 2008) and emission line surface brightnesses in these galaxies, we hypothesize that the high surface brightnesses and relationship between velocity dispersion and surface brightness in Hα, may be explained by postulating that the intense star formation is pressure-driven by mechanical energy input from the starburst itself and self-gravity of gas at high surface densities. In this sense, the star formation will be self-regulated. We will argue that these systems may be analogous to nearby starburst galaxies, such as M82, except that at high redshift, the intense star formation and strong mechanical energy injection must act over significantly larger areas (10-20 kpc compared to a few kpc, e.g., Heckman et al., 1990; Lehnert & Heckman, 1996a), but with a similar local surface brightness and similarly high pressures. However, this is not the only possibility and we will explicitly address different scenarios to investigate whether these relationship may be generated by cosmological

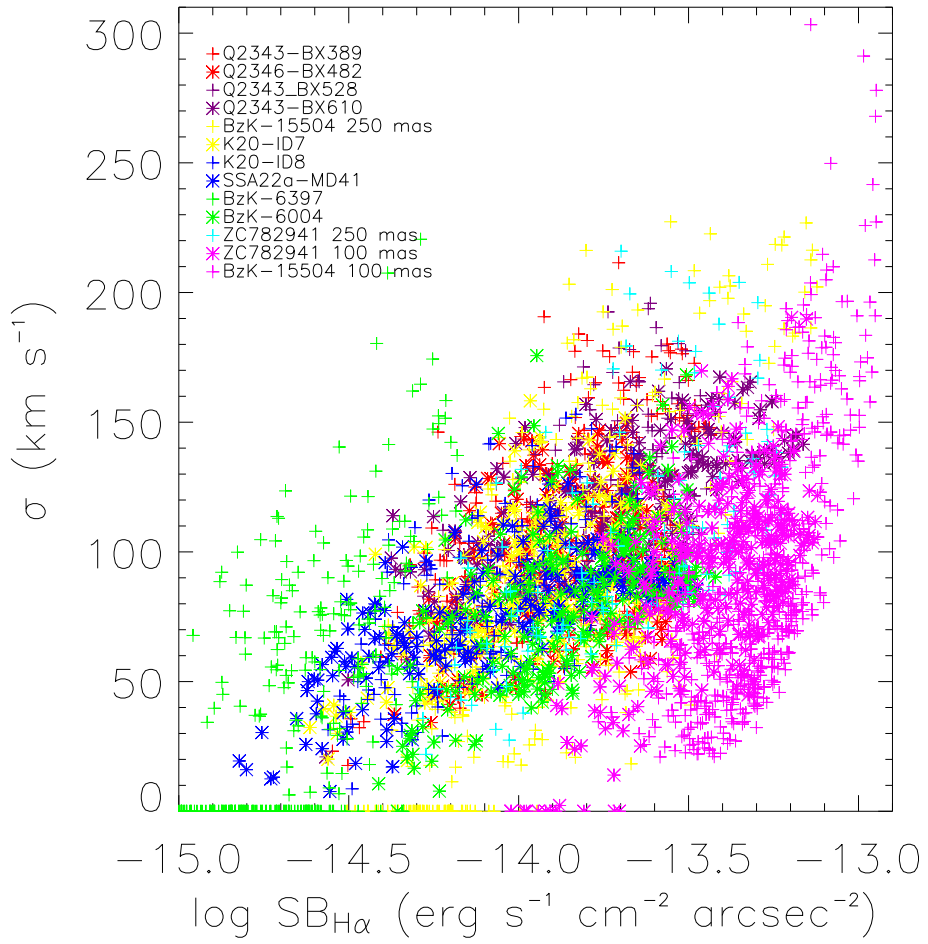

Figure 3.6 Plot of the Hα surface brightness (now corrected for surface brightness dimming) versus the observed velocity dispersion. See Figure 3.5 for details on the 3×3 pixel smoothing that was applied. The legend to the figure indicates which symbol represents which galaxy in our sample. There appears to be a relationship between surface brightness in Hα and the line width for both the ensemble of sources as well as within individual sources. Because of the trend between surface brightness and dispersion, velocity dispersions below the resolution of our data, about 50 km s^{-1} for the sources observed in the K-band (all but one of the sources shown here) and about 60 km s^{-1} for BzK-6397 have particularly large relative uncertainties.

gas accretion or gravitationally unstable disks. Some of our main arguments will rely on the detection of nebular emission lines like [NII]λ6583, [SII]$\lambda\lambda$6716,6731 or [OI]λ6300, which are relatively faint in high-redshift galaxies. We detected all of these lines in only one galaxy, while we detect all but [OI]λ6300 in 5 others. Where one of the lines is undetected or severely affected by a telluric night sky line, we give upper limits, provided that they are physically meaningful. For a subsample of 5 targets, our data include Hβ and [OIII]$\lambda\lambda$4959,5007, which fall into the near-infrared H-band for redshifts z>2. These data sets have not been discussed previously in the literature. We list the integrated emission line properties of these galaxies in Table 1. As the H-band data are rather shallow relative to the K-band, we typically detect only the highest surface brightness regions (and likely also regions of relatively low extinction).

We extracted emission line ratios from matched apertures in the H and K band data sets, covering the areas where line emission is detected in the H band. We use the measured, and not the extinction corrected line fluxes for the emission line diagnostics. This adds only a minor uncertainty, given the relatively low signal-to-noise ratio of our data, low luminosities of the low-ionization lines, and the fact that we will only use ratios of lines with very similar rest-frame wavelengths.

3.4.1 Extinctions

We estimated extinctions for the four objects with measured Hα and Hβ fluxes (Table 2). Hβ in Q2346-BX482, which would have been a fifth galaxy with a Hβ flux and extinction estimate, and the emission in the north of Q2343-BX389 are severely affected by night sky lines (so the measurement is only for the southern part of the galaxy), and for three other galaxies we identified the areas with reasonably bright Hβ emission, and extracted Hα from the same aperture (Table 2). For a galactic extinction law, and an intrinsic Balmer ratio of $F_{H\alpha}/F_{H\beta}$ =2.86, we find extinctions in the range of $A_V \sim 1-2$ magnitudes. This corresponds to correction factors of about 2−5 between observed and intrinsic Hα luminosities. We will neglect extinction in much of our subsequent discussion, but caution that intrinsic values are strict lower limits and may have been underestimated by factors of a few.

3.4.2 Electron densities and pressures

The line ratio of the [SII] doublet, [SII] λ6716/[SII] λ6731, is density-sensitive in the range of $\sim 10^{1-5}$ cm^{-3}. These lines are relatively faint, but we have robustly detected and spectrally resolved this doublet in six galaxies in our sample, at signal-to-noise ratios $\sim$ 10. We are thus able to measure electron densities directly, and to estimate the pressure in the partially ionized zones within the interstellar medium. Densities listed in Table 3.3 are in the range $\sim$ 100−1000 cm^{-3}. Such values are

typical, if not higher, than densities in the starburst regions of galaxies in the local Universe (such as M82; Lehnert & Heckman, 1996a) and suggest thermal pressures of about $10^{-8.5}$ – $10^{-9.5}$ dyne cm^{-2}, i.e., several orders of magnitude higher than in the interstellar medium in normal nearby galaxies. Similar pressures are found for the z=2.6 submillimeter galaxy SMMJ14011+0252 (Nesvadba et al., 2007). We will argue below that the ambient medium of our galaxies is highly pressurized, and show that these estimates are also consistent with pressures derived directly from photoionization models.

The high pressures may also explain another remarkable feature of our galaxies, namely their overall low ratios of low-ionization lines like [SII] $\lambda\lambda$6716,6731 and [NII] λ6583 compared to the high Hα luminosities. While the recombination lines increase linearly with increasing density and ionization parameter, the ratio of [SII] $\lambda\lambda$6716,6731 will decline with increasing ionization parameter (e.g., Wang et al., 1999). Since the gas with the highest surface brightness also has a declining ratio, measuring the density from the [SII] lines becomes more difficult as the surface brightness increases. Thus, it may not be surprising that we obtained [SII] measurements at sufficiently high signal-to-noise only for parts of our sample. This may also affect other diagnostic line ratios. Larger samples of high-redshift galaxies with deep spectroscopy of a comprehensive set of faint, diagnostic lines will help to secure these findings.

3.4.3 Diagnostic line ratios

Baldwin et al. (1981) and Veilleux & Osterbrock (1987) advocated the use of characteristic ratios of the bright optical nebular emission lines as diagnostics to differentiate between ionization due to starbursts and AGN. These so-called BPT diagrams relate the strengths of lines like [NII] λ6583, [OI] λ6300, or [SII] $\lambda\lambda$6716,6731 with those of the Balmer recombination lines and [OIII] λ5007, and gives us the ability to trace the physical conditions, namely temperature and ionization parameter, in the emission line gas. Due to the different ionizing spectra of starbursts and AGN, galaxies will fall into characteristic areas of the diagrams when their nebular emission is dominated by photoionization from young stars, or by an active nucleus.

We show the results in Figure 3.9 and 3.10, together with the loci of other galaxies at similarly high redshifts taken from the literature. It should be noted that all of these diagnostics are to a large degree empirical and developed for galaxies at low redshift, and that different evolutionary stages may influence the emission line diagnostics in a rather subtle way. As already stated by Erb et al. (2006a), many z$\sim$ 2 – 3 galaxies are shifted towards higher low-ionization line ratios relative to the low-redshift relationships. Brinchmann et al. (2008) argued by analogy with a subsample of local galaxies from the SDSS that this may be a result of higher

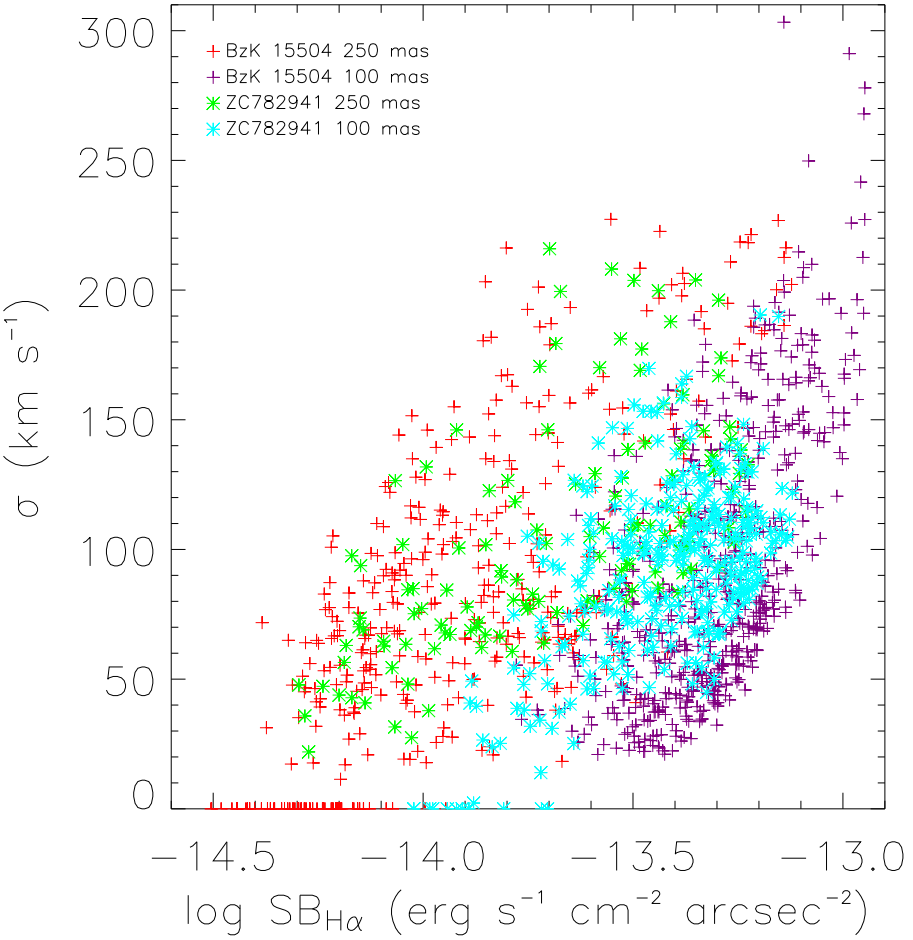

Figure 3.7 Plot of the rest-frame Hα surface brightness versus the observed velocity dispersion for the 2 galaxies for which we have both seeing limited and adaptive optics assisted data sets (ZC782941 and BzK-15504). Individual points in the data cubes were treated as shown in Figure 3.6. In the case of the data cubes that were taken with adaptive optics assistance, the pixel scale is 50 mas pixel^{-1} and they were also averaged over 3×3 pixels (Figure 3.5. There is an increase in the velocity dispersion of some of the regions within BzK-15504 but these are entirely associated with the region of and around the AGN, substantiating our claim that BzK-15504 hosts an AGN (see also Genzel et al., 2006).

pressures and higher ionization in high redshift galaxies.

However, this is not the only effect we may expect to take place. At low redshift, luminous AGNs reside predominantly in relatively massive galaxies which have comparably high ($\gtrsim$solar) metallicities. At high redshift, this is not necessarily the case. Groves et al. (2006) modeled the expected position of AGN in low-metallicity host galaxies in classical emission line/ionization diagrams (e.g., [NII]/Hα versus [OIII]/Hβ). They find that the metallicity-sensitive [NII]/Hα ratio will be shifted towards lower values for AGN with low-metallicity narrow line regions. Seyfert galaxies and QSOs have ratios of [OIII]/Hβ that are higher than those of HII regions and star-forming galaxies in such diagrams. Since the ratio of, for example, [OIII]/Hβ is not strongly affected by lower the metallicity, the position of low-metallicity AGN in ionization diagrams may lie above the locus occupied by HII regions. We illustrate this effect by showing the position of the low-redshift, low-metallicity AGN of Groves et al. (2006) in the same diagram. Interestingly, most optically or UV-selected starbursts fall very close to the region spanned by the Groves et al. sample. This is not to say that these will be low-metallicity AGN, in particular, since the observed strong starbursts will create high-ionization, high-pressure environments, which will shift the galaxies towards the AGN part of the diagram (Brinchmann et al., 2008). However, this does imply that we may significantly underestimate the fraction of high-redshift galaxies with AGN of rather moderate luminosity. In the following we discuss the specific example of an obscured quasar with relatively inauspicious diagnostic line ratios compared to optically selected QSOs.

3.5 The powerful Active Galactic Nucleus of BzK-15504

We will now give an example from among the galaxies of our sample, BzK-15504, where the AGN plays a role that is almost certainly non-negligible in interpreting the extended emission of the host galaxy. This galaxy falls within the range of low-metallicity AGN in the [NII]/Hα versus [OIII] /Hβ diagnostic diagram discussed by Groves et al. (2006), but also near the dividing line between AGN and starbursts. Thus, the impact of AGN photoionization will easily be missed with a diagnostic based only on local galaxies since powerful AGN embedded in low metallicity host galaxies are relatively rare (Groves et al., 2006). We use additional constraints, in particular the [OI]/Hα ratio and the near-nuclear [OIII] λ5007 luminosity to argue that this galaxy hosts an obscured quasar, and that most of the extended Hα emission may in fact be part of an AGN ionization cone. This calls into question previous interpretations of the star-formation properties and accretion rates in this galaxy (see also § 3.8.2). While this is the only clear case among the 11 galaxies

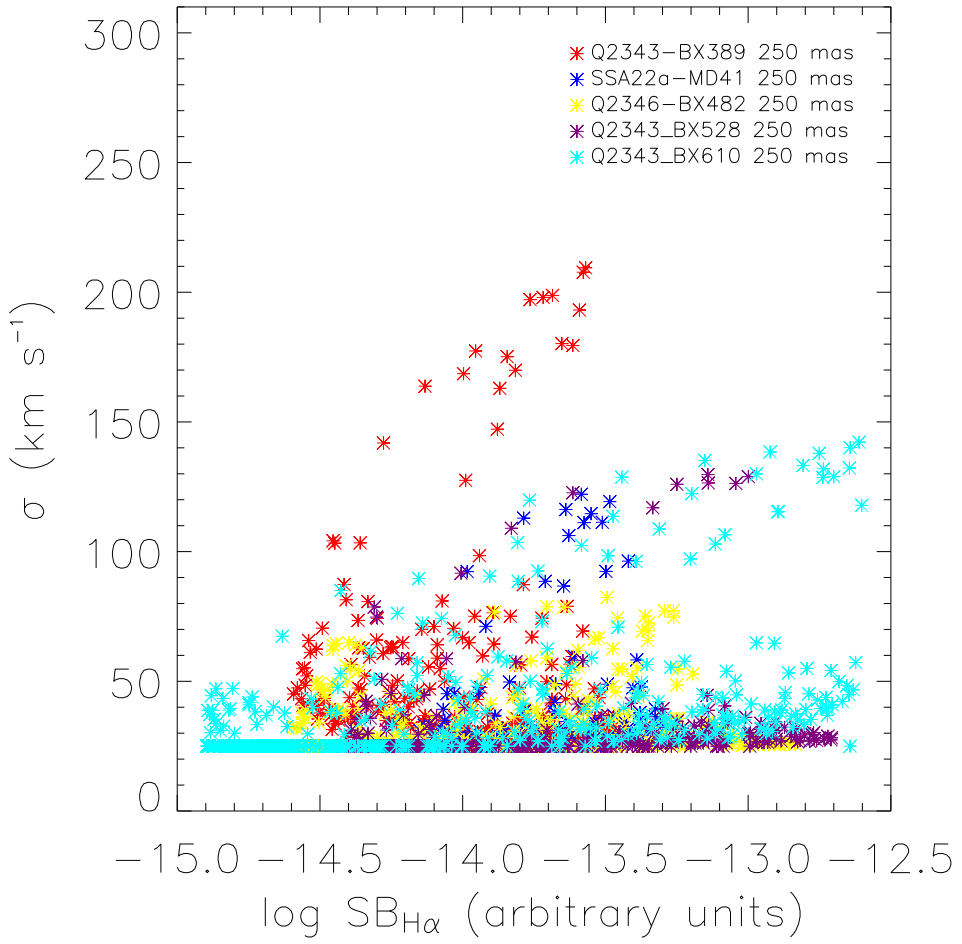

Figure 3.8 A plot of surface brightness versus velocity dispersion for a set of toy models. Each of the "models" was generated assuming the distribution of light of the HST/NICMOS image, an intrinsic and uniform velocity dispersion of 25 km s^{-1}, a distribution of rotation velocity and a velocity peak as given in Förster Schreiber et al. (2006), and a point spread function with a FWHM of 0″.6. Care was taken to ensure that the final resolution of the data set was 0″.6 and took into account the intrinsic resolution of NICMOS. For the presentation here, we did not include noise as it would simply tend to increase the scatter, especially at the low surface brightnesses, but not change the overall trend that the dispersion would remain roughly constant.

discussed here, it does illustrate that the rest-frame optical emission line diagnostics for z~ 2 galaxies, including the 11 discussed here, may be less straight-forward to interpret than previously realized.

3.5.1 The Bolometric Luminosity of the QSO in BzK-15504

It is clear that the nuclear emission lines of BzK-15504 lie within the region of the AGN in all of the emission line diagrams suggesting that it is indeed a powerful AGN (Figure 3.9 and 3.10). The bolometric luminosity is an important parameter as it sets the total energy output of the AGN. BzK-15504 has not been observed over a sufficiently wide range of wavelengths to estimate its bolometric luminosity accurately. Heckman et al. (2004) argue that [OIII] λ5007 luminosity can be used to estimate the bolometric luminosity of AGN over the range of $L_{[OIII]}=10^{6.5}$ to 10^{9} $L_{\odot}$. Their adopted relationship is $L_{bol}=3500L_{[OIII]}$ with a scatter of about a factor of 2 (see Heckman et al., 2004, and references therein for details). Using this relation for our [OIII] λ5007 flux from BzK-15504 centered on the brightest continuum and line emitting region suggests that it has $L_{[OIII]}=10^{9.5}$ $L_{\odot}$ and an implied $L_{bol}=10^{13.0}$ $L_{\odot}$. Extinction correcting the [OIII] λ5007 flux would increase it by 0.5 dex. BzK-15504 hosts a powerful AGN indeed – a QSO!

3.5.2 BzK-15504 as a giant Narrow Line Region?

In addition to the nuclear line ratios, the line ratios of the extended emission in BzK-15504 suggest that it could be photoionized by the AGN. In Figure 3.9 and 3.10, we show the BPT diagrams for various line emitting regions within BzK-15504, and the line ratios lie either near the star formation-AGN boundary, as in the diagrams of [OIII]/Hβ versus [SII]/Hα and [OIII]/Hβ versus [NII]/Hα, or clearly within the AGN region as in the [OIII]/Hβ versus [OI]/Hα diagram.

This of course is perhaps obvious from the fact that the surface brightness of the extended emission line region of BzK-15504 is very high, one of the highest in the sample (Figure 3.5). However, can illumination by a central AGN explain the light profile of BzK-15504? The light profile of BzK-15504 has a $\frac{1}{r^2}$ in its Hα surface brightness dependence and is thus consistent with photoionization from a point source such as an AGN. However, since the emission is somewhat complex, this is not a strong constraint as other light profiles might equally well fit the data. Our point here is to suggest that it is at least "consistent" with a $\frac{1}{r^2}$ profile. Making this assumption allows us to make a rough estimate of the ionization parameter,

$$\bar{U}_0 = S_{QSO}/c\bar{n}_H;\ \bar{n}_H = \frac{P_{gas}}{k10^4} \tag{3.1}$$

where c is the speed of light, S_{QSO} is the photon intensity at radius r from the

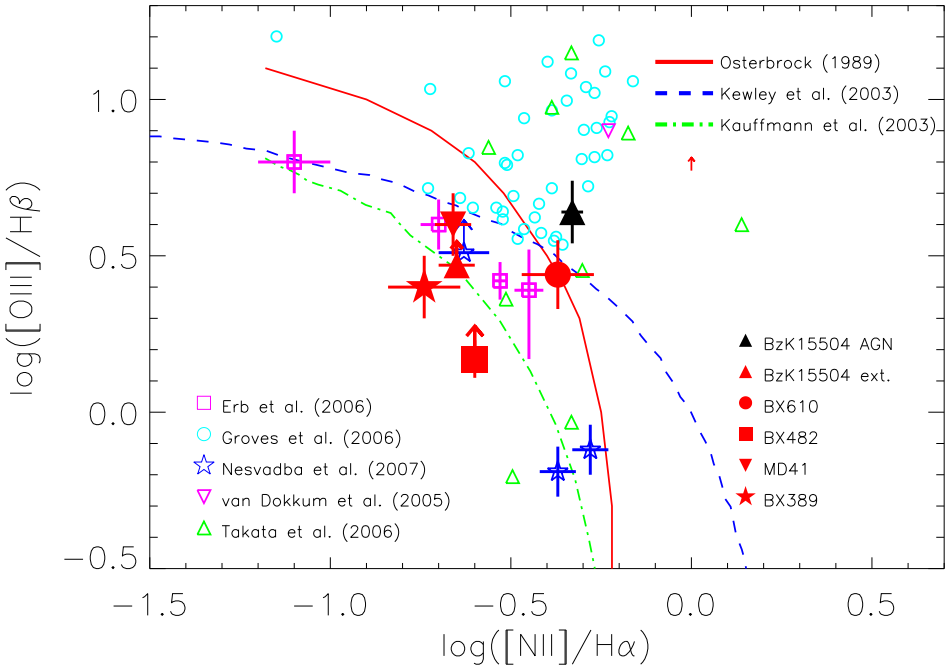

Figure 3.9 The optical emission line ratios, [Nii] λ6583/Hα versus [Oiii] λ5007/Hβ for some of the galaxies in our sample (BzK-15504, BX610, BX482, MD41, and BX389), as well as for some distant and local galaxies taken from the literature (Erb et al., 2006a; Groves et al., 2006; Nesvadba et al., 2007; van Dokkum et al., 2005; Takata et al., 2006). The dividing lines within the diagram demarcate the separate regions occupied by galaxies whose emission lines are dominated by heating due to star formation from those dominated by active galactic nuclei (Kauffmann et al., 2003; Kewley et al., 2001; Osterbrock, 1989). Interestingly, many of the galaxies in this sample fall near the dividing line, which is consistent with either heating due to AGN, as is the case for both the nucleus and the extended emission line gas in BzK-15506.

QSO, and where we used, $L_{QSO} = 10^{45.5}$ erg s^{-1} (or 1/10 of the total bolometric luminosity), a radius of about 6 kpc, a rough density of 500 cm^{-3} and a factor of 3 between the electron density and total density to reflect the fact that most of the [SII] $\lambda\lambda$6716,6731 forms in the partially ionized zone. Using these numbers suggests that $\bar{U}_0$ is about 10^{-3}. As we will see later, this is a rather canonical number for some of the other galaxies in the sample and not surprising given the surface brightness of all the galaxies.

Looking at this from another perspective, we can estimate that it takes a few percent of the total bolometric luminosity to explain the total Hα emission in BzK-15504, if we make a simple recombination estimate for the number of ionizing photons. This is less than the 10% we assumed above, but overall consistent with the nebula being completely powered by the QSO. We note that this is obviously a lower limit as we have not considered the extinction in the extended nebular emission.

The total ionized gas mass is straight-forward to estimate as well. If we assume simple case B recombination as we did previously to estimate the total ionizing luminosity necessary to power the nebula, we find that we need about,

$$\begin{aligned} \mathrm{M}_H &= \frac{L_{H\alpha}}{h\nu_{H\alpha}\alpha^{eff}_{H\alpha}} m_p n_e^{-1} \\ &= 9.73 \times 10^8 L_{H\alpha,43} n_{e,100}^{-1}\ \mathrm{M}_\odot \end{aligned} \tag{3.2}$$

Using n_e=500 cm^{-3} and $L_{H\alpha,43}$=$10^{0.8}$, we find a total mass necessary to sustain the Hα luminosity of about 3×10^8 $M_\odot$. This is a rather modest amount of mass and shows that it is very simple to have the AGN ionize this much gas, which is only a small fraction of the total mass.

Given these estimates, we appear to be able to explain the emission line ratios with our estimated ionization parameter, looking at the emission line diagrams and physical parameters for photoionized nebulae in Groves et al. (2004, 2006). The line ratios are indeed consistent with having Hydrogen number densities of-order 100-1000 cm^{-3} and a dilute ionizing energy field (log $\bar{U}_0 \sim -3$).

There are of course analogs to this situation in both the local and high redshift Universe. At high redshifts, optical emission line ionization cones over scales of kpc to 100 kpc are seen in powerful radio galaxies (e.g., Nesvadba et al., 2006b, 2008a). Emission line nebulae this large are generally seen in AGN with UV and emission line luminosities that are higher than observed for BzK-15504 (about a factor of a few to 10). However, the extended emission line region in BzK-15504 is consistent with luminosities observed in the "narrow line regions" of distant QSOs (Netzer et al., 2004).

AGN also show strong asymmetries in their emission line distributions. This may also explain the asymmetries seen in the emission line images of BzK-15504

(Genzel et al., 2006). It represents the asymmetry in the opening angle out of which the photons escape the AGN and where the gas falls within the beam. A local example of this is NGC 1068 (Veilleux et al., 2003). In NGC 1068, the circumnuclear ionization cone shows a strong asymmetry in its distribution of [OIII] λ5007 on both small scales (100s of parsecs; Evans et al., 1993) and large scale (kpc scales; Veilleux et al., 2003). Only in the areas of intense Hα emission are the line ratios consistent with photoionization of massive stars in HII regions. Over a much larger scale, 10s of kpc, in the areas of relatively low Hydrogen recombination line surface brightness are the line ratios consistent with photoionization by the AGN (Veilleux et al., 2003). Moreover, the emission line widths over the regions excited by the AGN (FWHM$\sim$100-few 100 km s^{-1}) are also in reasonable agreement with what is observed for BzK-15504. In many optically selected AGN, the line widths are not strongly influenced by the AGN despite the fact that the ionization state of the gas is (Nelson & Whittle, 1996). Of course, both the gas mass and the power of the AGN are larger in BzK-15504 and it may well be that as a result, the AGN can even outshine any star formation in the extended optical emission line emitting gas (Figure 3.9 and 3.10). Within this regard it is also important to note that BzK-15504 also has one of the highest Hα surface brightnesses in our sample. The AGN could be responsible for increasing its overall surface brightness as well as its AGN-like extended line emission. And like many classes of AGN (and in analogy with NGC1068 as just discussed) the radiation, although likely heavily attenuated, is able to escape to large distances despite the ionized gas representing a small fraction of the total gas mass of BzK-15504.

This last point is important. AGN host galaxies show a reasonable correlation between the size of their narrow line region and the luminosity in Hβ (Bennert et al., 2002, but see, Netzer et al. 2004). The Hβ luminosity of BzK-15504 would suggest a narrow line region size of a few to 10 kpc (this is without extinction correction). Interestingly, this is approximately the size of the emission line nebulae observed in Hα and [OIII]. Thus, in agreement with other arguments, there is evidence that the extended emission line region is nothing more than a narrow line region around a powerful QSO with line widths that are, by analogy with local AGN, influenced, perhaps dominated, by other processes.

3.6 Nature of the emission line gas in these galaxies

The surface brightness in our sample is both very high, and a function of radius, velocity dispersion, and low ionization line emission ratio (i.e., [NII]/Hα). This is in sharp contrast to what is observed for spiral galaxies in the local Universe where the velocity dispersion is roughly constant as the surface brightness declines exponentially. With the local trends in mind, we hypothesize that the trends seen in

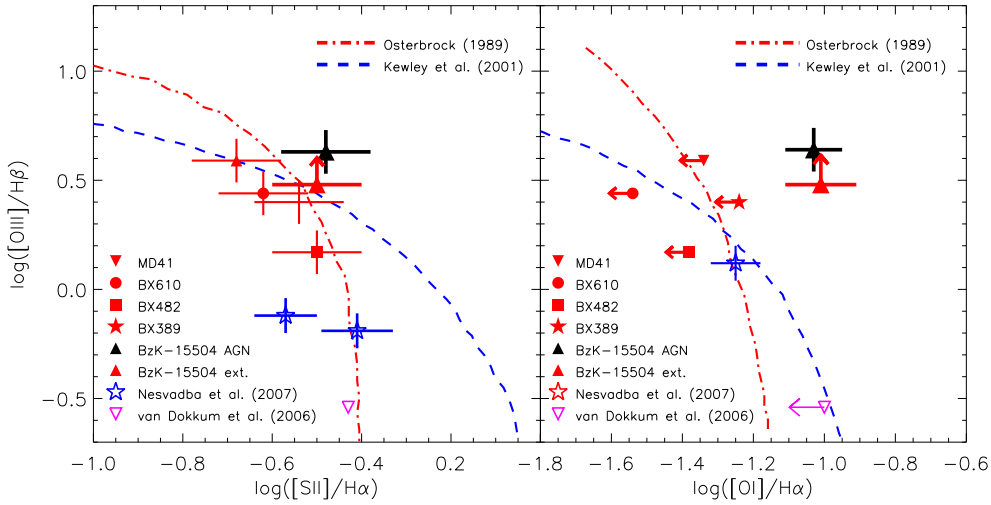

Figure 3.10 The optical emission line ratios, [SII] $\lambda\lambda$6716,6731/Hα versus [OIII] λ5007/Hβ *(left)*, and [OI] λ6300/Hα versus [OIII] λ5007/Hβ *(right)* for the same subsample as in Figure 3.9. Again, the lines demarcate the regions of the emission line diagrams where the photoionization is dominated by star formation or AGN(Kewley et al., 2001; Osterbrock, 1989). These diagrams again demonstrate the role of the AGN in photoionizing BzK-15504. The other galaxies in the sample lie close to the lines of demarcation in the [SII] $\lambda\lambda$6716,6731/Hα versus [OIII] λ5007/Hβ diagram, but have limits that are consistent with being photoionized mainly by massive stars.

the distant galaxy data can be explained by self-regulated star formation whereby the intense star formation is pressure driven by the gas motions induced by the star formation itself. We attempt to show that essentially, these systems are analogous to the nearby starburst galaxies, such as M82 (and regulated perhaps in the same way as the ISM of the Milky Way) with an overall similar surface brightness and similarly high pressure, but with their star formation occurring over a much larger area.

3.6.1 The relation between Hα surface brightness and [NII]/Hα

In Figure 3.11, we show the relationship between the emission line ratio [NII]/Hα and the surface brightness of Hα. An obvious way to understand such a relationship, in addition to the high Hα intensity, is through the gas pressure in the cloud or cloud interfaces that gives rise to the recombination line emission.

To test this hypothesis we ran some simple photoionization models using the code Cloudy[1]. The input spectrum was generated using Starburst99 (Leitherer et al., 1999) for a constant star formation rate and an age of 10^8 years (consistent with the estimated ages of galaxies at z≈2 Erb et al., 2006d). However, the exact age is not very important as long as it is sufficiently long for the spectral energy distribution, especially in the UV, to reach an equilibrium shape. It is thus appropriate for ages greater than about a few 10s Myrs and constant star-formation rate. We assumed a constant density slab with ionization parameters ranging from about log U=−5 to −1, initial densities log n=1, 2, and 3, and ISM metallicities and grain depletion which are kept constant for all calculations. These attempts at modeling are not intended to be exhaustive but illustrative. To gauge the impact of the ionization of the modeled cloud, we ran these calculations for two total column densities, 10^{20} and 10^{21} cm^{-2}. The results from this modeling are shown together with the data in Figure 3.11.

We can see that the range of [NII]/Hα and surface brightness can be explained by a combination of column density, volume densities, and moderately diffuse radiation fields. Obviously, such simple assumptions are not going to "fit" the data in any sense of the word, but show that the area of line ratio-surface brightness space covered by the data can be explained by a combination of these parameters, with each galaxy exhibiting some range in each of these. Surface brightness is linearly proportional to the density and ionization parameter, while the line ratio depends on roughly one over the square root of the ionization parameter for the range of ionization necessary to explain the line ratios. Such a high density and ionization rate implies that the ISM of these galaxies must in general exhibit high thermal pressures, P/k∼10^{6-7} K cm^{-3} or more. The true maximum pressures are likely to

[1]Calculations were performed with version 07.02.02 of Cloudy, last described by Ferland et al. (1998).

be higher as our physical resolution is only about a few kpc making it difficult to identify the regions of highest surface brightness.

These pressures are much higher than observed in the disk of our Milky Way or other nearby normal galaxies. As discussed in Blitz & Rosolowsky (2006), and references therein, the hydrostatic mid-plane pressure in the MW is about $10^{3.3-4.3}$ cm^{-3} K, while for other local spirals it can range up to about 10^{6} cm^{-3} K but is typically about $10^{4.6}$ cm^{-3} K. There have been fewer estimates of the more appropriate comparison, namely the thermal pressures. In the nuclear regions of local starburst galaxies, the thermal pressures as estimated from the ratio [SII] λ6716/[SII] λ6731 give values that range from $10^{-9.3}$ to $10^{-8.5}$ dyne cm^{-2} or typically about 10^{7} cm^{-3} K (Lehnert & Heckman, 1996a) similar to that observed here at z$\sim$2. Interestingly, Brinchmann et al. (2008) make a similar argument for galaxies that generally fall off the locus of the HII regions in the [OIII]/Hβ versus [NII]/Hα diagram and lie close to the dividing line between HII region and AGN excitation. They find that such galaxies have high specific star-formation rates, as do the general population of high redshift galaxies discussed here, and relatively large Hα equivalent widths. Brinchmann et al. suggest that the most likely explanation for this is higher density (pressure) and that the escape fraction may be higher in the star-forming regions implying that the nebulae are at least partially density bounded. Similarly, in Figure 3.11 we see that the clouds with column densities of log N_H=20 become density bounded at high ionization parameters and may explain the surface brightness limits we observe. Thus the pressures estimated from the photoionization models are consistent with those of nearby actively star-forming galaxies (Heckman et al., 1990; Wang et al., 1999).

3.6.2 Consistency with high ionization lines

In addition, for some of the galaxies we have H-band data cubes of sufficient signal-to-noise to investigate the ratio of [OIII] λ5007 and Hβ. The photoionization models would predict [OIII] λ5007/Hβ of about 0.5-2.0. Indeed, not considering BzK-15504, which is powered by a QSO, the other galaxies show ratios consistent with the high ionization line ratios and again amplifying the idea that these nebula have increased density compared to nearby galaxies as observed by Brinchmann et al. (2008).

3.7 Powering the local motions in these galaxies

We have argued that the ISM of these distant galaxies is under high pressure and that this high pressure could be induced by the intense star formation within these systems. Fundamentally, this argument is analogous to the situation in the most

intense starbursts in the local Universe such as M82 (e.g., Heckman et al., 1990; Lehnert & Heckman, 1996a; Lehnert et al., 1999). Such a hypothesis nicely explains some of the unusual features in these distant star-forming galaxies such as their high surface brightnesses in the recombination line(s) (which makes them observable in the first place), the low ionization line ratios, the ratio of the [SII] lines (suggestive of high densities), and the trend for more intense star formation to lead to broader lines. We observe low ratios (~2-4) of v/σ in the extended line emitting regions of our objects, much lower than the ratio of ~10 generally observed in local and intermediate redshift disk galaxies, and this appears to be driven mainly by unusually high velocity dispersions, not low velocity shears.

In principle, the high velocity dispersions observed in the ionized gas lines are likely not representative of the turbulence in the whole star-forming ISM. Nevertheless, the energy injection necessary to sustain the high velocity dispersions observed in the ionized gas should affect the atomic and molecular phases (although if it is a turbulent cascade, with energy injection on large scales, the velocity dispersion will likely be lower in denser gas but the $\rho\sigma^2$ will be the same; Joung et al., 2009b). Indeed, high dispersions in the gas out of which stars form is suggested by the large sizes and masses of high-redshift star-forming regions (giant clumps equaling the Jeans mass, Elmegreen & Elmegreen, 2005). This is also supported by the thickness of high-redshift disks when observed edge-on (Elmegreen & Elmegreen, 2006).

What is the power source of the high velocity dispersions that are observed, and that should affect the whole ISM of high-redshift galaxies? There are several possible mechanisms: (1) the conversion of potential energy of infalling material in turbulent gas which has sufficient angular momentum to relax into a disk configuration (cosmological accretion; Förster Schreiber et al., 2006; Dekel & Birnboim, 2008a); (2) peculiar motions in unstable disks that lead to perturbations in the velocity fields that are not resolved in our data and lead to a high σ without consisting of real small-scale turbulence (e.g., Bournaud & Elmegreen, 2009); (3) self-gravitationally generated turbulence (Wada et al., 2002); and/or (4) the combined effect of the intense star formation.

To characterize the order-of-magnitude needed to power the turbulence, we shall start by estimating its energy budget (if that is what these motions represent). Our low spatial resolution in the rest-frame of the galaxies does not allow us to cleanly separate these possible sources of the observed broad line emission. In fact, Mac Low (1999) as well as our astrophysical reasoning below imply that bulk motion and turbulence are intricately related in some of the scenarios, in the sense that bulk motion will inject kinetic energy into the system which will then be dissipated through turbulence. However, carefully examining the total energy contained within the emission line gas may help us constrain the mechanism responsible for its characteristics. We first consider the energy dissipated within the

turbulence and whether or not it is consistent with cosmological accretion of gas.

3.7.1 Turbulent energy dissipation

The violent motions observed in these distant galaxies are highly supersonic given the densities derived previously for the optical emission line gas and the turbulence generated, compressible. To estimate the dissipation of the turbulent energy therefore requires comparison with (magneto-)hydrodynamic simulations of a realistic interstellar medium. Mac Low (1999) provides an estimate of the energy dissipation rate for compressible turbulence as,

$$\dot{E}_{kin} \simeq -n_{\nu} m \tilde{k} v_{rms}^{3}$$

where n_{ν} is a constant of proportionality, which Mac Low (1999) estimates to be $0.21/\pi$, v_{rms} is the root mean square of the velocity in the region, m is the total mass, E_{kin} is the kinetic energy, and $\tilde{k}$ is the driving wavenumber. Although, the validity of this energy dissipation estimate on galaxy scales has yet to be verified, it is useful to give an order-of-magnitude estimate of the energy injection rate necessary to sustain the motions we observe.

The parameters necessary to estimate the energy dissipation rate of compressible turbulence span a wide range of values. For example, the velocity dispersions observed in the galaxies range from about <40 km s^{-1}, in the outer regions, to about 250 km s^{-1} in the inner, circum-nuclear regions (Figure 3.6). The typical velocity dispersion is of-order ~100-150 km s^{-1}. The driving scale is particularly difficult to estimate since the driving mechanisms likely operate over a wide range of scales (e.g., Joung et al., 2009b). For example, if the largest scale driving mechanism was the cosmological accretion of gas, we would expect this scale to be large (Dekel & Birnboim, 2008a) approximately that of the thickness of the disk. Alternatively, if the driving mechanism is star-formation, the size of the largest star-forming regions or associations in the galaxies might be the appropriate scale. The clumps seen in Figure 3.4 are approximately 100s of parsecs to kpc in diameter. Since the driving wavenumber is inversely proportional to the driving length, assuming a small scale for the driving length would tend to increase the energy dissipated through turbulence.

We cannot estimate the total mass of gas in the galaxies in a straight forward way. For simplicity, we will apply the Schmidt-Kennicutt law (Kennicutt, 1998a) to the star-formation intensities estimated from the Hα surface brightness distribution. This relation implies that the gas surface densities are of-order $\Sigma_{gas} = 10^{2.6} M_{\odot} pc^{-2}$ for star-formation intensities of 1 $M_{\odot}$ yr^{-1} kpc^{-2} (1 $M_{\odot}$ yr^{-1} kpc^{-2} is the typical average value for the star-formation intensity approximately averaged over the isophotal radius). This of course assumes that the molecular gas has same kinematics as the warm ionized gas. The high densities that we found in § 3.6.1 and the

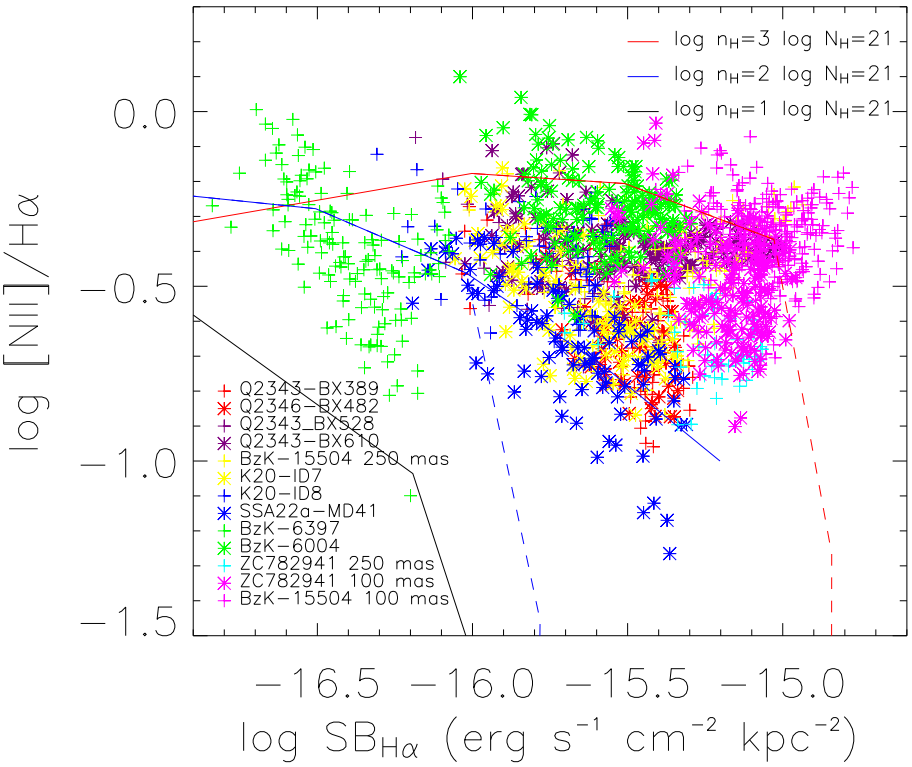

Figure 3.11 The Hα surface brightness (corrected for surface brightness dimming) versus the logarithm of the [NII] λ6583/Hα line ratio for all the individual spectra of the galaxies in our sample. The galaxies are labeled in the legend to the figure. The lines represent results for photoionization modeling (see text for details) for 6 set of conditions. The lines represent a range of density (log n$_H$=1 to 3) and column densities of log N$_H$=21 cm^{-2} (solid lines) and log N$_H$=20 cm^{-2} (dotted lines). The ionization parameters span from log U=−5 to −1.0 (which increases from left to right along the lines, meaning low ionization parameters have relatively high log [NII]/Hα and low Hα surface brightnesses).

course angular resolution of our data which averages the kinematics over a large region perhaps imply that this is not a bad assumption (but see Joung et al., 2009b; Walter et al., 2002).

If we adopt, v_{rms}=150 km s^{-1}, a mass surface density of 1000 M$_\odot$ pc^{-2}, a driving length of 1 kpc (which is a typical thickness of the "clumpy disks" observed at similar redshifts as our sample; Elmegreen & Elmegreen, 2006), we find that turbulence likely dissipates about 10^{42} erg s^{-1} kpc^{-2}. The surface area within the isophotal radius is approximately 200 kpc^2 (Table 1) giving a total energy dissipation of about $10^{44.3}$ erg s^{-1}. We emphasize given the uncertainties, the limits of our theoretical understanding of turbulence and untested assumptions, this estimate of the turbulent dissipation should be considered as order-of-magnitude only.

3.7.2 Cosmological gas accretion

We can compare this rough energy dissipation estimate with that of gas infalling on to the disk itself. The total energy accretion rate from gas falling onto the disk is given approximately by (Dekel & Birnboim, 2008b),

$$\begin{aligned} \dot{\mathrm{E}}_{heating} &= \mid \Delta\phi \mid \dot{M}_{gas} = 4.8 \dot{M}_{gas} V_c^2 \\ &= 10^{43.1} \dot{M}_{gas,100} V_{c,200}^2 \text{ erg s}^{-1} \end{aligned} \tag{3.3}$$

where $\mid \Delta\phi \mid$ is the potential energy of infall, $\dot{M}_{gas,100}$ is the halo gas accretion rate in units of 100 M$_\odot$ yr^{-1} and $V_{c,200}$ is the circular velocity of the halo in units of 200 km s^{-1}. Thus it appears that accretion of gas in itself cannot power the turbulent and bulk motions we observe in these galaxies if these motions decay as compressable turbulence. Dekel et al. (2009) also suggest that the main source of turbulence is not infalling gas, unless this infalling gas is itself also highly clumpy, something they themselves rule out as highly unlikely for a large fraction of the infalling gas.

3.7.3 Velocity dispersions in Jeans unstable clumps

The dynamics of these galaxies could be influenced by the mode of star formation. Elmegreen and collaborators have proposed that the large number of *clump-cluster* and *chain galaxies* observed at high resolution in deep HST imagery represent gas-rich Jeans unstable disks (review in Elmegreen, 2007). Clumpy galaxies are not rare. Their frequency and relatively fast dynamical evolution suggests that perhaps all galaxies pass through a "clumpy" stage in their evolution and that this process is a natural way of explaining phenomena like the growth of bulges and nuclear supermassive black holes (Bournaud et al., 2007; Elmegreen et al., 2008a).

HST/NICMOS images of five of our sample galaxies (Figure 3.4) do show that they have "clumpy" irregular morphologies consistent with this hypothesis.

The clumpiness of the disks is hypothesized to be driven by Jeans instability, which implies a relationship between the mass of collapsing gas and the velocity dispersion within the gas (e.g., Elmegreen et al., 2007). Specifically, the Jeans relationship implies that,

$$\sigma_{gas} \sim M_J^{1/4} G^{1/2} \Sigma_{gas}^{1/4} = 54 M_{J,9}^{1/4} \Sigma_{SFR}^{0.18} \text{ km s}^{-1} \tag{3.4}$$

where σ_{gas} is the velocity dispersion of the gas, G is the gravitational constant, Σ_{gas} is the gas surface density in $M_\odot$ pc^{-2}, $M_{J,9}$ is the Jeans mass in units of 10^9 $M_\odot$, and Σ_{SFR} is the star-formation intensity in units of $M_\odot$ yr^{-1} kpc^{-2}. We have used the Schmidt-Kennicutt relation (Kennicutt, 1998a) to convert from gas surface density to star-formation intensity. We show the relationship between the velocity dispersion and star-formation intensity for Jeans unstable clumps in Figure 3.12 for a clump of 10^9 $M_\odot$, similar to the largest masses estimated for clumps based on spectral energy distribution fitting (Elmegreen & Elmegreen, 2005). We chose 10^9 $M_\odot$ to put the weakest limit on the possible contribution of the clumps to the observed velocity dispersion.

The velocity dispersions predicted by Equation 3.4 generally lie below the data in Figure 3.12, especially at the highest intensities, and the relationship is also too flat as a function of star-formation intensity. Although this does not rule out clumps in a disk as a contributing source to the high velocity dispersions observed in our sample, especially for the gas with lowest dispersions, it cannot be the entire explanation. And taken at face value, the masses necessary to explain the average dispersion would be more like 10^{10} $M_\odot$, not 10^9 $M_\odot$ suggesting that the dispersions are not dominated by the internal dispersions of the clumps themselves.

3.7.4 Gravity powering turbulence in dense gas-rich galaxies

The clumpy light distributions observed suggest, in particular, that the clumps themselves may have required an earlier source of turbulence. This is necessary to ensure that the initial Jeans mass is as high as the clumps masses observed (up to more than $10^9 M_\odot$; Elmegreen et al., 2007). This implies that we may be obliged to hypothesize another source of turbulence, especially in initiating the intense star formation, to favor and encourage the growth of massive clumps. Perhaps self-gravity powering the initial turbulence would play the necessary role (see Thomasson et al., 1991; Wada et al., 2002).

A gas disk with a low turbulent speed σ may likely have a Toomre parameter $Q = \frac{\sigma\kappa}{\pi G\Sigma} < 1$, if the surface density Σ is high. As a result, gravitational instabilities will form and heat the gaseous medium, increasing its turbulent energy until Q

reaches ~ 1 and the process stops. The observation of clumps in our z~2 galaxies and others suggest that Q is close to one, so that this is the level at which gravity could indeed power the turbulence. In local flocculent spiral galaxies, Elmegreen et al. (2003) argued that gravity was triggering the turbulence through local instabilities.

The hydrodynamic simulations by Agertz et al. (2009) have shown that disk self-gravity likely triggers the 5-10 km s^{-1} turbulent speed of extended HI disks around local spirals – which could not result from star formation beyond the edge of star-forming disks (see also Wada et al., 2002). The density of these modeled disks is nevertheless far lower than the estimated density of gas disks at z~2. A gas fraction of ~50% in these disks (from Daddi et al., 2008, observations or inferred from the Schmidt law, Bouché et al. (2007)) indeed corresponds to typical gas surface densities of ~500 $M_\odot$ pc^{-2}. More direct hints on the role of self-gravity in high-redshift disks can be found in the models by Tasker & Bryan (2006, 2008), where gas disks with large-scale densities around 100 $M_\odot$ pc^{-2} are modeled, much closer to the hypothesized density at z~2 even if still somewhat lower. Interestingly, these models show larger clumps when the gas density is large, indicating larger Jeans masses and hence larger velocity dispersions. This is found in models of isolated disks without feedback, where only gravity can power turbulence. The addition of feedback from star-formation in these models does not change significantly the clump masses, hence the turbulent speed, suggesting that the early stages of turbulence development could be mostly powered by self-gravity. Direct models of disks at z~2 with high density would be desirable, but given that Tasker & Bryan (2008) have both the gas density and the clump masses/sizes somewhat lower than z~2 standards, it is reasonable to infer that disk self-gravity is likely important source of turbulence at high redshift but does not likely generate the extreme dispersions we observe (Figure 3.12). As we noted earlier, it may be that the formation of massive clumps themselves requires high turbulence initially (Equation 3.4).

In addition, high velocity dispersions could be a result of mergers. In the local Universe, intensely star-forming galaxies show very high velocity dispersions in their optical emission line gas, up to 200 km s^{-1} (Monreal-Ibero et al., 2006). To explain the low v/σ observed at high redshift (Förster Schreiber et al., 2006), Robertson & Bullock (2008) proposed that a disk settling after a major gas-rich merger would have low v/σ. In particular, they construct their model to match approximately the properties of BzK-15504 in detail including its high star-formation rate and intensity (without the AGN). Thus, it is not clear how much of the dispersion is due to the intense star-formation and how much is driven purely by gravity in their model. Moreover, recently Bournaud et al. (2008) have criticised the merger model in that it does not naturally produce the clumpy morphologies that are frequently observed in distant galaxies and would lead to disks that make up a rather small fraction of the total mass. Thus it is not clear if gravitationally driven

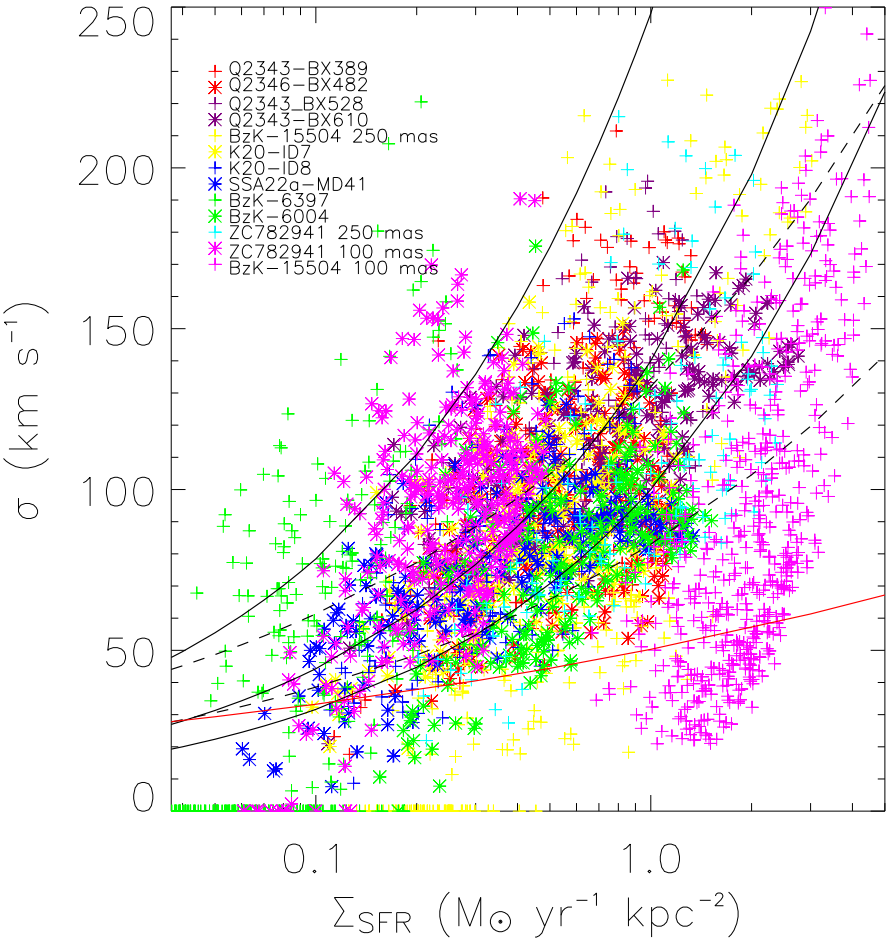

Figure 3.12 A plot of the star-formation intensity versus the Hα velocity dispersion in our sample of galaxies. See Figure 3.1 1 for details on the 3×3 pixel smoothing that was applied. The symbols for the different galaxies in our sample are shown in the legend to the figure. The solid black lines show three simple relationship of the form $\sigma = \sqrt{\varepsilon \dot{E}}$, where ε is the efficiency of coupling between the energy injected and the ISM. *(from bottom to top):* $\sigma = 100\sqrt{\Sigma_{SFR}}$ km s^{-1}, $\sigma = 140\sqrt{\Sigma_{SFR}}$ km s^{-1}, and $\sigma = 240\sqrt{\Sigma_{SFR}}$ km s^{-1} (see text for further details). We note that the overall trend seen in the diagram for the ensemble of galaxies is also traced by the data from individual galaxies but with a somewhat steeper slope. If the dispersions represented turbulent motions, we would expect a scaling, $\sigma = (\varepsilon \dot{E})^{1/3}$. Using two scalings for the coupling efficiency, 25% and 100% and a primary injection scale of 1 kpc, we find $\sigma = 80\Sigma_{SFR}^{1/3}$ km s^{-1} and $\sigma = 130\Sigma_{SFR}^{1/3}$ km s^{-1} (bottom and top black dashed curves respectively). The red solid line represents the velocity dispersion of a 10^9 M$_\odot$ clump using the simple Jeans relationship between mass and velocity dispersion (see text for details). The offset between galaxies may be due to a range of coupling efficiencies between the mechanical energy output from the on-going star formation, differences in the average pressure within the ISM, or geometrical factors such as inclination.

flows within mergers can produce the dispersions and high emission line surface brightness we observe without the accompanying intense star formation.

3.7.5 Hα surface brightness–velocity dispersion: Powering the kinematics through star formation

We argued above that self-gravity may be an important source of turbulence at high redshift, but does not seem sufficient to generate the observed velocity dispersions (see also Figure 3.12). This and the relationship between Hα surface brightness and velocity dispersion suggests that the star formation within the galaxies is powering the dynamics of the emission line gas. If the star formation is indeed inducing the high pressures, then this is what would be expected. On purely dimensional grounds, if the energy output from young stars is controlling the dynamics of the emission line gas, we would expect, that σ, the velocity dispersion, would be proportional to the square root of the energy injection rate, dE_{SF}/dt, due to stars. If the coupling efficiency of the mechanical energy output of the star formation does not depend on radius, then the energy injection rate is simply proportional to the star-formation rate. In this case of course, the energy injection per unit area is proportional to the star-formation intensity. This hypothesis is equivalent to conserving (with some efficiency) the mechanical energy output of the star-formation within the ISM of the galaxy and that the velocities of the warm ionized gas trace this energy injection rate.

In Figure 3.12, we have over-plotted just such a relationship. This is not a fit to the data, but a simple scaling law based on the star-formation rate per unit area and the velocity dispersion in the warm neutral/ionized gas in the disk of the MW and other nearby galaxies. The function is of the form, $\sigma=(\varepsilon\Sigma_{SFR})^{1/2}$ where ε has been determined for the MW and other nearby galaxies where the velocity dispersion in Hα and star-formation intensities have been related (see Dib et al., 2006, for details). There are several possible values for ε in this relationship. If we take a simple scaling from galaxies like the MW, they typically have star-formation intensities in the regime of $\Sigma_{SFR}=10^{-5}$ to 10^{-3} $M_\odot$ yr^{-1} kpc^{-2} and velocity dispersions in the warm ionized gas of-order 10 km s^{-1}. Dib et al. suggested that galaxies may change from a quiescent disk mode to a starburst mode at $\Sigma_{SFR}=10^{-2.5}$ to 10^{-2} $M_\odot$ yr^{-1} kpc^{-2}. This comes from modeling the ISM with a coupling efficiency of 25% to the supernova energy from disk star formation. Using these two values for the scaling relation yields the bottom two curves in Figure 3.12, whereas a coupling efficiency of 100% would yield the curve at the top in Figure 3.12. We emphasize that the axis of abscissa is a simple scaling between Hα surface brightness and the star-formation rate which was made assuming a relationship between star-formation rate and Hα luminosity (Kennicutt, 1998a). We have not taken into account the effect of extinction in making this scaling. If the galaxies for which

we have Hβ measurements for are representative of our entire sample. This would increase the star-formation intensities by a factor of a few (Table 2).

While such a toy model is not a particularly good fit, especially at the highest star-formation intensities, it has the virtue of having no free parameters. It is just a simple scaling based on the MW and other nearby galaxies. Although we put this in context of the modeling done by Dib et al. (2006), we could as well have simply used the MW scaling of star-formation intensity and velocity dispersion. Obviously, the true nature of the interstellar media of these distant galaxies cannot be so simple as the energy injection argument presented here. This argument simply shows that the star formation in the galaxies themselves is likely controlling the dynamics of the emission line gas.

3.7.5.1 Mechanical energy due to star formation

Given the relationship between star formation intensity and the velocity dispersion of the gas, it is logical to investigate whether the star formation has sufficient global energy injection rates to drive the high velocity dispersions – much like our previous estimate in § 3.7.1 comparing the accretion energy rate from infalling cosmological gas. Using the relationship from Kennicutt (1998a) between Hα luminosity and star-formation rate, we find that the total star-formation rate per unit area – the star-formation intensity – ranges from about 0.05-5 $M_\odot$ yr^{-1} kpc^{-2} (Figure 3.6). The dynamical time and integrated Hα equivalent width of our sample of galaxies and that from the Erb et al. (2006d) sample, suggests that they may have been forming stars continuously at the observed rate for the last few $\times$ 10^8 years. This implies that the ongoing star formation in this sample in total produces more than $10^{41-42.5}$ erg s^{-1} kpc^{-2} of mechanical energy (Leitherer et al., 1999) for the range of large scale star-formation intensities observed. These numbers are lower limits since we do not have sufficient data to constrain the spatially resolved extinction and so the true star-formation intensities are likely to be higher (Table 2).

We can now compare this total energy injection rate with the value estimated § 3.7.1, namely $10^{44.3}$ erg s^{-1}. For a fiducial value of 1 $M_\odot$ yr^{-1} kpc^{-2}, which is typical within a isophotal radius (Figure 3.6), and the mechanical energy output rate given above, would suggest total energy injection rates of $>10^{44.2}$ erg s^{-1}. Since the numbers are similar, we suggest that the star-formation is powerful enough to maintain the turbulent and bulk motions observed.

3.7.5.2 Accelerating the emission line clouds

Having now argued that the star formation is injecting energy into the ISM of these galaxies and is sufficient to explain the overall dynamics of the gas and to support dissipation through turbulence, can we make a plausible model for how the

clouds might be accelerated? Klein et al. (1994) and Nakamura et al. (2006) have developed both analytic models and simulations for clouds accelerated in a blast wave. Such a blast wave is expected to be generated by the intense star formation observed in our sample of galaxies. As the blast wave passes it shock heats the cloud and eventually destroys it through Kelvin-Helmholtz and Rayleigh-Taylor instabilities.

In this scenario, the turbulence is driven by large scale bulk motions induced by energy injection – blast waves generated by intense star-formation and other processes – over a wide range of scales, which then cascades into the denser gas and redistributes the energy over all scales in the medium finally dissipating mainly on the smallest scales (Joung et al., 2009b; Mac Low & Klessen, 2004, and references therein). The nature of turbulence emphasizes the importance of both bulk and random motions and estimating energy dissipation rates based on turbulence arguments while estimating velocities based on bulk motion arguments are thus appropriate.

Klein et al. (1994) have found relatively simple analytic approximations that can capture the destruction time of clouds with a range of properties like contrast with the inter-cloud material, Mach number of the blast wave, etc. Although there is a problem with simply using these formulae with the parameters from the photoionization calculations because those are aimed at providing the emission lines without consideration of the shock heating in the first place, we envision a scenario where shock heating, despite the intense energy input from the supernova and stellar winds, is only a small fraction of the total energy output of the star formation. For our zeroth order model of star formation proceeding for 10^8 years, we find that this condition is clearly satisfied (Leitherer et al., 1999). Thus we expect the emission lines to be dominated by the ionizing energy output from massive stars and not by the shock heating. The clouds could therefore be thought of as the ones that have yet to be destroyed or are simply the surfaces of sheets and filaments that will get eventually or are now being run over by the blast waves into the ISM.

The relationship for the acceleration of the cloud is given by (Klein et al., 1994, but see also Nakamura et al. 2006), as,

$$\mathrm{m_c}\frac{dv_c}{dt} = -1/2\mathrm{C_D}\rho_{i,1}\acute{v}_c^2 A \tag{3.5}$$

where, $\mathrm{m_c}$ is the mass of the cloud, $\frac{dv_c}{dt}$ is the acceleration of the cloud, $\mathrm{C_D} \sim 1$ is the drag coefficient, $\rho_{i,1}$ is the post-shock density and is approximately, $\rho_{i,1} \simeq 4\rho_{i,0}$ (we are assuming strong shocks), the pre-shock density of the inter-cloud medium, and $\acute{v}_c = \mid v_{i,1} - v_c \mid$ is the relative velocity of the shocked medium, where $v_{i,1}$ is the mean velocity of the cloud, and A is the cross-sectional area.

Does the star formation actually generate blast waves of sufficient energy to accelerate the clouds to the observed velocities? The total mass ejected by supernovae

and stellar winds in the star formation process, $\dot{M}_{SF}$ can be scaled as $\dot{M} = \beta\dot{M}_{SF}$, where β is the fraction of the total ejected mass that is entrained or mass loaded in the winds. Simple conservation arguments suggest the terminal velocity of the outflow is $v_\infty=(\dot{E}/\dot{M})^{0.5} \approx 2800(\varepsilon/\beta)^{0.5}$ km s^{-1}, where ε is the thermalization efficiency of the starburst mechanical energy (e.g., Marcolini et al., 2005; Strickland & Heckman, 2009). If we assume mass loading rates of 1-10, then the blast wave speed is about 1000-2000 km s^{-1}. Similarly, to first order the density of the blast wave is proportional to $\beta^{3/2}$, which would suggest densities of-order 10^{-3} cm^{-3} (e.g., Marcolini et al., 2005). Such low densities and high velocities meet the general criteria of being a blast wave, which is highly supersonic for all of the densities in the ISM and should be very efficient in destroying clouds as it passes through the ISM.

The modeling of the emission line gas in these galaxies suggest parameters for the clouds like density and column density, and assuming the ISM surrounding the pre-blast is like that typical of the ISM in local galaxies, implies log ρ_H=−3 to 0, log ρ_{cloud}=1 to 3 cm^{-3}, r_{cloud}=0.1-10 pc. Using these values for the clouds, the initial conditions for the ISM, and the blast wave formulation argued for previously as input to the simple cloud acceleration models, we find that the clouds could be accelerated up to 100 to a few 100 km s^{-1} before being destroyed. Thus it appears that at least in principle, the velocities of the outflows generated by intense star formation appear able to induce velocities like those observed.

3.7.6 Bulk and Turbulent motions

Ultimately, following the above reasoning, star formation may give rise to the observed line widths through a combination of bulk and turbulent motion. This would also help resolve an apparent inconsistency in our above arguments. If turbulent motions dominate the observed velocity dispersions, we may expect the relationship between the dispersion and star-formation intensity of the form, $\sigma=(\varepsilon\Sigma_{SFR})^{1/3}$ (ignoring the relationship between star-formation intensity and gas surface density which would tend to flatten this relationship). In Figure 3.12, we show this relationship based on Equation 3.3. To make this comparison with the data, we assume that the energy of star-formation is dissipated entirely as turbulence, i.e., $\dot{E}_{kin} = \dot{E}_{SF}$ (see § 3.7.5.1), assuming the same parameters used in § 3.7.1 and for two coupling efficiencies between the energy injected by stars with the ISM. We have ignored the increase in the gas surface density with star-formation (the Schmidt-Kennicutt relation). While this relationship does explain the overall trend in the data, data for individual galaxies are steeper than $\sigma=(\varepsilon\Sigma_{SFR})^{1/3}$ and in better agreement with $\sigma=(\varepsilon\Sigma_{SFR})^{1/2}$. It could be this mixture of bulk and turbulent velocities in the warm ionized gas steepens the relationship between the dispersion and star-formation intensity from $\sigma=(\varepsilon\Sigma_{SFR})^{1/3}$. But of course, as with the scaling $\sigma=(\varepsilon\Sigma_{SFR})^{1/2}$, this is

too simplistic. One would need to consider the scale of energy injection, what is the true nature of the warm ionized gas, the gas density, the dependence of the distribution of the gas phases with star-formation intensity, etc., in order to understand completely the underlying mechanisms exciting the gas.

We emphasize that this analysis does not apply to all the emission line gas, only the highest surface brightness gas. In nearby starburst galaxies, very high velocity gas is observed, up to several hundred to 1000 km s^{-1} (e.g., Heckman et al., 1990; Lehnert & Heckman, 1996a). However, such gas is generally of low surface brightness, well below the detection limit of the data presented here (e.g., Heckman et al., 1990; Lehnert & Heckman, 1996a; Lehnert et al., 1999). As pointed out in, e.g., Heckman et al. (1990) and Lehnert & Heckman (1996a), the pressure in the emission line gas outside of the intense star-forming regions in local starburst galaxies drops as roughly radius^{-2} and its surface brightness drops very rapidly as well. Only the nuclear regions with extremely high pressures reach surface brightnesses as observed in these distant galaxies and the molecular gas in such regions can share similar outflow velocities as the warm ionized gas (e.g., Walter et al., 2002, justifying our assumption that the kinematics of the warm ionized and molecular gas may be similar on the largest scales). We would therefore not expect to see the highest velocity gas in Hα or in the high and low ionization lines observed (see also Wang et al., 1998, 1999).

Turbulence is thought to be driven by large scale bulk motions induced by energy injection – blast waves generated by intense star-formation and other processes – over a wide range of scales, which then cascades into the denser gas and redistributes the energy over all scales in the medium finally dissipating mainly on the smallest scales (Joung et al., 2009b; Mac Low & Klessen, 2004, and references therein). The nature of turbulence emphasizes the importance of both bulk and random motions and estimating energy dissipation rates based on turbulence arguments while estimating velocities based on bulk motion arguments are perhaps appropriate. Most likely, and in analogy with local starbursts, the warm ionized gas is probing the interface between outflowing gas and dense clouds in the ISM of these galaxies (especially at the highest surface brightnesses). It is therefore probing the interface where bulk motion and thermal energy is transfered to denser phases of gas through several mechanism such as thermal instabilities, drag against the background flows, collisions of cloud fragments, gas cooling from warm HII to HI to denser H_2 (see Guillard et al., 2009, and references therein). Of course this requires efficient conversion of bulk motions into turbulent energy which is apparently the case (Mac Low, 1999). The complexity of the processes that control the dynamics and distribution of its various phases suggest that no simple scaling like $\sigma=(\varepsilon\Sigma_{SFR})^{1/2}$ can provide an ultimate understanding of the ISM. However, it does suggest that the ISM of these distant galaxies is controlled by the intense energy output of the star-formation within them. Not surprising, but something that

needed to be investigated and certainly needs further study.

3.8 Further Implications of Intense Star-formation

It appears that it is the intense star formation (or perhaps to some extent and in some cases the AGN) that is controlling the properties of the emission line gas within these galaxies. Given that we have found that the star formation has sufficient mechanical energy output in its own right to explain the characteristics of the emission line gas, it is unclear whether the gas is telling us much about the underlying mass distribution of these galaxies or their origins. For example, Genzel et al. (2008) have argued that high central velocity dispersions require mass concentrations that are consistent with bulges. We can now explain this using the intense mechanical energy output of massive stars (with a non-negligable contribution from AGN in some cases like BzK-15504) and thus the velocity dispersions do not appear to be a unique tracer of the underlying gravitational potential. Similarly, it is plausible that variations in the physical conditions of the gas will lead to variation in the line ratios (see discussion in § 3.6.1 and Figure 3.11). Although these variations do not appear sufficient to significantly affect the metallicity estimates based on integrated spectra (as argued by Brinchmann et al., 2008), they are sufficiently large that they may affect metallicity gradient estimates within individual high redshift galaxies.

Determining that the ISM of these distant galaxies appears regulated by the mechanical output of the intense star-formation, it is logical to investigate how this output might influence the nature of the star-formation itself and our understanding of the dynamics of distant galaxies. We do not as yet have a comprehensive theory of star formation or a complete understanding of all the processes that may limit both the efficiency and the rate at which stars can form. Global star-formation laws or thresholds are those that describe the gross characteristics of star formation on large scales and over dynamical times of galaxies. Several possibilities for explaining the global characteristics of star formation have been suggested: cloud-cloud collisions (e.g., Larson, 1988; Tan, 2000) and the growth of gravitational perturbations (Toomre, 1964), pressure and turbulence regulated media (e.g., Silk, 1997, 2001; Elmegreen, 2002; Mac Low & Klessen, 2004) and others. Models such as cloud-cloud collisions and pressure and turbulence regulated ISM seem particularly appropriate in understanding the role of self-regulation in intense star-formation. However, of particular interest in distant galaxies, and something that we can directly comment on given our results, are the questions of the star-formation efficiency and how does intense star-formation affect the structural properties of distant galaxies.

3.8.1 Efficiency of Star-Formation

Recently, Dekel & Birnboim (2008a) investigated whether or not cosmological gas accretion can sustain the star-formation rate of distant galaxies. Galaxies with high star formation rates as observed here require the star-formation rate to be close to the accretion rate of gas in this type of model. This, on the face of it, requires the gas infall time scale and the star-formation time scale to be close to equal which then implies that the star-formation efficiency is high.

Our results suggest that the star-formation intensity, gas pressure, and velocity dispersions in $z \sim 2$ star-forming galaxies are similar or higher than those in the most intense starbursting regions at $z = 0$. The efficiency of star-formation in local spirals is about a few percent, but can reach $\sim 10\%$ in starburst regions (e.g., Young et al., 1996; Solomon & Sage, 1988; Sanders et al., 1991). From this, we would infer efficiencies of at least 10% in our z~2 galaxies. As mentioned previously, we do not have a comprehensive theory of star formation. However, it has been suggested that there is a power-law dependence of the star formation rate on the total column density (Wang & Silk, 1994). Such a relationship implies that star-formation occurs on a dynamical time scale averaged over a large area. Elmegreen (2002) used this dependency to argue that this would lead to a star-formation law of the form, $SFI = \varepsilon_{SF}\Sigma_{gas}\omega$, where ε_{SF} is the star-formation efficiency and ω is a dynamical rate for the conversion of gas into dense, star-forming cloud cores. Interestingly, Elmegreen (2002) argue that this does not imply that gravitational forces are directly involved but that this dynamical rate of conversion is about equal to the turbulence crossing rate (which is also argued to be the inverse of the collapse time with modest over-pressures). Comparing the inverse of the relative crossing times of turbulence of our sample and local galaxies, $(v_{turb}/l)_{z\sim2}/(v_{turb}/l)_{z\sim0}$ ≈2−5 for v_{turb}=100−200 km s^{-1} and l~1 kpc (Elmegreen & Elmegreen, 2006) in the distant galaxies and v_{turb}=20−25 km s^{-1} and l~500 pc in local disks (Epinat et al., 2009). This suggests that the conversion efficiency of gas into dense star-forming cloud cores is higher in our sample of galaxies than for local disks. Thus the apparent efficiency of star-formation in our z~2 galaxies should be higher than in nearby disk galaxies, where by "apparent" we mean the product, $\varepsilon_{SF}\omega$. But it is important to note that the star-formation efficiency itself, ε_{SF}, can remain constant. On the other hand the efficiency can hardly exceed, say, 30%, since the star formation efficiency at the scale of individual cores is about 50% (Matzner & McKee, 2000) and the efficiency in molecular clouds is necessarily somewhat lower (Elmegreen, 2002). Our observations thus suggest "apparent" star-formation efficiencies between 10 and 30%, not just in a nuclear region but over the whole disk, which is globally starbursting and highly turbulent.

An increase in the apparent efficiency of star-formation can be understood with relation to the likely high surface density of gas in these galaxies. A high gas sur-

face density is supported by both the intense star-formation (through the Schmidt-Kennicutt relation) and by the high pressures inferred from the optical emission line gas. If this efficiency is related to the inverse of the gas consumption time and the Schmidt-Kennicutt relation, then the gas suface density divided by the star-formation intensity, the gas consumption time would be, $\Sigma_{gas}/\Sigma_{SFR} \propto \Sigma_{gas}^{-0.5}$ – a decreasing function of the gas density. Thus finding a high apparent efficiency of star-formation is a natural consequence of having faster dynamical processes such as faster collapse of gas due to high pressures, faster and greater turbulent compression, and stronger influence of self-gravity. Within this framework, it is easy to understand how the galaxies could be clumpy and highly unstable against rapid and intense star-formation.

3.8.2 Clumpy Disks and Dynamical Mass Estimates

Our results also have implications for the "clumpy disk hypothesis" (Elmegreen & Elmegreen, 2005; Elmegreen et al., 2007), whereby galaxy evolution is hypothesized to be driven by internal clump formation (Bournaud et al., 2007). Our results suggest that the clumpy disk model alone cannot explain the high dispersions observed and that an additional energy source is needed. Gravity can play a crucial role, generating the high masses observed in the clumps (Elmegreen & Elmegreen, 2005), but we have argued that star-formation must be an important source of energy too. The intense star-formation is a mechanism whereby further clump formation may be stimulated by maintaining the high dispersions. Bournaud & Elmegreen (2009) conclude that the observations of the "skywalker" in the UDF (UDF6462) and that the peculiar velocities observed are consistent with a clumpy disk. Peculiar clump motions, typically around 50 km s^{-1} (Bournaud et al., 2007), are likely masked by the turbulence and bulk velocities generated in the optical emission line gas by the intense star-formation. This implies that clump masses are difficult to infer from the dispersions of their optical emission line gas. Furthermore, while the clumpy disk model is certainly viable for a subset of the observed galaxies, it is also likely that the mechanical output from the intense star-formation within the clumps should not be ignored either and may have a profound influence on the evolution of the clumps.

Noguchi (1999) suggested that the bulges in local spiral galaxies form through the dynamical evolution of massive clumps of stars in high redshift galaxies. This model was further investigated by Elmegreen et al. (2008a): large massive clumps migrate towards the disk center, and coalesce into a slowly-rotating bulge. The limited observations available may support this picture (Elmegreen et al., 2009b). Could the high efficiency of star formation in our observations of z~2 clumpy galaxies question this model? Vigorous energy injection from intense star formation may disrupt the clumps just like this process disrupts the star-forming clouds in

low redshift galaxies. Actually, if the stars are forming in a higher density medium, which our observations may suggest, the clumps may be more tightly bound and more difficult to destroy with the mechanical energy output from massive stars (even with strong feedback from intense star formation, e.g., Tasker & Bryan, 2008). Therefore, it is likely that the energy output affects mainly the lower-density, inter-clump gas, but not the most massive clumps. Elmegreen et al. (2008a) have independently argued that star-formation feedback could regulate the bulge growth, but does not prevent this bulge-forming mechanism from taking place in high redshift galaxies.

Finally, we have argued that the emission line ratios for BzK-15504 are consistent with it harboring an AGN, and that this AGN is likely growing very rapidly. In this situation, it is difficult to know how much of the extended emission line gas is excited by star formation or the AGN and what drives the dynamics of the extended gas. BzK-15504, since it has an exquisite near-infrared data set, has been argued to be the archetypal growing disk at high redshift. In fact, Genzel et al. (2008) have recently proposed that this galaxy, and some others, represent a phase of rapid gas accretion from their dark matter halo that is feeding its intense star formation. If the extended emission line gas is influenced by a powerful AGN, then this cannot be the case. The necessary gas masses and growth rates would be lower, perhaps by factors of few or more, than previous estimates if the AGN is increasing the overall surface brightness of the extended emission line gas. We do not think that the AGN is the only power source, but our data do not support the notion that this galaxy must have an extreme accretion rate or a rapid rotation suggestive of a massive disk. The ionization, surface brightness distribution, emission line distribution asymmetry, and line widths are all consistent with there being a kpc scale narrow line region surrounding a powerful QSO in this object.

3.9 Conclusions

Our analysis of integral field spectroscopic data with SINFONI on the ESO/VLT and HST/NICMOS imaging of our sample of z~2 galaxies have revealed a number of interesting properties and relationships. Our results suggest that the feedback cycle between the ISM and star formation (and perhaps, more speculatively, AGN) plays an important, perhaps crucial role in regulating star formation at high redshift. In support of this overall conclusion, we find:

(1) These galaxies have surface brightnesses that are more than an order of magnitude greater than those of local disks. Our observations suggest that the ISM of these z~ 2 galaxies is starbursting over their whole area.

(2)These galaxies have line ratios that suggest the presence of an AGN, as in the case of BzK-15504, or high pressures and density bounded clouds.

(3) Cosmological gas accretion models cannot provide sufficient energy if its energy dissipates as compressible turbulence.
(4) A relationship between the star-formation intensity and the velocity dispersion of the emission line gas is found and it can be explained by a simple energy injection relation. At low velocity dispersions, self-gravity may play a role in generating turbulence.
(5) The explanations for the relationships we observe imply that the Hα surface brightness and the distribution of velocity dispersion may tell us little about the underlying mass distribution. Thus bright Hα emission and broad lines are likely not evidence for mass concentrations such as bulges or rings within these galaxies.
(6) Given the high pressures and velocity dispersions we observe, it is likely that the ISM (and perhaps star-formation) is turbulence and pressure moderated (e.g., Silk, 1997, 2001; Elmegreen, 2002; Mac Low & Klessen, 2004).
(7) Our results may imply apparent star-formation efficiencies as high as 10% to 30% (for the stellar mass formed per gas mass unit per dynamical time).

Through several lines of argument, we outlined a picture in which self-gravity generates high turbulence in gaseous disks. Massive, large and gas-rich clumps then form, triggering star formation with high intensities (>0.1 $M_\odot$ kpc^{-2}) and apparent efficiencies (10-30%), with the "starbursting" interstellar medium spreading over scales of 10-20 kpc. At this stage of intense star formation, the turbulence and pressure moderated ISM likely regulates the star formation through several possible mechanisms (e.g., Silk, 1997, 2001; Elmegreen, 2002; Mac Low & Klessen, 2004). The massive clumps however likely survive and form bulges following the mechanisms proposed by Noguchi (1999) and discussed in further detail by Elmegreen et al. (2008a). Such a picture has a myriad of implications for our understanding of the most rapid periods of star formation in distant galaxies and the ensemble properties of galaxies generally.

Object	Line	z	FWHM	flux	SB limit	r_{iso}
(1)	(2)	(3)	(4)	(5)	(6)	(7)
Q2343-BX610	Hα	2.2098±0.0018	382± 8	7.86±0.15	4.2	9.3
···	[NII]	2.2104±0.0019	400± 21	3.23±0.15	···	···
···	[OIII]	2.2090±0.0015	301± 30	0.67±0.06	···	···
···	Hβ	2.2096±0.0019	383± 62	0.50±0.07	···	···
ZC782941[a]	Hα	2.1812±0.0015	305± 13	5.23±0.21	8.9	7.2
···	[NII]	2.1816±0.0017	344± 75	1.15±0.22	···	···
ZC782941[b]	Hα	2.1814±0.0017	346± 13	3.05±0.11	3.8	4.2
···	[NII]	2.1815±0.0018	378± 42	1.09±0.11	···	···
Q2343-BX528	Hα	2.2684±0.0015	293± 8	2.28±0.05	4.3	7.5
···	[NII]	2.2689±0.0017	334± 63	0.43±0.06	···	···
BzK-15504[b]	Hα	2.3816±0.0014	260± 8	6.02±0.16	4.9	5.8
···	[NII]	2.3818±0.0017	327± 38	2.54±0.22	···	···
BzK-15504	Hα	2.3819±0.0020	400± 12	7.58±0.20	8.4	9.3
···	[NII]	2.3813±0.0032	661± 95	3.34±0.38	···	···
···	[OIII]	2.3833±0.0024	480± 15	8.68±0.24	···	···
···	Hβ	2.3841±0.0012	182± 50	0.73±0.17	···	···
BzK-6397	Hα	1.5132±0.0011	257± 8	3.18±0.09	2.3	10.5
···	[NII]	1.5135±0.0015	406± 46	1.08±0.11	···	···
BzK-6004K	Hα	2.3865±0.0013	245± 10	4.28±0.16	7.7	8.7
···	[NII]	2.3866±0.0015	274± 22	2.22±0.16	···	···
Q2346-BX482	Hα	2.2563±0.0016	312± 6	4.18±0.07	4.4	9.0
···	[NII]	2.2564±0.0016	313± 40	0.64±0.07	···	···
···	[OIII]	2.2569±0.0012	212± 11	1.62±0.07	···	···
···	Hβ	2.2589±0.0011	166	0.22	···	···
K20-ID7	Hα	2.2234±0.0016	313± 9	4.02±0.10	5.3	9.3
···	[NII]	2.2242±0.0014	282± 50	0.79±0.11	···	···
K20-ID8	Hα	2.2231±0.0014	267± 10	2.51±0.09	7.2	7.5
···	[NII]	2.2238±0.0014	264± 50	0.75±0.10	···	···
SSA22a-MD41	Hα	2.1632±0.0015	298± 12	3.71±0.13	5.2	8.3
···	[NII]	2.1627±0.0018	382± 89	0.72±0.16	···	···
···	[OIII]	2.1704±0.0016	323± 14	2.29±0.09	···	···
···	Hβ	2.1704±0.0009	96± 19	0.44±0.07	···	···
Q2343-BX389	Hα	2.1716±0.0024	525± 18	5.44±0.17	8.2	8.5
···	[NII]	2.1732±0.0031	681±112	1.65±0.22	···	···
···	[OIII]	2.1713±0.0019	393± 24	1.65±0.09	···	···
···	Hβ	2.1708±0.0010	141± 28	0.38±0.06	···	···

Table 3.1: Column (1) – Object designation. [a] implies 250 mas pixel scale plus adoptive optics, [b] implies 100 mas pixel scale plus adaptive optics. No indication implies that the data were taken without the benefit of AO and at 250 mas pixel^{-1}. Column (2) – Line identification. Column (3) – Redshift of the line in the integrated spectrum. By integrated spectrum, we mean that the sum of the flux from each pixel with a signal-to-noise greater than or equal to 3 in each data cube for Hα (see column 6 for this limiting value for Hα). All of the sums for the other emission lines are over the same aperture as for Hα. Column (4) – Full width at half maximum of the integrated spectrum of each galaxy, corrected for instrumental resolution and is in units of km s^{-1}. Column (5) – Line flux of the integrated spectrum in units of 10^{-16} erg s^{-1} cm^{-2}. Column (6) – Surface brightness detection limit in units of 10^{-19} erg s^{-1} cm^{-2} and defined at a signal to noise ratio, S/N≈3. This is for a pixel that has been averaged over 3 pixels x 3 pixels. Column (7) – Isophotal radius defined as Area = $\pi\, r_{\frac{1}{2}}^2$ where the Area is defined as the projected area on the sky above a significance of 3 in the data and is in units of kpc.

Source	$f_{H\beta}$	$f_{H\alpha}/f_{H\beta}$	$A_{H\beta}$	$corr_{H\alpha}$
(1)	(2)	(3)	(4)	(5)
Q2343-BX610	0.61±0.08	8.1	2.8	4.6
Q2343-BX389	0.37±0.05	4.1	1.0	1.7
SSA22a-MD41	0.35±0.05	7.2	2.5	3.9
BzK-15504	0.52±0.08	7.1	2.4	3.8

Table 3.2: Column (1) – Source designation. Column (2) – Measured line flux of Hβ in units of 10^{-16} erg s^{-1} cm^{-2} for the integrated spectrum. In this case, we mean that the spectrum is integrated over the region where the S/N is greater than 3 in Hβ. Column (3) – Line ratio $f_{H\alpha}/f_{H\beta}$ for the integrated spectrum as defined for column 2 in this table. Column (4) – The extinction in the Hβ using the Galactic extinction law. Column (5) – The multiplicative factor required to correct Hα for extinction assuming the Galactic extinction law.

Source	$f_{\lambda6716}$	$f_{\lambda6731}$	$f_{\lambda6716}/f_{\lambda6731}$	n_e
(1)	(2)	(3)	(4)	(5)
Q2343-BX389	5.9±0.1	7.5±0.1	0.8±0.1	1200^{+700}_{-400}
Q2343-BX610	1.7±0.1	1.5±0.1	1.1±0.1	400^{+700}_{-300}
Q2347-BX482	2.4±0.1	3.1±0.1	0.8±0.1	1200^{+700}_{-400}
BzK-15504	2.9±0.1	2.8±0.1	1.1±0.1	400^{+700}_{-300}
BzK-6397	1.1±0.1	0.9±0.1	1.2±0.1	260^{+150}_{-120}

Table 3.3: Column (1) – Source designation. Column (2) – Measured line flux of [SII] λ6716 in erg s^{-1} cm^{-2}. Column (3) – Measured line flux of [SII] λ6731 in erg s^{-1} cm^{-2}. Column (4) – Line ratio F(6716)/F(6731). Column (5) – Electron density corresponding to R±1σ for T= 10^4 K in cm^{-3}.

Chapter 4

Can evidence for cosmological accretion be observed in the Hα emission from galaxies at z~2?

Le Tiran, L., Lehnert, M. D., Di Matteo, P., Nesvadba, N. P. H. & van Driel, W.
Published on June 2011 in *Astronomy and Astrophysics*

Abstract: In previous studies, it has been shown that the large line widths observed in high surface brightness Hα emitters at low and high redshifts are likely due to the mechanical energy injected by intense star formation. Here we discuss the possibility that the high surface brightnesses observed are not due to star formation, but due to cosmological gas accretion. We assume that all of the accretion energy is dissipated as shocks from the accreting gas. We show that in order to explain the high surface brightnesses both the mass accretion rate and energy would have to be much higher than expected from simulations or from equating the star formation with the accretion rate. We also investigate scaling relations between the surface brightness expected from accretion and for star formation through mechanical heating and photo-ionization, trying to identify a regime where such accretion may become evident in galaxies. Unfortunately, the surface brightness necessary to detect the gas in optical line emission is about an order of magnitude lower than what has currently been achieved with near-infrared observations of distant galaxies.

Contents

4.1 Introduction

Various processes have been proposed to explain how galaxies obtain the amount of gas necessary to fuel star formation and their growth. In the early hierarchical models of galaxy growth (e.g. White & Rees, 1978) it was a combination of minor and major mergers, and gas cooling from a virialized dark matter halo, but it is now thought that much of the cooling may take place outside of the individual halos that subsequently accrete the gas, and that this gas will never be heated up to the virial temperature in the halo – such accretion mechanisms have been dubbed "cold flows" (e.g. Dekel et al., 2009; van de Voort et al., 2010).

All these ideas rely on the basic assumption that baryons are strongly coupled to the dark matter through gravity and thus robustly follow the collapse of the dark matter. Without such coupling and the relative amounts of heating and cooling that this entails, neither cooling virialized halo gas nor gas from cold flows would deposit as much material over the same time range as they have been hypothesized to do. However, there is scant observational evidence for such cold flows or even hot halos. Recently, Anderson & Bregman (2010) concluded that the missing baryons are not in the halos of nearby galaxies and likely never were part of the Milky Way. In addition, there is evidence that gas in halos of distant galaxies is due to starburst driven outflows and not to gas accretion (Steidel et al., 2010).

Nevertheless, many models (e.g. Dekel et al., 2009; Brooks et al., 2009; Kereš et al., 2009) suggest that cooling baryons in the halos and/or cold accretion flows are needed to explain the observations of distant galaxies, especially their large emission line widths, the apparent prevalence of rotating disks (as claimed by Förster Schreiber et al., 2006), and their high star-formation rates. On the other hand, Lehnert et al. (2009) (hereafter L09, chapter 3) proposed that the large line widths observed are not due to gas accretion but to the intense star formation in the observed high redshift (z~2) objects. The same conclusion has subsequently been reached by Green et al. (2010). Elmegreen & Burkert (2010) (hereafter EB10) modeled how accretion flows might explain the large line widths by dissipating the accretion energy as turbulence. They conclude that while large line widths are possible due to accretion, the phase when line widths are dominated by accretion must be short lived, about one dynamical time (~100 Myr), suggesting that intense, or more efficient, star formation may be more likely responsible for the large line widths.

Despite this work, many subsequent studies have continued to suggest that gas accretion is a viable mechanism for explaining some of the properties of high redshift galaxies. In this chapter, we examine the two following simple questions: (1.) Can the observed high Hα surface brightnesses in distant galaxies be explained by cosmological gas accretion at a rate sufficient to fuel their star formation? (2.) For what ratio of the star formation and accretion rates would we expect the emission

line luminosity generated from accretion to dominate? The impact of gas accretion can only be observed if the heating rate due to star formation is below some threshold. This threshold depends on the efficiency of (1.) the transformation of accretion energy into turbulence, (2.) gas heating and (3.) the transformation of the mechanical and ionizing energy of massive stars into turbulent and bulk motions, and heating.

Throughout this chapter we adopt a flat H_0 =70 km s^{-1} Mpc^{-3} concordance cosmology with $\Omega_\Lambda = 0.7$ and $\Omega_M = 0.3$.

4.2 Hα luminosity and velocity dispersion

We use ESO archival data from a variety of programs with SINFONI on the ESO-VLT of a sample of more than fifty galaxies in the redshift range 1.3-2.7, described in Chapter 2. The key to the sample is that all have sufficiently high Hα surface brightness to obtain spatially resolved line maps in a few hours integration time. The targets have Hα surface brightness levels exceeding a few $\times$ 10^{-18} erg cm^{-2} s^{-1} arcsec^{-2} over more than 1-2 arcsec^2 (10-20 kpc) in radius and total Hα luminosities above about 10^{42} erg s^{-1}. Due to cosmological dimming, there is a range of a factor of ~5 in the faintest surface brightness line emission levels that can be probed as a function of redshift in our sample. However, it is worth repeating the conclusion from L09 that even our lowest redshift SINFONI sources are extreme compared to galaxies in the local volume, where only a few of the most intense starbursts have such high Hα surface brightnesses, and this on smaller physical scales only.

Many studies which have analyzed the emission-line characteristics of distant galaxies examined velocity dispersions as an integrated property (e.g. Khochfar & Silk, 2009; Burkert et al., 2010; Ceverino et al., 2010). These analyses have tended to favor gravity as the source of the observed characteristics, whether driven by gas accretion energy derived from the potential energy of the halo or from gravitational contraction of a gaseous and stellar disk. L09, on the other hand, focused on the relationship they found between spatially resolved Hα surface brightness and velocity dispersion in 10 high redshift galaxies observed with SINFONI, a subset of the sample of over 50 galaxies discussed here. They suggest that neither smooth cosmological gas accretion, velocity dispersions driven by Jeans-unstable clumps, or turbulence generated by energy extracted by a collapsing disk can explain this relationship. They suggested instead that the velocity dispersion due to mechanical energy released by the observed intense star formation is of the form σ=$(\varepsilon\Sigma_{SFR})^{1/2}$, where ε is the efficiency at which the mechanical energy from a star-formation intensity Σ_{SFR} is converted into turbulence and bulk flows in the interstellar medium of galaxies. This model has the advantage of having no free parameters since the efficiency can be constrained by observations of nearby galaxies or models (Dib

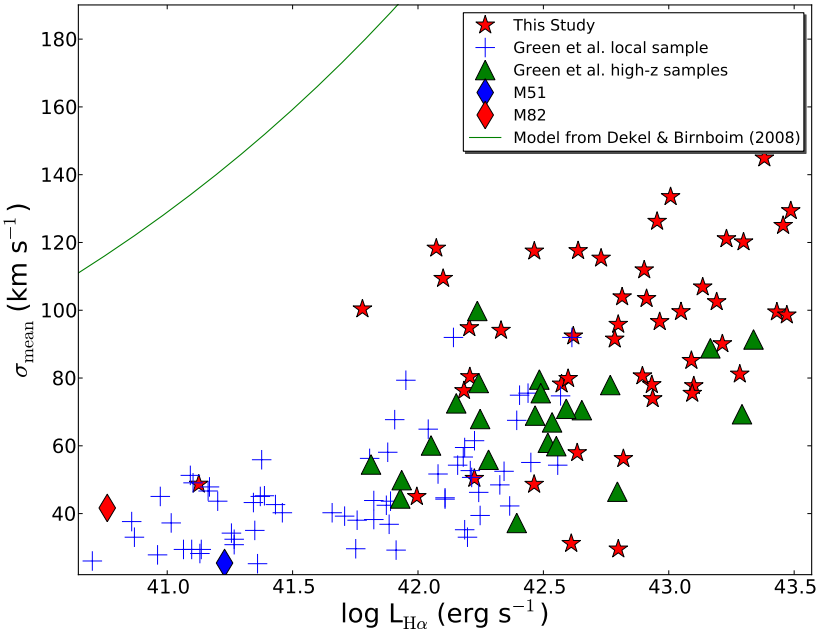

Figure 4.1 Intrinsic mean Hα velocity dispersion (in km s^{-1}) as function of total Hα luminosity (in erg s^{-1}) for different samples of local and high redshift galaxies (see § 5.2). The green line represents the Hα produced by a gas accretion model (Dekel & Birnboim, 2008a, see § 4.3).

et al., 2006, and references therein).

Rather than using spatially resolved spectrographic data for a pixel-by-pixel comparison, Green et al. (2010) constructed a single, integrated Hα spectrum per galaxy, through a flux-weighted averaging of their pixels. Figure 6.11 shows the relationship between the total Hα luminosity and the mean velocity dispersion measured using integrated spectra derived with flux weighting per pixel, for our sample of high redshift galaxies, as well as for the galaxies from Green et al. (2010), i.e., their selection of local SDSS galaxies, M51 (Tully, 1974), M82 (Lehnert et al., 1999) and diverse samples of high redshift galaxies taken from Epinat et al. (2009), Law et al. (2009) and Lemoine-Busserolle et al. (2010). The relationship shows a similar trend as the one found between surface brightness and dispersion per pixel in L09. For our purpose here, this remarkable similarity is important as it supports the notion that any hypothesis that explains the trend of increasing local optical emission line widths with local surface brightness, such as star formation (Lehnert et al., 2009), apparently also explains the similar relationship between the integrated quantities (something that was not pointed out by either L09 or Green et al. 2010). We will discuss this in greater depth in Chapter 6.

4.3 Can cosmological gas accretion shocks produce the observed Hα surface brightnesses?

L09 evaluated various mechanisms that can contribute to the large observed Hα line widths, such as clumps, gravitational instabilities, effects from the turbulence and smooth accretion, and suggested that only the mechanical output from star formation could power such large random motions. This chapter further examines the case for cold gas accretion and its observability in the z~2 Universe (e.g. Kereš et al., 2009; Dekel et al., 2009). Gas accretion onto galaxies is undoubtedly a complex process: this accreting gas would further cool through radiation and by generating shocks upon hitting the ISM of the galaxy. The highly radiative shocks are an effective mechanism through which infalling gas can lose its energy and momentum. But can we see direct evidence for this in our integral field Hα data sets?

The underlying assumption that the infalling gas dissipates energy by colliding with gas already in a galaxy disk and that all the accretion energy, extracted from the halo potential, is converted into supersonic turbulence which then dissipates as fast shocks is undoubtedly an over-simplification, as in reality only part of the energy will go into turbulence and some of it into bulk motions, and shock velocities will span a wide range of velocities which is dependent on the structure (density and temperature) of the ISM. Although some, and perhaps most, of the energy will be dissipated in slower shocks in denser gas, the Hα luminosity of the shock will not be very high in shocks below a few tens of km s^{-1} (Shull & McKee, 1979).

We can estimate the dissipation rate of the infalling gas using a range of shock models, as we assume that the shock velocities are equal to the observed velocity dispersions, which span the range of ~50-250 km s^{-1} in our sample. The shock models are complementary in the sense that some (Allen et al., 2008) focus on high velocity shocks where the precursor ionizing the gas in front of the shock is important ($v_{shock} \gtrsim$ 80-100 km s^{-1}, Dopita & Sutherland, 1995), and others on lower velocity shocks (Raymond, 1979; Shull & McKee, 1979).

This allows us to estimate the rate at which mass must pass through the shock in order to provide sufficient Hα surface brightness to be observable, as well as the total Hα luminosity produced by the accretion energy. Using the characteristics of the z~2 galaxies in our sample, we find a mean velocity dispersion of almost 100 km s^{-1} and a total Hα luminosity of $\sim 10^{43.0}$ erg s^{-1}. Correcting for the extinction typically observed for this kind of sources would increase their Hα luminosities by a factor of 2-5 (L09). Using the shock models of Allen et al. (2008), we find that about 2% of the shock energy is emitted in Hα for a shock velocity of 100 km s^{-1}, independent of the gas density. The conversion rate of 2% is near the maximum efficiency for this process.

An accretion energy extracted from the potential energy of the dark matter halo, of $\sim 10^{43.1}$ erg s^{-1} has been estimated for a baryonic accretion rate of about 100 M$_\odot$ yr^{-1} (Dekel & Birnboim, 2008a). Our typical Hα luminosity, if entirely due to star formation, would be consistent with a star-formation rate of $\sim$ 100 M$_\odot$ yr^{-1} for a Salpeter IMF with lower and upper mass limits of 0.1 and 100 M$_\odot$ (Kennicutt, 1998a, and a factor of a few lower for a more reasonable Kroupa IMF). The predicted Hα luminosity, if due to accretion, would then be about $10^{41.4}$ ($\dot{M}_{acc}$/100 M$_\odot$ yr^{-1}) erg s^{-1}, if the whole of the accretion energy is radiated through shocks with velocities of 100 km s^{-1}, with a conversion rate of 2%. With 10% of the accretion energy going into supersonic turbulence (Klessen & Hennebelle, 2010), gas accretion rates of many hundreds to thousands of M$_\odot$ yr^{-1} would be required for the total accretion energy to explain the Hα luminosity. Such high values for the gas accretion rate are well above what is commonly estimated from various models (e.g. Kereš et al., 2009; Genel et al., 2008). We demonstrate this in Figure 6.11 where we show the relationship between σ and $L_{H\alpha}$ for a gas accretion model. For this model, we have used the gas accretion rate as a function of virial velocity and the energy deposition rate due to accretion (Dekel & Birnboim, 2008a), a conversion rate of 2%, and assumed the virial velocity is equal to the shock velocity.

If gas accretion is truly happening at rates of up to several hundreds of M$_\odot$ yr^{-1} at z$\sim$2, it is likely that the integrated measures of Hα luminosity and velocity dispersion are due to a combination of star formation and gas accretion. We can use the spatially resolved data to investigate if part of the surface brightness of these galaxies may be explicable by gas accretion. For this we will estimate the amount of mass that would need to be shocked to explain the observed surface brightnesses as a function of dispersion. In Figure 4.2, we show the results for 10 representative galaxies in two redshift bins which, because of the strong dependence of surface brightness with redshift, allows us to show the full range of rest-frame Hα surface brightnesses within our sample of about 50 galaxies. We find that the surface brightnesses can be explained by shock models, but only if the mass flow rates through the shocks are very high, with accretion rate densities of over a few hundred M$_\odot$ yr^{-1} kpc^{-2} implied for the highest surface brightnesses, whereas only for the lowest surface brightnesses a more reasonable level of 25-50 M$_\odot$ yr^{-1} kpc^{-2} is indicated. In all cases, to explain the surface brightness requires gas of reasonably high density ($\gtrsim$100 cm^{-3}).

Taking a rate at which gas is shocked of 300 M$_\odot$ yr^{-1} kpc^{-2} would suggest 10^5 M$_\odot$ yr^{-1} of shock heated gas, or $\sim 10^3$ times the reasonable gas accretion rate (Dekel et al., 2009). To support star formation and to form a disk galaxy, the energy from accretion must not be dissipated too rapidly least the gas loses too much angular momentum. Over a dynamical time of about 200-300 Myr (EB10), the amount of gas that needs to be shock heated is of the order of 10^{13} M$_\odot$, two orders of magnitude larger than the total ISM mass in a disk galaxy.

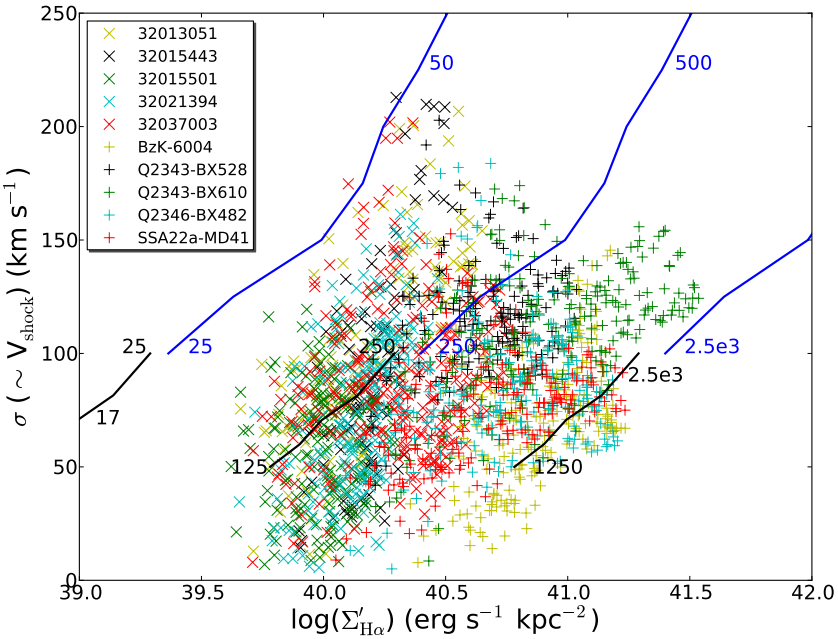

Figure 4.2 Observed pixel-by-pixel Hα line widths (assumed equal to the shock velocities) as function of Hα surface brightnesses (corrected for cosmological surface brightness dimming) in a sub-sample of 5 representative galaxies in each of two redshift bins, z~1.4 (+ symbols) and z~2.3 (×). Lines correspond to Hα surface brightnesses derived using shock models from Raymond (1979) (black) and Allen et al. (2008) (blue). The numbers along each line indicate the surface accretion rates (in $M_\odot$ yr^{-1} kpc^{-2}) which produce the Hα surface brightness. The 3 sets of lines are for pre-shock densities of 10, 100 and 1000 cm^{-3}, respectively, from left to right.

4.4 Discussion and Conclusions

The reason why it is likely difficult to note the effects of gas accretion on the ISM of presently observed galaxies is the relatively low efficiency of the conversion of accretion energy into line emission. An interesting question is under what circumstances a galaxy might be observed that is undergoing a (formative) phase of intense gas accretion.

We have attempted to quantify how the mass accretion rate would compare to the star-formation rate in both controlling the ionization of the gas and in mechanically exciting the gas (see Fig. 4.3). We estimated that the Hα luminosity is produced at the rate of 2.6×10^{41} erg s^{-1} M$_{\odot}^{-1}$ (Leitherer et al., 1999, appropriate for a Kroupa IMF), that there is a 90% contribution of ionizing photons ($\varepsilon_{\gamma,SF}$), which implies an escape fraction of 10%, that accretion shock energy is converted into Hα luminosity at the rate of 2% ($\varepsilon_{acc}^{shocks}$), and that 90% ($\varepsilon_{\rm acc}$) of the accretion energy is lost due to shocks which emit Hα at an efficiency of $\varepsilon_{acc}^{shocks}$. To compare this with the mechanical energy of the star formation we used a conversion factor of 7.4×10^{41} erg s^{-1} M$_{\odot}^{-1}$ (Leitherer et al., 1999) and a conversion efficiency of either 10 or 20% ($\varepsilon_{\rm SF}$).

This allows us to compare the relative efficiency of heating and ionization from the formation of massive stars with that of the mechanical heating through gas accretion. Can we identify areas in a plot comparing the rates of star formation and cosmological gas accretion where observations may be made to discover the duration and impact of gas accretion? To this end, we have used the simple model of the relationship between gas accretion and star formation of EB10. This model, which assumes a phase with constant accretion rate, allows us to compare, as a function of time, the expected total recombination line luminosity due to infalling gas dissipating its energy through shocks versus that produced by the ionizing radiation and mechanical energy from star formation, whose rate is estimated by the total gas mass multiplied by the gravitational instability growth rate (see EB10 for details).

In this comparison with the models of EB10 we see (Fig. 4.3) that very quickly, within 45-90 Myr depending on the gas mass accretion rate, photo-ionization from massive stars dominates over the heating due to gas accretion. This implies that shock-like line ratios are not expected to be observed even if the energy of the infalling gas dominates the dynamics of the ISM. After about 180 Myr, the mechanical energy of massive stars through supernovae and stellar winds begins to dominate, something already concluded by L09. While we should not take the numbers literally, the analysis suggests that the time over which the effects of gas accretion will be evident is relatively short – less than a dynamical (orbital) time within a galaxy.

So we expect to see the impact of gas accretion on either the ionization or dynamical state of the gas only early in the gas accretion process and only when the

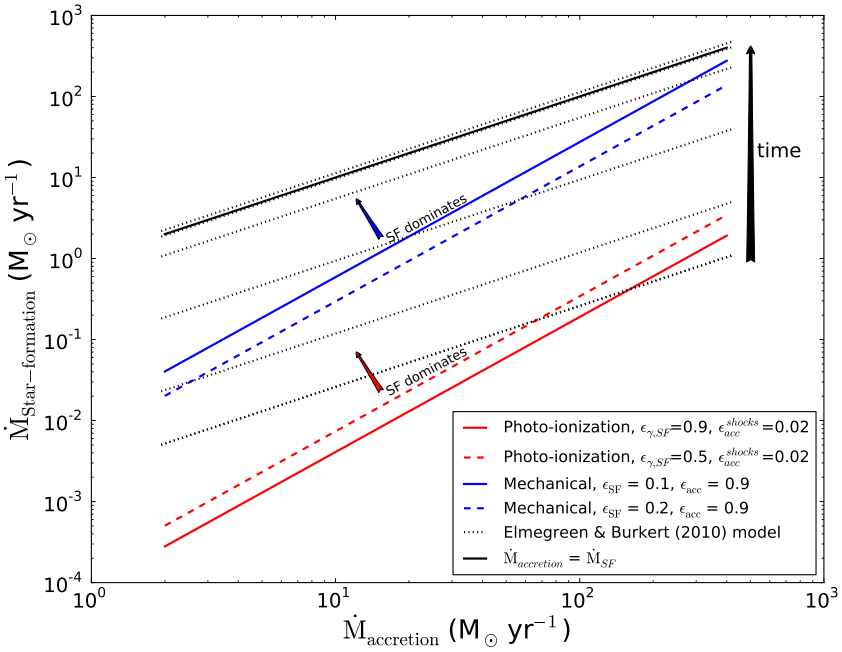

Figure 4.3 Comparison of the star formation rates and cosmological gas mass accretion rates (in $M_\odot$ yr^{-1}) at which accretion energy generates the same Hα luminosity as young stars through their ionizing photons (red solid and dashed lines) and as mechanical energy released by supernovae and stellar winds (blue lines); the difference between the two sets of lines is the efficiency at which the ionization or mechanical energy output couples to the ISM (see text for details). Both comparisons assume the same accretion model. Regions above the blue and red lines are dominated by the influence of the intense star formation. A comparison with the models by Elmegreen & Burkert (2010) is also shown for 0.5, 1, 2, 3, 4 and 5 $\times$ 90 Myr (from bottom to top, as indicated by the black arrow). The solid black line shows the situation when star formation and cosmological gas mass accretion rates are equal (which the model reaches after a couple of dynamical times).

star-formation rates are relatively low. Within the context of the EB10 model, the star formation will roughly reach equilibrium with the accretion rate after a couple of dynamical times. If this were the case for our intensely star-forming galaxies at high redshift, we should not see any impact on either the surface brightness or dynamics of the emission line gas, as these are both controlled by star formation, in agreement with what was first proposed by L09 and later supported by the findings of Green et al. (2010).

Can we actually observe this early phase of gas accretion and its impact on either the ionization or the mechanical energy? The answer is likely no, at least not through Hα observations. Star-forming galaxies at high redshift have star-formation rates above 10 $M_{\odot}$ yr^{-1} (Förster Schreiber et al., 2006). Comparing this with Figure 4.3 suggests there is only a small probability that the effect of gas accretion can be observed. Taking a relatively optimistic star-formation rate of less than 30 M$_{\odot}$ yr^{-1}, which is equivalent to the Hα surface brightness generated by a gas accretion rate of about 100 M$_{\odot}$ yr^{-1}, using our scaling for mechanical energy, suggests that the average surface brightness over 1 arcsec^2 (barely enough to resolve a galaxy) would be about 4×10^{-19} erg s^{-1} arcsec^{-2} at z=2.2. This is about an order of magnitude less than what can be detected in a few hours observation with a spectrograph like SINFONI on an 8-10m class telescope like the ESO-VLT, and even beyond the longest integrations made with SINFONI (Lehnert et al., 2010). Perhaps more unfortunately, given the difficulty in designing spectrographs with large pixels on the next generation of large telescopes, reaching surface brightness levels beyond the current limits will remain difficult in the foreseeable future.

Therefore, we conclude that currently, the impact of gas accretion on galaxies at high redshift cannot be observed using the optical emission line gas. This is true especially for the early phases of galaxy formation where the gas accretion rate, despite it being thought of order 100-300 M$_{\odot}$ yr^{-1} for massive galaxies and at high redshifts (Dekel et al., 2009; Kereš et al., 2009), will not be observable both because it does not liberate enough mechanical energy to be observable with integral field spectrometers and because it is relatively quickly over-whelmed by the heating due to star formation, even at relatively modest rates.

CHAPTER 5

The average optical spectra of intense starbursts at z∼2: Outflows and what pressurizes their ISM

Le Tiran, L., Lehnert, M. D., Di Matteo, P., Nesvadba, N. P. H. & van Driel, W.
Submitted on June 30th, 2011, in *Astronomy and Astrophysics*.

Abstract: An important property of star-forming galaxies at z∼1-2 is the high local star-formation intensities they maintain over tens of kiloparsecs at levels which are only observed in the nearby Universe in the most powerful nuclear starbursts. To investigate how these high star-formation intensities affect the warm ionized medium, we present an analysis of average spectrum of about 50 such galaxies at z≈1.2-2.6, and of subsamples selected according to their local and global star-formation intensity. Stacking allows us to probe relatively weak lines like [SII]$\lambda\lambda$6716,6731 and [OI]λ6300, which are tracers of the conditions of the ISM, and are undetectable in most individual targets. We find higher gas densities (and hence, pressures) in intensely star-forming regions compared to fainter diffuse gas, and overall, values that are comparable to starburst regions and the diffuse ISM in nearby galaxies. Photoionization modeling Hα surface brightnesses and [SII]/Hα line ratios with Cloudy, we find that our galaxies continue trends observed in local galaxies, where gas pressures scale with star-formation intensity. We discuss these results in the context of models of self-regulated star formation, where star formation determines the average thermal and turbulent pressure in the ISM, which in turn determines the rate at which stars can form, finding good agreement with our data. We also confirm the detection of broad, faint lines underlying Hα and [NII], which have previously been considered evidence of either outflows or active galactic nuclei. Finding that these lines scale with local and global star-formation intensity strongly supports the outflow interpretation, and further emphasizes the importance of star-formation feedback and self-regulation in the early Universe.

Contents

5.1 Introduction

The nature and evolution of galaxies is a result of the complex interplay between heating, cooling and dynamical processes in the interstellar medium (ISM). The cyclic, or competitive, nature of these processes determines the rate at which stars form and creates a feedback loop which determines the chemistry and structure of galaxies and their ISM. This interplay ultimately results in galaxies as we observe them today.

In starburst galaxies, where the energy injection rate per unit volume from young stars is high, we may see the effects of self-regulation of star-formation, a process in which supernova feedback with its strong energy injection may well play an important role (Silk, 2001) – and drive the cloud velocity dispersion (Joung & Mac Low, 2006; Tasker & Bryan, 2006) – as may turbulent pressure (Silk, 2001; Blitz & Rosolowsky, 2006). At low energy injection rates into the ISM, global shear is likely to play the most significant role in determining the peculiar velocities in dense massive clouds (Gammie et al., 1991). The observed turbulence is dominated by non-axisymmetric gravitational instabilities at low star-formation intensity levels, like the few to several tens of km s^{-1} seen in the Milky Way, but at high intensity levels mechanical energy from the stellar population may play the most significant role (Joung et al., 2009a; Agertz et al., 2009).

Recently, we have proposed that the large Hα line widths observed in distant (z$\sim$1-3) intensely star-forming galaxies are driven by the mechanical energy liberated by young stars, a relationship which can be understood within the context of self-regulated star-formation (Chapters 3 and 6). We hypothesized that mechanical energy is sufficient to keep the disk critically unstable against fragmentation and collapse and thus star-formation (Toomre Q$\sim$1). The intensity of the star-formation in these distant galaxies is very high, similar to those in local starbursts but over a much larger physical scale, and it is maintained by large gas fractions and high total mass surface densities. These line widths do not appear to be driven by either cosmological accretion (Le Tiran et al., 2011) or gravitational instabilities.

In this manuscript, we further these arguments through a stacking analysis of rest-frame optical emission lines of about 50 galaxies with redshifts of 1.2 to 2.6 and high Hα surface brightnesses. Stacking allows us to analyze emission lines that are too faint to be observed in most individual galaxies like [SII]$\lambda\lambda$6716,6731 or [OI]λ6300, which are key indicators of the pressure and sources of ionization in the emission line gas. We analyze stacks of subsamples to investigate how the gas properties scale with star-formation intensity (rate per unit area). In a stacking analysis of a very similar sample, but focusing on trends with stellar mass and radius, Shapiro et al. (2009) identified a broad line underlying Hα and [NII], but were unable to differentiate whether this broad line emission was from outflows or active galactic nuclei. We confirm the detection of a broad component and argue

that its presence in our stacks, where the significance of the broad component increases with increasing star-formation intensity, can be interpreted as confirming the outflow hypothesis.

5.2 Data analysis

We use ESO archival data from a variety of programs with SINFONI on the ESO-VLT of a sample of more than fifty galaxies in the redshift range 1.2-2.6, see Chapter 2 for further details. For this chapter, however, we have excluded all galaxies with recognizable AGN features in their data cubes – especially broad lines and high ratios of [NII]λ6583/Hα. We produce for each object an integrated spectrum using all the spectra in the data cube where Hα is detected above the 3-σ level, which are co-added after shifting Hα to its rest-wavelength in order to remove any broadening due to the velocity field and weighted by the Hα signal-to-noise ratio (SNR) of each object in order to maximize the final SNR. Uncertainties were measured using a Monte-Carlo method fitting 1000 realizations of the spectrum (Figure 5.2).

To investigate if the stacked emission line properties depend on the Hα surface brightness (and/or redshift) of the galaxies used, we also made comparative stacks of objects in three bins: (1) z < 1.8 and star-formation rate (SFR) < 100 $M_\odot$ yr^{-1}, (2) z > 1.8 and SFR < 100 $M_\odot$ yr^{-1} and (3) z > 1.8 and SFR > 100 $M_\odot$ yr^{-1} (Figure 5.1). All galaxies have similar isophotal size (Chapters 3 and 2). To investigate the role that star-formation intensity might play in determining the characteristics of the integrated spectrum, for each bin and for the entire sample we also made one sub-stack using only the 18 brightest pixels in the Hα distribution of individual galaxies, and another using only the remaining, fainter pixels. Eighteen pixels correspond to approximately the FWHM of the PSF (∼0″.6). On average, 25% of the total Hα luminosity is due to these brightest pixels (Table 5.1).

5.3 Emission line properties

We obtain log [NII]λ6583/Hα = −0.75 to −0.55 in all four stacks, and log [SII]$\lambda\lambda$6716,6731 = −0.5 to −0.75. We did not detect [OI]λ6300 in any of our stacks, with an upper limit of log [OI]/Hα = -1.4 to -1.9 (1σ), similar to those in the integrated spectra of nearby star-forming galaxies (Lehnert & Heckman, 1994) and HII regions. The flux ratio of [SII]λ6716/[SII]λ6731 is about 1.2 to 1.4, near the low density limit (1.45; Table 5.2), and the highest values are found in the stacks with the highest surface brightness Hα emission. For most of the stacks the density must be very low (n_e ∼ 10-100 cm^{-2}, see Figure 5.3), whereas in the regions of the highest Hα surface brightnesses in each galaxy we find values of about 100 to

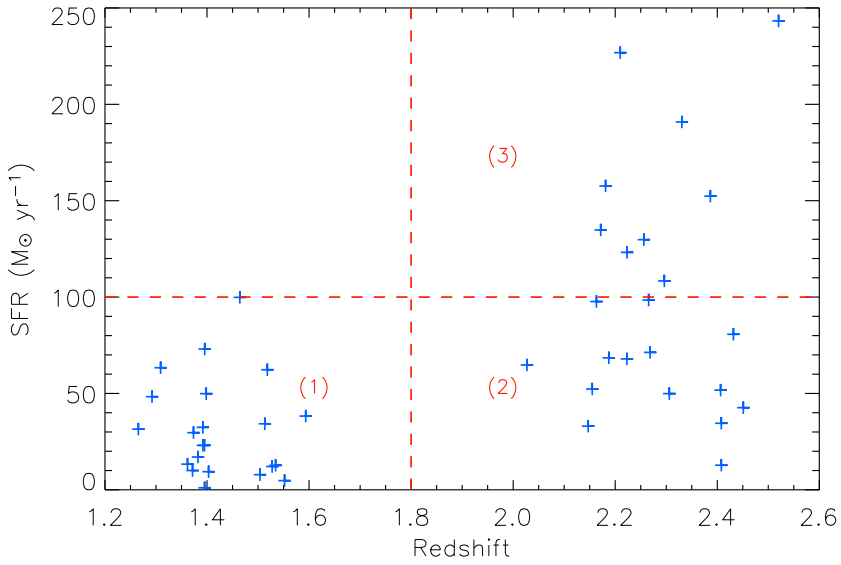

Figure 5.1 Star-formation rate as a function of redshift for all galaxies used. Red dashed lines correspond to the boundaries between the 3 different bins used to make comparative stacks, which are labeled (1), (2) and (3).

bin	# objects	$<\Sigma_{H\alpha}>$	$<\Sigma_{SFR}>$	$L_{H\alpha,brightest}/L_{H\alpha,whole}$
all	45	5.7	0.4	25
(1)	22	2.1	0.2	21
(2)	14	7.3	0.6	29
(3)	9	12.1	1.0	24

Table 5.1 Properties of the entire sample and the 3 different bins used for comparative stacking. $<\Sigma_{H\alpha}>$, in units of 10^{40} erg s^{-1} kpc^{-2}, is the average Hα surface brightness of the galaxies in the stack, calculated as $L_{H\alpha}/4\pi r_{iso}^2$, where $L_{H\alpha}$ is the Hα luminosity and r_{iso} is the isophotal radius at the surface brightness detection limit. r_{iso} is estimated using the total isophotal area at the detection limit, A_{iso}, and by requiring $r_{iso}=(A_{iso}/\pi)^{1/2}$ (see Lehnert et al. (2009) and Chapter 2 for details). $<\Sigma_{SFR}>$ is the average star-formation rate per unit area ($M_\odot$ yr^{-1} kpc^{-2}), calculated using the conversion factor for Hα luminosity to the star-formation rate from Kennicutt (1998a). $L_{H\alpha,brightest}/L_{H\alpha,whole}$ is the proportion of the Hα luminosity contained in the 18 brightest pixels stacks compared to the stacks of whole galaxies.

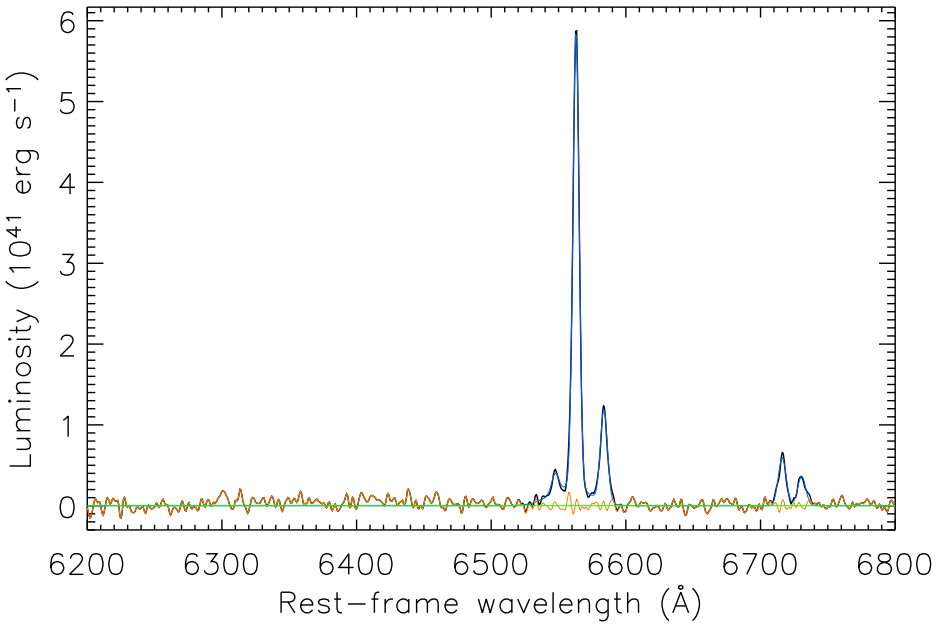

Figure 5.2 Stacked spectrum (signal-to-noise of Hα weighted average) of all the galaxies in the sample. The lines of Hα, [NII]$\lambda\lambda$6548,6583 and [SII]$\lambda\lambda$6716,6731 are all significantly detected, but we can only set an upper limit on the [OI]λ6300 emission.

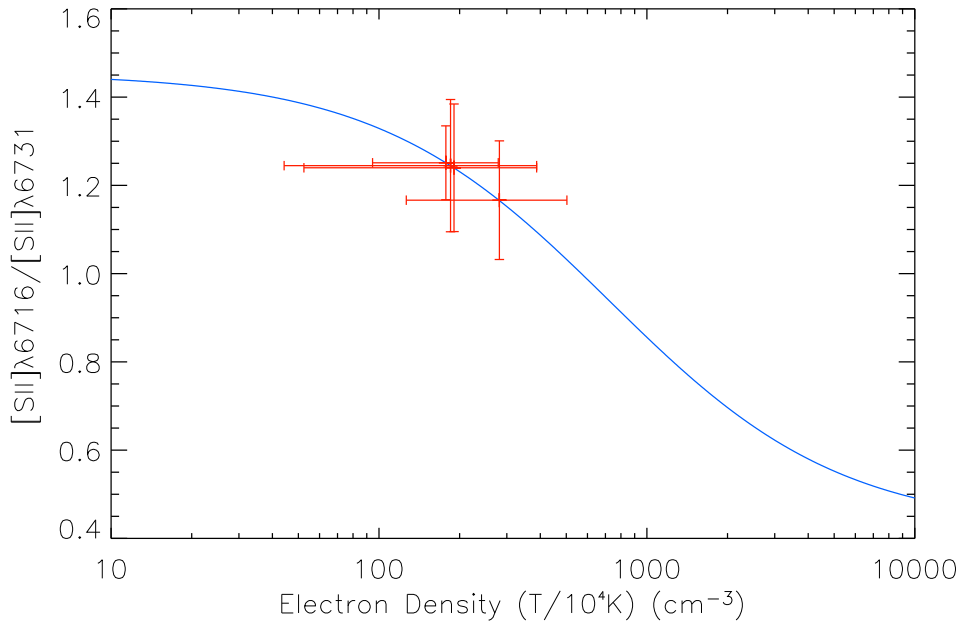

Figure 5.3 [SII]λ6716/[SII]λ6731 line flux ratio as a function of electron density (cm^{-3}), for a temperature of 10^4K (blue line; For derivation of this curve, see Appendix B). Only results for the stacks of the brightest pixels of Hα emission are indicated (red crosses). The error-bars indicate the 1σ uncertainties in the measurements. For clarity, stacks with [SII] line ratios below the low density limit are not shown.

500 cm^{-3}, with a mean of ~200 cm^{-3} (Table 5.2; Figure 5.4). These values are similar to nearby starbursts which have strong evidence for driving energetic outflows (Figure 5.4; Lehnert & Heckman, 1996a). Finding that the full stacks and the stacks excluding the brightest pixels are at (or near) the low density limit suggests that the most extended emission contributes most of the flux and indicates that these outer regions are more like the diffuse interstellar medium in nearby disk galaxies (Lehnert & Heckman, 1994; Wang et al., 1998).

We also find no significant differences in the widths of the various lines analyzed. Although there is a slight tendency of [NII]λ6583 to be systematically broader than Hα in all stacks, all individual width measurements are the same within the uncertainties. We do find a trend for the narrow components of both lines to be broader for the stacks with high average surface brightnesses. This is related to the trend for the most intense star-forming regions to have the broadest lines (Lehnert et al. (2009)).

Several of the spectral stacks have an apparent broad line underlying the region around Hα (Figure 5.5), as noted by Shapiro et al. (2009). We conducted

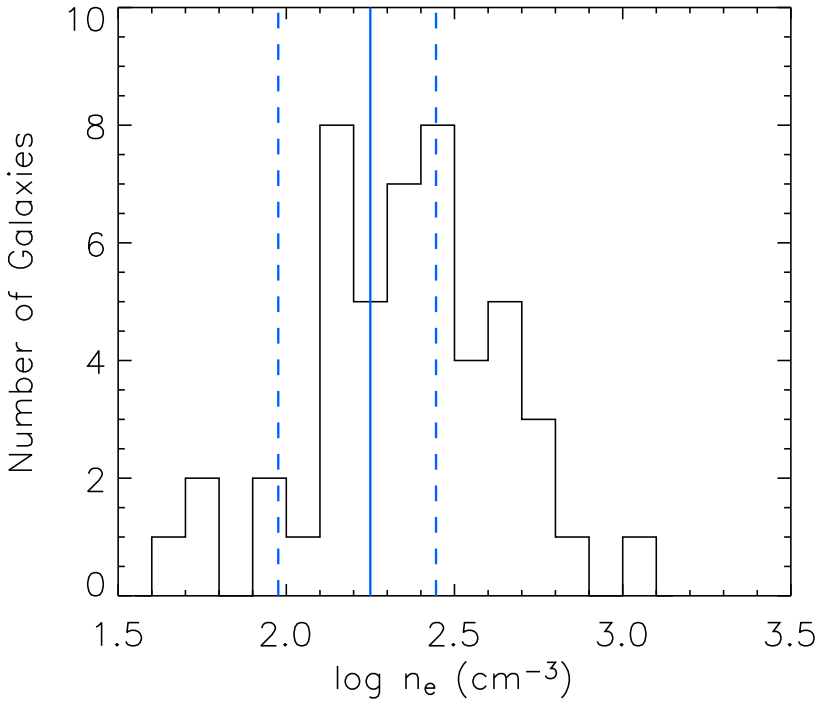

Figure 5.4 Distribution of electron densities n_e in the nuclear region of nearby starburst galaxies (Lehnert & Heckman, 1996a), as well as the mean electron density for the stack including only the brightest pixels of all our objects (solid blue line) and the corresponding $\pm 1\sigma$ uncertainties (dashed blue lines).

a Bayesian analysis to compute the relative strength of evidence, Bayes factor B, for a model which includes a broad line versus one without a broad component. Generally speaking, $ln(B) \geq 5$ is considered to be strong evidence in favor of the broad-line models (interpreted against the Jeffreys' scale; see Trotta, 2008, and references therein). We find strong evidence in favor of broad lines in the stacks with the highest average surface brightnesses (see B values listed in Table 5.2). In general, our fits (as derived from models with the highest values of B) agree well with Shapiro et al. (2009). We also find that the best fits are broad (FWHM~1500 km s^{-1}) and that the total flux ratio of the broad to narrow Hα emission lines is about 30% for those stacks with a significant broad feature.

5.4 Discussion and Conclusions

The results of the broad line analysis (§ 5.3) suggest a close relationship between the source of the broad emission and the star-formation intensity in these galaxies. Nearby galaxies whose starbursts are as intense as those observed in our distant sample show strong evidence for driving large-scale outflows (Lehnert & Heckman, 1996a). In fact, one can find close analogues between our spectra with or without a broad component and the low redshift starbursts galaxies in Lehnert & Heckman (1995), suggesting both samples must share a similar phenomenology. Although Shapiro et al. (2009) already suggested that broad lines in stacked spectra of z~2 intensely star-forming galaxies may indicate outflows, since they stacked according to stellar mass and radius (comparing nuclear and off-nuclear stacks) they were unable to rule out that the broad lines were due to AGN. The trends we see with average star-formation intensity contradicts the AGN hypothesis, simply because many intensely star-forming regions in these galaxies are off-nucleus, whereas the nuclear regions have often very low surface brightness (e.g. Förster Schreiber et al., 2009).

In the outflow scenario we expect, in addition to single narrow components of Hα and [NII]$\lambda\lambda$6548,6583, 3 more lines of Hα and [NII] that are offset and likely very broad (e.g. Lehnert & Heckman, 1996a). By making 5 physically motivated assumptions we avoid introducing 9 additional free parameters: (1) all three additional lines have the same offset velocity, (2) velocity dispersions are the same for each Hα and [NII] line component and are equal to the offset velocity, (3) the flux ratio of [NII]/Hα is that given by fast shock models (ratios ranging from ~0.2–1 for the velocities we considered in this modeling, see Allen et al., 2008), (4) the velocity offset and the shock speed are the same, and (5) the amplitude of the offset Hα component is 5% of that of the main Hα line. This last value matches the measured peak fluxes in the best-fit single broad component. This reduces the number of free parameters to only one, the offset velocity, while the other 8 are constrained.

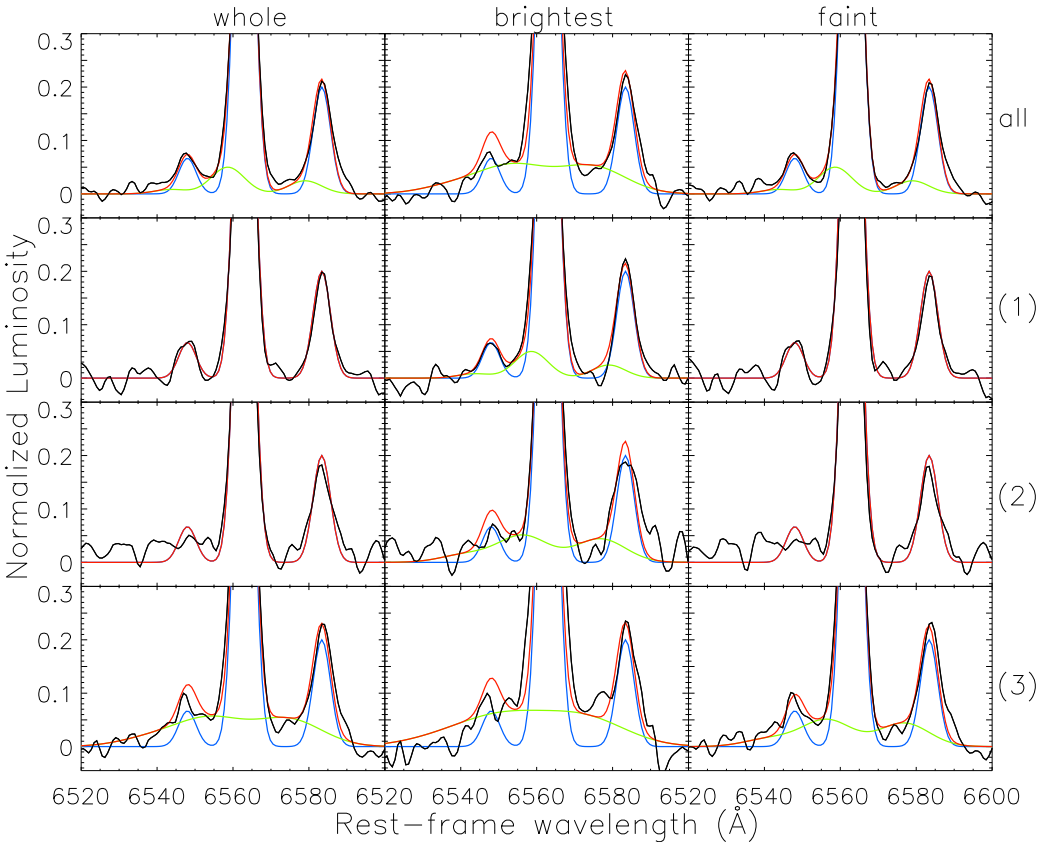

Figure 5.5 Zoom of the region of Hα and [NII] for 12 different stacks (black lines): from *left to right*: the integrated spectrum of all the emission from each galaxy (whole), only the brightest 18 pixels in Hα (brightest), and all other pixels (faint); from *top to bottom*: all spectral bins, bins (1), (2) and (3). The dashed blue line is the best fit to the strongest component of each line and the green dashed line the fit to the weaker offset component (the red line is the total of the fitted lines; see text for details). Velocity offsets range from ~100-500 km s^{-1} with the highest value seen in the stack with the highest average surface brightness.

We find that these fits are as significant as assuming a single broad component for velocity offsets of a few 100 km s^{-1} and narrow-to-broad Hα flux ratios of about 10% (although this is partially constrained by our assumption of a fixed 1:20 Hα peak ratio). These values are similar to those in the extended (i.e., wind) emission in nearby starbursts (Lehnert & Heckman, 1996a). The derived pressures are also similar to those in nearby starbursts, which is a necessary condition for driving winds (Figure 5.4). There is also sufficient mechanical energy in the shocks to power these flows. The mechanical energy output at a SFR of 150 $M_\odot$ yr^{-1} (typical for our high surface brightness sample) is about 10^{44} erg s^{-1}. The fraction of the total energy from fast enough shocks necessary to explain the broad lines observed is about 1-2% (Allen et al., 2008). If we assume that the mechanical energy output from stars is efficiently thermalized, we only require of-order 1-10% of the mechanical energy to energize the broad, blueshifted line emission.

What do these results imply about the nature of the ISM in these high redshift galaxies? We have already argued that the galaxies have high pressure. Figure5.6 illustrates that the warm ionized medium in nearby star-forming and starburst galaxies and in our galaxies forms a continuity – a one parameter family. Going from low to high Hα surface brightness we progress from diffuse ISM in nearby galaxies, through HII regions (and their surroundings) to nuclei of nearby starburst galaxies (e.g. Wang et al., 1998). On average our galaxies lie at the high surface brightness, low [SII]/Hα end of the relationship, similar to the positions of local powerful nuclear starbursts.

This continuity can be explained through a range of ISM pressures and radiation field intensities. We modeled the data as photo-ionized clouds (using the code Cloudy; Ferland et al., 1998), using the ionizing spectrum of a young (10^8 yrs) stellar population forming stars at a constant rate with a Salpeter IMF (Leitherer et al., 1999) and a range of column and volume densities. Our results suggest the galaxies have high average gas densities (~10–few $\times$ 100 cm^{-3}) and high ionization parameters (log U~ -2 to 0, where U is proportional to the relative intensity of the photon field divided by the total gas density). This supports the hypothesis of Wang et al. (1998) that this relationship can be understood as an underlying proportionality between the thermal pressure and the mean star-formation intensity in a photoionized gas.

What is the source of this underlying proportionality? Star formation might be regulated by the average pressure in the ISM (Silk, 1997), which Wang et al. (1998) suggested may itself be either regulated by the mechanical energy injection from star-formation, or related to the hydrostatic or turbulent pressure.

If the mechanical energy from massive stars is controlling the over-pressure, we would expect the pressure to increase linearly with the star-formation intensity. This can be estimated as, $P_{gas}=\dot{M}^{1/2}\dot{E}^{1/2}\ R_\star^{-2}$ (where P_{gas} is the gas pressure, $\dot{M}$ is the mass loss and entrainment rate, $\dot{E}$ is the mechanical energy output and $R_\star$ is the

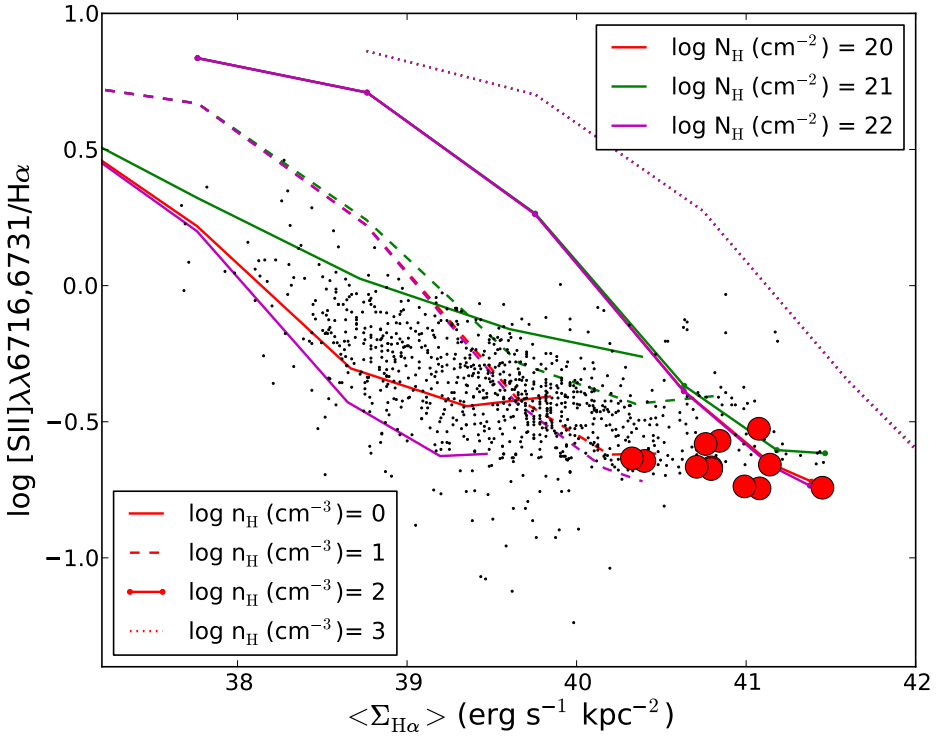

Figure 5.6 [SII]$\lambda\lambda$ 6716,6731/Hα flux ratio versus average Hα surface brightness for our 12 different stacks (see Table 2) of galaxies (red circles) superimposed on data for the diffuse emission in nearby star-forming and starburst galaxies from Wang et al. (1998) (black dots). The lines represent Cloudy photoionization models (Ferland et al., 1998) with various column densities (10^{20}, 10^{21} and 10^{22} cm^{-2} in green, red and purple, respectively), ionization parameters (U=10^{-5} to 1 from left to right along each line) and densities (1,10,100,1000 cm^{-3} as solid, dashed, dot-dash and dotted, respectively). The legend at the upper right indicates the colors of the lines for different column densities, while the legend at the lower left indicates the line styles for each volume density.

radius over which the energy and mass output occurs, e.g. Strickland & Heckman, 2009). From Leitherer et al. (1999), we can estimate the mechanical energy and mass output rate from star-formation. Adopting an equilibrium mass and energy output rate for continuous star-formation over 10^8 yrs, we estimate pressures of 1×10^{-10} dyne cm^{-2} (one-sided) for 0.5 M$_\odot$ yr^{-1} kpc^{-2}. If the mass entrainment rate is a factor of a few, this predicted pressure would be somewhat higher (consistent with that observed in M82 for example; Strickland & Heckman, 2009). For our stacks, the results of the photoionization models suggest thermal pressures of 6×10^{-10} to 6×10^{-11} dyne cm^{-2}.

In an alternative interpretation (which may be particularly appropriate at low star-formation intensities), the pressures are set by gravitational processes. Star-formation intensity is related to a cloud-cloud collision model, which gives $\Sigma_{\rm SFR} \propto \Sigma_{\rm gas}^{3/2}\Sigma_{\rm total}^{1/2}$ (Silk & Norman, 2009). The pressure in the ISM can be related to gravity or turbulence through $P_{\rm gas} = \rho_{\rm gas}\sigma_{\rm gas} = \pi G\Sigma_{\rm gas}\Sigma_{\rm total}$, where $P_{\rm gas}$ and $\rho_{\rm gas}$ are the gas pressure and density, respectively, and G is the gravitational constant. Combining these suggests that $\Sigma_{\rm SFR} \propto P(\Sigma_{\rm gas}/\Sigma_{\rm total})^{1/2}$. We can normalize this relationship empirically with the appropriate values for the Milky Way – ISM pressure of ~3000 K cm^{-3}, star-formation intensity ~2.5×10^{-3} M$_\odot$ yr^{-1} kpc^{-2} and a gas fraction of about 10%. The gas fraction in distant galaxies is likely to be higher, a few 10s of percent (Daddi et al., 2010). Using the average pressure from our photoionization modeling and the relation between star-formation intensity and pressure based on the Milky Way scaling suggests $\Sigma_{\rm SFR}$ ~1 M$_\odot$ yr^{-1} kpc^{-2}.

If star formation is driving the gas pressure, then it is likely that turbulent pressure is similar or even higher than thermal pressure, especially at high star-formation intensities (Joung et al., 2009a). In our stacking analysis, we find typical Hα line velocity dispersions of about 125 km s^{-1} and densities in the warm ionized gas of about 30-300 cm^{-3}. If the clouds formed through turbulent compression, the pre-shocked material would have turbulent pressures, $P_{\rm turb}=\rho_{\rm gas}\sigma_{\rm gas}\sim 10^{-9}$ to 10^{-10} dyne cm^{-2}. This is higher than the thermal pressures we observe in the emission line clouds of nearby galaxies, as suggested by models of ISM pressure regulated by feedback from star-formation (e.g. Joung et al., 2009a), but in the range of what we find at z~1-2.

In summary we find that these distant galaxies have high ISM pressures and drive outflows, at least at the highest average Hα surface brightnesses. These are two characteristics similar to intense starbursts at low redshift. Overall, we favor a picture where the pressure in the ISM is determined by the intensity of the star-formation and where feedback sets the scaling between pressure and star-formation intensity. Since the pressure is being regulated by the star-formation and pressure likely determines the nature of star-formation, this suggests that the star-formation in these high redshift galaxies is self-regulating (Silk, 1997). This extends our earlier conclusions that star-formation is likely to regulates the pressure of the ISM

based on spatially resolved properties of individual distant galaxies with high Hα surface brightness (Chapters 3 and 6).

Stack	$L_{H\alpha}$	$FWHM_{H\alpha}$	$FWHM_{H\alpha,int}$	L_{broad}	$FWHM_{broad}$	v_{off}	$L_{broad}/L_{H\alpha}$	ln(B)	[SII]λ6716/[SII]λ6731	n_e
(1)	(2)	(3)	(4)	(5)	(6)	(7)	(8)	(9)	(10)	(11)
all	32.9±0.5	250±3	254	8.4±1.5	1557±371	-183±142	0.3	24.6	1.6±0.2	...
all-brightest	7.8±0.2	271±4	288	2.8±0.4	999±140	-49±60	0.4	21.3	1.3±0.2	177^{+107}_{-86}
all-fainter	25.9±0.5	244±3	242	5.8±1.7	2031±872	-268±336	0.2	11.5	1.7±0.2	...
(1)	23.4±0.6	241±5	212	...	...	...	...	-0.1	1.6±0.3	...
(1)-brightest	5.6±0.2	270±8	230	...	...	...	...	-0.1	1.2±0.3	281^{+231}_{-160}
(1)-fainter	18.8±0.6	234±5	207	...	...	...	...	-1.6	1.7±0.4	...
(2)	24.7±0.8	236±5	231	...	...	...	...	5.0	1.7±0.3	...
(2)-brightest	7.2±0.3	265±8	247	...	...	...	...	4.6	1.2±0.3	184^{+203}_{-140}
(2)-fainter	18.0±0.7	227±6	224	...	...	...	...	2.4	1.9±0.5	...
(3)	57.0±1.3	264±4	278	19.9±3.2	1404±292	-149±113	0.3	22.6	1.6±0.3	...
(3)-brightest	13.5±0.4	292±7	322	7.1±0.8	1158±158	15±68	0.5	26.8	1.2±0.3	190^{+201}_{-141}
(3)-fainter	44.7±1.2	259±5	264	12.5±3.4	1555±629	-274±225	0.3	8.5	1.7±0.4	...

Table 5.2 Column (1) – The four bins used in the analysis are all objects, and bins (1), (2) and (3), see § 5.2, Table 5.1, and Figure 5.1 for details. Within each bin, – brightest refers to stacks made using only the brightest 18-pixels area (which roughly corresponds to the area of one seeing disk) of Hα emission per object, while –fainter refers to stacks made using only the remaining, less intense Hα emission pixels per object; Column (2) – Hα luminosity of the stack in units of 10^{41} erg s^{-1}; Column (3) – FWHM of the Hα line obtained without weighting the widths of individual objects by their Hα flux (in km s^{-1}); Column (4) – Hα FWHM obtained when weighting the widths of individual objects by their Hα flux (in km s^{-1}); In the next columns, 5–8, we provide the characteristics of our fits of a single broad component underlying the Hα and [NII] emission. However, we emphasize that we do not think of these fits as realistic (see text for details) but are given for comparison with Shapiro et al. (2009). The parameters are only provided for fits that have high significance; Column (5) – Hα luminosity of the single broad line component fitted to the spectrum (in units of 10^{41} erg s^{-1}); Column (6) – FWHM of the single broad component fitted to the spectrum (in km s^{-1}); Column (7) – velocity offset between the best-fit broad component and the narrow Hα line component (in km s^{-1}), where negative numbers indicate a blue-shifted broad component; Column (8) – flux ratio of the broad to narrow Hα line components; Column (9) – Bayesian likelihood, ln(B), of the model with a broad line compared to the model without, where values above 5 indicate a significant enhancement of the fit quality by including a broad line and negative values rule out a broad component; Column (10) – [SII]λ6716/[SII]λ6731 line flux ratios; Column (11) – electron densities (in cm^{-3}) derived from the [SII] ratios given in Column (10), with their 1σ uncertainties. Throughout our analysis, we adopt the cosmology H_0 =70 km s^{-1} Mpc^{-3}, Ω_Λ = 0.7 and Ω_M = 0.3.

Chapter 6

On the self-regulation of intense star-formation in galaxies at z=1-3

Le Tiran, L., Lehnert, M. D., Di Matteo, P., Nesvadba, N. P. H. & van Driel, W.
To be submitted in *Astronomy and Astrophysics*.

Abstract: We have analyzed the properties of the Hα and [NII]λ6583 rest-frame optical emission lines of a sample of 53 galaxies observed with SINFONI on the ESO-VLT. Our sample spans the redshift range z=1.3 to 2.7. All are intensely star-forming galaxies. We find that the large line velocity dispersions observed compared to nearby disk galaxies (few 10-250 km s^{-1} compared to $\sim$10 km s^{-1}) are most likely driven by the intense star-formation taking place within these galaxies. We reach this conclusion by comparing our data with those of simulations where we have applied a scaling relation of the form: velocity dispersion is proportional to the square root of the star-formation intensity (star-formation rate per unit surface area). We find good agreement between the observations and beam-smeared models with this underlying relationship between line dispersion and star-formation intensity. Furthermore, we generally show that the observed large line widths are largely driven by a selection effect whereby galaxies must have high enough average Hα surface brightness to be spatially resolved with SINFONI in a few hour exposure time. However, due to the relative decrease in cosmological dimming at z<2, for the more nearby galaxies in our sample the surface brightness requirement is relaxed such that we may be beginning to observe objects where the star-formation intensity may not be the predominate driver of the line dispersions. To explain the high surface brightness and line ratios, high thermal pressures in the warm ionized medium are required (P/k$\gtrsim$10^6–10^7 K cm^{-3}). Additionally, using mass surface density estimates from the literature we find roughly the same values for the hydrostatic pressure, the turbulent pressure in the warm ionized medium and the pressure generated by the mechanical energy output of massive stars. We make several arguments that the star-formation in these galaxies is self-regulated, due to star-formation controlling the overall average pressure in the ISM. This regulation of the pressure allows the galaxies to be unstable against star-formation (Toomre Q parameter $\sim$1) and is crucial for maintaining the intense star-formation we observe. Furthermore, this line of reasoning allows us

to predict the observed upper-envelope of the "star-formation rate-mass relationship" for galaxies at z∼1 and 2 based on a simple scaling of the properties of the ISM in nearby galaxies and reasonable values for the characteristics surface densities and gas fractions of galaxies at z∼1–3. Our results further emphasize the importance of star-formation feedback and self-regulation in the early Universe.

Contents

6.1 Introduction

Galaxies exhibit a wide range of phenomena some of which are apparently more important in the distant Universe than today. The global co-moving star-formation rate was higher by an order of magnitude (Madau et al., 1996), and so were the specific star-formation rates. Morphologies were increasingly irregular, an observation that cannot be explained with extinction alone (Conselice et al., 2008). Processes like starburst-driven outflows are obvious and ubiquitous in samples of high redshift galaxies (e.g., Shapley et al., 2003; Steidel et al., 2010) compared to only a small fraction of galaxies today (Lehnert & Heckman, 1996a), and the AGN fraction appears high (cf. 1% in LBGs, versus <<1% locally) even in optically-selected samples. The merger rate is also likely to be much higher (de Ravel et al., 2009). While the gas infall rates of nearby galaxies are apparently low, they were likely much higher in the early Universe (Croton et al., 2006). While today, the Universe could be considered in the "age of secular evolution", beyond about 8 Gyrs ago it was in the "age of feedback and self-regulation". It is the mix of physical processes that shaped the characteristics of the ensemble of galaxies we observe today and their early evolution.

Understanding this complexity and relative contribution from all of the physical processes that were likely significant in the shaping of distant galaxies is required before we can consider our understanding of galaxies in any sense complete. With the higher "activity levels" of galaxies at z~1-5 relative to the universe today, it is difficult to gauge the importance of each process by mere analogy. On the contrary, it can only be gained through careful, direct observations of distant galaxies.

A significant worry in this pursuit is that getting detailed spatial information from distant galaxies – as is required to probe the myriad of processes that may drive galaxy evolution – is hampered by the large impact of surface brightness dimming. Unfortunately, this limitation implies that only the highest surface brightness galaxies can be observed in their rest-frame UV or optical emission line gas. This then biases the samples where we can detect the spatially extended emission line gas to galaxies which have intense star-formation over many 10s of kpc^2 or extended emission line regions excited by powerful active galactic nuclei (e.g., Nesvadba et al., 2006b, 2008b). Of course the exact intensity or AGN luminosity necessary to excite large high-surface brightness nebulae will depend on the properties of the surrounding gas (e.g. higher density gas, for the equivalent excitation, will be brighter).

There is a significant controversy concerning the source of turbulence in distant galaxies that have been observed with integral field unit spectrographs, which mirrors well the discussion on explaining the amount of turbulence observed in the Milky Way and nearby galaxies. Simply put, it is a debate on whether the turbulent cascade is primarily driven by gravitational instabilities/perturbations/collapse,

self-gravity/cloud collapse and fluid instabilities, perhaps driven or aided by cosmological gas accretion (Brooks et al., 2009; Kereš et al., 2009; Dekel et al., 2009; Elmegreen & Burkert, 2010) or by energy injection from young stars (e.g., Elmegreen et al., 2004; Cox, 2005; Ferrara, 1993; Norman & Ferrara, 1996). Both of these general processes must contribute to the overall turbulence of the ISM, but which is most important is a function of the rate of energy injection, over what scales it is injected, and how rapidly the energy cascades and dissipates in various phases and over what time and size scales. Given this complexity, it is often not obvious which processes dominate (e.g., Elmegreen et al., 2004).

In our previous work (Chapter 3, Lehnert et al. (2009)), we suggested that the energy input from massive stars was sufficient to power the dynamics of intensely star-forming galaxies at high redshift – in particular line widths, which are likely representative of both bulk and turbulent motions in the ISM. This leads to a simple (perhaps unrealistically so) relation between optical emission line velocity dispersion, σ, and the star-formation rate intensity (star-formation rate per unit area, $\Sigma_{\rm SFR}$) of $\sigma \propto \Sigma^{0.5}$. This work has been criticized by a number of authors (e.g., Krumholz & Dekel, 2010; Burkert et al., 2010). Krumholz & Dekel (2010) suggest that this relationship can be "prosaically" explained by the Toomre stability criteria. Specifically, they state that the requirement for a Toomre parameter Q$\sim$1 for gas disks to be unstable against star-formation leads to a relationship of the type observed ($\sigma \propto \Sigma_{\rm SFR}^{0.6-0.7}$), after translating the mass surface density into a star-formation rate intensity via the Schmidt-Kennicutt relation). Although this relation is, given the uncertainties, consistent with the observations of Lehnert et al. (2009), adopting this relationship does not constrain the source of energy powering line width we observe in the Hα emitting gas.

Burkert et al. (2010) go further in this argument, and argue that disks must stay close to the gravitational stability line. They suggest that gravitational instabilities will generate density and velocity irregularities which drive turbulence and heats the gaseous disk. The process will saturate only close to the instability line and thus gravitational forcing is sufficient to explain the highly turbulent gas seen is high Hα surface brightness distant galaxies. However, that can only be true if the instability growth and heating rate is higher than the turbulent dissipation time scale. Since the dispersions observed in distant galaxies are so high, the gas will dissipate energy very quickly. It is hard to see how such an equilibrium will be reached through gravity alone. Moreover, if the dissipation rate of the turbulent cascade is higher than the gravitational heating rate, stars will form out of (some) of the dense gas, which will further remove gravitational energy. How then is this cycle sustained, given it is unlikely that we are observing these galaxies at the end of their intense star-formation (Erb et al., 2006c).

Furthermore, there are several other limitations in using this type of general explanation for the dispersions measured in the optical emission line gas of star-

forming galaxies at z=1-3. Although the Toomre criterion is appropriate for disk galaxies, ordinary rotating disks do not make up a majority of distant galaxies with high emission line surface brightnesses (Förster Schreiber et al., 2006; Law et al., 2007, 2009; Wright et al., 2009b; Epinat et al., 2010; Lemoine-Busserolle et al., 2010). But perhaps more importantly, it appears that gravitationally driven processes appear incapable of producing even the relatively modest dispersions observed in the warm neutral and ionized media in nearby galaxies (Tamburro et al., 2009; Leroy et al., 2008). In fact, it appears that the energy injection from supernovae and stellar winds is a more likely process, given the correlation between star-formation rate and observed velocity dispersions in HI (Tamburro et al., 2009) and the decrease in CO line dispersion with radius in some nearby galaxies (Wilson et al., 2011). In addition, the emission line velocity dispersion in the warm ionized medium is (at least partially) driven by star-formation in intensely star-forming galaxies in the nearby Universe (Basu-Zych et al., 2009; Gonçalves et al., 2010). The Toomre criterion only suggests that distant intensely star-forming galaxies are in a state where they can form stars intensely, but does not purport to explain the source of the turbulence.

Despite these caveats, it is interesting to interpret this relationship between dispersion and Σ_{SFR} within the context of the Toomre criterion, which has been suggested by many studies to play a role in understanding large scale star-formation, and likely to be of use in explaining why stars form so intensely (Leroy et al., 2008, and references therein). The fact that galaxies with high optical emission line surface brightness at high redshift may lie near the line of Toomre stability can be interpreted in another way, through star-formation that is self-regulating (and not for the first time; Silk, 1997, 2001, 2003; Silk & Norman, 2009). In other words, it could be that star-formation is driving the turbulence to a level at which it can be self-sustaining until the gas has decreased so much in surface density that it is no longer unstable against star-formation and the intensity of star-formation declines. This is the point of the current chapter – we discuss the possibility that star-formation in these high surface brightness galaxies is near the gravitational stability line because star-formation is self-regulating. We will show that the data are consistent with $\sigma \propto \Sigma_{SFR}^{0.5}$ and that the dispersions can be explained by the mechanical energy liberated by star-formation. However, it is also plausible that there is a balance between energy injection and shutting down star-formation, and it is this balance that allows both interpretations to be (approximately) correct.

The chapter is organized as follows: § 7.2 we limit our discussion to the characteristics of the sources and their general properties as seen in the SINFONI integral field unit (IFU) data. In § 6.3 we focus on the role that the surface brightness detection limits and cosmological surface brightness dimming play in limiting the overall dynamic range of the data and in requiring these galaxies (or basically any galaxy observed with IFU data which is spatially resolved) to have high – simi-

lar to nearby intense starbursts – surface brightnesses in their optical emission line gas. In § 6.4 we conduct a thorough analysis of beam smearing to investigate how robustly the velocity dispersion distribution of the spatially resolved IFU data can be recovered. We accomplish this by making an artificial data cube of a numerical simulation of disk galaxies including the effect of seeing, spectral resolution, and limited signal-to-noise as we have in our galaxy data. In § 6.5 we discuss the implications of our results of galaxy evolution and the nature of distant galaxies – particularly the so-called stellar mass-star-formation rate relation.

Throughout the chapter we adopt a flat H_0 =70 km s^{-1} Mpc^{-3} cosmology with $\Omega_\Lambda = 0.7$ and $\Omega_M = 0.3$.

6.2 Source characteristics

The sample of more than 50 galaxies was observed with SINFONI on the ESO-VLT. They span a redshift range of z= 1.3-2.7 (Fig 6.1). The data comes from a variety of programs in the ESO archives and the selection of the galaxies is very inhomogeneous. Basically, for the purposes of this chapter, we are not interested in how they were selected as this is not a population study. We focus here on the emission line properties of galaxies that are spatially resolved in SINFONI observations. The key to the sample is that all have sufficiently high Hα surface brightness to obtain spatially resolved line maps in a few hours integration time (which is typical for SINFONI observations of distant galaxies). Because of this necessity, our results are only applicable to galaxies with intense star-formation intensity (star-formation rate per unit area). This introduces strong biases as it necessitates a process that drives intense star-formation to 100 Myrs or more (Erb et al., 2006c). The properties of the 53 galaxies, including the integration times, are presented in Table 2.1 and 2.2. Details of the observations have been presented in various papers on the galaxies in this sample (see for example, Lehnert et al., 2009; Förster Schreiber et al., 2006, 2009, for summaries of the observations of the sources;).

The observations reach surface brightness detection limits in Hα of $\sim 2\times10^{-19}$ erg s^{-1} cm^{-2} pixel^{-1} (for the 125 mas pixel^{-1} scale and averaged over 3×3 pixels; "mas" is milliarcseconds). The spectral resolution is FWHM$\sim$115 and $\sim$150 km s^{-1} in the K and H bands, respectively. The observed surface brightnesses range from about 3.6-34 $\times$ 10^{-18} erg cm^{-2} s^{-1} arcsec^{-2} and the objects have isophotal radii, down to their surface brightness detection limits, of 1-2 arcsec^2, or on average $\sim$7±2 kpc (corresponding to an isophotal area of $\sim$150±15 kpc^2). . The point-spread function FWHM of the data is $\sim$0$''$.6, which at z=2 represents an area of $\sim$20 kpc^2, so we have generally $\sim$8 spatial resolution elements per object. With such low spatial resolution, it is necessary to discuss the impact of beam smearing on

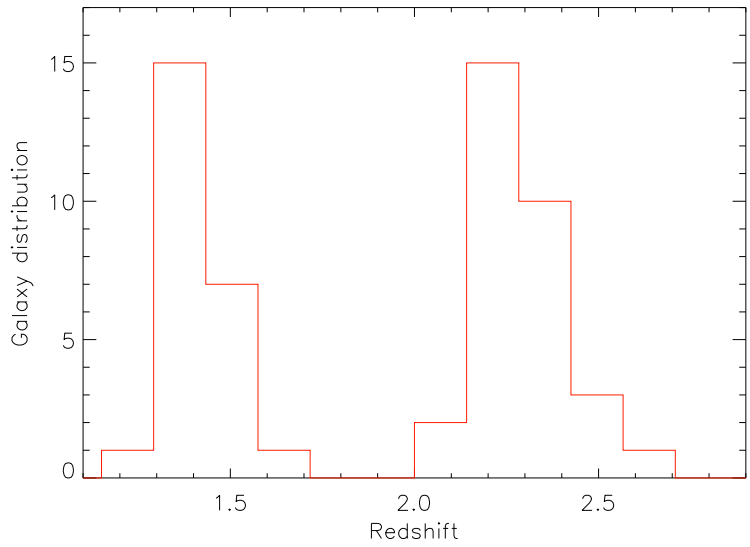

Figure 6.1 Redshift distribution of our sample of galaxies. The two groups of redshifts (z<1.8 and z>2) are due to atmospheric transmission and the limited wavelength coverage of the H-band and K-band. These limit the observable redshift range of the Hα and [NII]λ6583 lines.

the characteristics of our data (discussed in detail in § 6.4). In the present analysis, we will formally define the isophotal radius, r_{iso}, as $r_{iso} = (\pi\ A_{iso})^{1/2}$, where A_{iso} is the isophotal area, i.e. the total area of all pixels above the 3-σ surface brightness limit of the data (Table 2.2).

The total Hα luminosities of all galaxies in our sample are above 10^{41} erg s^{-1} but are mostly above about 10^{42} erg s^{-1}. Hα luminosities in this range imply an average star-formation rate of ~70 $M_\odot$ yr^{-1}. However, as these are not corrected for extinction our estimates are lower limits. For a sub-sample of these galaxies we have Hβ estimates, and the line ratios of Hα to Hβ suggest relatively modest extinction corrections to the star-formation rates, of a factor of few (Lehnert et al., 2009).

6.3 Surface brightness limits and selection effects

Due to cosmological surface brightness dimming, over the redshift range of a factor ~2 in our sample there is about a factor of 5 difference in the faintest rest-frame line emission surface brightness levels that can be probed, whereas the physical dimensions in the rest frame, i.e., length per arcsec, changes by only about 5%. Given this strong impact of cosmological surface brightness dimming, it is worth

repeating the conclusion from Lehnert et al. (2009) that even the lowest redshift sources in our SINFONI sample are extreme compared to galaxies in the local volume, where only most intense starbursts have such high Hα surface brightness, and this on smaller physical scales only.

The total range of surface brightness probed by the SINFONI observations of our ensemble of galaxies is ≈20 (Fig. 6.2). To investigate the dependence of this range on galaxy size, we divided our galaxies into 4 equally large bins based on their estimated isophotal areas (Fig. 6.3). For the 3 bins with the largest average isophotal sizes, the observed dynamic range in surface brightness is ≈20. However, for the apparently small galaxies, the dynamic range of the observations is only about a factor of 3. The relationship between surface brightnesses and projected distance is the same for all bins, indicating that their individual declines in surface brightness follow the same trend. The observations imply two things. The observations imply two things. First, although the effects of beam smearing cannot be ignored, as we will discuss extensively in the next sections, it does not dominate the overall distribution of the surface brightness (i.e., the distribution does not simply represent the PSF of the observations). Secondly, it implies that the reason the apparently small galaxies appear small is that the dynamic range of the observations is too low to detect their extended emission. As noted above, this is not due to the physical scale of the galaxies changing across our redshift range, as this effect amounts to only ∼5%. While we do not show it here, there is a crude trend for the galaxies with the highest total Hα fluxes to also have the largest isophotal sizes. Again, this suggests that we are limited by the overall dynamic range of the data and by the impact of surface brightness dimming, but not by differences in the scale sizes of the galaxies (Fig. 6.4). This is an important point to bear in mind when reading this manuscript.

Furthermore, if the trends in surface brightness and total Hα luminosity were dominated by cosmological surface brightness dimming, which is proportional to $(1+z)^4$, we would expect our data to show a slope of about 4 in a plot of the logarithmic relation between Hα luminosity and isophotal area. Indeed, we find such a trend in our data (Fig. 6.4). The range in surface brightness detection limits in our data trace out the ranges in size and luminosity we observe in our sample of galaxies. In addition, this confirms what we have already shown previously, that at the high redshift end of our sample the intrinsic surface brightnesses are very high and that they generally decline with redshift.

6.4 Analysis of the effect of beam smearing

In Lehnert et al. (2009), we proposed that the velocity dispersions of the high surface brightness Hα emitting galaxies observed with SINFONI (and other near-

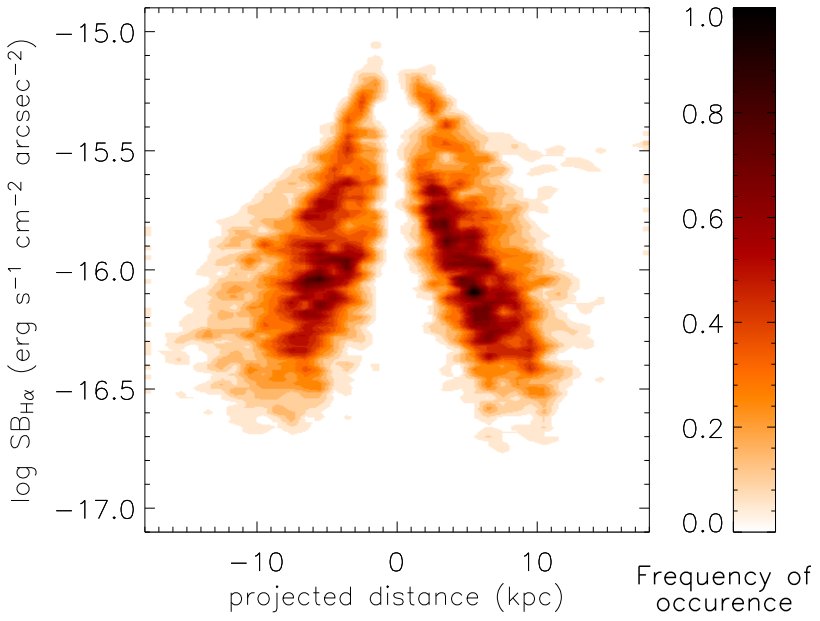

Figure 6.2 A 2-dimensional histogram of the frequency of occurrence of pixel values of Hα surface brightness versus the projected physical distance for the entire sample. As shown in the color bar, the darkest regions have the highest frequency of occurrence. The surface brightness has not been corrected for cosmological dimming. The zero radius was chosen to be the symmetry point in either the Hα velocity field or of 3-σ isophotes in the Hα surface brightness map.

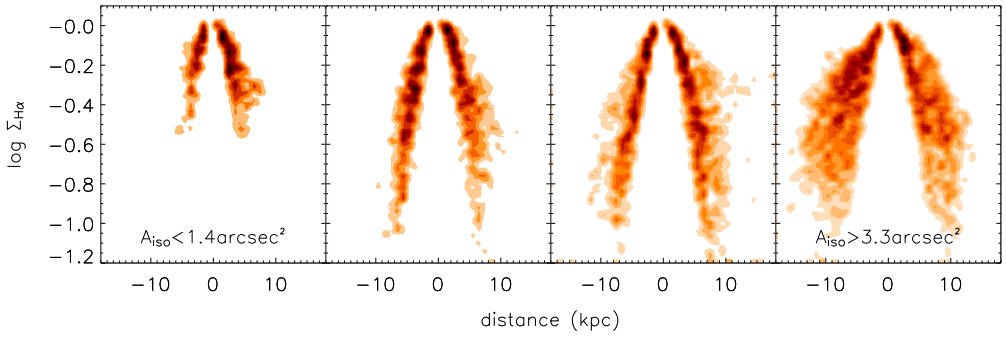

Figure 6.3 Two-dimensional histograms of the relative frequency of occurrence of normalized Hα surface brightness values versus radius for galaxies in 4 equal-size bins selected on their isophotal area (A_{iso}). The relative frequency of occurrence is scaled in the same way as in Fig. 6.2. We have normalized the distribution by setting to zero the level of the most intense emission region in each galaxy. From left to right, each panel represents an increasing angular size (i.e., $A_{iso} < 1.4$ arcsec^2, 1.4 arcsec^2 $\geq A_{iso} < 2.5$ arcsec^2, 2.5 arcsec^2 $\geq A_{iso} < 3.4$ arcsec^2 and A_{iso} ≥ 3.3 arcsec^2). The values of r_{iso}, which is derived from A_{iso}, for individual galaxies are given in Table 2.2. The galaxies with the lower dynamic range in the data are also smaller in isophotal size.

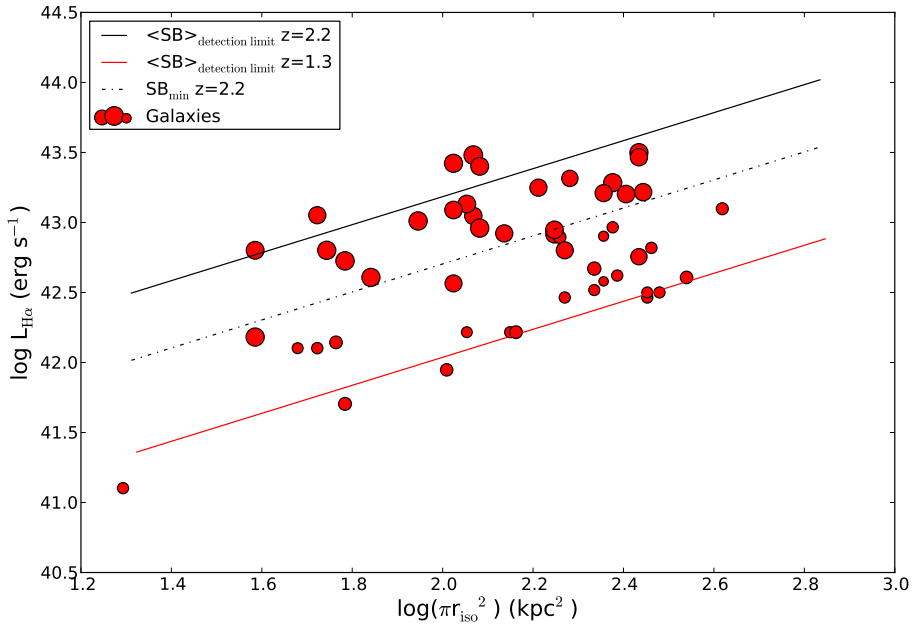

Figure 6.4 Plot of Hα luminosities versus isophotal area for the galaxies in our sample (red circles). The size of the circle is proportional to the redshift of the galaxy, with larger circles denoting higher redshifts (range in z is 1.3 to 2.7). The two solid lines show the relationship between the luminosity and area for the average surface brightness detection level of galaxies, 1.1×10^{-17} erg s^{-1} cm^{-2} arcsec^{-2} (black for galaxies at z=2.2 and red for z=1.3, respectively). The dot-dashed line shows the relationship for the minimum surface brightness detection limit of 3.6×10^{-18} erg s^{-1} cm^{-2} arcsec^{-2} for all galaxies with z$\approx$2.2. See Table 2.2 for the Hα luminosities, isophotal radii and surface brightness detection limits.

infrared integral field units) that yielded spatially resolved emission line data, could be explained by the mechanical output of young stellar populations within those galaxies. In fact, we framed the argument in the context of an overly simplified energy injection model of the form, $\sigma = \varepsilon \Sigma_{\rm SFR}^{1/2}$, where σ is the velocity dispersion of Hα, ε is the coupling efficiency of the mechanical energy output to the interstellar medium and $\Sigma_{\rm SFR}$ is the star-formation intensity. The energy due to the young stars is given for population synthesis models (Leitherer et al., 1999). Using scaling relations based on models and observations of nearby galaxies, we were able to explain the trends between dispersion and star-formation intensity with no free parameters (see Lehnert et al., 2009, for details of the scalings used in this analysis).

However, the limited spatial resolution of integral field spectroscopy of redshift 2 galaxies causes an artificial broadening of the emission lines due to large-scale kinematics, which can cause a significant radial velocity gradient across each pixel. While we argued that this would not have an important impact on our results in Lehnert et al. (2009) based on some simple modeling, we now feel it is important to revisit this issue in a more complete and detailed way.

6.4.1 Constructing artificial IFU observations

In order to study the effect of beam smearing, we made a simulation of isolated galaxies using a tree-SPH code (see Semelin & Combes, 2002; Di Matteo et al., 2009; Chilingarian et al., 2010, for a description). This model has a high gas fraction (50%) and galaxies were evolved in isolation, without companions or tidal interactions (Qu et al., 2011). We allowed the disk to go unstable against star-formation and it developed a "clumpy" morphology which evolved with time(see Di Matteo et al., 2008, for details of the initial conditions and evolution of the simulation). As the simulated galaxies have a ~15 kpc diameter, which is small compared to what we observe, we artificially increased their size by taking a sampling that was physically lower than our observations but gave a number of resolution elements consistent with our data. From these simulations we produce maps of the star-formation rate surface density, radial velocity field and velocity dispersion (Fig. 6.5). The simulations were viewed at an inclination angle of 45° and given a flat rotation curve with a projected amplitude of 110 km s^{-1}, a value derived from the average intrinsic full width at half maximum of the integrated spectra of our sample. This implies a rotation speed of about 160 km s^{-1}. Intrinsically, our simulations show low gas velocity dispersions, of-order 10 km s^{-1} (or less), which are roughly constant with radius. In Lehnert et al. 2009 we also proposed that the dispersion is proportional to the star-formation intensity. When making our artificial data cubes we include these two relationships for the intrinsic velocity dispersions of the warm ionized gas.

We then degraded the resolution of these simulations to produce synthetic ob-

servations similar to what we observed with SINFONI. We adopted a single redshift (z=2) for determining the scalings in the synthetic observations – the exact redshift chosen does not matter much as the physical scale per angular projected size (kpc/arcsec) changes little (~5%) over the redshift range of our sources. We also took into account the instrumental spectral resolution, the seeing using a FWHM for the PSF of 0.6″(and conducted experiments with the AO resolution of 0.2″) and added an amount of noise to the synthetic data consistent with the observations. The artificial datacubes created in this way were then analyzed using the same procedures as the real SINFONI observations.

In the following analysis, we will focus on the impact of beam smearing on the interpretation of the underlying cause of the high dispersion observed in distant galaxies with spatially-resolved line emission observations.

For our analysis of the effects of beam smearing, we make a comparison between the analogs produced using two sets of scaling relations for the velocity dispersions: (1) the dispersions taken directly from the simulation, $\sigma_{\rm sim}$, and (2) a function of the star formation rate surface density $\sigma = 140\sqrt{\Sigma_{\rm SFR}}$ – see Lehnert et al. (2009) for details concerning these scalings. The resulting Hα flux and kinematics maps made with our artificial SINFONI data sets and applying these two different types of dispersion show, as expected, that the surface brightness distribution is now smoother than in the original simulation (Fig. 6.6).

6.4.2 Effect of beam smearing on the star-formation intensities

The star-formation intensities – the star-formation rate per unit area – are related to the Hα surface brightness by a simple scaling (e.g. Kennicutt, 1998a).

The areas of intrinsically high star formation intensity – the star-formation rate per unit area – are blended after smearing the data, lowering their intensities (Fig. 6.6). Whether or not such peaks in the star-formation intensity can be observed in principle depends on their relative distribution and peak intensity relative to their surroundings within one or two PSFs (cf. Figs. 6.5 and 6.6). However, Fig. 6.7 demonstrates that, after smearing, the simulated final radial distribution of surface brightness is consistent with what we observe. The similarity seen does not depend on the assumed underlying velocity dispersion distribution in the construction of the synthetic data.

The star-formation intensities decline by $\lesssim$25% after beam smearing. While the precise value of this decrease is likely to depend on the initial spatial distribution of the surface brightness, it is always going to be small. The total star-formation rate, which in the simulations is typically about 60 $M_\odot$ yr^{-1}, remains essentially unchanged after making an artificial SINFONI data set. The largest impact of smearing is on the distribution of the star-formation intensities and in losing the lowest surface brightness emission because of noise and the relatively low dynamic

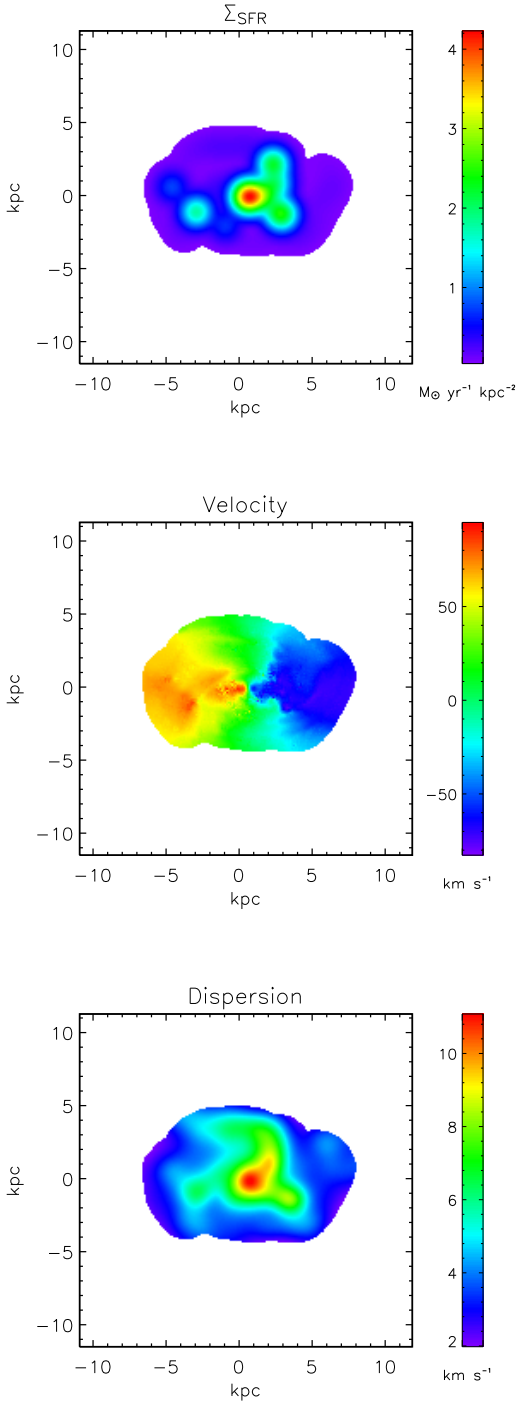

Figure 6.5 Output from the simulations of a star-forming disk galaxy at z=2 before they were beam smeared. Shown are the distribution of the star-formation rate surface density (top panel), Hα velocity field (center panel) and Hα dispersion map (bottom panel). The galaxy is projected at an inclination angle of 45° relative to face-on. The scale on the axes is in kpc and the kinematic axis is horizontal.

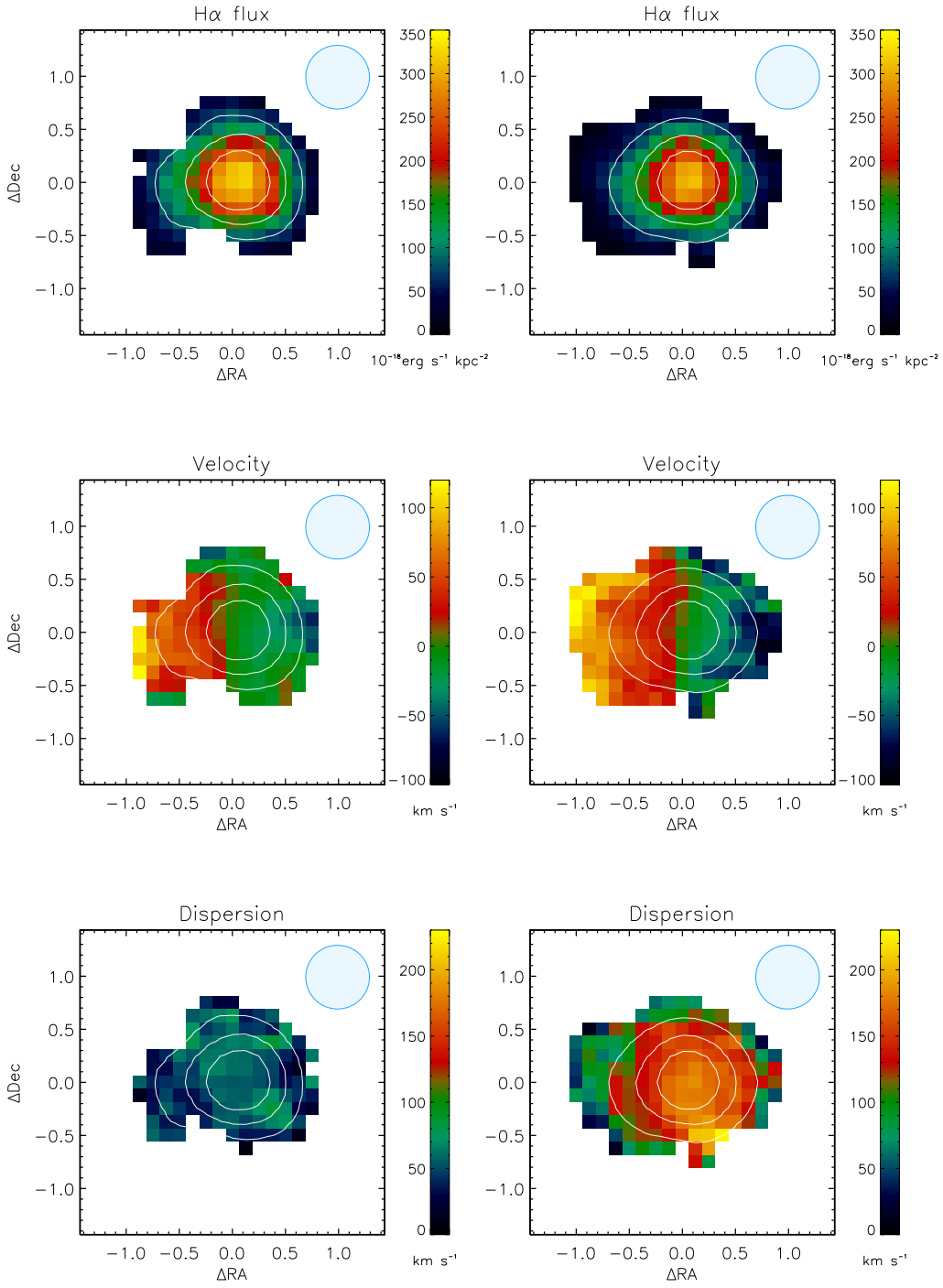

Figure 6.6 Simulated data sets of a star-forming disk galaxy at z=2 after beam smearing using different relationships for the velocity dispersions. Shown are the distribution of the Hα surface brightness (top), velocity field (center) and velocity dispersion map (bottom). In the left column, we have simply taken the velocity dispersions as estimated from the N-body/SPH simulation, while for the right column we assumed a relationship between the velocity dispersion and star-formation intensity of the form $\sigma = 140\ \sqrt{\Sigma_{\rm SFR}}$. The circle in the upper right of each plot represents the FWHM of the PSF used to make the artificial data set. The scales are in arc seconds. We have scaled the images such that the sizes of these panels and those in Fig. 6.5 are similar, for ease of direct comparison.

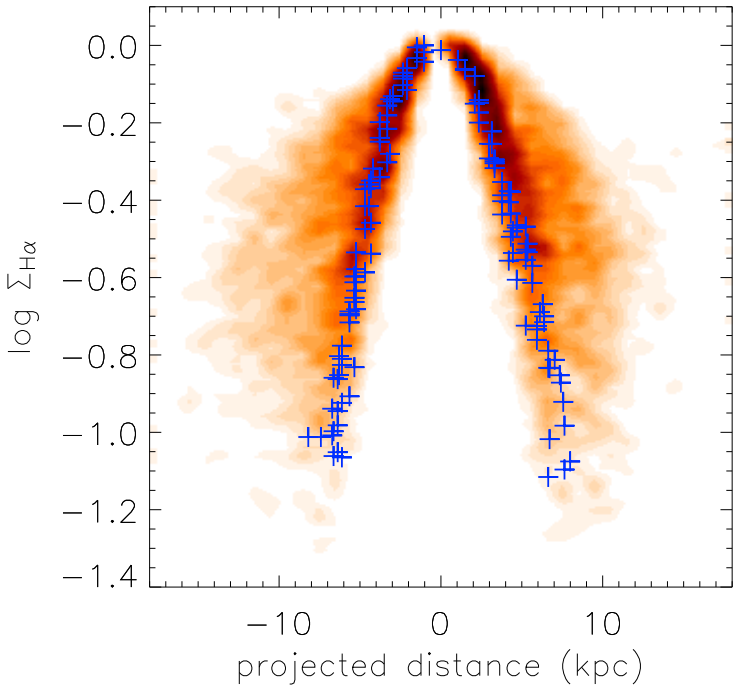

Figure 6.7 Comparison of the normalized per pixel Hα surface brightness distributions of the whole sample of galaxies (in shades of red) with superimposed an artificial SINFONI data set constructed from a N-body/SPH simulation (blue crosses). Both observations and simulation follow similar distributions.

range of the data.

6.4.3 Effect of beam smearing on velocity dispersions

Since we have assumed two relationships between velocity dispersions and star-formation intensity, it is in the resulting velocity dispersions that we see the most dramatic differences. In the model with $\sigma_{\rm sim}$, the dispersion is low (a few to 10 km s^{-1}) and almost constant as a function of radius and star-formation intensity (Fig. 6.8, left panel). In the synthetic observations however, the beam smearing (FWHM 0$''$.6) and low velocity? resolution of the data broadens all lines by about ∼40 km s^{-1} and the noise in the data increases the scatter about this mean increase. Even though we correct for the intrinsic resolution of the spectrograph, at relatively low S/N we tend to over-estimate the widths of lines that are only marginally resolved. Our results suggest that for galaxies with roughly constant and low dispersions, a spectrograph like SINFONI will tend to over-estimate the intrinsic widths of the lines but still produce a roughly constant trend of dispersion

with star-formation intensity.

For the model where the simulation dispersions are scaled to $\sigma = 140 \sqrt{\Sigma_{\rm SFR}}$, there are almost no differences between the mean velocity dispersions from the simulation itself and the the artificial data sets (Fig. 6.8, right panel). For this model, because of its large range of velocity dispersions, there is little effect of beam smearing on the average velocity dispersion. Looking at the pixel-by-pixel quantities, we obviously lose the relatively rare regions and peaks with the highest velocity dispersions (over 200 km s^{-1}). However, as suggested by the average and intrinsic dispersions, the decrease in the values (ranges and averages) is not large, even after the smoothing to low spatial and relatively low spectral resolution. Again, because of the loss of the lowest surface brightness regions, we also tend to lose information on the areas with the lowest velocity dispersions. However, in spite of all of this, the general trend for increasing star-formation intensity to result in increasing dispersion is maintained.

6.4.4 Other dependencies

We also varied the noise and increased the rotation speed of the simulated galaxy. The results did not quantitatively change, but can affect, the intrinsic scatter in the star-formation intensity-dispersion plane.

6.5 Discussion

6.5.1 Are the dispersions related to star-formation intensity?

We now compare the observed trend between star formation surface density and Hα line velocity dispersion with the models we used to make synthetic data sets, including the effects of beam smearing. For this purpose, we constructed 2-dimensional histograms which show the frequency of occurrence of each pair of Hα line width and star-formation rate surface density values in all pixels of our data set, after smearing to the spatial and spectral resolution of the real SINFONI observations. This is a cleaner way of visualizing the relationship than showing all single pixels and emphasizes the continuity of the data. Fig. 6.9 shows that the values of the simulated Hα line dispersion $\sigma_{\rm sim}$ are too low to explain the high values of the linewidths we generally observe in our sample of galaxies. On the other hand, models using the relationship, $\sigma \propto \sqrt{\Sigma_{\rm SFR}}$, are a good match to the overall distribution of the data (Fig. 6.9).

Figure 6.10 displays the differences in the Hα velocity vs SFR surface density distribution for the galaxies in two different redshift regimes, z<1.8 and z>2. The key result is that for both sub-samples the data are consistent with a simple scaling

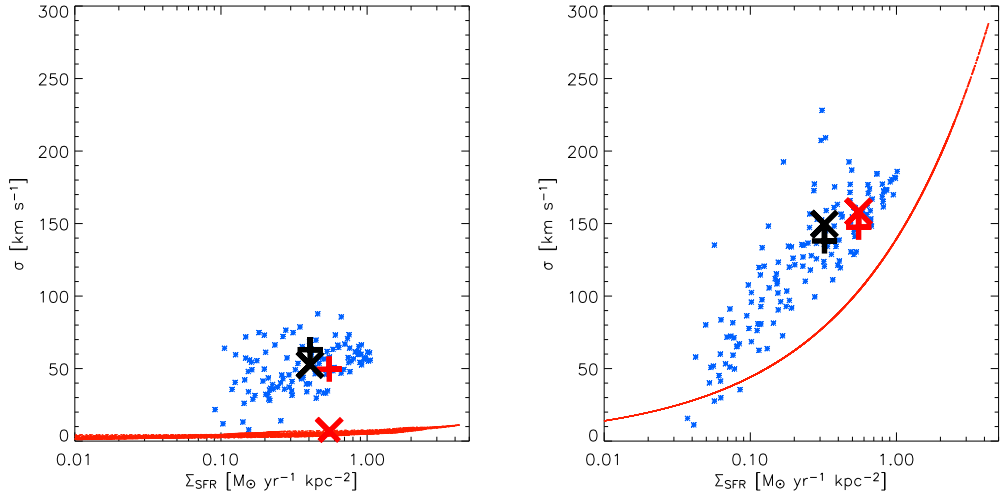

Figure 6.8 In our analysis of the impact of beam smearing on the velocity dispersion and star-formation intensity, we adopted two relationships between these two quantities. One taken directly from the simulations (*left panel*), and another where we assumed $\sigma \propto \Sigma_{\rm SFR}^{1/2}$ (*right panel*). The model velocity dispersions are shown in red (these are not lines but many individual points). We also show the points (blue) after analyzing the artificial data cubes derived from the simulation which include the effects of beam smearing. The red + (red $\times$) sign indicate the mean star-formation intensity and integrated (original input) velocity dispersion for the intrinsic relation between velocity dispersion and star-formation intensity, while the black + (black $\times$) sign has the same meaning but now for the beam smeared relationship.

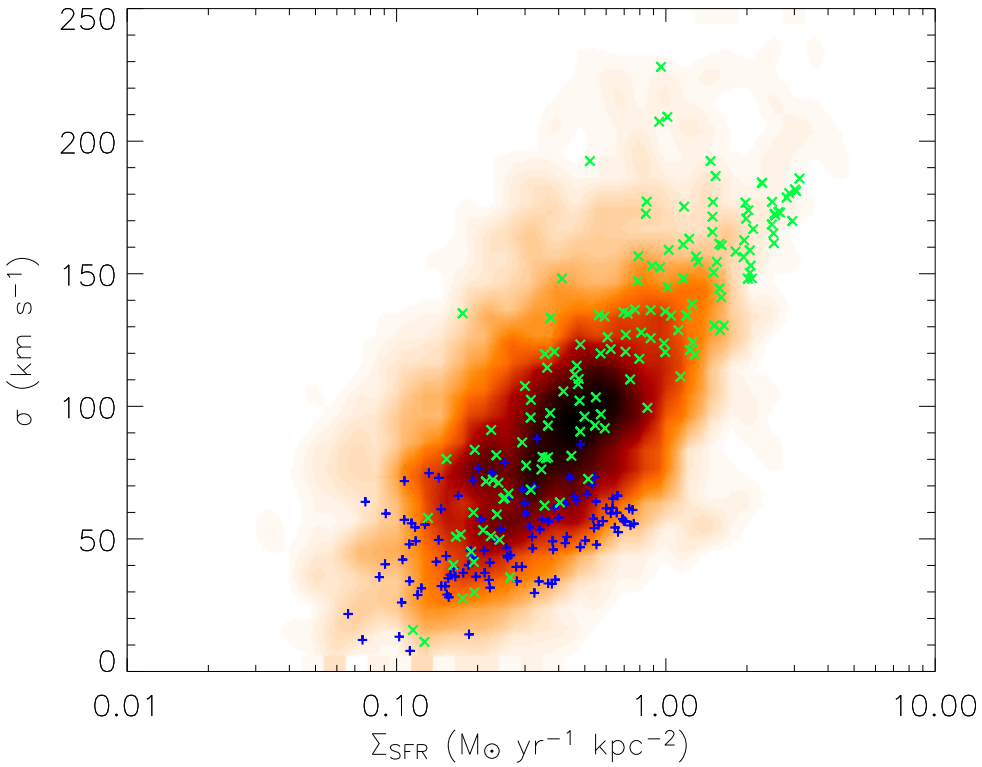

Figure 6.9 Normalized 2-dimensional histogram of the frequency of occurrence in the data set of Hα line widths as function of star formation rate surface density. The set of points for each galaxy are normalized such that all of the galaxies have the same mean star-formation rate intensity (their distribution of velocity dispersion of each galaxy is unaffected). The mean value was chosen to match the mean value of the star-formation intensity in the model $\sigma = \varepsilon \sqrt{\Sigma_{\rm SFR}}$ as indicated by the red + sign in the right panel of Fig. 6.8 (~0.5 $M_\odot$ yr^{-1} kpc^{-2}). As in Fig. 6.2, the darkest regions represent the highest frequency of occurrence in the data set. The green $\times$ and red + symbols represent our simulated data after beam smearing, assuming that the two quantities plotted are related as $\sigma = \varepsilon \sqrt{\Sigma_{\rm SFR}}$ and σ=$\sigma_{\rm sim}$, respectively.

between dispersion and star-formation intensity but that the low redshift galaxies appear to have on average lower dispersions and star-formation intensities. Also, the scatter is larger for the lower redshift galaxies, which perhaps indicates that a single relationship of the type $\sigma = 140\sqrt{\Sigma_{\rm SFR}}$ does not explain all of the trends in the data as well as it does for the higher redshift objects.

At the low end of the star-formation intensity within individual galaxies and over the ensemble of galaxies with lower average star-formation intensities, it is likely that we are over-estimating the velocity dispersions, and it could be that the dispersions are becoming roughly constant with radius. We say this, because our artificial model-based data cubes suggest that dispersions smaller than ~40-50 km s^{-1} are consistent with $\lesssim$10 km s^{-1}, a level at which we simply can no longer differentiate between a model where the line widths are proportional to $\sqrt{\Sigma_{\rm SFR}}$ or one where the line widths are consistent with what is observed in the MW and other nearby galaxies (see, e.g., Wada et al., 2002; Dib et al., 2006; Agertz et al., 2009).

6.5.2 The equivalence of integrated and spatially resolved measurements

So far, we have studied the spatially resolved relationship between the Hα velocity dispersion and the star-formation intensity as probed by the Hα emission. In Le Tiran et al. (2011), we argued that the relationship between the integrated Hα luminosity (or equivalently the total star-formation rate) and surface brightness-weighted mean dispersion of whole galaxies reveals the same underlying physical mechanism as the spatially resolved measurements – namely, that the intense star-formation is responsible for the dynamics of the warm ionized medium as probed through the Hα recombination line (see also Green et al., 2010).

To further investigate this relationship, we have tested the idea that the intense star-formation in these galaxies can even explain the integrated measurements of the total star-formation rate and the integrated velocity dispersion. This is important: if we can show that also these integrated measurements reveal this underlying relationship, then a greater wealth of data become available for analysis, since slit spectra are more commonly available then integral field spectra.

For this analysis to be robust, we first note that we find little difference in velocity dispersion for whole galaxies if we simply sum up the Hα emission pixel-by-pixel and estimate their integrated dispersion or if we weigh each measurement by surface brightness (or signal-to-noise). The difference between both method is only about 15 km s^{-1}, where flux weighting tends to give a lower value and a scatter of about 15 km s^{-1}. So compared to the mean integrated velocity dispersion of our sample, this represents a systematic offset of about 10% (Le Tiran et al., 2011).

To further test the relevance of a relationship of the form, σ=$\varepsilon\Sigma_{\rm SFR}{}^{1/2}$, where ε is the efficiency at which the mechanical energy from a star-formation intensity

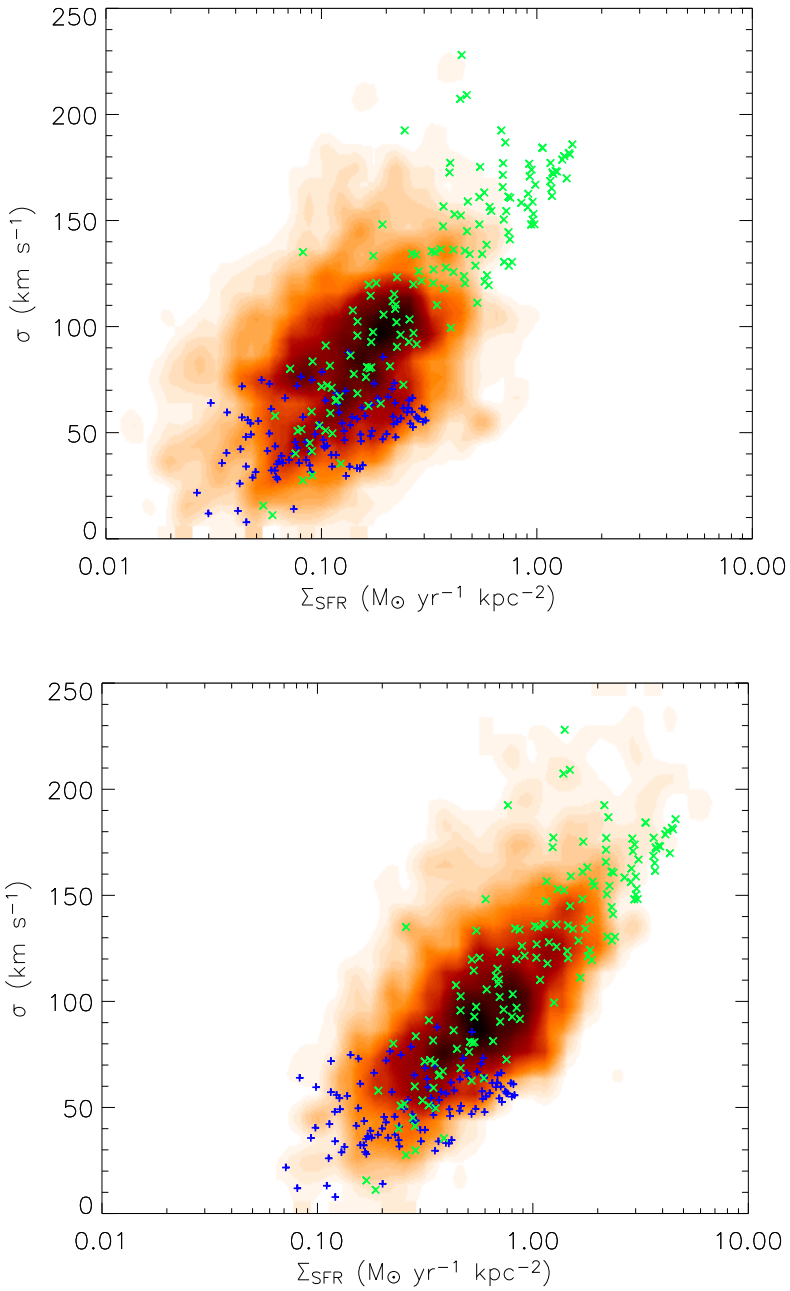

Figure 6.10 Plots of the normalized frequency of occurrence of Hα velocity dispersion versus star-formation intensity are similar to what was shown in Fig. 6.9 for the whole sample. However, here we have divided the sample into two redshift bins, galaxies with z<1.8 (*top*) and galaxies with z>2 (*bottom*). The normalizations are also different from that used in Fig. 6.9 and in the left and right panels. For the z<1.8 sample, the average star-formation intensities of each galaxy was shift to the average of the ensemble of galaxies with z<1.8 (0.16 $M_\odot$ yr^{-1} kpc^{-2}). Similarly, average star-formation intensity for galaxies in the z>2 sample were shifted to their ensemble average (0.73 $M_\odot$ yr^{-1} kpc^{-2}). Note that the two sub-samples tend to sample different ranges of both velocity dispersion and star-formation intensity. The model points shown in the green crosses and blue plus signs have been shifted to overlap with the data (the location of the modeled points along the axis of Σ_{SFR} is set by the coupling efficiency of the mechanical energy output of young stars to the ISM). Similar plots sorted in 6 different redshift bins are shown in Figure 6.17.

Σ_{SFR} is converted into turbulence and bulk flows in the interstellar medium, we applied it to the spatially resolved dispersion measurements, to estimate integrated quantities. Specifically, we used the spatially resolved, pixel-by-pixel Hα line velocity dispersion measurements to estimate the Hα surface brightness of each pixel. We then used these surface brightness estimates as weights when combining the individual pixel-by-pixel velocity dispersions, to estimate the integrated mean dispersion in Hα, $\sigma_{\rm mean}$. We summed these estimated surface brightness values to estimate the integrated Hα fluxes and then converted these to total luminosities using our adopted cosmology. The results of this analysis shows that we can reproduce the actual measurements quite well (Fig. 6.11). So not only does this simple scaling relationship reproduce the spatially resolved measurements, but it can also reproduce reasonably well the integrated measurements.

6.5.3 Densities and pressures in the ISM of distant galaxies

As discussed previously in Lehnert et al. (2009), lower [NII]λ6583/Hα line ratios correspond to higher Hα surface brightness levels. The emission line ratios and Hα surface brightnesses are related to the gas pressure, column density and radiation field present in the galaxy. The surface brightness is linearly proportional to the density and ionization parameter, while the line ratio depends on roughly one over the square root of the ionization parameter for the range of ionization necessary to explain the line ratios.

The new aspect we add to our previous analysis of this relationship is to expand it to the larger sample presented here which includes galaxies at lower redshift, which in turn allows us to probe pressures, column densities and radiation fields in galaxies with less extreme Hα surface brightnesses. Our expectation is that their ISM would also be less extreme (lower pressures and ionization rates). Using version 08.01 of the Cloudy code (Ferland et al., 1998), we ran a suite of models to show the relationship between the [NII]λ6583/Hα line ratio and the Hα surface brightness as a function of the hydrogen internal pressure, column density and ionization parameters (see Lehnert et al., 2009). Our objective is not an attempt to fit the data, but to examine the range of characteristics it may have.

As in some of the analyses we presented earlier, we noticed a difference in the region occupied in the [NII]λ6583/Hα versus Hα surface brightness plane between galaxies at z<1.8 and z>2. Over both redshift ranges, the span of [NII]/Hα and surface brightness can be explained by a combination of column density, volume densities and moderately diffuse radiation fields. The differences between the two redshift regimes is interesting. It appears that the relatively higher Hα surface brightnesses of the higher redshift (z>2) galaxies require somewhat higher gas densities, log n_H (cm^{-3}) = 2–3, for a column density of log N_H (cm^{-2}) = 21, and higher ionization parameters than the lower redshift sample. Such a high density and ion-

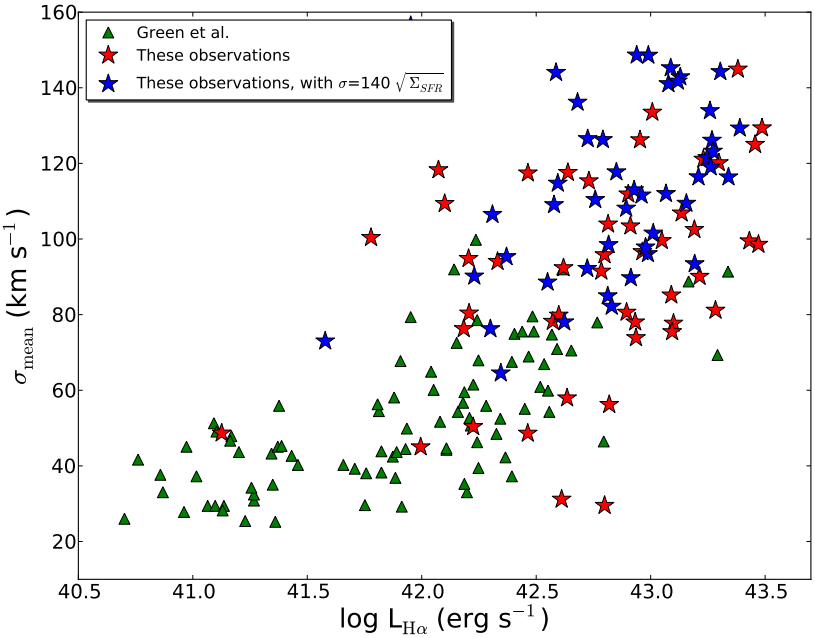

Figure 6.11 Mean Hα line velocity dispersion, $\sigma_{\rm mean}$ (in km s^{-1}), versus total Hα luminosity (in erg s^{-1}) for different samples of local and high redshift galaxies. Local galaxies (green triangles) are taken from Green et al. (2010) and the results for our sample are represented by red stars. The blue stars show the results where we assign to each pixel in a galaxy an Hα surface brightness based on the model relationship, $\sigma = 140\sqrt{\Sigma_{\rm SFR}}$ and use the observed local Hα velocity dispersion. We then estimate the total Hα luminosity by summing up the predicted pixel-by-pixel surface brightnesses. $\sigma_{\rm mean}$ is then estimated by weighting the pixel-by-pixel velocity dispersion measurements by the Hα surface brightnesses derived from the model.

ization rate implies that the ISM of these galaxies must in general exhibit high thermal pressures, P/k$\gtrsim 10^{6-7}$ K cm^{-3}. For the lower redshift sample, the properties are less extreme, and generally consistent with log n$_H$ (cm^{-3}) = 2 and ionization parameters that are about a factor of 10 lower. This suggests that thermal pressures in the lower redshift sources are about a factor of 10-100 lower compared to the more distant galaxies. We do not believe this to necessarily be an evolutionary effect, but rather a direct result of the fact that we can probe lower surface brightnesses (and hence lower pressures) at lower redshift. A complete census of both redshift regimes would be necessary to show that the average pressure in the warm ionized media of galaxies is declining with redshift.

These pressures are much higher than observed in the disk of our Milky Way or other nearby normal galaxies. The hydrostatic mid-plane pressure in the MW is about $10^{3.3-4.3}$ K cm^{-3}, while for other local spirals it can amount to about 10^6 K cm^{-3}, though it is typically about $10^{4.6}$ K cm^{-3} (Blitz & Rosolowsky, 2006, and references therein). In the nuclear regions of local starburst galaxies, thermal pressures are estimated to be typically about 10^7 K cm^{-3} (Lehnert & Heckman, 1996a). The pressures estimated from the photoionization models are consistent with those of nearby intensely star-forming galaxies (Heckman et al., 1990; Lehnert & Heckman, 1996a; Wang et al., 1998) and measurements of density-sensitive lines at high redshift (Lehnert et al., 2009; Nesvadba et al., 2007, ; Chapter 5). In addition, in Fig. 6.12 we see that the clouds with column densities of log N$_H$=20 become density bounded at high ionization parameters and may explain the upper limit to the observed surface brightness. Clouds being density bounded also explains why many intensely star-forming galaxies have line ratios in the [OIII]/Hβ versus [NII]/Hα diagnostic diagram that do not lie on the region of HII regions, but are more extreme. This further suggests that perhaps the escape fraction in the star-forming regions of these galaxies is high (see Brinchmann et al., 2008; Lehnert et al., 2009, for further discussion). These photons may not escape the galaxy proper but could simply go into heating and ionizing the surrounding diffuse gas. This may explain the extreme isophotal sizes of distant galaxies in Hα compared to local star-forming and starburst galaxies.

6.5.4 Self-regulation of star-formation in z~2 galaxies

In a study of the stacked integrated spectra of the galaxies in our sample (Chapter 5), we found that these galaxies must have high thermal pressures in their warm ionized media (P$_{gas}$~10^{-10} dyne cm^{-2}). We argued that this can also be understood in terms of self-regulation as the mechanical energy from star-formation is balancing cloud-cloud collisions or the equilibrium hydrostatic pressure in the ISM (see also Lehnert & Heckman, 1996a; Wang et al., 1998).

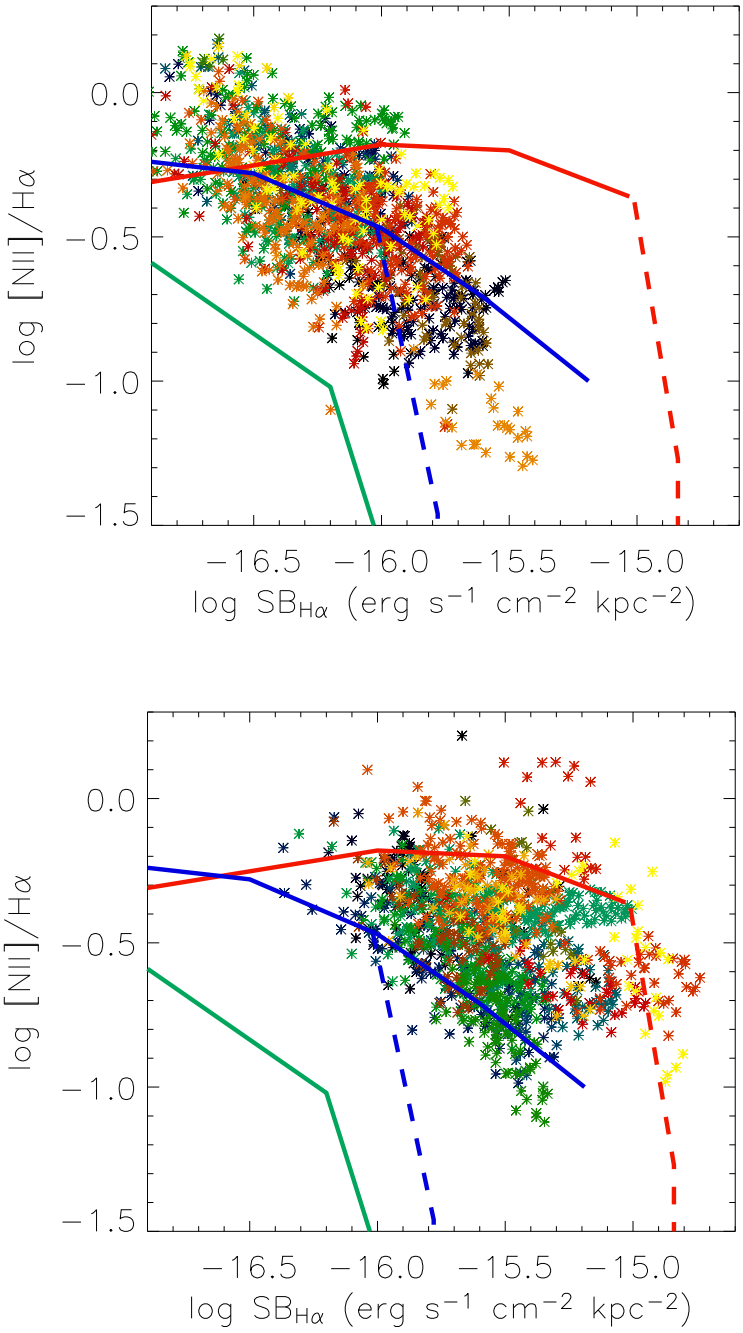

Figure 6.12 Hα surface brightness (corrected for cosmological surface brightness dimming) versus the logarithm of the [NII]λ6583/Hα line ratio. The galaxies have been separated into two redshift bins: z<1.8 (*top*) and z>2 (*bottom*). The lines represent results for photoionization modeling (see text for details) for 6 sets of conditions: a range of densities, log n_H (cm^{-3}) =1 (in green), 2 (in blue) and 3 (in red), and of column densities, log N_H (cm^{-2})=21 (solid lines) and log N_H (cm^{-2}) =20 (dashed lines). The ionization parameters span from log U=−5 to −1.0 (increasing from left to right along the lines, meaning low ionization parameters have relatively high log [NII]/Hα and low Hα surface brightnesses). At low ionization parameters the lines for the two column densities overlap until the lower column density cloud becomes density bounded, at which point the models reach very low ratios of [NII]λ6583/Hα.

Elmegreen & Burkert (2010) considered a model with a constant accretion rate onto a disk of fixed radius and potential, and another model where the potential is time dependent. The energy of the accretion is then balanced by the dissipation rate and loss of gas due to star-formation. The accretion rate is defined by accreting half of a fiducial mass scaling in one dynamical (orbital) time (in their model about 280 Myrs). We adopt the parameters of their model with two significant differences. The first is that we allow for a cut-off in the gas accretion at some point, and the second is that we include the mechanical energy of star-formation in the total energy budget. Since this is not included in their model, at some time the Toomre instability parameter Q drops to small values (<<1). To prevent this, they assume that when the star-formation becomes intense and the disk very unstable the star-formation will then regulate the ISM such that Q=1. Under this assumption they find that ultimately the disk equilibrates to $\dot{M}_{\rm accretion} = \dot{M}_{\rm star-formation}$.

To investigate the role of self-regulation through the mechanical energy output of the stellar population, we have modified the formulation of Elmegreen & Burkert (2010) to include the impact of this mechanical energy output. As they surmised, this energy should stabilize the disk at around Q∼1 allowing it to form stars continuously and rapidly. To do this, we have modified equation (11) from Elmegreen & Burkert (2010) as follows:

$$\frac{dE'}{dt'} = 1 - M'_{\rm disk}(E'M'_{\rm gas})^{1/2} - S'E'/M'_{\rm gas} + \varepsilon_{\rm SF}E_{\rm SF}S'M'_{\rm gas}{}^{3/2}E'^{1/2}$$

where E', $M'_{\rm disk}$, $M'_{\rm gas}$, and S' are the scaled energy, disk mass, gas mass and star-formation rate, respectively (see Elmegreen & Burkert, 2010, for details). The first terms are straight from Elmegreen & Burkert (2010). The first is constant (one), because we have assumed a constant potential (we note that the energy is normalized relative to the total accretion energy, which is extracted from the potential) and the second represents the energy dissipation due to turbulent losses, whereas the third term on the right hand side is the energy that is lost to the ISM when stars form. Adding a time dependence to the potential is quite straight-forward and we have conducted both types of analyses. To these first three terms we have added the energy injection rate due to star-formation, where $\varepsilon_{\rm SF}$ is the coupling efficiency of the mechanical energy to the interstellar medium of the galaxy and $E_{\rm SF}$ is the rate at which energy is ejected per unit of star-formation. The whole equation is normalized such that the accretion energy is one.

The scalings within this model are quite important. Using the estimates of the mechanical energy per unit star-formation (Leitherer et al., 1999) and a rotation speed of 220 km s^{-1} (which sets the potential energy of the galaxy from which the accretion energy is extracted), we estimate that the mechanical energy injected into the ISM by stars is 360 times greater than that generated by accretion. Thus star-formation can play an important role in injecting energy into the gas and per-

haps even stabilizing the disk against star-formation. The scalings for the original model (taken directly from Elmegreen & Burkert, 2010) are t′/t = 90 Myrs (or about one-third of an orbital time), S/S′ = 160 $M_\odot$ yr^{-1}, M_{gas}/M'_{gas} = 1.4 $\times 10^{10}$ $M_\odot$ and σ/σ'=70 km s^{-1}. The Toomre parameter, Q′ scales to Q with a coefficient of about 1/2 to 1 (depending on the efficiency at which accretion energy and the mechanical output from stars is converted into turbulence).

When the coupling efficiency of the mechanical energy from the young stellar population is high, around 10-20%, the Toomre Q parameter is about 1 through most of the evolution and because of this, the star-formation rate is roughly constant (Fig. 6.13). The energy injection into the ISM from both the accretion and the stars is high and thus the dispersions are also high throughout much of the evolution. With the adopted scalings, the dispersions are about 50-150 km s^{-1} and the star-formation rates about 50 $M_\odot$ yr^{-1} – both values are approximately as observed in our sample. The impact of the star-formation is such as to raise the Q-parameter to about 1 throughout the evolution and to stabilize the disk star-formation. At higher levels of coupling between the mechanical energy of the stars, the gas dispersion can be even higher but the star-formation suppressed. Notice that unlike the case of assuming Q=1 (as did Elmegreen & Burkert, 2010), the star-formation rate does not reach the accretion rate until well after the accretion has stopped and the gas fraction has dropped below 50%.

When the coupling between the mechanical energy output of the stellar population is low, we see that the disk is no longer stabilized at Q=1 but that Q becomes very small. This allows the star-formation to increase rapidly and exceed the accretion rate. This high star-formation rate again occurs when the gas fraction drops below about 50%. In this model, star-formation rates are ~200 $M_\odot$ yr^{-1}, high values but reasonable compared to the star-formation rates in our galaxies (the values in Table 2.1 have not been corrected for extinction, which is likely a factor of a few).

We note that during the early, gas-rich phase of evolution in these models the Jeans mass is relatively high which implies that the disks would then be very clumpy, especially in case of highly efficient coupling of the mechanical energy from stars (because such galaxies stay relatively gas rich Elmegreen et al., 2004, 2009a,b; Bournaud et al., 2007, 2008; Ceverino et al., 2010).

The basic point of this simple modeling is that the star-formation can play a key role in regulating the large scale instabilities within the disks of distant galaxies. This conclusion has been drawn before (e.g., Silk, 1997, 2001, 2003; Silk & Norman, 2009). What is new here is the use of the star-formation to drive the line widths (which are a combination of turbulent motions and bulk motions). In addition, given a high coupling efficiency, young stars can control the subsequent star-formation in distant galaxies. There does not need to be correspondence between the instantaneous cosmological gas accretion rate and the star-formation rate.

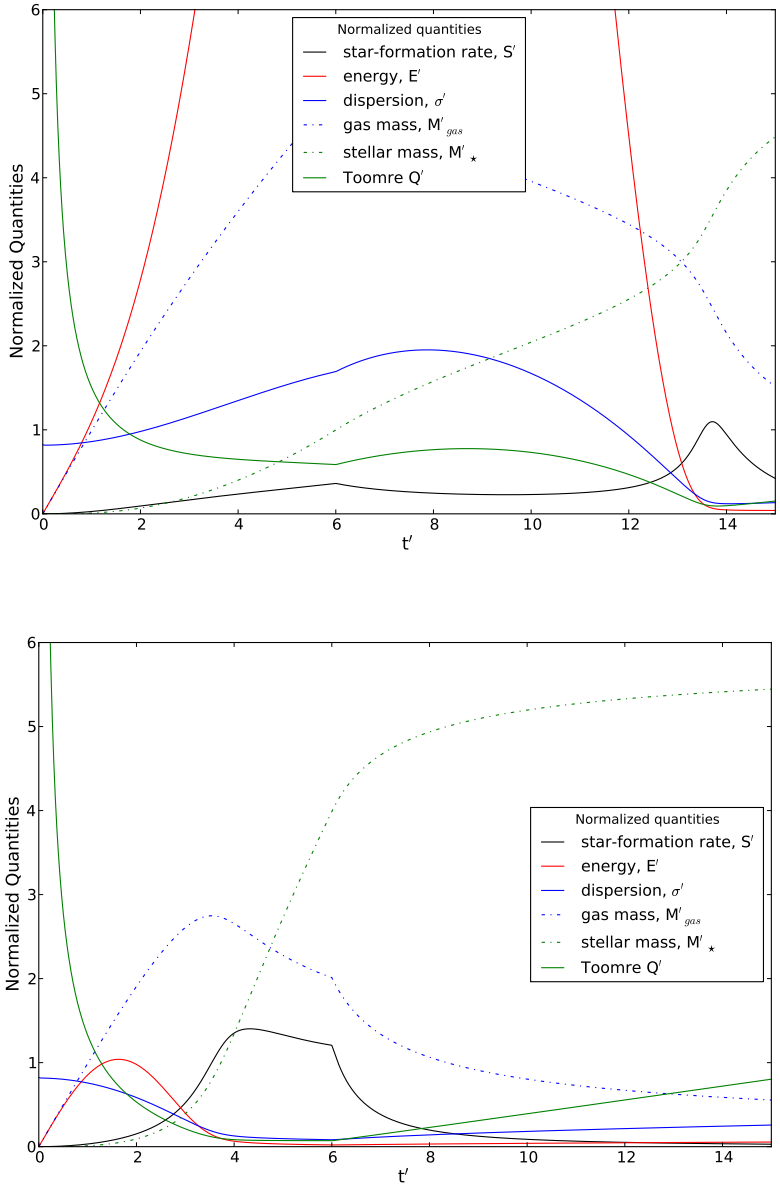

Figure 6.13 Six normalized quantities (see legend) as a function of time, where t/t′ = 90 Myrs or about 1/3 of a dynamical time of the potential. The accretion ended at t′=6 (about 540 Myrs or two dynamical times). The top panel is for a relatively high assumed efficiency of coupling of the mechanical energy output of the stellar population to the ISM (12%), whereas in the bottom panel is for a relatively low coupling efficiency (5%). The scalings for these normalized quantities are provided in the text (see Elmegreen & Burkert, 2010).

In fact, quite the opposite. Smooth constant accretion is probably unrealistic and what we have shown here is that star-formation, even if initiated by the accretion event, does not have to be related closely in time with accretion. The amount of energy available from the supernovae and stellar winds for the stellar population is much higher in comparison and very early in the evolution begins to control the star-formation history.

6.5.5 Surface densities and the Toomre Q parameter

Krumholz & Dekel (2010) favor disk instabilities as the source of the high velocity dispersion in galaxies with spatially-resolved kinematics and line emission. Their argument is that this is a more "prosaic" explanation, because it is based on the Toomre instability parameter, $Q=\kappa\sigma/\pi G\Sigma$. They suggest that the high velocity dispersions are a natural result of the need to keep the star-formation intense, which implies that Q~1. The results given above suggest perhaps that the star-formation itself may also lead to Q~1. Combining the Schmidt-Kennicutt relation with the Toomre instability criterion, Q=1, suggests that $\sigma \propto \Sigma_{SFR}^{0.7}$. This is similar enough to our suggested relationship as to be indistinguishable. However, such a solution does not explain how the observed high dispersions are maintained. This either requires a long dissipation time or a large source of mechanical energy. What maintains the instability such that Q~1? We suggest it is the star-formation itself that maintains the necessary dispersion in the gas phase.

The other criticism Krumholz & Dekel (2010) have made of Lehnert et al. 2009 is that the coupling efficiency between the mechanical energy from star-formation to the ambient ISM has to be high. Again, that is very uncertain in that we do not really know the dissipation time scales. We argued in Lehnert et al. (2009) that they must be short, approximately one turnover timescale of turbulence as suggested by simulations. However, a relatively small change in the dissipation rate would decrease the coupling efficiency. Our results in § 6.5.4 suggest the coupling efficiencies need not be very high. Furthermore, studies of low redshift intensely star-forming galaxies indicate the coupling efficiency could be high (Strickland & Heckman, 2009).

We have argued that the rest-frame optical line widths observed in the intensely star-forming galaxies are due to high rates of energy return from the massive, young-population stars. Further, we suggested that these intensities can be understood in terms of self-regulation (Silk, 1997, 2001). Such self-regulation would reveal itself through mass surface densities in the galaxies consistent with Q=1. The Toomre criterion is $Q=\kappa\sigma/\pi G\Sigma_{stars}$, where κ is the epicyclic frequency (which we have taken to be $2^{1/2}v/r$) and Σ_{stars} is the surface mass density of stars. For the galaxies we have presented here, the velocity shears are of-order 200 km s^{-1} (Förster Schreiber et al., 2006, 2009) and the radii are about a few to 10 kpc (Förster

Schreiber et al., 2011). These values can be used to estimate the epicyclic frequency. The mass surface density of our galaxies is difficult to estimate. Förster Schreiber et al. (2011), using NICMOS and other imaging data of 6 galaxies in our sample, have made crude estimates of stellar masses and sizes. From their results, we find that the mass surface densities within one effective radius, R_e, are ~100-1500 $M_\odot$ kpc^{-2}. Assuming Q=1, we can relate the velocity dispersion to the mass surface density (Fig. 6.14). It appears that the mass surface densities are consistent with Q=1.

Without considering the effects of beam smearing, this simple relation is actually also roughly consistent with our data on the emission line properties, as we can demonstrate rather simply: if we assume Q=1, apply the Toomre criterion to the gas, and adopt the Schmidt-Kennicutt relation (Kennicutt, 1998a), we find the relation, $\sigma = (\pi G Q/\kappa)(\Sigma_{SFR}/2.5\times10^{-4})^{0.7}$. For a variety of rotation speeds and disk radii, we find general consistency with our data (Fig. 6.15). Of course there are some caveats to this analysis, such as our assumption that the gas and stellar mass surface densities are roughly similar (Daddi et al., 2010), which may not be well justified.

This result is interesting. It is clear that the intense star-formation is energetically capable of driving the line widths we observe in the data as turbulence and bulk motions. Moreover, since the star-formation is currently very intense in these galaxies, the ISM must be globally near the line of stability (i.e., Q~1), and now we have shown that both the stellar mass surface densities, velocity dispersions and star-formation intensities are consistent with Q~1. There must be some underlying relationship tying all of these together. We suggest the most obvious: the star-formation must be self-regulating. That is, the star-formation is sufficient to render the whole of the galaxy near the line of stability. If the star-formation were even more intense, it would increase Q, perhaps to the point where it would extinguish the star-formation or consume the gas so rapidly as to quickly force Q upwards. Thus star-formation itself plays a key role in maintaining the ISM in a steady star, even if the overall star-formation is controlled by gravitational processes (i.e., dense clouds become self-gravitating in order to form stars, e.g., Bournaud et al., 2010).

6.5.6 High pressures: turbulent and hydrostatic pressures

Star-formation intensities as high as observed in our sample of galaxies suggest that they result in pressures of-order 10^{10} dyne cm^{-2} (Chapter 5). Our photoionization modeling suggests similar pressures, as does the direct observations of the [SII] lines (Lehnert et al., 2009) and analysis of the stacked spectra of the sources discussed here. If the pressure is due to star-formation, for the gas not to be expelled in a dynamical time and to suppress star-formation, it must be in or close to equilibrium with the hydrostatic pressure (see Lehnert & Heckman, 1996a, for

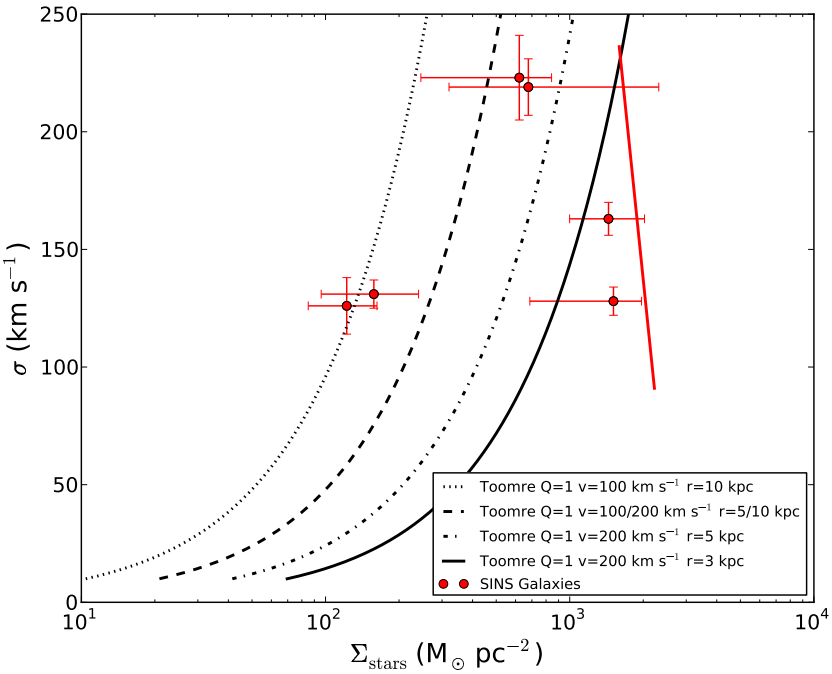

Figure 6.14 Stellar mass surface density, Σ_{stars} (M$_\odot$ kpc^{-2}), as function of Hα velocity dispersion, σ. The lines represent the Toomre criterion Q=1 for two rotation speeds (v=100 or 200 km s^{-1}) and three radii (r=3, 5, 10 kpc), as indicated in the legend. These values span the range of radii and velocity shears observed in these galaxies (Förster Schreiber et al., 2006, 2009). The points are estimates of the stellar mass surface densities (M$_{stars}$/2π(b/a)r$_e^2$, where M$_{stars}$ is the total stellar mass, b/a is the ratio of semi-minor to semi-major axis and r$_e$ is the effective radius) from several galaxies in our sample with NICMOS images from (Lehnert et al., 2009; Förster Schreiber et al., 2011). The red solid line shows the relationship between central velocity dispersion and stellar mass surface density for local early-type galaxies (Shen et al., 2003; Taylor et al., 2010).

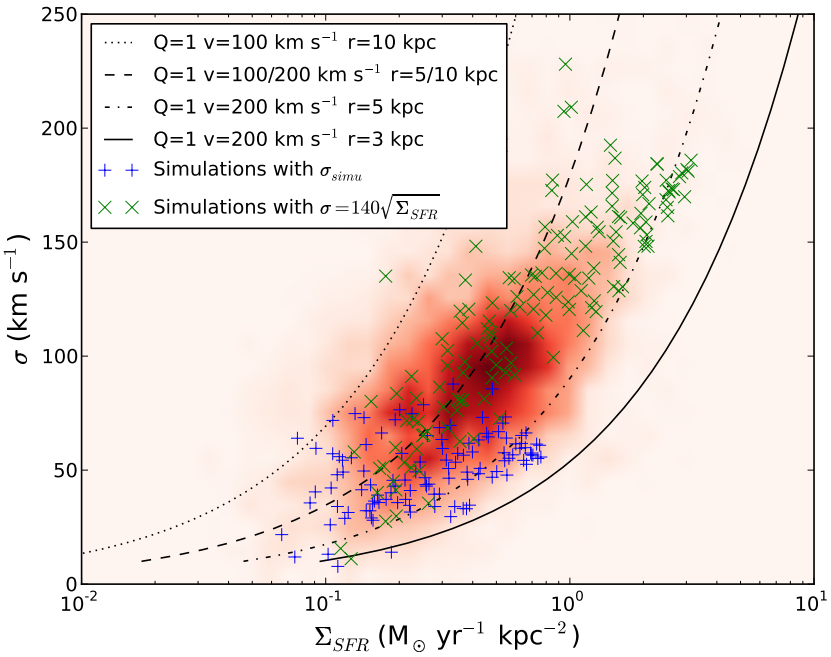

Figure 6.15 Hα velocity dispersion, σ, as function of star-formation intensity, $\Sigma_{\rm SFR}$ ($M_\odot$ yr^{-1} kpc^{-2}). The lines represent the Toomre criterion for gas,assuming both Q=1 and that the Schmidt-Kennicutt relation is appropriate for a variety of rotation speeds and radii, as in Fig. 6.14 and as indicated in the legend (see text for details).

this argument for nearby starbursts). While outflows are observed in z~2 galaxies, either directly in their absorption lines (Steidel et al., 2010) or through broad lines in their stacked spectra (Chapter 5; Shapiro et al. 2009), the star-formation in these galaxies appears to have been sustained for more than a dynamical time (~10^8 yr Erb et al., 2006c; Förster Schreiber et al., 2011).

If gravity plays a role in keeping the gas bound, then it is likely that the turbulent pressure and the hydrostatic pressure are related, $P_{gas} = \rho_{gas}\sigma_{gas} = \pi G \Sigma_{gas}\Sigma_{total}$ (where P_{gas} and ρ_{gas} are the gas pressure and density, respectively, and G the gravitational constant). While it is impossible to estimate directly the hydrostatic pressures for our sample of galaxies, measurements of gas mass surface densities are available for similar samples of galaxies (z~1 and 2; Daddi et al., 2010; Aravena et al., 2010; Dannerbauer et al., 2009; Tacconi et al., 2010). The hydrostatic pressure scales as $P_{gas}=7\times10^{-10}\ \Sigma_{gas,500}\Sigma_{total,1500}$ dyne cm^{-2}. Measurements of the gas mass surface densities of galaxies at z~2 suggest the mean gas surface density is about 500 $M_\odot$ pc^{-2} and total gas fractions are approximately 30–50% (Daddi et al., 2010; Tacconi et al., 2010). This suggest hydrostatic pressures of about 10^{-8} to 10^{-9} dyne cm^{-2}.

We can estimate the turbulent pressures in the warm ionized gas by relating the observed velocity dispersions to the gas density. If the gas that we observe is the post-shock heated gas that has been first accelerated and compressed, and then photoionized by massive stars, we can estimate the turbulent pressures by assuming a density of 1/4 of what we observe. The densities of the warm ionized media in these galaxies ranges from about 10-1000 cm^{-3} (Fig. 6.12; e.g., Chapter 5; Lehnert et al. 2009). Making this estimate, we find that the turbulent pressure for velocity dispersions in the range 50-150 km s^{-1} are of-order 10^{-8} to 10^{-10} dyne cm^{-2}. Of course, some of the observed dispersion is due to bulk motions, but Chapter 5 suggest that this likely does not involve a large fraction of the Hα emitting gas.

From these order-of-magnitude estimates of the various pressures in the warm ionized medium, we infer that the gas pressures are energized by massive stars and that there is sufficiently high gas and total mass surface densities for a significant fraction of this mechanical energy output that goes into supporting turbulent motions. It is this generation of high pressures that supports the intense star-formation we observe.

6.5.7 Consequences of self-regulation

The apparent SFR-$M_\star$ relation for galaxies from z=0–6 (e.g. Elbaz et al., 2007; Daddi et al., 2007; Stark et al., 2009; Oliver et al., 2010; Magdis et al., 2010a) provides valuable insight into how galaxies convert their gas into stars. As an upper envelope or ridge line to the distribution of galaxies in the SFR-stellar plane it shows in particular how the rates of vigorously star-forming galaxies evolve with

stellar mass and redshift. The slope of this envelope is roughly the same at every epoch, however, high-redshift galaxies can reach much higher star-formation rates per unit mass than galaxies at more moderate redshifts.

Currently there is no widely accepted explanation why galaxy the relative rate of growth depends on redshift in this way (Weinmann et al., 2011, and references therein). The rate of cosmological gas accretion into a galaxy halo is expected to be a function of mass and time, depending on redshift as $\dot{M}_{acc}/M \propto (1+z)^{2.5}$ (Dekel et al., 2009), contrary to the observed relationship sSFR $\propto (1+z)^3$ (Oliver et al., 2010; Elbaz et al., 2011). Our current understanding of gas accretion suggests that galaxies at $z \gtrsim 2$ are "gas saturated" having $\dot{M}_{acc}/M \gtrsim$ sSFR, while galaxies at $z \lesssim 2$ are "gas starved", $\dot{M}_{acc}/M \lesssim$ sSFR (Weinmann et al., 2011). This evolution of the specific cosmological gas accretion rate suggests that the specific star-formation rate is not controlled by the gas supply alone, but that galaxy growth must either be limited by the way how the gas is accreted, cools and collapses, or alternatively, by processes that are internal to the galaxy or the physics of star formation.

Any plausible explanation must reconcile the available gas supply with the star-formation rate per unit mass and as a function of mass. However, there is no *a priori* reason why the two should be related in a direct way. For example, Le Tiran et al. (2011, A&A submitted) have shown with a rather simple model based on recent work by Elmegreen & Burkert (2010), the baryonic mass accretion rate and star-formation rate do not need to be equal at any time after accounting for the effects of energy injection from young stellar populations into the interstellar medium of a galaxy. In the regime of efficient coupling of the energy injection to the ISM, the star-formation rate can often be less than the accretion rate. This would favor an explanation of the sSFR-stellar mass relationship through local processes, perhaps related to self-regulating star-formation (e.g. Silk, 1997; Silk & Norman, 2009). One observational signature of this self-regulation are galaxy-wide outflows, which are observed in intensely star-forming galaxies across all cosmic epochs (e.g. Lehnert & Heckman, 1996a; Weiner et al., 2009; Steidel et al., 2010).

We will now show that the SFR-$M_\star$ relationship may be explicable within a simple model which relates the overall star-formation rate in galaxies to the overall pressure of the ISM (Silk, 1997; Blitz & Rosolowsky, 2006; Silk & Norman, 2009). In such scenarios the star formation rate is limited to regimes below where the pressure induced by mechanical energy injection of star formation exceeds the hydrostatic mid-plane pressure in galaxies (e.g. Lehnert & Heckman, 1996a). In this context, the SFR-$M_\star$ relationship would be a consequence of the high gas mass surface densities and gas fractions of high-redshift galaxies, which allow for higher rates of star formation at which the feedback (i.e., the intense mechanical energy) shuts down star formation or the intense star formation depletes their total gas content significantly.

One simple analytic way of investigating if pressure is the driver of the star-

formation intensity is by relating the star-formation rate to the rate at which clouds collide with each other or in a generalized Schmidt law. In such scenarios, the star-formation is given by $\Sigma_{\rm SFR} \propto \Sigma_{\rm gas}^{3/2}\Sigma_{\rm total}^{1/2}$ (Dopita & Ryder, 1994; Silk & Norman, 2009). The pressure in the ISM can be related to gravity or turbulence through $P_{\rm gas} = \rho_{\rm gas}\sigma_{\rm gas} = \pi G\Sigma_{\rm gas}\Sigma_{\rm total}$, where $P_{\rm gas}$ and $\rho_{\rm gas}$ are the gas pressure and density, respectively. G is the gravitational constant, and $\sigma_{\rm gas}$ is the velocity dispersion of the turbulent gas. Combining these implies that $\Sigma_{\rm SFR} \propto P(\Sigma_{\rm gas}/\Sigma_{\rm total})^{1/2}$. This formulation includes hydrostatic as well as turbulent pressure driven by star formation.

Combining the equations given above relate the star-formation rate and the gas surface density,

$$\mathrm{SFR} \propto M_\star \frac{f_g^{1/2}}{(1-f_g)} \Sigma_{\rm gas} \tag{6.1}$$

where $M_\star$ is the total stellar mass and f_g is the average gas fraction, $M_{\rm gas}/M_{\rm total}$. We have assumed for this derivation that the area covered by the gas is the same as that of stars (and recent star-formation).

One of the difficulties in estimating the evolution of this relationship is its normalization. We can adopt a purely empirical approach by estimating the constant of proportionality from the average star-formation rate and gas-mass densities of nearby galaxies (see Le Tiran et al. 2011, A&A submitted). Unfortunately, galaxies for which such data are available, in particular the Milky Way (Elbaz et al., 2007) and the galaxies of Leroy et al. (2008), do not fall near the upper envelope of the SFR-$M_\star$ plane. We therefore adopt a more circuitous route and rely on a scaling that is derived from data from a variety of sources and satisfies the local SFR-mass relationship. At $M_\star \sim 10^{10}$ $M_\odot$, the local SFR-$M_\star$ relation has a SFR$\approx$2.5 $M_\odot$ yr^{-1} (Elbaz et al., 2011). To normalize the SFR-$M_\star$ relation, we will adopt the average values for late type spirals, namely, $<\Sigma_{\rm gas}> \sim 20$ $M_\odot$ pc^{-2} and $f_g \sim 10\%$ (Young et al., 1995; Young & Knezek, 1989).

Our scaling depends only mildly on gas fraction ($f_g^{1/2}$), but nonetheless, adopting a scaling based on local galaxy samples could bias the gas fraction and mass-surface densities necessary to explain the distant galaxy sSFR-$M_\star$ or SFR-$M_\star$ relations. Since these scalings can vary by factors of a few depending on what local sample one uses, any analysis that explicitly assumes a gas surface density or gas fraction will have uncertainties of this order. However, this uncertainty is comparable to the scatter in the observed relations, and therefore is not a dominant source of uncertainty.

The redshift regime where both the SFR-$M_\star$ relationship has been studied and also have a reasonable number of estimates of the molecular gas content in galaxies is z∼1–2 (e.g. Elbaz et al., 2007; Daddi et al., 2007; Tacconi et al., 2010). CO observations of galaxy samples in this redshift range have estimated $f_g \sim$20-40%

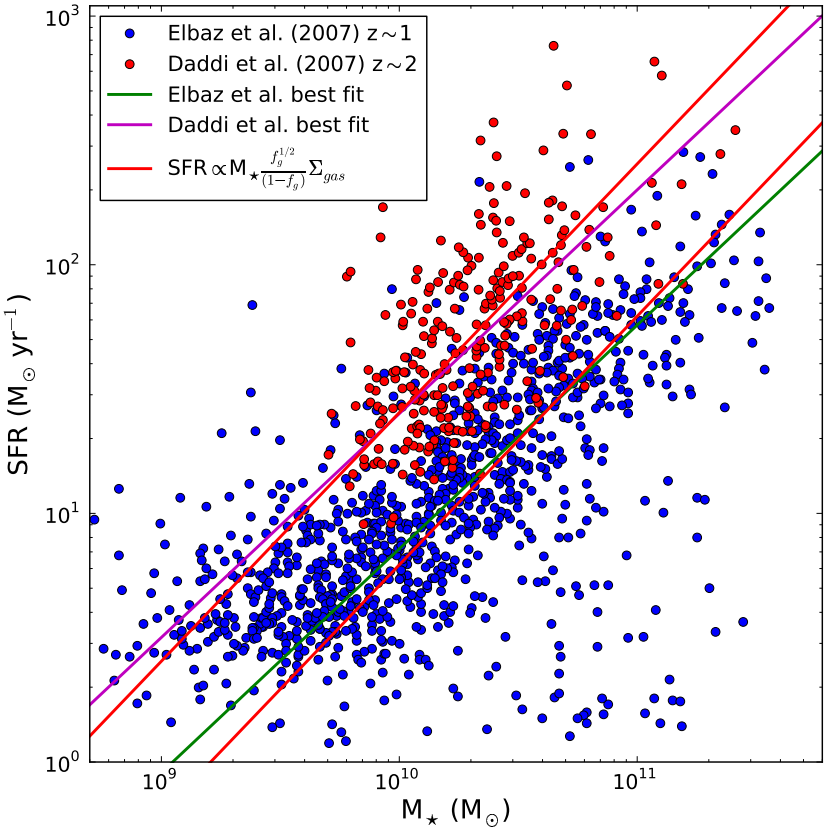

Figure 6.16 Star-formation rate ($M_\odot$ yr^{-1}) as function of total stellar mass ($M_\star$). The data points are estimates of the star-formation rate and stellar mass for samples of galaxies at z∼1 (blue circles Elbaz et al., 2007) and z∼2 (red circles; Daddi et al., 2007). The green and purple solid lines indicate the best fits to the data sets at z∼1 and z∼2 from the original papers. The two red lines indicate simple star-formation model where the star-formation rate SFR$\propto M_{total} f_g^{1/2} \Sigma_{gas}$, where M_{total} is the total mass, f_g is the gas fraction and Σ_{gas} is the gas surface density – see text for details.

and Σ_{gas}~100-2000 $M_\odot$ pc^{-2}(Daddi et al., 2010; Aravena et al., 2010; Dannerbauer et al., 2009; Tacconi et al., 2010). Using the normalization of Eqn. 6.1 based on nearby-late type galaxies and adopting Σ_{gas}=110 and 330 $M_\odot$ pc^{-2} and f_g=0.25 and 0.35 yields relationships that are statistically indistinguishable from the best fits of the ridge line in the SFR-$M_\star$ plane at z=1 and 2 respectively (Fig. 6.16; Elbaz et al., 2007; Daddi et al., 2007). The values for Σ_{gas} that provide these good fits to the SFR-$M_\star$ ridge line are below the mean, but well within the range of estimates based on CO observations in the mm for z=1–2 galaxies (Daddi et al., 2010; Aravena et al., 2010; Dannerbauer et al., 2009; Tacconi et al., 2010). However, this is not surprising given the large (systematic and random) uncertainties in the estimates of Σ_{gas}, the range of possible normalizations of the fitted relationship itself, and that some of the galaxies detected in CO are not typical of the galaxies that would lie along the mean relationship in the SFR-$M_\star$ plane(e.g. Tacconi et al., 2010).

In addition, the star-formation intensities observed in all the very distant (z>4-5) UV selected galaxies is high, $\gtrsim$1 $M_\odot$ yr^{-1} kpc^{-2} (Verma et al., 2007; Stark et al., 2009). Moreover, Verma et al. (2007) found that Lyman break galaxies at z~5 have mass surface densities consistent with early type galaxies in the local universe (similar to what is shown in Fig. 6.14). Within the context of self-regulating star-formation, this can be explained by the dual limitations of detecting low surface brightness galaxies due to cosmological surface brightness dimming and the overall low mass of galaxies at these redshifts. Thus only the highest surface brightness galaxies can be observed and by necessity, those must have high stellar mass surface densities and high gas fractions to support such intense star-formation.

6.6 Conclusions

From an analysis of optical rest-frame emission line properties (Hα and [NII]λ6583) of 53 galaxies at z~1.3-2.7 selected using a variety of techniques, we have come to a number of conclusions.

The surface brightness limits that can be achieved in a few hour integration with SINFONI (or any IFU for that matter), in combination with cosmological surface brightness dimming, strongly constrains the characteristics that can be observed, as we have shown for both the isophotal size and the total Hα luminosity.

We have attempted to quantify the effects of beam smearing on our results. Using an N-body/SPH simulation of a gas rich disk, we find that beam smearing and low spatial sampling of the data diffuse the highest and lowest line velocity dispersions; blend and lower the surface brightnesses (star-formation intensities) by a factor of a few (although this depends on the details of the light distribution); tend to increase the lowest dispersions from 10 km s^{-1} to about 50 km s^{-1} for simulations which intrinsically have a constant dispersion as function of radius ; roughly

preserve the slope of the data in the star-formation intensity-velocity dispersion plane. Therefore, we find through this exercise that if there is an underlying relationship of the type $\sigma = \varepsilon\Sigma_{\rm SFR}^{1/2}$, beam smearing will not totally remove evidence for this relation from the data, although its effects cannot be ignored, especially for galaxies or regions of galaxies with low intrinsic dispersions.

For the galaxies at the low redshift end of our sample distribution, it appears that we are (and can) probe the spatially resolved properties of galaxies at generally lower rest-frame Hα surface brightnesses. This has its consequences when interpreting observations of galaxies over a wide range of redshifts. While we also find that the galaxies at z$\gtrsim$2 are extreme (cf. Lehnert et al., 2009), our sample of lower redshift galaxies has ISM pressures that are a factor of 10-100 lower than the high redshift sample, but still higher than typical disks in the local universe. Probing lower surface brightnesses also allows us to study galaxies with less extreme internal dynamics (turbulent and bulk motions). Given the difficulties in resolving narrow lines at modest S/N and with the effects of beam smearing, it can be difficult to precisely determine the line widths of these lower surface brightness galaxies. Because the effects of beam smearing artificially increase the estimated dispersions if they intrinsically are below our resolution ($\sim$50 km s^{-1}), we conclude that galaxies with relatively low surface brightnesses and dispersions may actually have dispersions which are similar to the Milky Way and other nearby disk galaxies (i.e., $\sim$10 km s^{-1}), in both magnitude and radial dependence.

Using a simple model for star-formation and gas accretion, we suggest that star-formation plays a key role in energizing the dynamics of the warm ionized medium, but may also play a role in regulating star-formation itself. We find that by combining the simple scaling $\sigma \propto \Sigma_{\rm SFR}^{1/2}$, with a Toomre instability analysis, we conclude that star-formation may be balancing subsequent star-formation by driving the Toomre Q-parameters to be about one and thus making the galaxy critically unstable against star-formation.

We suggest that this self-regulation may manifest itself observationally in the ensemble properties of distant galaxies. A simple star-formation model where the star-formation rate is given as SFR $\propto$ M$_\star$ $\frac{\rm f_g^{1/2}}{\rm (1-f_g)}$ $\Sigma_{\rm gas}$ (where M$_\star$ is the total stellar mass, f$_g$ the gas fraction and Σ_{gas} the gas surface density) can explain the "star-formation-rate-stellar mass relation" found for star-forming galaxies at low and high redshifts (Elbaz et al., 2007; Daddi et al., 2007; Magdis et al., 2010b). Using a constant of proportionality based on the Milky Way and other nearby galaxies, and plausible values for the gas fractions and gas mass surface densities of high redshift galaxies, provides a reasonably good fit to the "star-formation rate-stellar mass" relation.

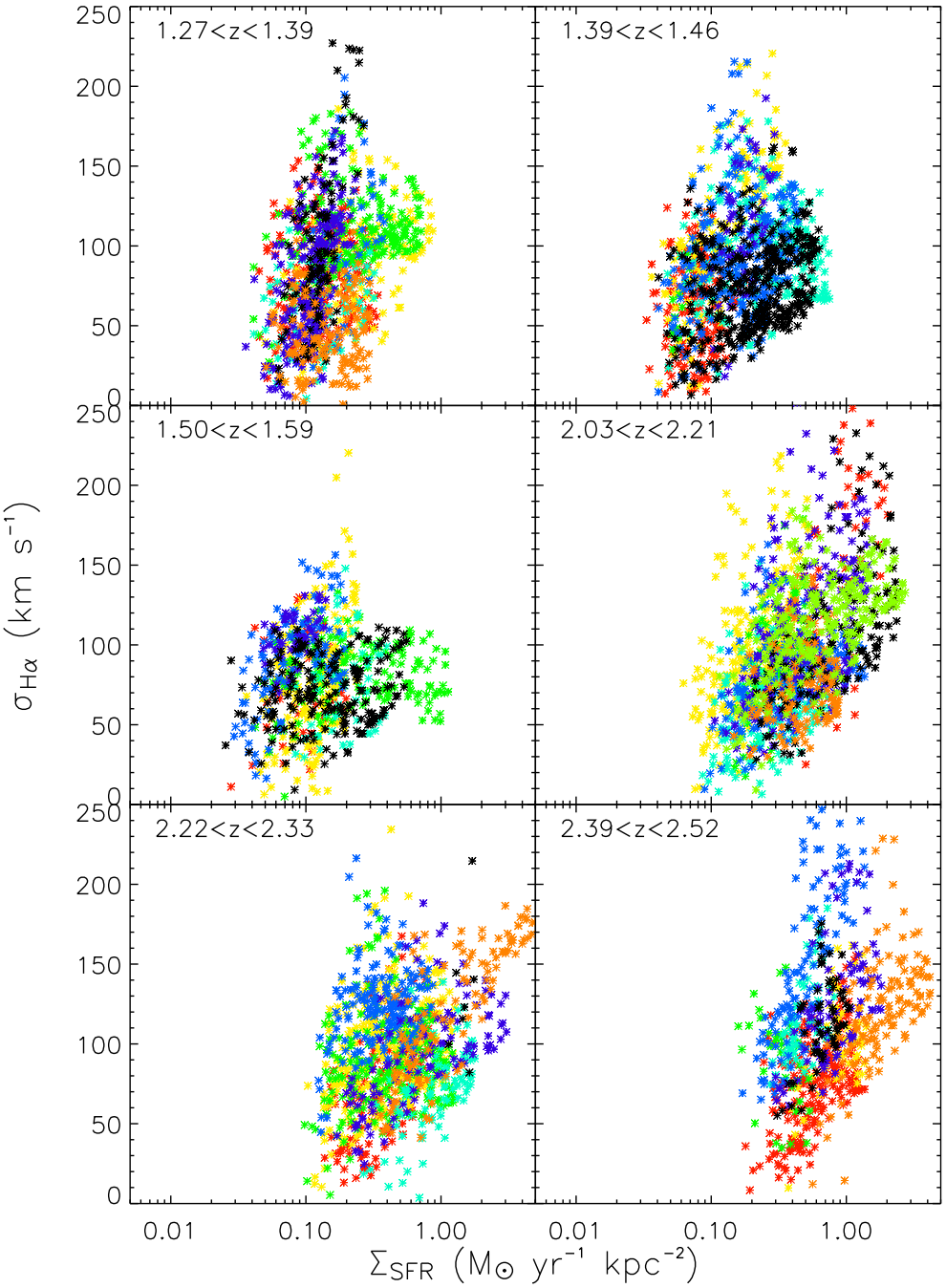

Figure 6.17 Plots of the Hα velocity dispersion as a function of the star formation rate surface density for all the galaxies presented in this chapter, sorted in 6 bins amongst their redshift.

Chapter 7

A Perspective: The Physical Conditions of the ISM in Massive Galaxies at redshift~1.4: Evidence for a "top-heavy" IMF, Bursty Star-Formation and/or High Pressures?

Abstract:

We analyze observations of 10 galaxies at z~1.38 based on integral-field spectroscopy using SINFONI from the ESO-VLT, combined with data obtained from the DEEP2 Survey. We focus on the continuum, Hα and [NII] fluxes to derive the dynamical and ionization properties of our sample. These objects often exhibit complex morphologies, disturbed velocity fields, and low projected v/σ ratios. In a diagram of v/σ versus axial ratio, these galaxies lie close to a region occupied by merger simulations (properly scaled to the resolution of our data). [NII]/Hα line ratios and Hα line widths studies show that two objects host AGN. The star formation rate intensities also indicate that these objects are likely to drive winds suggesting that they have high pressures in their warm ionized media. Moreover, their ratio of $F_{\mathrm{H}\alpha}/f_{\mathrm{FUV}}$ to Hα and R-band luminosity surface brightnesses follow the same overall trend as nearby HI selected galaxies, but populate the high end of $F_{\mathrm{H}\alpha}/f_{\mathrm{FUV}}$ to Hα and R-band luminosity surface brightnesses, forming a single parameter family. Other authors have suggested that this relationships may indicate a stellar initial mass function that is dependent on the mass of the galaxy or its average surface brightness, or that the star-formation history is "bursty" — short phases of intense star-formation — and/or the pressure of the ISM increases with mass or stellar surface density. Of course, high pressures in the ISM could lead to both a skewed IMF and bursty star-formation. We find all hypotheses for explaining the trends in $F_{\mathrm{H}\alpha}/f_{\mathrm{FUV}}$ with mass surface density and mass to be viable for the high redshift galaxies too, but favor either a top heavy IMF or high pressures.

Both fit the relations reasonably well. Future, more detailed observations of distant galaxies may help solve this issue as to why $F_{\mathrm{H}\alpha}/f_{\mathrm{FUV}}$ increases with increasing mass surface density and Hα surface brightness. Here we intend to simply give a perspective on this type of analysis, pose questions to be addressed with more work and how we might answer these questions.

Contents

7.1 Introduction

Distant galaxies at z=1-3, with spatially resolved spectra, appear to show high surface brightnesses in their hydrogen recombination lines, as high as those of nearby intense starbursts but over much larger areas, and often lie in the region of various optical emission line diagnostic plots, such as [OIII]λ5007/Hβ versus [NII]λ6583/Hα which are between the area occupied by HII regions and active galactic nuclei (AGN; Lehnert et al., 2009; Veilleux & Osterbrock, 1987). The observations can be explained by dense high pressure gas bathed by an intense radiation field (Lehnert et al., 2009, , see Chapter 3 and Le Tiran et al. 2011, A&A submitted, see Chapter 5). The velocity dispersions in the Hα emitting gas are also high (~50-200 km s^{-1}) in distant spatially resolved emission line galaxies and there is evidence for bulk flows (Le Tiran et al. 2011, A&A submitted, see Chapter 5 Shapiro et al., 2008; Steidel et al., 2010). This suggests that not only is the thermal pressure high, but so is the turbulent pressure. These high pressure and large line widths are likely powered by the intense star-formation taking place in these galaxies. High turbulent and thermal pressures will also have consequences for the star-formation.

The Jeans mass is $M_{Jeans} \propto T^{3/2}/\rho^{1/2} \sim T^2/P^{1/2}$, where T is the temperature, ρ is the density, and P is the pressure. Clouds with low temperature and/or high pressures would form clusters with IMFs weighted towards low mass stars. Conversely, clouds that are collapsing in relatively low extinction, gas poor, more quiescent regions might be influenced by the ionizing radiation of nearby young clusters raising its gas temperature. Such a situation would favor the formation of clusters with IMF that have relatively large fractions of high mass stars. However, the Jeans mass estimate only considers the internal pressure of the cloud, not the overlying or external pressure. In the case of generally high pressures in the ISM, this could act as an additional pressure source on the surface of the cloud. This additional source of pressure could shorten the collapse time of the cloud by compressing it without heating it significantly. If the density rises faster than the temperature or equivalently, if the cooling time becomes shorter than the dynamical time, the mass of the collapsing gas can be increased over the simple Jeans mass estimate (which would then be applicable not on large scale but on small scale embedded self-gravitating dense clouds). This increase may skew the IMF more towards massive stars.

The efficiency of star-formation in local spirals is about a few percent, but can reach ~ 10% in starburst regions (e.g., Young et al., 1996; Solomon & Sage, 1988; Sanders et al., 1991). Because of the high star-formation intensities in the z~2 galaxies and the high pressures, similar to those of local starburst regions, we would infer similarly high efficiencies of at least 10%. We do not have a comprehensive theory of star formation, however, it has been suggested that there is a power-law dependence of the star formation rate on the total column density and/or pressure

and density (e.g. Wang & Silk, 1994; Blitz & Rosolowsky, 2006). Relationships of these types can imply that star-formation occurs on a dynamical time scale averaged over a large area. Elmegreen (2002) used this dependency to argue that this would lead to a star-formation law of the form, $SFI = \varepsilon_{SF}\Sigma_{gas}\omega$, where ε_{SF} is the star-formation efficiency and ω is a dynamical rate for the conversion of gas into dense, star-forming cloud cores. Elmegreen 2002 argues that this does not imply that gravitational forces are directly involved but that this dynamical rate of conversion is about equal to the turbulence crossing rate (which is also argued to be the inverse of the collapse time with modest over-pressures). By comparing the inverse of the relative crossing times of turbulence at z~2 and local galaxies, Lehnert et al. (2009) argued that the conversion efficiency of gas into dense star-forming cloud cores is higher in z~2 galaxies than for local disks. Thus the apparent efficiency of star-formation in z~2 galaxies should be higher than in nearby disk galaxies ("apparent" means $\varepsilon_{SF}\omega$) while the star-formation efficiency itself, ε_{SF}, can remain constant.

The star-formation history of galaxies are generally thought to include episodes of intense star-formation, especially in the most and least massive systems (e.g. Mateo, 1998; Stinson et al., 2007; Thomas et al., 2005). During bursty star-formation the equivalent width and surface brightnesses of the recombination lines of hydrogen can reach large values (>50-100Å) and the UV emission can become intense. This "burstyness" may also be related to the high efficiency of star-formation which would allow the star-formation rate to go highly non-linear — the definition of burstyness.

Recently, Meurer et al. (2009, hereafter M09) investigated the relationships between the ratio of Hα to far-UV luminosity of a sample of nearby HI selected galaxies. M09 found that there is a linear relationship between the logarithm of the flux ratio of Hα and far-UV luminosity, $F_{\mathrm{H}\alpha}/f_{\mathrm{FUV}}$, and logarithm of both the surface brightnesses in Hα, $\Sigma_{\mathrm{H}\alpha}$ (erg s^{-1} kpc^{-2}), and the R-band surface brightness, Σ_{R} (L$_\odot$ kpc^{-2}). The relation is in the sense that galaxies with higher surface brightness in the line or continuum have higher values of $F_{\mathrm{H}\alpha}/f_{\mathrm{FUV}}$. They suggested this is one of the fundamental scaling relations for galaxies and hypothesized several underlying causes for this relationship among local star-forming galaxies. These include IMF variations, in the sense that perhaps the lower surface brightness galaxies have steeper high mass ends of their IMFs (or reach a less extreme upper mass end), the star-formation in their sample is "bursty", the escape fraction of ionizing photons is higher in low mass galaxies, and/or the pressure increases along the sequence since the relation is with both $\Sigma_{\mathrm{H}\alpha}$ and Σ_{R}. Ultimately, investigating each of these hypotheses in turn, they favored an IMF variation but could not rule out conclusively other explanations (the pressure in particular was not argued thoroughly in M09). Lee et al. (2009) furthered this discussion by investigating the $F_{\mathrm{H}\alpha}/f_{\mathrm{FUV}}$ as function of mass (low mass galaxies tend to have lower Σ_{R}, for example). They

suggested that the trend at the high mass end is simply due to extinction and that at the low masses even after extinction correcting the $F_{H\alpha}/f_{FUV}$, the Hα luminosity still under-predicts the star-formation rate (assuming the UV is the better tracer of the star-formation rate). They suggest that either perhaps star-formation becomes inefficient to low mass and low star-formation intensities or the IMF really is stepper in low mass galaxies.

Here our goal is to present how we might begin to understand the physical processes that underpin the relationships between $\Sigma_{H\alpha}$ and Σ_R and $F_{H\alpha}/f_{FUV}$. Since our data are rather limited we cannot reach a firm conclusion of why local and distant galaxies appear to fall on these relations. M09 suggested that the IMF may be the culprit at least for the low mass galaxies. Recently, it appears that this is unlikely and that perhaps inefficient star-formation is related (R. Kennicutt, private communication). However, we will make a crude analysis of each of these to determine how high redshift galaxies might help solve the issue as to the nature of the relationships between $\Sigma_{H\alpha}$ and Σ_R with $F_{H\alpha}/f_{FUV}$. It is only meant to be a perspective for future work, not to give definitive answers.

7.2 Observations and Data Reduction

This analysis of the physical properties of strongly star-forming, high-redshift galaxies, is based on the observations of a sample of 10 mass selected galaxies at z$\sim$1.38 from the DEEP2 Redshift Survey, in rest-frame optical with integral-field spectroscopy.

Data were taken with the near-infrared integral-field spectrograph SINFONI on the ESO Very Large Telescope in several service mode runs between June and September 2007. Observation times are given in Table 7.1. We reduced these data independently from any other previous work, using the IRAF (Tody, 1993) standard tools for the reduction of long slit spectra, modified to meet the special requirements of integral-field spectroscopy, and complemented by a dedicated set of IDL routines. Data are dark-frame subtracted and flat-fielded. The position of each slitlet is measured from a set of standard SINFONI calibration data, measuring the position of an artificial point source. Rectification along the spectral dimension and wavelength calibration are done before night sky subtraction to account for some spectral flexure between the frames. Curvature is measured and removed using an arc lamp, before shifting the spectra to an absolute (vacuum) wavelength scale with reference to the OH lines in the data. To account for variations in the night sky emission, we normalize the sky frame to the average of the object frame separately for each wavelength before sky subtraction, correcting for residuals of the background subtraction and uncertainties in the flux calibration by subsequently subtracting the (empty sky) background separately from each wavelength plane.

The three-dimensional data are then reconstructed and spatially aligned using the telescope offsets as recorded in the header within the same sequence of dithered exposures (about one hour of exposure), and by cross-correlating the line images from the combined data in each sequence, to eliminate relative offsets between different sequences. Telluric correction is applied to each final cube. Flux scales are obtained from standard star observations.

We also used the standard stars to monitor the seeing during observations, and we find an effective seeing in the combined cubes of typically FWHM 0″.5 −0″.8. The spectral resolution was measured from night-sky lines and is FWHM∼150 km s^{-1} in the H band, for the 250 mas pixel scale (where "mas" means milli-arcseconds).

7.3 Results

7.3.1 Spatial properties

Maps of emission lines flux, dispersion and radial velocity have been obtained from the three-dimensional data (see Chapter 2). Every spectrum has been fitted using IDL routines with a combination of a low-order polynomial, to fit the continuum and a series of gaussians to fit the emission lines. In order to improve the signal-to-noise ratio (S/N), we averaged each spaxel over a region of 3x3 spaxels which is approximately the width of the seeing disk in our data.

Noise has been measured on a subset of each spectra close to the emission lines. Regions of strong night sky line emission were not considered when determining the noise of the spectrum. A Monte-Carlo (hereafter MC) has been used to compute maps of the S/N: the measured signal is fitted with different realizations of the noise having the same amplitude as the noise in our data and assuming it was distributed as a gaussian. The dispersion of the obtained values for these MC fits then gives the uncertainty in each measurement. Continuum maps have been obtained using parts of the spectrum which do not have overlying strong night sky lines. The regions of strong night sky line emission where interpolated over before collapsing the spectrum, for each spatial pixel separately, and clipped to include the wavelengths of the H band only (the spectral region partly goes beyond the formal range of the H band but these regions are affected by strong absorption due to the atmosphere).

Our results imply typical isophotal areas of ∼200 kpc^2 in Hα, with values between 20 kpc^2 and 300 kpc^2, but detection in [NII] is, as expected, less extended. The area is determined by summing up the area of all spaxels which have a S/N>3 in the line. Two galaxies are very poorly resolved in Hα to derive accurate dynamical properties. Two of these objects have broad emission lines and large Hα/[NII] emission and therefore mostly likely host AGN. Among the eight other objects,

more than a half exhibit multiple components, usually in the continuum morphology as well as in the Hα distribution. For half of these galaxies, Hα appears to be slightly offset from the continuum center (which is defined as the highest surface brightness region in the continuum data). None of the observed velocity fields is simple and regular: most of them appear very disturbed and even the smoother ones exhibit distortions. Overall the galaxies, at different degrees, seem to have complex velocity fields and morphologies. Individual descriptions of these objects can be found in Appendix C.

7.3.2 Integrated properties

The integrated properties of each galaxy were derived by summing all the spectra of every pixel that has a S/N>3 in Hα or [NII] emission line. Uncertainties in the flux and dispersion are computed using a MC as we did for the individual spectra of our cubes (see Section 7.3.1). For both the line maps and the values obtained from the integrated spectrum, the instrumental spectral resolution has been subtracted. Redshift uncertainties correspond to the 1σ dispersion in the distribution of the MC realizations. The surface brightness limit corresponds to the lowest flux per pixel estimated for pixels with S/N>3. These estimates are presented in Table 7.1. The previous spectroscopic measurements of the redshifts in the DEEP2 survey are confirmed: all these objects have very similar redshifts, with a mean value of $< z >= 1.387$ and a range z=1.3716 to 1.3985. In our assumed cosmology (§7.1), the age of the Universe at this mean redshift is ~4.5 Gyr, with a corresponding lookback time of ~9 Gyr. The measured line fluxes lie around $<F_{H\alpha}>\sim 2.6\times10^{-16}$ erg s^{-1} cm^{-2} for Hα and slightly less than the half for [NII]: $<F_{[NII]}>\sim 1.2\times10^{-16}$ erg s^{-1} cm^{-2}. Dispersions for both lines lie around 120±70 km s^{-1} in the integrated spectra.

The rest-frame equivalent widths were estimated by integrating over the region where the signal-to-noise was greater than 3-σ in the continuum to estimate both the emission line flux of Hα and the total continuum magnitude of each galaxy. The continuum maps were smoothed over a 3x3 pixel box and then σ-filtered to include only those individual pixels that were 3 times greater than the background noise level. The continuum maps were then fitted by a 2d-gaussian in order to derive an estimation of the continuum intensity in function of the distance along the major axis. The obtained curve has been subtracted to its own 20 pixels smooth, to suppress the low frequency component, i.e., the random noise, that can now be calculated. For both the continuum and Hα, the final values of the fluxes are the sum of the values of every pixel above the 3-σ detection limit in the continuum. For two objects, 32007614 and 32029850, the surface of detection of Hα is small, and we integrated over the continuum aperture. The results of this analysis are shown in Table 7.2. The flux density in H on the best detection areas (over 3-σ

detection) is typically around 11×10^{-19} erg s^{-1} cm^{-2} Å^{-1}. Luminosities in Hα are $\sim 3 \times 10^{42}$ erg s^{-1}. We obtain equivalent widths (with both continuum and Hα fluxes measured on the same continuum 3-σ detection region) usually around 50 Å.

In addition, from the total Hα fluxes, we have estimated the star-formation rate using the standard relationship (Kennicutt, 1998b). Our results are presented in Table 7.2. As for other values measured previously, we have not corrected for extinction in making this estimate. We obtain star formation rates typically around 25 M$_\odot$ yr^{-1} which implies star formation rate surface densities of $\sim$0.1 M$_\odot$ kpc^{-2}.

7.3.3 Ordered and random motions

The v_{shear}/σ_{mean} (hereafter referred to simply as v/σ) have been derived using a method similar to that used in Law et al. (2009). σ_{mean} is the flux-weighted mean dispersion as estimated by taking the velocity dispersion for each pixel in the dispersion map above a S/N>3. The velocity shear is estimated along the axis which exhibits the maximum velocity difference. V_{shear} refers to half the maximum velocity difference determined along this axis. The results of this analysis are shown in Table 7.1. We obtain velocity shears around 140km s^{-1} and weighted velocity dispersions around 110km s^{-1}, and a mean v/σ of about 1.3. This result demonstrates that random motions are a major contribution of the total mechanical energy of these galaxies, which is very different from the ordered motions and large v/σ observed in local disk galaxies.

7.3.4 Axial ratios

The complex morphologies of the sources precludes a good estimate of the axial ratio of our sources and thus it is difficult to robustly de-project the estimated velocity shear for the sources. Despite the uncertainties, we estimated the semi-major to semi-minor axis ratios (hereafter a/b) of our sample of galaxies (and in §7.4.2, we compared them with other values of simulations "analogued" to be as if they were observed with SINFONI). The axial ratios, a/b, were estimated by fitting the continuum map with a two-dimensional gaussian. All lie around 1.3, except for objects 32015443 (a/b$\sim$2) and 32002481 (a/b$\sim$3.7) which appears to have two well separated components (Table 7.1).

7.3.5 Other quantities used in the analysis

To further our analysis, in addition to the morphological, dynamical and integrated properties, we estimate the effective surface brightness of Hα, the Hα flux, the far-UV flux, the H-band flux measured from the SINFONI data directly, the rest-frame R-band effective surface brightness, and the apertures used to estimate both the

effective Hα and R band surface brightness (Table 7.2). We now describe how they were estimated.

7.3.5.1 Quantities derived from SINFONI observations

$\Sigma'_{H\alpha}$ and Σ'_{R} are respectively the effective surface brightness of Hα and rest-frame R-band. Both quantities were calculated by taking the total integrated fluxes of Hα and H band, calculating the luminosity of each (the H band corresponding approximately to rest-frame R band in these galaxies) and dividing by the total area of the Hα and H band emission respectively. The exponentiated primes in the symbols indicate that these quantities have not been corrected for the effect of extinction. The aperture used for this estimate is the total number of pixels having a S/N>3 on the Hα or H-band flux map and where this total pixel area has been tabulated in units of kpc^2 ($A_{H\alpha}$ or A_R respectively). The Hα effective surface brightness is given by $\Sigma'_{H\alpha}$=4π D_L^2 $F'_{H\alpha}/A_{H\alpha}$, where D_L is the luminosity distance of the object derived from the redshift, $F'_{H\alpha}$ is the integrated Hα flux measured and $A_{rmH\alpha}$ the projected surface of the object in kpc^2. The tabulated uncertainties only include uncertainties in $F'_{H\alpha}$. A formula similar in spirit is used to calculate the effective R band surface brightness. Namely, the R-band surface brightness is obtained from the H-band continuum flux f'$_{H-band}$, Σ'_R = 4π D_L^2 (1+z) f'_{H-band}/A_{H-band}. The uncertainties are derived from the measure of the random noise in the continuum maps. The value is given in units of solar luminosities in the band, using $L_{R,\odot}$=4.39×10^{22} W Å^{-1}.

7.3.5.2 Quantities derived from the DEEP2 survey

The far-UV flux density f'_{FUV} is estimated using the B magnitude given by the DEEP2 survey (e.g., Coil et al., 2004). This estimate was made using f'_{FUV} = (1+z) ((1+z) λ_{FUV}/λ_B)$^{\beta}$ $\frac{c}{\lambda_B{}^2}$10$^{-0.4(mag_B+48.6)}$, where mag_B is the CFHT B magnitude centred on λ_B=4451 Å, and β is the slope of the UV between the λ_B/(1+z) and λ_{FUV}. This correction is due to the fact that in the CFHT B filter the central wavelength is 4451 Å, corresponding to a rest frame of $\sim$ 1870 Åfor a redshift of 1.38, while for the GALEX FUV channel, the central wavelength, λ_{FUV}, is at 1528 Å. We used a conservative value with β = 2. β is typically between 1 and 2 for star-forming galaxies, as measured at higher redshifts (Bouwens et al., 2009). A value of β = 1.5, more likely to be found at z = 1.4, would increase the f'_{FUV} by 10%, up to 22% for β=1. We estimated the uncertainties following Coil et al. (2004) which at the flux levels of these sources, is dominated by the calibration and systematic uncertainties in the data. We have assigned each magnitude an uncertainty of 0.04 dex. This definition of FUV is very close to what was used in M09 and thus our comparison is fair.

7.4 Discussion

7.4.1 These Are Massive Galaxies

The high luminosity observed in the H band continuum, probing the rest frame optical, suggests that these galaxies are massive. In order to obtain a simple estimate of their masses, we have used the observed parameters together with models made using the software GALAXEV (Bruzual & Charlot, 2003).

We used a τ-model (where SFR $\propto e^{-t/\tau}$). This model does not describe the real star formation history (SFH) of our galaxies: a τ-model is more accurate for modelling quiet galaxies in the local universe, whose major star formation episodes are finished since a long time. Other forms of SFHs may be more reliable, especially in the high redshift Universe (constant star formation, inverted-τ models, see Maraston et al., 2010)). Moreover, this model does not take in account any recent burst of star formation which would affect it (especially the Hα emission). This is however the model we will use, considering we are only looking for an estimate of these masses. Moreover, this is the typically used model, which allows more direct comparisons with other works (e.g. Shapley et al., 2005).

We used a Salpeter initial mass function extending from 0.1 to 100 $M_\odot$, solar metallicity, and the Padova 1994 stellar evolution tracks (as recommended in Bruzual & Charlot, 2003).

We constrained τ using a series of models with different e-folding times (0.1, 0.3, 0.5, 0.7, 1.0, 1.5, 2.0 Gyr). This range of e-folding times represents a reasonable span encompassing the likely evolutionary times of distant galaxies. It turns out using an e-folding time of 0.7 Gyr in our models allows acceptable Hα equivalent widths while for longer e-folding times, the models would have Hα equivalent widths greater than a significant fraction of our sample of galaxies over the whole age of the universe at redshift of 1.4. Therefore, we used this value to determinate the masses of our objects.

We used the stellar mass to luminosity in the visible $M_\star/L_R$ given by the models at a time corresponding to the observed Hα equivalent width to obtain $M_\star$ from our measurements of the rest frame visible luminosity (approximately that of the SINFONI H band). We find that plausibly, $M_\star/L_R$ ranges from about 0.3 to 1.3, with about 0.7 being a reasonable "mid-point" value for the ensemble of Hα equivalent widths and range of plausible ages and model e-folding times. We used however a different $M_\star/L_R$ for each object.

Adopting the absolute magnitude of the sun in the R band of 4.46, we find that the average R-band luminosity of our objects is about 7×10^{10} $L_\odot$ with a range of about 4-13$\times10^{10}$ $L_\odot$. Although 2 sources are likely to harbor AGN, they are not amongst the brightest in the continuum nor is there any evidence for nuclear point sources in the continuum images. For a $M_\star/L_v$ ratio of about 0.7, this would

suggest that the galaxies in this sample have masses of order 3-8$\times10^{10}$M$_\odot$. Of course, this is the unextincted stellar mass and does not include any contribution from the interstellar medium. It is thus a lower limit to the true baryonic masses of these galaxies. Nonetheless, in comparison with the stellar mass distribution of galaxies in the local universe, these would qualify as massive galaxies as they are roughly twice more massive than local M* galaxies (e.g., Smith et al., 2009).

7.4.2 What Could be the Source of the Large Scale Motions and Complex Morphologies?

On Table 7.1 we show the values we obtained for the projected v/σ. We find a mean value around 1.5 (excluding the values of two objects having very low Hα detection), with a range between 0.5 and 2.3. This maximal value still lies down compared to the observations of disk galaxies today, and is close to random motion dominated like ellipticals and bulges. The mechanical energy of these objects cannot be only rotational and must be mostly random motions or winds.

We also used the results of the axial ratios obtained in §7.3.4, on which we can add analogs of different simulations. By analogs, we mean that we used simulated data and virtually observed them as if they were observed with SINFONI: placed at redshift 1.4, smoothed by our observations point spread function (FWHM of 0$''$.6), and treated with the same analysis techniques to obtain continuum maps, Hα flux and kinematic maps. We used two samples of these objects. The first one is an isolated spiral galaxy seen at different angles, from face-on to edge-on. The second one is a set of mergers of the previous isolated galaxy with an other self, with different angles between these objects, at different times of the merging process, and seen from different points of view. The results we obtain for our observed sample and for this two analogued samples, together with their projected v/σ, are plotted in Figure 7.1. Our galaxies lie in a low a/b region, close to the isolated galaxies, which tends to shows that our objects are not generally in the process of a violent merger. The red circle with high axial ratios is 32002481 which is composed of two well separated components and thus may not be a flattened system.

7.4.3 Are These Galaxies Driving Winds?

The SFR spatial density of our objects varies between 50 and 200 $\times10^{-3}$M$_\odot$yr^{-1}kpc^{-2}. The high pressures generated by the supernovae are likely to drive winds around these values of the spatial SFR density. Heckman (2001) and Lehnert & Heckman (1996b) suggest the limit above which the SFR produces large scale winds lies around 100 $\times10^{-3}$ M$_\odot$ yr^{-1} kpc^{-2}. Most of our sample lies above this limit (see Figure 7.2). Even though it is not possible to demonstrate that

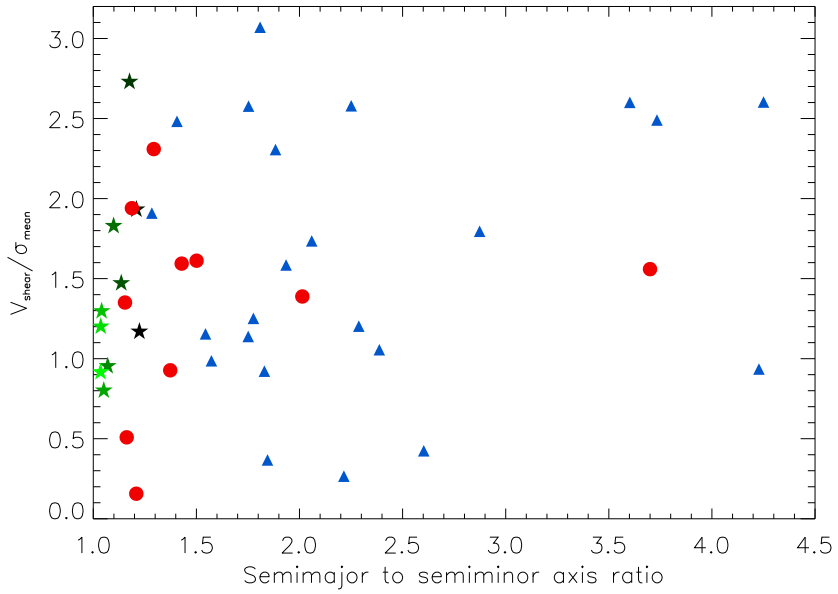

Figure 7.1 Distribution of the v_{shear}/σ_{mean} as a function of the semi-major to semi-minor axis ratio of three samples of objects: The sample presented in this paper appears as red filled circles; the green stars represent analogs of simulations of spiral galaxies in isolation. The shade of the star corresponds to the inclination of observation: the lightest shade corresponds to a face-on observation, while the darkest star corresponds to an edge-on observation; the blue triangles are analogs of simulations of different mergers of the same spiral galaxies, seen from different points of view.

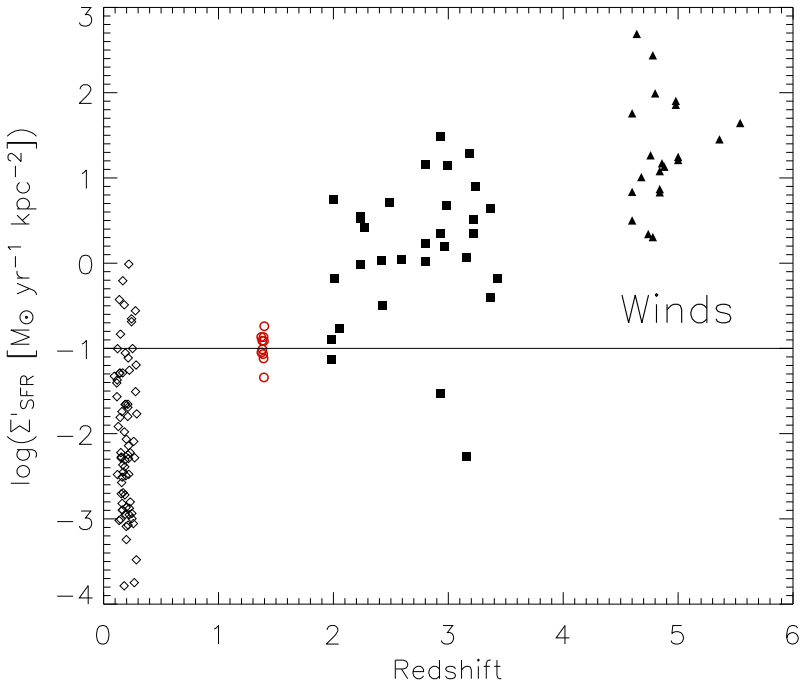

Figure 7.2 We compare the star-formation rate intensities — the rate of star-formation per unit projected area — of this work (red circles), to the z≈5 LBGs (black triangles; Verma et al. 2007), z≈3 LBGs (black squares; Papovich et al. 2001), and a local sample of UV selected galaxies (diamonds; Heckman et al. 2005). The horizontal line indicates the threshold above which local starbursts exhibit large scale outflows (Heckman, 2001; Lehnert & Heckman, 1996b).

all these galaxies are driving winds, the pressure due to the recent and ongoing star formation must play a major role in the galaxy internal kinematics. This is similar to what we have found for other galaxies in our entire sample as discussed in previous chapters.

7.4.4 On the ratio of ionizing continuum to non-ionizing continuum

A way to distinguish between the most massive stars in galaxies is through the ratio of ionizing to non-ionizing photons that are emitted by a sample of stars. Only the most massive stars emit strongly ionizing photons. The Hα luminosity emitted by the ionized hydrogen regions around the most massive stars decreases quickly between 100 and 10 $M_{\odot}$, while on the same range, the FUV luminosity remains quite high. It is therefore possible to link the ratio of the O to B stars to the Hα

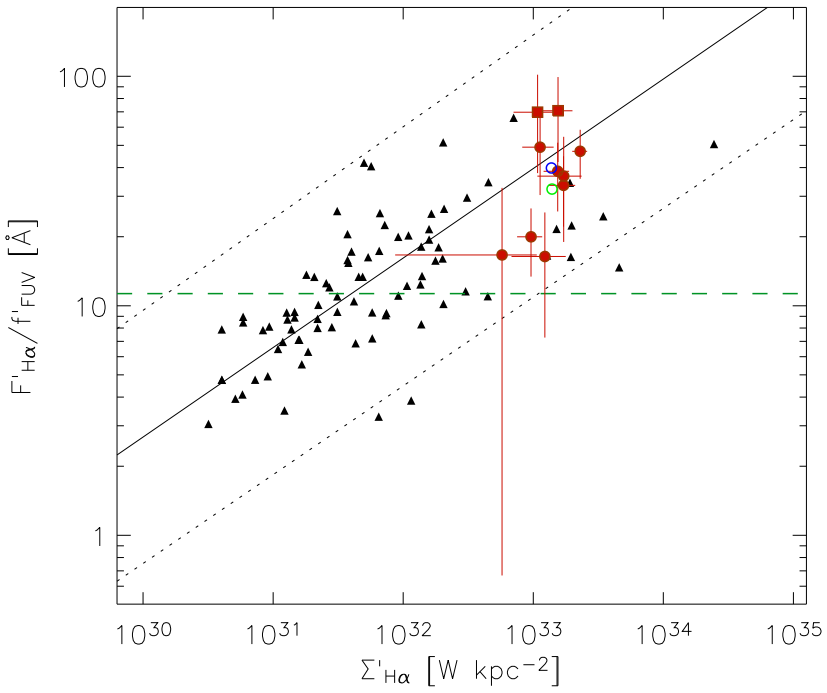

Figure 7.3 The ratio of Hα line flux to FUV flux-density as a function of the Hα effective surface brightness. Black triangles are the local galaxies data from Meurer et al. (2009), red circles are data from this work as well as red squares that represent AGN. The blue and green circles are the mean points for our sample, respectively with and without the AGN. The uncertainties are 3 σ. Galactic and internal dust absorption have not been corrected on this plot. The solid line shows the iteratively clipped least squares fit to the Meurer et al. (2009) data, while the dashed lines show the final clipping limits. The green dashed line is the fiducial value for constant star formation.

line flux to FUV flux-density ratio (for a more detailed analysis, see M09). These quantities are dependent on the IMF upper mass limit and inclination. In the case of a constant SFR we should expect, from the UV and Hα calibrations of SFRs, $F_{H\alpha}/f_{FUV} = 11.3$ for the fiducial model (Kennicutt, 1998b).

From the data derived in Section 7.3.5 and presented in Table 7.3, obtained using our observations as well as DEEP2 measurements, we can derive $F_{H\alpha}/f_{FUV}$ for our sample. The data we obtain, together with the low redshift data from M09 are presented on Figure 7.3 (as a function of the Hα surface brightness) and Figure 7.4 (as a function of the R-band surface brightness). From both figures, we observe that we can extend the local relationship to high redshifts, towards higher Hα and R-band surface brightnesses. The continuum surface brightness is evaluated on the

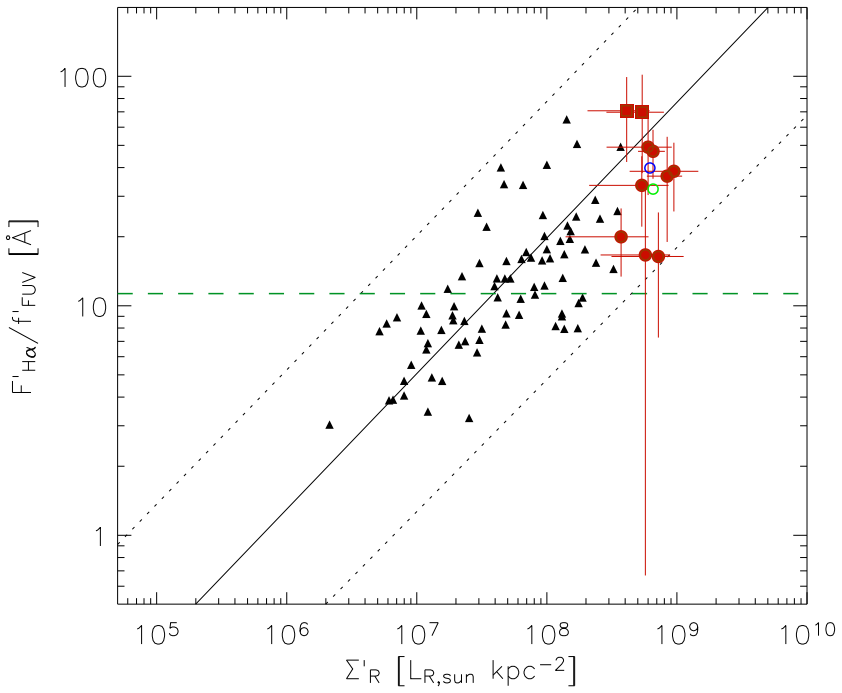

Figure 7.4 The ratio of Hα line flux to FUV flux-density as a function of the R-band effective surface brightness. Black triangles are the local galaxies data from Meurer et al. (2009), red circles are data from this work as well as red squares that represent AGN. The blue and green circles are the mean points for our sample, respectively with and without the AGN. The uncertainties are 3 σ. Galactic and internal dust absorption have not been corrected on this plot. The solid line shows the iteratively clipped least squares fit to the Meurer et al. (2009) data, while the dashed lines show the final clipping limits. The green dashed line is the fiducial value for constant star formation.

brightest regions, where the continuum is resolved enough. This tends to slightly over-evaluate the R-band surface brightness. In this case, our points on Figure 7.4 should move slightly towards lower surface brightnesses, therefore being closer to the mean trend observed on local objects.

What is responsible for the high values of $F_{H\alpha}/f_{FUV}$ we observe? We will now look at the different processes that may explain our measurements. The following study will not take in account the AGN hosts, whose luminosities are dominated by their nucleus and not by their stellar components.

7.4.4.1 Extinction

Unfortunately, we do not have extinction measurements for our sample. The unextincted relationship of M09 seems to be well extended by our data points. This should not change with the extinction, which should vary smoothly towards higher Hα and R-band surface brightnesses. A large differential extinction between our measurements and the "fourth quartile" of M09 (the quartile of highest surface brightness galaxies in M09) is very unlikely. Using M09 fourth quartile extinction, around 0.25 dex towards decreasing $F_{\mathrm{H}\alpha}/f_{\mathrm{FUV}}$, we can estimate the extincted $F_{\mathrm{H}\alpha}/f_{\mathrm{FUV}}$. Results are given in Table 7.3. We obtain two sets of values: a lower bin, composed of objects 32015443, 32029850 and 32015501 whose extincted $F_{\mathrm{H}\alpha}/f_{\mathrm{FUV}}$ lie around 10 Åand a higher bin, composed of objects 32007614, 32013051, 32021394, 32037003 and 32100778 with values around 23 Å. Galaxies in the lower bin follow the fiducial model, but we need to explain why objects in the higher bin do not.

7.4.4.2 Bursty star formation

Could changes in $F_{\mathrm{H}\alpha}/f_{\mathrm{FUV}}$ be due to a rapidly evolving and increasing star formation history? The ratio of Hα flux to FUV flux density is mainly proportional to the relative number of O- and early B-stars (B2–O5) to the number of O- and late B-stars (B9–O2). Obviously, this ratio depends on the age of the stellar population. For constant or declining star-formation rates and ages of ∼100 Myr, $F_{\mathrm{H}\alpha}/f_{\mathrm{FUV}}$ probes the ratio of the relative number of O and B-stars directly and therefore is sensitive to the slope of the high mass initial mass function. Unfortunately, this sensitivity also comes with the proviso that the star-formation history is well-understood and is approximately constant. If the star-formation undergoes a rapid burst then the approximately constant (or declining) criteria is no longer met and the stellar population, essentially the relative number of O-stars compared to B-stars is not fixed by the IMF but by the details of the changing star-formation rate.

Because of this, it is therefore necessary to evaluate the contribution a burst of star-formation can produce. We say burst because it is too time consuming to consider a wide range of star-formation histories, we prefer to make models defined by the amplitude and duration of a burst. That is why we created a range of models using GALAXEV to model the effects of a burst in the star formation history of galaxies. A burst is added to a τ-model (using τ=0.7 Gyr). We also add to this SFH a smaller continuous contribution corresponding to less than 8% of the galaxy total mass at 15 Gyrs. We used a Salpeter IMF extending from 0.1 to 100 $M_{\odot}$, with solar metallicity. We ran our models for a series of varying burst widths and amplitudes. Our bursts FWHM vary between 10 Myr and 3 Gyr. The burst amplitude varies to generate from 1 to 66% of the total mass of the galaxy.

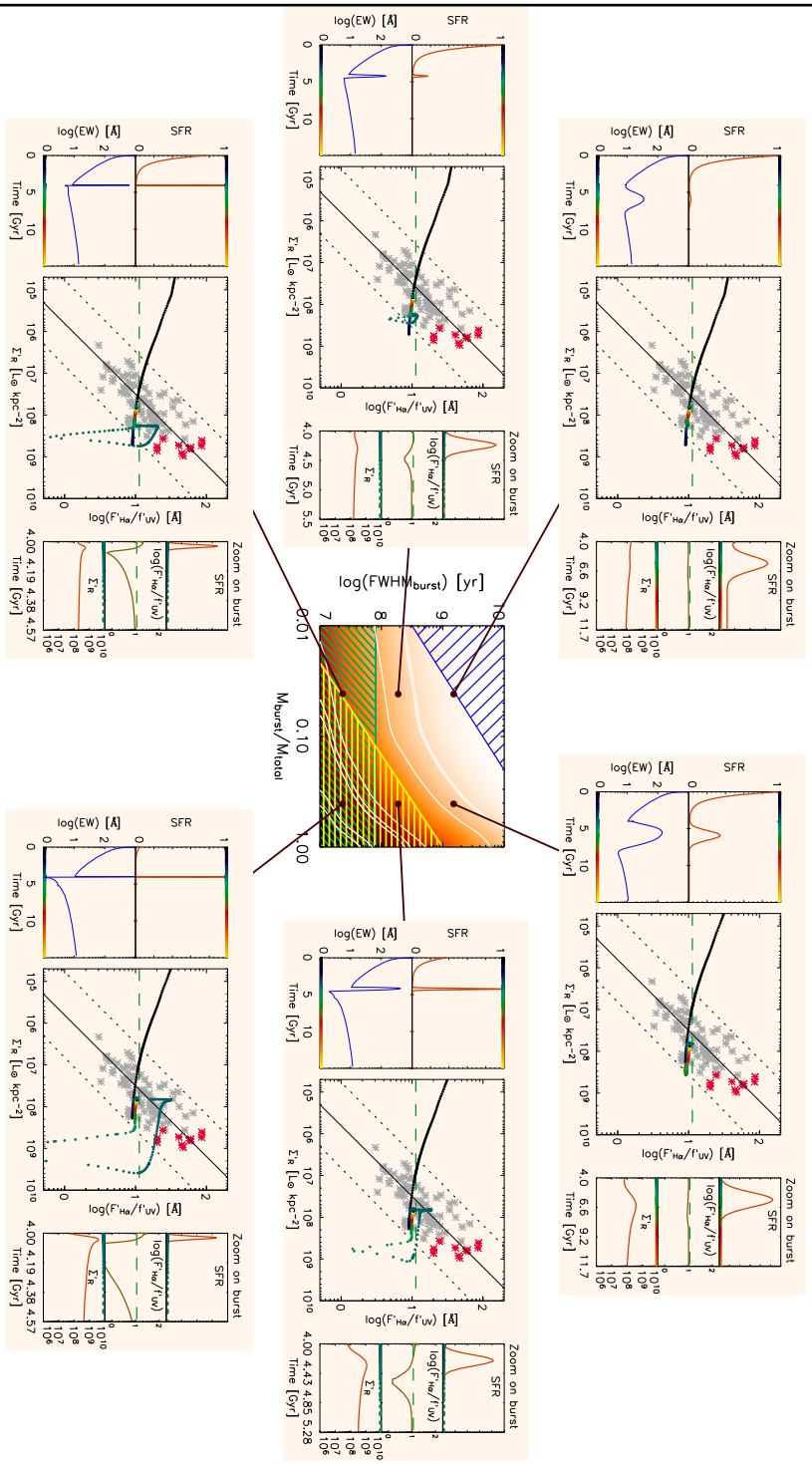

Figure 7.5 Representation of different models used to evaluate the importance of bursty star formation in the ratio $F_{\mathrm{H}\alpha}/f_{\mathrm{FUV}}$. The central panel is the same than Figure 7.6. The 6 outer panels represent the different parameters taken in account for 6 realizations of the bursts. On each of these panels, the center figure is the same that Figure 7.4 (local points in gray, high-redshift points in red, green dashed line is the fiducial value for constant star formation), with a track that represents the positions of the points in time in our model. The color of the track corresponds to the time in the side plots. All side plots are values evolving with time: during 15 billion years on the left: upper-left plot is the normalized star-formation rate; bottom-left plot is the Hα equivalent widths; centered on the burst on the right: upper-right is the normalized star-formation rate, center-right is the $F_{\mathrm{H}\alpha}/f_{\mathrm{FUV}}$ ratio (green dashed line is again the fiducial value for constant star- formation), bottom-right is the R-band surface brightness.

The beginning of the burst is placed at 4 Gyr, which is about the age of our sample. An earlier burst would results in lower $F_{H\alpha}/f_{FUV}$: the more the galaxy has time to acquire mass, the more luminous the R-band flux will be. Therefore values we obtained are higher limits.

The Hα line flux has been computed using the rate of H-ionizing photons N(H^0), output by BC03, using $L_{H\alpha}$=1.36×10^{-12} N(H^0) (Leitherer & Heckman, 1995). The FUV and R-band flux-densities has been obtained from the Spectral Energy Distributions (SEDs) output by BC03.

Figure 7.6 presents the maximal values of $F_{H\alpha}/f_{FUV}$ obtained by covering the parameter space of FHWM and amplitude of the bursts. Darker regions correspond to $F_{H\alpha}/f_{FUV}$ up to 40Å, obtained for strong short bursts, while lighter regions correspond to low $F_{H\alpha}/f_{FUV}$, down to the fiducial model, obtained typically for soft long bursts. The white tracks represent the extincted values of $F_{H\alpha}/f_{FUV}$ obtained for our galaxies. 32015443 and 32029850 have too low values for this plot, and therefore are not shown there. The tinted sectors are the regions of the bursts parameters space which can be ruled out for the following reasons:

- The blue tinted region represents the region in which the computed Hα equivalent widths are too low to explain the ones we observe in our objects.

- The green tinted region represents bursts FWHMs under the mean dynamical time t_{dyn} of our objects. t_{dyn} was calculated from $t_{dyn} = 0.6 \times \frac{\sqrt{A_{H\alpha}/\pi}}{V_{shear}}$, where 0.6 is a factor taking account for the random inclinations of our objects, $A_{H\alpha}$ is the area on which Hα is detected over 3-σ signal-to-noise, and V_{shear} is defined in section 7.3.3. We obtain $t_{dyn} \sim 6.\pm2 \times 10^7$ yr.

- The yellow tinted region represents models where the mean SFR over the whole duration of the burst is greater than 100 $M_\odot$ yr^{-1}. These galaxies already have a large population of old stars, as we can see from the R band fluxes, which means these galaxies are old. Taking a high value of 4Gyrs, for an average mass $< M_* > = 5.6\pm3.0 \times 10^{10} M_\odot$, we obtain an average SFR over time <SFR> = 14±7$M_\odot$ yr^{-1}. The average momentaneous SFR of our sample is $<SFR_t> = 24.\pm14. M_\odot$ yr^{-1}, which gives a present to past averaged SFR b=$<SFR_t>$/<SFR>~ 2. A burst of star formation of average intensity 100 $M_\odot$ yr^{-1}, with values up to 200 $M_\odot$ yr^{-1}, is impossible in the very recent history of these objects.

The largest values of $F_{H\alpha}/f_{FUV}$ observed in some of our objects cannot be explained by a recent burst of star formation. Burst can only explain an increase of a few Å given the already high R-band continuum luminosity.

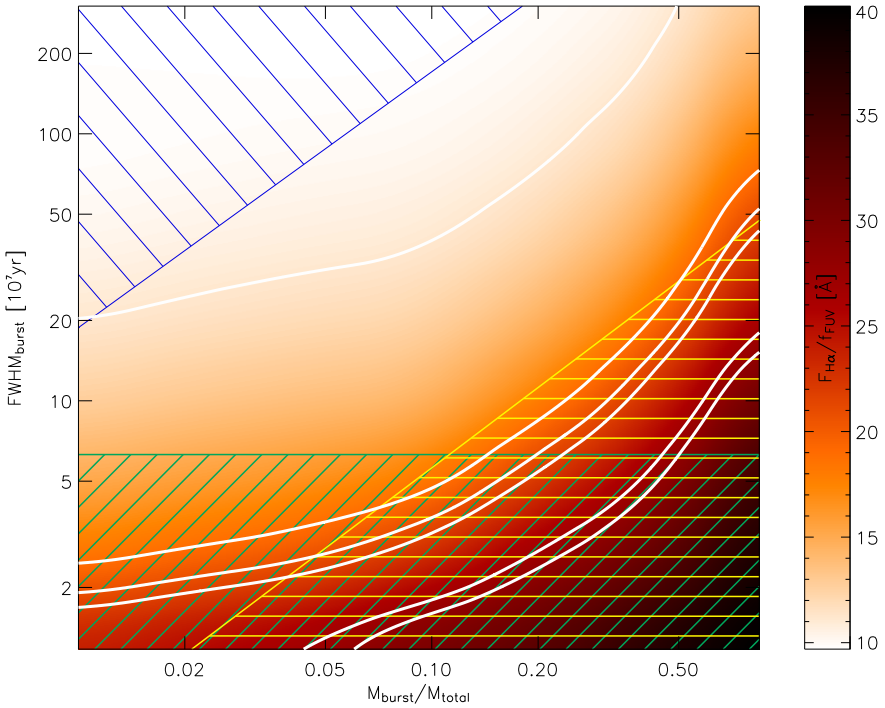

Figure 7.6 Maximal values of $F_{\mathrm{H}\alpha}/f_{\mathrm{FUV}}$ obtained with star formation bursts of variable intensities and variable durations. Higher values correspond to darker shades. The white tracks represent the extincted values of $F_{\mathrm{H}\alpha}/f_{\mathrm{FUV}}$ obtained for our galaxies. *32015443* and *32029850* have too low values for this plot, and therefore are not represented there, as well as AGN hosts. Blue tinted region represents the region in which the computed Hα equivalent widths are too low to explain the ones we observe in our objects. The green tinted region represents bursts FWHMs under the mean dynamical time t_{dyn} of our objects. The yellow tinted region represents models where the mean SFR over the whole duration of the burst is greater than 100 $M_{\odot}\ yr^{-1}$.

7.4.4.3 Metallicity

The local thermal Jeans mass for an isothermal gas, which is considered to play a role in setting the characteristic mass scale for the initial mass function is proportional to $T^{3/2}n^{-1/2}$, where T and n are the temperature and gas density. It is not clear if the extreme conditions we observe in these distant galaxies would tend to increase or decrease the characteristic mass. To first order, we observe generally higher densities which would favor the formation of low mass stars. On the other hand, the metallicity may be overall lower which would tend to increase the temperature of the gas and the radiation field is likely to be more intense, further increasing the gas temperature. Elmegreen et al. (2008b) have argued that there is only a weak dependence of the characteristic mass of sthe IMF on intensity of the radiation field (likely to be high in our galaxies), density (also likely to be high), column density (also likely to be high), or metallicity (which is likely not quite solar, e.g. at $z \sim 2$: **?**, between $z \sim 4$ and $z \sim 4$: Rodrigues et al. (2008)). Our modeling with BC03 has mostly been done assuming a solar metalicity ($Z_\odot$=0.02), but also with other sub solar values (Z = 0.2 $Z_\odot$, Z=0.4 $Z_\odot$) and super solar (Z=2.5$Z_\odot$). There was no significant changes with these values: whatever the metallicity we used, the maximum values of $F_{H\alpha}/f_{FUV}$ never rose more than 4 Å. Only extremely low values of the metallicities could be resulting in a significant change in $F_{H\alpha}/f_{FUV}$ but these values of the metallicity are ruled out by the previous studies on mass-metallicity relation in high redshift galaxies.

7.4.4.4 IMF slope and upper mass limit

The previous explanations are not sufficient to explain the higher values of $F_{H\alpha}/f_{FUV}$ we measure. The most favorable explanation, with star formation bursts, can explain values up to $\sim$ 18 Å, 10 Åbeyond our higher values. A last possibility would be to suggest a variable IMF upper-end, which would create more O stars relatively to lower mass stars. This could be a higher upper-mass as well as a flatter slope.

To study the impact of varying high-end of the IMF, we used Starburst99 from Leitherer et al. (1999) and built synthesis models for a Salpeter IMF with varying slopes from γ= 1.25 to 3, and upper-masses from M = 60 –120 $M_\odot$. We present our results for a constant SFR after 100 Myr and 1 Gyr, enough to reach an equilibrium state. These results are presented in Figure 7.8 for a varying slope and Figure 7.7 for a varying upper mass limit. Unfortunately, there is no model for stars with masses higher than 120 $M_\odot$, which could however be present in these galaxies. A higher upper-mass limit, as well as a flatter slope, could explain an increase of $F_{H\alpha}/f_{FUV}$. From works on Galactic Field IMF (IGIMF) ((Kroupa & Weidner, 2003)), we would expect a steeper slope ($\gamma \geq 2.8$) at the high-end of the IMF. The

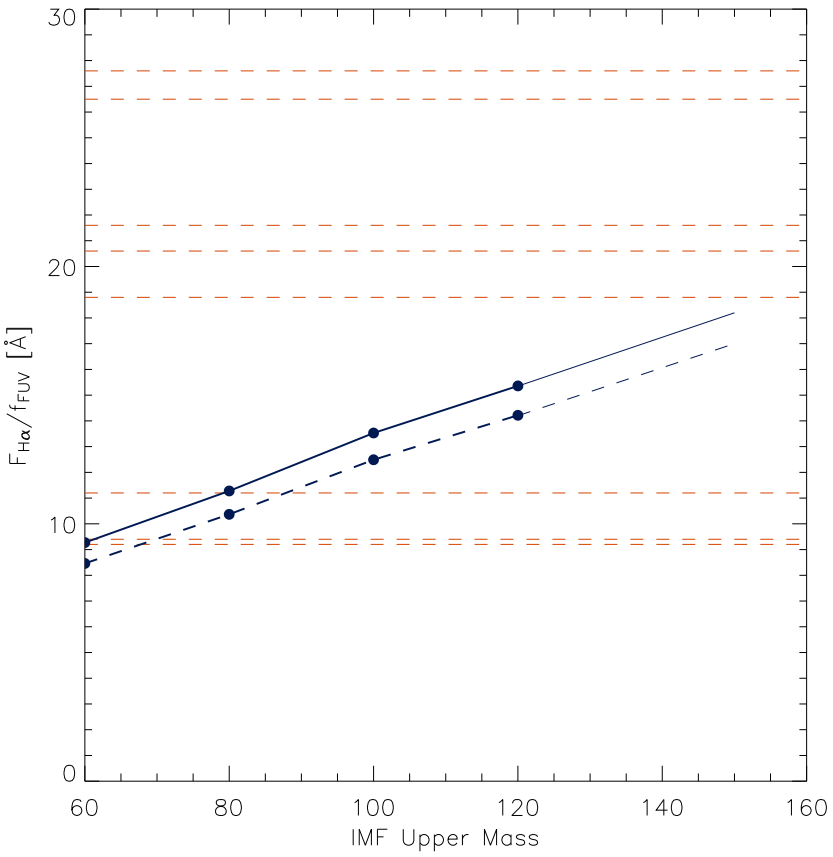

Figure 7.7 $F_{\mathrm{H}\alpha}/f_{\mathrm{FUV}}$ obtained for a constant SFR of 100 Myr (dashed line) and 1 Gyr (plain line), for different values of the IMF upper mass. These values have been modeled until 120 $\mathrm{M}_{\odot}$. The thiner lines are extrapolations. Horizontal dashed lines represent the extinction corrected values of $F_{\mathrm{H}\alpha}/f_{\mathrm{FUV}}$ for our sample.

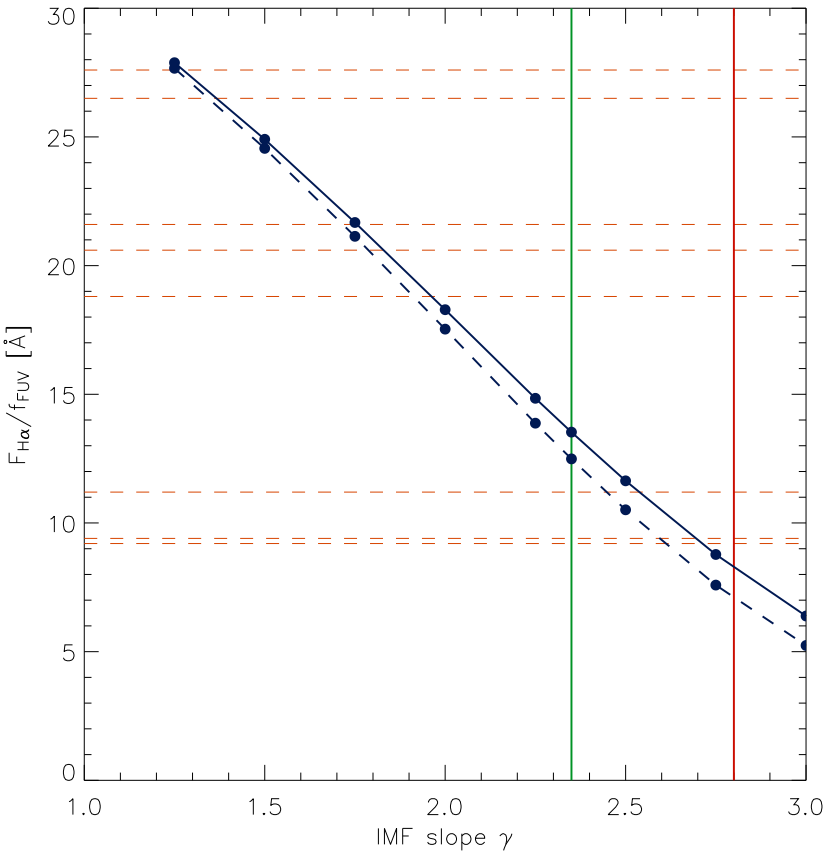

Figure 7.8 $F_{\mathrm{H}\alpha}/f_{\mathrm{FUV}}$ obtained for a constant SFR of 100 Myr (dashed line) and 1 Gyr (plain line), for different values of the slope of the IMF. The vertical green line is the Salpeter IMF slope, the vertical red line is the Kroupa IGIMF slope. Horizontal dashed lines represent the extinction corrected values of $F_{\mathrm{H}\alpha}/f_{\mathrm{FUV}}$ for our sample.

flatter slope we expect may be due to the size of the area of high star formation rate, conditions that differ strongly from the typical clusters observed in the local universe, integrated in the works on IGIMF.

7.4.4.5 Other limitations

Both the porosity of the ISM and the stochastic variations in the IMF have been studied in M09. They conclude that they likely do not have a strong influence on the observed values of $F_{\mathrm{H}\alpha}/f_{\mathrm{FUV}}$. Moreover, stochastic variations in the IMF are likely to result in fewer O stars. Few O stars should then decrease $F_{\mathrm{H}\alpha}/f_{\mathrm{FUV}}$ and therefore cannot explain the continuity we find between the low and high redshift

data sets. However, such an explanation may be appropriate for the results of Lee et al. (2009) which show that there may be a relative deficit of Hα relative to the UV in low mass galaxies.

7.5 The Meurer relations and Interstellar pressure

What is interesting about the findings of M09 is that they relate not the total mass to the ratio of $F_{\mathrm{H}\alpha}/f_{\mathrm{FUV}}$ but the surface brightness of both Hα and the R band. The interstellar mid-plane pressure, if the galaxy is in hydrostatic equilibrium, is $\mathrm{P_{hydro}} = \pi \mathrm{G} \Sigma_{\mathrm{gas}} \Sigma_{\mathrm{total}}$. Both the surface brightness of the FUV emission and the R-band surface brightness are related to the stellar mass surface densities (modulo the extinction). The constant of proportionality is given by the star-formation history of the stellar population. The surface brightness of Hα is dependent on the pressure of the ISM as well as on the ionization parameter (proportional to the ratio of the intensity of the radiation field divided by density of ionized gas).

As part of our analysis in previous chapters, we have generated a series of model results on photoionized clouds using the publicly available code Cloudy (Ferland et al., 1998). We modeled the data as photo-ionized clouds. For this we used an ionizing spectrum of a young (10^8 yr) stellar population forming stars at a constant rate with a Salpeter IMF (Leitherer et al., 1999) and a range of column (10^{19} to 10^{21} cm^{-2} in steps of factors of 10), volume densities (0.1-1000 cm^{-3} in steps of factors of 10), and ionization parameters (log U$\sim$ -5 to 0 again in steps of factors of 10). For the results of the models that were not density bounded (meaning that the photons passed through the clouds), we fitted a plane in the 3D space modeled. For this, we find that the surface brightness of Hα, $\mathrm{SB_{H\alpha}}$ is proportional to $\mathrm{n}^{0.93}$ $\mathrm{U}^{0.80}$.

Since we know that the surface brightness of Hα is controlled not only by the rate at which stars form, but also by the density and distribution of the gas relative to the ionizing field, we might expect $F_{\mathrm{H}\alpha}/f_{\mathrm{FUV}}$ to show a similar complex behavior too. For the moment, let us isolate the dependence on the Hα SB to only include the density. If the total far-UV flux density can be related as $\mathrm{f}_{FUV} = 2\pi \mathrm{r}_e^2 \, \Sigma_{FUV} \propto 2\pi \mathrm{r}_e^2 \, \Sigma_\star$ (where $\Sigma_\star$ is the average stellar surface density within r_e) and similarly, $\mathrm{f}_{\mathrm{H}\alpha} = 2\pi \mathrm{r}_e^2 \, \Sigma_{\mathrm{H}\alpha}$, then $F_{\mathrm{H}\alpha}/f_{\mathrm{FUV}} \propto \Sigma_{\mathrm{H}\alpha}/\Sigma_\star$. If we suppose that the gas fractions of these galaxies is relatively small and the total mass surface density is dominated by the stellar mass surface density, then $F_{\mathrm{H}\alpha}/f_{\mathrm{FUV}} \propto \Sigma_{\mathrm{H}\alpha}/\Sigma_{\mathrm{total}}$. Using both hydrostatic equilibrium and our relationship between the Hα SB and the density (or pressure assuming approximately constant temperatures) yields, $F_{\mathrm{H}\alpha}/f_{\mathrm{FUV}} \propto \mathrm{P}^{0.43}$. If we plot the relationship between $F_{\mathrm{H}\alpha}/f_{\mathrm{FUV}}$ and $\Sigma_{\mathrm{H}\alpha}$ as a function of the pressure and ionization we actually find a good agreement (Fig. 7.9). The models have been scaled so that log U=-2 and log n = 0, log $F_{\mathrm{H}\alpha}/f_{\mathrm{FUV}}$ = 1.04 (the equi-

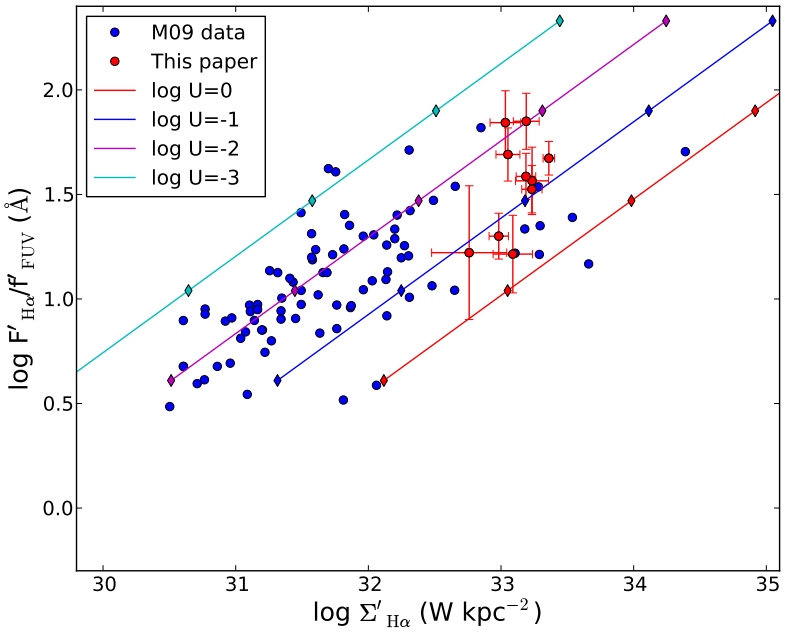

Figure 7.9 We now show the same data as in Fig. 7.3, where the blue circles are the data from M09, while the red circles with error bars represent our sample. Superimposed are lines of constant ionization parameter as given in the legend for a range of densities in the logarithm ranging from -1 to 3 (lower left to upper right along each line with the colored diamonds representing each density in steps of one in the logarithm). See text for details.

librium value of $F_{\mathrm{H}\alpha}/f_{\mathrm{FUV}}$ from M09 when the star-formation is constant and these values of log U and log n where chosen to roughly match values from the typical diffuse interstellar media in nearby galaxies).

Explaining the data for nearby and our more distant galaxies in the Σ_R–$F_{\mathrm{H}\alpha}/f_{\mathrm{FUV}}$ plane is somewhat more difficult. Again, assuming hydrostatic equilibrium and that the gas fractions in this galaxies is small (<0.2 or so) leads to a relationship $F_{\mathrm{H}\alpha}/f_{\mathrm{FUV}} \propto (\Sigma_\star \Sigma_{gas})^{0.43}$. This complicates this argument simply because there is likely a complex relationship between the gas and total mass surface densities, $\Sigma_{\mathrm{H}\alpha}$, the distribution and filling factor of HII regions, and the overall pressure. Without more information, we cannot solve for these uniquely. There are two hypotheses we can make to remove some of the complexity in resolving the relationship between these quantities. We could suppose first that Σ_{gas} is not a strong function of $\Sigma_\star$. However, this seems unlikely. The sample of M09 is HI selected and thus is likely gas-rich compared to the ensemble of galaxies and is late-type generally (see M09). This being the case, these galaxies probably have gas fractions which are still small, but at the upper end of the local galaxy distribution, and therefore would likely have increasing Σ_{gas} with $\Sigma_\star$. The other possibility is the relationship between the stellar mass surface density and the conversion between $\Sigma_\star$ and Σ_R is a function of both $\Sigma_\star$ and Σ_{gas}. This could come about if relatively gas rich galaxies had on average a younger stellar population which would tend to move then to the right and upwards in the Σ_R–$F_{\mathrm{H}\alpha}/f_{\mathrm{FUV}}$ plane for constant stellar mass surface density. If we scale the relationship such that the local MW gas and stellar surface densities give the equilibrium value of M09 (namely, 11.06), then we also find a good fit to the data (Fig. 7.10).

Scaling $F_{\mathrm{H}\alpha}/f_{\mathrm{FUV}}$ is perhaps also telling us something about the way the star-formation and pressure in galaxies is related. While we have not attempted to fully model these relationships in any complete way — that will take more time and better data to constraint the various parameters within our simple scaling relations — we have shown that the pressure and gas surface densities should be considered before suggesting that such relationships as that between $F_{\mathrm{H}\alpha}/f_{\mathrm{FUV}}$ and Σ_R and $\Sigma_{\mathrm{H}\alpha}$ are related only to the star-formation history or the IMF. Only through a complete modeling of the properties of the ISM can the conclusion as to the ultimate underlying cause or causes of these relations be understood.

7.6 Preliminary Conclusions of this Perspective

Our analysis of integral field spectroscopic data with SINFONI on the ESO/VLT and DEEP2 redshift Survey of our sample of z∼1.38 galaxies have revealed a number of interesting properties and relationships.

(1) These galaxies exhibit complex morphologies and disturbed velocity fields.

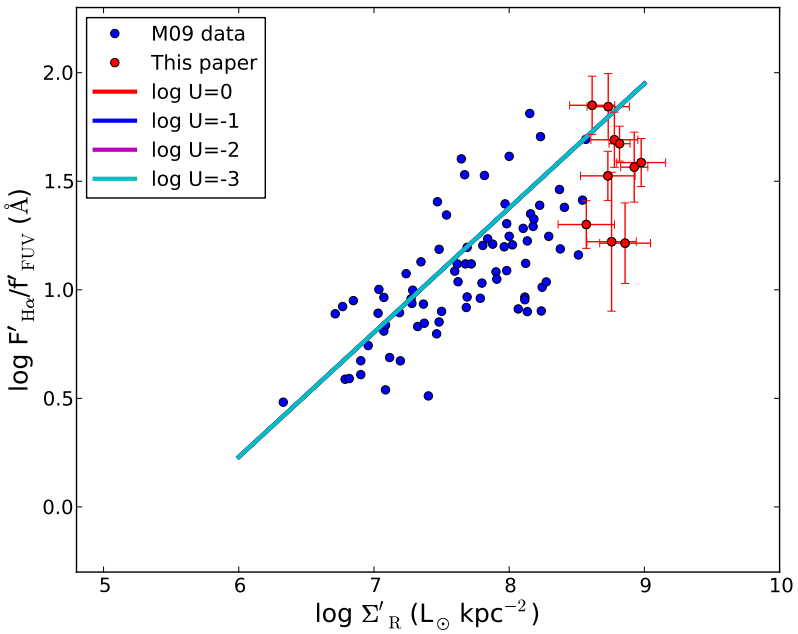

Figure 7.10 We now show the same data as in Fig. 7.4, where the blue circles are the data from M09, while the red circles with error bars represent our sample. Superimposed is the relationship between $F_{\mathrm{H}\alpha}/f_{\mathrm{FUV}}$ and Σ_R with a scaling appropriate for log Σ_R=7.42 (which is appropriate value for the solar neighborhood assuming an M/L=1 for the R-band and $F_{\mathrm{H}\alpha}/f_{\mathrm{FUV}}$ =11.06, the equilibrium value from M09). See text for details.

Line ratios and linewidths suggest that two of these objects host AGN.
(2) We measure low projected v/σ that indicates a strong conponent of random motions in these objects. Overall, these galaxies have v/σ and axial ratios consistent with merger models when scaled to the appropriate resolution of our data. This does not suggest that they are mergers given our ignorance of all the process that could disturb the kinematics of distant galaxies.
(3) Neither the models or local mergers show surface brightnesses as high as we observe over large (10 Kpc) scales. We suggest this is due to the ISM reaching generally higher densities in the optical emission line gas (likely due to strong compression of the high turbulence; see Lehnert et al., 2009) and possibly the addition ionization rate to a flatter IMF. The last of these is obviously more speculative.
(4) Our measurements of the SFR surface densities suggests these objects are likely to drive winds, or at least, must be subject to high pressures from the SN explosions.
(5) The addition of high redshift data to the local relation between $F_{\mathrm{H}\alpha}/f_{\mathrm{FUV}}$ and R-band and Hα surface luminosity from M09 provides new insight into the underlying processes producing it. Our measurements reach higher values in both the R-band and Hα surface luminosities and thus extend these relations to more extreme galaxies. This may suggest that these galaxies have generally higher internal pressures as already suggested by the high dispersions and high star formation intensities they exhibit. A bursty star formation rate, as well as systematic changes in the metallicity, seems to be unable to explain these values. It may be that a shallower IMF is necessary to explain the high values of $F_{\mathrm{H}\alpha}/f_{\mathrm{FUV}}$ that some galaxies, especially in our sample, reach for their given Hα or R-band surface brightnesses.
(6) Alternatively, we show, somewhat crudely, that it is also possible that pressure and ionization effects may also explain the relationships between $F_{\mathrm{H}\alpha}/f_{\mathrm{FUV}}$ and Hα and R-band surface luminosities. To explain the relationship and the range of scatter in each of these diagrams a variation in the ionization parameter, relative gas surface densities, and gas densities. In terms of the locations of galaxies within each of these diagrams, galaxies with relatively low $F_{\mathrm{H}\alpha}/f_{\mathrm{FUV}}$, $\Sigma_{\mathrm{H}\alpha}$, and Σ_R would have lower gas mass surface densities, stellar mass surface densities, and densities or pressures than galaxies with higher $F_{\mathrm{H}\alpha}/f_{\mathrm{FUV}}$, $\Sigma_{\mathrm{H}\alpha}$, and Σ_R. This naturally follows on from assuming hydrostatic pressure equilibrium and that both the Σ_R and Σ_{FUV} are related to the stellar mass surface densities. All of these assumptions are reasonable.

However, this chapter is intended to only open up new questions and is not meant to be definitive. Much more work is needed as we will outline in the next section.

Object	Int time	Line	z	$\sigma_{\rm line}$	F′	SB limit	$r_{\rm iso}$	$V_{\rm shear}$	$\sigma_{\rm mean}$	$V_{\rm shear}/\sigma_{\rm mean}$	a/b
(1)	(2)	(3)	(4)	(5)	(6)	(7)	(8)	(9)	(10)	(11)	(12)
32007614 †	5400	Hα	1.3716±0.0011	142± 17	1.79±0.22	6.9	3.9	18.	114.	0.2	1.2
···		[NII]	1.3718±0.0010	100± 14	0.56±0.07	···	···				
32013051	5400	Hα	1.3950±0.0011	118± 9	2.45±0.18	2.8	7.7	66.	130.	0.5	1.2
···		[NII]	1.3951±0.0011	124± 16	1.57±0.19	···	···				
32015443	6600	Hα	1.3822±0.0009	85± 13	1.47±0.22	6.0	6.7	152.	109.	1.4	2.0
···		[NII]	1.3824±0.0009	83± 28	0.54±0.18	···	···				
32015501	10800	Hα	1.3919±0.0007	57± 5	2.47±0.18	3.8	9.8	87.	64.	1.4	1.2
···		[NII]	1.3921±0.0006	31± 12	0.38±0.14	···	···				
32021317*	5400	Hα	1.3814±0.0016	196± 19	2.88±0.28	4.3	8.3	201.	216.	0.9	1.4
···		[NII]	1.3821±0.0028	350± 39	3.36±0.37	···	···				
32021394	5400	Hα	1.3735±0.0009	92± 9	2.78±0.25	4.0	9.5	205.	89.	2.3	1.3
···		[NII]	1.3753±0.0013	156± 34	1.29±0.27	···	···				
32029850 †	6600	Hα	1.3952±0.0009	81± 23	0.39±0.11	3.6	2.5	99.	62.	1.6	1.4
···		[NII]	1.3961±0.0010	110± 40	0.10±0.03	···	···				
32037003	5400	Hα	1.3985±0.0014	157± 7	5.50±0.24	3.6	9.6	189.	97.	1.9	1.2
···		[NII]	1.3987±0.0010	101± 14	1.39±0.19	···	···				
32002481*	6600	Hα	1.3880±0.0014	155± 19	2.76±0.32	2.5	9.8	270.	173.	1.6	3.7
···		[NII]	1.3897±0.0017	208± 65	1.20±0.37	···	···				
32100778	6600	Hα	1.3918±0.0006	41± 4	3.54±0.27	3.9	8.8	72.	45.	1.6	1.5
···		[NII]	1.3919±0.0007	59± 14	1.36±0.31	···	···				

Table 7.1 Column (1) — Object designation (DEEP2 catalog number). Column (2) — Integration time in seconds. Column (3) — Line identification. Column (4) — Redshift of the line in the integrated spectrum. By integrated spectrum, we mean the sum of the flux from each pixel with a signal-to-noise greater than or equal to 3 in each data cube for Hα (see column 7 for this limiting value for Hα). All of the sums for the other emission lines are over the same aperture as for Hα. Column (5) — Dispersion of the integrated spectrum of each galaxy, corrected for instrumental resolution and in units of km s^{-1}. Column (6) — Line flux of the integrated spectrum in units of 10^{-16} erg s^{-1} cm^{-2}, not corrected for extinction. Column (7) — Surface brightness detection limit in units of 10^{-19} erg s^{-1} cm^{-2} and defined at a signal to noise ratio S/N≈3. This is for a pixel that has been averaged over a 3x3 pixel region. Column (8) — The isophotal radius is defined as $A_{iso}= \pi\ r_{iso}^2$ where A_{iso}, the isophotal radius, is defined as the projected area on the sky above a significance of 3-σ in the data and is in units of kpc. The Hα line widths and fluxes of these objects have been derived using integration over the continuum 3-σ detection area. Column (9) — Hα velocity shear $V_{\rm shear}$ in units of km s^{-1}. Column (10) — Hα mean dispersion $\Sigma'_{\rm mean}$ in units of km s^{-1}. Column (11) — $V_{\rm shear}/\sigma_{\rm mean}$. Column (12) — Semi-major to semi-minor axis ratios estimated using the lowest detected isophot (column 7). *Objects hosting AGN. †Hα line fluxes derived by integration over the continuum 3-σ detection aperture, instead of the Hα spatial detection.

Object	f'_{H-band}	W	$L'_{H\alpha}$	SFR	$A_{int,H\alpha}$	Σ'_{SFR}
(1)	(2)	(3)	(4)	(5)	(6)	(7)
32007614 †	16.2±1.6	31.±7.	2.0 ±0.3	16±2	119.	13.6±1.7
32013051	16.2±2.9	51.±13.	2.9 ±0.2	23±2	189.	12.3±0.9
32015443	5.7±1.0	26.±9.	1.7 ±0.3	14±2	140.	9.7±1.4
32015501	6.2±1.3	65.±19.	2.9 ±0.2	23±2	304.	7.6±0.6
32021317 *	11.6±1.9	113.±29.	3.4 ±0.3	27±3	216.	12.5±1.2
32021394	21.1±3.6	37.±10.	3.2 ±0.3	25±2	282.	9.0±0.8
32029850 †	7.1±1.3	22.±11.	0.47±0.13	4±1	81.	4.5±1.3
32037003	12.1±1.0	47.±6.	6.6 ±0.3	52±2	288.	18.1±0.8
32002481 *	6.2±1.0	47.±15.	3.2 ±0.4	26±3	302.	8.5±1.0
32100778	8.0±1.6	75.±21.	4.2 ±0.3	33±3	245.	13.6±1.0

Table 7.2 Column (1) — Object designation (DEEP2 catalog number). Column (2) — H-band flux density in units of 10^{-19} erg s^{-1} cm^{-2} Å^{-1}. The estimate was made by averaging the continuum over the band pass (removing spectral regions severely affected by night sky line emission), centered on ∼1.65 μm or about 6900 Å in the rest frame. Column (3) — Integrated Hα equivalent width of the object in Å. The Hα flux used here is integrated only over the pixels having a continuum detection over 3 σ. Column (4) — Hα effective luminosity in units of 10^{42} erg s^{-1}. Column (5) — Star-formation rate estimated from the total integrated Hα flux for each source in $M_\odot$ yr^{-1}. Column (6) — Aperture on which Hα has been integrated in kpc^2: for most objects, it corresponds to the Hα detection, except for objects having the smallest spatial extend, marked †, where the continuum 3-σ detection area is used for the integration. Column (7) — Star-formation rate surface density in units of 10^{-2} $M_\odot$ yr^{-1} kpc^{-2}. The symbol * signifies the object hosts an AGN.

Object	$\Sigma_{H\alpha}$	mag_B	f'_{FUV}	f'_{H-band}	L'_R	Σ'_R	A_R	$A_{H\alpha}$	$F'_{H\alpha}/f'_{FUV}$	$F_{H\alpha}/f_{FUV}$
(1)	(2)	(3)	(4)	(5)	(6)	(7)	(8)	(9)	(10)	(11)
32007614 †	1.71±0.21	24.02	5.0±0.2	16.2±1.6	10.0±1.0	8.4±0.8	119.	48.	37.±6.	21.±3.
32013051	1.55±0.11	23.72	6.6±0.3	16.2±2.9	10.6±1.9	9.4±1.7	111.	189.	39.±4.	22.±2.
32015443	1.21±0.18	23.34	9.4±0.4	5.7±1.0	3.6±0.7	7.2±1.4	50.	140.	16.±3.	9.±2.
32015501	0.96±0.07	23.00	12.8±0.5	6.2±1.3	4.1±0.8	3.7±0.7	109.	304.	20.±2.	11.±1.
32021317 *	1.56±0.15	24.21	4.2±0.2	11.6±1.9	7.3±1.2	4.1±0.7	178.	216.	71.±9.	40.±5.
32021394	1.13±0.10	23.86	5.9±0.3	21.1±3.6	13.1±2.3	6.0±1.0	218.	282.	49.±6.	28.±4.
32029850 †	0.58±0.16	24.79	2.5±0.1	7.2±1.3	4.7±0.8	5.7±1.0	81.	20.	17.±5.	9.±3.
32037003	2.29±0.10	23.05	12.1±0.5	12.1±1.0	7.9±0.6	6.6±0.6	121.	288.	47.±4.	26.±2.
32002481 *	1.08±0.12	24.23	4.1±0.2	6.2±1.0	4.0±0.6	5.4±0.8	74.	302.	70.±11.	39.±6.
32100778	1.71±0.13	23.16	11.0±0.4	8.0±1.6	5.1±1.0	5.4±1.1	96.	245.	33.±4.	19.±2.
							Mean values[a]			
							Whole sample	39.9±20.	22.4±11.	
							Without AGN	32.3±13.	18.1±7.	

Table 7.3 Column (1) — Object designation (DEEP2 catalog number). Column (2) — Hα surface brightness in units of 10^{33} W kpc^{-2}. Column (3) — AB magnitude in the B band from the DEEP2 catalog. Uncertainties are for all measurements ±0.04 dex. Column (4) — Far-UV flux density in units of 10^{-19} erg s^{-1} cm^{-2} Å^{-1}. Column (5) — H band flux density in units of 10^{-19} erg s^{-1} cm^{-2} Å^{-1}. The estimate was made by averaging the continuum over the band pass (removing spectral regions severely affected by night sky line emission), centered on ∼1.65 μm or about 6900 Å in the rest frame. Column (6) — R band total luminosity in units of 10^{10} solar luminosities in the R band, using $L_{R,\odot}$=4.39×10^{22} W Å^{-1}. Column (7) — R band surface brightness in units of 10^8 $L_\odot$ kpc^{-2}. Column (8) — Area on which the R band has been integrated (3-σ detection) in kpc^2. Column (9) — Area on which Hα has been detected (3-σ detection) in kpc^2. Column (10) — $F'_{H\alpha}/f'_{FUV}$ in Å, unextincted, with 1-σ uncertainties. Column (11) — $F_{H\alpha}/f_{FUV}$ in Å, extincted by 0.25 dex, with 1-σ uncertainties. [a]Uncertainties for the mean values are the standard deviation of the measurements. *Objects hosting AGN. †Hα line fluxes derived by integration over the continuum 3-σ detection aperture, instead of the Hα spatial detection.

Chapter 8

Conclusions and perspectives

Contents

8.1 Conclusions

This thesis presents the analysis of a sample of 53 galaxies at z∼1.3–2.7 observed with the integral-field spectroscopy unit SINFONI on ESO/VLT. These galaxies have surface brightnesses that are more than an order of magnitude larger than those of local disks. These observations suggest that their ISM is likely dominated by the intense star-formation taking place over large scales (∼10-20 kpc). The high optical emission line surface brightnesses are likely are likely a selection or "publication" bias in that they must have high surface brightness galaxies in order to be spatially resolved and detected at high significance in a few hour integration with current integral-field units. Only galaxies that have such surface brightnesses will yield interesting data and thus get published or even observed. This problem or bias is largely an effect of the strong cosmological surface brightness dimming ($[1+z]^4$).

Gas accretion has often been suggested as a viable mechanism for driving the ionized gas line dispersions of high redshift galaxies, among other things (likely clumpiness of the galaxies, the perhaps large fraction of disks, etc.). We showed that the mass accretion rate as well as the energy injection would have to be much higher than expected from simulations or from simply equating the star formation with the accretion rate to explain the high Hα surface brightnesses we observe in high-redshift galaxies. The surface brightness detection limit which is required to detect the effects of gas accretion is about an order of magnitude lower than what is achieved with current near-infrared integral-field units. Because it is difficult to build integral field spectrographs with large areal areas on the sky, even with an IFU on a 40-m class telescope, it is still unlikely that we will reach the surface brightnesses necessary to detect the direct effects of cosmological accretion in the optical emission line gas.

We suggest that star-formation plays a key role in the dynamics, ionization, and other characteristics of the warm ionized medium: the observed trend between the star- formation intensity and the velocity dispersion of the emission line gas can be modeled by a simple energy injection relationship of the form $\sigma \propto \Sigma_{\rm SFR}^{1/2}$. By combining this simple scaling relationship with a Toomre instability analysis, we conclude that star-formation may be balancing subsequent star-formation by setting the Toomre Q-parameter to about one and thus making the galaxy critically unstable against star-formation.

Using a stacking analysis, we demonstrate that these distant galaxies have high ISM pressures and these pressures are sufficiently high to drive vigorous outflows and strong turbulence, at least at the highest Hα surface brightnesses. These characteristics are similar to intense starbursts found in the nearby universe. This leads to a picture where the pressure in the ISM is determined by the intensity of the star-formation and where feedback sets the scaling between pressure and star-formation intensity. This is another piece of evidence in favor of star-formation being self-regulating, as pressure is being regulated by the star-formation and pressure likely determines the nature of star-formation. This is star-formation feedback.

Observations of galaxies in the lower redshift galaxies in our sample exhibit generally lower rest-frame Hα surface brightnesses. This sub-sample has ISM pressures that are a factor of 10-100 lower than the high redshift sample, but still higher than typical disks in the local universe. Because of the effect of beam smearing, these galaxies may have dispersions that are well below our resolution ($\sim$50 km s^{-1}) and in fact may be similar to nearby disk galaxies or the Milky-Way ($\sim$10 km s^{-1}). This may imply that it is a more promising avenue to observe galaxies at more moderate redshifts, say z<1.5, where the impact of cosmological surface brightness dimming is less severe and allow us to probe galaxies that are more like nearby spirals.

8.2 Perspectives for future work related to this thesis

This thesis leaves a number of outstanding issues, completely open, and these may be interesting to pursue in future work. Our analysis points towards what may be interesting differences in the processes that control the physics of the ISM in galaxies at redshift $\sim$1.4 compared to galaxies at $\sim$2.2. While the latter are in a regime where there ISM are dominated by very intense star-formation dominated, galaxies at more moderate redshifts, z$\sim$1-1.5, may be entering a regime where gravitational processes also become a competitive driver of large scale internal motions and turbulence. Probing lower mass galaxies at z$\sim$2.2, where there star-formation intensity may be less, and observing more galaxies at lower redshift is an interesting step to understand how the mixture of underlying physics that

dominates their ISM – i.e., between star-formation and gravity dominated regimes. In galaxies around z=1.4, the effect of beam smearing is large compared to the observed velocity dispersions. Adaptive optics assisted observations, although they do not probe the same range of surface brightnesses as non-AO observations, are necessary to quantify the relative distribution of velocity dispersions in the ionized gas in these objects and therefore to study the transition phase between these two regimes. In addition, in some rare cases, with long integration times, it may be possible to get some information about the dispersions of the stellar component. This comparison would allow us to make significant progress in understanding the nature and underlying processes driving the dynamics we observe.

In the perspectives chapter (Chapter 7), we emphasized a relationship between $F_{\mathrm{H}\alpha}/f_{\mathrm{FUV}}$ and Hα or R-band surface brightnesses, followed by local galaxies but also by z=1.4 massive objects. Can we extend this relationship to higher redshifts and higher average Hα surface brightnesses? Will this relationship stay linear? Is there a limit in Hα surface brightness for which it will saturate? These results are sensitive to the star-formation history and especially to recent bursts of star-formation: a larger set of photometric measurements may better constrain the star-formation histories of these objects and rule-out the impact of bursts. Testing the validity of integrated-light methods for reconstructing star-formation histories, as it has been done for stellar clusters but not over complex objects such as galaxies may be necessary to critically evaluate their accuracy.

Is there a relationship between the dynamics of the galaxies and their position on the $\Sigma_{\mathrm{H}\alpha}$–$F_{\mathrm{H}\alpha}/f_{\mathrm{FUV}}$ and Σ_R–$F_{\mathrm{H}\alpha}/f_{\mathrm{FUV}}$ planes? Are the most extreme galaxies on this plot mergers? Does the star-formation itself ultimately limits the maximal $\Sigma_{\mathrm{H}\alpha}$ and $F_{\mathrm{H}\alpha}/f_{\mathrm{FUV}}$ that galaxies can reach?

Rest-frame UV data for the whole sample of galaxies presented in this thesis, compared to 10 galaxies as it is the case today, would greatly improve our understanding of the physics that underlie this relationship, and the importance of all the possible effects such as IMF variations, turbulences, and star formation, and the competition between them. Meanwhile, probing the higher density medium with CO and other line observations from new facilities such as ALMA will provide information on the denser material that carries much more mass than the warm ionized medium. Relating these two phases at subarcsecond resolution will increase our understanding of these distant galaxies substantially.

Appendix A

Analysis of SINFONI observations

Contents

A.1 Introduction

Our SINFONI observations of high redshift galaxies produce datacubes that require a very careful data analysis process. The signal-to-noise Ratio (derived using the method presented in § A.7) for the detectable lines in each spatial pixel is low (the SNR median value for all our the pixels in this thesis sample is ~5, as shown in Figure A.1), and these observations sometimes only just reach the detection limit of the instrument for the brightest regions of an object. The following sections will introduce some of the relevant techniques used to extract robust quantitative measurements and spatial distributions from J, H and K band observations of galaxies with redshifts between 1.3 and 2.7, providing morphological, dynamical and ionization information. These observations have been reduced by Nicole Nesvadba and the following sections present only the analysis of these cubes. The reduction process is described in Nesvadba (2005, Chapter 3).

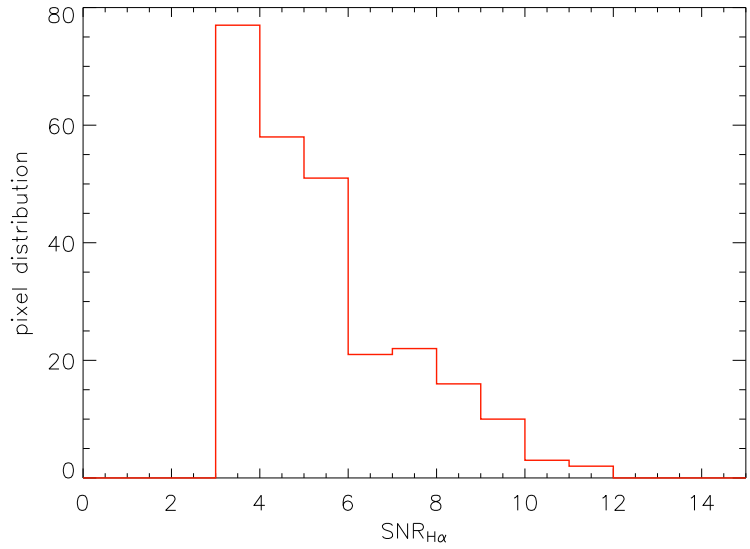

Figure A.1 Distribution of the Signal to Noise Ratio for all the pixels of the sample of galaxies used in this thesis. Each pixel analyzed is the average over a 0″.375 × 0″.375 area in a SINFONI datacube.

A.2 Spatial averaging

The first step consists of averaging the spatial pixels in 3×3 pixel boxes. SINFONI allows use of different pixel sizes. For the observations of high redshift galaxies, the physical pixels size used is usually the largest one: 0″.125 × 0″.250 (each physical pixel is cut in 2 similar square pixels). We will use square averaging boxes of 0″.375 size, slightly smaller than the typical PSF of our observations (FWHM ∼ 0″.6): this spatial smoothing allows us to work on stronger signals without degrading significantly our spatial resolution, determined by the PSF size. Using the adaptive optics mode of SINFONI, the PSF can reach a FWHM of ∼ 0″.2, and therefore a pixel size of 0″.05 × 0″.1 is usually selected. This method has been used in all the works considered in this thesis. Although it is possible, in principle, to average over a larger box, or to use tesselation techniques to increase the SNR in some regions (see Cappellari & Copin, 2003, for the techniques employed for data analysis with the SAURON IFU), these techniques are in practice employed only for local galaxy observations with high spatial resolution.

A.3 Spectral averaging

The spectral dimension has also been averaged, using a 3 pixel-sized box over the whole spectral range, for all observations. With a spectral pixel size around 2.5Å, the size of this averaging box is close to the spectral resolution of SINFONI (~6Å), but usually smaller than the widths of emission lines. Similar to the case of the spatial averaging used, the spectral averaging is set to the effective physical resolution of the instrument.

A.4 Fitting procedure

The emission line properties of each galaxy are obtained by fitting them with a gaussian profile. The fit is made simultaneously of all the lines visible in the observed band. The most frequently detected emission lines are Hα and the [NII]$\lambda\lambda$6548, 6583 doublet. In a few cases, another band is observed and Hβ and the [OIII]$\lambda\lambda$4959, 5700 doublet are detected. Other lines, like the [SII]$\lambda\lambda$6716, 6730 doublet, are usually too faint to appear in spatially resolved data, and often even in the integrated data for an entire object. There are two sets of physical constraints between these lines, which can be used for fitting them: the position of one of them gives the position of the others, and in the case of doublets, we can constrain their flux ratio to [NII]λ6583/[NII]λ6548 ~ [OIII]λ5007/[OIII]λ4959 ~ 3, as dictated by atomic physics (Osterbrock, 1989). Fitting Hα and the [NII] doublet for example, we used the following constraints:

$$\lambda_{\mathrm{obs,[NII]}\lambda6583} = \frac{6583}{6563}\,\lambda_{\mathrm{obs,H}\alpha} \tag{A.1}$$

$$\lambda_{\mathrm{obs,[NII]}\lambda6548} = \frac{6548}{6563}\,\lambda_{\mathrm{obs,H}\alpha} \tag{A.2}$$

$$\sigma_{\mathrm{[NII]}\lambda6583} = \frac{6583}{6563}\,\sigma_{\mathrm{H}\alpha} \tag{A.3}$$

$$\sigma_{\mathrm{[NII]}\lambda6548} = \frac{6548}{6563}\,\sigma_{\mathrm{H}\alpha} \tag{A.4}$$

$$A_{\mathrm{[NII]}\lambda6583} = 3 \cdot A_{\mathrm{[NII]}\lambda6548} \tag{A.5}$$

Where λ_{obs} is the observer frame position of the emission line, σ the velocity dispersion of the emission line, and A is the amplitude of the line.

In order to fit the emission lines accurately, it is necessary to also fit the underlying continuum component. This is done using a simple polynomial function

$\sum_i n_i x^i$ with $0 < i < N$: where N must be large enough to account for the low order shape of the continuum but avoid the higher order structures produced by the noise (usually N=9). The continuum fit needs to be accurate only in the region of the emission lines (the spatial distribution of the continuum is already evaluated during the data reduction). The fit is realized using the IDL code `mpfitexpr.pro` (Markwardt, 2009) which allows the usage of a large set of embedded constraints and fitting parameters. Figure A.2 gives an example of a fit centered on the Hα emission line region.

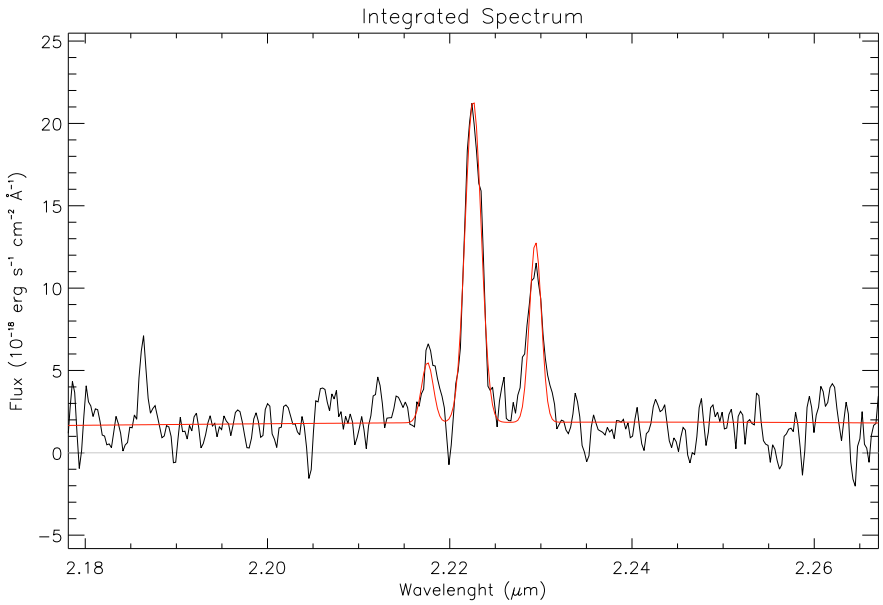

Figure A.2 Example of continuum fitting. Shown are an integrated spectrum (black) and fit (red curve) of the Hα and [NII] doublet emission lines region. This spectrum has a very distinct continuum emission which has been fitted as well as the emission lines.

A.5 Night Sky Emission Lines

A major source of noise and possible confusion in spectroscopic observations is the numerous emission lines from the night sky. This non-gaussian noise can strongly perturb a signal, especially if it lies on top of an emission line, making it very hard to fit and therefore strongly reducing the quality of the measurements. In some cases it may not be detected and will affect the measurement adversely. However, night sky emission line positions are well known (see Figure A.3) and observers select objects whose emission lines will lie as far as possible from the night sky lines. Therefore, night sky emission lines are usually not a problem.

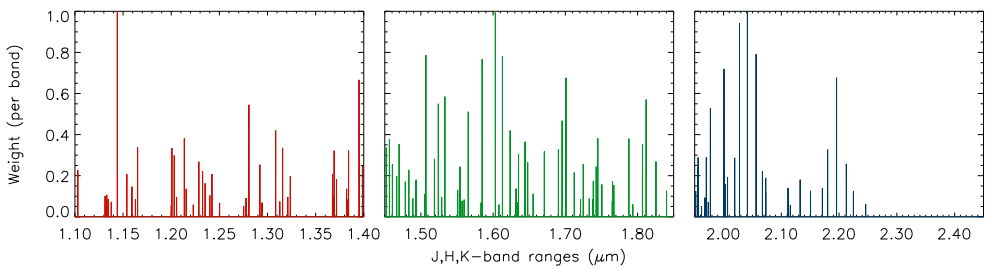

Figure A.3 Principal Night Sky Emission Lines in the *J* (red), *H* (green), and *K* (blue) bands of SINFONI. Amplitudes of the lines are normalized for each band separately.

Correcting the effects of the night sky lines is done by applying different weights to the different spectral pixels of the spectrum during the fit: corrupted pixels are given a weight of 0 and therefore are not be considered in the fit, while the other pixels, weighted to 1, are fully considered. Correcting the night sky lines by using a template of their theoretical positions and amplitudes (see Figure A.3) is complicated and unnecessary. A simple `sigma_filter`[1] operation on the line-free regions of the spectrum corrects the first-order effect of the strongest lines. This step is especially important in order to accurately fit the continuum. Closer to the ionization lines, the treatment of the sky lines has been done manually, when required, by weighting the corrupted pixels to 0 previously to the fitting. This is what has been done for the fit presented in Figure A.4.

A.6 Random noise properties

Besides the aforementioned possible adverse effect of night sky lines, the main source of noise in these observation is random noise. An automated process was used to evaluate for each spatial pixel the amount of random noise near the fitted lines. In order to do so, we sample a large section of noise around the ionized gas emission lines (usually 200 spectral pixels) and evaluate its properties. Only 90% of each "noise-spectrum" is conserved: the 10% most extreme points are automatically deleted, in order to sample only the random noise and not night sky lines. The measurement of the noise RMS is done on the remaining 90% of the spectral pixels and corrected to take in account these removed values. This process

[1]This routine computes the mean and standard deviation of pixels in a box centered on each pixel of the image, excluding the center pixel. If the center pixel value exceeds a chosen multiple of the standard deviation from the mean, it is replaced by the mean in the box. `http://idlastro.gsfc.nasa.gov/ftp/!pro/image/sigma_filter.pro`

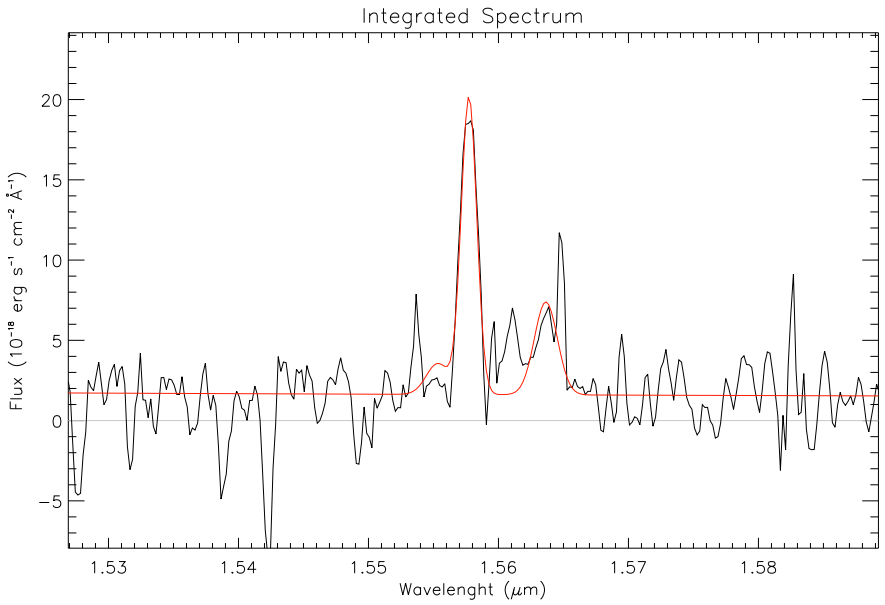

Figure A.4 Example of a spectral line fit in the presence of a night sky line. Shown are an integrated spectrum (black) and fit (red curve) of the Hα and [NII] doublet emission lines region. The fit is correct despite the presence of a sky line on top of [NII] λ6568.

reduces this particular effect of night sky lines, which are rare but can be very strong and bias the measurement of the noise RMS. Figure A.5 shows that the noise values follow a gaussian distribution, although it should be noted that two consecutive spectral pixels are not independent and therefore the noise is not randomly sampled.

A.7 Signal to Noise Ratio evaluation

In order to measure the statistical effect of the random noise on the emission line fit, we used a series of Monte Carlo simulations. The previously measured signal S (for example the gaussian fit of the Hα line) is added for each iteration to a sample of generated random noise values N_i having the properties measured from the observed noise (see Section A.6), as shown in Figure A.6 (On this example, the signal is set to a position of 150, an amplitude of 5, and a dispersion of 8. The noise distribution has a dispersion of 1. All values are normalized in pixels). We take account of the fact that two consecutive spectral pixels are not independent by smoothing the generated noise in order to mimic the observed noise properties. We usually run 1000 iterations for each spatial pixel and obtain the fitted line parameters: position (λ), amplitude (A), and dispersion (σ). The distribution of the 1000 triplets of parameters therefore obtained, each of them corresponding to a different

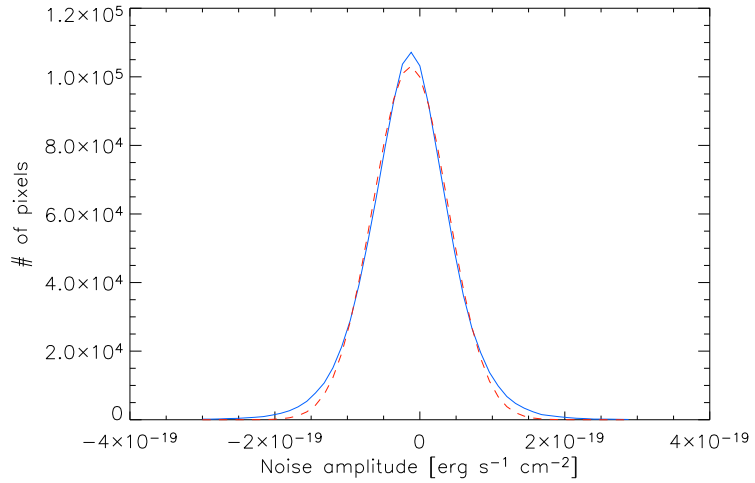

Figure A.5 Histogram of the measured values of the RMS noise in a subsection of a SINFONI obervation cube (solid blue line) and its associated gaussian fit (dashed red line).

realization of the noise, corresponds to the statistical uncertainty on the parameter triplet. Examples of these distributions, with the precedent input values for the signal and the noise, are presented in Figure A.7. Here, we obtain an accurate mean value of the distributions the input parameters of the fit: λ=150, A=5, and σ=8. The dispersion of values for each parameter corresponds to the effect of the noise for this parameter.

Evaluating the SNR for each pixel using 1000 realizations of the noise each time is a time-consuming task. Therefore, instead of doing so for each new cube analysis, we constructed tables of the SNR as a function of dispersion and amplitude of the signal relative to the noise. Once this table was constructed, it was no longer necessary to make the calculation of the noise for each new fit. This table is presented graphically in Figure A.8.

A.8 Visual verification of the fitted profiles

In order to improve the data analysis, all the spectra for each spatial pixel have been compared to their fits using an IDL code that has been developed to allow a quick look at the spectra and their fits over the whole cube, as well as the single-click selection or rejection of these spectra depending on their quality. As each analyzed object has been through this process, ultimately all individual spectra have been visually verified. Figure A.9 shows a screenshot taken during the use of this software. It is particularly useful for detecting the night sky line effects.

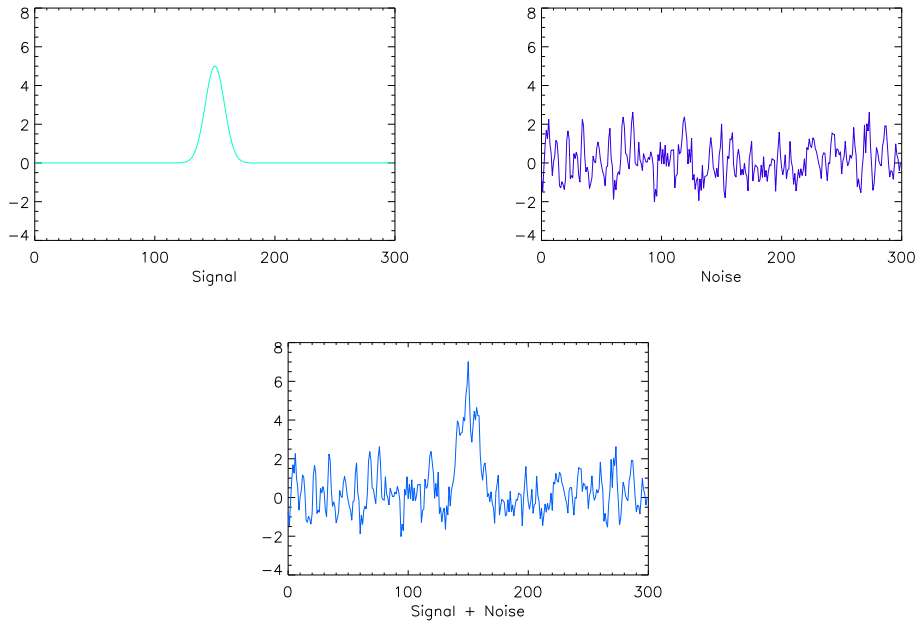

Figure A.6 Realized series of random noise added to a gaussian signal. This signal and the noise parameters are the ones used in Figure A.7.

In this case, the fit is corrected (see Section A.5). In other cases and especially at very low SNR (therefore generally at the periphery of the observed objects), it is common to fit a noise feature instead of a signal: by comparing the position and width with nearby pixels, or comparing with stronger emission lines, it is possible to disentangle the signal from noise realizations.

A.9 Instrumental resolution

An important systematic effect to take into account is the broadening of the lines by the instrumental resolution. This effect has been quantified in Nesvadba (2005, Chapter 3, Section 7, Page 30), using measurements of the telluric OH lines. These lines have a dispersion well below the instruments spectral resolution, and their line widths observed by SINFONI therefore correspond to the instrumental resolution at a certain wavelength. For a 0″.250 pixel scale, with averaging over 3×3 spatial pixels and 3 spectral pixels, we obtained the real FWHM by quadratically substracting the measured FWHM as in the following equation:

$$\mathrm{FWHM}^2_{\mathrm{line}} = \mathrm{FWHM}^2_{\mathrm{observed}} - \mathrm{FWHM}^2_{\mathrm{Instrumental\ Resolution}} \quad \text{(A.6)}$$

Where $\mathrm{FWHM}_{\mathrm{line}}$ is the FWHM of the emission line, $\mathrm{FWHM}_{\mathrm{observed}}$ is the

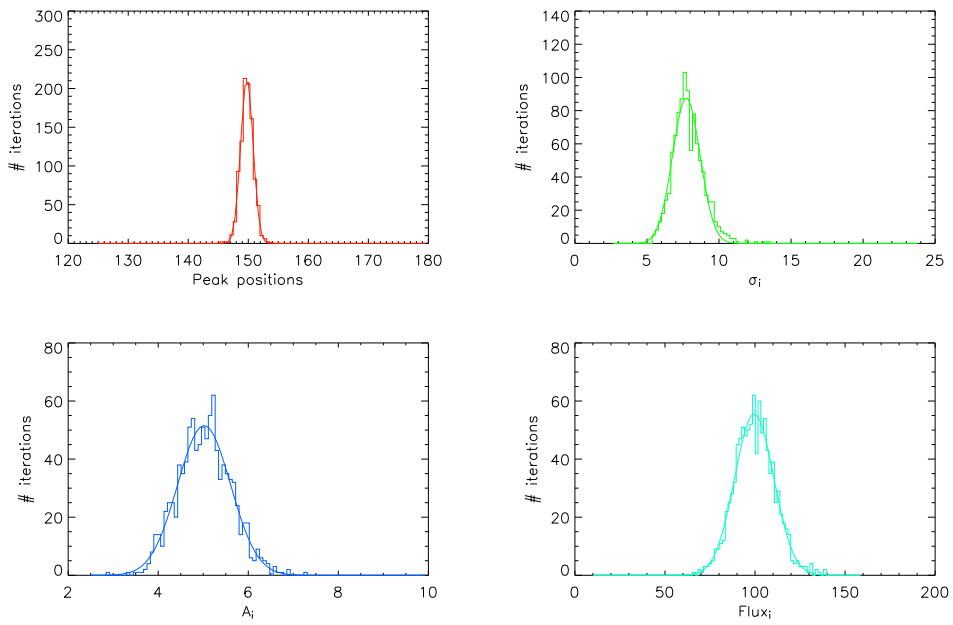

Figure A.7 Distribution of the obtained parameters after fitting the signal with 1000 realizations of superimposed noise. Upper left: distribution of the peak position (λ); Upper right: velocity dispersion distribution (σ); Lower left: normalized amplitude distribution (A); Lower right: flux distribution ($\sqrt{2\pi} \cdot A \cdot \sigma$). The signal and noise input values correspond are the same that in Figure A.6.

FWHM measured in the spectrum and $\mathrm{FWHM}_{\text{Instrumental Resolution}}$ is the instrumental resolution for the corresponding observing frame wavelength.

We used the following values for the instrumental resolution, measured in Nesvadba (2005, Chapter 3, Section 7, Page 30):

$$\mathrm{FWHM}_{\mathrm{J-band}}[\mathrm{km\ s^{-1}}] = 342 - 127 \times \lambda[\mu m] \tag{A.7}$$

$$\mathrm{FWHM}_{\mathrm{H-band}}[\mathrm{km\ s^{-1}}] = 274 - 71 \times \lambda[\mu m] \tag{A.8}$$

$$\mathrm{FWHM}_{\mathrm{K-band}}[\mathrm{km\ s^{-1}}] = 256 - 56 \times \lambda[\mu m] \tag{A.9}$$

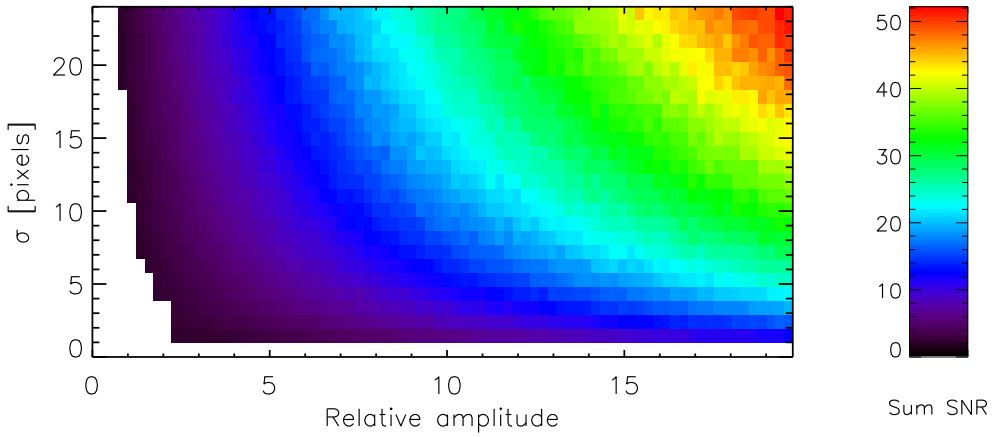

Figure A.8 Table of the signal to noise ratio for the line fluxes, as a function of their dispersion and amplitude. Line amplitude is relative to the noise dispersion and line velocity dispersion is in pixels. The SNR increases with increasing signal amplitude (relative to the noise) as well as with increasing line velocity dispersion (for a fixed amplitude).

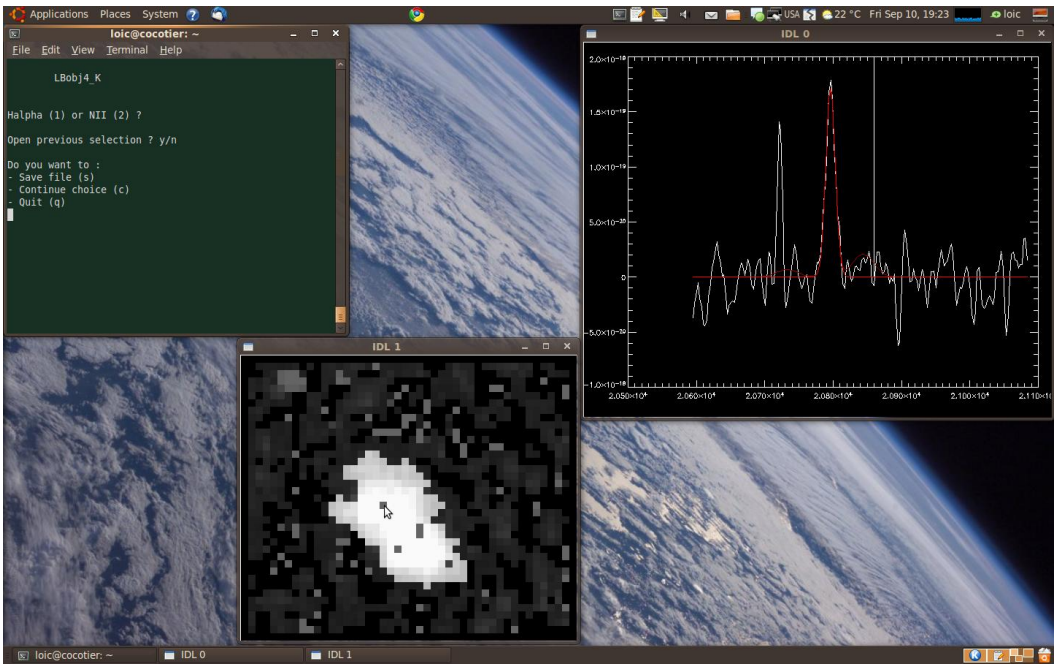

Figure A.9 Screenshot of the selection/rejection program used to verify the quality of each fit.

Appendix B

Deriving electron densities

The intensity ratio of two lines of the same ion with very close excitation levels provides a way to evaluate the electronic density in the ISM of distant galaxies. Lines close to each other in wavelength have the advantage not to suffer from differential extinction. We use the doublet [SII]λ6716 / [SII]λ6731 (hereafter [SII]$_R$) as it lies close to Hα and is frequently observed. However, since its SNR is usually very low in integrated spectra of individual galaxies, the use of a stacking analysis is required to accurately measure the mean electronic density in a sample of galaxies.

Collisionally excited (or "forbidden") lines are only visible in very low density environments. This is why they are only observed in some astrophysical objects, where the probability of collisional de-excitation is lower than for the "forbidden" decay by emission of a photon. Although the ions that produce these lines are rare compared to H or He, this cooling process is very effective.

Here we explain how we derive electronic densities from the "5-level atom problem" of [SII]. Other levels can be included, although for the [SII] ion, at the temperatures and densities we are considering in astrophysical plasmas, these 5 levels are enough to measure accurate densities. The atomic levels considered for [SII] are $^4L_{3/2}$, $^2D_{3/2}$, $^2D_{5/2}$, $^2P_{1/2}$ and $^2P_{3/2}$, which will be noted i (or j). Any transition, in both directions, is possible, with different probabilities. Collisional excitation (and de-excitation) probabilities from level i to level j, q_{ij} (and q_{ji}) can be calculated from the collision strength Ω(j,i) whose values can be derived from quantum- mechanical calculations. These values and the following equations are taken from Osterbrock (1989).

$$q_{ji} = \left(\frac{2\pi}{kT}\right)^{1/2} \frac{\hbar 2}{m_e^{3/2}} \frac{\Omega(i,j)}{\omega_j} \tag{B.1}$$

$$q_{ij} = (\frac{\omega_j}{\omega_i}) q_{ji} e^{-\chi/kT} \tag{B.2}$$

Where $\omega_i = 2J_i + 1$, and m_e is the electron mass, and $\chi = \frac{1}{2} m_e v_i 2 - \frac{1}{2} m_e v_j 2$.

The transition probabilities A_{ji} by decay to a lower level through photon emission are also derived.

Taking N_i to be the densities of each quantum state, we have:

$$\sum_{j\neq i} N_j N_e q_{ji} + \sum_{j>i} N_j A_{ji} = \sum_{j\neq i} N_i N_e q_{ij} + \sum_{j<i} N_i A_{ij} \tag{B.3}$$

and

$$\sum_j N_j = 1 \tag{B.4}$$

Where N_e is the electron density. We therefore have to solve a six linear equations problem (5 equations of the form B.3 and the closing equation B.4). We will normalize the total number of states to 1 (right hand term of equation B.4), which is permitted as we are determining line ratios.

The first five equations can be put in the following form:

$$[L_{equilibrium}] = [N] * (N_e[Q] + [A] - Ne[Q_{self}] - [A_{self}]) = [0] \tag{B.5}$$

With the following matrices :

$$[N] = \begin{bmatrix} N_{^4L_{3/2}} & N_{^2D_{3/2}} & N_{^2D_{5/2}} & N_{^2P_{1/2}} & N_{^2P_{3/2}} \end{bmatrix} = \begin{bmatrix} N_1 & N_2 & N_3 & N_4 & N_5 \end{bmatrix} \tag{B.6}$$

$$[Q] = \begin{bmatrix} 0 & q_{21} & q_{31} & q_{41} & q_{51} \\ q_{12} & 0 & q_{32} & q_{42} & q_{52} \\ q_{13} & q_{23} & 0 & q_{43} & q_{53} \\ q_{14} & q_{24} & q_{34} & 0 & q_{54} \\ q_{15} & q_{25} & q_{35} & q_{45} & 0 \end{bmatrix} \tag{B.7}$$

$$[A] = \begin{bmatrix} 0 & A_{21} & A_{31} & A_{41} & A_{51} \\ 0 & 0 & A_{32} & A_{42} & A_{52} \\ 0 & 0 & 0 & A_{43} & A_{53} \\ 0 & 0 & 0 & 0 & A_{54} \\ 0 & 0 & 0 & 0 & 0 \end{bmatrix} \tag{B.8}$$

$$[Q_{self}] = \begin{bmatrix} \sum_{j>1} q_{1j} & 0 & 0 & 0 & 0 \\ 0 & \sum_{j>2} q_{2j} & 0 & 0 & 0 \\ 0 & 0 & \sum_{j>3} q_{3j} & 0 & 0 \\ 0 & 0 & 0 & q_{45} & 0 \\ 0 & 0 & 0 & 0 & 0 \end{bmatrix} \tag{B.9}$$

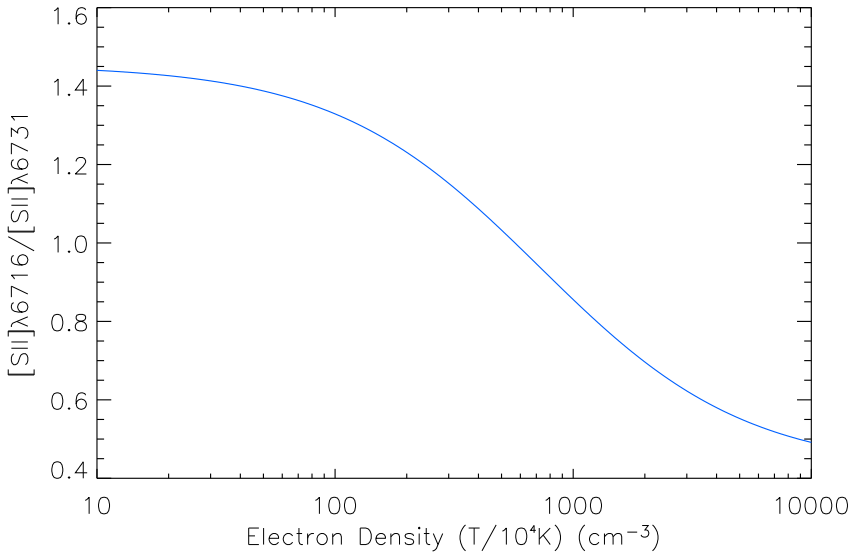

Figure B.1 The [SII]λ6716 / [SII]λ6731 ratio as a function of electron density (in cm^{-3}), for a temperature of 10^4K.

$$[A_{self}] = \begin{bmatrix} 0 & 0 & 0 & 0 & 0 \\ 0 & A_{21} & 0 & 0 & 0 \\ 0 & 0 & \sum_{j<3} A_{3j} & 0 & 0 \\ 0 & 0 & 0 & \sum_{j<4} A_{4j} & 0 \\ 0 & 0 & 0 & 0 & \sum_{j<5} A_{5j} \end{bmatrix} \tag{B.10}$$

To the sum of matrices $[L_{equilibrium}]$ in B.5 we can add the closing relation B.4 as a sixth line in the matrix:

$$\begin{bmatrix} [L_{equilibrium}] \\ \begin{bmatrix} 1 & 1 & 1 & 1 & 1 \end{bmatrix} \end{bmatrix} = \begin{bmatrix} [0] \\ 1 \end{bmatrix} \tag{B.11}$$

We can solve this equation for a given pair of (N_e, T) values, using single-values decomposition. We therefore obtain for each value of temperature and electron density:

$$[SII]_R = \frac{N_3 A_{31}}{N_2 A_{21}} \tag{B.12}$$

Figure B shows $[SII]_R$ as a function of the electron density N_e for a temperature of 10^4K.

Appendix C

Description of the Objects from Chapter 7

Contents

The various emission lines and kinematic maps, as well as the continuum image for the objects we will describe now, are presented in Chapter 2. Integration times for these observations are given in Table 7.1.

C.1 DEEP2-32007614

Despite having one of the strongest continuum flux (and therefore being one of our most massive objects), this small size object (almost the smallest detected size, around 90 kpc^2) has one of the weakest Hα flux density, corresponding to a SFR of 16 $M_\odot$ yr^{-1}, making it one of the least active galaxy in our sample. The star formation seems to be slightly offset from the continuum center by 2 kpc, where a strong but very localized Hα emission zone lies. Quite a strong [NII] emission (until half of the Hα flux) is also observed more smoothly around the object, with

its largest relative flux maybe forming a ring around it. It is however hard to tell considering the poor resolution of our observations, especially for such a weak line.

We do not detect a velocity shear, however, there is a gradient of velocity dispersion from South (~50 km s^{-1}) to North (~180 km s^{-1}). At first sight it may be corresponding to the region where Hα is stronger (in the Northern part of the object), however, it really seems to follow a linear trend from South to North, consequently not caused by the Hα emission. Eventually, the phenomenon responsible for this high dispersions may be causing part of the Hα emission.

C.2 DEEP2-32013051

This intermediate size (~250 kpc^2) object seems to have a simple circular morphology. There are quite a strong Hα and [NII] emission, which are spatially distributed similarly as the continuum, all centered in the same region. Hα line shifts exhibits a velocity shear on a scale of ~200 km s^{-1}, suggesting that there is some ordered motion. This velocity field is however distorted and does not exhibit clear signs of rotation. Kinematics also display a large zone of high dispersion values around 150 km s^{-1}, centered similarly as the emission lines and the continuum. Even higher values of the dispersions can be observed at $3kpc$ North West from the center of this zone, which may be a clue for a galactic wind. The luminosity of [NII] at the center of the object can approach those of approach Hα (with a ratio [NII]/Hα ~0.8). This strong ratio, together with the observed velocity dispersion, could be indicating the presence of an AGN. However, the velocity dispersion is not high enough and we lack other ionization parameters to make this claim. It might simply due to the effect of an high star formation at work (~23 $M_\odot$ yr^{-1}).

C.3 DEEP2-32015443

This object has quite a more complex morphology than the precedent. The continuum emission is here slightly extended from North to South and the center seems to be offset on the South of the object. Unfortunately, the signal to noise ratio is quite low and a skyline on top of Hα disrupts its measurement. The Hα emission does not exhibit a clear center but what seems to be a smoother emission along the whole galaxy. The two stronger emission zones on the Hα flux map could be simply due to an enlargement effect of the skyline and may not be real. Considering this, the most reliable center of emission could be slightly offset from the continuum emission, ~2.5 kpc toward the North. Considering the quality of the data, the [NII] emission cannot be interpreted.

We observe a velocity shear which could be as large as 200 or 300 km s^{-1}, directed South-East to North-West, maybe along the major axis of the highest con-

tinuum values zone. The dispersion map, also affected by the skyline, shows that the dispersion on its most reliable zones should lie around 100 km s^{-1}. Due to its enlarged morphology and its distorted velocity shear, this object may be the result of a recent merger.

C.4 DEEP2-32015501

This object exhibits an obviously complex morphology over its 250 kpc^2. The center of the continuum seems to be elongated on 5×8 kpc^2, eventually displaying two close zones of equally strong emission. A foreground object on the South-West disrupts the continuum map and should not be considered. The Hα emission also exhibits a complex spatial distribution. The most luminous emission is centered over the Southern area of the strong continuum emission, but does not fill the Northern area. Around this central emission of 20 kpc^2 lies three other smaller emission regions, which do not seem to be linked with the continuum at all. Overall, the cutting of this object seems to follow a pattern with three "arms" (East, North-West, South-West). The total [NII] emission is quite small, around a tenth of the total Hα emission. Therefore it is observed only in a small central region superposed to the central Hα emission.

The velocity field is also perturbed, with an amplitude around 150 km s^{-1}. There might be a clue for a motion around the continuum center, with an axis along a line North-East to South-West. Dispersion map is quite messy, with a lot of the Hα lines being very thin and therefore falling beneath the instrumental resolution.

C.5 DEEP2-32021317

This slightly elongated object (∼12×16 kpc^2) exhibits a simple continuum morphology. The Hα and [NII] emissions follow the same morphology. The very central regions of emission for these two lines are the strongest we obtain in this whole sample. The total [NII] emission is also the largest of this sample. There is a strong velocity field, which has an amplitude over 400 km s^{-1}. This field is disturbed but clearly exhibiting a trend across the galaxy with a North-East to South-West axis crossing the luminous center of the object.

The kinematic data shows very large lines in the central region, with a dispersion over 400 km s^{-1}. [NII]/Hα often exceeds 1 or even 1.5. This object is obviously hosting an AGN.

C.6 DEEP2-32021394

While this intermediate size (~240 kpc^2) object has a simple circular continuum morphology, its emission lines maps exhibit more complex features. The Hα emission is not superposed to the continuum emission but lies around it, mostly on the Eastern side, with a weaker component on the Western side. It is probably that the star forming regions lie on a ring around the center of this object. On the extreme South of the object, where the Hα line emission seems to be extended, we observe a small area (~20 kpc^2) of [NII] emission, which is the main contribution of the observable [NII] luminosity (a skyline on top of it prevents us to detect the whole emission, especially in the center of the object).

The velocity field exhibits a strong amplitude (~ 300 km s^{-1}) and seems to follow a North-East to South-West axis centered on the continuum emission, with an extra component from the Southern feature.

C.7 DEEP2-32029850

This is the smallest object we observe in size (~ 50 kpc^2). It is weak in continuum emission, and it is the weaker object in Hα emission. Therefore, because of the very low number of elements of resolution (two elements for the continuum, only one for Hα), it is impossible to interpret spatial data.

C.8 DEEP2-32037003

This is a particularly interesting object: it is large (~ 300 kpc^2) and exhibits interesting morphological and dynamical features. It has a strong continuum emission but above all the stronger Hα emission of our sample.

The continuum emission exhibits a circular emission, with a small elongation on the North-West (and eventually the South-East). This elongation is in fact clear on the Hα emission map where we observe the presence of a second component. The weight in Hα emission of this second component is ~20% of the total emission. The [NII] emission traces the Hα emission with smaller extends. It reproduces well the overall shape of the object, with its two components.

Kinematical analysis also exhibits clear trends. The velocity map displays a clear shear of amplitude over 300 km s^{-1}. Its gradient is oriented toward the secondary component. Therefore, it is possible that part of the velocity field is due to the secondary component. However there are no clear signs of distortion expected if this component had a strong impact on the kinematics of this objects. This is in agreement with the fact that the minor component has a weak continuum and therefore must have a light mass.

We also observe nice features in the dispersion map. Looking only at the main component, we see a line enlargement on the center, joining the South-East and South-West extremities of the object. This dispersion features, together with the velocity field, could be a clue for a rotating disk motion. High dispersion on the extremities may also indicate the presence of galactic winds, which may be present in many of these galaxies, considering their high star formation rate. Focusing on the minor component, we observe a reduction of the linewidths on an area which could be between the components. However, the spatial resolution is too low to distinguish the effect of the component on the dispersion field.

The morphological and dynamical features, together with the secondary Hα emission suggest that this object may be a clumpy disk.

C.9 DEEP2-32002481

This is our biggest object with an area around 350 kpc^2. It is clearly composed of two components. Seen in the continuum, the Northern component is ∼25% of the total luminosity. However, the same component is 60% of the flux in Hα, though only a weak fraction in [NII]. The Hα emission, with fainter densities in the Northern component, is more extended than on the Southern component. The difference with the continuum may also come from the fact that the continuum emission is way harder to measure and extended low emission are less likely to be detected than compact strong emission. On the Northern emission, Hα is slightly offset from the continuum emission (∼2 kpc), while the Southern Hα emission seems to overlie the continuum.

The Hα line dispersion exhibits very broad lines on the Southern components ($\sim$ 300 km s^{-1}). The [NII]/Hα in this region is also high (∼0.8). These are clues for the presence of an AGN.

The velocity map shows that the two components are clearly separated by $\sim$ 300 km s^{-1}. There seems to be velocity gradients on both components. The gradient on the Northern component is clearer, because of its spatial extension but also because the large linewidths of the Southern components cause larger uncertainties on the measurement of the Southern velocity field. The Northern component has a velocity gradient around 150 km s^{-1} which is directed perpendicularly to the direction of the AGN, which indicates that it is not due to its presence. However, this field is smoother in the South, which must be a tidal effect of the Southern component.

C.10 DEEP2-32100778

This large object ($\sim$ 270 kpc^2) exhibits multiple components, as well in the continuum that in Hα. The continuum displays three components of similar sizes (the Southern one seems to be the heavier one). All three are very close to each other (Eastern and Western component are both $\sim$5 kpc from the Southern component).

The Hα flux map exhibits two close components of equal weights. Both are offset from the continuum emission. One seems to be in between the three sources of continuum emission. The other one seems to be between the Southern and the Western components, slightly offset toward the West. The [NII] spatial distribution somewhat follows Hα.

Kinematical data display a very disturbed velocity field, although a gradient is observed between East to West of about 100 kpc. The velocity field is also disturbed, with a gradient around 150 km s^{-1}. [NII] lies on the same region, with ratios to Hα around 0.5.

C.11 Previous spectroscopic observations of DEEP2-32037003 and DEEP2-32100778

Two of these objects, 32037003 and 32100778, have been studied spectroscopically using Keck II NIRSPEC in the same band by Shapley et al. (2005). The measured fluxes in Hα and [NII] are respectively around 3 and 5 times lower for both lines. This is due to the NIRSPEC slit which is $0''.7\ 6 \times 42''.$, too narrow to enclose the whole object.

Appendix D

International Conferences: Oral Presentation Proceedings

D.1 "UP: Have Observations Revealed a Variable Upper End of the Initial Mass Function?"

June 20-25, 2010, Sedona, Arizona, USA

Up2010: Have Observations Revealed a Variable Upper End of the Initial Mass Function?
ASP Conference Series, Vol. 440
Marie Treyer, Ted K. Wyder, James D. Neill, Mark Seibert, and Janice C. Lee, eds.

The Turbulent ISM of Galaxies about 10 Gyrs Ago: An Impact on their IMF?

L. Le Tiran and M. D. Lehnert

Laboratoire d'Etude des Galaxies, Etoiles, Physique et Instrumentation GEPI, Observatoire de Paris, 92195 Meudon, France

Abstract. The utilization of integral-field spectroscopy has led us to a new understanding of the physical conditions in galaxies within the first few billion years after the Big Bang. The combination of the kinematics and emission line diagnostics is a powerful technique to discern the physical processes that are at work in distant galaxies. In these proceedings, we present observations of 10 massive galaxies as seen as they were 9 Gyrs ago using SINFONI from the ESO-VLT, combined with photometry from the DEEP2 Survey. We first portray a brief picture of the physical conditions in the warm ionized medium of these galaxies; they exhibit complex morphologies, high star formation and are so pressure dominated they are likely to drive winds and high turbulence. Moreover, their ratio of Hα to FUV flux to their *R*-band luminosity surface brightnesses indicates that perhaps their initial mass function is flatter than Salpeter at the high mass end, as has been suggested recently for some local galaxies. It may be that high turbulence is responsible for skewing the IMF towards more massive stars as suggested by some theories of star-formation.

1. Introduction

The IMF is one of the most important underlying parameters which determines some of the most obvious characteristics of galaxies as observed in the local universe – their emission line equivalent widths, their metal abundance and ratios, the total mass in stellar remnants and hence their mass-to-light ratios, etc. A change in the IMF in simulations leads to changes in the galaxy mass function, the metal content within galaxies and the IGM, as well as changing the luminosity (per unit mass) evolution of galaxies. Wide swaths of the astronomical community consider the IMF to be universal – an assumption that is however often criticized. Recently, many authors have been trying to characterize the global nature of the IMF using integrated galactic properties, especially $F_{\mathrm{H}\alpha}/f_{\mathrm{FUV}}$ (Meurer et al. 2009; Lee et al. 2009; Boselli et al. 2009), but not exclusively (Hoversten & Glazebrook 2008). Perhaps though, galaxies in the early Universe, with their generally more extreme properties are interesting targets for studying star formation under extreme physical conditions, high turbulence and thermal pressures, which might impact the overall shape of the IMF.

2. Integral-Field Spectroscopy of a Sample of 10 Galaxies at $z \sim 1.4$

We use here a sample of 10 galaxies around redshift 1.38, extracted from the DEEP2 Redshift Survey and observed with the integral field unit SINFONI on VLT. These galaxies are selected in the infrared to be massive (they have an estimated mass of a few $\times 10^{10}$ $\mathrm{M}_{\odot}$ or more). In order to get a better idea of the information we can extract from our data, as well as the different kinds of morphological and dynamical features that are present in these galaxies, we present

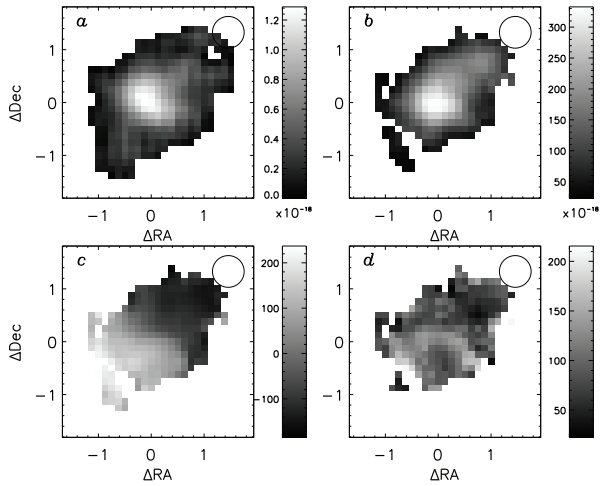

Figure 1. Continuum and Hα emission line properties for DEEP2-32037003: *Panel a*: *R*-band continuum flux density in 10^{-18} erg s^{-1} cm^{-2} arcsec^{-2} Å^{-1} (observed in *H*-band corresponding to rest-frame visible); *Panel b*: Hα flux density in 10^{-18} erg s^{-1} cm^{-2} arcsec^{-2}; *Panel c*: Hα line velocity field in km s^{-1}; *Panel d*: Hα line dispersion in km s^{-1}. On the upper-right corner of each pannel, we show the approximate size of the full width at half-maximum of the seeing disk. The relative positions are in arc seconds. All maps were centered on the peak in the Hα surface brightness distribution which defines the (0,0) in each panel.

three objects chosen to represent particular features of the whole range of characteristics of galaxies in our sample. In the following analysis, it is important to consider that the spatial resolution of these observations is very low. We show this by representing the FWHM of the PSF (around 0.6 arc seconds) as circles in the upper-right of each panel. These objects have only a few spatial resolution elements within their isophotes which can lead to mis-interpretations of the their characteristics.

2.1. 32037003

This object's main spatial features are presented in Figure 1. It is large ($\sim 300 kpc^2$, with a major axis around $25 kpc$) which exhibits interesting morphological and dynamical features. It has the highest star-formation rate in our sample (around $50 M_\odot yr^{-1}$, more than an order of magnitude above the typical galaxies in the nearby Universe), and also appears to be very red. Its continuum map exhibits a smooth and quite circular morphology, with a small elongation on the North-West. By looking at the Hα emission map, this elongation becomes somehow clearer to form a secondary component, which accounts for ~20% of the total Hα emission.

The kinematics also shows clear trends. The velocity map displays a smooth shear of amplitude over 300km s^{-1}. While this gradient is oriented toward the secondary component, the velocity field shows clear signs of distortion expected if this component is interacting/merging. Moreover, this minor component is far weaker in the continuum than in Hα, hence must have a comparatively low mass, but a relatively high star formation rate. This is borne out by the dispersion map in which we see a wide line in the center, with narrower feature farther out. Perhaps this is a rotating clumpy disk (Elmegreen et al. 2009) where the second component is a region of intense star-formation.

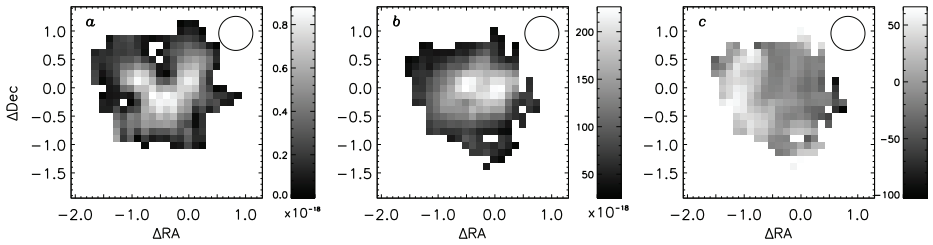

Figure 2. Continuum and Hα emission line properties for DEEP2-32100778: *Panel a*: *R*-band continuum flux density in 10^{-18} erg s^{-1} cm^{-2} arcsec^{-2} Å^{-1} (observed in *H*-band corresponding to rest-frame visible); *Panel b*: Hα flux density in 10^{-18} erg s^{-1} cm^{-2} arcsec^{-2}; *Panel c*: Hα line velocity field in km s^{-1}.

2.2. 32100778

The regular velocity field is not typical however. The object, 32100778, is much more typical of the kind of things we observed in this sample (Fig. 2). Its size is similar to the object just discussed, but exhibits very clear multiple components, in the continuum as well as in Hα. In fact, the continuum displays three components of similar sizes (the southern one must be a bit more massive). All three are very close to each other, with distances around $5kpc$. However, looking at the Hα flux map, we do not see three components but only two of equal brightnesses, in the area but apparently not directly related to the three continuum components. As might be expected from the morphologies, the velocity field is very disturbed (although an E-W gradient is observed of about 100 km s^{-1}).

2.2.1. 32002481

We also find two AGN, one of which we show here (Fig. 3). This is our most extended object, and consists of two completely distinct components, with an total area around 350 kpc^2. Seen in the continuum, the northern component is $\sim$ 25% of the total luminosity. However, the same component is 60% of the flux in Hα, and more extended than the southern component. The Hα line dispersion exhibits very broad lines on the southern components ($\sim$ 300km s^{-1}) and the [NII] /Hα in this region is also high ($\sim$ 0.8). The velocity map shows that the two components are clearly separated by $\sim$ 300km s^{-1}. The northern component has a velocity gradient around 150 km s^{-1} which is perpendicular to the direction of the AGN and is likely not related. However, this field is smoother in the south, which must be a tidal effect of the southern component. In the following analysis, we will of course take care of the fact that the Hα emission in the southern component is related to the presence of an AGN, and is therefore not a tracer of the star formation.

2.3. These are Multi-Component Objects with High Dispersion

As we can see in these three objects, the galaxies in this sample share many common features. They tend to have many components, whether these are clearly separated, late in a merger phase, or with different relative masses. Their velocity dispersions can reach quite high values. Understanding what is powering these motions is a major question in our understanding of galaxy evolution.

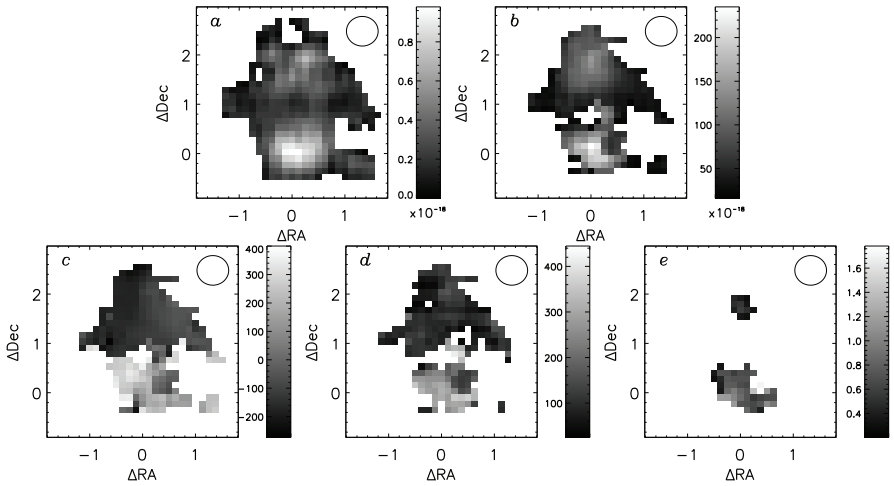

Figure 3. Continuum and Hα emission line properties for DEEP2-32002481: *Panel a*: *R*-band continuum flux density in 10^{-18} erg s^{-1} cm^{-2} arcsec^{-2} Å^{-1} (observed in *H*-band corresponding to rest-frame visible); *Panel b*: Hα flux density in 10^{-18} erg s^{-1} cm^{-2} arcsec^{-2}; *Panel c*: Hα line velocity field in km s^{-1}; *Panel d*: Hα line dispersion in km s^{-1}; *Panel e*: [NII]$_{\lambda 6583}$/Hα flux densities ratio.

3. What is Powering the Local Motions in these Galaxies?

3.1. Energy Injection from Massive Stars

The SFR surface densities of our objects vary between 50 and 200 $\times 10^{-3} M_{\odot} yr^{-1} kpc^{-2}$. Such high intensity star formation will create high pressures due to the thermalization of the mechanical energy output of the massive stars. Lehnert & Heckman (1996) and Heckman (2001) suggest the limit above which the SFR produces large scale winds lies around $100 \times 10^{-3} M_{\odot} yr^{-1} kpc^{-2}$. Most of our sample lies above this limit. Even though it is not possible to demonstrate that all these galaxies are driving winds, the pressure due to the recent and ongoing star formation must play a major role in driving the galaxy internal kinematics.

3.2. High Densities and Internal Pressures

Beyond just measuring the kinematics of the gas, we can also analyze the line ratios. Figure 4 presents the relationships between the emission line ratio [NII] /Hα and the surface brightness of Hα for each galaxy in our sample. On this plot, we superimposed three models made using the photoionization code Cloudy (Ferland et al. 1998) and Starburst99 (Leitherer et al. 1999). Output spectra generated by Starburst99 for young galaxies with constant star formation rate are used in Cloudy with different initial densities (corresponding to the three lines in the plots, log n_H [cm^{-3}] = 1, 2, and 3), and ionization parameter ranging from about log U=−5 to −1. More details are available in Lehnert et al. (2009).

These zero order models can only give a crude estimate of the expected [NII] /Hα. They suggest, however, high ISM densities in these galaxies. This, in turn, implies thermal pressures similar to the pressures in the center of local starbursts such as M82, i.e., pressures much higher than observed in typical nearby galaxies.

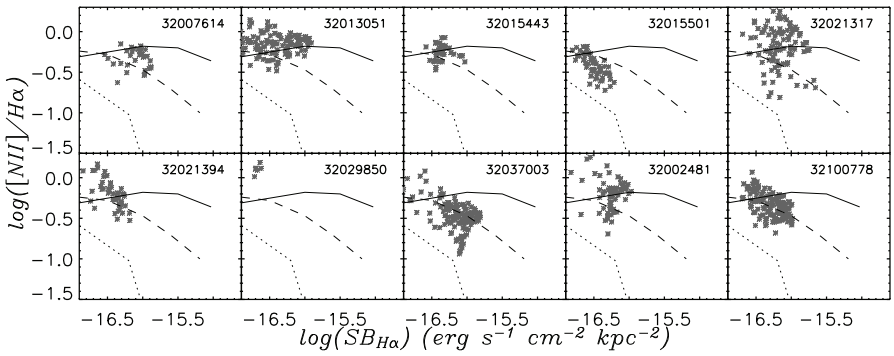

Figure 4. The Hα surface brightness (corrected for surface brightness dimming) versus the logarithm of the [NII] λ6583/Hα line ratio for all the individual spectra of the galaxies in our sample. The DEEP2 names of these galaxies are labeled in the upper-right corner of each panel. Lines represent results for photoionization modeling (see text for details) for different hydrogen densities: log n_H=1 (short dashed line), log n_H=2 (long dashed line), log n_H=3 (solid line). The ionization parameters span from log U=−5 to −1.0 (which increases from left to right along the lines, meaning low ionization parameters have relatively high log [NII] /Hα and low Hα surface brightnesses).

3.3. Is Mechanical Energy from Intense Star Formation the Key to the Kinematics?

Several explanations have been proposed for the underlying physical mechanism that drives the high dispersions we observe in these objects. The dispersions we observe could be generated by Jeans instabilities in the gas, the infall of gas from cosmic accretion, or general gravitational instabilities in the cooling gaseous disks of galaxies. However, none of these proposed mechanisms appears sufficient to reproduce the high velocity dispersions we observe.

In Figure 5, we show the relationship between Hα surface brightness and velocity dispersion for each of the galaxies in our sample. This suggests that the mechanical energy of star formation is powering the dynamics of the emission line gas inside the galaxy. In fact, with a simple dimensional analysis, and making the hypothesis that the mechanical energy output of the star formation is roughly conserved in the ISM, we expect the velocity dispersion to be proportional to the square root of the energy injection rate of the stars, dE_{SF}/dt. We have overplotted such a relationship on Figure 5 using a simple scaling law based on the star-formation rate per unit area and the velocity dispersion in the warm neutral/ionized gas in the disk of the MW and other nearby galaxies. This is a simple toy-model, but it uses no free parameters and reproduces the observed trend between the velocity dispersion and the star formation intensity (a more detailed analysis can be found in Lehnert et al. 2009). This shows that it is the star formation itself that is controlling the dynamics of the emission line gas.

4. Evidence for a Top-Heavy IMF?

Using measurements from SINFONI and DEEP2, we can estimate $F_{\mathrm{H}\alpha}/f_{\mathrm{FUV}}$ which is sensitive to the relative fractions of high mass (ionizing) to lower mass (non-ionizing) stars. The Hα emission traces the rate of ionization which is dominated by the massive O stars (>20$M_\odot$), while the FUV emission mainly traces somewhat less massive O and B stars (>3$M_\odot$). Making these measurements for our sample, we find that these distant galaxies "extend" the relationship

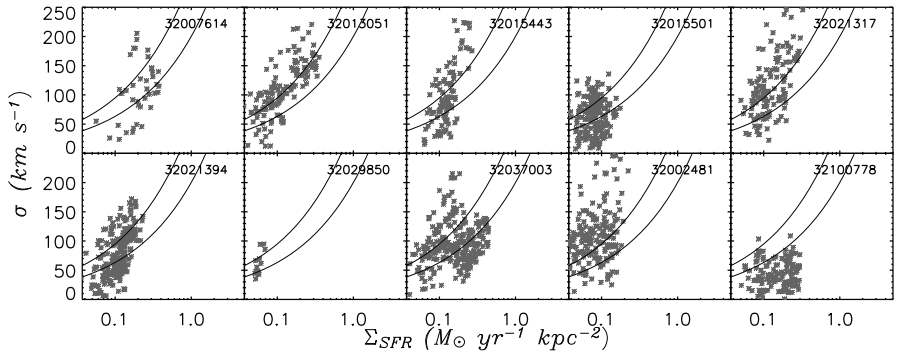

Figure 5. Star-formation intensity versus Hα velocity dispersion in our sample of galaxies. The DEEP2 names of these galaxies are labeled in the upper-right corner of each panel.The solid black lines show two simple relationship of the form $\sigma = \sqrt{\epsilon \dot{E}}$, where ϵ is the efficiency of coupling between the energy injected and the ISM. *(from bottom to top):* $\sigma = 200\sqrt{\Sigma_{SFR}}$ km s^{-1}, $\sigma = 300\sqrt{\Sigma_{SFR}}$ km s^{-1}.

found in Meurer et al. (2009) to higher surface brightnesses (Fig. 6) and more extreme $F_{\mathrm{H}\alpha}/f_{\mathrm{FUV}}$ ratios. At a minimum, this suggests the relationship between $F_{\mathrm{H}\alpha}/f_{\mathrm{FUV}}$ and surface brightness is one of the fundamental scaling relationships for galaxies as emphasized by Meurer et al. (2009). The high values we obtain for $F_{\mathrm{H}\alpha}/f_{\mathrm{FUV}}$ and high surface brightnesses may suggest a top-heavy IMF in these galaxies. Due to the lack of the necessary data, the relationship we present is unfortunately unextincted. Extinction should not however change the global trend which we have extended. Although metallicity variations can play a role in $F_{\mathrm{H}\alpha}/f_{\mathrm{FUV}}$, the metallicity of such galaxies is expected to be around solar (Erb et al. 2006), and models made with metallicities ranging from $Z = 0.2Z_{\odot}$ to $Z = 2.5Z_{\odot}$ suggest that this effect is negligible.

4.1. Effects of Bursts of Star Formation

$F_{\mathrm{H}\alpha}/f_{\mathrm{FUV}}$ is sensitive to variation in the star formation rate because of the differences in the lifetimes of O and B stars. Using GALAXEV (Bruzual & Charlot 2003), we modeled the impact of bursts on this relationship. We created different simulations adding bursts to a τ-model (using $\tau = 0.7Gyrs$) of galaxy formation. These bursts vary in intensity as well as in duration. Strong short bursts are obviously the most likely to produce high $F_{\mathrm{H}\alpha}/f_{\mathrm{FUV}}$. However, these bursts cannot be shorter than the dynamical time of these galaxies, estimated to be $\sim 70Myrs$. Using our observed constraint on the Hα equivalent widths, we can also estimate the maximum possible burst for each duration. With all these constraints, we find that bursts cannot explain the values of the extended relationship.

4.2. IMF Variations

To study the impact of varying the high-end of the IMF, we used Starburst99 to build synthesis models for IMFs with varying slopes from $\gamma = 1.25$ to 3.0 and upper-masses from $M = 60\mathrm{M}_{\odot}$ to $120\mathrm{M}_{\odot}$. We present our results for a constant SFR after 100 Myr and 1 Gyr (time enough to obtain an equilibrium in the number of O and B stars with time) in Figure 7. Our measurements of $F_{\mathrm{H}\alpha}/f_{\mathrm{FUV}}$ have been corrected by 0.25 dex towards decreasing $F_{\mathrm{H}\alpha}/f_{\mathrm{FUV}}$ to account for $\sim$1 mag of extinction. This shows that a flatter slope would be an easy way to explain the high values of $F_{\mathrm{H}\alpha}/f_{\mathrm{FUV}}$ we observe without having a more extreme upper-mass limit.

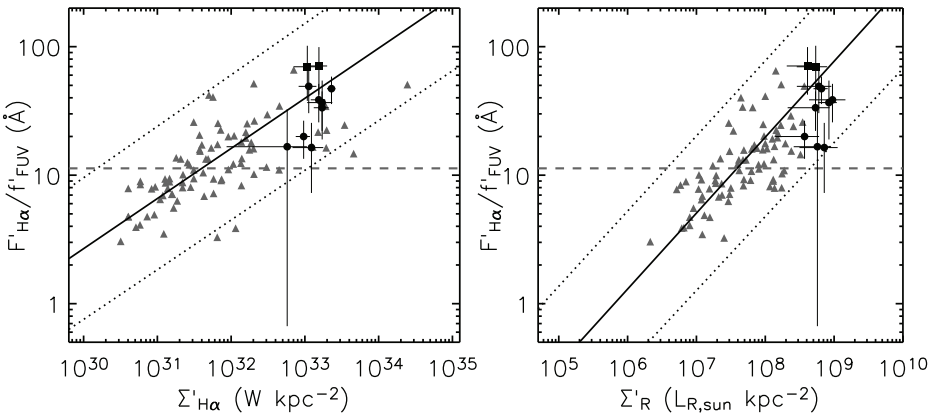

Figure 6. The ratio of Hα line flux to FUV flux-density as a function of the Hα effective surface brightness (right panel) and as a function of the *R*-band effective surface brightness (left panel). Grey triangles are the local galaxies data from Meurer et al. (2009), dark circles are data from this work as well as dark squares that represent AGN. The uncertainties are 3 σ. Galactic and internal dust absorption have not been taken into account in the data. The solid line shows the iteratively clipped least squares fit to the Meurer et al. (2009) data, while the dotted lines show the final clipping limits. The dashed line corresponds to the $F_{\mathrm{H}\alpha}/f_{\mathrm{FUV}}$ fiducial value of $F_{\mathrm{H}\alpha}/f_{\mathrm{FUV}}$ for a constant star-formation rate.

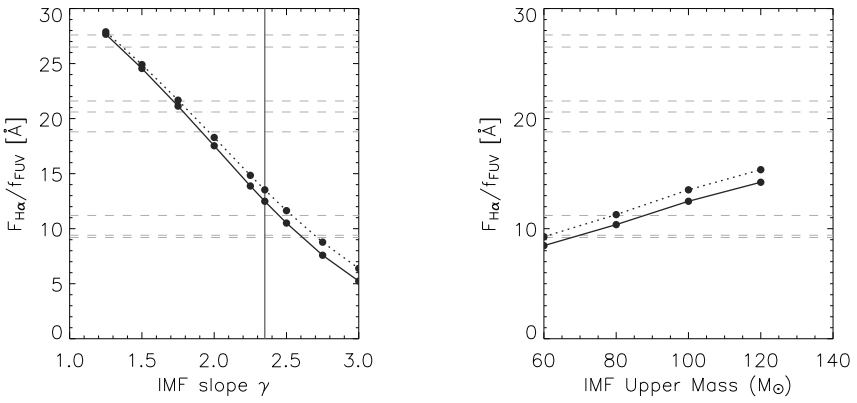

Figure 7. $F_{\mathrm{H}\alpha}/f_{\mathrm{FUV}}$ obtained for a constant SFR of 100 Myr (short-dashed line) and 1Gyr (plain line), for different values of the slope (left panel) and the upper-mass (right panel) of the IMF. Horizontal dashed lines represent the extinction corrected values of $F_{\mathrm{H}\alpha}/f_{\mathrm{FUV}}$ for our sample. On the left panel, the vertical plain line is the slope of a Salpeter IMF.

5. Conclusion

Galaxies within the first few Gyrs in the age of the universe provide extreme conditions which may impact the nature of galaxies and their star-formation. Galaxies in our sample have star formation rates more than one order of magnitude higher than typical galaxies in the local Universe, creating the high velocity dispersions we observe in ionized gas. In this dense medium and under such high internal pressures, it is interesting to test whether these extreme conditions impact the nature of star formation producing differences from star-formation that occurs in more quiescent environments. Using the relationship between $F_{\mathrm{H}\alpha}/f_{\mathrm{FUV}}$ and surface brightness as a diagnostic, we find that perhaps there is a top-heavy IMF in these high redshift galaxies. This may be a result of the relative high pressures and turbulence we find for galaxies at high redshift.

Acknowledgments. I would like to thank the organizers for their dedication and kindness during the whole process of organizing and conducting this conference, as well as for their generous grant and advice. Obviously, this meeting was a great success, from a scientific point of view (bringing together astronomers from different fields to discuss this interesting subject) as well as on many others: a perfectly and smoothly run organization in a wonderful place!

References

Boselli, A., Boissier, S., & Cortese 2009, ApJ, 706, 1527
Bruzual, G., & Charlot, S. 2003, MNRAS, 344, 1000
Elmegreen, D. M., Elmegreen, B. G., & Marcus 2009, ApJ, 701, 306
Erb, D. K., Shapley, A. E., & Pettini 2006, ApJ, 644, 813
Ferland, G. J., Korista, K. T., & Verner 1998, PASP, 110, 761
Heckman, T. M. 2001, in Gas and Galaxy Evolution, edited by J. E. Hibbard, M. Rupen, & J. H. van Gorkom, vol. 240 of Astronomical Society of the Pacific Conference Series, 345
Hoversten, E. A., & Glazebrook, K. 2008, ApJ, 675, 163
Lee, J. C., Gil de Paz, A., Tremonti, C., Kennicutt, R. C., Salim, S., Bothwell, M., Calzetti, D., et al. 2009, ApJ, 706, 599
Lehnert, M. D., & Heckman, T. M. 1996, ApJ, 472, 546
Lehnert, M. D., Nesvadba, N. P. H., & Tiran, L. L. 2009, ApJ, 699, 1660
Leitherer, C., Schaerer, D., Goldader, J. D., González Delgado, R. M., Robert, C., Kune, D. F., de Mello, D. F., Devost, D., & Heckman, T. M. 1999, ApJS, 123, 3
Meurer, G. R., Wong, O. I., Kim, J. H., Hanish, D. J., Heckman, T. M., Werk, J., Bland-Hawthorn, J., et al. 2009, ApJ, 695, 765

D.2 IAU Symposium 277: "Tracing the Ancestries of Galaxies on the Land of our Ancestors"

December 13-17, 2010, Ouagadougou, Burkina Faso

Tracing the Ancestry of Galaxies on the Land of our Ancestors
Proceedings IAU Symposium No. 277, 2011
A.C. Editor, B.D. Editor & C.E. Editor, eds.

DOI: 00.0000/X000000000000000X

The turbulent ISM of galaxies 10 Gyrs ago: Star-formation, gas accretion, and IMF

Loïc Le Tiran and Matthew D. Lehnert

Laboratoire d'étude des Galaxies, Etoiles, Physique et Instrumentation
GEPI, Observatoire de Paris, UMR8111 du CNRS, 92195 meudon, France

Abstract. The utilization of integral-field spectroscopy has led us to a new understanding of the physical conditions in galaxies within the first few billion years after the Big Bang. In this proceedings, we analyze observations of ∼50 massive galaxies as seen as they were 10 Gyrs ago using SINFONI from the ESO-VLT. We show that the large line width they exhibit can be explained by the intense mechanical energy output from the young stars. We also study the influence of cold gas accretion upon these galaxies: We show that an unrealistic amount of shocked gas would be needed in order to explain the Hα emission from these galaxies through shocks from gas accretion with velocity about the Hα line widths of these galaxies. We also use DEEP2 photometric measurements for a sub-sample of 10 of these galaxies to evaluate their ratio of Hα to FUV flux as a function of their Hα and R-band luminosity surface brightnesses. Our data suggests that perhaps their initial mass function (IMF) is flatter than Salpeter at the high mass end, as has been suggested recently for some local galaxies. It may be that high turbulence is responsible for skewing the IMF towards more massive stars as suggested by some theories of star-formation. Much work is however needed to accredit this hypothesis.

Keywords. galaxies: high-redshift — galaxies: evolution — galaxies: ISM — galaxies: kinematics and dynamics — infrared: galaxies

1. Introduction

Galaxies in the early Universe exhibit many complex features. An interesting example is their large Hα line width, which suggests that a high amount of turbulences is at work in the warm gas of these objects. Many models have been trying to reproduce these different observations, especially with inflows of cold gas (e.g. Dekel *et al.* (2009)). It is therefore important to distinguish the different contributions to the observables from gas accretion, gravitational instabilities, or mechanical energy output from star formation (which major role is emphasized in Lehnert *et al.* (2009)). The IMF is another important underlying parameter which determines some of the most obvious characteristics of galaxies as observed in the local universe. Many recent studies have been studied this assumption, using for example the quantity $F_{\mathrm{H}\alpha}/f_{\mathrm{FUV}}$ (but only in the local universe, e.g. Meurer *et al.* (2009)). Perhaps though, galaxies in the early Universe, with their generally more extreme properties are interesting targets for studying star formation under extreme physical conditions, high turbulence and thermal pressures, which might impact the overall shape of the IMF.

In this proceedings we use SINFONI observations on the ESO-VLT of a sample of fifty galaxies around z∼2±1. This sample will be described in details in Le Tiran et al. (2011, in preparation).

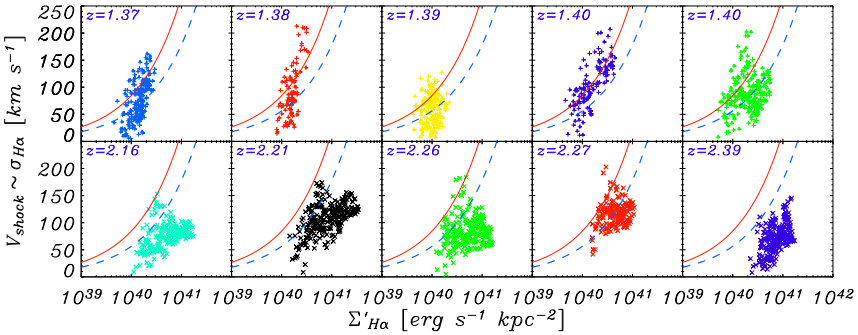

Figure 1. Observed Hα surface brightness values (in erg s^{-1} kpc^{-2}) as a function of Hα line width (in km s^{-1}) for a representative sub-sample of 10 galaxies. Redshifts of these galaxies are labeled in the upper-left corner of each panel. The solid lines show two simple relationships of the form $\sigma = \sqrt{\epsilon \dot{E}}$, where ϵ is the efficiency of coupling between the energy injected and the ISM: $\sigma = 200\sqrt{\Sigma_{SFR}}$ km s^{-1} (in dashed blue), $\sigma = 300\sqrt{\Sigma_{SFR}}$ km s^{-1} (in plain red).

2. What is driving the internal motions of these galaxies?

Galaxies at high redshift exhibit surprisingly high values of their Hα line widths. During the last years several explanations have been suggested for the underlying physical mechanism that drives these high dispersions. They could be for example generated by Jeans instabilities in the gas, by the general gravitational instabilities in the cooling gaseous disks of galaxies, or by the infall of gas from cosmic accretion (an effect studied in more details in Le Tiran et al. (2011, submitted) and briefly in Section 3). However, as developed in Lehnert *et al.* (2009), none of these proposed mechanisms appears sufficient to reproduce the high velocity dispersions we observe.

Lehnert *et al.* (2009) suggested that the dynamics of the emission line gas inside the galaxy is powered by the mechanical energy of star formation. If we make the hypothesis that the mechanical energy output of the star formation is roughly conserved in the ISM, by using a simple dimensional analysis we expect the velocity dispersion to be proportional to the square root of the energy injection rate of the stars, dE_{SF}/dt. This relationship is over-plotted on Fig. 1: using a simple scaling law based on the star-formation rate per unit area and the velocity dispersion in the warm neutral/ionized gas in the disk of the MW and other nearby galaxies. This simple toy-model, which has the advantage of using no free parameter, reproduces the observed trend between the velocity dispersion and the star formation intensity (a more detailed analysis can be found in Lehnert *et al.* (2009)). It is therefore the star formation itself that is controlling the dynamics of the emission line gas.

3. Can shocks induced by cosmological gas accretion produce the observed Hα brightnesses?

Gas accretion onto galaxies is undoubtedly a complex process. To explain cold gas accretion, the gas has to lose its energy and momentum through radiation and shocks upon hitting the ISM of the galaxy. Can we see direct evidence for this in our integral field Hα data sets?

If the infalling gas dissipates energy by colliding with gas already in a galaxy disk, we can estimate the rate at which it dissipates using various complementary shock models (Raymond (1979), Shull & McKee(1979), Allen *et al.* (2008)). We will assume that the

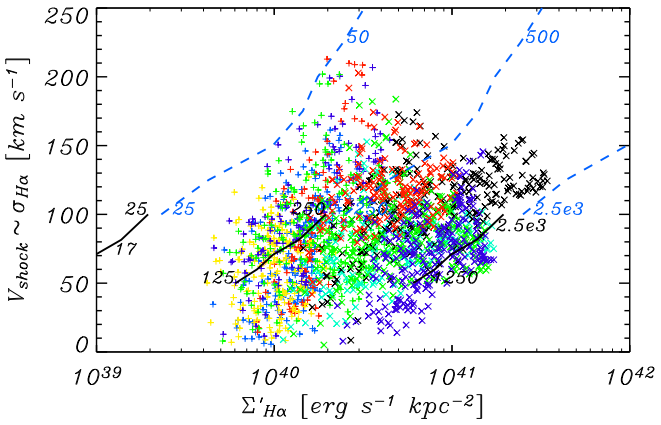

Figure 2. Observed Hα surface brightness values (in erg s^{-1} kpc^{-2}) as a function of Hα line width (in km s^{-1}) for a representative sub-sample of 10 galaxies. Colors and symbols are the same than in Fig. 1. Lines correspond to the Hα surface brightnesses which would be generated by shocks with a velocity equal to the velocity dispersion of the Hα line. Models from Raymond (1979) are in plain black and from Allen *et al.* (2008) in dashed blue. The numbers along each line indicate the surface accretion rate (in M$_\odot$ yr^{-1} kpc^{-2}) necessary to produce the observed Hα surface brightnesses. The 3 sets of lines are for a different pre-shock density, 10, 100, 1000 cm^{-3}, from left to right.

observed velocity dispersion in distant galaxies is about the shock velocity range (∼50-250 km s^{-1}). The underlying assumption is that all the accretion energy is converted into supersonic turbulence which then dissipates as fast shocks. We can then estimate the amount of mass that would be need to be shocked to explain the observed surface brightnesses as a function of dispersion. The results are shown in Fig. 2. We find that to explain the surface brightnesses with these shock models, the necessary mass flow rates through the shocks are unrealistically high, implying accretion rate densities of over a few hundred M$_\odot$ yr^{-1} kpc^{-2}. Therefore, over a dynamical time of about 200-300 Myrs, the amount of gas that would need to be shock heated is of the order of 10^{13} M$_\odot$, two orders of magnitude larger than the total ISM mass. A more complete analysis of the influence of the gas accretion, and its importance relative to Hα emission from star formation, will be presented in Le Tiran et al. (2011, submitted).

4. Evidence for a top-heavy IMF?

This section focuses on a sub-sample of 10 galaxies, for which we have DEEP2 data. We can therefore estimate $F_{\mathrm{H}\alpha}/f_{\mathrm{FUV}}$, a quantity which is sensitive to the relative fractions of high mass (ionizing) to lower mass (non-ionizing) stars. The Hα emission traces the rate of ionization which is dominated by the massive O stars, over 20 M$_\odot$, while the FUV emission mainly traces somewhat less massive (O and B) stars, over 3 M$_\odot$. Making these measurements for our sample, we find that these distant galaxies "extend" the relationship found in Meurer *et al.* (2009) to higher surface brightnesses and more extreme ratios, as seen in Fig. 3. This suggests that the relationship between $F_{\mathrm{H}\alpha}/f_{\mathrm{FUV}}$ and surface brightness is one of the fundamental scaling relationships for galaxies as emphasized by Meurer *et al.* (2009). The high values we obtain for $F_{\mathrm{H}\alpha}/f_{\mathrm{FUV}}$ and high surface brightnesses may suggest a top-heavy IMF in these galaxies. Due to the lack of the necessary data, the relationship we present is unfortunately unextincted. Our model-

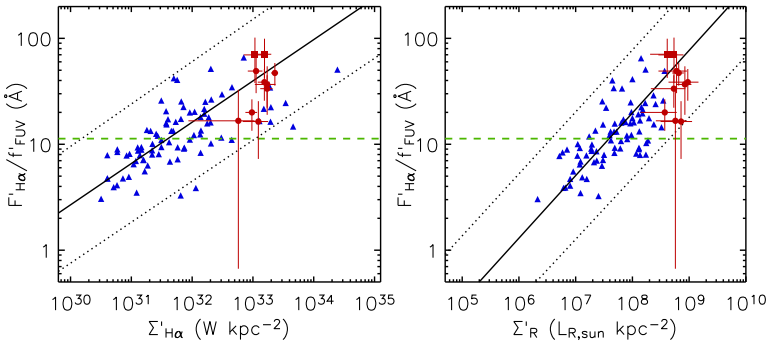

Figure 3. The ratio of Hα line flux to FUV flux-density as a function of the Hα effective surface brightness (right panel) and as a function of the R-band effective surface brightness (left panel). Blue triangles are the local galaxies data from Meurer *et al.* (2009), red circles are data from this work as well as red squares that represent AGN. The uncertainties are 3 σ. Galactic and internal dust absorption have not been taken into account in any of these data. The solid line shows the iteratively clipped least squares fit to the Meurer *et al.* (2009) data, while the dotted lines show the final clipping limits. The green dashed line corresponds to the $F_{\mathrm{H}\alpha}/f_{\mathrm{FUV}}$ fiducial value of $F_{\mathrm{H}\alpha}/f_{\mathrm{FUV}}$ for a constant star-formation rate.

ing shows that neither bursts of star-formation nor changes in the metallicity can explain our measurements.

To study the impact of varying high-end of the IMF, we used Starburst99 (Leitherer *et al.* (1999)) to build synthesis models for IMFs with varying slopes from $\gamma = 1.25$ to 3. and varying upper-masses from $M = 60\mathrm{M}_{\odot}$ to $120\mathrm{M}_{\odot}$. While variations of the upper-mass limit of the IMF cannot explain our measurements, a flatter slope would be a possible explanation to the high values of $F_{\mathrm{H}\alpha}/f_{\mathrm{FUV}}$. These results, although preliminary, suggest that perhaps the very particular physical conditions at work in high redshift galaxies favor a top-heavy IMF. Additonal data is needed to investigate this hypothesis.

5. Conclusion

Galaxies within the first few Gyrs in the age of the universe provide extreme conditions which may impact the nature of galaxies and their star-formation. Galaxies in our sample have star formation rate more than one order higher than typical galaxies in the local Universe, creating the high velocity dispersions we observe in ionized gas. In the case of cold flows of gas accreting upon a galaxy, the amount of shocked gas that would be needed to explain such Hα emission would be unrealisticaly high. Using the relationship between $F_{\mathrm{H}\alpha}/f_{\mathrm{FUV}}$ and surface brightness as a diagnostic, we find that perhaps there is a top-heavy IMF in these high redshift galaxies. This may be a result of the relative high pressures and turbulence we find for galaxies at high redshift.

References

Allen, M. G., Groves, B. A., Dopita, M. A., Sutherland, R. S., et al. 2008, *ApJS*, 178, 20
Dekel, A., et al. 2009, *Nature*, 457, 451
Lehnert, M. D., Nesvadba, N. P. H., Le Tiran, L., et al. 2009, *ApJ*, 699, 1660
Leitherer, C., et al. 1999, *ApJ*, 123, 3
Meurer, G. R., et al. 2009, *ApJ*, 695, 765
Raymond, J. C. 1979, *ApJS*, 39, 1
Shull, J. M., & McKee, C. F. 1979, *ApJ*, 227, 131

Discussion

L. Ho: I don't understand the argument that these large line widths are not due to beam smearing. You only reduced the beam by factor of 3 for 0.6" - 0.2". 0.2" = 2 kpc; and there can be a lot of rotation within that scale (e.g. Milky-Way).

L. Le Tiran: You are totally right. Using our adaptive optics data and comparing it to the same data without AO, we can constrain the effect of beam smearing from 0.6" to 0.2". Which still accounts for 2 kpc, effectively. However, we have also modeled the effect of beam smearing in our observations: using NICMOS observations of a few of these galaxies, we can have a more precise idea of the stellar distribution in these objects than in the SINFONI data. We then use the SINFONI velocity map and typical line widths observed in the local universe to reconstruct a simulated high spatial resolution model of our data. We then apply an artificial beam smearing. These analogues of observations display line width that are still low compared to what we observe. We therefore think this effect is small compared to the effect of mechanical output from star formation. However, a more complete analysis of the effect of beam smearing should be published soon in le Tiran et al. (2011, in preparation).

L. Ho: You say that it is not an effect of clumps. How are these sources related to the clumps seen in "clump clusters" or "chain galaxies", which are "clumpy" ?

L. Le Tiran: An important fraction of these observations can effectively be categorized as "clump clusters".

B. Partridge: If you change the IMF at the bright end, you will alter the formation FIR/ratio correlation. Is there any evidence for such a change in L_{FIR}/Lratio ?

L. Le Tiran: You are right. Unfortunately, we have too few data on these galaxies to answer this question.

M. Dickinson: Do you interpret the slope of f(Halpha)/f(FUV) vs $\Sigma H\alpha$ as implying that the IMF slope varies as a function of $\Sigma H\alpha$?

L. Le Tiran: These results have to be taken very carefully. Especially, more data is needed to constraint more accurately different effects like the extinction. Such work has been done by Boselli et al. (2009) or Lee et al. (2009) on a sample of local galaxies only. The high redshift universe is an interesting laboratory to study galactic processes in more extreme conditions. One could imagine that star formation could be affected by the particular conditions of pressure, high turbulences, UV radiations etc... In these conditions, an evolution of f(Halpha)/f(FUV) vs $\Sigma H\alpha$ could be very enlightening, as it could be linked to the quantity of UV radiation or turbulence in the ISM.

Bibliography

Adelberger, K. L., Steidel, C. C., Shapley, A. E., Hunt, M. P., Erb, D. K., Reddy, N. A. & Pettini, M. (2004) Optical Selection of Star-forming Galaxies at Redshifts 1 < z < 3. ApJ, 607:226–240. 13

Agertz, O., Lake, G., Teyssier, R., Moore, B., Mayer, L. & Romeo, A. B. (2009) Large-scale galactic turbulence: can self-gravity drive the observed HI velocity dispersions? MNRAS, 392:294–308. 114, 143, 177

Allen, M. G., Groves, B. A., Dopita, M. A., Sutherland, R. S. & Kewley, L. J. (2008) The MAPPINGS III Library of Fast Radiative Shock Models. ApJS, 178:20–55. 134, 136, 149, 151

Anderson, M. E. & Bregman, J. N. (2010) Do Hot Halos Around Galaxies Contain the Missing Baryons? ApJ, 714:320–331. 4, 131

Aravena, M., Carilli, C., Daddi, E., Wagg, J., Walter, F., Riechers, D., Dannerbauer, H., Morrison, G. E., Stern, D. & Krips, M. (2010) Cold Molecular Gas in Massive, Star-forming Disk Galaxies at z = 1.5. ApJ, 718:177–183. 190, 194

Armus, L., Heckman, T. M. & Miley, G. K. (1989) Long-slit optical spectroscopy of powerful far-infrared galaxies - The nature of the nuclear energy source. ApJ, 347:727–742. 90

Armus, L., Heckman, T. M. & Miley, G. K. (1990) The optical emission-line nebulae of powerful far-infrared galaxies. ApJ, 364:471–495. 90

Baldwin, J. A., Phillips, M. M. & Terlevich, R. (1981) Classification parameters for the emission-line spectra of extragalactic objects. PASP, 93:5–19. 6, 85, 98

Basu-Zych, A. R., Gonçalves, T. S., Overzier, R., Law, D. R., Schiminovich, D., Heckman, T., Martin, C., Wyder, T. & O'Dowd, M. (2009) An OSIRIS Study of the Gas Kinematics in a Sample of UV-Selected Galaxies: Evidence of "Hot and Bothered" Starbursts in the Local Universe. ApJ, 699:L118–L124. 7, 162

Bennert, N., Falcke, H., Schulz, H., Wilson, A. S. & Wills, B. J. (2002) Size and Structure of the Narrow-Line Region of Quasars. ApJ, 574:L105–L109. 105

Blitz, L. & Rosolowsky, E. (2006) The Role of Pressure in GMC Formation II: The H2-Pressure Relation. ApJ, 650:933–944. 7, 108, 143, 181, 191, 201

Bouché, N., Cresci, G., Davies, R., Eisenhauer, F., Förster Schreiber, N. M., Genzel, R., Gillessen, S., Lehnert, M., Lutz, D., Nesvadba, N., Shapiro, K. L., Sternberg, A., Tacconi, L. J., Verma, A., Cimatti, A., Daddi, E., Renzini, A., Erb, D. K., Shapley, A. & Steidel, C. C. (2007) Dynamical Properties of z ˜ 2 Star-forming Galaxies and a Universal Star Formation Relation. ApJ, 671:303–309. 114

Bournaud, F. & Elmegreen, B. G. (2009) Unstable Disks at High Redshift: Evidence for Smooth Accretion in Galaxy Formation. ApJ, 694:L158–L161. 109, 123

Bournaud, F., Elmegreen, B. G. & Elmegreen, D. M. (2007) Rapid Formation of Exponential Disks and Bulges at High Redshift from the Dynamical Evolution of Clump-Cluster and Chain Galaxies. ApJ, 670:237–248. 112, 123, 184

Bournaud, F., Daddi, E., Elmegreen, B. G., Elmegreen, D. M., Nesvadba, N., Vanzella, E., Di Matteo, P., Le Tiran, L., Lehnert, M. & Elbaz, D. (2008) Observations and modeling of a clumpy galaxy at z = 1.6. Spectroscopic clues to the origin and evolution of chain galaxies. A&A, 486:741–753. 114, 184

Bournaud, F., Elmegreen, B. G., Teyssier, R., Block, D. L. & Puerari, I. (2010) ISM properties in hydrodynamic galaxy simulations: turbulence cascades, cloud formation, role of gravity and feedback. MNRAS, 409:1088–1099. 187

Bouwens, R. J., Illingworth, G. D., Franx, M., Chary, R.-R., Meurer, G. R., Conselice, C. J., Ford, H., Giavalisco, M. & van Dokkum, P. (2009) UV Continuum Slope and Dust Obscuration from z ˜ 6 to z ˜ 2: The Star Formation Rate Density at High Redshift. ApJ, 705:936–961. 206

Brinchmann, J., Pettini, M. & Charlot, S. (2008) New insights into the stellar content and physical conditions of star-forming galaxies at z = 2-3 from spectral modelling. MNRAS, 385:769–782. 6, 85, 98, 100, 108, 121, 181

Brooks, A. M., Governato, F., Quinn, T., Brook, C. B. & Wadsley, J. (2009) The Role of Cold Flows in the Assembly of Galaxy Disks. ApJ, 694:396–410. 5, 7, 131, 161

Bruzual, G. & Charlot, S. (2003) Stellar population synthesis at the resolution of 2003. MNRAS, 344:1000–1028. 207

Burkert, A., Genzel, R., Bouche, N., Cresci, G., Khochfar, S., Sommer-Larsen, J., Sternberg, A., Naab, T., Forster Schreiber, N., Tacconi, L., Shapiro, K., Hicks, E., Lutz, D., Davies, R., Buschkamp, P. & Genel, S. (2010) High-redshift Star-forming Galaxies: Angular Momentum and Baryon Fraction, Turbulent Pressure Effects, and the Origin of Turbulence. ApJ, 725:2324–2332. 7, 132, 161

Cappellari, M. & Copin, Y. (2003) Adaptive spatial binning of integral-field spectroscopic data using Voronoi tessellations. MNRAS, 342:345–354. 234

Ceverino, D., Dekel, A. & Bournaud, F. (2010) High-redshift clumpy discs and bulges in cosmological simulations. MNRAS, 404:2151–2169. 132, 184

Chemin, L., Carignan, C. & Foster, T. (2009) H I Kinematics and Dynamics of Messier 31. ApJ, 705:1395–1415. 8

Chilingarian, I. V., Di Matteo, P., Combes, F., Melchior, A. & Semelin, B. (2010) The GalMer database: galaxy mergers in the virtual observatory. A&A, 518:A61+. 169

Cimatti, A., Daddi, E., Mignoli, M., Pozzetti, L., Renzini, A., Zamorani, G., Broadhurst, T., Fontana, A., Saracco, P., Poli, F., Cristiani, S., D'Odorico, S., Giallongo, E., Gilmozzi, R. & Menci, N. (2002) The K20 survey. I. Disentangling old and dusty star-forming galaxies in the ERO population. A&A, 381:L68–L72. 14

Coil, A. L., Newman, J. A., Kaiser, N., Davis, M., Ma, C.-P., Kocevski, D. D. & Koo, D. C. (2004) Evolution and Color Dependence of the Galaxy Angular Correlation Function: 350,000 Galaxies in 5 Square Degrees. ApJ, 617:765–781. 206

Conselice, C. J., Rajgor, S. & Myers, R. (2008) The structures of distant galaxies - I. Galaxy structures and the merger rate to z ˜ 3 in the Hubble Ultra-Deep Field. MNRAS, 386:909–927. 2, 160

Contini, T., Epinat, B., Queyrel, J., Vergani, D., Tasca, L., Amram, P., Garilli, B., Kissler-Patig, M., Le Fèvre, O., Moultaka, J., Paioro, L., Tresse, L., Bournaud, F. & Perez-Montero, E. (2011) ArXiv e-prints. 6

Cox, D. P. (2005) The Three-Phase Interstellar Medium Revisited. ARA&A, 43:337–385. 7, 161

Croton, D. J., Springel, V., White, S. D. M., De Lucia, G., Frenk, C. S., Gao, L., Jenkins, A., Kauffmann, G., Navarro, J. F. & Yoshida, N. (2006) The many lives of active galactic nuclei: cooling flows, black holes and the luminosities and colours of galaxies. MNRAS, 365:11–28. 2, 160

Daddi, E., Cimatti, A., Renzini, A., Fontana, A., Mignoli, M., Pozzetti, L., Tozzi, P. & Zamorani, G. (2004) A New Photometric Technique for the Joint Selection of Star-forming and Passive Galaxies at 1.4 < z < 2.5. ApJ, 617:746–764. 13

Daddi, E., Dickinson, M., Morrison, G., Chary, R., Cimatti, A., Elbaz, D., Frayer, D., Renzini, A., Pope, A., Alexander, D. M., Bauer, F. E., Giavalisco, M., Huynh, M., Kurk, J. & Mignoli, M. (2007) Multiwavelength Study of Massive Galaxies at z˜2. I. Star Formation and Galaxy Growth. ApJ, 670:156–172. 190, 192, 193, 194, 195

Daddi, E., Dannerbauer, H., Elbaz, D., Dickinson, M., Morrison, G., Stern, D. & Ravindranath, S. (2008) Vigorous Star Formation with Low Efficiency in Massive Disk Galaxies at z = 1.5. ApJ, 673:L21–L24. 114

Daddi, E., Bournaud, F., Walter, F., Dannerbauer, H., Carilli, C. L., Dickinson, M., Elbaz, D., Morrison, G. E., Riechers, D., Onodera, M., Salmi, F., Krips, M. & Stern, D. (2010) Very High Gas Fractions and Extended Gas Reservoirs in z = 1.5 Disk Galaxies. ApJ, 713:686–707. 153, 187, 190, 194

Dannerbauer, H., Daddi, E., Riechers, D. A., Walter, F., Carilli, C. L., Dickinson, M., Elbaz, D. & Morrison, G. E. (2009) Low Milky-Way-Like Molecular Gas Excitation of Massive Disk Galaxies at z ˜ 1.5. ApJ, 698:L178–L182. 190, 194

de Ravel, L., Le Fèvre, O., Tresse, L., Bottini, D., Garilli, B., Le Brun, V., Maccagni, D., Scaramella, R., Scodeggio, M., Vettolani, G., Zanichelli, A., Adami, C., Arnouts, S., Bardelli, S., Bolzonella, M., Cappi, A., Charlot, S., Ciliegi, P., Contini, T., Foucaud, S., Franzetti, P., Gavignaud, I., Guzzo, L., Ilbert, O., Iovino, A., Lamareille, F., McCracken, H. J., Marano, B., Marinoni, C., Mazure, A., Meneux, B., Merighi, R., Paltani, S., Pellò, R., Pollo, A., Pozzetti, L., Radovich, M., Vergani, D., Zamorani, G., Zucca, E., Bondi, M., Bongiorno, A., Brinchmann, J., Cucciati, O., de La Torre, S., Gregorini, L., Memeo, P., Perez-Montero, E., Mellier, Y., Merluzzi, P. & Temporin, S. (2009) The VIMOS VLT Deep Survey. Evolution of the major merger rate since z ˜ 1 from spectroscopically confirmed galaxy pairs. A&A, 498:379–397. 2, 160

Dekel, A. & Birnboim, Y. (2008a) Gravitational quenching in massive galaxies and clusters by clumpy accretion. MNRAS, 383:119–138. 3, 4, 83, 84, 109, 110, 122, 133, 135

Dekel, A. & Birnboim, Y. (2008b) Gravitational quenching in massive galaxies and clusters by clumpy accretion. MNRAS, 383:119–138. 112

Dekel, A., Birnboim, Y., Engel, G., Freundlich, J., Goerdt, T., Mumcuoglu, M., Neistein, E., Pichon, C., Teyssier, R. & Zinger, E. (2009) Cold streams in early massive hot haloes as the main mode of galaxy formation. Nature, 457:451–454. 5, 7, 112, 131, 134, 135, 139, 161, 191

Di Matteo, P., Bournaud, F., Martig, M., Combes, F., Melchior, A.-L. & Semelin, B. (2008) On the frequency, intensity, and duration of starburst episodes triggered by galaxy interactions and mergers. A&A, 492:31–49. 169

Di Matteo, P., Jog, C. J., Lehnert, M. D., Combes, F. & Semelin, B. (2009) Generation of rotationally dominated galaxies by mergers of pressure-supported progenitors. A&A, 501:L9–L13. 169

Dib, S., Bell, E. & Burkert, A. (2006) The Supernova Rate-Velocity Dispersion Relation in the Interstellar Medium. ApJ, 638:797–810. 8, 116, 117, 132, 177

Dopita, M. A. & Ryder, S. D. (1994) On the law of star formation in disk galaxies. ApJ, 430:163–178. 84, 192

Dopita, M. A. & Sutherland, R. S. (1995) Spectral Signatures of Fast Shocks. II. Optical Diagnostic Diagrams. ApJ, 455:468–+. 134

Elbaz, D., Daddi, E., Le Borgne, D., Dickinson, M., Alexander, D. M., Chary, R., Starck, J., Brandt, W. N., Kitzbichler, M., MacDonald, E., Nonino, M., Popesso, P., Stern, D. & Vanzella, E. (2007) The reversal of the star formation-density relation in the distant universe. A&A, 468:33–48. 190, 192, 193, 194, 195

Elbaz, D., Dickinson, M., Hwang, H. S., Diaz-Santos, T., Magdis, G., Magnelli, B., Le Borgne, D., Galliano, F., Pannella, M., Chanial, P., Armus, L., Charmandaris, V., Daddi, E., Aussel, H., Popesso, P., Kartaltepe, J., Altieri, B., Valtchanov, I., Coia, D., Dannerbauer, H., Dasyra, K., Leiton, R., Mazzarella, J., Buat, V., Burgarella, D., Chary, R. ., Gilli, R., Ivison, R. J., Juneau, S., LeFloc'h, E., Lutz, D., Morrison, G. E., Mullaney, J., Murphy, E., Pope, A., Scott, D., Alexander, D., Brodwin, M., Calzetti, D., Cesarsky, C., Charlot, S., Dole, H., Eisenhardt, P., Ferguson, H. C., Foerster-Schreiber, N., Frayer, D., Giavalisco, M., Huynh, M., Koekemoer, A. M., Papovich, C., Reddy, N., Surace, C., Teplitz, H., Yun, M. S. & Wilson, G. (2011) ArXiv e-prints. 191, 192

Elmegreen, B. G. (2002) Star Formation from Galaxies to Globules. ApJ, 577:206–220. 121, 122, 125, 201

Elmegreen, B. G. & Burkert, A. (2010) Accretion-Driven Turbulence and the Transition to Global Instability in Young Galaxy Disks. ApJ, 712:294–302. 7, 131, 138, 161, 181, 183, 184, 185, 191

Elmegreen, B. G. & Elmegreen, D. M. (2005) Stellar Populations in 10 Clump-Cluster Galaxies of the Hubble Ultra Deep Field. ApJ, 627:632–646. 109, 113, 123

Elmegreen, B. G. & Elmegreen, D. M. (2006) Observations of Thick Disks in the Hubble Space Telescope Ultra Deep Field. ApJ, 650:644–660. 109, 112, 122

Elmegreen, B. G., Elmegreen, D. M. & Leitner, S. N. (2003) A Turbulent Origin for Flocculent Spiral Structure in Galaxies. ApJ, 590:271–283. 114

Elmegreen, B. G., Bournaud, F. & Elmegreen, D. M. (2008a) Bulge Formation by the Coalescence of Giant Clumps in Primordial Disk Galaxies. ApJ, 688:67–77. 112, 123, 124, 125

Elmegreen, B. G., Klessen, R. S. & Wilson, C. D. (2008b) On the Constancy of the Characteristic Mass of Young Stars. ApJ, 681:365–374. 217

Elmegreen, B. G., Elmegreen, D. M., Fernandez, M. X. & Lemonias, J. J. (2009a) ApJ. 184

Elmegreen, D. M. (2007) Clumpy Galaxies in the Early Universe. In: F. Combes & J. Palous (ed.), IAU Symposium. vol. 235 of *IAU Symposium*, pp. 376–380. 112

Elmegreen, D. M., Elmegreen, B. G. & Hirst, A. C. (2004) Discovery of Face-on Counterparts of Chain Galaxies in the Tadpole Advanced Camera for Surveys Field. ApJ, 604:L21–L23. 7, 161, 184

Elmegreen, D. M., Elmegreen, B. G., Ravindranath, S. & Coe, D. A. (2007) Resolved Galaxies in the Hubble Ultra Deep Field: Star Formation in Disks at High Redshift. ApJ, 658:763–777. 113, 123

Elmegreen, D. M., Elmegreen, B. G., Marcus, M. T., Shahinyan, K., Yau, A. & Petersen, M. (2009b) Clumpy Galaxies in Goods and Gems: Massive Analogs of Local Dwarf Irregulars. ApJ, 701:306–329. 123, 184

Epinat, B., Amram, P., Marcelin, M., Balkowski, C., Daigle, O., Hernandez, O., Chemin, L., Carignan, C., Gach, J.-L. & Balard, P. (2008) GHASP: an Hα kinematic survey of spiral and irregular galaxies - VI. New Hα data cubes for 108 galaxies. MNRAS, 388:500–550. 8

Epinat, B., Contini, T., Le Fèvre, O., Vergani, D., Garilli, B., Amram, P., Queyrel, J., Tasca, L. & Tresse, L. (2009) Integral field spectroscopy with SINFONI of VVDS galaxies. I. Galaxy dynamics and mass assembly at $1.2 < z < 1.6$. A&A, 504:789–805. 95, 122, 133

Epinat, B., Amram, P., Balkowski, C. & Marcelin, M. (2010) Evidence for strong dynamical evolution in disc galaxies through the last 11 Gyr. GHASP VIII - a local reference sample of rotating disc galaxies for high-redshift studies. MNRAS, 401:2113–2147. 162

Erb, D. K., Steidel, C. C., Shapley, A. E., Pettini, M. & Adelberger, K. L. (2004) The Kinematics of Morphologically Selected z˜2 Galaxies in the GOODS-North Field. ApJ, 612:122–130. 6, 84

Erb, D. K., Shapley, A. E., Pettini, M., Steidel, C. C., Reddy, N. A. & Adelberger, K. L. (2006a) The Mass-Metallicity Relation at z gt 2. ApJ, 644:813–828. 6, 8, 84, 85, 98, 103

Erb, D. K., Steidel, C. C., Shapley, A. E., Pettini, M., Reddy, N. A. & Adelberger, K. L. (2006b) Hα Observations of a Large Sample of Galaxies at z ˜ 2: Implications for Star Formation in High-Redshift Galaxies. ApJ, 647:128–139. 5, 84

Erb, D. K., Steidel, C. C., Shapley, A. E., Pettini, M., Reddy, N. A. & Adelberger, K. L. (2006c) Hα Observations of a Large Sample of Galaxies at z ˜ 2: Implications for Star Formation in High-Redshift Galaxies. ApJ, 647:128–139. 161, 163, 190

Erb, D. K., Steidel, C. C., Shapley, A. E., Pettini, M., Reddy, N. A. & Adelberger, K. L. (2006d) The Stellar, Gas, and Dynamical Masses of Star-forming Galaxies at z ˜ 2. ApJ, 646:107–132. 107, 117

Evans, I. N., Tsvetanov, Z., Kriss, G. A., Ford, H. C., Caganoff, S. & Koratkar, A. P. (1993) Hubble Space Telescope Imaging of the Narrow-Line Region of NGC 4151. ApJ, 417:82–+. 105

Ferland, G. J., Korista, K. T., Verner, D. A., Ferguson, J. W., Kingdon, J. B. & Verner, E. M. (1998) CLOUDY 90: Numerical Simulation of Plasmas and Their Spectra. PASP, 110:761–778. 107, 151, 152, 179, 220

Ferrara, A. (1993) Can Galactic H I be radiatively supported? ApJ, 407:157–162. 7, 161

Förster Schreiber, N. M., Lehnert, M. D., Bouché, N., Verma, A., Erb, D. K., Shapley, A. E., Steidel, C. C., Davies, R., Lutz, D., Nesvadba, N., Tacconi, L. J., Eisenhauer, F., Abuter, R., Gilbert, A., Gillessen, S. & Sternberg, A. (2006) SINFONI Integral Field Spectroscopy of z ˜ 2 UV-selected Galaxies: Rotation Curves and Dynamical Evolution. ApJ, 645:1062–1075. 3, 5, 8, 83, 87, 88, 95, 101, 109, 114, 131, 139, 162, 163, 186, 188

Förster Schreiber, N. M., Genzel, R., Bouché, N., Cresci, G., Davies, R., Buschkamp, P., Shapiro, K., Tacconi, L. J., Hicks, E. K. S., Genel, S., Shapley, A. E., Erb, D. K., Steidel, C. C., Lutz, D., Eisenhauer, F., Gillessen, S., Sternberg, A., Renzini, A., Cimatti, A., Daddi, E., Kurk, J., Lilly, S., Kong,

X., Lehnert, M. D., Nesvadba, N., Verma, A., McCracken, H., Arimoto, N., Mignoli, M. & Onodera, M. (2009) The SINS Survey: SINFONI Integral Field Spectroscopy of z ˜ 2 Star-forming Galaxies. ApJ, 706:1364–1428. 5, 149, 163, 186, 188

Förster Schreiber, N. M., Shapley, A. E., Erb, D. K., Genzel, R., Steidel, C. C., Bouché, N., Cresci, G. & Davies, R. (2011) Constraints on the Assembly and Dynamics of Galaxies. I. Detailed Rest-frame Optical Morphologies on Kiloparsec Scale of z ˜ 2 Star-forming Galaxies. ApJ, 731:65–+. 186, 187, 188, 190

Gammie, C. F., Ostriker, J. P. & Jog, C. J. (1991) The velocity dispersion of giant molecular clouds. II - Mathematical and numerical refinements. ApJ, 378:565–575. 143

Genel, S., Genzel, R., Bouché, N., Sternberg, A., Naab, T., Schreiber, N. M. F., Shapiro, K. L., Tacconi, L. J., Lutz, D., Cresci, G., Buschkamp, P., Davies, R. I. & Hicks, E. K. S. (2008) Mergers and Mass Accretion Rates in Galaxy Assembly: The Millennium Simulation Compared to Observations of z ˜ 2 Galaxies. ApJ, 688:789–793. 135

Genzel, R., Tacconi, L. J., Eisenhauer, F., Förster Schreiber, N. M., Cimatti, A., Daddi, E., Bouché, N., Davies, R., Lehnert, M. D., Lutz, D., Nesvadba, N., Verma, A., Abuter, R., Shapiro, K., Sternberg, A., Renzini, A., Kong, X., Arimoto, N. & Mignoli, M. (2006) The rapid formation of a large rotating disk galaxy three billion years after the Big Bang. Nature, 442:786–789. 3, 6, 8, 83, 84, 88, 99, 105

Genzel, R., Burkert, A., Bouché, N., Cresci, G., Förster Schreiber, N. M., Shapley, A., Shapiro, K., Tacconi, L. J., Buschkamp, P., Cimatti, A., Daddi, E., Davies, R., Eisenhauer, F., Erb, D. K., Genel, S., Gerhard, O., Hicks, E., Lutz, D., Naab, T., Ott, T., Rabien, S., Renzini, A., Steidel, C. C., Sternberg, A. & Lilly, S. J. (2008) From Rings to Bulges: Evidence for Rapid Secular Galaxy Evolution at z ˜ 2 from Integral Field Spectroscopy in the SINS Survey. ApJ, 687:59–77. 4, 6, 84, 87, 88, 95, 121, 124

Gonçalves, T. S., Basu-Zych, A., Overzier, R., Martin, D. C., Law, D. R., Schiminovich, D., Wyder, T. K., Mallery, R., Rich, R. M. & Heckman, T. H. (2010) The Kinematics of Ionized Gas in Lyman-break Analogs at z ˜ 0.2. ApJ, 724:1373–1388. 6, 7, 162

Green, A. W., Glazebrook, K., McGregor, P. J., Abraham, R. G., Poole, G. B., Damjanov, I., McCarthy, P. J., Colless, M. & Sharp, R. G. (2010) High star

formation rates as the origin of turbulence in early and modern disk galaxies. Nature, 467:684–686. 7, 131, 133, 139, 177, 180

Groves, B. A., Dopita, M. A. & Sutherland, R. S. (2004) Dusty, Radiation Pressure-Dominated Photoionization. II. Multiwavelength Emission Line Diagnostics for Narrow-Line Regions. ApJS, 153:75–91. 104

Groves, B. A., Heckman, T. M. & Kauffmann, G. (2006) Emission-line diagnostics of low-metallicity active galactic nuclei. MNRAS, 371:1559–1569. 6, 85, 100, 103, 104

Guillard, P., Boulanger, F., Pineau Des Forêts, G. & Appleton, P. N. (2009) H2 formation and excitation in the Stephan's Quintet galaxy-wide collision. A&A, 502:515–528. 120

Heckman, T. M. (2001) Galactic Superwinds at Low and High Redshift. In: J. E. Hibbard, M. Rupen, & J. H. van Gorkom (ed.), Gas and Galaxy Evolution. vol. 240 of *Astronomical Society of the Pacific Conference Series*, pp. 345–+. 208, 210

Heckman, T. M. (2003) Starburst-Driven Galactic Winds. In: V. Avila-Reese, C. Firmani, C. S. Frenk, & C. Allen (ed.), Revista Mexicana de Astronomia y Astrofisica Conference Series. vol. 17 of *Revista Mexicana de Astronomia y Astrofisica, vol. 27*, pp. 47–55. 6, 84

Heckman, T. M., Armus, L. & Miley, G. K. (1990) On the nature and implications of starburst-driven galactic superwinds. ApJS, 74:833–868. 6, 84, 95, 108, 109, 120, 181

Heckman, T. M., Kauffmann, G., Brinchmann, J., Charlot, S., Tremonti, C. & White, S. D. M. (2004) Present-Day Growth of Black Holes and Bulges: The Sloan Digital Sky Survey Perspective. ApJ, 613:109–118. 102

Heckman, T. M., Hoopes, C. G., Seibert, M., Martin, D. C., Salim, S., Rich, R. M., Kauffmann, G., Charlot, S., Barlow, T. A., Bianchi, L., Byun, Y.-I., Donas, J., Forster, K., Friedman, P. G., Jelinsky, P. N., Lee, Y.-W., Madore, B. F., Malina, R. F., Milliard, B., Morrissey, P. F., Neff, S. G., Schiminovich, D., Siegmund, O. H. W., Small, T., Szalay, A. S., Welsh, B. Y. & Wyder, T. K. (2005) The Properties of Ultraviolet-luminous Galaxies at the Current Epoch. ApJ, 619:L35–L38. 210

Joung, M. K. R. & Mac Low, M.-M. (2006) Turbulent Structure of a Stratified Supernova-driven Interstellar Medium. ApJ, 653:1266–1279. 143

Joung, M. R., Mac Low, M. & Bryan, G. L. (2009a) Dependence of Interstellar Turbulent Pressure on Supernova Rate. ApJ, 704:137–149. 143, 153

Joung, M. R., Mac Low, M.-M. & Bryan, G. L. (2009b) Dependence of Interstellar Turbulent Pressure on Supernova Rate. ApJ, 704:137–149. 109, 110, 112, 118, 120

Kauffmann, G., Heckman, T. M., Tremonti, C., Brinchmann, J., Charlot, S., White, S. D. M., Ridgway, S. E., Brinkmann, J., Fukugita, M., Hall, P. B., Ivezić, Ž., Richards, G. T. & Schneider, D. P. (2003) The host galaxies of active galactic nuclei. MNRAS, 346:1055–1077. 85, 103

Kennicutt, Jr., R. C. (1998a) Star Formation in Galaxies Along the Hubble Sequence. ARA&A, 36:189–232. 15, 19, 110, 113, 116, 117, 135, 145, 170, 187

Kennicutt, Jr., R. C. (1998b) Star Formation in Galaxies Along the Hubble Sequence. ARA&A, 36:189–232. 205, 211

Kennicutt, Jr., R. C. (1998c) The Global Schmidt Law in Star-forming Galaxies. ApJ, 498:541–+. 5

Kennicutt, Jr., R. C., Calzetti, D., Walter, F., Helou, G., Hollenbach, D. J., Armus, L., Bendo, G., Dale, D. A., Draine, B. T., Engelbracht, C. W., Gordon, K. D., Prescott, M. K. M., Regan, M. W., Thornley, M. D., Bot, C., Brinks, E., de Blok, E., de Mello, D., Meyer, M., Moustakas, J., Murphy, E. J., Sheth, K. & Smith, J. D. T. (2007) Star Formation in NGC 5194 (M51a). II. The Spatially Resolved Star Formation Law. ApJ, 671:333–348. 3, 83

Kereš, D., Katz, N., Weinberg, D. H. & Davé, R. (2005) How do galaxies get their gas? MNRAS, 363:2–28. 3, 8, 83

Kereš, D., Katz, N., Fardal, M., Davé, R. & Weinberg, D. H. (2009) Galaxies in a simulated ΛCDM Universe - I. Cold mode and hot cores. MNRAS, 395:160–179. 3, 5, 7, 83, 131, 134, 135, 139, 161

Kewley, L. J., Dopita, M. A., Sutherland, R. S., Heisler, C. A. & Trevena, J. (2001) Theoretical Modeling of Starburst Galaxies. ApJ, 556:121–140. 103, 106

Khochfar, S. & Silk, J. (2009) Modeling the Star-Forming Universe at z = 2: Impact of Cold Accretion Flows. ApJ, 700:L21–L24. 132

Klein, R. I., McKee, C. F. & Colella, P. (1994) On the hydrodynamic interaction of shock waves with interstellar clouds. 1: Nonradiative shocks in small clouds. ApJ, 420:213–236. 118

Klessen, R. S. & Hennebelle, P. (2010) Accretion-driven turbulence as universal process: galaxies, molecular clouds, and protostellar disks. A&A, 520:A17. 135

Koopmann, R. A. & Kenney, J. D. P. (2004a) Hα Morphologies and Environmental Effects in Virgo Cluster Spiral Galaxies. ApJ, 613:866–885. 90

Koopmann, R. A. & Kenney, J. D. P. (2004b) Massive Star Formation Rates and Radial Distributions from Hα Imaging of 84 Virgo Cluster and Isolated Spiral Galaxies. ApJ, 613:851–865. 90

Koopmann, R. A. & Kenney, J. D. P. (2006) An Atlas of Hα and R Images and Radial Profiles of 29 Bright Isolated Spiral Galaxies. ApJS, 162:97–112. 90

Koopmann, R. A., Kenney, J. D. P. & Young, J. (2001) An Atlas of Hα and R Images and Radial Profiles of 63 Bright Virgo Cluster Spiral Galaxies. ApJS, 135:125–154. 90

Koopmann, R. A., Haynes, M. P. & Catinella, B. (2006) A Comparison of Hα and Stellar Scale Lengths in Virgo and Field Spirals. AJ, 131:716–735. 90

Kroupa, P. & Weidner, C. (2003) Galactic-Field Initial Mass Functions of Massive Stars. ApJ, 598:1076–1078. 217

Krumholz, M. R. & Dekel, A. (2010) Survival of star-forming giant clumps in high-redshift galaxies. MNRAS, 406:112–120. 161, 186

Larson, R. B. (1988) Large-Scale Aspects of Star Formation and Galactic Evolution. In: R. E. Pudritz & M. Fich (ed.), NATO ASIC Proc. 232: Galactic and Extragalactic Star Formation. pp. 459–+. 121

Law, D. R., Steidel, C. C., Erb, D. K., Larkin, J. E., Pettini, M., Shapley, A. E. & Wright, S. A. (2007) Integral Field Spectroscopy of High-Redshift Star-forming Galaxies with Laser-guided Adaptive Optics: Evidence for Dispersion-dominated Kinematics. ApJ, 669:929–946. 8, 83, 162

Law, D. R., Steidel, C. C., Erb, D. K., Larkin, J. E., Pettini, M., Shapley, A. E. & Wright, S. A. (2009) The Kiloparsec-scale Kinematics of High-redshift Star-forming Galaxies. ApJ, 697:2057–2082. 133, 162, 205

Le Borgne, D., Elbaz, D., Ocvirk, P. & Pichon, C. (2009) Cosmic star-formation history from a non-parametric inversion of infrared galaxy counts. A&A, 504:727–740. 2, 4, 8

Le Tiran, L., Lehnert, M. D., Di Matteo, P., Nesvadba, N. P. H. & van Driel, W. (2011) Can evidence for cosmological accretion be observed in the Hα emission from galaxies at z ˜ 2? A&A, 530:L6. 143, 177

Lee, J. C., Gil de Paz, A., Tremonti, C., Kennicutt, Jr., R. C., Salim, S., Bothwell, M., Calzetti, D., Dalcanton, J., Dale, D., Engelbracht, C., Funes, S. J. J. G., Johnson, B., Sakai, S., Skillman, E., van Zee, L., Walter, F. & Weisz, D. (2009) Comparison of Hα and UV Star Formation Rates in the Local Volume: Systematic Discrepancies for Dwarf Galaxies. ApJ, 706:599–613. 201, 220

Lehnert, M. D. & Heckman, T. M. (1994) Emission-line ratios of the integrated spectra of galaxies: Evidence for a diffuse ionized medium in other galaxies? ApJ, 426:L27–L30. 144, 147

Lehnert, M. D. & Heckman, T. M. (1995) Ionized gas in the halos of edge-on, starburst galaxies: Data and results. ApJS, 97:89–139. 90, 149

Lehnert, M. D. & Heckman, T. M. (1996a) Ionized Gas in the Halos of Edge-on Starburst Galaxies: Evidence for Supernova-driven Superwinds. ApJ, 462:651–+. 3, 6, 83, 84, 90, 95, 98, 108, 109, 120, 147, 148, 149, 151, 160, 181, 187, 191

Lehnert, M. D. & Heckman, T. M. (1996b) Ionized Gas in the Halos of Edge-on Starburst Galaxies: Evidence for Supernova-driven Superwinds. ApJ, 462:651–+. 208, 210

Lehnert, M. D. & Heckman, T. M. (1996c) The Nature of Starburst Galaxies. ApJ, 472:546–+. 6, 84, 90

Lehnert, M. D., Heckman, T. M. & Weaver, K. A. (1999) Very Extended X-Ray and Hα Emission in M82: Implications for the Superwind Phenomenon. ApJ, 523:575–584. 109, 120, 133

Lehnert, M. D., Nesvadba, N. P. H., Tiran, L. L., Matteo, P. D., van Driel, W., Douglas, L. S., Chemin, L. & Bournaud, F. (2009) Physical Conditions in the Interstellar Medium of Intensely Star-Forming Galaxies at Redshift˜2. ApJ, 699:1660–1678. 131, 133, 145, 147, 161, 163, 164, 165, 169, 170, 179, 181, 186, 187, 188, 190, 195, 200, 201, 224

Lehnert, M. D., Nesvadba, N. P. H., Cuby, J., Swinbank, A. M., Morris, S., Clément, B., Evans, C. J., Bremer, M. N. & Basa, S. (2010) Spectroscopic confirmation of a galaxy at redshift z = 8.6. Nature, 467:940–942. 139

Leitherer, C. & Heckman, T. M. (1995) Synthetic properties of starburst galaxies. ApJS, 96:9–38. 215

Leitherer, C., Schaerer, D., Goldader, J. D., González Delgado, R. M., Robert, C., Kune, D. F., de Mello, D. F., Devost, D. & Heckman, T. M. (1999) Starburst99:

Synthesis Models for Galaxies with Active Star Formation. ApJS, 123:3–40. 107, 117, 118, 137, 151, 153, 169, 183, 217, 220

Lemoine-Busserolle, M., Bunker, A., Lamareille, F. & Kissler-Patig, M. (2010) 2D kinematics and physical properties of z ˜ 3 star-forming galaxies. MNRAS, 401:1657–1669. 133, 162

Leroy, A. K., Walter, F., Brinks, E., Bigiel, F., de Blok, W. J. G., Madore, B. & Thornley, M. D. (2008) The Star Formation Efficiency in Nearby Galaxies: Measuring Where Gas Forms Stars Effectively. AJ, 136:2782–2845. 7, 162, 192

Mac Low, M.-M. (1999) The Energy Dissipation Rate of Supersonic, Magneto-hydrodynamic Turbulence in Molecular Clouds. ApJ, 524:169–178. 109, 110, 120

Mac Low, M.-M. & Klessen, R. S. (2004) Control of star formation by supersonic turbulence. Reviews of Modern Physics, 76:125–194. 118, 120, 121, 125

Madau, P., Ferguson, H. C., Dickinson, M. E., Giavalisco, M., Steidel, C. C. & Fruchter, A. (1996) MNRAS, 283:1388–1404. 2, 8, 160

Magdis, G. E., Elbaz, D., Daddi, E., Morrison, G. E., Dickinson, M., Rigopoulou, D., Gobat, R. & Hwang, H. S. (2010a) A Multi-wavelength View of the Star Formation Activity at z ˜ 3. ApJ, 714:1740–1745. 190

Magdis, G. E., Rigopoulou, D., Huang, J.-S. & Fazio, G. G. (2010b) On the stellar masses of IRAC detected Lyman Break Galaxies at z ˜ 3. MNRAS, 401:1521–1531. 195

Maiolino, R., Nagao, T., Grazian, A., Cocchia, F., Marconi, A., Mannucci, F., Cimatti, A., Pipino, A., Ballero, S., Calura, F., Chiappini, C., Fontana, A., Granato, G. L., Matteucci, F., Pastorini, G., Pentericci, L., Risaliti, G., Salvati, M. & Silva, L. (2008) AMAZE. I. The evolution of the mass-metallicity relation at z gt 3. A&A, 488:463–479. 6, 84

Maraston, C., Pforr, J., Renzini, A., Daddi, E., Dickinson, M., Cimatti, A. & Tonini, C. (2010) Star formation rates and masses of z ˜ 2 galaxies from multicolour photometry. MNRAS, 407:830–845. 207

Marcolini, A., Strickland, D. K., D'Ercole, A., Heckman, T. M. & Hoopes, C. G. (2005) The dynamics and high-energy emission of conductive gas clouds in supernova-driven galactic superwinds. MNRAS, 362:626–648. 119

Markwardt, C. B. (2009) Non-linear Least-squares Fitting in IDL with MPFIT. In: D. A. Bohlender, D. Durand, & P. Dowler (ed.), Astronomical Society of the Pacific Conference Series. vol. 411 of *Astronomical Society of the Pacific Conference Series*, pp. 251–+. 236

Mateo, M. L. (1998) Dwarf Galaxies of the Local Group. ARA&A, 36:435–506. 201

Matzner, C. D. & McKee, C. F. (2000) Efficiencies of Low-Mass Star and Star Cluster Formation. ApJ, 545:364–378. 122

Meurer, G. R., Wong, O. I., Kim, J. H., Hanish, D. J., Heckman, T. M., Werk, J., Bland-Hawthorn, J., Dopita, M. A., Zwaan, M. A., Koribalski, B., Seibert, M., Thilker, D. A., Ferguson, H. C., Webster, R. L., Putman, M. E., Knezek, P. M., Doyle, M. T., Drinkwater, M. J., Hoopes, C. G., Kilborn, V. A., Meyer, M., Ryan-Weber, E. V., Smith, R. C. & Staveley-Smith, L. (2009) Evidence for a Nonuniform Initial Mass Function in the Local Universe. ApJ, 695:765–780. 201, 211, 212

Monreal-Ibero, A., Arribas, S. & Colina, L. (2006) LINER-like Extended Nebulae in ULIRGs: Shocks Generated by Merger-Induced Flows. ApJ, 637:138–146. 114

Nakamura, F., McKee, C. F., Klein, R. I. & Fisher, R. T. (2006) On the Hydrodynamic Interaction of Shock Waves with Interstellar Clouds. II. The Effect of Smooth Cloud Boundaries on Cloud Destruction and Cloud Turbulence. ApJS, 164:477–505. 118

Nelson, C. H. & Whittle, M. (1996) Stellar and Gaseous Kinematics of Seyfert Galaxies. II. The Role of the Bulge. ApJ, 465:96–+. 105

Nesvadba, N. P. H. (2005) Integral-Field Spectroscopy of High-Redshift Galaxies: Implications for Early Galaxy Evolution. Ph.D. thesis, Ludwig-Maximilians-Universität München. 233, 240, 241

Nesvadba, N. P. H., Lehnert, M. D., Eisenhauer, F., Genzel, R., Seitz, S., Davies, R. I., Saglia, R. P., Lutz, D., Tacconi, L., Bender, R. & Abuter, R. (2006a) Lyman Break Galaxies under a Microscope: The Small-Scale Dynamics and Mass of an Arc in the Cluster 1E 0657-56. ApJ, 650:661–668. 6, 83, 84

Nesvadba, N. P. H., Lehnert, M. D., Eisenhauer, F., Gilbert, A., Tecza, M. & Abuter, R. (2006b) Extreme Gas Kinematics in the z=2.2 Powerful Radio Galaxy MRC 1138-262: Evidence for Efficient Active Galactic Nucleus Feedback in the Early Universe? ApJ, 650:693–705. 6, 104, 160

Nesvadba, N. P. H., Lehnert, M. D., Genzel, R., Eisenhauer, F., Baker, A. J., Seitz, S., Davies, R., Lutz, D., Tacconi, L., Tecza, M., Bender, R. & Abuter, R. (2007) Intense Star Formation and Feedback at High Redshift: Spatially Resolved Properties of the z = 2.6 Submillimeter Galaxy SMM J14011+0252. ApJ, 657:725–737. 6, 84, 85, 98, 103, 181

Nesvadba, N. P. H., Lehnert, M. D., Davies, R. I., Verma, A. & Eisenhauer, F. (2008a) Integral-field spectroscopy of a Lyman-break galaxy at z = 3.2: evidence for merging. A&A, 479:67–73. 104

Nesvadba, N. P. H., Lehnert, M. D., De Breuck, C., Gilbert, A. M. & van Breugel, W. (2008b) Evidence for powerful AGN winds at high redshift: dynamics of galactic outflows in radio galaxies during the "Quasar Era". A&A, 491:407–424. 6, 8, 83, 160

Netzer, H., Shemmer, O., Maiolino, R., Oliva, E., Croom, S., Corbett, E. & di Fabrizio, L. (2004) Near-Infrared Spectroscopy of High-Redshift Active Galactic Nuclei. II. Disappearing Narrow-Line Regions and the Role of Accretion. ApJ, 614:558–567. 104, 105

Noguchi, M. (1999) Early Evolution of Disk Galaxies: Formation of Bulges in Clumpy Young Galactic Disks. ApJ, 514:77–95. 123, 125

Norman, C. A. & Ferrara, A. (1996) The Turbulent Interstellar Medium: Generalizing to a Scale-dependent Phase Continuum. ApJ, 467:280–+. 7, 161

Ocvirk, P., Pichon, C. & Teyssier, R. (2008) Bimodal gas accretion in the Horizon-MareNostrum galaxy formation simulation. MNRAS, 390:1326–1338. 3, 83

Oliver, S., Frost, M., Farrah, D., Gonzalez-Solares, E., Shupe, D. L., Henriques, B., Roseboom, I., Alfonso-Luis, A., Babbedge, T. S. R., Frayer, D., Lencz, C., Lonsdale, C. J., Masci, F., Padgett, D., Polletta, M., Rowan-Robinson, M., Siana, B., Smith, H. E., Surace, J. A. & Vaccari, M. (2010) Specific star formation and the relation to stellar mass from $0 < z < 2$ as seen in the far-infrared at 70 and 160 μm. MNRAS, 405:2279–2294. 190, 191

Osterbrock, D. E. (1989) Astrophysics of gaseous nebulae and active galactic nuclei. 103, 106, 235, 243

Papovich, C., Dickinson, M. & Ferguson, H. C. (2001) The Stellar Populations and Evolution of Lyman Break Galaxies. ApJ, 559:620–653. 210

Pettini, M., Steidel, C. C., Adelberger, K. L., Dickinson, M. & Giavalisco, M. (2000) The Ultraviolet Spectrum of MS 1512-CB58: An Insight into Lyman-Break Galaxies. ApJ, 528:96–107. 6, 84

Qu, Y., Di Matteo, P., Lehnert, M. D. & van Driel, W. (2011) ArXiv e-prints. 169

Raymond, J. C. (1979) Shock waves in the interstellar medium. ApJS, 39:1–27. 134, 136

Robertson, B. E. & Bullock, J. S. (2008) High-Redshift Galaxy Kinematics: Constraints on Models of Disk Formation. ApJ, 685:L27–L30. 6, 84, 114

Rodrigues, M., Hammer, F., Flores, H., Puech, M., Liang, Y. C., Fuentes-Carrera, I., Nesvadba, N., Lehnert, M., Yang, Y., Amram, P., Balkowski, C., Cesarsky, C., Dannerbauer, H., Delgado, R., Guiderdoni, B., Kembhavi, A., Neichel, B., Östlin, G., Pozzetti, L., Ravikumar, C. D., Rawat, A., di Serego Alighieri, S., Vergani, D., Vernet, J. & Wozniak, H. (2008) IMAGES IV: strong evolution of the oxygen abundance in gaseous phases of intermediate mass galaxies from z ˜ 0.8. A&A, 492:371–388. 6, 217

Sanders, D. B., Scoville, N. Z. & Soifer, B. T. (1991) Molecular gas in luminous infrared galaxies. ApJ, 370:158–171. 122, 200

Sarzi, M., Falcón-Barroso, J., Davies, R. L., Bacon, R., Bureau, M., Cappellari, M., de Zeeuw, P. T., Emsellem, E., Fathi, K., Krajnović, D., Kuntschner, H., McDermid, R. M. & Peletier, R. F. (2006) The SAURON project - V. Integral-field emission-line kinematics of 48 elliptical and lenticular galaxies. MNRAS, 366:1151–1200. 8

Semelin, B. & Combes, F. (2002) Formation and evolution of galactic disks with a multiphase numerical model. A&A, 388:826–841. 169

Shapiro, K. L., Genzel, R., Förster Schreiber, N. M., Tacconi, L. J., Bouché, N., Cresci, G., Davies, R., Eisenhauer, F., Johansson, P. H., Krajnović, D., Lutz, D., Naab, T., Arimoto, N., Arribas, S., Cimatti, A., Colina, L., Daddi, E., Daigle, O., Erb, D., Hernandez, O., Kong, X., Mignoli, M., Onodera, M., Renzini, A., Shapley, A. & Steidel, C. (2008) Kinemetry of SINS High-Redshift Star-Forming Galaxies: Distinguishing Rotating Disks from Major Mergers. ApJ, 682:231–251. 94, 200

Shapiro, K. L., Genzel, R., Quataert, E., Förster Schreiber, N. M., Davies, R., Tacconi, L., Armus, L., Bouché, N., Buschkamp, P., Cimatti, A., Cresci, G., Daddi, E., Eisenhauer, F., Erb, D. K., Genel, S., Hicks, E. K. S., Lilly, S. J., Lutz, D., Renzini, A., Shapley, A., Steidel, C. C. & Sternberg, A. (2009) The SINS Survey: Broad Emission Lines in High-Redshift Star-Forming Galaxies. ApJ, 701:955–963. 6, 143, 147, 149, 155, 190

Shapley, A. E., Steidel, C. C., Pettini, M. & Adelberger, K. L. (2003) Rest-Frame Ultraviolet Spectra of z˜3 Lyman Break Galaxies. ApJ, 588:65–89. 2, 3, 83, 160

Shapley, A. E., Coil, A. L., Ma, C.-P. & Bundy, K. (2005) Chemical Abundances of DEEP2 Star-forming Galaxies at z˜1.0-1.5. ApJ, 635:1006–1021. 207, 252

Shen, S., Mo, H. J., White, S. D. M., Blanton, M. R., Kauffmann, G., Voges, W., Brinkmann, J. & Csabai, I. (2003) The size distribution of galaxies in the Sloan Digital Sky Survey. MNRAS, 343:978–994. 188

Shull, J. M. & McKee, C. F. (1979) Theoretical models of interstellar shocks. I - Radiative transfer and UV precursors. ApJ, 227:131–149. 134

Silk, J. (1997) Feedback, Disk Self-Regulation, and Galaxy Formation. ApJ, 481:703–+. 84, 121, 125, 151, 153, 162, 184, 186, 191

Silk, J. (2001) The formation of galaxy discs. MNRAS, 324:313–318. 7, 121, 125, 143, 162, 184, 186

Silk, J. (2003) A new prescription for protogalactic feedback and outflows: where have all the baryons gone? MNRAS, 343:249–254. 162, 184

Silk, J. & Norman, C. (2009) Global Star Formation Revisited. ApJ, 700:262–275. 153, 162, 184, 191, 192

Smith, A. J., Loveday, J. & Cross, N. J. G. (2009) Luminosity and surface brightness distribution of K-band galaxies from the UKIDSS Large Area Survey. MNRAS, 397:868–882. 208

Solomon, P. M. & Sage, L. J. (1988) Star-formation rates, molecular clouds, and the origin of the far-infrared luminosity of isolated and interacting galaxies. ApJ, 334:613–625. 122, 200

Stark, D. P., Ellis, R. S., Bunker, A., Bundy, K., Targett, T., Benson, A. & Lacy, M. (2009) The Evolutionary History of Lyman Break Galaxies Between Redshift 4 and 6: Observing Successive Generations of Massive Galaxies in Formation. ApJ, 697:1493–1511. 190, 194

Steidel, C. C., Erb, D. K., Shapley, A. E., Pettini, M., Reddy, N., Bogosavljević, M., Rudie, G. C. & Rakic, O. (2010) The Structure and Kinematics of the Circumgalactic Medium from Far-ultraviolet Spectra of z ˜= 2-3 Galaxies. ApJ, 717:289–322. 2, 4, 131, 160, 190, 191, 200

Stinson, G. S., Dalcanton, J. J., Quinn, T., Kaufmann, T. & Wadsley, J. (2007) Breathing in Low-Mass Galaxies: A Study of Episodic Star Formation. ApJ, 667:170–175. 201

Strickland, D. K. & Heckman, T. M. (2009) Supernova Feedback Efficiency and Mass Loading in the Starburst and Galactic Superwind Exemplar M82. ApJ, 697:2030–2056. 119, 153, 186

Swinbank, A. M., Bower, R. G., Smith, G. P., Wilman, R. J., Smail, I., Ellis, R. S., Morris, S. L. & Kneib, J.-P. (2007) Resolved spectroscopy of a gravitationally lensed L* Lyman-break galaxy at z ˜ 5. MNRAS, 376:479–491. 8

Tacconi, L. J., Genzel, R., Neri, R., Cox, P., Cooper, M. C., Shapiro, K., Bolatto, A., Bouché, N., Bournaud, F., Burkert, A., Combes, F., Comerford, J., Davis, M., Schreiber, N. M. F., Garcia-Burillo, S., Gracia-Carpio, J., Lutz, D., Naab, T., Omont, A., Shapley, A., Sternberg, A. & Weiner, B. (2010) High molecular gas fractions in normal massive star-forming galaxies in the young Universe. Nature, 463:781–784. 190, 192, 194

Takata, T., Sekiguchi, K., Smail, I., Chapman, S. C., Geach, J. E., Swinbank, A. M., Blain, A. & Ivison, R. J. (2006) Rest-Frame Optical Spectroscopic Classifications for Submillimeter Galaxies. ApJ, 651:713–727. 103

Tamburro, D., Rix, H.-W., Leroy, A. K., Mac Low, M.-M., Walter, F., Kennicutt, R. C., Brinks, E. & de Blok, W. J. G. (2009) What is Driving the H I Velocity Dispersion? AJ, 137:4424–4435. 7, 162

Tan, J. C. (2000) Star Formation Rates in Disk Galaxies and Circumnuclear Starbursts from Cloud Collisions. ApJ, 536:173–184. 121

Tasker, E. J. & Bryan, G. L. (2006) Simulating Star Formation and Feedback in Galactic Disk Models. ApJ, 641:878–890. 114, 143

Tasker, E. J. & Bryan, G. L. (2008) The Effect of the Interstellar Model on Star Formation Properties in Galactic Disks. ApJ, 673:810–831. 114, 124

Taylor, E. N., Franx, M., Glazebrook, K., Brinchmann, J., van der Wel, A. & van Dokkum, P. G. (2010) On the Dearth of Compact, Massive, Red Sequence Galaxies in the Local Universe. ApJ, 720:723–741. 188

Thomas, D., Maraston, C., Bender, R. & Mendes de Oliveira, C. (2005) The Epochs of Early-Type Galaxy Formation as a Function of Environment. ApJ, 621:673–694. 201

Thomasson, M., Donner, K. J. & Elmegreen, B. G. (1991) A&A, 250:316–323. 113

Tody, D. (1993) IRAF in the Nineties. In: R. J. Hanisch, R. J. V. Brissenden, & J. Barnes (ed.), Astronomical Data Analysis Software and Systems II. vol. 52 of *Astronomical Society of the Pacific Conference Series*, pp. 173–+. 87, 202

Tolman, R. C. (1930) On the Estimation of Distances in a Curved Universe with a Non-Static Line Element. Proceedings of the National Academy of Science, 16:511–520. 6, 84

Toomre, A. (1964) On the gravitational stability of a disk of stars. ApJ, 139:1217–1238. 121

Tremonti, C. A., Heckman, T. M., Kauffmann, G., Brinchmann, J., Charlot, S., White, S. D. M., Seibert, M., Peng, E. W., Schlegel, D. J., Uomoto, A., Fukugita, M. & Brinkmann, J. (2004) The Origin of the Mass-Metallicity Relation: Insights from 53,000 Star-forming Galaxies in the Sloan Digital Sky Survey. ApJ, 613:898–913. 85

Trotta, R. (2008) Bayes in the sky: Bayesian inference and model selection in cosmology. Contemporary Physics, 49:71–104. 149

Tully, R. B. (1974) The Kinematics and Dynamics of M51. 1. the Observations. ApJS, 27:415–+. 133

van de Voort, F., Schaye, J., Booth, C. M., Haas, M. R. & Dalla Vecchia, C. (2010) ArXiv e-prints. 131

van Dokkum, P. G., Kriek, M., Rodgers, B., Franx, M. & Puxley, P. (2005) Gemini Near-Infrared Spectrograph Observations of a Red Star-forming Galaxy at z=2.225: Evidence of Shock Ionization Due to a Galactic Wind. ApJ, 622:L13–L16. 103

van Starkenburg, L., van der Werf, P. P., Franx, M., Labbé, I., Rudnick, G. & Wuyts, S. (2008) Dynamical properties of a large young disk galaxy at z = 2.03. A&A, 488:99–112. 8, 83

Veilleux, S. & Osterbrock, D. E. (1987) Spectral classification of emission-line galaxies. ApJS, 63:295–310. 6, 85, 98, 200

Veilleux, S., Shopbell, P. L., Rupke, D. S., Bland-Hawthorn, J. & Cecil, G. (2003) A Search for Very Extended Ionized Gas in Nearby Starburst and Active Galaxies. AJ, 126:2185–2208. 105

Verma, A., Lehnert, M. D., Förster Schreiber, N. M., Bremer, M. N. & Douglas, L. (2007) Lyman-break galaxies at z ˜ 5 - I. First significant stellar mass assembly in galaxies that are not simply z ˜ 3 LBGs at higher redshift. MNRAS, 377:1024–1042. 3, 83, 194, 210

Wada, K., Meurer, G. & Norman, C. A. (2002) Gravity-driven Turbulence in Galactic Disks. ApJ, 577:197–205. 109, 113, 114, 177

Walter, F., Weiss, A. & Scoville, N. (2002) Molecular Gas in M82: Resolving the Outflow and Streamers. ApJ, 580:L21–L25. 112, 120

Wang, B. & Silk, J. (1994) Gravitational instability and disk star formation. ApJ, 427:759–769. 122, 201

Wang, J., Heckman, T. M. & Lehnert, M. D. (1998) Toward a Unified Model for the "Diffuse Ionized Medium" in Normal and Starburst Galaxies. ApJ, 509:93–102. 120, 147, 151, 152, 181

Wang, J., Heckman, T. M. & Lehnert, M. D. (1999) On the Structure and Morphology of the "Diffuse Ionized Medium" in Star-forming Galaxies. ApJ, 515:97–107. 98, 108, 120

Weiner, B. J., Coil, A. L., Prochaska, J. X., Newman, J. A., Cooper, M. C., Bundy, K., Conselice, C. J., Dutton, A. A., Faber, S. M., Koo, D. C., Lotz, J. M., Rieke, G. H. & Rubin, K. H. R. (2009) Ubiquitous Outflows in DEEP2 Spectra of Star-Forming Galaxies at z = 1.4. ApJ, 692:187–211. 191

Weinmann, S. M., Neistein, E. & Dekel, A. (2011) ArXiv e-prints. 191

White, S. D. M. & Rees, M. J. (1978) MNRAS, 183:341–358. 4, 131

Wilson, C. D., Warren, B. E., Irwin, J., Knapen, J. H., Israel, F. P., Serjeant, S., Attewell, D., Bendo, G. J., Brinks, E., Butner, H. M., Clements, D. L., Leech, J., Matthews, H. E., Mühle, S., Mortier, A. M. J., Parkin, T. J., Petitpas, G., Tan, B. K., Tilanus, R. P. J., Usero, A., Vaccari, M., van der Werf, P., Wiegert, T. & Zhu, M. (2011) The JCMT Nearby Galaxies Legacy Survey - IV. Velocity dispersions in the molecular interstellar medium in spiral galaxies. MNRAS, 410:1409–1422. 162

Wright, S. A., Larkin, J. E., Barczys, M., Erb, D. K., Iserlohe, C., Krabbe, A., Law, D. R., McElwain, M. W., Quirrenbach, A., Steidel, C. C. & Weiss, J. (2007) Integral Field Spectroscopy of a Candidate Disk Galaxy at z ˜ 1.5 Using Laser Guide Star Adaptive Optics. ApJ, 658:78–84. 8, 83

Wright, S. A., Larkin, J. E., Law, D. R., Steidel, C. C., Shapley, A. E. & Erb, D. K. (2009a) Dynamics of Galactic Disks and Mergers at z ˜ 1.6: Spatially Resolved Spectroscopy with Keck Laser Guide Star Adaptive Optics. ApJ, 699:421–440. 6, 84, 95

Wright, S. A., Larkin, J. E., Law, D. R., Steidel, C. C., Shapley, A. E. & Erb, D. K. (2009b) Dynamics of Galactic Disks and Mergers at z ˜ 1.6: Spatially Resolved Spectroscopy with Keck Laser Guide Star Adaptive Optics. ApJ, 699:421–440. 162

Young, J. S. & Knezek, P. M. (1989) The ratio of molecular to atomic gas in spiral galaxies as a function of morphological type. ApJ, 347:L55–L58. 192

Young, J. S., Xie, S., Tacconi, L., Knezek, P., Viscuso, P., Tacconi-Garman, L., Scoville, N., Schneider, S., Schloerb, F. P., Lord, S., Lesser, A., Kenney, J., Huang, Y.-L., Devereux, N., Claussen, M., Case, J., Carpenter, J., Berry, M. & Allen, L. (1995) The FCRAO Extragalactic CO Survey. I. The Data. ApJS, 98:219–+. 192

Young, J. S., Allen, L., Kenney, J. D. P., Lesser, A. & Rownd, B. (1996) The Global Rate and Efficiency of Star Formation in Spiral Galaxies as a Function of Morphology and Environment. AJ, 112:1903–+. 122, 200

List of Abbreviations

AO Adaptive Optics

ESO European Southern Observatory

GEPI Laboratoire d'Etudes des Galaxies, Etoiles, Physique et Instrumentation

HST Hubble Space Telescope

IFS Integral Field Spectroscopy

IFU Integral Field Unit

IGIMF Integrated Galaxial Initial Mass Function

IMF Initial Mass Function

MASSIV Mass Assembly Survey with SINFONI in VVDS

MC Monte Carlo

MPE Max-Planck-Institut für extraterrestrische Physik

OSIRIS OH Suppressing Infra-Red Imaging Spectrograph

PSF Point Spread Function

RMS Root Mean Square

SAURON Spectroscopic Areal Unit for Research on Optical Nebulae

SED Spectral Energy Density

SFH Star Formation History

SINFONI Spectrograph for INtegral Field Observations in the Near Infrared

SINS Spectroscopic Imaging survey of high redshift galaxies in the Near-infrared with SINFONI

SMG Submillimeter Galaxies

SNe Supernovae

SNR Signal to Noise Ratio

VLT Very Large Telescope

ZAMS Zero Age Main Sequence